A Mathematical Model of an Electromechanically Coupled Poroelastic Medium

by

Jeffrey R. Sachs

Sc. B., Sc. M., Brown University (1981)

Submitted to the
Department of Mathematics
in Partial Fulfillment of the Requirements for the Degree of

Doctor of Philosophy
at the

Massachusetts Institute of Technology

June 1987

© Massachusetts Institute of Technology, 1987

Signature of Author___ ____________________
Department of Mathematics
June 30, 1987

Certified by__________ ____________________
Professor Alan J. Grodzinsky
Thesis Supervisor

Accepted by____
Professor Willem V. R. Malkus, Chairman
Committee on Applied Mathematics

Accepted by___ ____________________
Professor Sigurdur Helgason, Chairman
Departmental Graduate Committee
Department of Mathematics

MASSACHUSETTS INSTITUTE
OF TECHNOLOGY
AUG 22 1988
LIBRARIES
Vol. 1

A Mathematical Model of an Electromechanically Coupled Poroelastic Medium

by

Jeffrey R. Sachs

Submitted to the Department of Mathematics
on June 30, 1987 in partial fulfillment
of the requirements for the Degree of
Doctor of Philosophy

ABSTRACT

A three-dimensional model of electromechanically coupled poroelastic systems is developed, and general two-dimensional solutions are found for the case of an isotropic, homogeneous biphasic layer of finite thickness. All processes are assumed to be governed by a linearized theory. Limitations of the model are discussed both in terms of mathematical considerations and with regard to application of the model to articular cartilage. The solid displacement, fluid velocity, stress, and the electrical current density and potential within the layer are predicted for boundary conditions representing:

- electrical to mechanical transduction, with potential or current stimulation;
- mechanical to electrical transduction, with and without fluid flow normal to the tissue surface;

and

- an electrically driven mixed boundary value problem with intervals of prescribed displacements and intervals of prescribed stress.

The general solutions for the case with zero current density are interpreted physically. Numerical solutions for the fields are obtained for all three cases, with a special algorithm presented for the rapid solution of the third case. Asymptotic solutions are found for the first two cases in the short-wave (infinite-depth) and long-wave (one-dimensional) limits, and are found to agree with the numerical solutions. Numerical solutions are found in the long-wave limit of the first case with boundary conditions that correspond to those of experiments in the literature. The theoretical predictions are in good agreement with the data when parameter values from the literature are used. Such agreement is also shown in the long-wave limit of the second case. The results of all cases are interpreted in terms of the feasibility of an electrokinetic surface probe for measuring the electromechanical properties of biphasic materials such as articular cartilage. It is found that material properties can be inferred for depths on the order of the imposed wavelength or the diffusion boundary layer thickness (whichever is smaller) when surface stress and potential are measured as a function of frequency, wavelength, and the amplitudes (at the surface) of the vertical current and displacement.

Thesis Supervisor: Alan J. Grodzinsky

Title: Professor

Department of Electrical Engineering and Computer Science,

Massachusetts Institute of Technology

Acknowledgements

Special thanks go to my advisor, Prof. Alan "$\jmath$" Grodzinsky, for the phenomenal integrity of his scientific work, and for the tremendous encouragement he has given me. The genuine interest he has taken in the completeness of my scientific education will continue to influence me for a long time.

Prof. Alar Toomre has given me more questions and answers than I can remember, particularly during the five months during which he acted as my tutor in fluid mechanics. He has supported me in every aspect of my education since my arrival at M.I.T., and has taught me a lot about the art of teaching. For all of this I am deeply grateful.

My father's love of science has always been an inspiration for me. He showed me the joy of inquiring into the nature of anything and everything. I am profoundly thankful for his love and support.

The rest of my family has also been tremendously supportive, especially my siblings Tom, Jen, Kate, Reb, Jackie, Joel, and Judy (and their spouses ...). Many thanks for good company over good food. I would also like to thank my step-mother Carolyn for her encouragement.

My relationship with Priscilla Cehelsky has been a constant source of joy and inspiration. She has been extremely supportive, and her help as a technical advisor and as an editor has been indispensable. Her hours of help collating this thesis are deeply appreciated.

I would also like to thank Prof. Harvey P. Greenspan and Prof. Ali Nadim. Prof. Greenspan has been generous with his time, and has made many insightful suggestions about my research. Ali was kind enough to join my committee at the last minute, and I am grateful for his careful reading of and comments on this work.

Some other professors who inspired and encouraged me: Prof. H. T. Banks (Brown Univ.), whose spirited lectures on differential equations convinced me to go into Applied Math; Prof. W. Flemming (Brown), who advised and taught me; Prof. S. Fallieros (Brown), whose comraderie and extemporaneous lectures where a true joy; Prof. J. Mallet-Paret (Brown), who spent many hours revealing the rigors of analysis to me; and Prof. H. Cheng (M.I.T.), in whose enjoyable company I have learned a lot.

Other friends who helped: Alayne Barnicoat and Victoria and Ian Drew, without whom I couldn't have survived those first two years; Dana Fine and Susan Coombs whose supportive friendship (along with Dana's technical consulting) have been invaluable; Adi Shwartz and Shuli Cohen, whose love and friendship are very dear to me; Bill Aiello and Karen Parrish, whose spirited friendship made a difference; and Phyllis Ruby, who always knew who, what, where, when, why, and how, and was willing to work on all six.

I also received immense support from: Prof. L Nick Trefethen and Louis Howell on numerics; Robert P. Thurstans and Steve A. Lowe on graphics, LaTeXand general hacking; Chris Snyder and Kwok Chow on technicalities and humour; Dave Macdonald on copying; George Fann and Dale R. Worley on hacking; and Ray Hirschfeld on hardware, *etc.* Thanks also to the cartilage crushers and veal verifiers at Honest Al's chop shop, especially Sol Eisenberg and Eliot Frank for experimental support. And thanks to Dave Benney for his spirit and the job connection.

In loving memory of Jean W. Sachs.

"Minasama ni, sukkari osewa ni narimashita. Iroiro dōmo arigatō gozaimashita."

This work was supported in part by a National Science Foundation Graduate Fellowship, and grants from the National Institute of Health.

Contents

Abstract ii

Acknowledgments iv

1 Introduction 13

1.1 The Structure of Articular Cartilage 14

1.1.1 The Extracellular Matrix of Articular Cartilage 15

1.1.2 Implications for Diagnostic Measurements 21

1.2 Background for Electromechanically Coupled Poroelasticity 23

2 Governing Equations 32

2.1 Introduction 32

2.2 The Model 33

2.3 Limitations 36

2.3.1 Relevance to Properties of Articular Cartilage 37

2.3.2 Mathematical Considerations 40

2.A The Response of a Rigid Conductor 43

2.B The Momentum Equations in Radial Coordinates 45

3 Solution of the Governing Equations 47

3.1 Non-dimensionalization and Transformation 47

3.2 Solution 50

3.2.1 The Particular Solutions 50

3.2.2 The Homogeneous Solutions 52

3.3 Physical Interpretation of the Homogeneous Solutions 53

4 The Current Forced Response **58**

4.1 Introduction 58

4.2 Results 60

4.2.1 Numerical Results 62

4.2.2 Asymptotic Results 69

4.3 Comparison with Experimental Data 81

4.4 Discussion 86

5 The Mechanically Forced Response **90**

5.1 Introduction 90

5.2 Results 91

5.2.1 Case Descriptions and Consequences of the Boundary Conditions 91

5.2.2 Numerical Results 95

5.2.3 Asymptotic Results 106

5.3 Discussion 119

6 The Mixed Boundary Value Problem **127**

6.1 Introduction 127

6.2 Statement of the Problem 127

6.3 The Algorithm for Solution of the Mixed Problem 131

6.3.1 Introduction 131
6.3.2 The Current Density Field and Particular Solutions 132
6.3.3 Solution for the Non-Mixed Problem:
Problems "A" and "B" 137
6.3.4 The Basis Coefficients:
Reducing the Number of Degrees of Freedom 140
6.3.5 Solution for the Basis Functions and their Coefficients 142
6.4 Results 144
6.5 Discussion 157
6.5.1 Convergence 157
6.5.2 Comparison with Previous Results 163
6.5.3 The Nature of the Singularity 166

7 Conclusion **171**

A Plots **175**

A.1 Current-Forced Fields 175
A.1.1 Numerical Results 175
A.1.2 Asymptotic Results 245
A.1.3 Development of Long-Wave Behavior in Section 4.3 293
A.2 Mechanically Forced Fields 300
A.2.1 Case Three: Impermeable Surface 300
A.2.2 Case Four: Infinitely Permeable Surface 366
A.3 Fields Resulting from Mixed Boundary Conditions 395

B Fortran Code for the Mixed Boundary Value Problem **434**

C Notation **464**

List of Figures

1.1 The function of cartilage in a synovial or hinge joint. 16

1.2 The structure of proteoglycans and proteoglycan aggregates. 19

1.3 The structure and composition of the glycosaminoglycans hyaluronic acid, chondroitin sulfate, and keratan sulfate. 20

1.4 Streaming potential induced by a macroscopic flow. 22

4.1 Geometry and boundary conditions for current forcing. 59

4.2 The current density field $\vec{J}/J_0$. 65

4.3 Magnitude of the horizontal and vertical displacements, $|u_y|$ and $|u_z|$, $\lambda = 1\,mm, f = .001$ to $.1\,Hz$. 66

4.4 Magnitude of the horizontal and vertical relative velocities divided by frequency, $|V_y|/f$ and $|V_z|/f$, $\lambda = 1\,mm, f = .001$ to $.1\,Hz$. 67

4.5 Magnitude of the pressure and electrical potential, $|p|$ and $|\phi|$, $\lambda = 1\,mm, f = .001$ to $.1\,Hz$. 68

4.6 Phase of the horizontal displacement, $\arg(u_y)$, $\lambda = 1\,mm, f = .001$ to $.1\,Hz$. 70

4.7 Magnitude of the pressure, $|p|$, $f = .001\,Hz, \lambda = .1$ to $10\,mm$. 71

4.8 Magnitude of relative velocities, $|V_y|$ and $|V_z|$, $f = .1\,Hz, \lambda = .1\,mm$. 74

4.9 Magnitude and phase of the surface stress, $s(0), f = .001\,Hz$, *vs.* $\log_{10}\lambda$. 75

4.10 Magnitude of the horizontal and vertical displacements, $|u_y|$ and $|u_z|$, $\lambda = 10\,mm$, $f = .001\,Hz$ *vs.* depth z. 79

4.11 Magnitude of the horizontal and vertical relative velocities, $|V_y|$ and $|V_z|$, $\lambda = 10\,mm$, $f = .1\,Hz$ *vs.* depth z. 80

4.12 Experimental setup and magnitude of the surface stress, $|s(0)|$ *vs.* frequency f. 84

4.13 Phase of the surface stress, $|s(0)|$ *vs.* frequency f. 85

4.14 Magnitude of the pressure, $|p|, \lambda = .1\,mm, f = .001$ to $.1\,Hz$. 89

5.1 Geometry and boundary conditions for mechanical forcing. 92

5.2 Phase of the vertical displacement, u_z, *vs.* depth for a permeable surface, $\lambda = 10.\,mm, f = 2.5 \cdot 10^{-2}, 5 \cdot 10^{-2}$, and $0.1\,Hz$. 96

5.3 Magnitude of the vertical displacement, u_z, for a permeable surface, $\lambda = 10\,mm$, $f = 10^{-3}$ to $10^{-1}\,Hz$ logarithmically. 99

5.4 Magnitude of the vertical displacement, u_z, for an impermeable surface, $\lambda = 10\,mm$, $f = 10^{-3}$ and $10^{-1}\,Hz$. 100

5.5 Magnitude of the horizontal displacement, u_y, for an impermeable surface, $f = 10^{-3}\,Hz$, $\lambda = 0.1$ to $10.\,mm$ logarithmically. 101

5.6 Magnitude of the relative horizontal velocity, V_y, for an impermeable surface, $f = 10^{-3}\,Hz$, $\lambda = 0.1$ to $10.\,mm$ logarithmically. 103

5.7 Magnitude of the relative vertical velocity, V_z, for a permeable surface, $f = 10^{-1}\,Hz$, $\lambda = 0.1$ to $10.1\,mm$ linearly. 104

5.8 Phase of the vertical displacement, u_z, for an impermeable surface, $\lambda = 10\,mm$, $f = 10^{-3}$ to $10^{-1}\,Hz$ logarithmically. 105

5.9 Magnitude of the relative vertical velocity, V_z, for an impermeable surface, $\lambda = 10\,mm$, $f = 10^{-3}$ to $10^{-1}\,Hz$ logarithmically. 107

5.10 Phase of the relative vertical velocity, V_z, for an impermeable surface, $\lambda = 10\,mm$, $f = 10^{-3}$ to $10^{-1}\,Hz$ logarithmically. 108

5.11 Magnitude of horizontal and vertical displacements, u_y, and u_z, for a permeable surface, $f = 0.001\ Hz$, $\lambda = 0.1\ mm$. 111

5.12 Magnitude and phase of the surface stress, $s(0)$, for a permeable surface, $f = .001\ Hz$, *vs.* $\log_{10}\lambda$. 112

5.13 Magnitude of vertical relative velocity, V_z, for a permeable surface, $f = 0.001, 0.1\ Hz$, $\lambda = 0.1\ mm$. 113

5.14 Magnitude of the horizontal and vertical displacements, $|u_y|$ and $|u_z|$, for a permeable surface, $\lambda = 10^2\ mm$, $f = 0.001\ Hz$ *vs.* depth z. . . 116

5.15 Magnitude of the vertical relative velocity, $|V_z|$, for a permeable surface, $\lambda = 10^2\ mm$, $f = 10^{-3}, 6.85 \cdot 10^{-2}\ Hz$ *vs.* depth z. 117

5.16 Phase of the vertical relative velocity, $|V_z|$, for a permeable surface, $\lambda = 10^2\ mm$, $f = 10^{-3}, 6.85 \cdot 10^{-2}\ Hz$ *vs.* depth z. 118

5.17 Theoretical and experimental magnitude of the surface electrical ("streaming") potential, $|\phi(0)|$ *vs.* frequency f, for a permeable surface. . . 120

5.18 Magnitude of the relative horizontal velocity, V_y, for an impermeable surface, $\lambda = 1\ mm$, $f = 0.001$ to $0.1\ Hz$ logarithmically. 122

5.19 Magnitude of the relative vertical velocity, V_z, for a permeable surface, $\lambda = 10\ mm$, $f = 0.001$ to $0.1\ Hz$ logarithmically. 123

5.20 Magnitude of the relative horizontal velocity, V_y, for an impermeable surface, $\lambda = 10\ mm$, $f = 0.001$ to $0.1\ Hz$ logarithmically. 126

6.1 Boundary conditions for the mixed boundary condition problem . . 129

6.2 Current density field for mixed boundary conditions. 134

6.3 Boundary conditions for problems "A" and "B" 138

6.4 Magnitude of the horizontal displacement, $|\bar{u}_y|$, $f = 10^{-3}\ Hz$ 147

6.5 Magnitude of the vertical displacement, $|\bar{u}_z|$, $f = 10^{-5}$ and $10^{-3}\ Hz$. 148

6.6 Magnitude and phase of the relative horizontal velocity, $\bar{V}_y$, $f = 10^{-5}\ Hz$. 150

6.7 Magnitude of the relative vertical velocity, $|\bar{V}_z|$, for $f = 10^{-5}$ and 10^{-3} Hz. 151
6.8 Phase of the relative vertical velocity, $\bar{V}_z$, $f = 10^{-3}$. 152
6.9 Magnitude of the pressure, $|\bar{p}|$, for $f = 10^{-5}$. 153
6.10 Magnitude of the normal stress, $|\bar{s}|$, for $f = 10^{-3}$. 155
6.11 Magnitude of the shear stress, $|\bar{\sigma}_{yz}|$, $f = 10^{-5}$ and 10^{-3} 156
6.12 Magnitude of the potential, $|\bar{\phi}|$, $f = 10^{-3}$. 158
6.13 Magnitude of the pressure, $|\bar{p}|$, $f = 10^{-3}$, $M = 36$, 70, and 120. . . . 159
6.14 Magnitude of the relative horizontal velocity, $|\bar{V}_y|$, $f = 10^{-3}$, $M = 36$, 70, and 120. 160
6.15 Convergence rate for the field maxima at $z = -0.5$, $f = 10^{-3}$, $l = 1$, $l_1 = 0.5$. 162
6.16 Convergence of the relative velocity fields, V_y, and V_z at $z = 0$, $f = 10^{-3}$, $l = 1$, $l_1 = 0.5$. 164
6.17 Local coordinate system and boundary conditions for analysis of the singularity, ... 167

List of Tables

4.1 Maximum field magnitudes for current forcing. 64

5.1 Maximum field magnitudes for vertical displacement forcing. 97

6.1 Field values for mixed boundary condition forcing. 146

Chapter 1

Introduction

This thesis presents a model of electromechanically coupled poroelastic systems. A poroelastic medium will here be taken to be a medium for which any macroscopic volume element contains both a solid and fluid continuum. The first version of a poroelastic theory was developed in the early 1920's [99] to study consolidation of soil under a load. Later versions have been used in a variety of fields such as reservoir modeling and petroleum exploration [7,91]. Electromechanical coupling has also long been recognized as important in poroelastic media, with applications such as geological exploration [37]. More recently, electromechanical phenomena have been identified as fundamental to the behavior of biological connective tissues such as bone [45,94,95,105], and cartilage [4,33,44,67].

The model presented here will be general enough for all of these applications, and the range of parameters used should allow applications in many areas. The computations presented here, however, were performed using parameters pertaining to electrokinetic transduction in soft connective tissues such as articular cartilage. This is a particularly fruitful use of the theory as it suggests a non-destructive method for the measurement of certain physical and biochemical parameters of cartilage, *e.g.* mechanical or electrical stimulation of the surface [34,35]. Since these parameters are greatly altered with the onset of cartilage degeneration in joint disease [33,51,74], a device ("probe") based on this model could detect changes in cartilage properties associated with, *e.g.*, the early development of osteoarthritis [51]. Even though several relevant one-dimensional models have been presented (*cf.* §1.2), a one-dimensional model is insufficient for the geometry of an *in vivo* measurement.

This introductory chapter will describe the microstructure of cartilage. This will motivate the use of electromechanical coupling to model the properties of this particular medium. The historical background of the field of electromechanically coupled poroelasticity will then be presented. The mathematical model used here will then be developed, and the following chapters will describe case studies of a finite-thickness, two-dimensional layer of a poroelastic medium under boundary conditions describing different idealized configurations of the aforementioned probe. The boundary conditions include current driving, in which the mechanical and electrical fields resulting from an injection of current are studied, mechanical driving, in which the fields resulting from a mechanical displacement at the surface are studied, and a mixed boundary condition representing a probe with spaces between electrodes.

1.1 The Structure of Articular Cartilage

The purpose of this section is to acquaint the reader with the basic macro- and microstructure of cartilage and to motivate the macroscopic electromechanical model presented herein. The changes which occur in osteoarthritis will also be briefly discussed so that the utility of the above probe may be seen. The descriptions provided here are based on information gathered in the last decade [44,71,74,88], and are not intended to be complete. Because details are constantly changing, the reader is referred to the literature for further information.

Articular cartilage is a multiphasic, polydisperse, inhomogeneous, anisotropic medium. Articular cartilage is found covering the ends of bones in diarthroidal joints (*cf.* figure 1.1), and serves two basic functions there. First, it serves as a lubricating layer which drastically reduces friction in joints [84]. Second, it helps to distribute the load imposed on the bones forming these joints, especially in the case of weight-bearing joints. The thickness of the layer is on the order of millimeters, and depends on the joint and species being considered [74]. Adult articular cartilage has no blood, nerve, or lymph supply [71]. The interface between the deep ("bottom") zone of the cartilage and the underlying ("subchondral") bone is referred to as the "tidemark." The top "articular surface" is in contact with synovial fluid in the joint and with the opposing articular surface. Even though there are living cells (termed chondrocytes) present in cartilage, in the adult they constitute only 1 – 10% of the wet weight [44]. They do not appear to contribute significantly to the mechanical and electromechanical properties of the tissue, which are determined largely by the extracellular matrix.

1.1.1 The Extracellular Matrix of Articular Cartilage

The extracellular matrix consists mainly of proteoglycans, collagen, and the interstitial fluid phase. These three constituents determine such macroscopic parameters as the elastic moduli, fluid permeability, and electromechanical coupling of the cartilage.

Water makes up 65% to 80% of the wet weight of cartilage [44,74]. Most investigators believe that the majority of fluid in cartilage is unbound and freely exchangeable with the surrounding media. This view was recently challenged by Torzilli *et al.* [101], who reported that as much as 30% of cartilage water may be bound. However, Maroudas *et al.* [76] performed a series of experiments including a repeat of Torzilli's, and reported values closer to 1%. The exact content varies with depth from the surface, age, and with the degree of degeneration, if any. *In vivo*

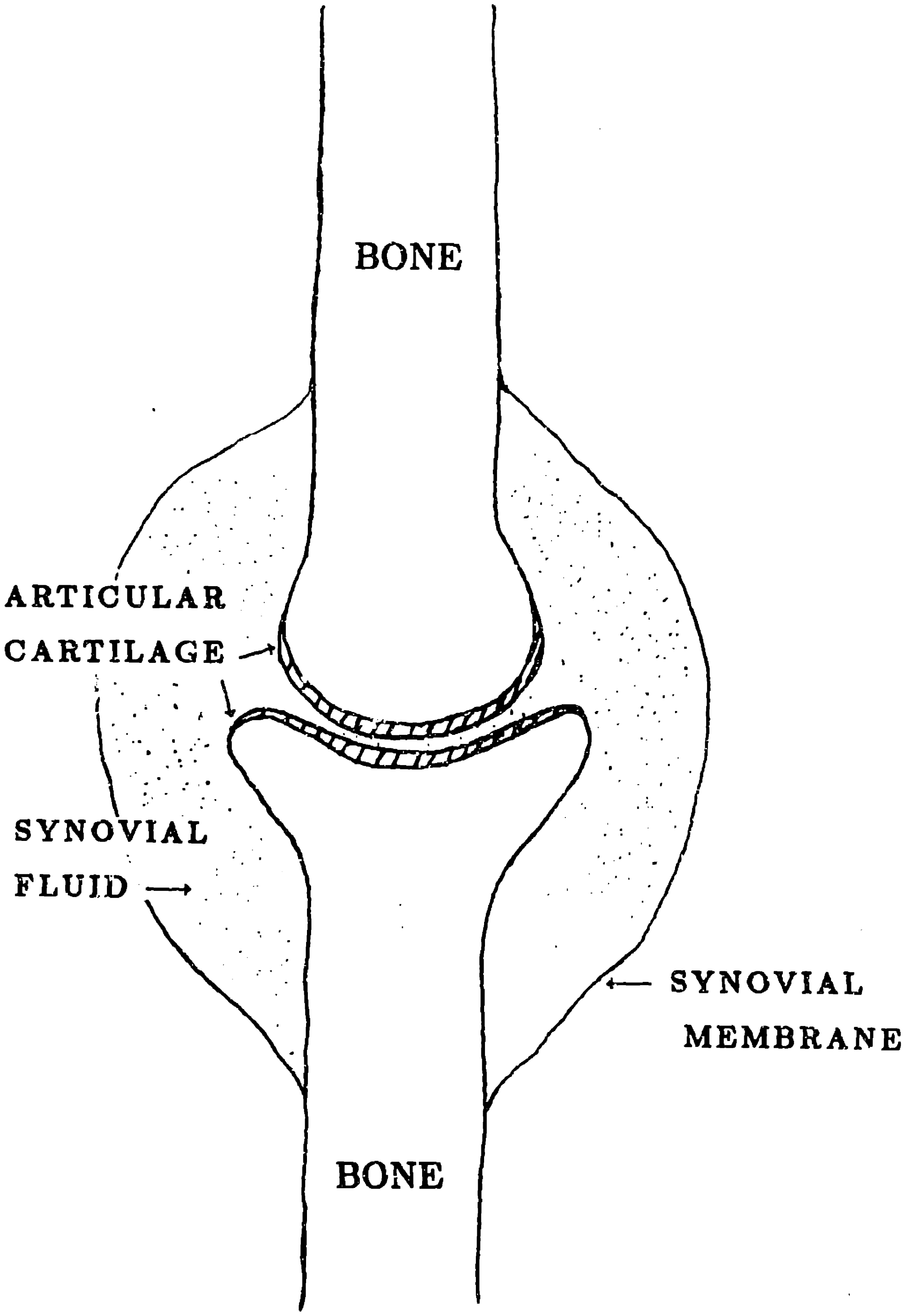
BONE
ARTICULAR
CARTILAGE
SYNOVIAL
FLUID
SYNOVIAL
MEMBRANE
BONE

Figure 1.1: The function of cartilage in a synovial or hinge joint.

the fluid phase contains numerous electrolytes which balance the net charge of the proteoglycans, and, along with oxygen and nutrients, supply the physiological needs of the chondrocytes [44,71].

Most of the dry weight of articular cartilage (65% to 75%, see [44,71]) is collagen. Cartilage ("type II") collagen, like other collagens, consists of triple helical macromolecules. The basic subunit is a polypeptide chain wound in a left-handed helix. Three of these helicies are then wound around each other in a right-handed super-helix, with both hydrogen and covalent bonding between the constituents, forming tropocollagen, which is the basic unit of the collagen molecule. Tropocollagen molecules are about $1.5nm$ in diameter, $300nm$ in length, and have molecular weights on the order of $3 \cdot 10^5$ daltons. Collagen molecules further aggregate to form fibrils. In many connective tissues, fibrils are found to group together to form larger fibers of different diameters [104].

The fibrils of collagen form a loose mesh in cartilage. Collagen is woven fairly tightly near the surface, but it is randomly oriented and dispersed more homogeneously throughout the bulk of the volume [84]. The $\sim 100\ nm$ gaps between the fibrils are significantly larger than the 2 to 10 nm "pore" size relevant for the exclusion of solutes in diffusion and for the fluid permeability [74]. The woven network of cross-linked collagen fibrils gives a large tensile strength to this loose mesh. The collagen is largely responsible for the shear strength of cartilage and for its resistance to the swelling pressure generated by the proteoglycans [74,84].

Proteoglycan aggregates (PGAs) are large, complex polyelectrolytes woven through and tightly associated with the collagen matrix, and make up about 20% of the dry weight of articular cartilage [44,71]. These aggregates resemble test tube brushes in structure (*cf.* figure 1.2). They are roughly 1 μm in length and .7 μm in diameter, and have a molecular weight of about 10^8 daltons [88,44]. Each aggregate is made up of proteoglycan monomers attached to a chain polymer of hyaluronic acid (*cf.* figure 1.3). The monomers consist of glycosaminoglycans ("GAGs", once known as mucopolysaccharides) attached to a protein core. The GAGs, which weigh $\sim 10^6$ daltons, are linear polymers of disaccharides, principally chondroitin sulfate ("CS") and keratan sulfate ("KS",*cf.* figure 1.3), attached by a special linking region to a core protein.

At physiological pH of about 7.4, the CS dimer has two negative charges, and the KS has one, on the average. This results in a fixed charge density of about 0.1 M/l for normal articular cartilage [44]. On a macroscopic scale this charge is neutralized by the presence of mobile positive ("counter") ions in the fluid within the cartilage. The concentration of all the coions and counterions in the cartilage is determined by the Donnan equilibrium relations, and results in an osmotic pressure difference between the fluid in the matrix and the external bathing solution [74]. This osmotic pressure, which may also be regarded as a result of electrostatic repulsion between the GAG constituents ([44]), results in a swelling pressure. This pressure, which indicates a tendency for the matrix to absorb fluid, is a major component of the compressive modulus of cartilage [26,74,87].

The presence of the PGAs in cartilage has two other consequences of note. First, there is a significant change in several of the mechanical properties. For instance, the size of a solute which is free to diffuse or be advected into the matrix is reduced to roughly $5nm$ (*cf.* above). Thus it is seen that the PGAs act like a swollen gel which is constrained by the collagen matrix. This is particularly apparent in terms of the changes of stiffness and volume of cartilage with changes in the pH or solute concentration of its external bath [44]. Also, experiments have shown that the mechanical response to a difference in osmotic pressure across the surface of the cartilage is directly related to the response to a mechanical load applied to the surface [74]. Thus if we define

$$\mathcal{P} = P - \Delta\pi, \tag{1.1}$$

PROTEOGLYCAN AGGREGATE

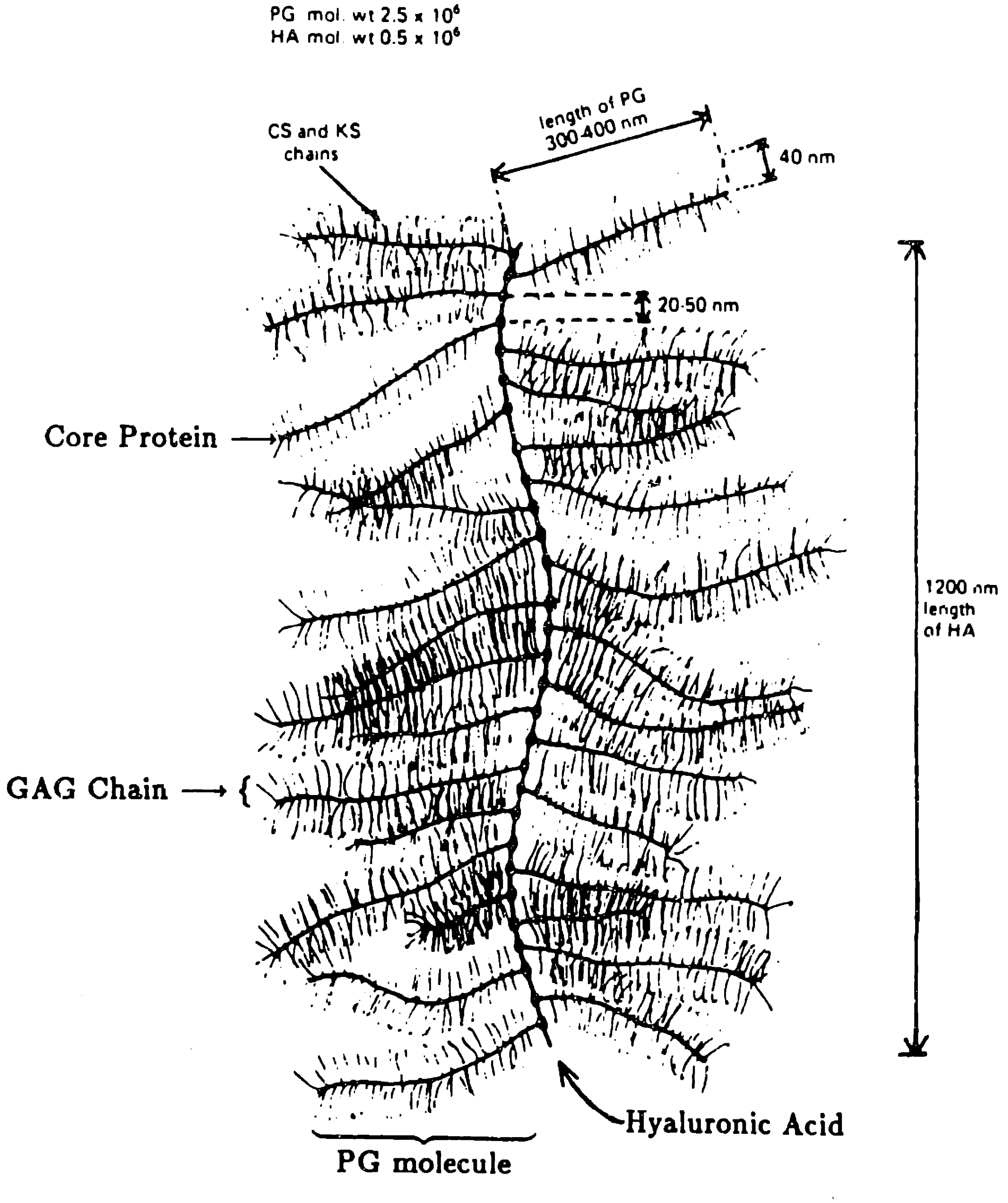
PG mol. wt 2.5 x 10⁶
HA mol. wt 0.5 x 10⁶
CS and KS chains
length of PG 300-400 nm
40 nm
20-50 nm
1200 nm length of HA
Core Protein
GAG Chain
Hyaluronic Acid
PG molecule

Figure 1.2: The structure of proteoglycans and proteoglycan aggregates. Adapted from [88], page 164. Key: PG, proteoglycan molecule or subunit; HA, hyaluronic acid; CS, chondroitin sulfate; KS, keratan sulfate, GAG, glycosaminoglycan. HA, CS, and KS are glycosaminoclycans.

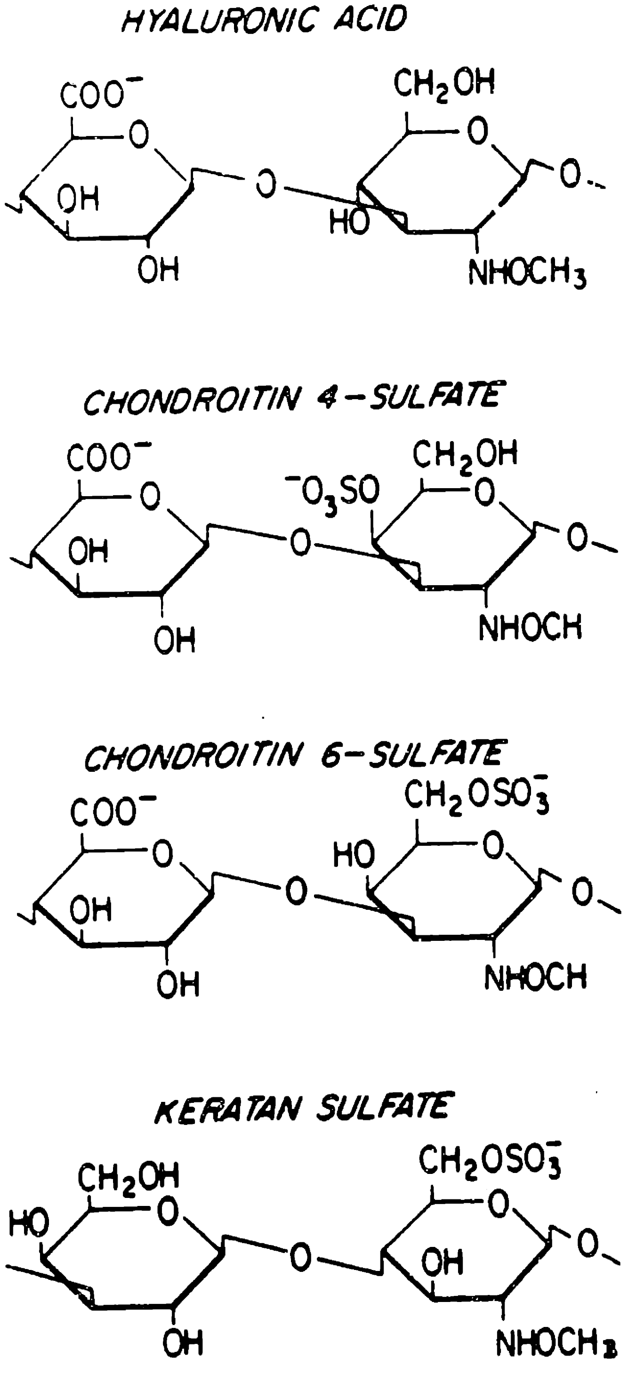
HYALURONIC ACID
COO⁻
O
OH
OH
O
CH₂OH
O
HO
O
NHOCH₃
CHONDROITIN 4-SULFATE
COO⁻
O
OH
OH
⁻O₃SO
O
CH₂OH
O
O
NHOCH
CHONDROITIN 6-SULFATE
COO⁻
O
OH
OH
O
HO
CH₂OSO₃⁻
O
O
NHOCH
KERATAN SULFATE
CH₂OH
HO
O
OH
O
CH₂OSO₃⁻
O
OH
O
NHOCH₃

Figure 1.3: The structure and composition of the glycosaminoglycans hyaluronic acid, chondroitin sulfate, and keratan sulfate [71].

with hydrostatic pressure P, and osmotic pressure difference $\Delta\pi$ (relative to the point of fluid pressure reference), $\mathcal{P}$ may now be used in place of P within a single domain or across an interface (*e.g.* the cartilage surface) to predict a mechanical response (see also [26]).

The second major consequence of the presence of PGAs in articular cartilage is the existence of electrokinetic coupling. When there is macroscopic fluid motion in cartilage due to a pressure gradient, the counterions are dragged in the direction of the flow (*cf.* figure 1.4). This results in a macroscopically measurable streaming potential, which is on the order of a 10 mV drop over a 1 mm sample if a 1 $\mu m/s$ flow is induced, requiring a pressure drop on the order of $10^6\ N/m^2 \equiv 1M\ Pa \approx 10atm$.

1.1.2 Implications for Diagnostic Measurements

It is now possible to see what some macroscopic measurements imply about the physicochemical state of the material. For example, if the proteoglycan content is reduced, then the concentration of excess counterions necessary to balance the fixed charge density will also be reduced. This will result in a drop in the osmotic pressure, and thus the compressive stiffness of the cartilage. Since the conductivity of a (dilute) ionic solution is proportional to the concentration of mobile ions ([44]), the electrical conductivity of the medium will also be reduced. Lastly, the decrease in fixed charge density will clearly result in a weakening of the electrokinetic coupling.

Several changes occur in diseased tissue. Osteoarthritic tissue, for instance, is known to have a lower concentration of proteoglycans and a larger water content [71]. This excess water has been associated with a fibrillated or damaged collagen matrix [75]. Such tissue has lost some ability to resist the swelling pressure. Furthermore, it appears that the PGA content decreases in direct proportion to the severity of the disease [71].

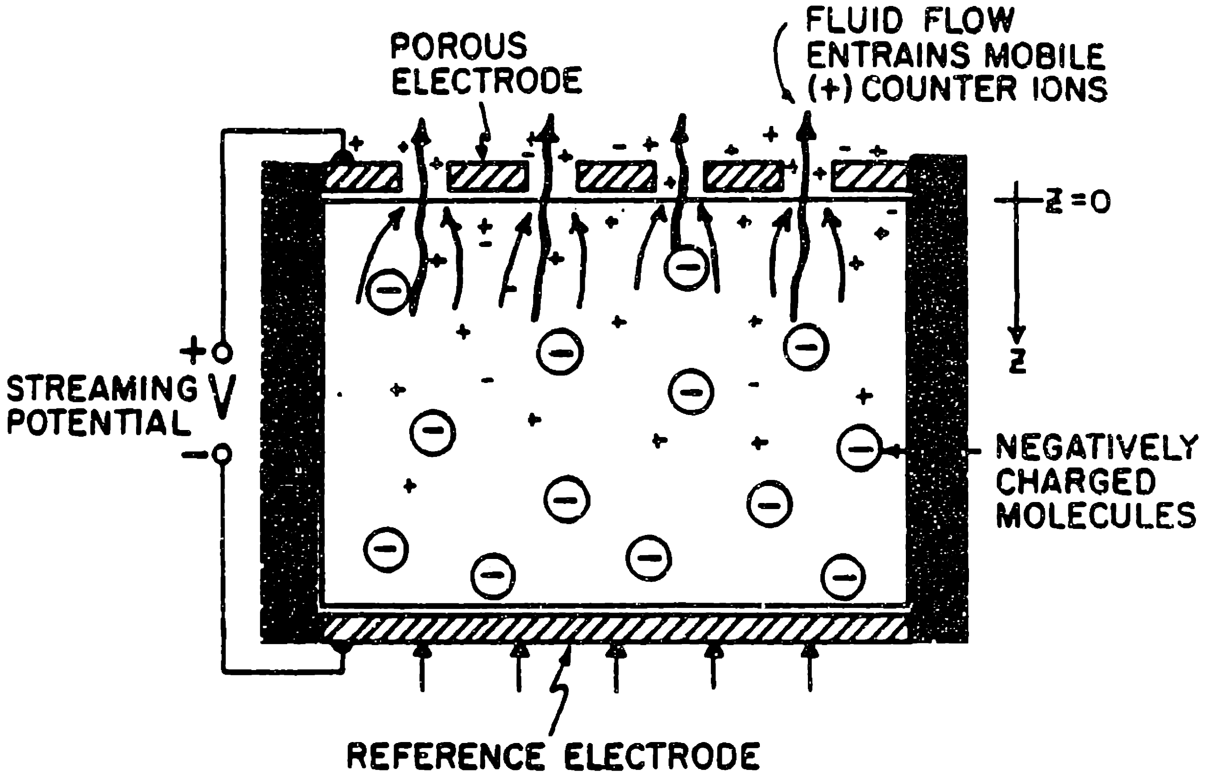
POROUS ELECTRODE
FLUID FLOW ENTRAINS MOBILE (+) COUNTER IONS
z=0
z
+
STREAMING POTENTIAL V
−
NEGATIVELY CHARGED MOLECULES
REFERENCE ELECTRODE

Figure 1.4: Streaming potential induced by a macroscopic flow. The mobile, "counter" ions ("+") in the interstices are dragged by the fluid, and constitute a streaming current. The potential measured will be in a direction opposing this current and the implied charge separation, as expected from Le Chatelier's principle. Reproduced from [35] with permission of the authors.

Experimental evidence suggests that all of the parameters which describe the electrokinetic coupling undergo significant changes during the onset of osteoarthritis. First, it is known that the fixed charge density measures the proteoglycan content of the cartilage [74]. It is also known that if the charge density is varied by modification of the PGA content (as opposed to, *e.g.*, external bath concentrations), the Darcy permeability of the tissue varies approximately like the inverse of the charge density. Thus knowledge of the permeability alone gives significant information about the status of the cartilage.

Further, both the stiffness [74] and the coupling parameter which determines the streaming potential [44,35] change in enzymatically modified cartilage. On the basis of experiments involving artificially induced arthritis in laboratory animals and enzymatic degradation of excised articular cartilage, it has been conjectured that the changes in the streaming potential can be detected at an earlier stage than those of stiffness alone [35,82]. Also, visual inspection alone is not always sufficient to detect even large scale changes in, *e.g.*, proteoglycan content of osteoarthritic tissue [74]. Thus a probe able to measure non-destructively the electromechanical parameters of cartilage *in vivo* could well be beneficial to the early detection of osteoarthritis.

1.2 Background for Electromechanically Coupled Poroelasticity

Mathematical models of biphasic media have been used to describe phenomena from acoustic waves in saturated soil [11] to the electromechanochemical response of articular cartilage [35]. The earliest published use was Darcy's 1856 treatise [23] on the public springs in the city of Dijon, in which he stated the proportionality between pressure gradients and relative velocity of fluid and solid. The motion of the solid phase was taken into account by Terzaghi [99] in the early 1920's, and his theory was generalized by Biot [6,7] in the mid-1930's. This section gives a brief summary of approaches to poroelastic modeling that have been used in various contexts.

Swelling gels are frequently modeled as poroelastic media with high porosities (fluid volume fractions) $\phi \sim 1$. Because of the high porosity of cartilage, these models can be used in some situations. One such theory has been proposed by Tanaka and co-workers [97,98], who assumed that $\phi = 1$, and that, as a result, the fluid is stationary while the solid matrix moves through it. They also assumed that the solid matrix obeys a linearly elastic, isotropic constitutive relation whose stiffness parameters are properties of "the fiber network alone" [98]. The only solid-fluid interaction in this model arose from a Darcy's law body force which is equivalent to

$$\vec{\nabla} p = -f \partial_t \vec{u} \tag{1.2}$$

where p is fluid pressure (force / total area), $\vec{u}$ is displacement of the solid, and f is a friction coefficient. In the low-frequency limit of the (one-dimensional) momentum balance, this produced a diffusion equation:

$$f \partial_t u = (K + \frac{4}{3} G) \partial_z{}^2 u \tag{1.3}$$

(G and K are the shear and bulk compressibility moduli for the solid matrix, respectively). Good agreement was obtained with data from both light-scattering [98] and free-swelling [97] experiments.

A somewhat different approach to free-swelling was taken by Friedman [38,39]. Because of the large volume changes exhibited by cornea (the subject of his theory), a Lagrangian coordinate system was used. Friedman wrote equations of conservation of mass for the solid and fluid, a momentum-conserving form of Darcy's law, and a relation conserving total momentum. It should be noted that conservation of momentum had not been used by other authors [29], making it necessary to introduce *ad hoc* assumptions and extraneous parameters. By using experimental data relating equilibrium swelling pressure [29] (defined to be that force / total area exerted by the solid on an infinitely fluid-permeable surface) and tissue permeability [50] to tissue hydration (*i.e.* porosity), an irreducible system of hyperbolic equations was obtained. Numerical solutions fit available data somewhat better than previous theories.

A much more general approach to biphasic problems has been taken by Mow and co-workers [3,52,58,60,61,69,83,84,85,86,102,103]. Mow developed a mixture ("two variable") description based on the work of Craine, Green and Naghdi [21,43], and Bowen [16]. In this system, density, displacement, stress, and constitutive relations of the fluid and solid are kept separate. By considering a system in which the solid and fluid elements are incompressible, Mow obtained the equation of mass conservation [83]

$$\phi\vec{\nabla}\cdot\vec{u}^f + (1-\phi)\vec{\nabla}\cdot\vec{u}^s = 0, \tag{1.4}$$

where $\vec{u}^f, \vec{u}^s$ are fluid and solid displacements, respectively. This intuitive result was also written down by Biot [8]. The separate momentum equations are (without body forces):

$$\begin{aligned} \rho^s \frac{D\vec{v}^s}{Dt} &= \vec{\nabla}\cdot\mathbf{T}^s + \vec{\pi}^s \\ \rho^f \frac{D\vec{v}^f}{Dt} &= \vec{\nabla}\cdot\mathbf{T}^f + \vec{\pi}^f, \end{aligned}$$

with

$$\vec{\pi}^s = -\vec{\pi}^f = K(\ \vec{v}^s - \vec{v}^f\ ). \tag{1.5}$$

Here ρ^i is the mass per unit total (tissue) volume, $\vec{v}^i$ the velocity, $\mathbf{T}^i$ the partial stress field, $\vec{\pi}^i$ the interaction body force, all of species i, and K is inversely proportional to the Darcy permeability.

The constitutive equations also set this approach apart from others. They are derived from very general mixture-theoretic, thermodynamic considerations. After linearizing this theory, it is assumed that: the system is isotropic; the solid is strictly elastic (*i.e.* non-dissipative); the fluid is inviscid; and there is no stress produced by relative vorticity of fluid and solid. The resulting equations are [83]:

$$\mathbf{T}^s = -\alpha p\mathbf{I} + Ae\mathbf{I} + 2N\mathbf{e}$$

and,

$$\mathbf{T}^f = -p\mathbf{I} - Qe\mathbf{I} \ , \tag{1.6}$$

where p is (ϕ times) the fluid pressure, **I** is the unit tensor, α is the solid to fluid ratio $(1-\phi)/\phi$, **e** is the small strain tensor, with

$$e_{ij} \equiv \frac{1}{2}(\partial_{x_i} u_j + \partial_{x_j} u_i) \ , \tag{1.7}$$

$e \equiv \text{tr}\ \mathbf{e} = \vec{\nabla} \cdot \vec{u}^s$, and the parameter Q defines the change in fluid pressure due to dilitation of the solid matrix. Here p is the fluid force per total (as opposed to fluid) area. Some authors [26,35,83,92] have used the total area as a basis, while others have used either fluid area [91,7], or both [15]. By considering a free surface of tissue at equilibrium with a fluid bath, the fluid area basis explains the unusual factor of α in $\mathbf{T}^s$.

Two noteworthy features of this model are the distinction of the stress fields for the fluid and solid phases, and the use of Q. Other developments [7,15,26,35,91,92] neither consider two separate stress fields for the fluid and solid phases, nor describe explicitly the pressure force of the fluid acting on the solid. Also, the fluid stress here contains a contribution other than the pressure. Others (*cf.* below) consider the pressure to be the fluid stress field. It should be noted, however, that this contribution was eliminated [3] by setting $Q = 0$, making the stress fields consistent with those of other authors.

Another important contribution by Mow and co-workers is the consideration of the nonlinearities produced by strain-dependent permeability. The results of several experiments led to the introduction of a dependence of K (*cf.* equation 1.5) on the strain in the solid [52,58,60,69,83,84].

$$K = K_0 \exp(-M_0 e), \tag{1.8}$$

where K_0 and M_0 are constants, and $e = \partial_z v$ is the (one-dimensional) matrix consolidation. The resulting nonlinear equations were solved exactly for the one-dimensional static case, and demonstrate good agreement with available data [60]. Creep and stress relaxation solutions have been examined [52]. The effects of finite deformation theory have also been investigated [58].

Another approach is the "single variable" representation founded by Biot [6–13,15]. He considered strain and porosity to be natural variables with which to describe the status of the medium. (This was strictly true only of his later works [8–13]: his first work and that of Rice and Cleary [91] are similar — *cf.* below.) A completely phenomenological approach was used to linearly relate the stresses and the fluid pressure to strain and porosity of an isotropic system [8]:

$$\begin{aligned} \sigma_{ij} &= 2Ne_{ij} + (Ae + Q\epsilon)\delta_{ij} \\ p &= Q_1 e + R\epsilon \,. \end{aligned}$$

Here N, A, Q, Q_1, and R are elastic constants, δ_{ij} is the Kronecker delta, e_{ij} is the strain in the solid matrix (*cf.* equation 1.7), p is the force on the fluid per unit total area (as $\mathbf{T}^f$, above), $\sigma_{ij} = \mathbf{T}^s_{ij}$, and $\epsilon = \vec{\nabla} \cdot \vec{U}$, where $\vec{U}$ is the displacement of the fluid. Consideration of thermodynamic reversibility and the existence of an elastic potential showed that $Q_1 = Q$, but it should be noted that the arguments given in the first work [7] are not valid for compressible fluids. A similar error led to the conservation of mass equation

$$\vec{\nabla} \cdot (\vec{v}^s - \vec{v}^f) + \partial_t \phi = 0,$$

but equation 1.4 was properly used for the case of incompressible constituents. Biot used Darcy's law

$$\vec{\nabla} p = -k(\vec{v}^f - \vec{v}^s) \tag{1.9}$$

for time-dependent problems. Recently the equations of this theory, including the extension to anisotropic media with compressible constituents, were rigorously re-derived by Burridge and Keller using the method of spacial homogenization [17].

Several differences from the Mow approach are apparent here. First, Biot used the fluid pressure variable, p, to represent all of the forces on the fluid. Also, the pressure exerted by the fluid on the solid is not (explicitly) contained in his expression for solid stress. Furthermore, Biot was allowing both the fluid and solid constituents to be compressible. In the limit of incompressible constituents (also taken by Mow), we have the relations [15]:

$$\phi\frac{Q+R}{R} = 1 \quad \text{and} \quad \phi^2 R^{-1} = 0.$$

Under additional non-restrictive assumptions, however, the approach taken by Mow *et al.* is completely equivalent to that of Biot.

The roles of Biot's parameters A, Q, and R are not, however, easily visualized. Biot and Willis [15] presented a number of intuitive *Gedanken* experiments relating the naturally measured experimental parameters to these phenomenological parameters. Rice and Cleary [20,91], on the other hand, started with the more readily visualized parameters from Biot's first work [7]. In this approach, stress (now $\mathbb{T}$ represents total force / unit total area) and fluid pressure (force per unit fluid area) are naturally controllable variables, and strain and porosity are expressed as linear functions of these variables. The constitutive laws are [91]:

$$2Ge_{ij} = (T_{ij} + p\delta_{ij}) - \frac{\nu}{1+\nu}(T_{kk} + 3p)\delta_{ij} + \frac{2G}{3}\left(\frac{1}{H} - \frac{1}{K}\right)p\delta_{ij} \tag{1.10}$$

and

$$\phi - \phi_0 = \frac{1}{3H}(T_{kk} + 3p) - \frac{\phi_0}{K_s''}p, \tag{1.11}$$

where G is the shear modulus, ν is Poisson's ratio, $K \equiv \frac{2G(1+\nu)}{3(1-2\nu)}$, H is a modulus related to compressibility of constituents, and ϕ_0 is the undeformed porosity of the material. Darcy's law is still used for (inertia free) time-dependent problems, but it should be noted that because it is stated in terms of mass flux ($\vec{q}$) and equilibrium fluid density ρ_0 [91] using,

$$\vec{q} = -\rho_0 \, \kappa \, \vec{\nabla} p \ ,$$

the permeability κ may be pressure dependent for a compressible fluid. The equation of conservation of mass, now valid for compressible constituents is

$$\partial_t m + \vec{\nabla} \cdot \vec{q} + \vec{\nabla} \cdot (m\vec{v}^s) = 0 \quad ,$$

with $m = \phi\rho$.

By considering two time scales, Rice and Cleary developed what they termed the "drained" and "undrained" elastic coefficients. The "drained" parameters refer to the static response of the medium after infinite time. This allows all relative solid and fluid motion to cease, and yields the familiar G and ν of linear elasticity. If, however, the response is considered after a time short enough that no fluid motion has occurred (*i.e.* the mass of fluid per unit volume, m, is unchanged), the "undrained" parameters are evoked. One of these is the undrained Poisson's ratio ν_u, and the other, B, relates fluid pressure to total normal stresses on a surface element by

$$\Delta p \ = \ -B\frac{\Delta\sigma_{kk}}{3} \ .$$

Since ν_u and B can be expressed in terms of the parameters of equations 1.10 and 1.11, the entire theory is reformulated using the intuitive parameters ϕ, G, ν, ν_u, B, and κ.

This theory was also utilized by Chandler and Johnson [19,54]. First, equations 1.10 and 1.11 were re-written in terms of ϕ, k (*cf.* equation 1.9), k_b, k_s, and k_f. Here, k_b, k_s, and k_f are the bulk compressibilities of the ("drained") solid matrix, solid constituent, and fluid phase, respectively. The authors then developed several limiting cases of the acoustic propagation theory of Biot [11,13]. Specifically, they showed that the "slow" compressional mode predicted by Biot is equivalent to the diffusive behavior predicted by others. In so doing, they found and corrected errors (in predicted mechanical diffusion coefficients) made by other authors [54]. They also verified that fluid motion is negligible in the gel limit $\phi \rightarrow 1$.

While the application of poroelastic theories to the purely mechanical behavior of connective tissues has now matured, the electromechanical transduction processes described in the previous section have only recently begun to be elucidated. In several recent works [18,65], classical theories relating pressure gradients to potential gradients have been utilized to good effect. In particular, Salzstein and Pollack [94,95] have predicted stress generated potentials in bone using the poroelastic theory of Mow along with electrokinetic coupling virtually identical to that below in equation 1.12.

A somewhat different approach has been taken by Grodzinsky and co-workers [25–28, 32–36,44,56, 63,64]. Their stress-strain relations [25] are those of the single variable approach of Biot and of Rice and Cleary, modified to include effects of chemical gradients:

$$\sigma_{ij} = 2G(c)\epsilon_{ij} + [\lambda(c)\epsilon_{kk} - \beta(c) - (p - \Delta\pi)]\delta_{ij}$$

where c is a local electrolyte concentration, β is a "chemical stress" (used to account for changes in equilibrium strain with c), and $\Delta\pi$ is again the osmotic pressure (*cf.* §1.1.1). The constituents are considered to be incompressible. Thus, for a one-dimensional problem in which an infinitely permeable platen compresses cartilage against an impervious surface, mass conservation requires

$$\phi v_z^f = -v_z^s \, ,$$

where v_z^i denotes the z-component of velocity $\vec{v}^i$.

The electrokinetic interactions are described by a modified form of Darcy's law:

$$\begin{pmatrix} v_z^f - v_z^s \\ J_z \end{pmatrix} = \begin{pmatrix} -k_{11} & k_{12} \\ k_{21} & -k_{22} \end{pmatrix} \begin{pmatrix} \partial_z(p - \Delta\pi) \\ \partial_z V \end{pmatrix} \tag{1.12}$$

Here, k_{11} is the (short-circuited) Darcy permeability, k_{22} is the (null-pressure) electrical conductivity, and k_{12} and k_{21} are coupling coefficients that are equal by Onsager reciprocity. This model has been successfully used to describe the results of one-dimensional experiments involving mechanically generated streaming potentials and current-generated mechanical stress in articular cartilage [25,35,64]. Also, electrical, mechanical, and chemical properties of the fluid and solid constituents (along with an idealized geometric representation of the extracellular matrix) have been used to predict the k_{ij} with some success [25,26,62,94].

Chapter 2

Governing Equations

2.1 Introduction

This chapter presents the differential equations and parameters of the model used to describe a homogeneous, linearly-elastic, isotropic, electromechanically coupled, poroelastic medium. The first section will state the governing equations of the system, along with the primary assumptions on which the equations are based. Working equations will then be developed, and the two-dimensional version will be stated in terms of partial differential equations in rectangular coordinates. (The equations are developed in cylindrical coordinates in appendix 2.3.2.) The second section will discuss the assumptions in more detail. In particular, the relation of the model assumptions to the measured properties of articular cartilage will be considered. Also, the equation of conservation of mass will be derived more carefully, showing the order of terms dropped in linearizing this equation.

2.2 The Model

The three-dimensional model presented here is based primarily on the electrokinetic coupling approach used by Eisenberg [25] and Frank [35] (*cf.* §1.2). The mechanical development is also strongly influenced by that of Biot [7] and that of Rice and Cleary [91]. The following assumptions are made concerning the poroelastic two-phase continuum and the disturbance to be analyzed:

1. The electromagnetic wavelengths are much longer than the length scale of the layer so that the electroquasistatic form of Maxwell's equations is applicable;
2. the disturbance wavelength (λ) is sufficiently long compared to the intermolecular spacing of the tissue matrix that a continuum model may be used;
3. the frequencies (f) of interest are such that the charge relaxation time in the fluid (about 1 ns for cartilage) is much smaller than $1/f$;
4. the frequency of disturbances (f) is low enough that inertial and acoustical effects are negligible;
5. all processes are isothermal, and chemical reactions are negligible;
6. the individual solid and fluid constituents are isotropic, homogeneous, and incompressible;
7. motion of the fluid phase can be modeled by Darcy flow – the fluid phase may be considered to be inviscid at macroscopic solid boundaries;

and

8. the amplitude of the solid displacement field is small enough that the mechanics of the solid matrix can be represented by a linear, elastic model.

These assumptions are discussed more thoroughly in section 2.3.

Using assumption 6, conservation of mass is [8,3, *cf.* §2.3.2 below]

$$\alpha_0 \vec{\nabla} \cdot \vec{v}^s + \vec{\nabla} \cdot \vec{v}^f = 0, \tag{2.1}$$

where α_0 is the solid volume fraction, $\vec{v}^s$ is the local velocity of the solid matrix, and $\vec{v}^f$ is the local velocity of the fluid[1]. Conservation of momentum is (from assumption 4)

$$\vec{\nabla} \cdot \underline{\underline{\sigma}} = \vec{0} \tag{2.2}$$

where the solid stress $\underline{\underline{\sigma}}$ measured per unit total area is given by the constitutive relation [15,25,26] (using 6 and 8)

$$\sigma_{ij} = 2G\epsilon_{ij} + \delta_{ij}(\lambda_L \epsilon_{kk} - P). \tag{2.3}$$

Here, G and λ_L are the Lamé coefficients of the solid matrix, P is the fluid pressure (per unit total area) including both hydrostatic and osmotic pressure [26], and ϵ_{ij} is the small-strain tensor

$$\epsilon_{ij} \equiv \frac{1}{2}\left(\frac{\partial u_i}{\partial x_j} + \frac{\partial u_j}{\partial x_i}\right), \tag{2.4}$$

$i, j = 1, 2, 3.$

To describe electrical interactions two more equations are needed. First, under the assumption 3, the current density is solenoidal, corresponding to instantaneous charge relaxation, so that

$$\vec{\nabla} \cdot \vec{J} = 0, \tag{2.5}$$

where $\vec{J}$ is the current density. The solid-fluid interaction is governed by linearized electrokinetics (which encompasses both Ohm's and Darcy's laws as special cases):

$$\begin{pmatrix} \vec{\nabla} P \\ \vec{\nabla} \Phi \end{pmatrix} = \begin{pmatrix} -b_{11} & b_{12} \\ b_{21} & -b_{22} \end{pmatrix} \begin{pmatrix} \vec{V}^s \\ \vec{J} \end{pmatrix}, \tag{2.6}$$

---

[1] Notation is defined in Appendix C.

where Φ is the electrical potential, and $\vec{V}^*$ is the relative fluid velocity $\vec{v}^f - \vec{v}^s$. Here, b_{11} is the (open-circuit) Darcy hydraulic resistivity, b_{22} is the (no flow) electrical resistivity and b_{12} and b_{21} are coupling coefficients that are equal by Onsager reciprocity. The coupling exists because ions in the Debye layer near the charged moieties of the solid matrix are being dragged by the fluid. Details of the derivation of equation 2.6 may be found in the literature [24,55]. It should be emphasized that ***electrical interactions influence the measured*** b_{11}***, and mechanical interactions influence*** b_{22}. For example, open- and closed-circuit measurements of permeability for bovine articular cartilage differ by roughly 10% [34].

Two additional relations are useful. By taking the curl of the first and second rows of equation 2.6, assumption (6) and $\det(b_{ij}) \neq 0$ yield

$$\begin{aligned} \vec{\nabla} \times \vec{V}^* &= \vec{0} && (a) \\ \text{and,} \qquad\qquad\qquad\qquad &&& \qquad (2.7) \\ \vec{\nabla} \times \vec{J} &= \vec{0}. && (b) \end{aligned}$$

The latter equation also arises in the electroquasistatic case of a homogeneous, isotropic, monophasic medium (*cf.* Appendix 2.3.2), but is arrived at differently.

The above differential equations are easily written in rectilinear coordinates. Because only two-dimensional (plane-strain) geometries are considered in this work, the two-dimensional equations will be presented. By writing the local velocity of the solid matrix as

$$\vec{v}^s \equiv \partial_t \vec{u} \tag{2.8}$$

the equation of conservation of mass 2.1 becomes

$$\alpha_0(\partial_y \partial_t u_y + \partial_z \partial_t u_z) + \partial_y v_y + \partial_z v_z = 0\,. \tag{2.9}$$

(All field and coordinate variables will be dimensional for the rest of this section: “*”’s have been omitted for clarity.) The conservation of momentum is expressed in terms of the solid displacements and pressure by substituting equations 2.4 and 2.3 into 2.2, yielding

$$\begin{aligned}(2G+\lambda_L)\nabla^2 u_y + (G+\lambda_L)(\partial_y\partial_z u_z - \partial_z^2 u_y) - \partial_y P &= 0\\ (2G+\lambda_L)\nabla^2 u_z + (G+\lambda_L)(\partial_y\partial_z u_y - \partial_y^2 u_z) - \partial_z P &= 0\,,\end{aligned} \tag{2.10}$$

where homogeneity of the Lamé coefficients and equivalence of the mixed partials $\partial_y\partial_z = \partial_z\partial_y$ have been assumed. If the electrokinetic coefficients b_{ij} are also homogeneous, then equations 2.6 become

$$\begin{aligned}\partial_{\{y,z\}} P &= -b_{11} V_{\{y,z\}} + b_{12} J_{\{y,z\}}\\ \partial_{\{y,z\}} P &= b_{21} V_{\{y,z\}} - b_{22} J_{\{y,z\}}\,,\end{aligned} \tag{2.11}$$

where $\{y,z\}$ represents the y or z component, as appropriate. Equation 2.5 is just

$$\partial_y J_y + \partial_z J_z = 0\,. \tag{2.12}$$

Given appropriate boundary conditions, the preceding eight equations may now be solved for $u_y, u_z, V_y, V_z, P, J_y, J_z$, and ϕ. Equations 2.7 may be used in place of two of the equations 2.6. In rectangular coordinates, equations 2.7 become

$$\begin{aligned}\partial_y V_z - \partial_z V_y &= 0\\ \text{and,}\qquad & \\ \partial_y J_z - \partial_z J_y &= 0\,.\end{aligned} \tag{2.13}$$

2.3 Limitations

This section will discuss the limitations of the model in terms of the assumptions made in deriving the model equations (page 33). First, the implications of the physical assumptions will be compared to properties of articular cartilage which have been investigated experimentally. Then purely mathematical limitations of the model will be discussed. In particular, the size of the non-linear terms ignored in the equations of conservation of mass will be discussed.

2.3.1 Relevance to Properties of Articular Cartilage

The purpose of this section is to examine the assumptions of the model (on page 33) in light of experimentally measured properties of articular cartilage. The basis of each assumption will be discussed, and implications of simplifications examined.

1. The assumption of electroquasistatics is valid so long as $f \ll c/L$, where f is the frequency of the applied disturbance (*cf.* §3), c is the speed of light, and L is the smallest length scale being considered. The thickness of the cartilage layers being considered here is approximately 1 mm, and the shortest wavelengths will be about 1 μm. Since the highest frequency considered in this work is considerably less than 1 Hz, this assumption is well founded.

2. The longest length scale for which the microstructure of the extracellular matrix is relevant is roughly either the largest dimension of a collagen fibril or proteoglycan aggregate, or the interstitial pore size. In articular cartilage, the collagen fibrils and PGA's both have length scales on the order of 1 μm (§1.1), and the pore size is roughly 2 to 10 nm. Thus the 1 μm wavelengths mentioned above are at the limits of validity of this assumption.

   Two facts ameliorate the seriousness of this situation. First, the highest wavelengths will appear only as short-wavelength terms in Fourier series solutions. Second, an $\mathcal{O}(1)$-amplitude driving field (*e.g.* $\vec{J}$ in chapter 4) with a small wavelength λ will be seen to produce a response (*e.g.* $\vec{u}$) with amplitude proportional to a power of $1/\lambda$. Thus the small Fourier coefficient and the natural size of the response combine to reduce the effects of constituents of finite size.

3. The theory of electric fields in electrolyte solutions [65] predicts that the time τ required for concentration gradients on the scale of a Debye length $\kappa^{-1} \sim \sqrt{(\epsilon/\sigma)D}$ to equilibrate, is roughly ϵ/σ [81]. Here $\sigma \approx 1$ mho/m

is the conductivity of the solution in the vicinity of the Debye layer, and $\epsilon \approx 80\epsilon_0 \approx 7 \cdot 10^{-10}$ $farads/m$, so that $\tau \sim 10^{-9}$ s [48]. Since the highest frequency considered below is 0.1 Hz, and because macroscopic concentration gradients are not imposed (*cf.* assumption 5), the Debye layers may be considered to be in quasi-equilibrium.

4. The equation of momentum conservation (2.2) ignores an acceleration term which has the form [11,12,13] $\rho\partial_t^2\vec{u}$, where ρ is an average mass density. To estimate the error incurred by dropping this term, consider its size relative to the terms kept, *e.g.* $(2G+\lambda_l)\nabla^2 u_y$, where u_y is a horizontal displacement (§3). If the ∇ operator has length scale at most L, then the acceleration term would have a non-dimensional coefficient c of the form $c = \rho L^2 f^2/(2G + \lambda_L)$. Since gradients will occur over a length scale on the order of the cartilage depth, $L = 10^{-3}$ m is a reasonable choice here. Using $\rho = 10^3$ kg/m^3,, $f = 1Hz$, and $2G + \lambda_L = 10^5$ Nm^{-2} gives $c = 10^{-8}$. Thus inertia and acoustic propagation are not significant for the range of frequencies or material properties studied here.

5. *In vitro* experiments have been successful at maintaining constant temperatures, and show that the chemical composition of the cartilage samples are not drastically different after mechanical and or electrical stimuli are imposed [32,33,34,63]. Also, the majority of researchers have found that nearly 100% of the interstitial water in cartilage is freely exchangeable, *i.e.* is not reacting with the collagen or PGAs [76]. Further, there is substantial evidence that the major ionic solutes in the interstitial fluid (*e.g.* Na^+ and Cl^-) do not react or bind chemically with the macromolecules of the extracellular matrix [44,74]. There is little or no evidence suggesting that the assumptions of constant temperature and no reaction could not be realized in an *in vivo*

experiment of a sufficiently short time duration.

6. There is strong evidence suggesting that both the solid matrix and the interstitial fluid in articular cartilage act as though incompressible under the experimental conditions relevant to the current work [74]. By comparing the change of volume under load with the volume of fluid expressed, Maroudas [73] showed that the change in volume is virtually identical to the fluid lost. Also, there is evidence that the Darcy permeability (b_{11}^{-1} in equations 2.6) of cartilage is approximately isotropic in spite of the highly anisotropic structure of the material (*cf.* below). This was suggested by experiments by McCutchen [78], and verified more directly by Maroudas [72], who measured normal and tangential permeabilities. Because of the close relation between the Darcy permeability and the other electrokinetic coupling coefficients suggested by micromodels [25], the scalar (rather than tensor) form of the b_{ij} used in equations 2.6 is reasonably justified. The tensor form would be appropriate in cases for which anisotropy is deemed important.

   Further, in spite of the fact that articular cartilage is neither isotropic nor homogeneous, many predictions based on isotropy and homogeneity have closely matched experimental results [35,36,60,61,64,83]. It is clear, however that the porosity, charge density, and collagen structure and content, are all dependent on depth from the articular surface [44,71,74,84,88]. Furthermore, the total collagen and proteoglycan contents and content profiles (as a function of depth) varies significantly between individuals, and between joints of a given individual [88]. Neighboring regions from a given joint, however, have less marked differences. Diagnostic interpretations of electromechanical measurements will thus depend strongly on the latter.

7. The use of Darcy's law and equations like 2.6 have also had a great deal of success in predicting one-dimensional experiments [35,64,83]. The main consideration which must be addressed in using this law is the dependence of the permeability (and, by implication, the other b_{ij}) on such factors as strain and pressure. Mow and co-workers [52,84] have used pressure and strain-dependent permeability to fit one-dimensional permeation data [83] using a phenomenological relationship like equation 1.8. Maroudas [74] has also measured a dependence of permeability on porosity (and thus strain), but did not find a pressure dependence. The effect of non-linearities in the poroelastic behavior of articular cartilage is a topic of current investigation [52,58,60,69,83,84]. The inclusion of non-linear effects may improve the fit of some types of material parameters [64], but for small, one-dimensional deformations the linear relation 2.6 is able to accurately predict data values under a wide variety of conditions.

8. The use of linear mechanics is consistent with the use of a linear phenomenological relation 2.6, and linear conservation of mass equation 2.1 (*cf.* §2.3.2). In fact, linear elasticity seems to predict the one-dimensional equilibrium stress-strain relation for strains as high as 15% [25,26]. Also, the effects of the intrinsic viscoelasticity of the solid matrix on the time dependent behavior of articular cartilage are currently being examined [68,84].

2.3.2 Mathematical Considerations

This section will derive the equation of conservation of mass 2.1 in detail. In particular, the size of non-linear terms left out of the equations of mass will be considered. The error due to ignoring the quadratic terms in the stress and strain tensors is similar to that in single-phase elasticity, and is discussed by other authors [70].

The roles of inhomogeneities and non-linear constitutive properties was discussed in §2.3.1. Also, the assumption that there is no coupling of the relative rotation of the fluid to the stress tensor in the solid made by some authors [83] is not required in the current model because of equation 2.7. The development of this section is based in part on analysis done by Mow *et al.* [83].

Consider first the separate equations of mass conservation for the fluid and solid constituents. If there is no chemical reaction, then

$$\partial_t \rho^{s,f} + \vec{\nabla} \cdot (\rho^{s,f} \vec{v}^{s,f}) = 0 \, , \tag{2.14}$$

where $\rho^{s,f}$ is the mass of solid (fluid) per unit total volume. The densities also obey the relation [83]

$$\rho^s \rho_T^f + \rho^f \rho_T^s = 0 \, , \tag{2.15}$$

where $\rho_T^{s,f}$ is the "true" density: solid (fluid) mass per unit solid (fluid) volume. Assuming that the constituents are incompressible gives

$$\rho^{s,f}(t) = \rho^{s,f}(0) \, ,$$

so that taking ∂_t of equation 2.15, solving 2.15 for ρ^f, and using 2.14 gives the kinematic relation (also stated by [83])

$$\vec{\nabla} \cdot \vec{v}^f + \alpha \vec{\nabla} \cdot \vec{v}^s + (\vec{v}^s - \vec{v}^f) \cdot \vec{\nabla} \ln \rho^s = 0 \, , \tag{2.16}$$

where

$$\alpha \equiv \frac{\rho_T^f \rho^s}{\rho_T^s \rho^f} \equiv \phi^{f^{-1}} - 1 \, ,$$

is the solid content volume of solid per volume of fluid, and ϕ^f is the porosity, volume of fluid per total volume.

The usual solid and fluid dilitations (in equation 2.1),

$$e \equiv \vec{\nabla} \cdot \vec{u} \qquad \text{and} \qquad \partial_t \eta \equiv -\vec{\nabla} \cdot \vec{v}^s \, . \tag{2.17}$$

must now be expressed in terms of the above notation. First, define $\tilde{\eta}$ and $\tilde{e}$ by

$$\rho^f = \rho^f(t=0)\;(1+\tilde{\eta}) \qquad \text{and} \qquad \rho^s = \rho^s(t=0)\;(1-\tilde{e})\;. \tag{2.18}$$

Using $\vec{v}^s = \partial_t \vec{u}$, assuming that the initial density of the solid is uniform, $grad\rho^s(t=0)=0$, substituting 2.10 into 2.1 and dividing by $-\rho^s$ gives

$$\partial_t \tilde{e} + (\tilde{e}-1)\partial_t e + \vec{\nabla} e \cdot \vec{v}^s = 0\;. \tag{2.19}$$

Thus

$$e = \tilde{e} + \int_0^t \vec{\nabla}\cdot(\tilde{e}\vec{v}^s)dt\;, \tag{2.20}$$

where $\tilde{e}(t=0) = e(t=0) = 0$ has been used. Thus the total error in assuming that the relative change in mass density of the solid phase is e is the integral of the divergence of a field proportional to the actual change in relative density and to the velocity of the solid matrix. A parallel for the fluid phase gives ($\eta(t=0)\equiv 0$)

$$\eta = \tilde{\eta} + \int_0^t \vec{\nabla}\cdot(\tilde{\eta}\vec{v}^f)dt\;, \tag{2.21}$$

which has a similar interpretation. It is thus reasonable to make the linear approximations

$$e = \tilde{e} \qquad \text{and} \qquad \eta = \tilde{\eta} \tag{2.22}$$

in 2.18 as long as fluid and solid displacements are small, *e.g.* ,

$$\int_0^t \vec{\nabla}\cdot(\eta\vec{v}^f)dt/\eta \ll 1\,. \tag{2.23}$$

Note that the only integrals of fluid and solid velocities appear in equations 2.20 and 2.21, so that it is only the magnitude of the displacements are relevant to the approximations 2.22.

To complete the derivation of 2.1, equations 2.22 will be used to simplify 2.16.

To this end, expand α in terms of $\tilde{e}$ and $\tilde{\eta}$:

$$\begin{aligned} \alpha &= \frac{\rho_T^f \rho^s(t=0)}{\rho_T^s \rho^f(t=0)} \frac{1-\tilde{e}}{1+\tilde{\eta}} \\ &= \frac{\rho_T^f \rho^s(t=0)}{\rho_T^s \rho^f(t=0)} (1 + O(\tilde{\eta}^2, \tilde{e}^2, \tilde{\eta}\tilde{e})) \\ &= \alpha(t=0) + \text{h.o.t.} \equiv \alpha_0 + \text{h.o.t.}. \end{aligned} \tag{2.24}$$

Also, using $\vec{\nabla}\rho^s(t=0) = 0$ yields

$$\begin{aligned} \vec{\nabla} \ln \rho^s &= \vec{\nabla} \ln \rho^s(t=0)\ (1-\tilde{e}) \\ &= \tfrac{-\vec{\nabla}\tilde{e}}{1-\tilde{e}}\,. \end{aligned} \tag{2.25}$$

Now substituting 2.22, 2.24 and 2.25 into 2.16 gives

$$-\partial_t \eta + \alpha_0(1-e-\eta)\partial_t e - \alpha_0(1-e-\eta)(\vec{v}^s - \vec{v}^f)\vec{\nabla} e + \text{h.o.t.} = 0\,. \tag{2.26}$$

This may be recognized, by using 2.17, to be equation 2.1 with (lowest order) error terms

$$\alpha_0(e+\eta)\partial_t e + \alpha_0(\vec{v}^s - \vec{v}^f)\vec{\nabla} e\,.$$

Integrating these terms in time shows, as for equations 2.20 and 2.21, that the mass relation 2.1 does not require that fluid or solid velocities are small, but only that the dilitations and displacements are small. This implies that constraints on using the linear differential form of mass conservation for poroelastic media are no more stringent than those on using the linear equations of momentum conservation.

Appendix 2A: The Response of a Rigid Conductor

To judge the magnitude of Φ it is useful to consider the response of a rigid, single phase conducting slab of thickness δ^s and conductivity σ. Inside the conductor we have

$$\begin{aligned} \vec{\nabla} \times \vec{E} &= 0 \\ \vec{\nabla} \cdot \epsilon\vec{E} &= \rho \\ \vec{\nabla} \cdot \vec{J} &= -\partial_t \rho \\ \vec{J} &= \sigma\vec{E} \end{aligned} \qquad (2.27)$$

which correspond to Faraday's law, Gauss' law, conservation of charge, and Ohm's law. The electroquasistatic assumption 3 on page 33 now gives $\partial_t \rho \ll \partial_y J_y,\ \partial_z J_z$. Assuming further that $\vec{\nabla}\sigma = 0$, equations 2.27a, 2.27c and 2.27d give

$$\vec{\nabla}^2 \Phi = 0.$$

where Φ is the electrical potential with $\vec{E} = -\vec{\nabla}\Phi$. If subjected to the electrical boundary conditions in equations 4.1, the result is

$$\vec{J} = \begin{pmatrix} i \cosh \delta(z+1) \\ \sinh \delta(z+1) \end{pmatrix} \frac{J_0}{\sinh \delta} e^{i(ky-\omega t)} \qquad (2.28)$$

and,

$$\Phi = -\frac{\cosh \delta(z+1)}{k\sigma \sinh \delta}. \qquad (2.29)$$

The maximum magnitude of Φ in 2.29 corresponding to the values used above ($J = 1\mu A/mm^2$, $\sigma = 1mho/m$, and $\delta = 10^{-3}m$) is

$$|\Phi|_{max} = \begin{cases} 2.86mV & \lambda = 10mm \\ 0.159mv & \lambda = 1mm \\ 0.0159mv & \lambda = .1mm \end{cases} \qquad (2.30)$$

These values are very close to those in table 1.

There are two additional considerations. First, if the fixed charge density of the solid matrix reverses sign, so do b_{12} and b_{21}, but Φ does not. This property is preserved by equations 3.24, 4.5, and 2.29. Second, there are two choices for σ

in 2.29:

$$\begin{aligned} \sigma = \quad & b_{22}^{-1} && = \text{no-flow conductivity, } \vec{U} = 0 \end{aligned} \tag{2.31}$$

and,

$$\sigma = \quad (b_{22} - \tfrac{b_{12}b_{21}}{b_{11}})^{-1} \quad = \text{open-flow conductivity, } \vec{\nabla} P = 0.$$

The former is necessarily smaller, as the fluid drag on migrating ions is larger with the fluid "held in place." Since the boundary conditions 4.1 in §4.1 resemble this more closely, $\sigma = b_{22}^{-1}$ was used in equation 2.30 above.

Appendix 2B: The Momentum Equations in Radial Coordinates

Many problems in poroelasticity have boundary conditions for which cylindrical polar coordinates are more appropriate, The momentum equations 2.2 are thus presented here in cylindrical radial coordinates for reference. (The other model equations, 2.1, 2.5, 2.6, and 2.7 are easily written in coordinate form using standard vector identities.) In these coordinates, equations 2.2 become [40]

$$\begin{aligned}
\frac{1}{r}(\partial_r(r\sigma_{rr}) + \partial_\theta\sigma_{rz} - \sigma_{\theta\theta}) + \partial_z\sigma_{rz} - \partial_r P &= 0 \\
\frac{1}{r}(\partial_r(r\sigma_{\theta r}) + \sigma_{\theta r} + \partial_\theta\sigma_{\theta\theta}) + \partial_\theta\sigma_{\theta z} - \frac{1}{r}\partial_\theta P &= 0 \qquad (2.32) \\
\frac{1}{r}(\partial_r(r\sigma_{zr}) + \sigma_{z\theta} + \partial_z\sigma_{zz} - \partial_z P &= 0\,. \qquad (2.33)
\end{aligned}$$

The six independent strain coordinates are now

$$\begin{aligned}
\epsilon_{rr} &= \partial_r u_r & \epsilon_{r\theta} &= \tfrac{1}{2}(\partial_r u_\theta + \tfrac{1}{r}(\partial_\theta u_r - u_\theta)) \\
\epsilon_{\theta\theta} &= \tfrac{1}{r}(\partial_\theta u_\theta + u_r) & \epsilon_{\theta z} &= \tfrac{1}{2}(\partial_z u_\theta + \tfrac{1}{r}\partial_\theta u_z) \\
\epsilon_{zz} &= \partial_z u_z & \epsilon_{zr} &= \tfrac{1}{r}(\partial_z u_r + \partial_r u_z)\,.
\end{aligned} \tag{2.34}$$

If $\partial_z = u_z = 0$ is assumed, substituting 2.34 into 2.3 and the result into 2.32 yields

$$\begin{aligned}(2G+\lambda_L)[\partial_r \tfrac{1}{r}\partial_r r u_r + \partial_r \tfrac{1}{r}\partial_\theta u_\theta] + G\tfrac{1}{r^2}[\partial_\theta^2 u_r - \partial_\theta \partial_r r u_\theta] - \partial_r P &= 0 \\ (2G+\lambda_L)\tfrac{1}{r^2}[\partial_\theta \partial_r r u_r + \partial_\theta^2 u_\theta] + G[\partial_r \tfrac{1}{r}\partial_r r u_\theta - \partial_r \tfrac{1}{r}\partial_\theta u_r] - \tfrac{1}{r}\partial_\theta P &= 0.\end{aligned}$$

Chapter 3

Solution of the Governing Equations

This chapter presents the general, two-dimensional solutions of the governing equations 2.1 – 2.6. In the first section the equations will be non-dimensionalized and Fourier transformed, while the following sections will present "particular" and "homogeneous" solutions. The homogeneous solutions will then be interpreted physically to gain insight into the implications of the model.

3.1 Non-dimensionalization and Transformation

Because equations (2.1-2.6) are linear, superposing solutions that have a single wavelength and frequency yields solutions to a large class of time and space dependent problems. Because of the isotropy and homogeneity of the problem, rotating and superposing the solutions to such two-dimensional problems produces the solutions to three-dimensional problems.

Because of the above characteristics, the solutions to two dimensional cases will be found *via* complex amplitudes. This is equivalent to using Fourier transforms and assuming all fields have a single wavelength and frequency. To do this, the equations will first be non-dimensionalized by assuming that there is a current or potential excitation with angular frequency ω $(= 2\pi f)$ and wavenumber k $(= 2\pi/\lambda)$ imposed on the surface. The choice of current is due to convenience in finding the "particular solns" (*cf.* below) and in solving problems with electrical forcing (as will be seen in Chapter 4); displacement or velocity would have been equally appropriate. This generates solutions which may be expressed in the form

$$\begin{aligned} u_y^* &= a_J u_y(z) e^{i(ky^*-\omega t)} \\ u_z^* &= a_J u_z(z) e^{i(ky^*-\omega t)} \end{aligned} \tag{3.1}$$

$$\begin{aligned} v_y^* &= J_0 \tfrac{b_{12}}{b_{11}} v_y(z) e^{i(ky^*-\omega t)} \\ v_z^* &= J_0 \tfrac{b_{12}}{b_{11}} v_z(z) e^{i(ky^*-\omega t)} \end{aligned} \tag{3.2}$$

$$\begin{aligned} V_y^* &= J_0 \tfrac{b_{12}}{b_{11}} V_y(z) e^{i(ky^*-\omega t)} \\ V_z^* &= J_0 \tfrac{b_{12}}{b_{11}} V_z(z) e^{i(ky^*-\omega t)} \end{aligned} \tag{3.3}$$

$$\begin{aligned} P &= J_0 \delta^* b_{12} p(z) e^{i(ky^*-\omega t)} \\ S &= J_0 \delta^* b_{12} s(z) e^{i(ky^*-\omega t)} \\ \sigma_{yz}^* &= J_0 \delta^* b_{12} \sigma_{yz}(z) e^{i(ky^*-\omega t)} \end{aligned} \tag{3.4}$$

$$\begin{aligned} J_y &= J_0 j_y(z) e^{i(ky^*-\omega t)} \\ J_z &= J_0 j_z(z) e^{i(ky^*-\omega t)} \end{aligned} \tag{3.5}$$

and,

$$\Phi = J_0 \delta^* b_{22} \phi(z) e^{i(ky^*-\omega t)} \tag{3.6}$$

with

$$z = \frac{z^*}{\delta^*}, \qquad \text{and} \qquad a_J = J_0 \frac{\delta^{*2} b_{12}}{G + \lambda_L}, \tag{3.7}$$

where u_y and u_z are the horizontal and vertical solid displacement fields, v_y, v_z, V_y, and V_z are the horizontal and vertical laboratory frame and relative fluid velocities

(respectively), $S = -\sigma_{33}$ is the force per unit total area exerted on a plane of constant z (defined so as to be positive in compression), σ_{yz} is the shear force in the y direction on a plane of constant z, J_y and J_z are horizontal and vertical current densities, δ^* is the (dimensional) thickness of the layer, and b_{ij} are the coupling coefficients of equation 2.6. All "$*$" variables are dimensional (*cf.* Appendix C for notation).

The transformed equations are found by substituting equations 3.1 through 3.6 into 2.1 through 2.7a, giving

$$\alpha_0 r(\delta u_y - iu'_z) + i\delta v_y + v'_z = 0 \tag{3.8}$$

$$\left.\begin{aligned} p - i\delta^{-1}V_y &= -i\delta^{-1}\dot{j}_y & (a) \\ p' + V_z &= \dot{j}_z & (b) \\ \phi + ib_c\delta^{-1}V_y &= i\delta^{-1}\dot{j}_y & (c) \\ \phi' - b_c V_z &= -\dot{j}_z & (d) \end{aligned}\right\} \tag{3.9}$$

$$i\delta v_z - \delta r u_z - v'_y - iru'_y = 0 \tag{3.10}$$

and,

$$\left.\begin{aligned} 2(1-\nu)(u''_y - \delta^2 u_y) + i\delta u'_z - u''_y - i\delta p &= 0 \\ 2(1-\nu)(u''_z - \delta^2 u_z) + \delta^2 u_z + i\delta u'_y - p' &= 0\,. \end{aligned}\right\} \tag{3.11}$$

These equations use the relation $\frac{2G+\lambda_L}{G+\lambda_L} = 2(1-\nu)$, with ν the Poisson ratio, and the definitions

$$r \equiv \frac{\omega b_{11}\delta^{*2}}{\lambda_L + G} = \left(\frac{\delta^*}{\Delta^*}\right)^2 2(1-\nu)\phi_0 \tag{3.12}$$

$$b_c \equiv \frac{b_{12}b_{21}}{b_{11}b_{22}} \tag{3.13}$$

$$\delta \equiv k\tilde{\delta} \tag{3.14}$$

and,

$$\left.\begin{aligned} V_y &= v_y + iru_y \\ V_z &= v_z + iru_z \end{aligned}\right\} \tag{3.15}$$

for the relative velocity. (Δ^* is discussed below equation 3.26 and in §3.3.)

3.2 Solution

3.2.1 The Particular Solutions

To find a general solution to the above equations, we proceed as follows. If " ′ " denotes $\frac{d}{dz}$, then substituting 3.6 into 2.5 and 2.7b gives

$$j_z'' - \delta^2 j_z = 0 \tag{3.16}$$

where $\delta = k\delta^*$. Thus the current density satisfies

$$j_z = k_7 e^{\delta z} + k_8 e^{-\delta z}, \tag{3.17}$$

with k_7, and k_8 constants to be determined. Also (from 2.5 and 2.7b),

$$j_y = i\delta^{-1} j_z' = ik_7 e^{z} - ik_8 e^{-z}. \tag{3.18}$$

Thus $\vec{J}$ will be treated as a known inhomogeneity in equations 3.8 to 3.11.

To obtain the general particular solutions, it is assumed that there exists a particular solution for which there is no relative velocity, *i.e.* $\vec{V} = 0$. In this case equations 3.9 give p^p and ϕ^p immediately (below). Using 3.15 and 3.8 we find that

$$u_z^{p\,\prime} = -i\delta u_y^p\,. \tag{3.19}$$

Substituting for u_y and u_z in 3.11 gives the two equations

$$\begin{aligned} n(u_z^{p\,\prime\prime\prime} - u_z^{p\,\prime}) &= \delta^2 p^p \\ n(u_z^{p\,\prime\prime} - u_z^p) &= p^{p\,\prime}\,, \end{aligned} \tag{3.20}$$

where $n \equiv 1 - 2\nu$. These two equations are consistent, however, and lead to the general particular solutions to equations 3.8 to 3.11:

$$X^P(z; k_7, k_8) \equiv (u_y^p, u_z^p, v_y^p, v_z^p, p^p, s^p, \sigma_{yz}^p, \phi^p, j_y^p, j_z^p)^T$$

are given by (j_z^p and j_y^p are j_z and j_y of equations 3.17 and 3.18)

$$\begin{array}{rcll} u_y^p & = & \frac{i}{2n\delta^2}[k_7e^{\delta z} - k_8e^{-\delta z} + \gamma(k_7e^{\delta z} + k_8e^{-\delta z}) & \\ & & \qquad + \delta(k_8 - k_7)\cosh\gamma/\sinh\delta] & (a) \\ u_z^p & = & \frac{1}{2n\delta^2}[\gamma(k_7e^{\delta z} - k_8e^{-\delta z}) + \delta(k_8 - k_7)\sinh\gamma/\sinh\delta] & (b) \\ v_y^p & = & -iru_y^p & (c) \\ v_z^p & = & -iru_z^p & (d) \\ p^p & = & \delta^{-1}(k_7e^{\delta z} - k_8e^{-\delta z}) & (e) \\ s^p & = & p^p + 2in\delta u_y^p & (f) \\ \sigma_{yz}^p & = & i\delta^{-1}[k_7e^{\delta z} + k_8e^{-\delta z} + \gamma(k_7e^{\delta z} - k_8e^{-\delta z}) & \\ & & \qquad + \delta(k_8 - k_7)\sinh\gamma/\sinh\delta] & (g) \\ \phi^p & = & -p^p & (h) \end{array} \qquad (3.21)$$

In the above, $\gamma = \delta(z+1)$, and equations 3.4 and 2.3 have been used in the form

$$s = p - 2(1-\nu)u_z' - 2i\delta\nu u_y \; . \qquad (3.22)$$

The same two equations yield

$$\sigma_{yz} = 2n(u_y' + i\delta u_z) \; , \qquad (3.23)$$

from which 3.21g was derived. Note that because $\vec{V}^p = 0$, the particular solutions should have no dissipative loss from the Darcy's law part of equation 2.6. This is true, as evidenced by the frequency only appearing as a scaling factor in the velocities in the equations above (r is the non-dimensional frequency).

3.2.2 The Homogeneous Solutions

Now the task is to find the homogeneous solutions to equations 3.8 through 3.11 corresponding to $k_7 = k_8 = 0$ (*i.e.* $\vec{J} = 0$) and a particular solution due to the current in equations 3.9. By substituting constants multiplied by exponentials of z into the equations, the solutions are easily found to be

$X^H(z; k_1, k_2, k_3, k_4, k_5, k_6, k_7, k_8) \equiv$

$$\begin{pmatrix} u_y^H \\ u_z^H \\ v_y^H \\ v_z^H \\ p^H \\ s^H \\ \sigma_{yz} \end{pmatrix} = k_1 \begin{pmatrix} i \\ 1 \\ r \\ -ir \\ 0 \\ -2n\delta \\ 2in\delta \end{pmatrix} e^{\delta z} + k_2 \begin{pmatrix} -i \\ 1 \\ -r \\ -ir \\ 0 \\ 2n\delta \\ 2in\delta \end{pmatrix} e^{-\delta z} + k_3 \begin{pmatrix} i\delta^{-1} + iz \\ z \\ \frac{r}{\delta} - 2in\delta + rz \\ -2n\delta - irz \\ 2n \\ -2n\delta z \\ 2in(\delta z + 1) \end{pmatrix} e^{\delta z} \quad (3.24)$$

$$+ k_4 \begin{pmatrix} i\delta^{-1} - iz \\ z \\ \frac{r}{\delta} - 2in\delta - rz \\ 2n\delta - irz \\ 2n \\ 2n\delta z \\ 2in(\delta z - 1) \end{pmatrix} e^{-\delta z} + k_5 \begin{pmatrix} i \\ \Lambda \\ -\alpha_0 r \\ i\alpha_0 \Lambda r \\ -i\frac{r}{\delta\phi_0} \\ -2n\delta \\ 2in\delta\Lambda \end{pmatrix} e^{\Lambda\delta z} + k_6 \begin{pmatrix} -i \\ \Lambda \\ \alpha_0 r \\ i\alpha_0 \Lambda r \\ i\frac{r}{\delta\phi_0} \\ 2n\delta \\ 2in\delta\Lambda \end{pmatrix} e^{-\Lambda\delta z},$$

where $k_1, \cdots, k_6$ are constants (in y, z, and t) to be determined, and

$$\begin{aligned} \Lambda &= \sqrt{1 - i\Delta^{-2}} \\ &(\Re(\Lambda) > 1). \end{aligned} \quad (3.25)$$

Here

$$\Delta = k\Delta^*,$$

and

$$\Delta^* \equiv \sqrt{\frac{(2G+\lambda_L)\phi_0}{b_{11}\omega}} \tag{3.26}$$

is the diffusion boundary layer thickness. Note also that

$$\phi^H = -b_c p^H \; . \tag{3.27}$$

Given the general particular solutions, X^P, in §3.2.1, the complete solution of equations 3.8 to 3.11 are now simply $X^H + X^P$. Thus any solution to the untransformed equations 2.1 to 2.6 (with well-posed boundary conditions) may be constructed by superposing (properly rotated) this solution over k and ω.

The crux of the solution now lies in the determination of $k_1, \cdots, k_8$.

3.3 Physical Interpretation of the Homogeneous Solutions

Each of the six solution vectors of equation 3.24 may be understood in terms of a specific physical behavior. The first two (those multiplied by k_1 and k_2) satisfy

$$\vec{\nabla} \cdot \vec{u} = \vec{\nabla} \cdot \vec{v}^f = 0. \tag{3.28}$$

Further, there is no relative motion between the fluid and the solid, resulting in the lack of pressure or potential fields. Thus these "modes" represent the motion of a monophasic incompressible medium of moduli G and λ_L. The motion is a quasi-static two-dimensional shear wave traveling in the y-direction. (This wave is not acoustic; *cf.* assumption 4 on page 33 .) Because of the isotropy of the model, there exist similar waves traveling in the x- and z-directions, decaying in planes normal to the direction of travel[1]. The vertical decay of the fields over a length scale of λ is not due to damping, as there is no frictional loss in this motion. The decay results from the Laplacian nature of the momentum equations.

---

[1] Analogous statements may be made about the other four solutions as well. The symmetry of all six solutions with respect to reflection about the x, y-plane is also due to the isotropy of the model.

The second pair of solutions also obeys equations 3.28. Thus this motion also represents shear waves traveling through the biphasic medium. In this case, though, the relative motion is given by

$$V_y = \pm V_z = -2in\delta e^{\pm\delta z}.$$

Both the decay length and the amplitude of the pressure field are independent of the frequency of the imposed disturbance (for a fixed $\vec{V}$). Further, the amplitude of the pressure is proportional to b_{11}, the Darcy resistivity. From equation 3.24 we see that these modes have a plane of zero normal stress at $z = 0$. These solutions thus correspond to a semi-infinite slab driven by shear with no normal surface ($z = 0$) stress. For example, with displacement applied at $z = 0$ such that there is no normal stress (at $z = 0$), there is damping and energy dissipation in the bulk. This mode is like a steady Darcy flow through a medium, here modified to satisfy the two-dimensional drive and mechanics of the system. Displacement does not change with f, while the relative velocities are proportional to f. In the limit $\lambda \to \infty$, the resulting Darcy-like flow corresponds to a y-directed relative velocity which decreases linearly with depth. Note, however, that

$$\phi^H = -b_e p^H,$$

so that there is a streaming potential here which is not predicted by the Darcy law limit ($\vec{J} = 0$) of our coupling equations 2.6. There is electrical energy dissipation here, so that strictly energetic considerations show that the "Darcy" coefficient is different here than that predicted in a system not including electrokinetic effects.

The last two modes contain all of the dynamics of the system. For these two solutions, equation 3.28 no longer holds, and both phases undergo both shear and compression. These modes are most easily understood by considering the two limits $\Delta \to 0$ and $\Delta \to \infty$.

$\Delta \to 0$:

In this limit the frequency is high enough that the diffusion boundary layer thickness is a vanishing fraction of a wavelength. Thus it will be important in the long-wave limit (*cf.* §4.2.2). We have

$$\Lambda \sim \Delta^{-1} e^{-i\frac{\pi}{4}} + O(\Delta), \tag{3.29}$$

so that

$$\Lambda \delta z \sim \frac{z^*}{\Delta^*} e^{-i\frac{\pi}{4}} + O(\Delta k z^*). \tag{3.30}$$

It is now clear that, in these modes, all of the fields oscillate and decay over a length of order Δ^*: the behavior is that of a diffusive boundary layer of thickness Δ^*.

The relative magnitudes of the fields are also easily interpreted. If the fifth mode is scaled so that we have a solution to the problem of a semi-infinite slab with a displacement of magnitude a_J at the surface we obtain (dimensionally)

$$\left.\begin{pmatrix} u_y^H \\ u_z^H \\ v_y^H \\ v_z^H \\ p^H \end{pmatrix}\right|_{k_5 = \delta/\Lambda} \sim \begin{pmatrix} \Delta e^{3i\frac{\pi}{4}} \\ 1 \\ \alpha_0 \omega \Delta e^{-3i\frac{\pi}{4}} \\ i\alpha_0\omega \\ (2G + \lambda_L)\frac{1}{\Delta^*} e^{-i\frac{\pi}{4}} \end{pmatrix} a_J e^{i(ky^* - \omega t) + \Lambda \delta z} \tag{3.31}$$

(once again, $\phi^H = -b_c p^H$). First, note that the ratio of fluid velocity to displacement (in the y- or z-direction) is that of solid to fluid volume. Since both constituents are here modeled as incompressible, the conservation of mass is accomplished by the exchange of volume between fluid and solid. Also, the horizontal motions are a factor of Δ smaller than the vertical. As expected in a normal boundary layer, the secondary, or generated motion is much smaller than that imposed.

The characteristic pressure is also informative. Equation 3.31e shows that the pressure is proportional to the uniaxial modulus of the material, with the force increasing with the ratio of displacement to boundary layer thickness. $\mathcal{P}$ may also be written

$$\mathcal{P} = \begin{cases} \phi_0^{-1} b_{11} \Delta^* \omega a_J \, e^{-i\frac{\pi}{4}} \cdots & (a) \\ \sqrt{\phi_0^{-1}(2G + \lambda_L) b_{11} a_J^2 \omega} \, e^{-i\frac{\pi}{4}} & (b) \end{cases} \tag{3.32}$$

Equation 3.32a has $\mathcal{P}$ proportional to the matrix resistance b_{11} acting over a length Δ^* on a characteristic velocity ωa_J. Equation 3.32b gives $\mathcal{P}$ as the geometric average of the modulus of the solid matrix and the matrix resistance b_{11} acting over a length a_J on the velocity ωa_J. The dynamics are thus expressed as the balance of the elastic (solid) and resistive (dissipative) forces.

The relative phases of the variables are also understandable. The fluid and solid velocities are 180° out of phase, as expected in a dissipative limit. Also, the pressure leads the vertical displacement by 45°.

$\Delta \rightarrow \infty$:

In this limit, f is so low (or λ so short) that the diffusion depth is much greater than the length scale of the disturbance (λ). This is the quasistatic limit, which yields

$$\Lambda \sim 1 - \frac{i}{2}\Delta^{-2} + \mathcal{O}(\Delta^{-4}) \tag{3.33}$$

so that

$$\Lambda \delta z \sim kz^* + \mathcal{O}\left(\frac{z^*/\Delta^*}{\Delta}\right). \tag{3.34}$$

Thus none of the three pairs of homogeneous solutions have any frequency dependence (to first order), as expected. Note, however, that $V_y, V_z \neq 0$ in these (k_5, k_6) modes, and that they are still the only way to transmit compression waves. The frequency is now so low that the only length scale (other than a_J) is λ. Further, equations 3.31 and 3.32a are now true if Δ^* is replaced by k^{-1}. Thus the interpretations given to equations 3.31 and 3.32a are easily modified to this case.

Chapter 4

The Current Forced Response

4.1 Introduction

This chapter describes the response of an infinite sheet of "tissue" of finite thickness to a surface probe which imposes a known normal current density to the articular surface. We consider an infinite, planar, poroelastic sheet of finite thickness (figure 4.1). There is no displacement or transverse fluid flow at the bottom surface, and the top is covered by a fluid and subjected to one of a variety of mechanical and electrical boundary conditions (discussed below). The desired results are *e.g.*, the solid displacement, fluid velocity, and electric fields in the bulk, and the mechanical stress and electrical potential at the surface.

First, a method of solution appropriate for the boundary conditions of interest will be described. Next, the results of numerical calculations and asymptotic long- and short-wave analyses for two cases will be presented. The predictions of the long-wave limit of the model will be found to agree with data from experiments corresponding to this limit.

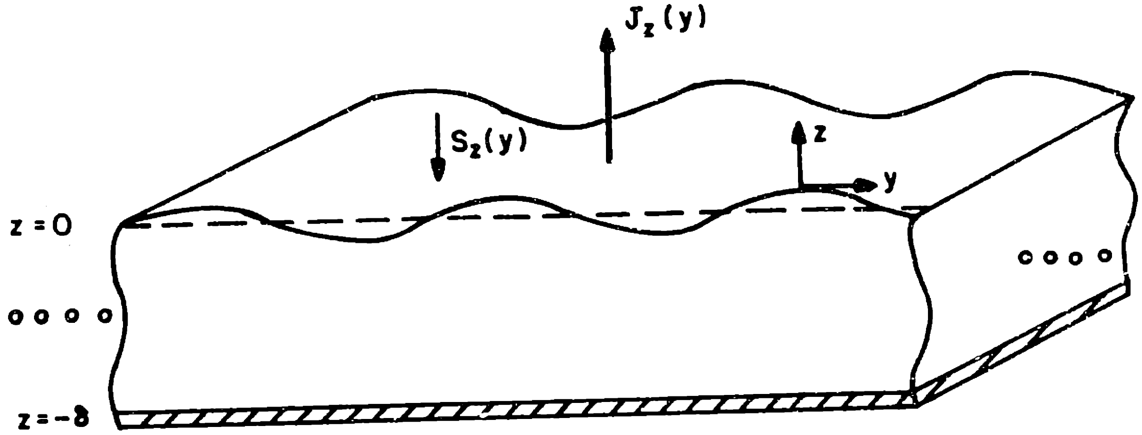

Figure 4.1: Geometry and boundary conditions for current forcing. A two-dimensional sinusoidal current density is applied to the top of a δ^*-thick layer. The top and bottom are constrained so that there is no motion of the solid matrix or normal fluid flow. The bottom is in contact with an insulator, so there is no vertical current density there. The top electrode is segmented to allow measurement of $\Phi(y, z = 0)$.

4.2 Results

This chapter treats two boundary value problems involving two-dimensional surface stimulation of the tissue layer of figure 4.1:

Case 1: the displacement, velocity, pressure, potential, and current density fields due to a vertical current density applied to the top surface;

and

Case 2: the displacement, velocity, pressure, potential, and current density fields due to a potential applied to the top surface.

The corresponding boundary conditions are:

Case 1:

$$\begin{array}{llll} u_y(0)=0 & u_z(0)=0 & V_z(0)=0 & j_z(0)=1 \\ u_y(-1)=0 & u_z(-1)=0 & V_z(-1)=0 & j_z(-1)=0 \end{array} \tag{4.1}$$

and

Case 2:

$$\begin{array}{llll} u_y(0)=0 & u_z(0)=0 & V_z(0)=0 & \phi(0)=1 \\ u_y(-1)=0 & u_z(-1)=0 & V_z(-1)=0 & j_z(-1)=0 \end{array}$$

The mechanical boundary conditions correspond to no displacement of the solid matrix at the top or bottom surface, and no normal fluid flow at the top or bottom surfaces. Note that the condition $V_z(0) = 0$ for no normal velocity relative to the top surface is the linearization of the condition

$$\hat{n} \cdot \vec{V} = J_0 \frac{b_{12}}{b_{11}} (V_z - \frac{a_J}{\delta_*} V_y \partial_y u_z) , \tag{4.2}$$

where V_y, V_z, and u_z are considered to be non-dimensional (*à la* equations 3.3 and 3.1) functions of y, z, and t. Thus this condition will only be valid when the second term above is small. Because $u_z(y, z = 0, -1) = 0$ here, however, this linearization becomes exact at both boundaries.

The electrical conditions represent the material being supported by an insulating substance. At the top surface either a normal current is injected or a potential is prescribed. These conditions were chosen because they simulate a probe that could measure the electromechanical properties of, *e.g.*, a layer of cartilage on bone *in vivo*[1]. With the given boundary conditions, it would be appropriate to measure the resulting surface stress ($s(0)$) and potential (or current) at the surface.

It is clear from these boundary conditions and the linearity of the model that the solution to case 2 may be obtained by rescaling that of case 1:

$$A_{\text{case 2}} = \frac{A_{\text{case 1}}}{\phi(0)_{\text{case 1}}},$$

where A is any field variable. Since, the denominator above is always very close to unity (*cf.* §4.2.2), the second case will not be described in detail in this work.

To solve the above problem it is only necessary to determine the $k_1, \cdots, k_8$ of §3.2. It is evident from equations 4.1 and 3.17 that

$$j_z = \sinh\gamma / \sinh\delta, \tag{4.3}$$

where $\gamma = \delta(z+1)$, so that

$$k_7 = \frac{e^{\delta}}{2\sinh\delta} \qquad \text{and} \qquad k_8 = -\frac{e^{-\delta}}{2\sinh\delta}. \tag{4.4}$$

The current density is thus known in closed form, and has the same form as that for a rigid conductor (*cf.* §2.3.2).The particular solutions corresponding to these

---

[1] It is known that $v_z(-1) \approx 0$ in adult articular cartilage due to the relative impermeability of the so-called "tidemark" interface between cartilage and subchondral bone [79]. In addition, the conductivity of the subcondral bone is known to be at least one to two orders of magnitude lower than that of cartilage [57].

k_7 and k_8 may be found from equations 3.21 of §3.2.1 to be:

$$\begin{aligned}
j_z^p &= \sinh\gamma/\sinh\delta \\
j_y^p &= i\cosh\gamma/\sinh\delta \\
u_y^p &= i\,\frac{(1-\delta\coth\delta)\cosh\gamma+\gamma\sinh\gamma}{2n\delta^2\sinh\delta} \\
u_z^p &= \frac{\gamma\cosh\gamma-\delta\coth\delta\sinh\gamma}{2n\delta^2\sinh\delta} \\
p^p &= \delta^{-1}\cosh\gamma/\sinh\delta \\
s^p &= p^p+2in\delta u_y^p \\
\sigma_{yz}^p &= i\,\frac{(1-\delta\coth\delta)\sinh\gamma+\gamma\cosh\gamma}{\delta\sinh\delta}
\end{aligned} \tag{4.5}$$

These particular solutions, along with the mechanical boundary conditions from equation 4.1, determine the boundary conditions appropriate for the homogeneous solutions, X^H.

4.2.1 Numerical Results

The coefficients k_1 through k_6 were calculated by inverting the matrix determined by equations 3.24, the six mechanical boundary conditions of equations 4.1, and the boundary contributions of equations 4.5. Matrix inversion was performed by the NAG Library routines F03ADF and F04AHF using double precision arithmetic. The parameter values used in the calculations correspond to those measured for cartilaginous connective tissue [25,34]:

$$\begin{pmatrix} b_{11} & b_{12} \\ b_{21} & b_{22} \end{pmatrix} = \begin{pmatrix} 1\cdot 10^{15}\frac{N\cdot s}{m^4} & 1\cdot 10^{7}\frac{V\cdot s}{m^2} \\ 1\cdot 10^{7}\frac{N}{A\cdot m} & 1\Omega\cdot m \end{pmatrix} \tag{4.6}$$

$$\begin{aligned}
&(2G+\lambda_L) = 5\cdot 10^6\frac{N}{m^2} \quad && \delta^* = 1mm \\
&\nu = 0.4 && \phi_0 = 0.8
\end{aligned} \tag{4.7}$$

Note that since the ratio Δ^*/δ^* ranged from .25 to .025, and because the wavelength was varied from ten times to one tenth the thickness of the medium, the results presented will be appropriate to many applications (the dimensional magnitudes may be rescaled easily). Thus the specific values chosen for $f, \lambda, 2G + \lambda_L$, and b_{ij} are not crucial. Studies of the effects of varying ν and ϕ_0 have only been performed for a slightly different set of boundary conditions in a long-wave case (§4.3).

Five sets of values were obtained. These correspond to λ fixed at $.1\,mm$ ("short-wave"), $1\,mm$, or $10\,mm$ ("long-wave") while f swept logarithmically through $.001\,Hz$ to $.1\,Hz$, and f fixed at $.001\,Hz$ ("low-frequency") or $.1\,Hz$ ("high-frequency") while λ swept logarithmically from $.1\,mm$ to $10\,mm$. The boundary conditions implied by the calculated k_i were checked against equations 4.1. The error in the boundary conditions was generally less than $10^{-8}\%$ over the range $\lambda > .1$mm, $.001\,Hz \leq f \leq .1\,Hz$, though errors as high as .03% occurred near $f = .1\,Hz$ and $\lambda = .1\,mm$. (Errors were calculated relative to the maximum amplitude at the corresponding f and λ.) Table 4.1 lists the maximum (over z) values obtained for various frequency and wavelength combinations. The driving current density fields, which are known in closed form, are plotted in figure 4.2, which shows the value for $\lambda = 2\,mm$ (j_y and j_z are independent of frequency).

Most of the results are plotted as surfaces of magnitude or phase of a non-dimensional transform variable *versus* depth (z) and either $\log f$ or $\log \lambda$. Plots of all of the fields calculated for each set of values are in Appendix A.1. In figure 4.3, the change in $|u_y|$ and $|u_z|$ with frequency with constant $\lambda = 1$ can be seen. Note the shift of the maximum amplitude of u_z towards $z = 0$ as the frequency rises. The values of $|V_y|$ and $|V_z|$ are similarly presented in figure 4.4. Here it may be seen that there is a significant horizontal ("slip") velocity at both $z = 0$ and $z = 1$, along with a similar trend in amplitude maxima for V_z. Figure 4.5b is an example of the insensitivity of the potential, ϕ, to frequency. This holds throughout the range of λ for which calculations were performed.

The length scale for significant changes in the fields is found to be the lesser of λ

$f\ (Hz)/$	u_y	u_z	V_y	V_z	p	$\phi = \Phi\ (mV)$	$s(0)$
$\lambda\ (mm)$	$u_y^*\ (\mu m)$	$u_z^*\ (\mu m)$	$V_y^*\ (nm/s)$	$V_z^*\ (nm/s)$	$P\ (kPa)$		$S(0)\ (kPa)$
0.001/10	0.125	$3.12 \cdot 10^{-2}$	1.67 (1.48)	0.516	0.552 (.309)	2.60 (2.14)	0.335
	3.00	0.749	16.7	5.16	5.52		3.35
0.001/1	$6.37 \cdot 10^{-3}$	$6.47 \cdot 10^{-3}$	0.164	$6.19 \cdot 10^{-2}$	0.155	0.159	$2.19 \cdot 10^{-2}$
	0.153	0.155	1.64	0.619	1.55		0.219
0.001/0.1	$6.65 \cdot 10^{-5}$	$6.65 \cdot 10^{-5}$	$1.71 \cdot 10^{-3}$	$6.27 \cdot 10^{-4}$	$1.59 \cdot 10^{-2}$	$1.59 \cdot 10^{-2}$	$2.27 \cdot 10^{-3}$
	$1.60 \cdot 10^{-3}$	$1.60 \cdot 10^{-3}$	$1.71 \cdot 10^{-2}$	$6.27 \cdot 10^{-3}$	0.159		$2.27 \cdot 10^{-2}$
0.01/10	$1.26 \cdot 10^{-2}$	$4.99 \cdot 10^{-3}$	1.76 (1.49)	0.833	0.107 (0.031)	2.58 (2.14)	$3.46 \cdot 10^{-2}$
	0.302	0.120	17.6	8.33	1.07		0.346
0.01/1	$2.18 \cdot 10^{-3}$	$3.21 \cdot 10^{-3}$	0.664	0.371	$8.46 \cdot 10^{-2}$	0.150	$8.86 \cdot 10^{-3}$
	$5.23 \cdot 10^{-2}$	$7.70 \cdot 10^{-2}$	6.64	3.71	0.846		$8.86 \cdot 10^{-2}$
0.01/0.1	$6.65 \cdot 10^{-5}$	$6.65 \cdot 10^{-5}$	$1.70 \cdot 10^{-2}$	$6.27 \cdot 10^{-3}$	$1.59 \cdot 10^{-2}$	$1.59 \cdot 10^{-2}$	$2.27 \cdot 10^{-3}$
	$1.60 \cdot 10^{-3}$	$1.60 \cdot 10^{-3}$	0.170	$6.27 \cdot 10^{-2}$	0.159		$2.27 \cdot 10^{-2}$
0.1/10	$1.26 \cdot 10^{-3}$	$5.57 \cdot 10^{-4}$	1.78 (1.49)	0.984	$2.78 \cdot 10^{-2}$	2.57 (2.14)	$3.48 \cdot 10^{-3}$
	$3.02 \cdot 10^{-2}$	$1.34 \cdot 10^{-2}$	17.8	9.84	0.278		$3.48 \cdot 10^{-2}$
0.1/1	$1.97 \cdot 10^{-4}$	$5.08 \cdot 10^{-4}$	0.893	0.728	$2.61 \cdot 10^{-2}$	0.145	$1.19 \cdot 10^{-3}$
	$4.73 \cdot 10^{-3}$	$1.22 \cdot 10^{-2}$	8.93	7.28	0.261		$1.19 \cdot 10^{-2}$
0.1/0.1	$6.36 \cdot 10^{-5}$	$6.48 \cdot 10^{-5}$	0.164	$6.19 \cdot 10^{-2}$	$1.55 \cdot 10^{-2}$	$1.59 \cdot 10^{-2}$	$2.19 \cdot 10^{-3}$
	$1.53 \cdot 10^{-3}$	$1.56 \cdot 10^{-3}$	1.64	0.619	0.155		$2.19 \cdot 10^{-2}$

Table 4.1: Maximum field magnitudes for current forcing. These are the values of the maxima (over z) of the magnitudes of the indicated field variables. The upper value at a given f/λ is the non-dimensional value, while the lower one is a dimensional one based on the parameter values given in equations 4.6 and 4.7, with $J_0 = 1A/m^2$. The values in parentheses are minima, and are included where deemed significant. The values of the surface stress, $s(0)$ (and $S(0)$), are given instead of the maxima of s over z.

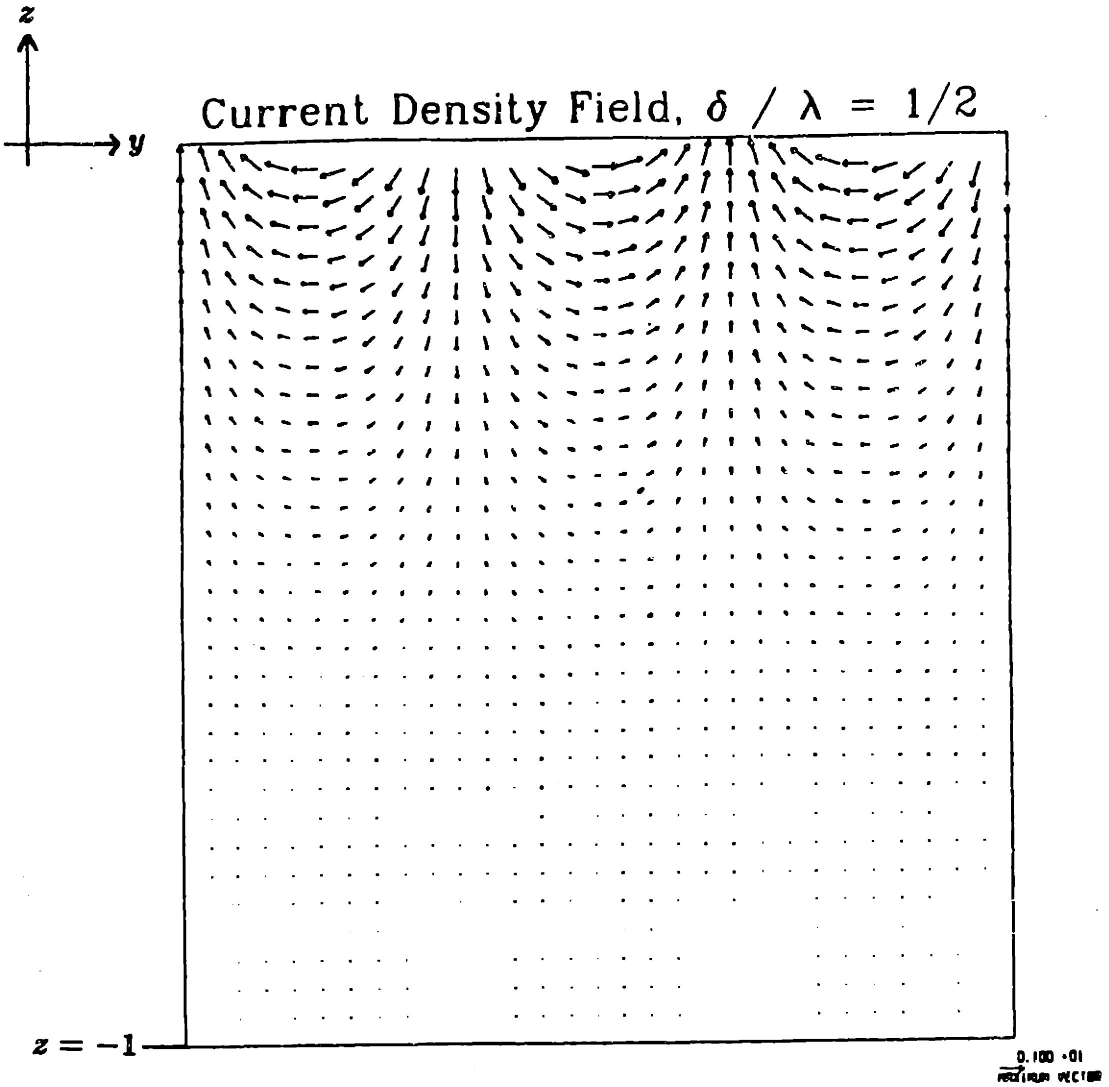

Figure 4.2: The Current Density Field $\vec{J}/J_0$. The case with $\delta/\lambda = 1/2$ is pictured.

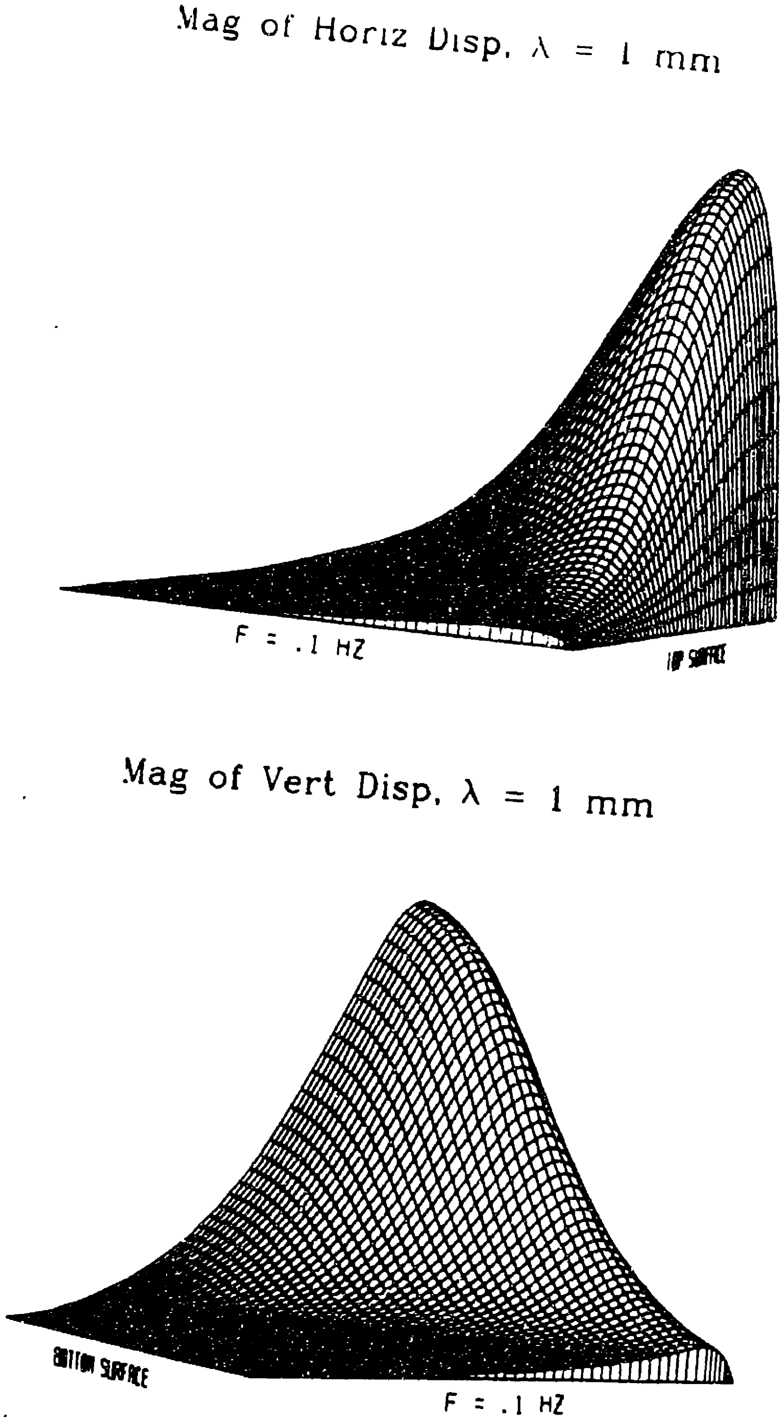

Figure 4.3: **Magnitude of the horizontal and vertical displacements, $|u_y|$ and $|u_z|$, $\lambda = 1\,mm, f = .001$ to $.1\,Hz$. The maximum values in the two diagrams are $0.153\,\mu m$ and $0.155\,\mu m$ respectively. The minimum is zero.**

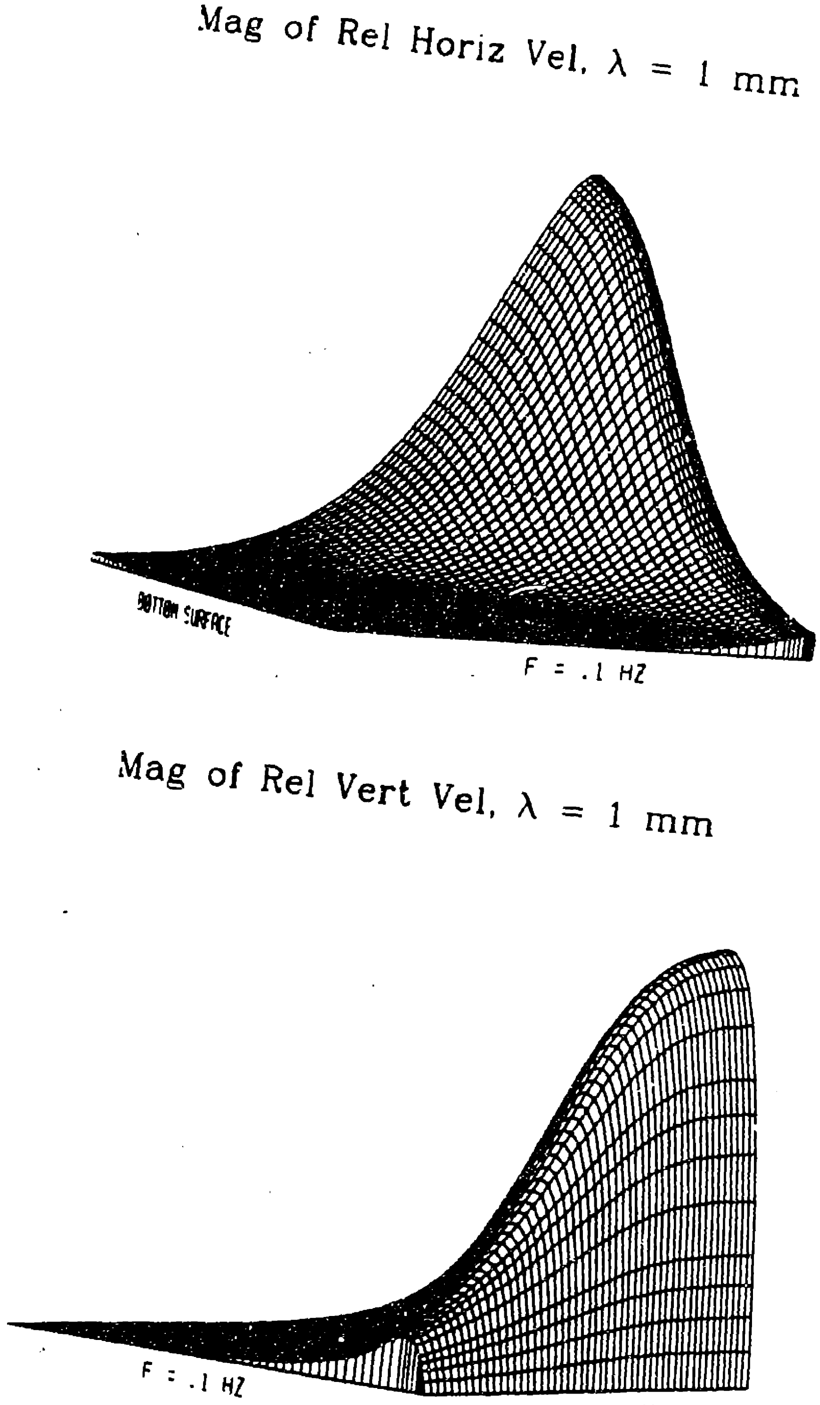

Figure 4.4: Magnitude of the horizontal and vertical relative velocities divided by frequency, $|V_y|/f$ and $|V_z|/f$, $\lambda = 1\,mm, f = .001$ to $.1\,Hz$. The maximum values in the diagrams are $1.64\,\mu m$ and $0.619\,\mu m$ respectively. The minimum value is zero.

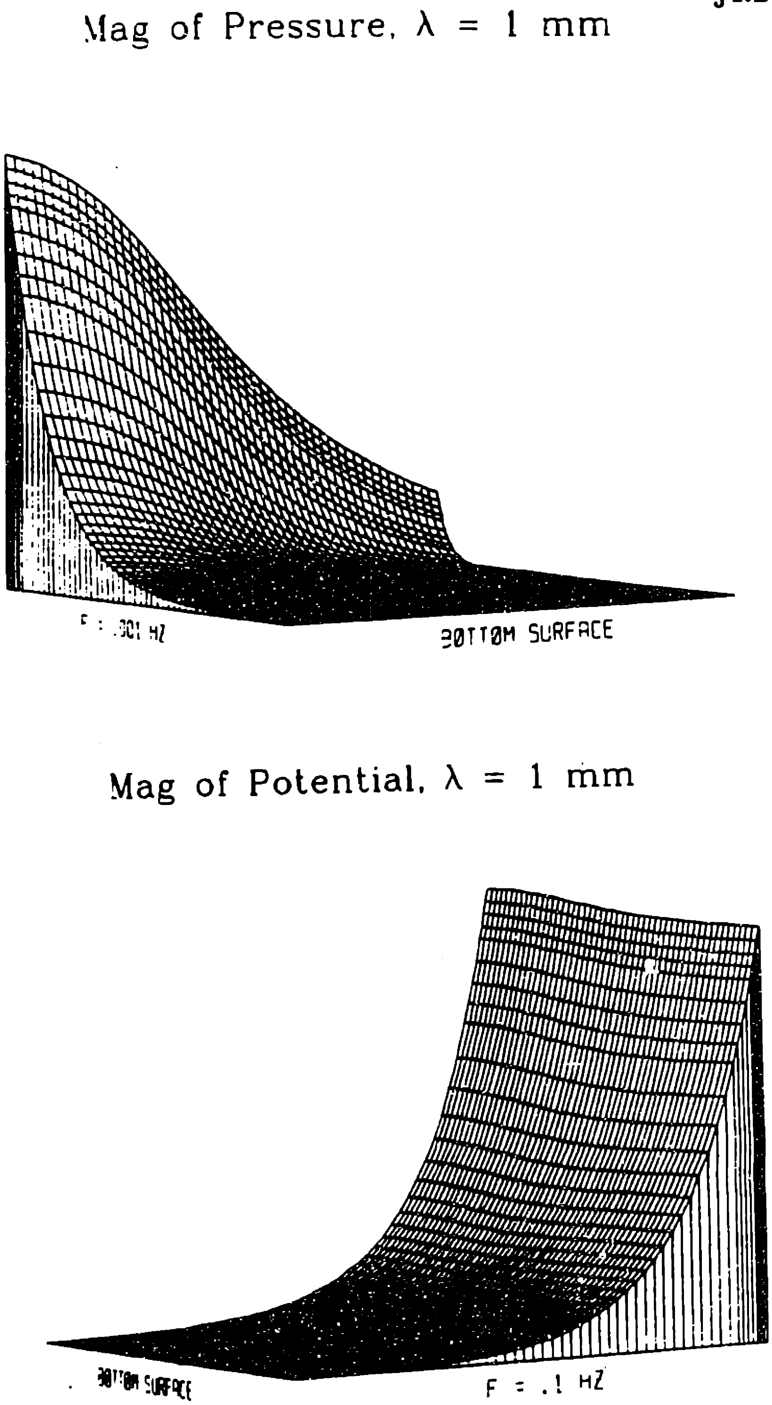

Mag of Pressure, λ = 1 mm

Mag of Potential, λ = 1 mm

Figure 4.5: Magnitude of the pressure and electrical potential, $|p|$ and $|\phi|$, $\lambda = 1\,mm, f = .001$ to $.1\,Hz$. The maximum values in the diagrams are $1.55\,kPa$ and $0.159\,mV$ respectively. The minimum is zero. Note that the maximum value of Φ at $f = .1\,Hz$ is only $0.145\,mV$.

and Δ^*. This trend can be viewed as a competition between equations 3.29, and 3.33, and can be seen in the. $|u_z|$ and $|V_z|$ of figures 4.3b and 4.4b,. This trend is also noticeable in the phases of all of the fields, as is exemplified by $\arg(u_y)$ at $\lambda = 1\,mm$, plotted in figure 4.6. Note that the phase changes in the top .08 mm, or roughly $3\Delta^*$, when $f = .1\,Hz$, but changes over .3 mm, or roughly $4\Delta^*$, at $f = .01\,Hz$. For lower frequencies the same trend is observed but the boundary conditions at $z = -1$ have a stronger influence.

There are two readily observed effects of wavelength. One is that the penetration depth of the disturbance is proportional to the wavelength, as is demonstrated by the pressure distribution in figure 4.7. This is to be expected from equations 3.24, especially in light of the approximation 3.33. For the case of short wavelengths, $|u_y|, |u_z|, |p|$, and $|\phi|$ are independent of frequency. This is demonstrated for the pressure in figure 4.14 (inset). Further, $|V_y^*|$ and $|V_z^*|$ are proportional to the frequency, as expected. For lower frequencies, the phases of all field variables are roughly constant over the region of significant magnitude. At higher frequencies the slope of the phase change rises so that, in some cases, there is a significant phase change even over the boundary layer.

4.2.2 Asymptotic Results

To gain physical insight and to verify the numerical solutions, we now consider two limits. The short-wave limit corresponds to $\delta \equiv 2\pi\delta^*/\lambda \rightarrow \infty$, or a wave of finite wavelength on an infinitely deep layer. The long-wave limit corresponds to $\delta \rightarrow 0$, or a one-dimensional surface disturbance.

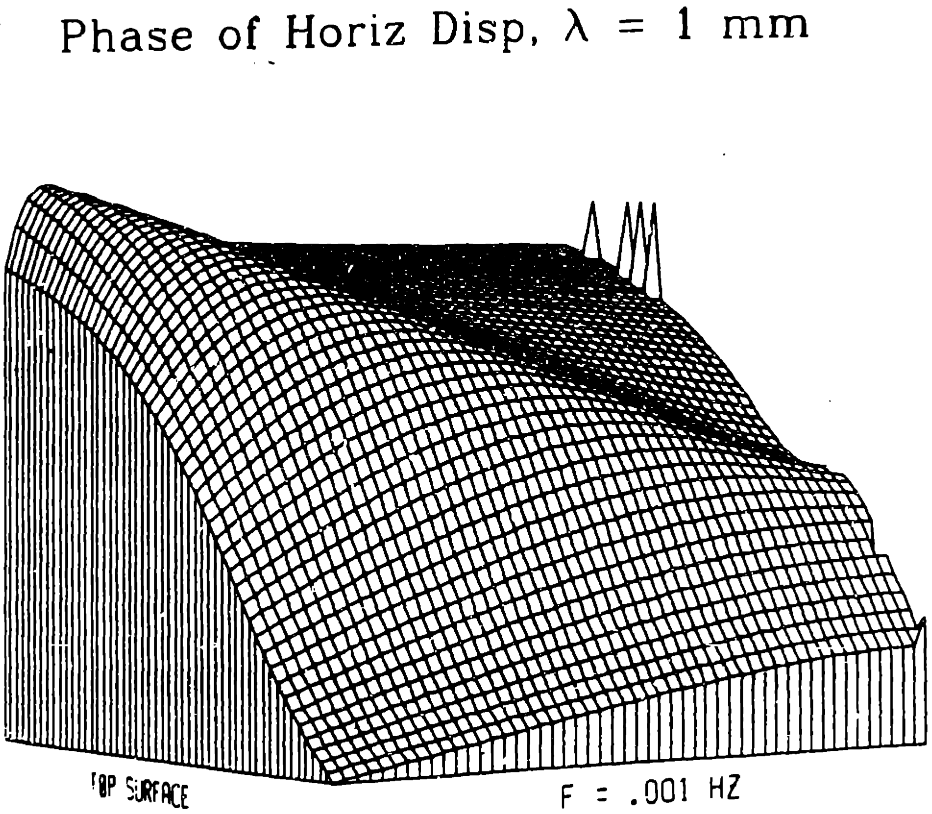

Figure 4.6: Phase of the horizontal displacement, $\arg(u_y)$, $\lambda = 1\,mm, f = .001$ to $.1\,Hz$. The range is from -1.32 to 0.079 radians. The spikes at the bottom surface come from the difficulty of determining the phase of a variable whose magnitude is approaching zero. Other, similar spikes were removed by linearizing the data when a large (> 0.3 radians) jump occurred.

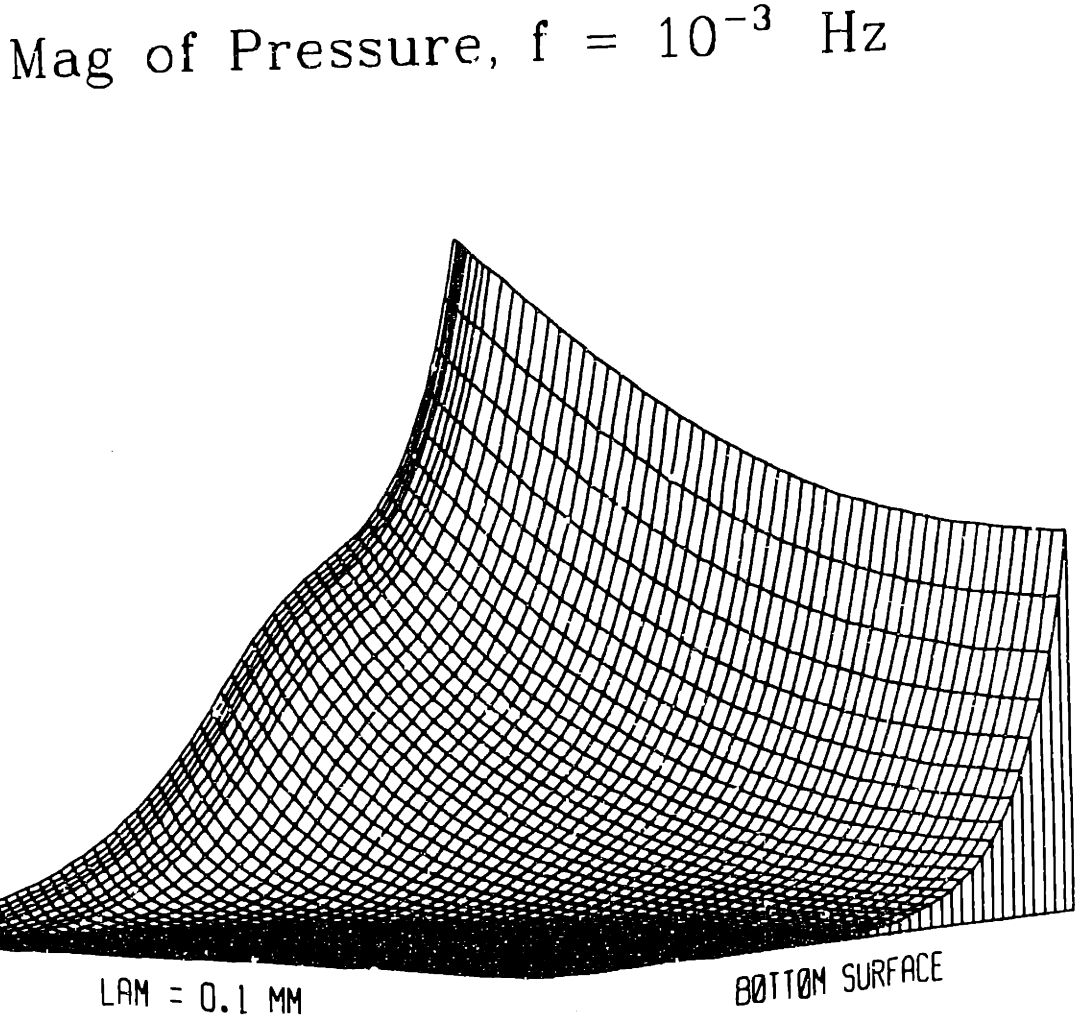

Figure 4.7: Magnitude of the pressure, $|p|$, $f = .001\,Hz, \lambda = .1$ to $10\,mm$. The maximum value is $5.52\,kPa$, the minimum is zero.

The Short-Wave Limit

In the short-wave limit $\delta \to \infty$, so that equations 3.24 suggest that all of the boundary conditions 4.1 at $z = -1$ may be used at $z = -\infty$, thus treating the problem in terms of boundary layer theory. To implement this, the particular solutions of §4.2 must be expanded to order $\exp(-\delta)$, yielding

$$\begin{aligned}
j_z^p &= e^{\hat{z}} & j_y^p &= ie^{\hat{z}} \\
p^p &= -\delta^{-1}e^{\hat{z}} & \phi^p &= -p^p \\
u_y^p &= \tfrac{i}{2n}\delta^{-2}(1+\hat{z})e^{\hat{z}} & u_z^p &= \tfrac{1}{2n}\delta^{-2}\hat{z}e^{\hat{z}} \\
v_y^p &= -iru_y^p & v_z^p &= -iru_z^p\,,
\end{aligned} \tag{4.8}$$

where $\hat{z} \equiv \delta z = kz^*$. If the values of the above particular solutions are subtracted from the boundary conditions 4.1 and equations 3.24 are used, the equations for $k_1, \cdots, k_6$ are obtained:

$$\begin{aligned}
u_y^H(0) &= -\frac{1}{2n\delta^2} &&= \delta^{-1}[k_1 - k_2 + k_3 + k_4 + k_5 - k_6] \\
u_y^H(-1) &= 0 &&= k_1e^{-\delta} - k_2e^{\delta} + k_3(1-\delta)e^{-\delta} + k_4(1+\delta)e^{\delta} \\
& && \quad +k_5e^{-\Lambda\delta} - k_6e^{\Lambda\delta} \\
u_z^H(0) &= 0 &&= k_1 + k_2 + k_5\Lambda + k_6\Lambda \\
u_z^H(-1) &= 0 &&= k_1e^{-\delta} + k_2e^{\delta} - k_3\delta e^{-\delta} + k_4\delta e^{\delta} + k_5\Lambda e^{-\Lambda\delta} + k_6\Lambda e^{\Lambda\delta} \\
v_z^H(0) &= 0 &&= -k_1 - k_2 + k_3 2in\tfrac{\delta}{r} - k_4 2in\tfrac{\delta}{r} + k_5\alpha_0\Lambda + k_6\alpha_0\Lambda \\
v_z^H(-1) &= 0 &&= -k_1e^{-\delta} - k_2e^{\delta} + k_3(2in\tfrac{\delta}{r} - 1)e^{-\delta} - k_4(2in\tfrac{\delta}{r} + 1)e^{\delta} \\
& && \quad +k_5\alpha_0\Lambda e^{-\Lambda\delta} + k_6\alpha_0\Lambda e^{\Lambda\delta}
\end{aligned} \tag{4.9}$$

It is now assumed that

$$k_2, k_4, k_6 = O(e^{-2\delta})\,, \tag{4.10}$$

and 4.9 are solved to $O(e^{-\delta})$, consistent with the expansion of the particular solutions 4.8. Because all terms with k_2, k_4, and k_6 are now a factor of $e^{-\delta}$ smaller than the others, the system 4.9 need only be solved for k_1, k_3, and k_5. The values of the latter three coefficients, when used in 3.24 give

$$\begin{aligned}
u_y &\sim \phi_0 C\delta^{-2}[1-\hat{z}(\Lambda-1)-e^{(\Lambda-1)\hat{z}}]e^{\hat{z}} \\
u_z &\sim i\phi_0 C\delta^{-2}[(\Lambda-1)\hat{z}+\Lambda(e^{(\Lambda-1)\hat{z}}-1)]e^{\hat{z}} \\
v_y &\sim i\phi_0 Cr\delta^{-2}[(\Lambda-1)(1+\hat{z})+\alpha_0(\Lambda-e^{(\Lambda-1)\hat{z}})]e^{\hat{z}} \\
v_z &\sim \phi_0 Cr\delta^{-2}[\Lambda\alpha_0(1-e^{(\Lambda-1)\hat{z}})+(\Lambda-1)\hat{z}]e^{\hat{z}} \\
V_y &\sim iCr\delta^{-2}[\Lambda-e^{(\Lambda-1)\hat{z}}]e^{\hat{z}} \\
V_z &\sim \Lambda Cr\delta^{-2}[1-e^{(\Lambda-1)\hat{z}}]e^{\hat{z}} \\
p &\sim [\delta^{-1}-Cr\delta^{-2}(\Lambda-e^{(\Lambda-1)\hat{z}})]e^{\hat{z}} \\
\phi &\sim -[\delta^{-1}-b_c Cr\delta^{-2}(\Lambda-e^{(\Lambda-1)\hat{z}})]e^{\hat{z}} \\
j_y &\sim ie^{\hat{z}} \\
j_z &\sim e^{\hat{z}}
\end{aligned} \qquad (4.11)$$

and,

$$s(0) \sim 2in\phi_0\delta^{-1}C(\Lambda-1),$$

where

$$C \equiv [\Lambda r/\delta^2 + 2in\phi_0(\Lambda-1)]^{-1}.$$

It should be noted that these solutions satisfy the differential equations of the model exactly: only the boundary conditions (*i.e.* 4.9) are approximated. Also, if the values of k_1, k_3, and k_5 are substituted into equations 4.9, the resulting k_2, k_4, and k_6 are found to be consistent with the assumptions 4.10. The boundary layer nature of solutions 4.11 is exemplified by the velocity and pressure fields of figure 4.8. Further, the good agreement between numerical and asymptotic results can be seen in the predicted surface stress of figure 4.9, as well as the velocity amplitudes of figure 4.8.

The above solutions can be simplified in the low frequency limit, $\Delta \gg 1$. In this case equation 3.33 holds so that

$$C \sim \phi_0^{-1}(3-4\nu)^{-1}\Delta^2.$$

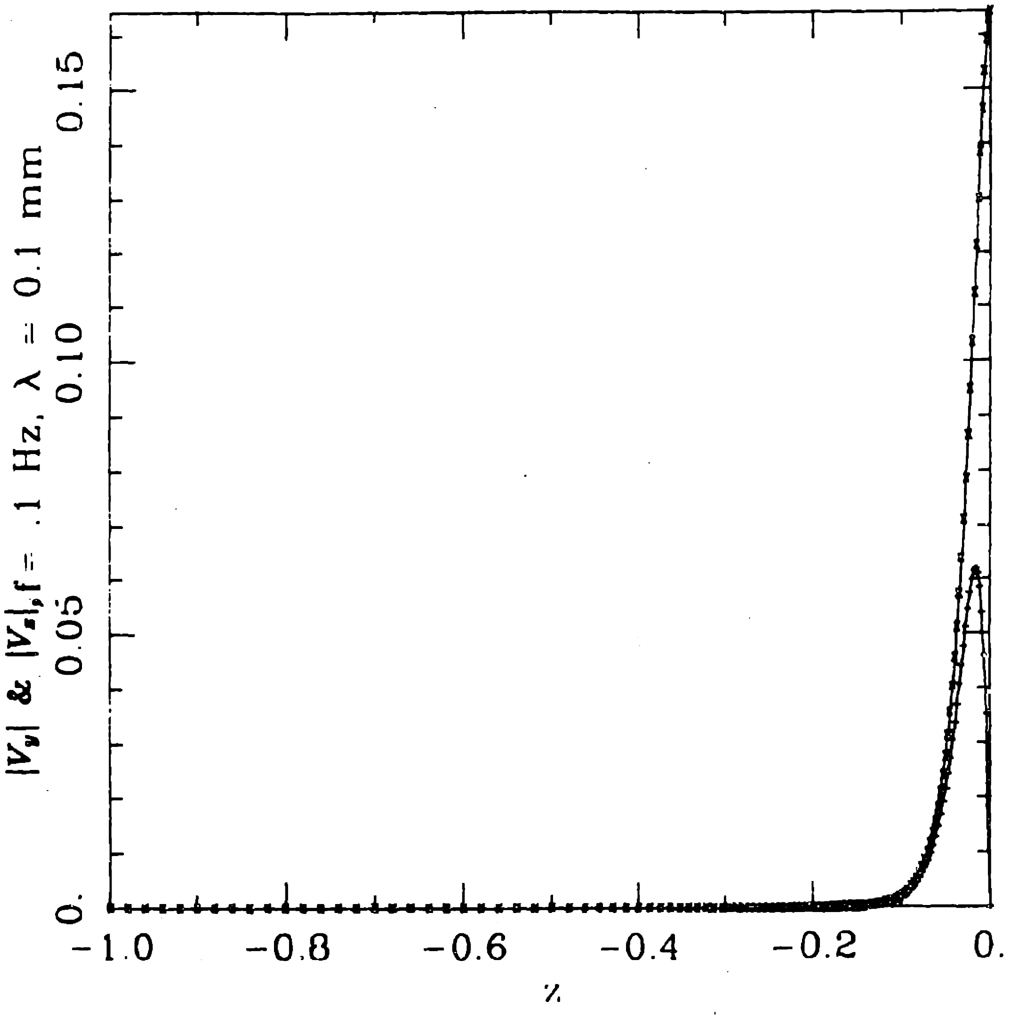

Figure 4.8: Magnitude of relative velocities, $|V_y|$ and $|V_z|$, $f = .1\,Hz, \lambda = .1\,mm$. The solid lines show the numerical results, and those of equations 4.11e and f are marked with "x"'s (V_y) and "+"'s (V_z).

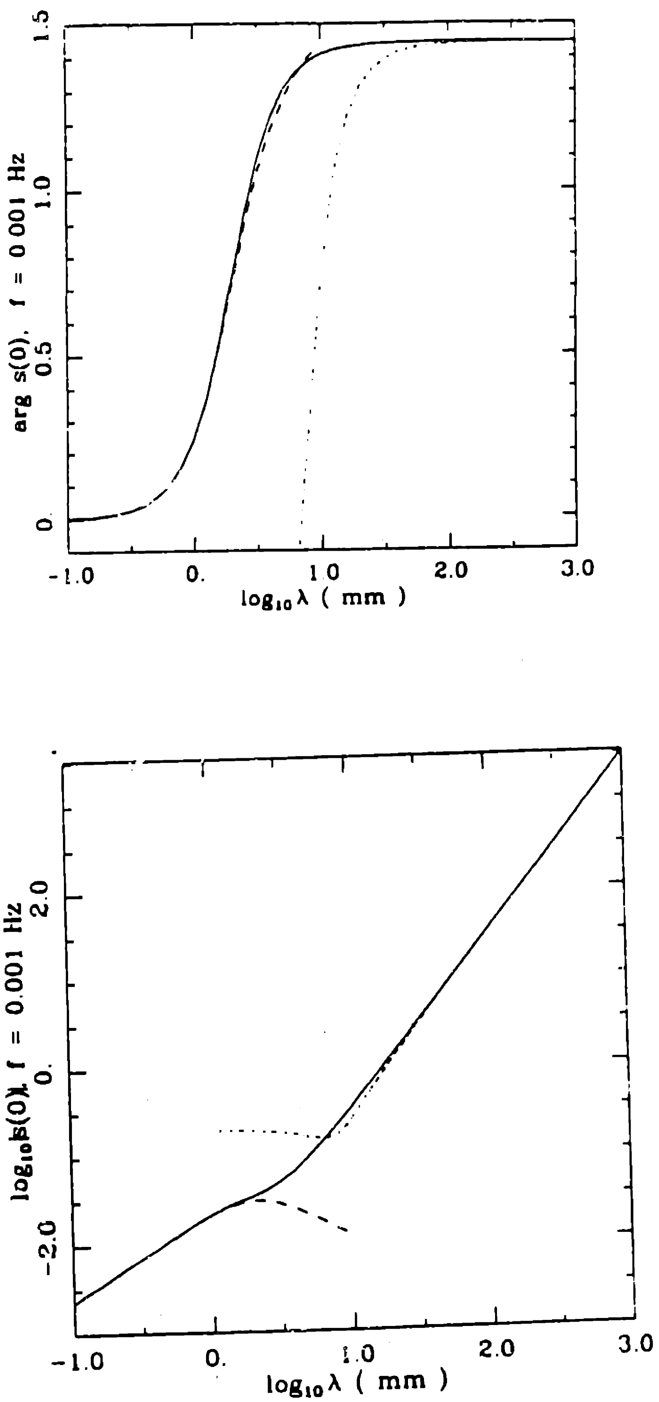

Figure 4.9: Magnitude and phase of the surface stress, $s(0), f = .001\,Hz$, *vs.* $\log_{10}\lambda$. The solid lines show the numerical results, and those of equations 4.11k and 4.20 are marked with dashed and dotted lines, respectively.

Thus, for $\delta \gg 1, \Delta \gg 1$,

$$
\begin{aligned}
u_y &\sim e^{z}\delta^{-2}\tfrac{i}{(3-4\nu)}\hat{z} \\
u_z &\sim e^{z}\delta^{-2}\tfrac{1}{(3-4\nu)}\hat{z} \\
v_y &\sim e^{z}\Delta^{-2}\tfrac{1-\nu}{3-4\nu}(1+(2\phi_0-1)\hat{z}) \\
v_z &\sim -ie^{z}\Delta^{-2}\tfrac{1-\nu}{3-4\nu}(2\phi_0-1)\hat{z} \\
V_y &\sim e^{z}\Delta^{-2}\tfrac{1-\nu}{3-4\nu}(1-\hat{z}) \\
V_z &\sim e^{z}\Delta^{-2}\tfrac{1-\nu}{3-4\nu}(1-\hat{z}) \\
p &\sim e^{z}\delta^{-1} \\
\phi &\sim -e^{z}\delta^{-1}[1+b_c i\tfrac{1-\nu}{3-4\nu}\Delta^{-2}(1-\hat{z})]+O(\Delta^{-4})
\end{aligned}
\tag{4.12}
$$

and

$$
s(0) \sim \delta^{-1}(\tfrac{1-2\nu}{3-4\nu}). \tag{4.13}
$$

The pressure field is that generated by the current $\vec{J}$ through equation 2.6. The (dimensional) velocities are proportional to the frequency and (through $\vec{J}$) the pressure, so that the current drives the pressure and relative velocity fields *via* the coupling parameter b_{12}. Because the mechanical resistivity (b_{11}) does not appear in the (dimensional) velocities, the solid displacement must be driven by mass conservation. Now the force balance is strictly between elastic compression and shear. This system is weakly coupled in that the current is not significantly affected by the mechanical fields.

Using the parameter values above in §4.2.1, the extra term kept in the expansion of ϕ (in equation 4.12) shows that $|\phi(z=0)| = 1$ to one part in 10^8 at $\lambda = .1mm, f = 10^{-3}Hz$. Since there is very little frequency dependence at this value of λ, this exemplifies the claim (in §4.2) that $|\phi(z=0)|$ is close to unity.

The Long-Wave Limit

In this limit, $\delta \to 0$, so that the scale of the imposed wave is much larger than the thickness of the layer. In this case a formal perturbation expansion

$$\begin{aligned} u_y^H &= \delta^{-1}(u_{y0} + \delta^2 u_{y1} + \ldots) \quad & u_z^H &= u_{z0} + \delta^2 u_{z1} + \ldots \\ v_y^H &= \delta^{-1}(v_{y0} + \delta^2 v_{y1} + \ldots) \quad & v_z^H &= v_{z0} + \delta^2 v_{z1} + \ldots \end{aligned} \tag{4.14}$$

was used. The ratio of magnitudes of the vertical and horizontal components of $y-$ and $z-$directed fields was chosen to be consistent the Taylor series expansions of the particular solutions 4.5 with $\delta \ll 1$. Reducing (3.8)-(3.11) to four equations in u_y, u_z, v_y, and v_z and substituting 4.14 gives:

$$\begin{aligned} \alpha_0 r(u_{y0} - iu'_{z0}) + iv_{y0} + v'_{z0} &= O(\delta^2) \\ v'_{y0} + iru'_{y0} &= O(\delta^2) \\ nu''_{y0} + v_{y0} + iru_{y0} &= O(\delta^2) \\ (1+n)u''_{z0} + iu'_{y0} + v_{z0} + iru_{z0} &= O(\delta^2) \end{aligned} \tag{4.15}$$

Keeping terms of the same order in the boundary conditions 4.1 and the particular solutions (*cf.* §3.2.1) results in

$$\begin{aligned} u_{y0} &= -\frac{\gamma}{n\delta} z(z+1) \\ u_{z0} &= \frac{1}{6n} z(z+1)(z+2) - \frac{\phi_0}{r}[(\gamma+i)(1 - \frac{\sinh\varsigma(z+1)}{\sinh\varsigma}) - \gamma\frac{\sinh\varsigma z}{\sinh\varsigma}] \\ &\quad + \frac{z}{n}[\frac{z^2}{3}(i\gamma - \frac{1}{2}) + \frac{z}{2}(i\gamma - 1) - \frac{1}{3}] \\ v_{y0} &= ir\frac{\gamma}{\delta n}(z(z+1) + \frac{1}{6\phi_0} \\ v_{z0} &= -ir\frac{1}{6n} z(z+1)(z+2) + z(1-2i\gamma) + (1-\phi_0)(1-i\gamma) \\ &\quad -i\frac{r}{n} z[\frac{z^2}{3}(i\gamma - \frac{1}{2}) + \frac{z}{2}(i\gamma - 1) - \frac{1}{3}] \\ &\quad +i\frac{1-\phi_0}{\sinh\varsigma}[\gamma\sinh\varsigma z + (\gamma+i)\sinh\varsigma(z+1)] \\ V_{y0} &= (2\gamma+i)/\delta \\ V_{z0} &= i\gamma\frac{\sinh\varsigma z}{\sinh\varsigma} + (i\gamma-1)\frac{\sinh\varsigma(z+1)}{\sinh\varsigma} - z(2i\gamma-1) + 1 - i\gamma \end{aligned} \tag{4.16}$$

where

$$\gamma = (2i + \frac{r}{6\phi_0 n})^{-1}$$

and,

$$\varsigma \equiv \sqrt{\frac{-ir}{2(1-\nu)\phi_0}} = \frac{\delta^*}{\Delta^*} e^{-i\frac{\pi}{4}}. \tag{4.17}$$

Note that the factor ς is exactly the expected first order approximation to Λ that one would expect from equation 3.29.

The displacements and velocities agree well with those calculated numerically at $\lambda = 10mm$, as is seen in figures 4.10 and 4.11. Here it is seen that u_y is parabolic, while u_z is skewed towards the top. This makes sense in view of the relative velocity and current density fields. J_y is nearly constant in z, and thus so is V_y. The mechanical displacements u_y and u_z are zero at the top and bottom and are driven *via* fluid drag. J_z has a linear profile, and the higher value at the top drives an asymmetric relative velocity and, hence, an asymmetric displacement.

At higher frequencies this skewing effect is exaggerated, as seen in figure 4.11. Now the displacement and velocity fields are even more biased towards the top of the layer ($|u_z|$ and $|V_z|$ are very similar at any f in the long-wave limit). This change with frequency is due to the change in Δ. It is also visible in the phases of the fields (*cf.* §4.2.1). It should be noted that, especially for the relative velocities, the phases behave as one would expect from two decoupled, one-dimensional analyses of the problem: V_y is in phase with j_y, and similarly for V_z and j_z. Also, the agreement between numerical and asymptotic values of u_y, u_z, and V_z is better at high frequencies. This makes sense, as the imposed length scale should be as large as possible relative to both δ^* and Δ^* to apply this limit.

The pressure and potential are not as easily obtained in this limit. To see why, note that only an average value of V_y is obtained from the lowest order analyses, and that the value of $V_y(0)$ is not well estimated. Because of equations 3.9a and b, this means that it is difficult to find the value of $p(0)$ (and thus $s(0)$). Further, all

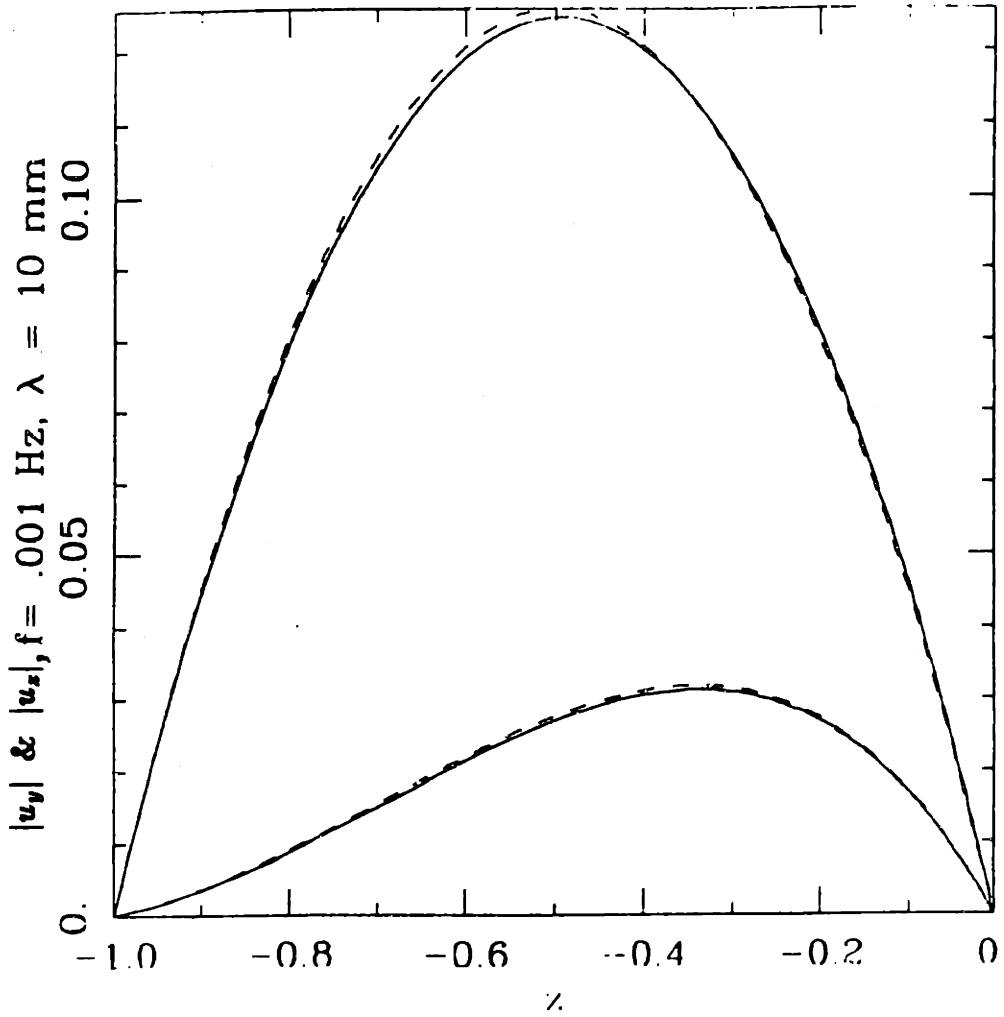

Figure 4.10: Magnitude of the horizontal and vertical displacements, $|u_y|$ and $|u_z|$, $\lambda = 10\,mm$, $f = .001\,Hz$ *vs.* depth z. The solid lines show the numerical results, while the dashed lines show the results of equations 4.16a (upper) and b (lower).

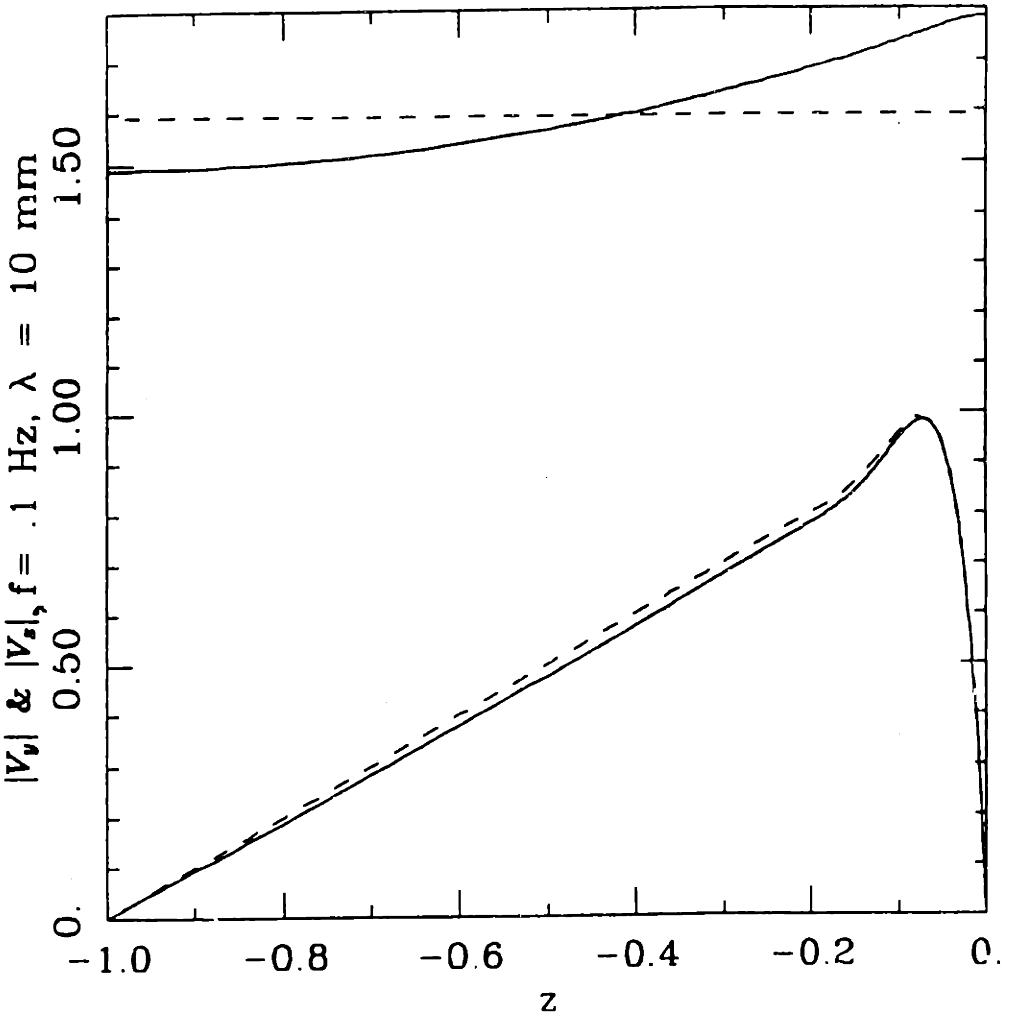

Figure 4.11: Magnitude of the horizontal and vertical relative velocities, $|V_y|$ and $|V_z|$, $\lambda = 10\,mm$, $f = .1\,Hz$ *vs.* depth z. The solid lines show the numerical results, while the dashed lines show the results of equations 4.16c (upper) and d (lower).

of the vertical field terms have been dropped from equation 4.15b. This equation is from 2.7a, which expresses the consistency of the vertical field values with the coupling equation 2.6. Because of the terms dropped from this equation, it is possible to derive two separate values for each of p and ϕ:

$$\begin{aligned} p_a &= 2i\gamma/\delta^2 + z^2/2 + z + \tfrac{1}{3} \\ \phi_a &= -(z^2/2 + z + \tfrac{1}{3}) - (b_c(2i\gamma - 1) + 1)/\delta^2 \end{aligned} \tag{4.18}$$

from equations 3.9a and 3.9c; and

$$\begin{aligned} p_b &= p_a(0) + i\gamma z(z+1) - \tfrac{1}{\varsigma \sinh \varsigma}[i\gamma(\cosh \varsigma z - 1) \\ &\qquad\qquad + (i\gamma - 1)(\cosh \varsigma(z+1) - \cosh \varsigma)] \\ \phi_b &= \phi_a(0) + \tfrac{b_c}{\varsigma \sinh \varsigma}[(\text{as above})] + (b_c(1 - i\gamma) - 1)z + \tfrac{z^2}{2}(b_c(1 - 2i\gamma) - 1) \end{aligned} \tag{4.19}$$

from 3.9b and 3.9d. In either case, the resultant normal surface stress is

$$s(0) = i\gamma(2\delta^{-2} - \frac{n+1}{6n}\varsigma \coth \varsigma) + 1/3\,. \tag{4.20}$$

This equation gives a good fit to the numerically calculated value of $s(0)$ for $\lambda > 9\,mm$, as can be seen in figure 4.9, which shows the value of s *vs.* $\log \lambda$ at $f = 0.001\,Hz$. Because of the difficulty of approximating the value of $V_y(0)$, the agreement between the numerical and long-wave pressure or stress is not very good at high frequencies. The agreement with ϕ is still very good, as V_y does not effect it very much when $b_c = 0.1$.

4.3 Comparison with Experimental Data

Even though there are no available data which use every facet of the current model, some comparisons can be made. Frank [34] used a one-dimensional confined compression geometry and boundary conditions very close to equations 4.1. He applied a current density of the form $\vec{J} = \hat{\imath}_z J_0 \cos \omega t$ across a cylindrical disk of cartilage and measured the resulting stress at $z = 0$ (*cf.* figure 4.12). There are two differences between the boundary conditions of equations 4.1 and those of the experiment. First, the no flow condition at $z = 0$ is replaced by one of infinite fluid permeability (and thus zero pressure, by equation 2.6).

The second difference is that the vertical displacement is applied to the electrode structure which contacts the top surface at $z = 0$. Because of the compliance of the porous platen used for the top electrode, the vertical displacement changes to maintain quasi-static stress equilibrium at the top surface. This is derived by requiring stress continuity at $z = 0$. In the one-dimensional limit, the only contribution to the platen stress is from its vertical displacement. (Also note that, if a no-slip condition is imposed at the surface, the $u_y = 0$ boundary condition below would preclude any contribution from a horizontal displacement or its tangential derivative, as in the $i\delta u_y$ term in equation 3.22.) Thus, the equilibrium stress that the platen produces when its surface is displaced (vertically) by a distance $u_z^*(z = 0)$ must be equal to the tissue normal stress $S^*(z = 0)$. If the platen is assumed to be a linear, elastic material, then the relation between $S^*(0)$ and the displacement at its surface may be written

$$\Lambda_s \frac{u_z^*(z = 0)}{\delta^*} = S^*(z = 0) \ ,$$

where Λ_s is a modulus which is proportional to the uniaxial compressional modulus of the platen and to the ratio of tissue to platen thickness. Further, there is zero shear in the one-dimensional limit. Thus the long-wave results discussed here, which use continuity of horizontal displacement ("no-slip"), should be the same as those derived from shear continuity.

Thus the appropriate non-dimensional boundary conditions are:

$$\begin{array}{llll} u_y(0) = 0 & u_z(0) - \frac{2G+\lambda_L}{2(1-\nu)\Lambda_s} s(0) = 0 & p(0) = 0 & j_z(0) = 1 \\ u_y(-1) = 0 & u_z(-1) = 0 & v_z(-1) = 0 & j_z(-1) = 0 \, . \end{array} \tag{4.21}$$

A current density, J_0, of $\approx 3.8A/m^2$ was applied, and the resultant surface stress was measured. This was repeated at frequencies between 0.005 and 1 Hz. To simulate these data, the following parameter values were taken from the literature:

$$\begin{pmatrix} b_{11} & b_{12} \\ b_{21} & b_{22} \end{pmatrix} = \begin{pmatrix} 3.3 \cdot 10^{14} \frac{Ns}{m^4} & 6.9 \cdot 10^6 \frac{Vs}{m^2} \\ 7.3 \cdot 10^6 \frac{N}{Am} & 1.1\,\Omega m \end{pmatrix} \tag{4.22}$$

$$\begin{array}{lll} 2G + \lambda_L = 1.1 \cdot 10^6 \frac{N}{m^2} & & \Lambda_s = 10. \cdot 10^6 \frac{N}{m^2} \\ \delta^* = .68mm & \nu = 0.4 & \phi_0 = 0.8 \end{array} \tag{4.23}$$

No adjustable parameters were used to fit the data. All of the parameter values were calculated by using those given in Frank [35] except for b_{22} which was estimated using bulk electroneutrality and linearity of solution conductivity with concentration (of mono:monovalent species at low concentrations) and data from Lee *et al.* [63]. Also, the parameter values determined by Frank were verified by a measurement which had no adjustable parameters. Note that $2G + \lambda_L, \Lambda_s, b_{11}, \phi$, and b_{22} were all determined by independent measurements; only the four parameters ν, b_{11}, b_{12}, and b_{21} are left to be determined. ν does not appear in the one-dimensional theory. Frank [34] used four independent configurations to measure the remaining 3 parameters in such a way that there was no parameter to be fit to the last set of data. It is in this sense that the above set of parameter values has not been fit to the data.

Since the experiment was reasonably one-dimensional, $\lambda = \infty$ should have been used, but actual calculations were carried out for λ ranging from 100 mm to 10^5 mm. This was found to make less than 0.5% difference in the calculated value of $s(0)$ for $f = 10^{-5}$ and 0.2 Hz. The value of $s(0)$ was also virtually unchanged for ν ranging from $0.35 < \nu < 0.49$[2]. The results of calculations using $\lambda = 1000\,mm$ are shown in figures 4.12 and 4.13. The calculations agree quite well with the data.

---

[2] The value of $s(0)$ was found to vary nearly linearly in ϕ_0, as expected, with slope about $4.80 \cdot 10^{-2} e^{1.08i}$ at $f = 0.1\,Hz$, and to be constant in ϕ_0 at $f = 10^{-5}\,Hz$.

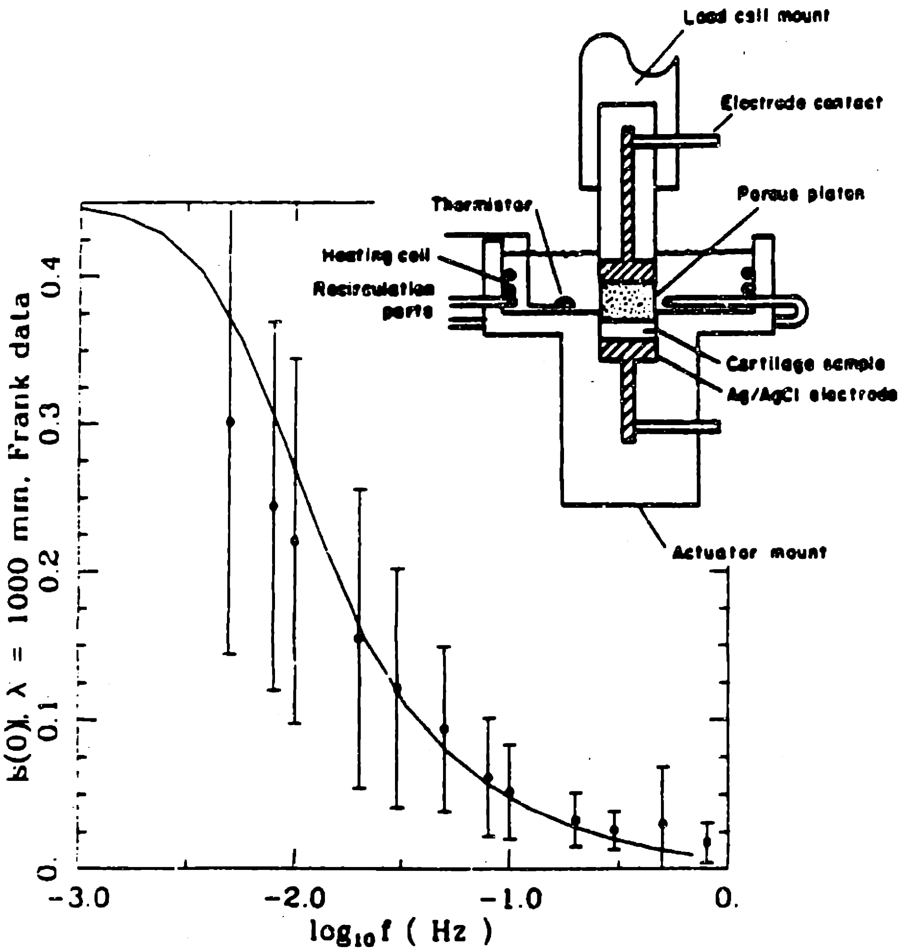

Figure 4.12: Magnitude of the surface stress, $|s(0)|$ *vs.* frequency f. The solid curve is the result of numerical calculations (§4.3). The data are from Frank [34]. A schematic of the experimental setup is shown in the inset: a sinusoidally varying, vertically directed current density is applied directly to the bottom of the cylindrical, confined sample, while at the top the current must pass through a porous platen designed so as to let the pressure equilibrate. The magnitude and phase of the compressive force on the top electrode was measured and recorded. The data are presented as mean plus or minus a standard deviation based on 9 different samples of bovine femoropatellar cartilage.

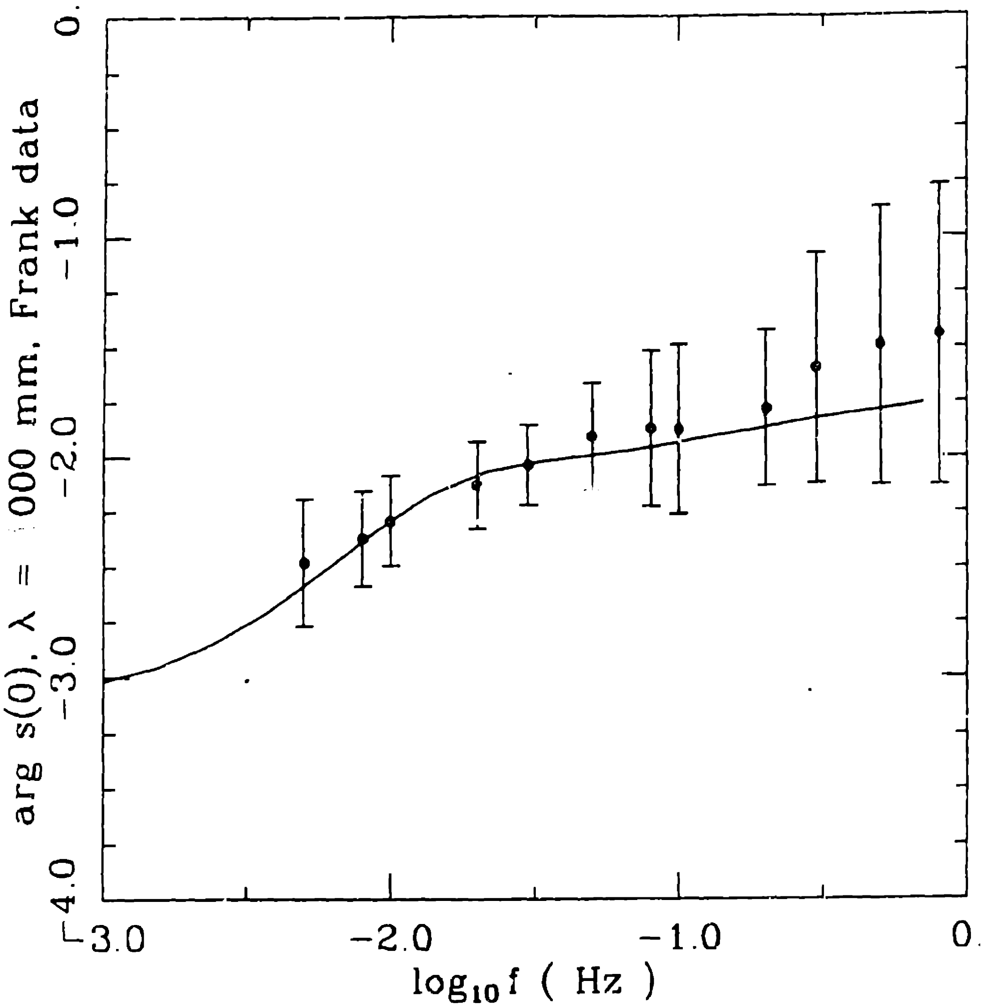

Figure 4.13: Phase of the surface stress, $|s(0)|$ *vs.* frequency f. As in figure 4.12, but phase instead of magnitude.

4.4 Discussion

Using the above model, it is possible to make some predictions regarding a surface probe used to measure electromechanical parameters($\delta^*, b_{11}, b_{12}, b_{21}, b_{22}, G, \nu$, and ϕ_0) of a biphasic medium. The interpretation of the values of these parameters will depend on the exact nature of the material being studied, but in all cases they give information about the material. For cartilage, for example, knowledge of b_{22} is useful because it gives information about the fixed charge density of the solid matrix [44]. The values of b_{12} and b_{21}, which should be equal by Onsager's analysis [90], give additional information about the electrochemical state of the medium, such as the proteoglycan concentration within the matrix. The other parameters give additional structural and compositional information as discussed in §1.1.

One strategy for measuring the above parameters is as follows. For each of two significantly different wavelength (λ) disturbances, the following experiments would be performed using the geometry of figure 4.1:

1. a current density like that of equation 3.5 is applied to the surface with the displacement held fixed, and the resultant stress $s(0)$ and potential $\phi(0)$ are measured (magnitude and phase for each) as a function of frequency;

2. a potential like that of equation 3.6 is applied to the surface with the displacement held fixed, and the resultant stress $s(0)$ and current density $J_z(0)$ are measured;

3. a vertical displacement like that of equation 3.1 is applied to the surface with an open circuit ($J_z(0) = 0$) boundary condition and the resultant stress $s(0)$ and potential $\phi(0)$ are measured;

and

4. a vertical displacement like that of equation 3.1 is applied to the surface with

a short circuit ($\phi(0) = 0$) boundary condition and the resultant stress $s(0)$ and current density $J_z(0)$ are measured.

The first two experiments are those of cases one and two (*cf.* page 60). The third is examined in chapter 5. Each of the above experiments gives four measurements (as a function of frequency) at each of two wavelengths, so that a total of 32 independently measured quantities. Since there are only eight parameters, this allows sufficient redundancy to check the consistency of any predictions.

The model suggests several issues regarding the ability to make such measurements. First, over the two decades of frequency used, the penetration depth is proportional to the wavelength of the imposed disturbance. Thus any predictions about material properties based on short-wave disturbances will only be sensing those relevant to a layer of material about one wavelength thick, as suggested by figure 4.14. This implies that it is possible to selectively measure properties of all of the material, or to measure properties relevant near the surface.

Arbitrarily short wavelengths may not be used, however. Equations 4.12 show that $|u_y|$, $|u_z|$, $|V_y|$, $|V_z| \propto \lambda^2$, and $|p|$, $|\phi|$, and, as seen in figure 4.9, $|s| \propto \lambda$. The latter demonstrates that shorter wavelengths produce smaller signals. The approximation to the stress in equation 4.13 suggests that $|s(0)|$ should be independent of frequency for wavelengths small compared to the layer thickness, δ^*, and diffusion thickness, Δ^*. The inset in figure 4.14 and other results show that this independence extends at least to frequencies so high that $\Delta^*/\lambda = 0.25$, far beyond the expected range of validity of equations 4.12.

Short-wave measurements may, therefore, be taken at relatively high frequencies without a decrease of the response amplitude. Thus, the nature of the electromechanical interactions near the surface can be determined using a short-wave disturbance. This could be beneficial, as these properties determine how the biphasic layer interfaces with any sensing device placed on its surface. Further, the decrease in surface stress for short wavelengths implies that surface imperfections (*e.g.* roughness or lack of control over the exact disturbance waveform) will not cause severe changes in the anticipated response. This is roughly equivalent to St. Venant's principle in that it implies that local changes in boundary conditions will produce only local changes in fields. Note that the requirement that the net applied stress be zero is met if a large-scale or a single-period average is taken.

For the medium to long wavelength disturbances, the fields develop phase lags over a depth of several Δ. Thus the diffusive nature of the process is manifested by a time delay in the propagation of the disturbance into the material, in addition to changing the location (in z) of amplitude maxima (*cf.* §4.2.2). This suggests that some information about seemingly strictly mechanical parameters (*e.g.* G, λ, b_{11}, and ϕ_0) may be obtained from an electrical disturbance.

Because of the limit on the penetration depth, a device used to measure bulk properties must have a length scale the same as that of the medium to be investigated. For longer wavelengths ($\lambda > O(1mm)$), $|s(0)|$ is decreasing in f, roughly like the inverse of a fractional power of f. Thus the largest field amplitudes, and (possibly) the easiest measurements, are at lower frequencies. This is also shown by the results in table 4.1.

The results suggest possible limitations to probe measurements which should be considered. First, the dimensional values of the velocities and stresses suggest that, for some applications with weak coupling and/or high stiffness, a large current density would be required. This could result in chemical reactions, heat generation, and other behavior not incorporated in the present work. Second, nonlinear effects may have to be considered. These effects could be important, especially under conditions of higher strain [83,84]. Further, the effects of three-dimensional boundary conditions may have to be included.

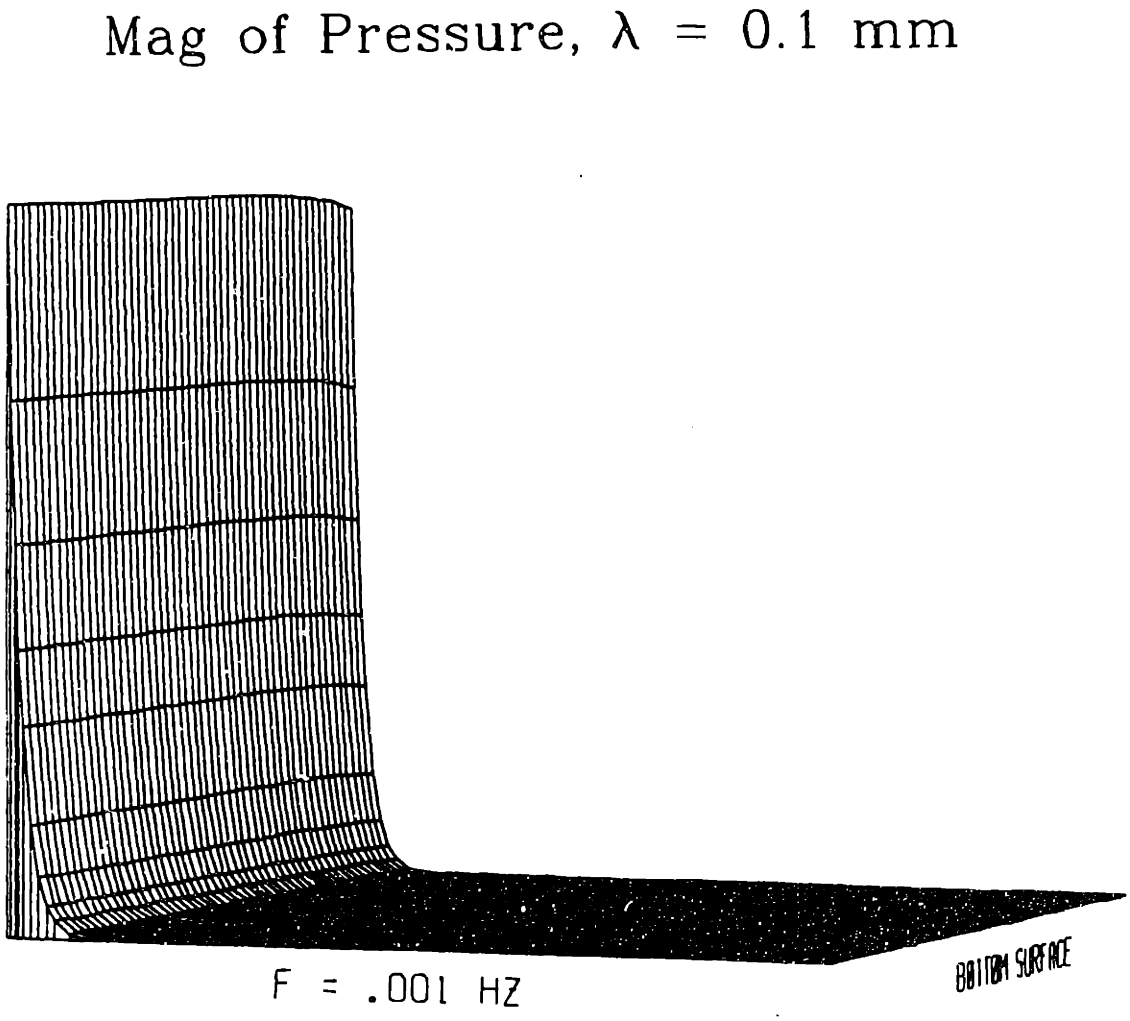

Figure 4.14: Magnitude of the pressure, $|p|, \lambda = .1\,mm, f = .001$ to $.1\,Hz$. The maximum value is $.159\,kPa$ at $.001\,Hz$, $.155\,kPa$ at $.1\,Hz$. The minimum value is zero.

Chapter 5

The Mechanically Forced Response

5.1 Introduction

This chapter describes the electromechanical response of the poroelastic "tissue" layer of previous chapters to a probe which imposes a known, periodic, vertical displacement at the top surface. The desired results will, as before, be the solid displacement, fluid velocity, electrical potential, and current density fields in the bulk, and the mechanical stress and electrical potential at the surface. First, some preliminary analytical results will be discussed. Then the numerical and asymptotic short- and long-wave results will be presented. Finally, a limiting case of the model will be compared with experimental data.

5.2 Results

5.2.1 Case Descriptions and Consequences of the Boundary Conditions

The geometry and boundary conditions considered here may be seen in figure 5.1. The boundary conditions provide a mechanical drive instead of the current drive of the previous chapter(*cf.* §4.1). Two cases will be compared with each other and to case one of the previous chapter:

Case 3: the displacement, velocity, pressure, potential and current density fields due to a vertical displacement applied to top surface of the layer, with no fluid flow normal to the top surface;

and

Case 4: the displacement, velocity, pressure, potential and current density fields due to a vertical displacement applied to the top surface of the layer, with no resistance to fluid flow normal to the top surface.

In terms of the non-dimensional variables of the last chapter, the corresponding boundary conditions are:

Case 3:

$$\begin{array}{llll} u_y(0) = 0 & u_z(0) = 1 & V_z(0) = 0 & j_z(0) = 0 \\ u_y(-1) = 0 & u_z(-1) = 0 & V_z(-1) = 0 & j_z(-1) = 0 \end{array} \tag{5.1}$$

and

Case 4:

$$\begin{array}{llll} u_y(0) = 0 & u_z(0) = 1 & p(0) = 0 & j_z(0) = 0 \\ u_y(-1) = 0 & u_z(-1) = 0 & V_z(-1) = 0 & j_z(-1) = 0 \end{array} \tag{5.2}$$

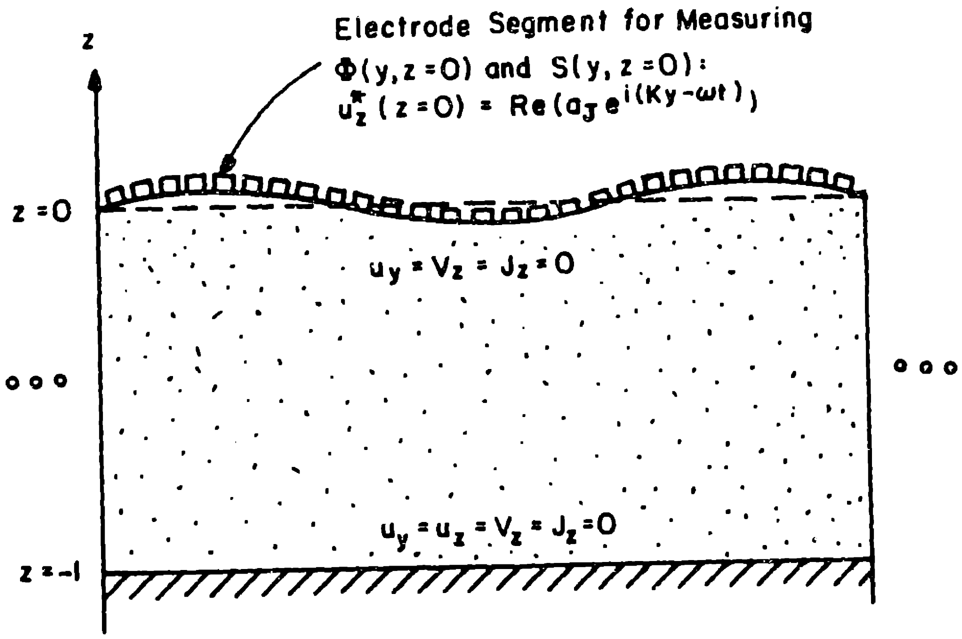
z
Electrode Segment for Measuring
Φ(y,z=0) and S(y,z=0):
$u_z^*(z=0) = \mathrm{Re}(a_J e^{i(Ky-\omega t)})$
z=0
$u_y = V_z = J_z = 0$
o o o
o o o
$u_y = u_z = V_z = J_z = 0$
z=-1

Figure 5.1: Geometry and boundary conditions for mechanical forcing. A two-dimensional sinusoidal current density is applied to the top of a δ^*-thick layer. The top and bottom are constrained so that there is no motion of the solid matrix or normal current density. At the top surface there is either no flow through the surface (case three, as shown) or no pressure gradient along the surface (case four). The electrode in contact with the top surface is segmented to allow measurement of $\Phi(y, z=0)$.

The drive in each of these cases is a unit amplitude cosinusoidal vertical displacement. Both cases have no displacement, vertical velocity or vertical current density at the bottom surface, and no horizontal displacement or current density at the top. Case three allows no fluid flow normal to the surface. Note, however, that the non-zero vertical displacement of the top surface now requires that the non-linear term in equation 4.2 be dropped. This is easily justified if the amplitude of the imposed displacement is sufficiently small relative to its wavelength. Case four assumes that the top surface, along with whatever is in contact with it, is infinitely permeable, so that the pressure will be the same at every point along the surface. The value of the transform of the pressure is thus zero at ($z = 0$) for any non-zero wavenumber k (*cf.* equation 3.1).

The above boundary conditions are again intended to simulate the action of an electromechanical probe to be used on articular cartilage *in vivo*. In order to simulate the boundary conditions of interest, the surface electrode can be thought of as a line of isolated, segmented electrodes connected to a high impedance amplifier so that there is no normal current (*cf.* figure 5.1). The segmentation of the electrode allows for the measurement of $\Phi(y, z = 0)$ along the surface. Also, in case four the electrode is considered to be made of an infinitely porous material, like that in the experiments of Frank [34] described in figure 4.12.

The first fact to note about the above cases is that the current density field $\vec{J}$ is everywhere zero. This is easily seen from equations 3.16 or 3.17 and the homogeneous boundary conditions (on J_z) above. A simple consequence of this fact is that the potential is proportional to the pressure *via* $\phi^H = -b_c p^H$ (equation 3.27). Thus the potential will not be discussed separately in this chapter.

The vanishing of the current density also implies that a maximum or minimum in the magnitude of the (transformed) pressure p occurs only when the relative velocity fields V_y and V_z are co-linear in the complex plane. To see this, note that, from equations 3.9,

$$
\begin{aligned}
\frac{\delta}{2}\partial_z|p|^2 &= \delta(\,\mathrm{Re}\,p'\,\mathrm{Re}\,p + \,\mathrm{Im}\,p'\,\mathrm{Im}\,p) \\
&= (-\,\mathrm{Re}\,V_z)(-\,\mathrm{Im}\,V_y) + (-\,\mathrm{Im}\,V_z)(\,\mathrm{Re}\,V_y) \qquad (5.3) \\
&= (\,\mathrm{Re}\,V_z,\ \mathrm{Im}\,V_z)\cdot\begin{pmatrix} \mathrm{Im}\,V_y \\ -\,\mathrm{Re}\,V_y \end{pmatrix}.
\end{aligned}
$$

Since the last vector is normal to V_y in the complex plane, $\partial_z|p(z)| = 0$ iff V_z is colinear with V_y. The latter condition is equivalent to V_y and V_z being in phase or 180° out of phase. Thus at points where the pressure is a local maximum or minimum in z, either V_y is maximum at the same time as V_z is minimum, or *vice versa*.

It is now also possible to derive a condition necessary for mechanical energy dissipation. If the mechanical work done on the solid per unit time and per unit length in the x-direction is denoted W^*, then by appropriately choosing the phase (or time origin) in equations 3.1 through 3.6 we have

$$
\begin{aligned}
W^* &= S(z=0)\cdot(-\partial_t u_z(z=0)) \ = \ \sigma_{zz}(0)\partial_t u_z^*(0) \\
&= -\omega(2G+\lambda_L)\,\mathrm{Re}\,\epsilon_{zz}^*(0)\,\mathrm{Re}\,iu_z^*(0) \qquad (5.4) \\
&= -\omega(2G+\lambda_L)\,\mathrm{Re}\,u_z^*(0)\partial_z\cdot\ \mathrm{Re}\,iu_z^*(0)\ .
\end{aligned}
$$

Note that this uses the fact that no shear work is being done (as $u_y(0) = 0$), and that there is no pressure work done on the fluid because either $u_z(0) = 0$ (case three), or $p(0) = 0$ (case four). If $\langle\cdot\rangle$ now denotes a time average over one period ($2\pi/\omega$), then the relation

$$
\langle\,\mathrm{Re}\,(Ae^{-i\omega t})\,\mathrm{Re}\,(Be^{-i\omega t})\rangle = \frac{1}{2}\,\mathrm{Re}\,(A\bar{B})
$$

(A and B constant in t) gives

$$
\langle W^*\rangle = \frac{1}{2}\omega(2G+\lambda_L)\,\mathrm{Re}\,[i\partial_z u_z(0)\bar{u}_z(0)]\,, \qquad (5.5)
$$

where $\bar{u}_z$ denotes the complex conjugate of u_z. Since the energy put into a dissipative system is expected to be positive, and because $u_z(0) = 1$ by equations 5.1 and 5.2, we now require

$$0 < \langle W^* \rangle = \operatorname{Re}\left(i\partial_{z^*} u_z(z=0)\right). \tag{5.6}$$

By letting $u_z = Ae^{i\psi}$ and noting that $\psi(0) = 0$, and $A(0) = 1$, we obtain (for cases three and four)

$$\langle W^* \rangle > 0 \qquad \text{iff} \qquad \partial_z \arg u_z < 0\,. \tag{5.7}$$

Thus energy is dissipated in this system if and only if the phase of the vertical displacement is increasing as one moves down into the layer. Since the phase is a measure of the time lag with respect to the profile of the drive at $z = 0$ (u_z, in these cases), this means that energy is dissipated only if the vertical displacement has a time lag just below the surface. This intuitive result has been verified for the calculations in a number of parameter regimes. It is exemplified by figure 5.2, which shows that $\arg u_z$, though an increasing function of z on a larger scale, is strictly decreasing in z in a thin layer near the top surface, for at least $\lambda = 10\,mm$ and the frequencies shown. (Parameters and calculation methods are discussed in §5.2.2, *cf.* also appendix A.2). Thus the model is known to have an appropriate behavior with respect to energy dissipation.

5.2.2 Numerical Results

The calculations performed in this section used exactly the same methods and parameter values as section 4.2.1. Because the current density $\vec{J}$ is zero everywhere, the equations for $k_1, \ldots, k_6$ are now obtained directly from the boundary conditions 5.1 or 5.2 and the equations for the homogeneous solutions 3.24. For case three (which has no flow through the top surface), the studies done were the same as those for the current-forced problem listed on page 63. For case four (which has an infinitely

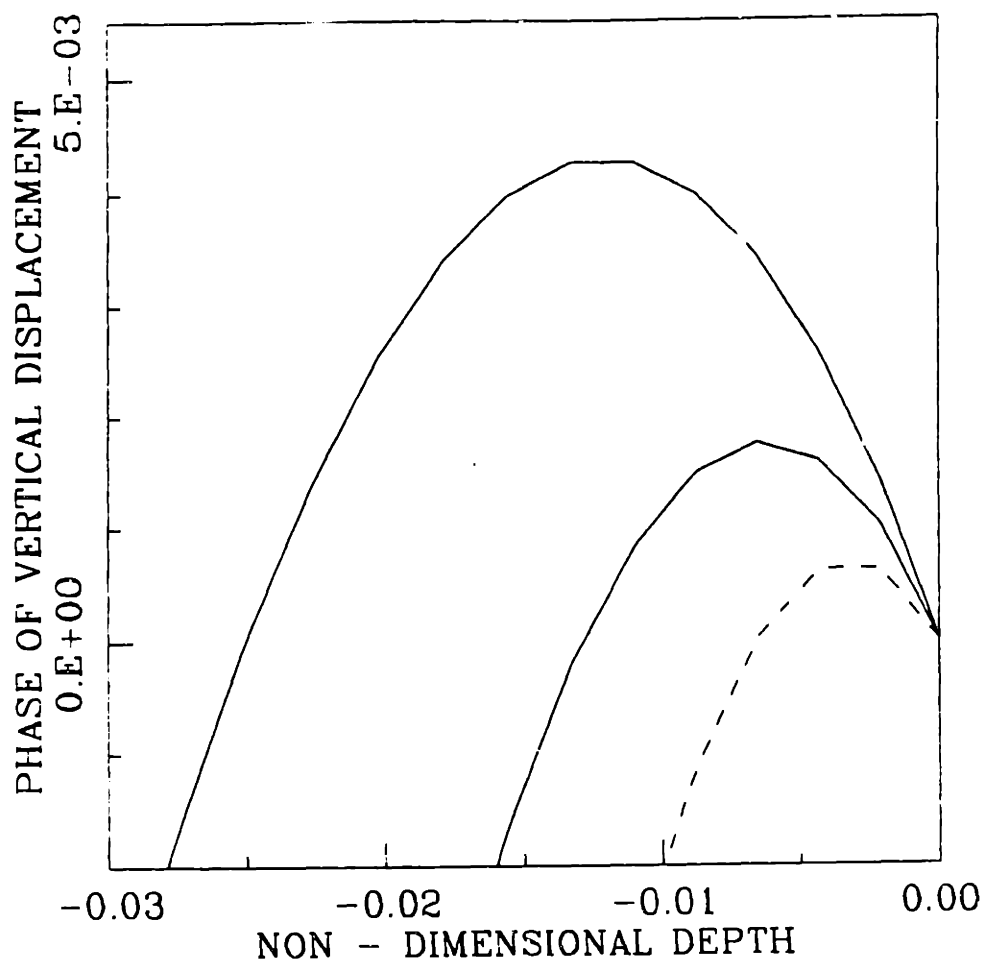

Figure 5.2: Phase of the vertical displacement *vs.* depth for $\lambda = 10.\ mm, f = 2.5 \cdot 10^{-2}, 5 \cdot 10^{-2}$, and 0.1 Hz. The highest curve is the lowest frequency, while the lowest, dashed curve is the highest frequency. Even though on a large scale the phase of the displacement decreases into the layer, closer examination reveals a phase increase, consistent with energy dissipation.

$f\ (Hz)/$ $\lambda\ (mm)$	$u_y^*\ (mm)$	$V_y^*\ (\mu m/s)$	$V_z^*\ (\mu m/s)$	$P\ (kPa)$	$\Phi\ (mV)$	$S(0)\ (kPa)$
0.001/10.	0.106	$8.36 \cdot 10^{-2}$	0.476	133.	1.33	124.
0.001/1.0	$2.66 \cdot 10^{-2}$	$4.04 \cdot 10^{-2}$	0.111	6.44	$6.44 \cdot 10^{-2}$	90.0
0.001/0.1	$2.62 \cdot 10^{-2}$	$4.12 \cdot 10^{-2}$	0.112	0.657	$6.57 \cdot 10^{-3}$	898.
0.01/10.	0.177	0.133	2.53	210.	2.10	204.
0.01/1.0	$3.20 \cdot 10^{-2}$	0.227	0.823	36.1	0.361	94.8
0.01/0.1	$2.62 \cdot 10^{-2}$	0.412	1.12	6.54	$6.54 \cdot 10^{-2}$	898.
0.1/10.	0.216	0.165	9.86	262.0	2.62	249.
0.1/1.0	$3.55 \cdot 10^{-2}$	0.462	3.58	73.6	0.736	101.
0.1/0.1	$2.65 \cdot 10^{-2}$	4.03	11.1	64.1	0.641	900.0

Table 5.1: Maximum field magnitudes for vertical displacement forcing of an infinitely permeable surface (case four). These are the dimensional values of the maxima (over 400 evenly spaced values of z) of the magnitudes of the indicated field variables. They are based on the parameter values given in equations 4.6 and 4.7, and use a displacement amplitude of $a_J = 0.1\ mm$. The magnitude of the surface stress, $S(0)$, is given instead of the maxima of $|S|$ over z.

permeable surface), the fields were found for $f = 10^{-3}\ Hz$ and $f = 0.1\ Hz$ with λ varying linearly from 0.1 to 10.1 mm in steps of 0.2. They were also found for $\lambda = 0.1\ mm$, with f varying linearly from 0.001 to 0.101 Hz by steps of 0.002, and $\lambda = 10\ mm$ with f varying logarithmically from 10^{-3} to 0.1 Hz. As for the current forced cases, the errors in meeting the boundary conditions (and thus, it is inferred, in the fields) are negligible relative to the overall magnitudes of the fields. Table 5.1 lists the maximum (over z) values obtained for various frequency and wavelength combinations.

The fields were again plotted as surfaces of magnitude or phase of a non-dimensional, transformed variable versus depth (z) and either λ, f, or $\log f$. Plots of all of the fields calculated for each set of values are in Appendix A.2. The magnitude of the vertical displacement, $|u_z|$, is shown in figure 5.3 for case four (permeable surface) for $\lambda = 10\ mm$. The effect of the diffusion boundary layer thickness, Δ, can be readily seen from the change in depth of the inflection point, even though the overall amplitude does not change. The two profiles given for the same field in case three (impermeable surface) show little frequency dependence of any kind (figure 5.4). These profiles, however, are similar to those of figure 5.3 in that the overall amplitude changes very little with frequency. Note that the overall frequency independence of the vertical displacements for both mechanically forced cases is in sharp contrast with the results of the current forcing of case one, as exemplified by figure 4.3 on page 66.

The magnitudes of the horizontal displacements are also relatively frequency independent, but, in contrast with those above, are virtually identical for the two cases. The magnitude of the horizontal displacement for case three is plotted in figure 5.5. Because of the significant difference between the fluid flow fields (discussed below), the similarity of the horizontal displacement fields is very likely an indication that the horizontal motion is largely driven by the conservation of mass.

The horizontal relative velocity is generally much larger than the vertical velocity in the third case, and is plotted in figure 5.6. The minimum at $\lambda \sim 2\ mm$ of the magnitude (evaluated at $z = 0$) seems to represent the crossover from the long-wave to short-wave behavior. A similar minimum in amplitude at the surface occurs for the relative vertical velocity in case four, as can be seen in figure 5.7. Here the minimum may be explained as follows: for shorter wavelengths there is a large normal flow due to the amount of displacement per unit volume near the surface. For longer wavelengths, the geometry is increasingly that of uniaxial compression, and

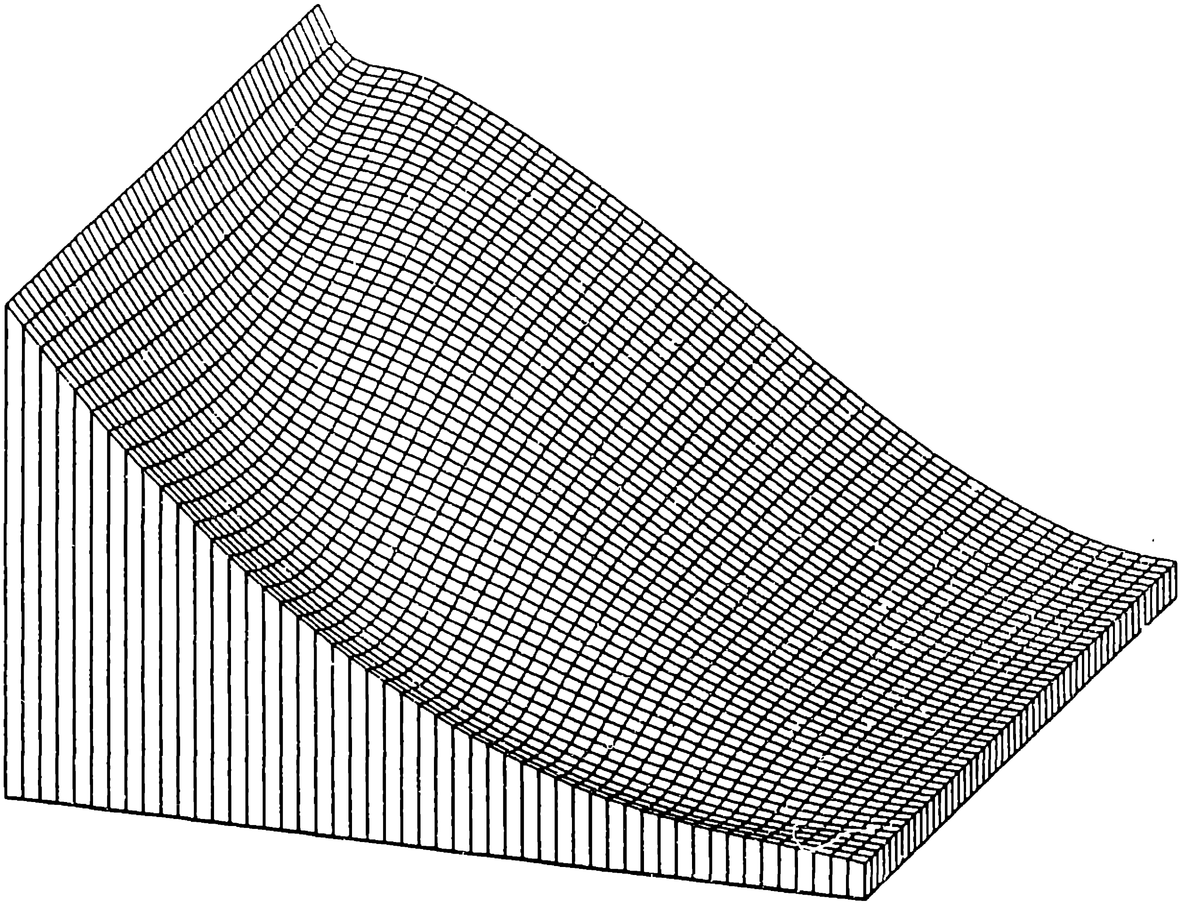

Figure 5.3: Magnitude of the vertical displacement, u_z, for a permeable surface, $\lambda = 10\ mm$, $f = 10^{-3}$ to $10^{-1}\ Hz$ logarithmically. The upper left-hand side is the top surface (z=0), and $f = 0.1\ Hz$ is at the back. The amplitude varies from exactly 1 (by equations 5.2: a_J is the dimensional value) to 0.

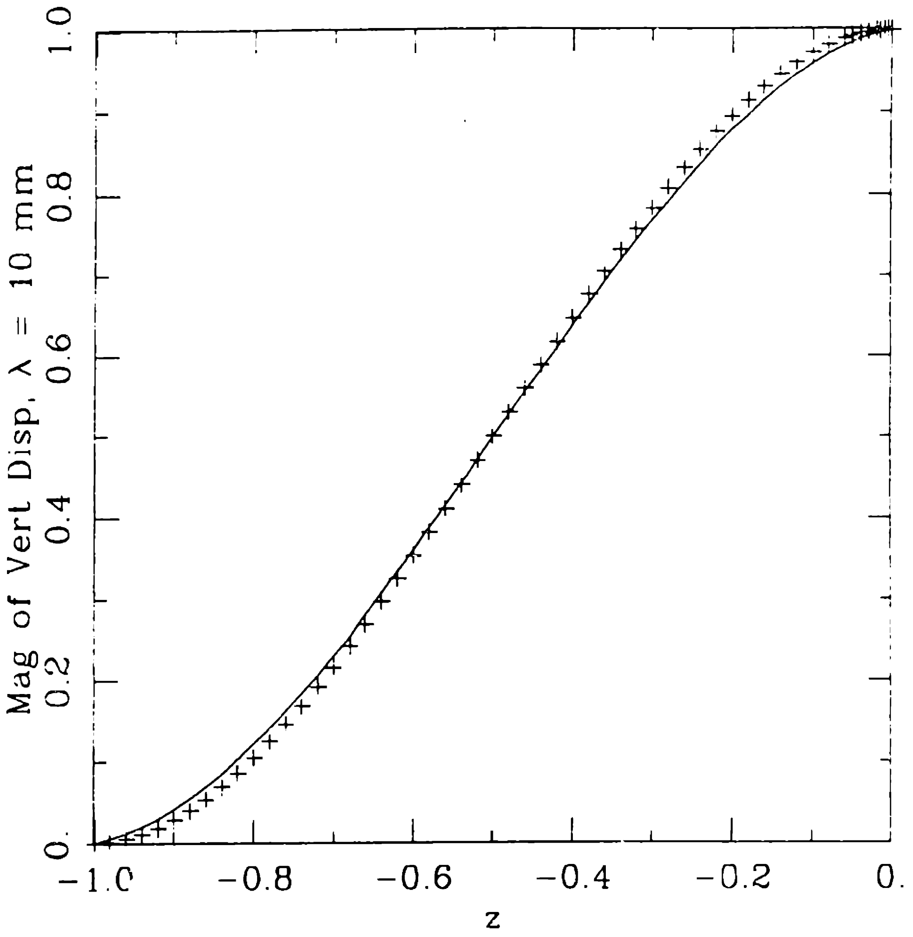

Figure 5.4: Magnitude of the vertical displacement, u_z, for an impermeable surface, $\lambda = 10\ mm$, $f = 10^{-3}$ (solid line) and 10^{-1} Hz.

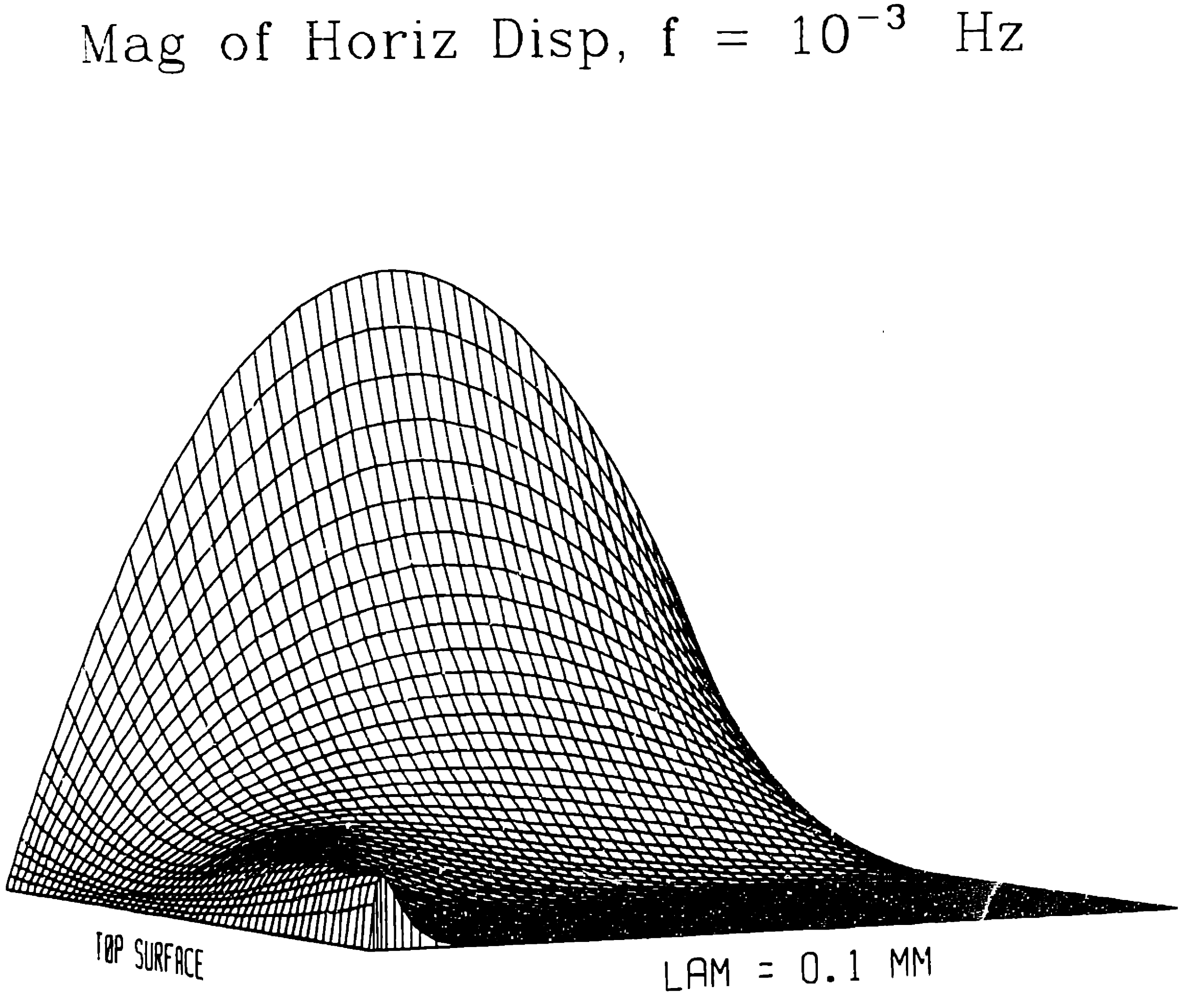

Figure 5.5: Magnitude of the horizontal displacement, u_y, for an impermeable surface, $f = 10^{-3}$ *Hz*, $\lambda = 0.1$ to 10. *mm* logarithmically. The maximum amplitude is 2.35 *mm* per *mm* of a_J.

the relative vertical velocity will increase to a level which obeys the one-dimensional conservation of fluid volume and the no-flow condition at the bottom, $z = -1$.

For case four the horizontal relative velocity is, for a wide range of frequencies and wavelengths, two orders of magnitude smaller than the vertical. This could be expected, as equation 3.9a with $\vec{J} = 0$ gives $\delta p = iV_y$. Since $p(z = 0) = 0$ in this case, $V_y(z = 0)$ is also constrained to zero. Similarly, $V_y \gg V_z$ for a large range of parameters in case three. This is a result of the fact that the fluid is constrained to horizontal (relative) motion at the top and bottom boundaries.

Two other results are especially noteworthy. First, there is a rise of the phase of the vertical displacement near the bottom boundary in almost every parameter range (with frequency $f \gtrsim 10^{-2}\ Hz$). In case three with $\lambda = 10\ mm$, shown in figure 5.8, this rise is about $\pi/5$. It is possible that this change in phase is related to the dissipation of energy expressed in equation 5.7.

Second, the frequency dependence of the fields of case three is very similar, at $\lambda = 10\ mm$, to the behavior expected in a one-dimensional experiment. From figure 5.5 it is clear that the parabolic displacement field expected for long-wave behavior (*cf.* §5.2.3) is only obtained for λ sufficiently greater than δ^*. In a truly one-dimensional situation, the vertical relative velocity is expected to be proportional to the frequency of the stimulus (*cf.*, *e.g.*, equation 5.13). In figure 5.9, however, the amplitude only increases by roughly one order of magnitude when the frequency increases by two. (V_z/f is shown on this plot, so exact proportionality would be demonstrated by a surface independent of f). Note however, that the amplitude is roughly symmetric about $z = -1/2$. This should be the case for a one-dimensional system with the boundary conditions here: the system is symmetric about this depth if considered in a frame moving with half the velocity of the top boundary – remember that inertia is being ignored here.

Further, at $f \sim 10^{-2}\ Hz$ the phase undergoes a violent transition from being

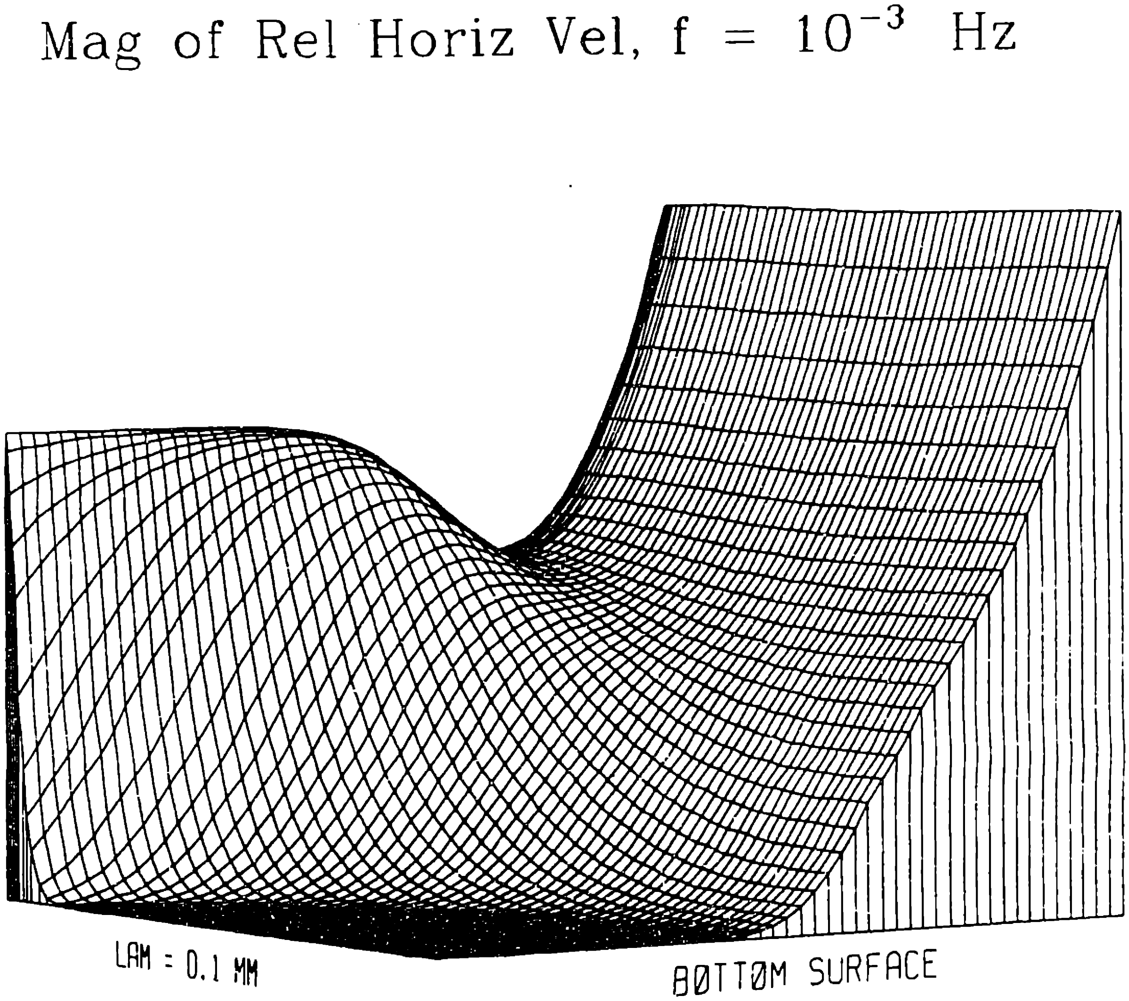

Figure 5.6: Magnitude of the relative horizontal velocity, V_y, for an impermeable surface, $f = 10^{-3}$ Hz, $\lambda = 0.1$ to 10. mm logarithmically. The maximum amplitude is 1.65 $\mu m/s$ per mm of a_J.

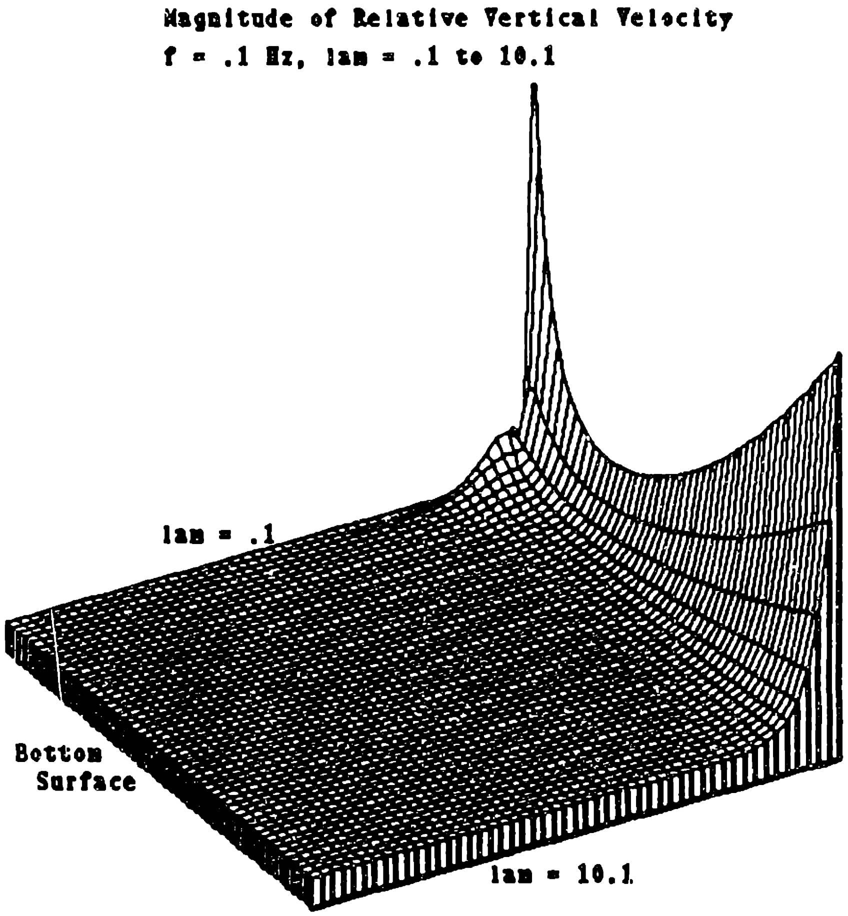

Figure 5.7: Magnitude of the relative vertical velocity, V_z, for a permeable surface, $f = 10^{-1}\ Hz$, $\lambda = 0.1$ to $10.1\ mm$ linearly. The maximum amplitude is 1.11 $\mu m/s$ per mm of a_J.

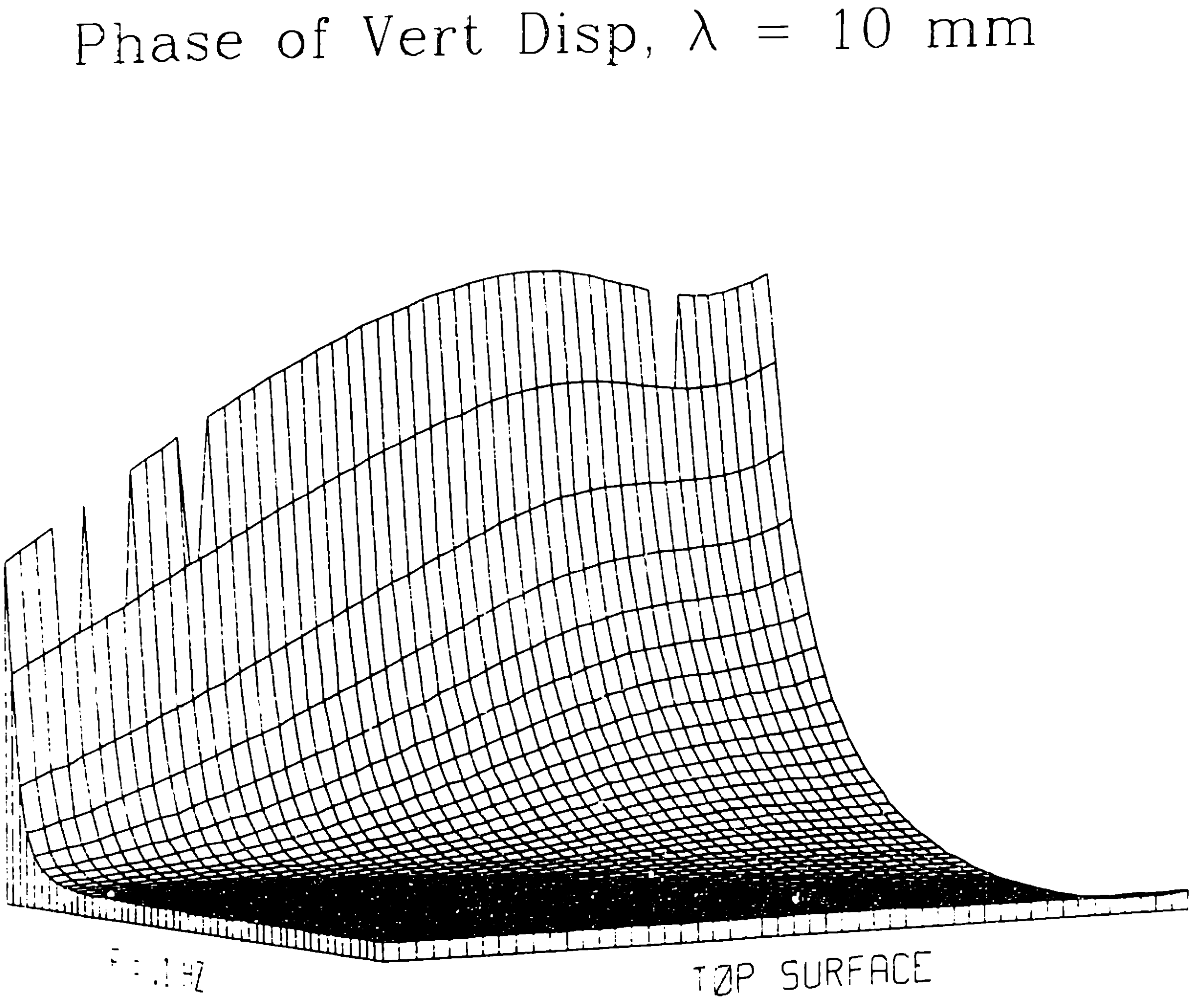

Figure 5.8: Phase of the vertical displacement, u_z, for an impermeable surface, $\lambda = 10$ *mm*, $f = 10^{-3}$ to 10^{-1} *Hz* logarithmically. The minimum value is -0.02 radians, the maximum is 0.66.

nearly constant in z (at about 0) for higher frequencies, to a step-function symmetric about the center (with values $\sim -\pi/2$ at the top and $\sim \pi/2$ at the bottom) for lower frequencies. The system is now acting as though it is being uniformly, periodically pressurized, which is the expected low-frequency behavior. The presence of this behavior for a Δ^* of only about $\delta^*/3$ ($f = 10^{-3}$ Hz) is a familiar case of an asymptotic behavior appearing before it can be rigorously justified. In addition, for frequencies above that of the transition, the depth over which the phase changes significantly seems to be proportional to Δ^*, as expected.

5.2.3 Asymptotic Results

This section presents the long and short wave asymptotic limits (*cf.* §4.2.2 for the case of a mechanically driven layer with an infinitely permeable surface (case four). Only case four is being presented since the two cases are very similar. More important, however, is the fact that a one-dimensional experiment in the case of an impermeable surface would effectively measure the compressibility of the material. Since the constituents have been assumed to be incompressible, the present model would not be expected to properly predict the behavior of the material under these conditions.

The Short-Wave Limit

This section considers the short-wave limit $\delta \rightarrow \infty$. The procedure here is similar to that of section §4.2.2. The wavelength of the disturbance is so short compared to the thickness of the layer that the bottom of the layer may be considered to be at $z = -\infty$. Thus, as in §4.2.2, the boundary conditions 5.2 at $z = 0$ and the homogeneous solutions 3.24 now determine the equations for the k_i:

$$u_y(0) \quad = 0 = \quad k_1 + k_3/\delta + k_5$$

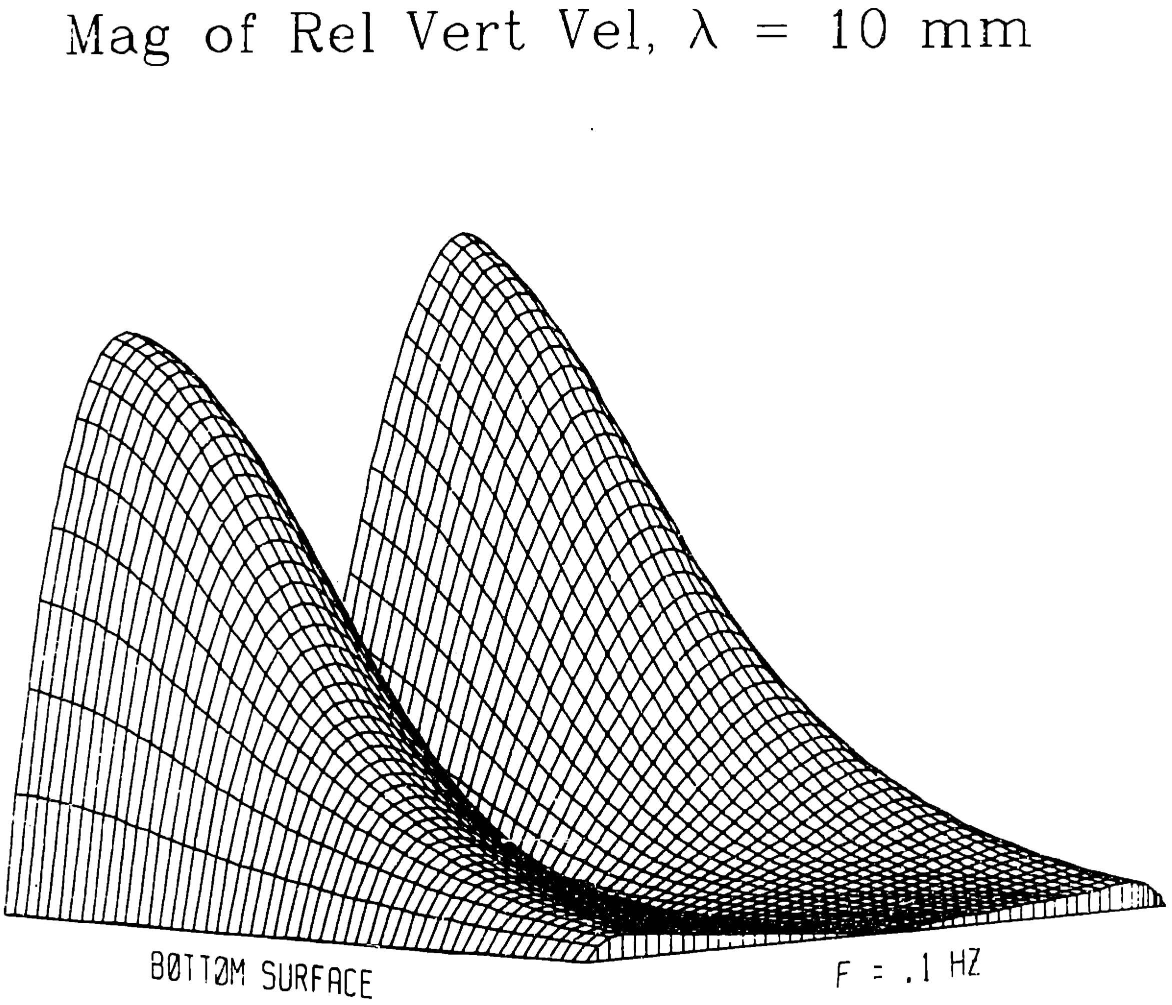

Figure 5.9: Magnitude of the relative vertical velocity, V_z, for an impermeable surface, $\lambda = 10\ mm$, $f = 10^{-3}$ to $10^{-1}\ Hz$ logarithmically. The maximum amplitude is 0.128 $\mu m/s$ per mm of a_J.

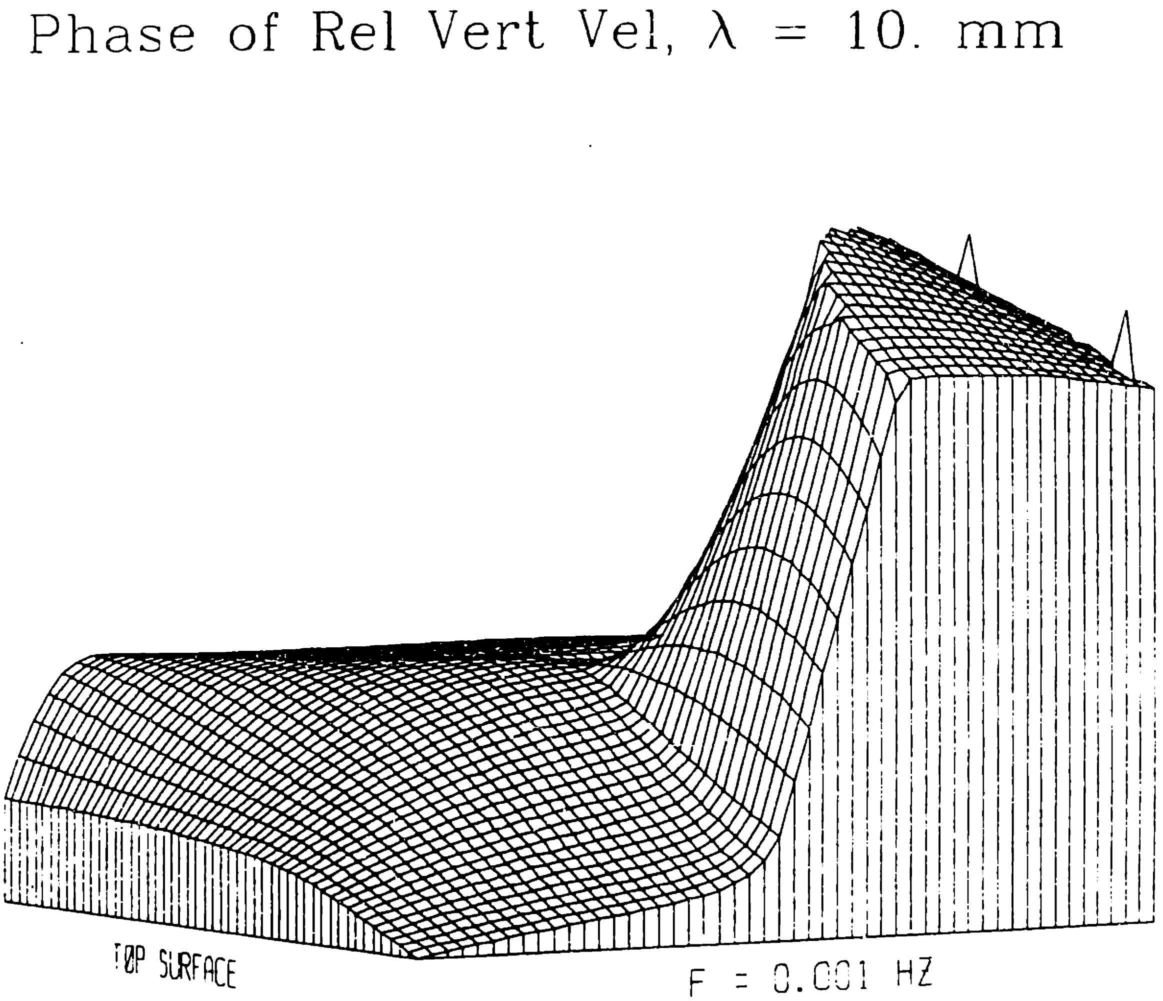

Figure 5.10: Phase of the relative vertical velocity, V_z, for an impermeable surface, $\lambda = 10\,mm$, $f = 10^{-3}$ to 10^{-1} Hz logarithmically. The range is from -1.43 to 2.58 radians, with a jump tolerance of 0.4 (*cf.* figure 4.6).

$$\begin{aligned} u_z(0) &= 1 = & k_1 + \Lambda k_5 \\ p(0) &= 0 = & 2nk_3 - i\frac{r}{\delta\phi_0}k_5 \end{aligned} \tag{5.8}$$

The solution to this system is

$$\begin{aligned} k_1 &= -(1 + \frac{ir}{2n\delta^2\phi_0})k_5 \\ k_3 &= \frac{ir}{2n\delta\phi_0}k_5 \\ k_5 &= [\Lambda - 1 - \frac{ir}{2n\delta^2\phi_0}]^{-1} \end{aligned} \tag{5.9}$$

As before these equations along with equations 3.24 determine a solution which satisfies the differential equations exactly, and satisfies the boundary conditions at the bottom to order $\mathcal{O}(e^{-\delta})$. These solutions are:

$$\begin{aligned} u_y &\sim k_5[\tfrac{-r}{2n\delta\phi_0}z + i(e^{(\Lambda-1)\hat{z}} - 1)]e^{\hat{z}} \\ u_z &\sim k_5e^{\hat{z}} + k_5[\tfrac{ir}{2n\delta\phi_0}z + \Lambda(e^{(\Lambda-1)\hat{z}} - 1)]e^{\hat{z}} \\ v_y &\sim k_5r[\tfrac{ir}{2n\delta\phi_0}z + \alpha_0(1 - e^{(\Lambda-1)\hat{z}})]e^{\hat{z}} \\ v_z &\sim k_5r[\tfrac{r}{2n\delta\phi_0}(z - \delta^{-1}) + i\alpha_0(\Lambda e^{(\Lambda-1)\hat{z}} - 1)]e^{\hat{z}} \\ V_y &\sim k_5r\phi_0^{-1}(e^{(\Lambda-1)\hat{z}} - 1)e^{\hat{z}} \\ V_z &\sim ik_5r\phi_0^{-1}(e^{(\Lambda-1)\hat{z}} - 1)e^{\hat{z}} \\ p &\sim ik_5\tfrac{r}{\delta\phi_0}(1 - e^{(\Lambda-1)\hat{z}})e^{\hat{z}} \\ \phi &\sim -b_cp \end{aligned} \tag{5.10}$$

and,

$$s(0) \sim k_5\tfrac{ir}{\delta\phi_0},$$

where once again $\hat{z} = kz^*$ is the boundary layer variable.

These asymptotic solutions agree extremely well with the numerically calculated ones, as can be seen in figures 5.11 and 5.12. The former shows that the numerical and asymptotic values for the horizontal and vertical displacements agree well for $\lambda = 0.1$ *mm*, and $f = 10^{-3}$ *Hz*. All of the fields have the boundary layer characteristics exhibited by these displacements. Figure 5.12 shows that the predicted stress also agrees quite well with that predicted numerically. Also, the agreement through $\lambda \approx 2\ mm$ (where $\lambda > \delta$) is again better than might be expected from purely physical reasoning.

Equations 5.10 may be simplified in the low frequency limit $\Delta \gg 1$. In this limit for any $\hat{z}$ satisfying $|\hat{z}|/\Delta^2 \ll 1$ and $|\hat{z}| \ll \delta$ (so that the field magnitudes are significant),

$$e^{(\Lambda-1)\hat{z}} - 1 \sim (\Lambda - 1)\hat{z} \sim \frac{-ib}{4(1-\nu)\phi_0}\hat{z}.$$

Further,

$$k_5 \sim \frac{4i\delta^2\phi_0 n(1-\nu)}{(3-4\nu)r}.$$

Using this in the above yields

$$\begin{aligned}
u_y &\sim \tfrac{-i}{3-4\nu}\hat{z}e^{\hat{z}} \\
u_z &\sim [1 - \tfrac{z}{3-4\nu}\hat{z}]e^{\hat{z}} \\
v_y &\sim \tfrac{2\nu(\alpha_0-1)-(2+\alpha_0)}{3-4\nu}r\hat{z}e^{\hat{z}} \\
v_z &\sim \tfrac{i}{3-4nu}[(n\phi_0^{-1}+1)\hat{z} + n(\alpha_0 - 1) - 1]re^{\hat{z}} \\
V_y &\sim -\tfrac{n\phi_0^{-1}+4\nu}{3-4\nu}r\hat{z}e^{\hat{z}} \\
V_z &\sim \tfrac{in}{\phi_0(3-4\nu)}[1+\hat{z}]re^{\hat{z}} \\
p &\sim -\tfrac{irn}{\phi_0\delta(3-4\nu)}\hat{z}e^{\hat{z}}
\end{aligned}$$

These equations show that the maximum pressure is proportional to the frequency and wavelength of the disturbance (the pressure is zero at the surface). They also demonstrate that the maximum velocities are proportional to frequency. Further, figure 5.13, which shows the magnitude of the vertical velocity divided by frequency for $\lambda = 0.1\ mm$ at $f = 10^{-3}$ and 0.1 Hz, exemplifies the frequency proportionality which the pressure and velocity fields exhibit for short-wave disturbances. (The phases do change somewhat with frequency.) The displacements are similarly frequency independent. It may thus be surmised that equations 5.10 are valid over the range of frequencies considered in this work.

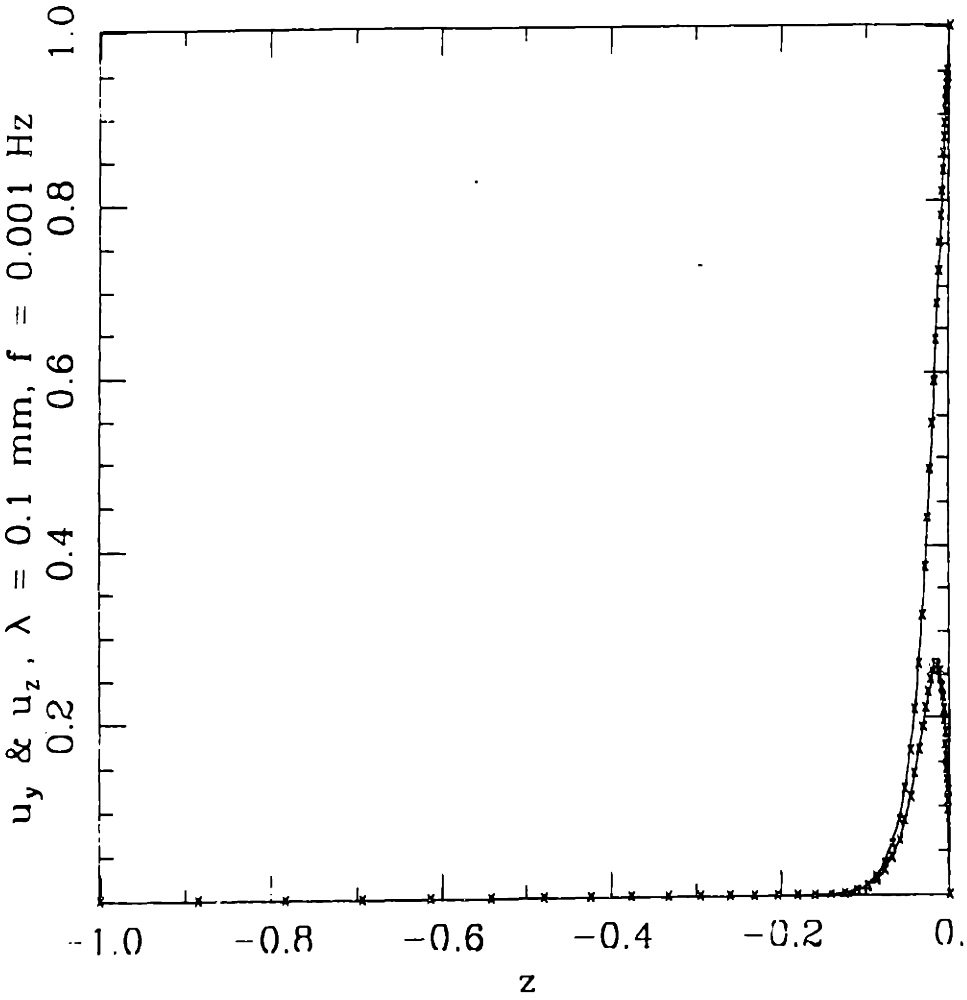

Figure 5.11: Magnitude of horizontal and vertical displacements, u_y, and u_z, for a permeable surface, $f = 0.001$ Hz, $\lambda = 0.1$ mm. The units are normalized to the vertical displacement at $z = 0$. The solid lines show the numerical results, while the "x"'s mark the those of equations 5.10a (lower) and b (upper).

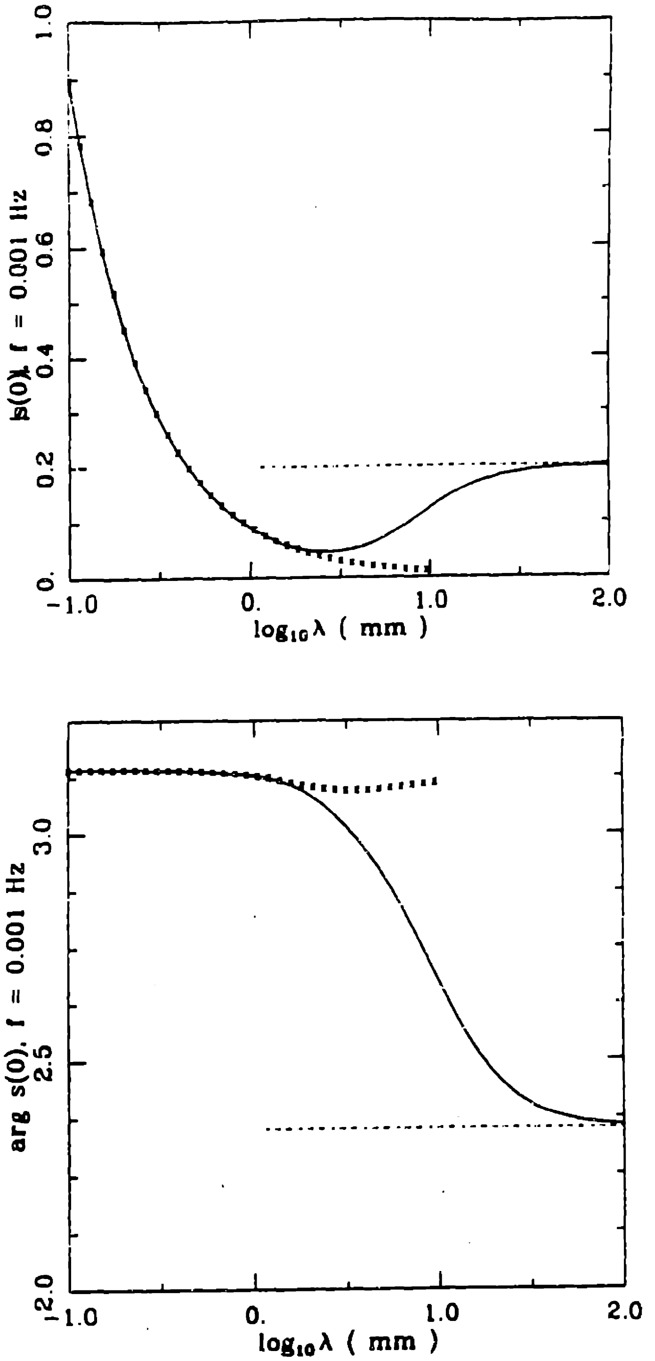

Figure 5.12: Magnitude and phase of the surface stress, $s(0)$, for a permeable surface, $f = .001\,Hz$, vs. $\log_{10}\lambda$. The solid lines show the numerical results, and those of equations 5.10i and 5.13f are marked with dashed and dotted lines, respectively. The units are $10^5\ N/m^2$ per mm of a_J.

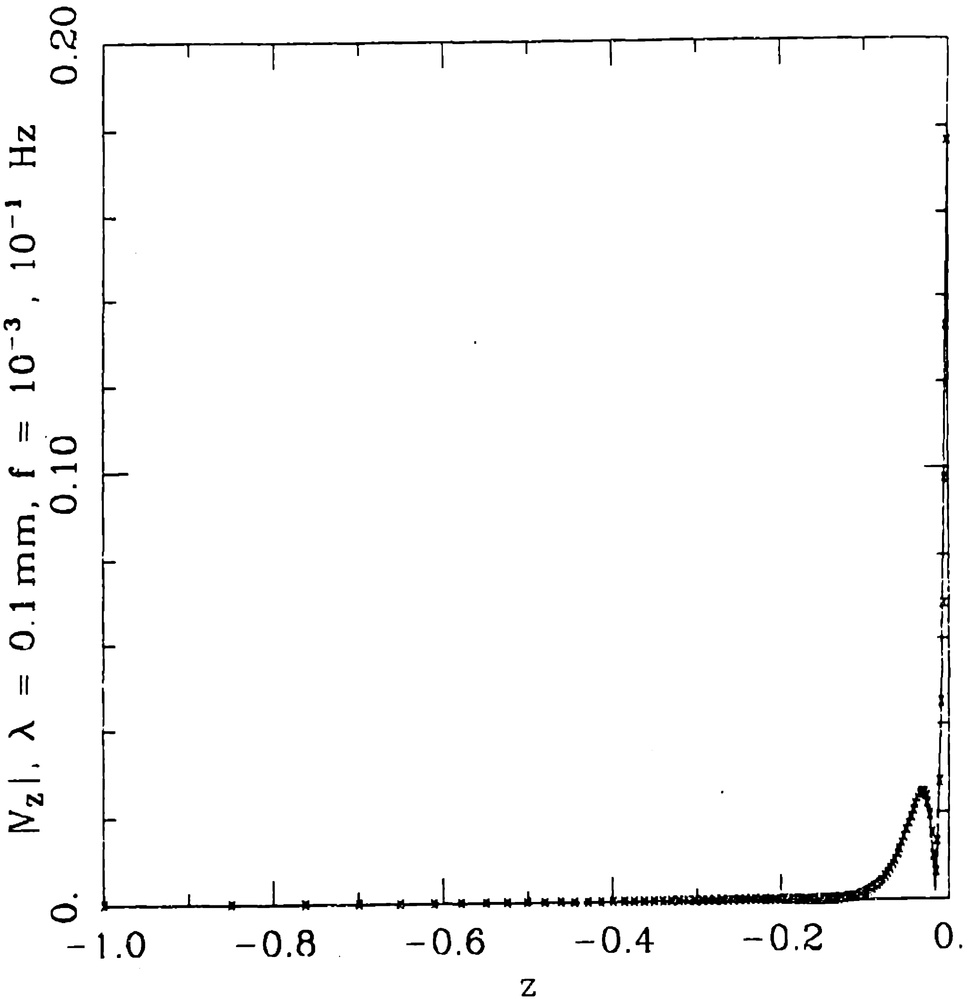

Figure 5.13: Numerically calculated magnitude of vertical relative velocity, V_z, for a permeable surface, $f = 0.001, 0.1\,Hz$, $\lambda = 0.1\ mm$. The numerical results for $f = 0.001$ are shown by a solid line, and those for $f = 0.1$ are drawn with "x"'s. The dimensional values are the value shown times ω times the amplitude of the imposed vertical displacement, a_f.

The Long-Wave Limit

This section considers case four in the limit $\delta \to 0$, for which the wavelength of the imposed wave is much larger than the thickness of the layer. In this case a formal perturbation expansion

$$\begin{aligned} u_y &= \delta(u_{y0} + \delta^2 u_{y1} + \dots) & u_z &= u_{z0} + \delta^2 u_{z1} + \dots \\ V_y &= \delta(V_{y0} + \delta^2 V_{y1} + \dots) & V_z &= V_{z0} + \delta^2 V_{z1} + \dots \\ p &= p_0 + \delta^2 p_1 + \dots & s &= s_0 + \delta^2 s_1 + \dots \end{aligned} \tag{5.11}$$

was used. The relative magnitudes of the lowest order fields was chosen to be consistent with the boundary conditions 5.2 and the expected resemblance to one-dimensional fields. Using equations 3.15 to reduce (3.8)-(3.11) to five equations in u_y, u_z, V_y, and V_z, and p and substituting 5.11 gives:

$$\begin{aligned} -iru'_{z0} + \phi_0 V'_{z0} &= O(\delta^2) \\ p_0 - iV_{y0} &= O(\delta^2) \\ p'_0 + V_{z0} &= O(\delta^2) \\ iV_{z0} - V'_{y0} &= O(\delta^2) \\ nu''_{y0} + iu'_{z0} - ip_0 &= O(\delta^2)\,, \end{aligned} \tag{5.12}$$

The solution to these equations using boundary conditions 5.2 is

$$\begin{aligned} u_{z0} &= \frac{\sinh\zeta(z+1)}{\sinh\zeta} \\ u_{y0} &= \frac{i}{\zeta\sinh\zeta}(\cosh\zeta(z+1) + \frac{ir}{n\phi_0}\frac{z^2}{2}\cosh\zeta + L(z)) \\ p_0 &= -\frac{ir}{\phi_0}\frac{\cosh\zeta(z+1) - \cosh\zeta}{\zeta\sinh\zeta} \\ V_{z0} &= \frac{ir}{\phi_0}u_{z0} \\ V_{y0} &= -ip_0 \\ s_0(0) &= -2(1-\nu)\zeta\frac{\cosh\zeta}{\sinh\zeta}\,, \end{aligned} \tag{5.13}$$

where

$$L(z) = [1 + (\frac{ir}{2n\phi_0} - 1)\cosh\zeta]z - \cosh\zeta\,,$$

and, as in equation 4.17 on page 78,

$$\varsigma \equiv \sqrt{\frac{-ir}{2(1-\nu)\phi_0}} = \frac{\delta^*}{\Delta^*} e^{-i\frac{\pi}{4}}.$$

For the boundary conditions used in this case, the approach to long wave behavior is slower than that investigated in section 4.2.2. This may be seen in figure 5.14 which shows the horizontal and vertical displacements for $\lambda = 100\ mm$ and $f = 10^{-3}\ Hz$. Even though the maximum horizontal displacement is expected to decay in proportion to the wavenumber, at this wavelength it is still nearly 20% of that of the vertical. In spite of this fact, the agreement between the numerics and asymptotics is quite good. (At $\lambda = 10\,mm$, $\max u_y \approx \max u_z$, and there is little agreement between numerics and asymptotics.) Also, the pressure (and potential) field is unambiguously defined here (in contrast with §4.2.2), and the agreement is as good as that for the displacements. Because of the good agreement of the numerical and asymptotic vertical displacements (for sufficiently high λ), and because the pressure at $z = 0$ is zero by the boundary conditions 5.2, the prediction of the surface stress is also very good, as can be seen in figure 5.12.

The frequency dependence of this case does have some similarities with that of the current forced problem. Figure 5.15 demonstrates how the penetration depth of the relative vertical velocity (and, in fact, all of the fields) depends on the frequency. For the long wave case, the disturbance only propagates for a distance comparable to the diffusion boundary layer thickness, Δ^*. Figure 5.16 shows that even though the value of the phase of the velocity field is constant in frequency at $z = 0$, the phase increases (*i.e.* a lag develops) much more rapidly at high frequencies. This behavior is familiar from the short-wave behavior of both this case and case one (*cf.* §4.2.2).

One of the most salient features of the long-wave limit, however, is that it agrees with one-dimensional analytic and experimental results of other authors [25,35]. If

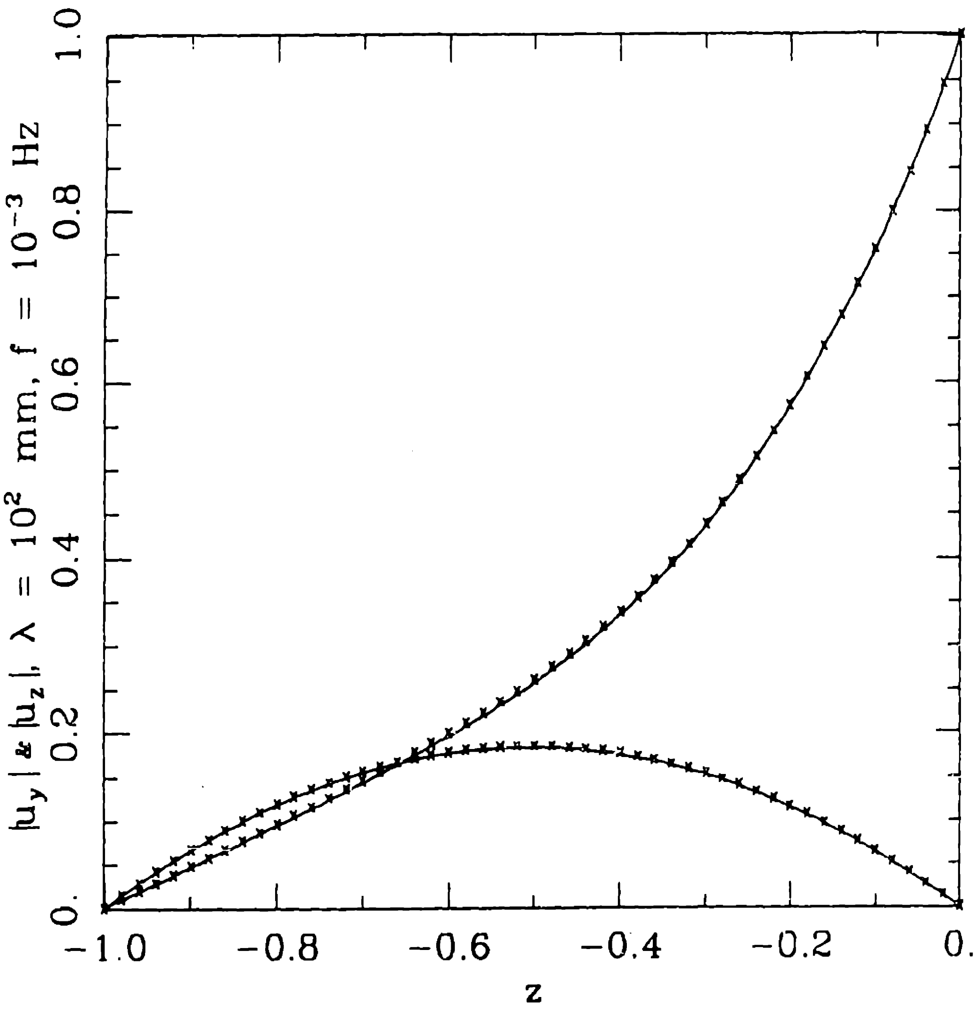

Figure 5.14: Magnitude of the horizontal and vertical displacements, $|u_y|$ and $|u_z|$, for a permeable surface, $\lambda = 10^2\,mm$, $f = 0.001\,Hz$ *vs.* depth z. The solid lines show the numerical results, while the "x"'s show the results of equations 5.13a (upper) and b (lower). Magnitude is normalized by a_J.

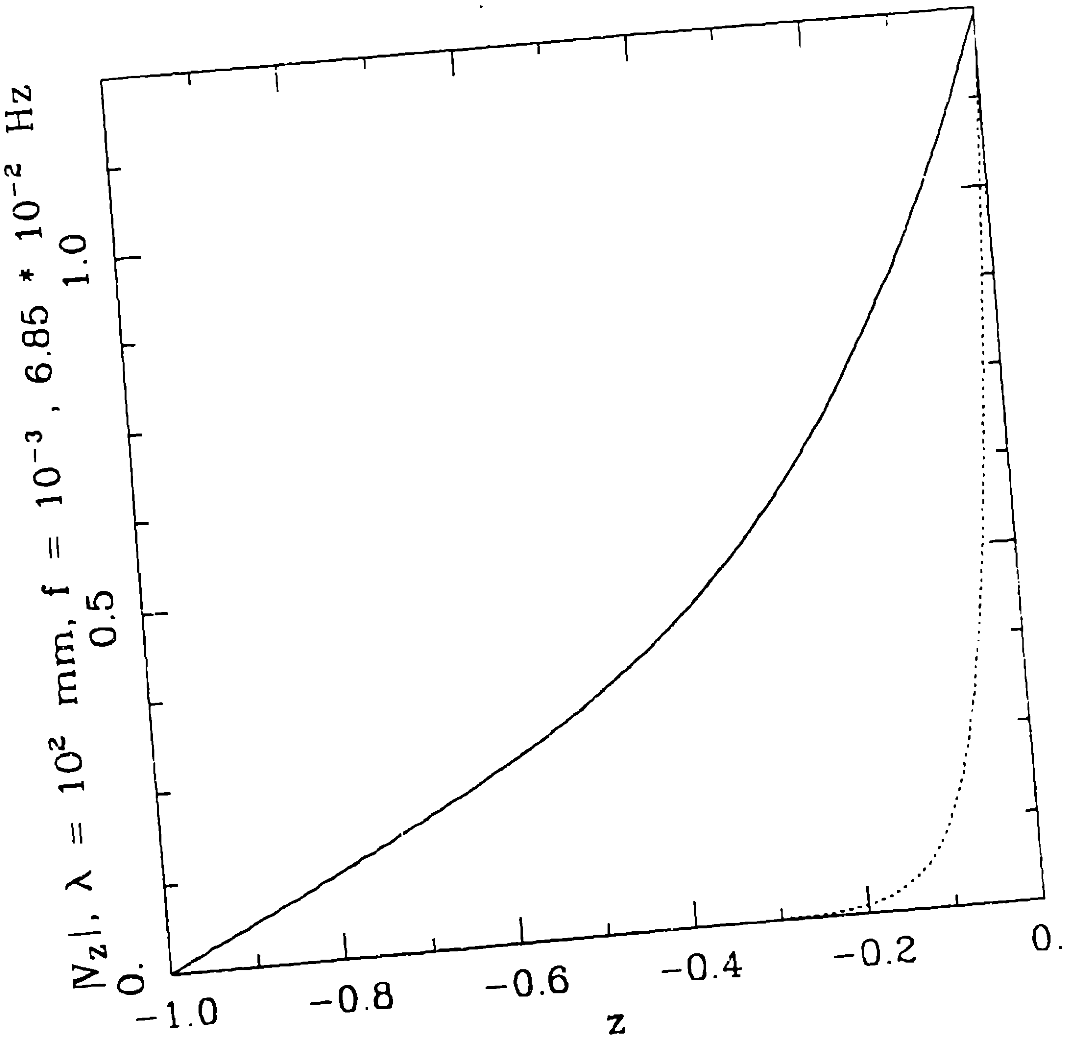

Figure 5.15: Numerically calculated magnitude of the vertical relative velocity, $|V_z|$, for a permeable surface, $\lambda = 10^2$ *mm*, $f = 10^{-3}, 6.85 \cdot 10^{-2}$ *Hz* *vs.* depth z. The dimensional values are the value shown times ω times the amplitude of the imposed vertical displacement. The frequency $6.85 \cdot 10^{-2}$ was chosen because it is near the highest value for which the numerical results converge.

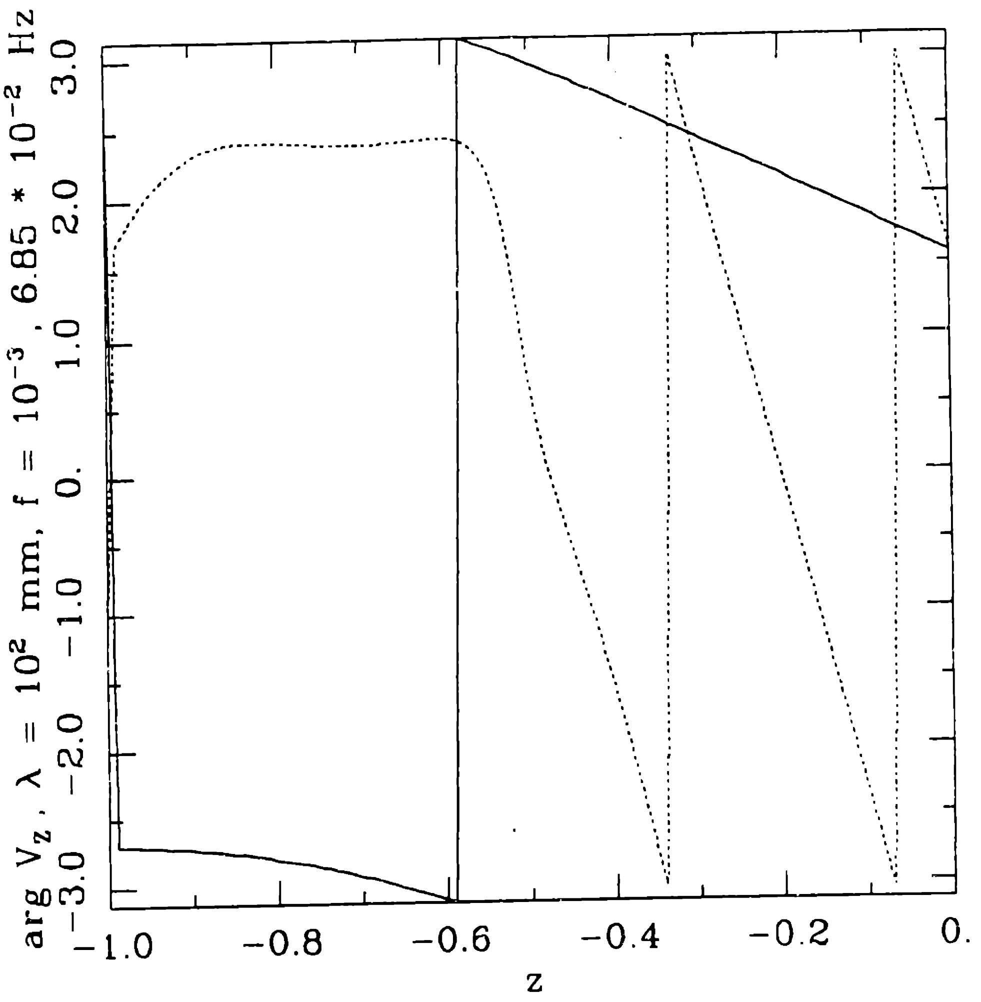

Figure 5.16: Numerically calculated phase of the vertical relative velocity, $|V_z|$, for a permeable surface, $\lambda = 10^2$ *mm*, $f = 10^{-3}, 6.85 \cdot 10^{-2}$ *Hz vs.* depth z.

the notation is changed so that the relative velocity is defined as $\phi_0 V_y$ and $\phi_0 V_z$ (flow is defined as flux per unit total area), and the k_{ij} defined appropriately *via* equation 2.6, then Eisenberg's 25 and Frank's [35] analytical results agree exactly with those in equations 5.13. Furthermore, if the boundary conditions are slightly modified to account for the application of the surface displacement *via* a compressible porous platen (as in §4.3), then there is good agreement with experimental data. The analysis of these modified boundary conditions has been performed by Frank [35], who also performed experiments using vertical displacement driving and confined uniaxial compression. A plot of the magnitude of both experimentally measured and analytically determined streaming potential is shown in figure 5.17.

5.3 Discussion

The use of mechanical stimulation to estimate the values of physical parameters of a layer of electromechanically coupled material may now be seen to have several characteristics in common with the current stimulation (case one) of Chapter 4. These similarities are particularly visible through the dependence of the fields on the frequency and wavelength of the imposed disturbance, as will be discussed below. A significant difference, though, is that fewer data values are available for a given f and λ because, at $z = 0$, $J = 0$. In case four, for which the top surface is infinitely permeable, we found that $\phi = p = 0$, so that even one less measurement (that of $\phi(0)$) may be used to estimate parameter values. If $\phi(0)$ is measured, however, the resulting value may be used as measure of linearity, the degree to which the boundary conditions are physically realized, *etc.*

As in Chapter 4, the penetration depth of the disturbance is limited by both the wavelength, λ, and diffusion boundary layer thickness, Δ^*, of the imposed surface displacement. In the short wave limit, the fields are only significant in a boundary

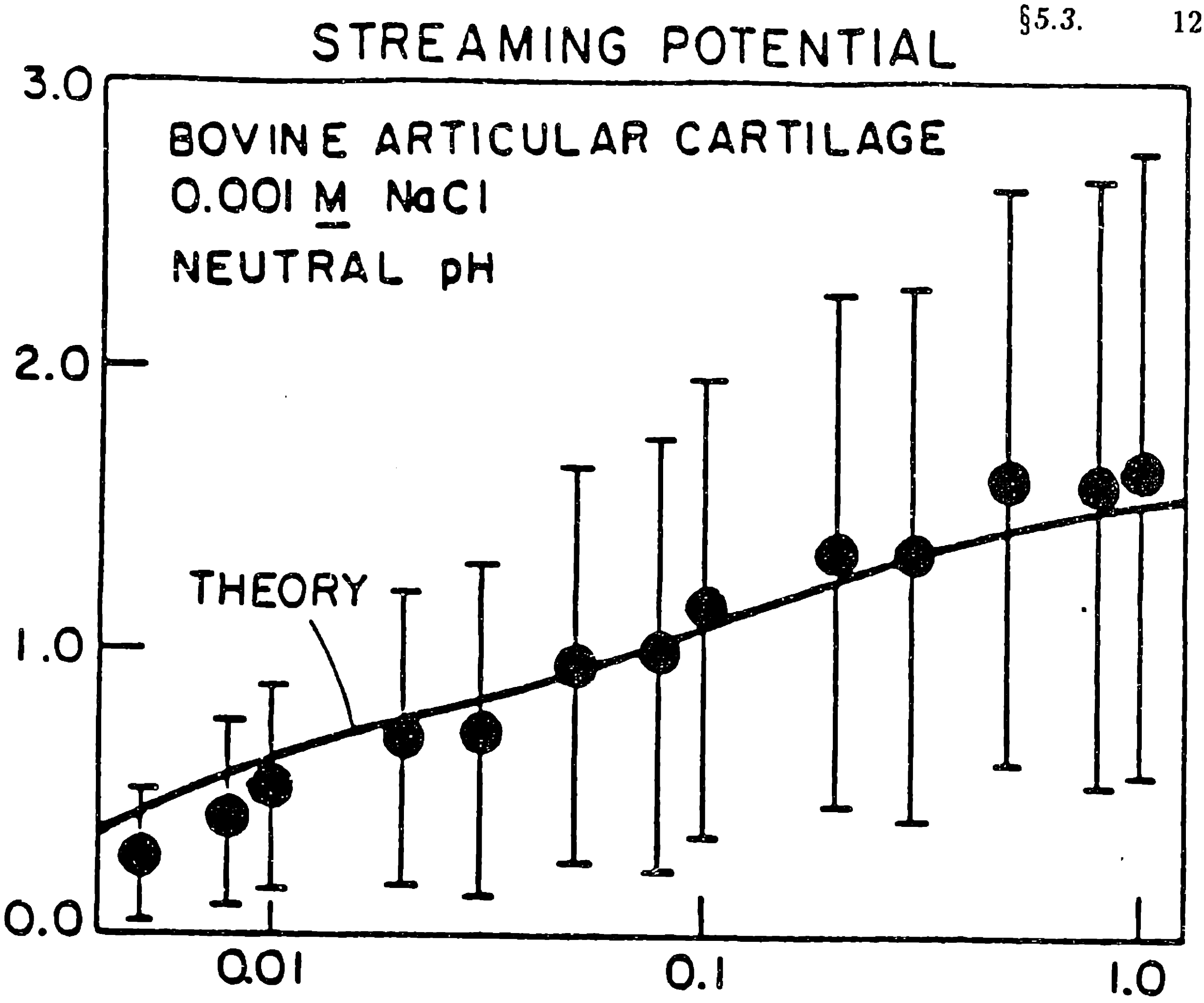

Figure 5.17: Theoretical and experimental magnitude of the surface electrical ("streaming") potential, $|\phi(0)|$ (in mV) *vs.* frequency f, for a permeable surface. The solid curve is the theoretical prediction [35], and the data are from Frank [35]. The experimental setup is similar to that shown in figure 4.12. Here, a sinusoidally varying vertical displacement is applied to the top of a cylindrical, confined sample *via* a compressible, porous platen, and the resulting electrical potential difference between the top and bottom surfaces measured. The applied displacement represents a 1% strain amplitude superimposed on a static displacement of 15%. The data are presented as mean plus or minus a standard deviation based on 9 different samples of bovine femoropatellar cartilage.

layer of thickness roughly equal to λ. In case four (permeable surface), it was shown that the maximum pressure (the pressure is zero at the surface) is proportional to frequency and wavelength while the velocities are proportional to frequency. In case three (impermeable surface) the asymptotics have not been performed, but the same frequency proportionality has been observed numerically, and it is surmised that the wavelength dependence is likely to be similar. Thus, short wave stimulation produces smaller signals, as before in case one, so that surface irregularities and non-uniform application of the boundary conditions on a small scale will not introduce large errors in the measured field values. This is again related to St. Venant's principle (*cf.* 88). Further, by using a surface disturbance composed of short-wave harmonics at a high frequency, it should be possible to obtain significant information about the values of the material parameters near the surface.

For wavelengths on the order of the depth, the frequency dependence is observable in at least two ways. First, the penetration depth of all of the displacement and velocity fields are roughly proportional to Δ^*. Similar behavior is seen for both the permeable and impermeable surface boundary conditions, as demonstrated by figures 5.18 and 5.19. Both of these show that the relative velocity has a significant amplitude for a depth of about $\Delta*$. Note that the vertical velocity is larger in the permeable case, as is the horizontal (by an order of magnitude) in the impermeable case. This is consistent with the intuitive idea that in the permeable case the fluid will just be squeezed out through the top surface, and that the mechanical displacement will thus be converted to a relative vertical velocity. In the impermeable case, the fluid is, for the most part, restricted to horizontal relative motion.

Further, changes in the frequency of the imposed disturbance effect the overall amplitude of the velocity fields for intermediate wavelengths. In figure 5.18 the maximum magnitude of the horizontal velocity increases by an order of magnitude when the frequency increases by two orders of magnitude. This suggests that the

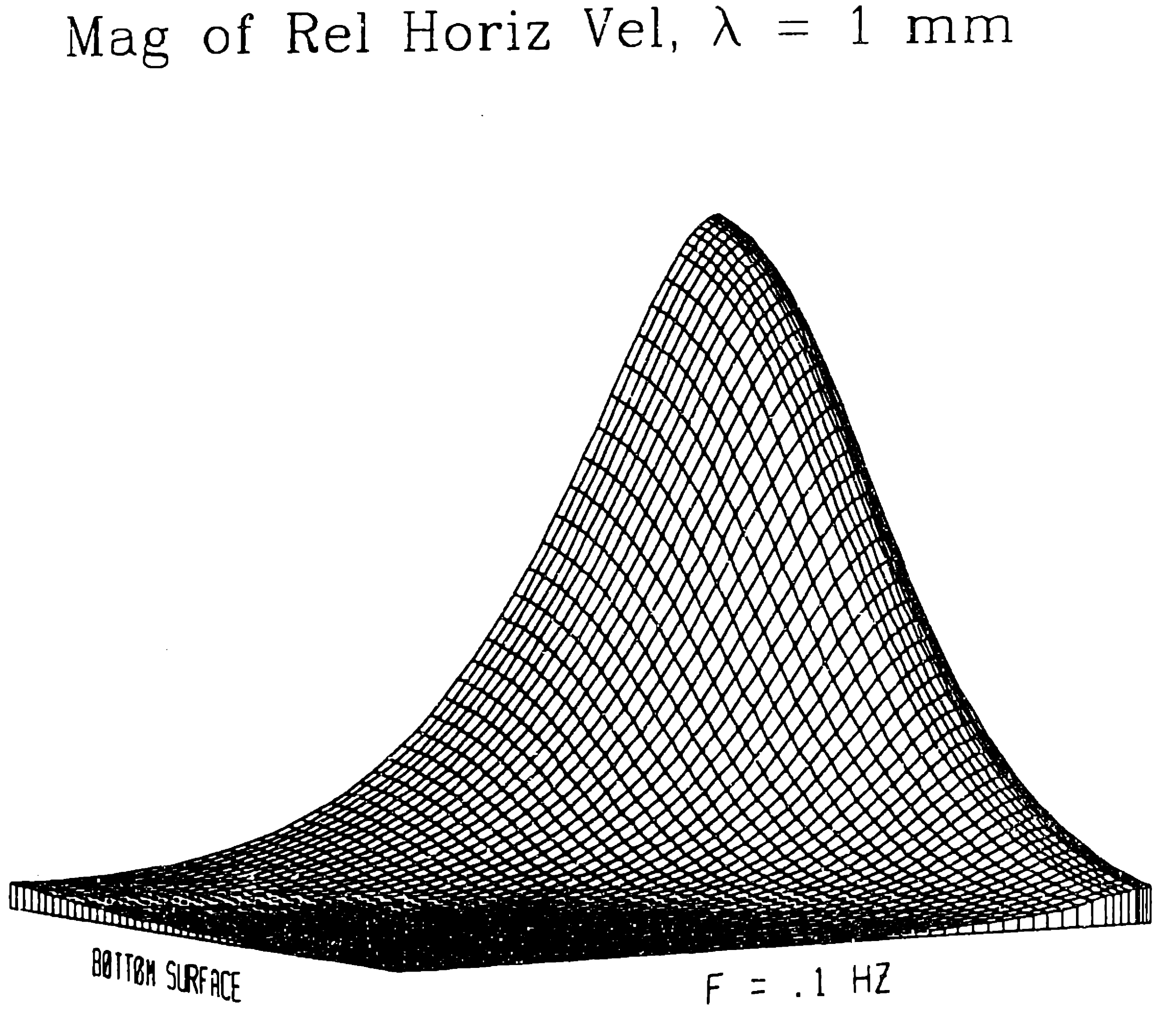

Figure 5.18: **Magnitude of the relative horizontal velocity divided by frequency, V_y/ω, for an impermeable surface, $\lambda = 1\ mm$, $f = 0.001$ to $0.1\ Hz$ logarithmically. The maximum amplitude shown corresponds to $1.08 \cdot 10^{-3}\ mm/s$ per mm of a_J.**

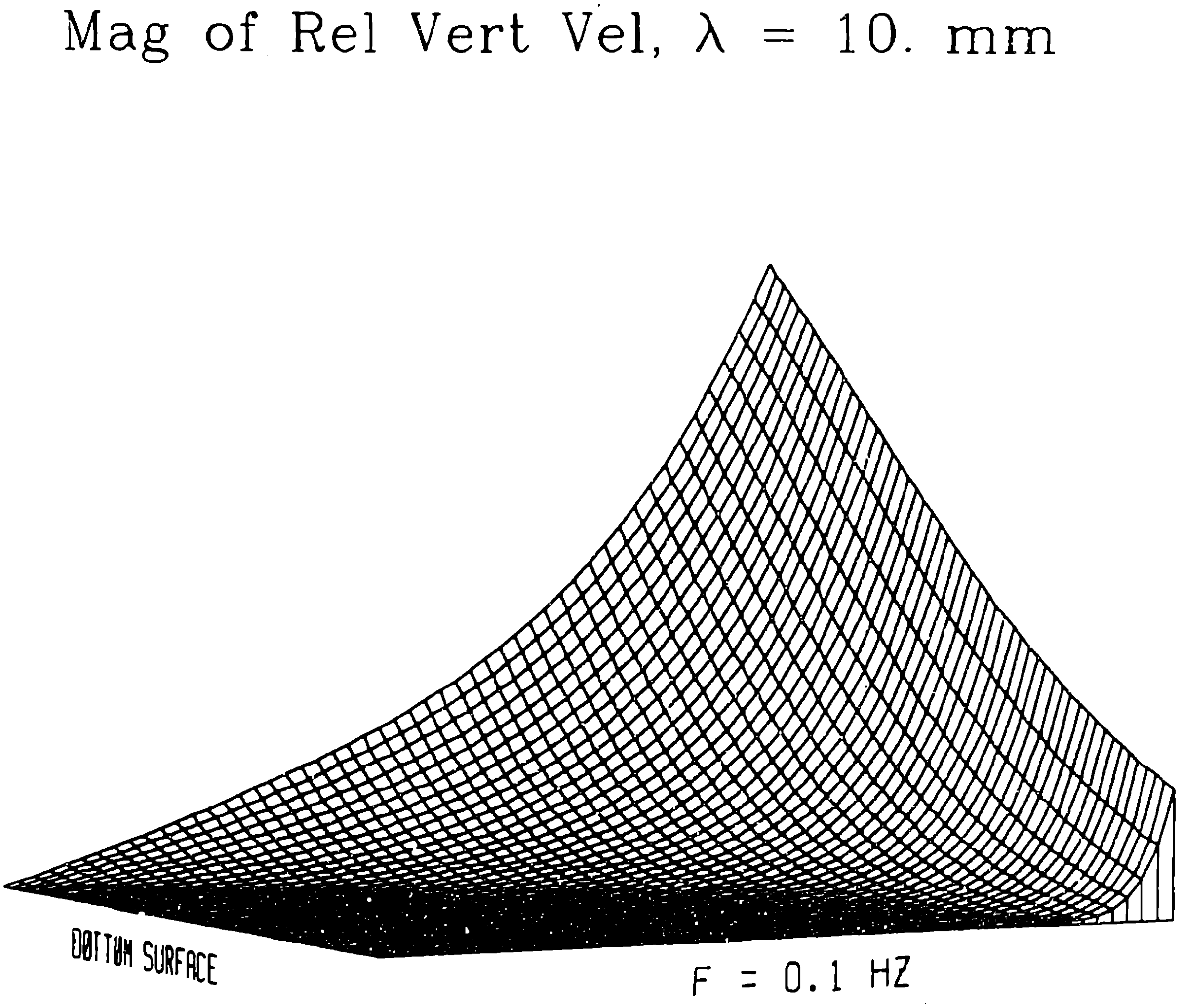

Figure 5.19: Magnitude of the relative vertical velocity divided by frequency, V_z/ω, for a permeable surface, $\lambda = 10\ mm$, $f = 0.001$ to $0.1\ Hz$ logarithmically. The maximum amplitude shown corresponds to $4.76 \cdot 10^{-3}\ mm/s$ per mm of a_J. From this graph may be approximated that the dimensional value at $f = 0.1$ is about $0.3\ mm/s$ per mm of a_J.

amplitude is proportional to Δ^*. The ratio V_y/f does seem to be asymptoting to a constant at either end of the frequency domain, however. The change in magnitude with f is shown for the relative vertical velocity for a longer wavelength for case four in figure 5.19. In the latter case the (dimensional) amplitude is roughly proportional to the frequency, perhaps due to the increased wavelength of the disturbance.

The most striking contrast between the permeable and impermeable cases may be seen at longer wavelengths, as shown in figures 5.15 and 5.20. In the former the more significant relative velocity (V_x) is shown to have a magnitude which is very nearly proportional to the frequency of the surface disturbance. In the latter, however, the more significant velocity (V_y) is (dimensionally) nearly constant in frequency. (This may also be surmised from the coupling equation 2.6, the fact that $\vec{J} = 0$, and the fact that the pressure field is nearly constant in f.) Further, full penetration seems to occur at this wavelength regardless of frequency. This contrasts sharply with the behavior of V_x shown for the permeable case in figure 5.15, in which the penetration depth is seen to be roughly proportional to the diffusion boundary layer thickness. Thus wavelength is a much more important factor than frequency in determining the depth over which parameters are being measured in the impermeable case. This is shown clearly in figure 5.6, which shows that the relative horizontal velocity is only significant near the bottom of the layer if the wavelength is on the order of or larger than the depth.

Finally, several other factors may need to be considered in comparing these results to experimental data. First, the linearity of the model requires that the displacement amplitude (a_J) be much smaller than the depth (δ). Thus the effects of finite stress and strain have not been accounted for. Similarly, in some cases inhomogeneity and anisotropy of the material could produce significant changes in estimated parameter values. Lastly, the application of the boundary conditions used here to a three dimensional problem of finite extent is not yet clear. The latter concern was one of the particular motivations for the material in the next chapter.

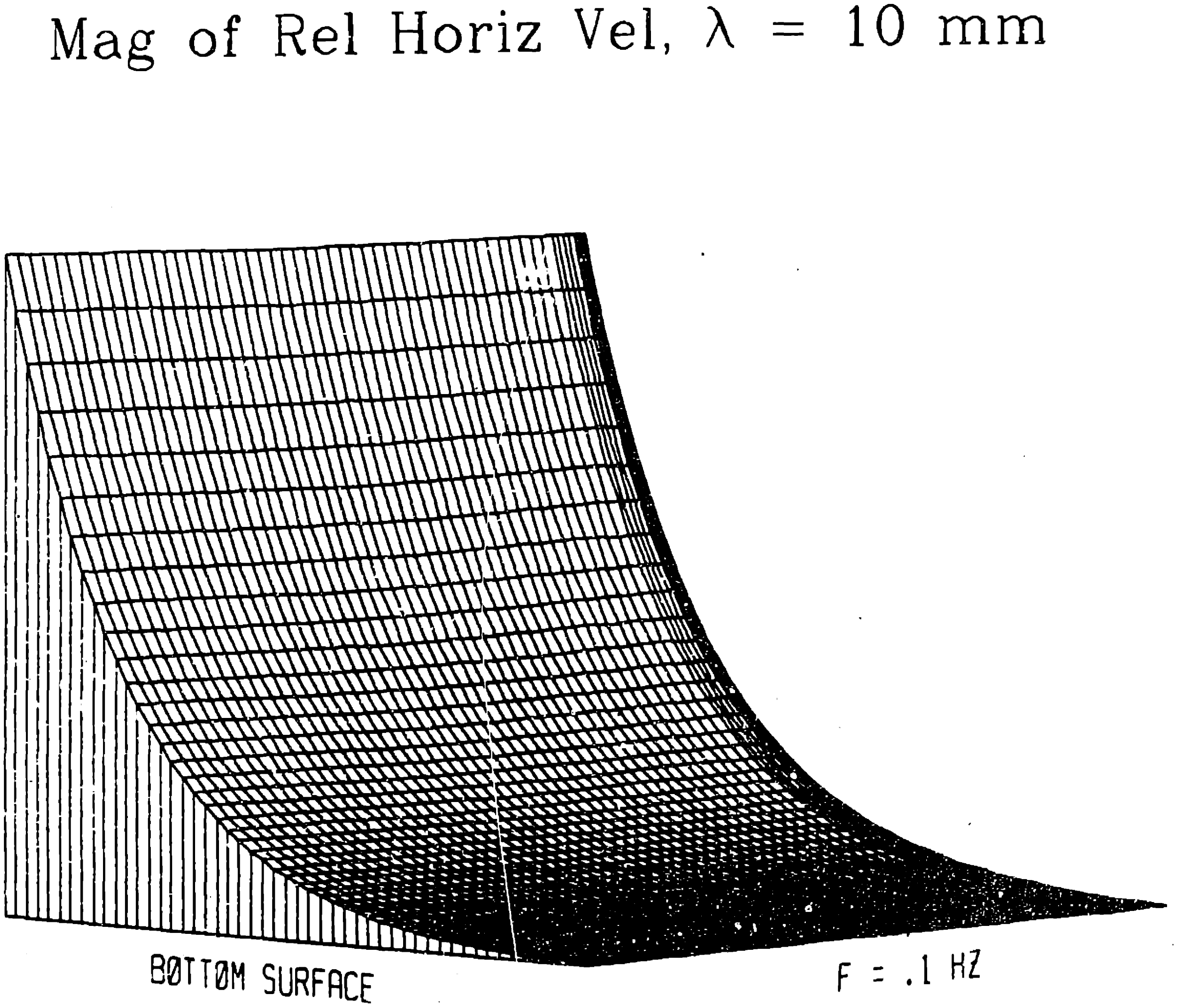

Figure 5.20: Magnitude of the relative horizontal velocity divided by frequency, V_y/ω, for an impermeable surface, $\lambda = 10\ mm$, $f = 0.001$ to $0.1\ Hz$ logarithmically. The maximum amplitude shown corresponds to $1.65 \cdot 10^{-3}\ mm/s$ per mm of a_J. The dimensional value at $f = 0.1$ is $1.71 \cdot 10^{-3}\ mm/s$ per mm.

Chapter 6

The Mixed Boundary Value Problem

6.1 Introduction

This chapter addresses a problem which satisfies boundary conditions thought to be closer to those present when the electromechanical probe is used for *in vivo* measurements. The next section will state the problem and its boundary conditions. The following section will explain the algorithm developed to solve the given system of equations and boundary conditions. The numerical results will then be presented and discussed.

6.2 Statement of the Problem

The boundary conditions considered in this chapter are similar to those of a contact problem in pure elasticity, in which displacement is specified on one region, and stress on another. Specifically, the top ($z = 0$)surface of the δ^*-thick layer of material of previous chapters is divided into two types of regions which are extended periodically in both y-directions. These are (*cf.* figure 6.1):

Region I: $0 \leq y < l_1$ ($y = y^*/\delta^*$, y and l_1 are non-dimensional), on which

$$u_z^*(y, z = 0, t) = 0 \qquad V_z^*(y, z, t) = 0 \qquad \sigma_{yz}^*(y, z, t) = 0$$
$$J_z(y, 0, t) = J_0[1 - (\frac{y}{l_1})^4]e^{i\omega t} \tag{6.1}$$

and

Region II: $l_1 \leq y < l$, on which

$$\mathcal{P}(y, z = 0, t) = 0 \quad S(y, z, t) = 0 \quad \sigma_{yz}^*(y, z, t) = 0 \quad J_z(y, 0, t) = 0\,, \tag{6.2}$$

where $l\delta^*$ is the total dimensional width of region I and region II. These correspond to the surfaces under the electrodes of a segmented electromechanical probe, and those between the electrodes, respectively. The conditions on region I are like those of case one of Chapter 4 in that a known current density is applied to a surface through which there is no fluid flow and at which the solid matrix is not allowed any vertical displacement. It is different in that the condition of no horizontal displacement has been replaced by one of free slip: there is no shear force at the top surface. Thus the surface of the electrode is assumed to be sufficiently smooth, and the normal forces sufficiently small, so that the solid matrix is free to slip along the surface of the electrode. This is consistent with the boundary conditions used by other authors [3] along boundaries with relative motion between cartilage and a smooth solid.

The second region represents the free surface in the space between the two electrodes. Here again there is no shear force on the surface. In addition, however, there is no pressure, so that the fluid is free to exchange with a "reservoir" between the electrodes. Lastly, the normal force is zero, as there is nothing to constrain the vertical motion of the solid matrix.

The two regions are now repeated in such a way that J_z is even about the line $y = 0$, and odd about the line $y = l$. The boundary conditions on the top surface are now $4l$-periodic in y, as may be seen in figure 6.1. The profile of J_z was

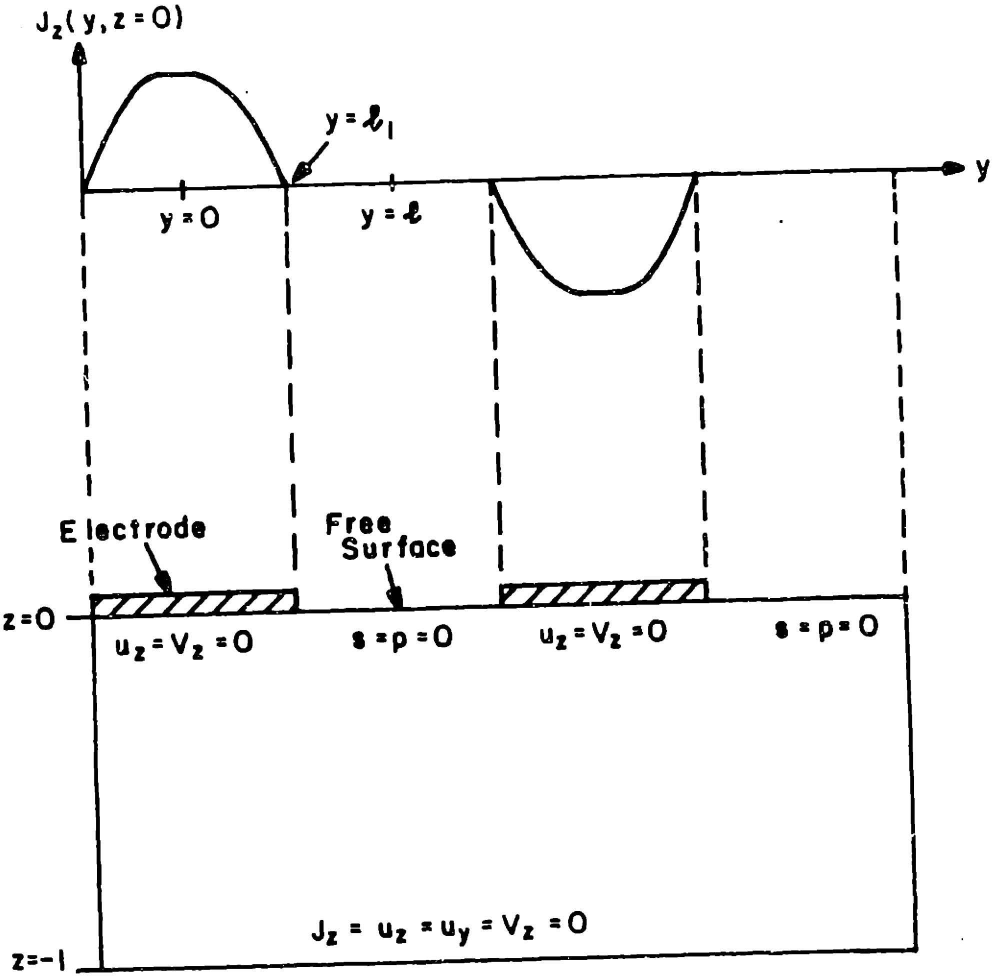
$J_z(y, z=0)$
$y=\ell_1$
y
$y=0$
$y=\ell$
Electrode
Free Surface
$z=0$
$u_z=V_z=0$
$s=p=0$
$u_z=V_z=0$
$s=p=0$
$J_z=u_z=u_y=V_z=0$
$z=-1$

Figure 6.1: Boundary conditions for the mixed boundary condition problem. Above: The segmented electrode is shown. The areas in which the electrode is in contact with the surface obey a type I boundary conditions 6.1, or a symmetric variant thereof. The regions not in contact with an electrode are subject to the type II boundary conditions 6.2. Below: The graph of $J_z(z=0)$ shows how the boundary conditions are extended periodically with the symmetries described on page 130.

chosen to represent a current injecting electrode next to an insulating region. Since a discontinuous profile is not physically realizable, the given "continuous square-wave" was chosen (*cf.* figure 6.1). The particular functional dependence was chosen for ease of analysis in finding the particular solutions (*cf.* below).

The boundary conditions at the bottom (z=-1) are the same as in previous chapters. These are:

$$u_y^*(y, z = -1, t) = 0 \quad u_z^*(y, -1, t) = 0 \quad V_z^*(y, -1, t) = 0 \quad j_z^*(y, -1, t) = 0 \qquad (6.3)$$

These again correspond to no horizontal or vertical displacement of the solid matrix, and no fluid or current flow through the surface. Note that equations 2.12.1 through 2.62.6 now immediately show that $u_z^*, V_z^*, \mathcal{P}$, and S have the same symmetries as J_z. The variables $u_y^*, V_y^*, \sigma_{yz}^*$, and J_y, on the other hand, are odd symmetric about $y = 0$, and even symmetric about $y = l$.

There are at least three major reasons for considering the above configuration. First, it is impossible to perform an experiment on a layer which extends indefinitely in the x- and y-directions. Thus it would be useful to model a structure of finite extent. Second, a practically designed probe probably will not cover the whole surface of the material whose properties are being measured. Thus, the top surface will most likely be subjected to more than one type of boundary condition, including one representing the forcing of the probe, and the other accounting for the areas not in contact with the probe. Third, a periodic probe is a natural implementation of both the segmented electrode structure, and the periodic transform methods used in previous chapters. Further, periodic probes have been used successfully to probe electrical properties in other applications [107]. Lastly, a probe with the above configuration could be used to apply both electrical and mechanical stimuli, thus obviating the need to change probes during a measurement.

Even though the problem being considered is of infinite extent, the above boundary conditions are still appropriate as a first step towards fulfilling the ideals described above. First, multiple boundary conditions have been imposed, and a periodic structure has been used. Moreover, since the probe is truncated to a finite width (in the y-direction), the Fourier spectrum of the input current is changed primarily by spreading into the high-k regions. (This is just a result of the exchange between bandwidth in physical and Fourier spaces.) Because short wave forcings are known to produce only small signals at the surface under a wide variety of boundary conditions, the problem described above should provide a reasonable approximation to the result of a finite width probe.

6.3 The Algorithm for Solution of the Mixed Problem

6.3.1 Introduction

This section describes the algorithm used to find the fields satisfying the boundary conditions 6.1 and 6.2 described in the previous section. However, the details of the algorithm's operation are more easily understood if the general idea behind it is understood first. Since a great deal of information is contained in the solutions of §3.2, it seems reasonable to try to use these solutions to solve the problem at hand. Noting that the current can be solved for in advance (as in Chapter 4, this will be explained in more detail below), only the coefficients of the homogeneous solutions need to be calculated. Because there are six homogeneous solutions (for a given wavelength and frequency) if a solution containing M Fourier components is desired, there will be $6M$ degrees of freedom. The most direct approach to solving the problem, then, would be to use M collocation points on each of the top and bottom surfaces, and require that each of the three boundary conditions hold at each point. This yields $6M$ linear equations in the $6M$ coefficients corresponding to the $k_1, \ldots, k_6$ of equation 3.24. The solution of these equations, and thus this algorithm, requires a time on the order of $(6M)^3$.

The algorithm developed for this problem, however, has an asymptotic time bound of M^3, thus providing a solution 216 times as fast. To do this, the three boundary conditions at the bottom of the layer and the zero-shear condition are first used to reduce the number of degrees of freedom to $2M$. Further, the information contained in the zero pressure and shear conditions of region II are used to eliminate one more degree of freedom. The method used to remove the degrees of freedom is effectively that of posing the problem in terms of Green's functions for other, related problems. This results in a problem of M degrees of freedom, which takes $O(M^3)$ time to solve. Even though the set up time is lengthened considerably, the reduction in time for the major matrix inversion step more than compensates when M is large enough to provide reasonable resolution.

6.3.2 The Current Density Field and Particular Solutions

Because the vertical current density is known at the top and bottom surfaces (from equations 6.1, 6.2, and 6.3), the current density field is known in closed form. The symmetry of the stated problem makes it convenient to use a slightly different notation than that of the previous chapters. Specifically, for the current density we define

$$\begin{aligned} J_y(y^*, z^*, t) &= J_0 e^{-i\omega t} \textstyle\sum_{m=1}^{\infty} \jmath_m \jmath_y^m(z) \sin k_m y \\ J_z(y^*, z^*, t) &= J_0 e^{-i\omega t} \textstyle\sum_{m=1}^{\infty} \jmath_m \jmath_z^m(z) \cos k_m y \; , \end{aligned} \tag{6.4}$$

where $\jmath_m$ is a Fourier coefficient, k_m is a wavenumber (given below), and $(y, z) = (y^*, z^*)/\delta^*$, as before. Here, $\jmath_y^m$ and $\jmath_z^m$ are related to the previously used $\jmath_y$ and $\jmath_z$ by

$$\begin{aligned} \jmath_y^m &= i \jmath_y \,|_{\delta = k_m} \\ \jmath_z^m &= \jmath_z \,|_{\delta = k_m} \; . \end{aligned} \tag{6.5}$$

The sin and cos functions were chosen according to the symmetries mentioned on page 130. It is also useful to define non-dimensional variables

$$\begin{aligned} \bar{j}_y(y,z,t) &= J_y/J_0 \\ \bar{j}_z(y,z,t) &= J_z/J_0 \,. \end{aligned} \tag{6.6}$$

The superscript "S" and over-bar will be omitted for the remainder of this chapter, except where necessary for clarity.

To find the current density field, note that if ij_y and j_z of equations 4.5 are used for j_y^m and j_z^m, then j_m will simply be the Fourier series for the profile of J_z given by equations 6.1 and 6.2. The coefficients j_m are thus found to be:

$$\begin{aligned} j_m = & -\frac{8l_1}{l}[(k_m l_1)^{-2}\cos(k_m l_1) - 3(k_m l_1)^{-3}\sin(k_m l_1) \\ & - 6(k_m l_1)^{-4}\cos(k_m l_1) + 6(k_m l_1)^{-5}\sin(k_m l_1)] \end{aligned} \tag{6.7}$$

with

$$k_m \equiv \frac{(2m-1)\pi}{2l} \,. \tag{6.8}$$

The current density field solution is completed by using equations 4.5a and b with k_m substituted for δ, so that

$$\begin{aligned} \bar{j}_z &= \sinh\gamma/\sinh k_m \\ \bar{j}_y &= -\cosh\gamma/\sinh k_m \,, \end{aligned} \tag{6.9}$$

with $\gamma = k_m(z+1)$. The current density field $\vec{J}$ is shown in figure 6.2.

As in the case of Chapter 4, the current density field produces a mechanical response which does not satisfy the given boundary conditions. The response is described here using a notation analogous to that of equations 6.4 and 6.6 above.

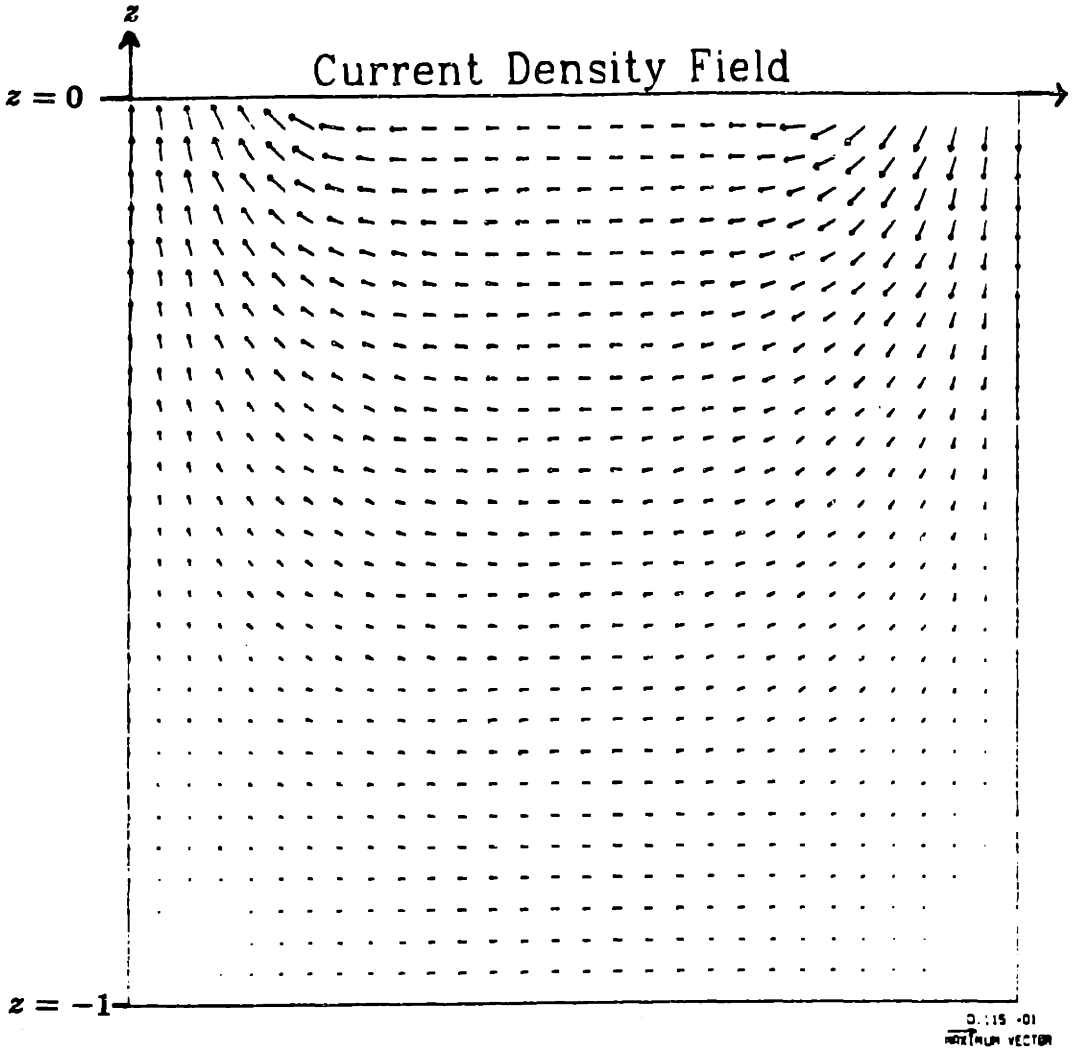

Figure 6.2: Current density field for mixed boundary conditions.

Thus we define

$$
\begin{aligned}
u_y^*(y^*, z^*, t) &= a_J c^{-i\omega t} \textstyle\sum_{m=1}^{\infty} j_m u_y^{Pm}(z) \sin k_m y \\
&\quad + \textstyle\sum_{m=1}^{\infty} \left[\sin k_m y \sum_{l=1}^{6} c_l^m u_{yl}^m(z)\right] \\
u_z^*(y^*, z^*, t) &= a_J e^{-i\omega t} \textstyle\sum_{m=1}^{\infty} j_m u_z^{Pm}(z) \cos k_m y \\
&\quad + \textstyle\sum_{m=1}^{\infty} \left[\cos k_m y \sum_{l=1}^{6} c_l^m u_{zl}^m(z)\right] \\
v_y^*(y^*, z^*, t) &= J_0 \tfrac{b_{12}}{b_{11}} e^{-i\omega t} \textstyle\sum_{m=1}^{\infty} j_m v_y^{Pm}(z) \sin k_m y \\
&\quad + \textstyle\sum_{m=1}^{\infty} \left[\sin k_m y \sum_{l=1}^{6} c_l^m v_{yl}^m(z)\right] \\
v_z^*(y^*, z^*, t) &= J_0 \tfrac{b_{12}}{b_{11}} e^{-i\omega t} \textstyle\sum_{m=1}^{\infty} j_m v_z^{Pm}(z) \cos k_m y \\
&\quad + \textstyle\sum_{m=1}^{\infty} \left[\cos k_m y \sum_{l=1}^{6} c_l^m v_{zl}^m(z)\right] \\
V_y^*(y^*, z^*, t) &= J_0 \tfrac{b_{12}}{b_{11}} e^{-i\omega t} \textstyle\sum_{m=1}^{\infty} j_m V_y^{Pm}(z) \sin k_m y \\
&\quad + \textstyle\sum_{m=1}^{\infty} \left[\sin k_m y \sum_{l=1}^{6} c_l^m V_{yl}^m(z)\right] \\
V_z^*(y^*, z^*, t) &= J_0 \tfrac{b_{12}}{b_{11}} e^{-i\omega t} \textstyle\sum_{m=1}^{\infty} j_m V_z^{Pm}(z) \cos k_m y \\
&\quad + \textstyle\sum_{m=1}^{\infty} \left[\cos k_m y \sum_{l=1}^{6} c_l^m V_{zl}^m(z)\right] \\
\mathcal{P}(y^*, z^*, t) &= J_0 \delta^* b_{12} e^{-i\omega t} \textstyle\sum_{m=1}^{\infty} j_m p^{Pm}(z) \cos k_m y \\
&\quad + \textstyle\sum_{m=1}^{\infty} \left[\cos k_m y \sum_{l=1}^{6} c_l^m p_l^m(z)\right] \\
S(y^*, z^*, t) &= J_0 \delta^* b_{12} e^{-i\omega t} \textstyle\sum_{m=1}^{\infty} j_m s^{Pm}(z) \cos k_m y \\
&\quad + \textstyle\sum_{m=1}^{\infty} \left[\cos k_m y \sum_{l=1}^{6} c_l^m s_l^m(z)\right] \\
\sigma_{yz}^*(y^*, z^*, t) &= J_0 \delta^* b_{12} e^{-i\omega t} \textstyle\sum_{m=1}^{\infty} j_m \sigma^{Pm}(z) \sin k_m y \\
&\quad + \textstyle\sum_{m=1}^{\infty} \left[\sin k_m y \sum l = 1^6 c_l^m \sigma_l^m(z)\right] \\
\Phi(y^*, z^*, t) &= J_0 \delta^* b_{22} e^{-i\omega t} \textstyle\sum_{m=1}^{\infty} j_m \phi^{Pm}(z) \cos k_m y \\
&\quad + \textstyle\sum_{m=1}^{\infty} \left[\cos k_m y \;\; \sum_{l=1}^{6} c_l^m \phi_l^m(z)\right]
\end{aligned}
\qquad (6.10)
$$

Also, a set of non-dimensionalized variables $\bar{u}_y, \ldots, \bar{\phi}$ may be defined analogously to $\bar{j}_y$ in equation 6.6 using the non-dimensionalizations above. These will also be used, and overbar will be dropped where non-dimensionality is clear from the context.

The superscript "P" in equation 6.10 represents the aforementioned response to the current density. These particular solutions are given by (see equations 4.5 and the procedure for deriving the homogeneous solutions, below)

$$
\begin{aligned}
u_y^{Pm} &= -\frac{(1-k_m\coth k_m)\cosh\gamma+\gamma\sinh\gamma}{2nk_m^2\sinh k_m} \\
u_z^{Pm} &= \frac{\gamma\cosh\gamma-k_m\coth k_m\sinh\gamma}{2nk_m^2\sinh k_m} \\
V_y^{Pm} &= 0 \\
V_z^{Pm} &= 0 \\
p^{Pm} &= k_m^{-1}\cosh\gamma/\sinh k_m \\
s^{Pm} &= p^p+2nk_m u_y^p \\
\sigma_{yz}^p &= -\frac{(1-k_m\coth k_m)\sinh\gamma+\gamma\cosh\gamma}{k_m\sinh k_m} .
\end{aligned}
\tag{6.11}
$$

The terms of equations 6.10 which are summed over l are the homogeneous solutions, which are derived from those of equations 3.24. The functions of z which are associated with c_l^m (*e.g.* $u_{zl}^m(z)$) are obtained from the homogeneous solutions of equations 3.24 as follows. First, δ, which was the product of the imposed wavenumber and the dimensional thickness, is replaced by k_m. Then, for any field component A which is even in y, the A_l^m are identical to the appropriate homogeneous solution for that component. For any field component A which is odd in y, the A_l^m are i times the homogeneous solutions for that component. For example, for the horizontal displacement (u_y), which is odd in y,

$$u_{y3}^m = -(z+k_m^{-1})e^{k_m z}$$

(*cf.* equations 3.24). For the vertical displacement (u_z), which is even in y,

$$u_{z3}^m = ze^{k_m z} .$$

The c_l^m are analogous to the k_l of equation 3.24. Since j_m are given in equations 6.7, the solution of the problem again lies in the determination of the coefficients of the homogeneous solutions.

6.3.3 Solution for the Non-Mixed Problem: Problems "A" and "B"

The first step in solving this problem is to change it into a convenient homogeneous problem, *i.e.* , one with current density $\vec{J} = 0$. To do this, the problem is divided into two subproblems, denoted "A" and "B". The current density for problem A is that given by equations 6.4, 6.7, and 6.9. The mechanical boundary conditions for A are

$$\begin{array}{lll} p(0) = 0 & s(0) = 0 & \sigma_{yz}(0) = 0 \\ u_y(-1) = 0 & u_z(-1) = 0 & V_z(-1) = 0\,. \end{array} \tag{6.12}$$

Problem B has $J_z = 0$ and mechanical boundary conditions

Region I ($0 \leq y < l_1$) :

$$\begin{array}{cc} u_z^*(y, z = 0, t) = -u_z^A(y, z = 0, t) & V_z(y, z, t) = -V_z^A(y, z = 0, t) \\ \multicolumn{2}{c}{\sigma_{yz}^*(y, z, t) = 0} \end{array} \tag{6.13}$$

Region II ($l_1 \leq y < l$):

$$p(y, z = 0, t) = 0 \quad s(y, z, t) = 0 \quad \sigma_{yz}(y, z, t) = 0 \tag{6.14}$$

and

Bottom Surface ($z = -1$):

$$u_y(-1) = 0 \quad u_z(-1) = 0 \quad V_z(-1) = 0\,. \tag{6.15}$$

In equations 6.13, the u_z^A and V_z^A refer to the solution to problem A at the given location. The above equations are shown schematically in figure 6.3. From the linearity of the problem it is evident that the sum of the solutions to problems A and B is the desired solution.

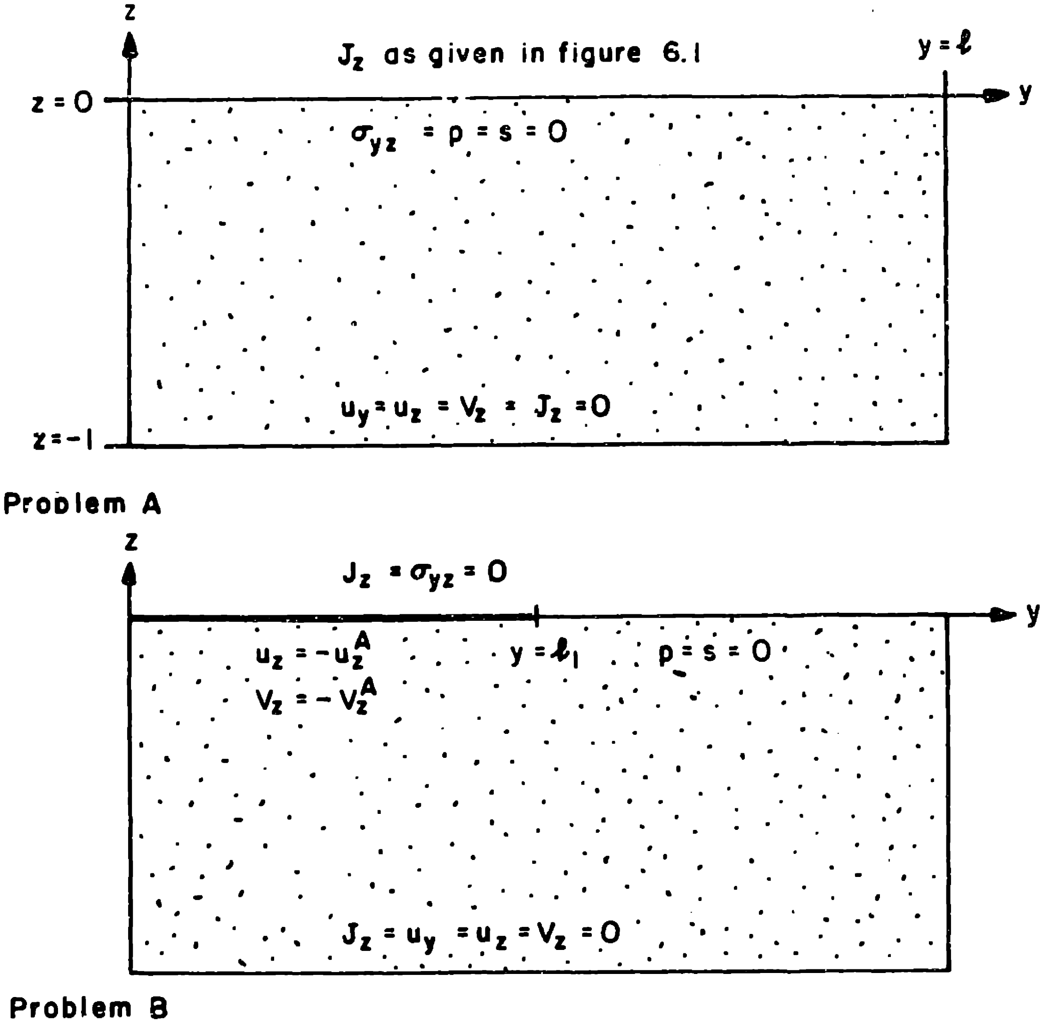
z
J_z as given in figure 6.1
$y=\ell$
$z=0$
y
$\sigma_{yz} = p = s = 0$
$u_y = u_z = V_z = J_z = 0$
$z=-1$
Problem A
z
$J_z = \sigma_{yz} = 0$
y
$u_z = -u_z^A$
$V_z = -V_z^A$
$y=\ell_1$
$p = s = 0$
$J_z = u_y = u_z = V_z = 0$
Problem B

Figure 6.3: Boundary conditions for problems "A" and "B." Problem A is inhomogeneous but has no mixing of boundary conditions. Problem B is homogeneous but has mixed boundary conditions.

The solution to problem A is obtained easily by the methods of Chapter 4. For each wavenumber k_m, the following boundary conditions are applied:

$$\begin{aligned}
\textstyle\sum_{l=1}^{6} c_l^{Am} p_l^m(0) &= -j_m p^{Pm}(0) \\
\textstyle\sum_{l=1}^{6} c_l^{Am} s_l^m(0) &= -j_m s^{Pm}(0) \\
\textstyle\sum_{l=1}^{6} c_l^{Am} \sigma_l^m(0) &= -j_m \sigma_{yz}^{Pm}(0) \\
\textstyle\sum_{l=1}^{6} c_l^{Am} u_{yl}^m(-1) &= -j_m u_y^{Pm}(-1) \\
\textstyle\sum_{l=1}^{6} c_l^{Am} u_{zl}^m(-1) &= -j_m u_z^{Pm}(-1) \\
\textstyle\sum_{l=1}^{6} c_l^{Am} V_{zl}^m(-1) &= -j_m V_z^{Pm}(-1)\ ,
\end{aligned}$$

$m = 1, \ldots, M$, where j_m are given in equation 6.7. This is a set of M six by six linear equations in the complex constants $c_1^A, \ldots, c_6^A$. If the time required to solve one such six by six equation is T_6, this step requires a time of MT_6. Note that the infinite sums of equations 6.4 and 6.10 have necessarily been truncated at a finite number of Fourier modes, M.

Note, however, for m sufficiently large $k_m \gg 1$, and the solution to equations 6.3.3 approaches that of the short-wave approximation defined by

$$c_2^{Am} = c_4^{Am} = c_6^{Am} = 0 \tag{6.16}$$

(*cf.* §4.2.2 and §5.2.3). Because equations 6.3.3 are ill-conditioned in this parameter regime, and because short-wave analytical results agreed well with numerical ones (in previous chapters), equation 6.16 was substituted into 6.3.3 when $k_m \geq 6\pi$. This means that the time required to solve 6.3.3 is reduced to $O(MT_3)$, where T_3 is the time required to solve the resulting three equations in c_2^{Am}, c_4^{Am}, and c_6^{Am}. Any errors in the values of the c_l^m which could result from this approximation would show up as deviations of the fields from the desired boundary conditions. As will be seen in §6.4, these errors were not significant.

6.3.4 The Basis Coefficients: Reducing the Number of Degrees of Freedom

Even though problem B has no current density, and may thus be solved in terms of strictly mechanical boundary conditions, it has the mixed condition at the top which is the crux of the present inquiry. To solve this efficiently the homogeneous coefficients (c_l^m) of two sets of fields will be used. It is the use of these "basis" coefficients, the affiliated fields, and the fast Fourier transform which effectively reduces the number of degrees of freedom.

To define the basis coefficients, we will use Green's function-like boundary conditions on the pressure at $z = 0$ for one set, and on the normal stress at $z = 0$ for the other. We will be rephrasing the boundary conditions of the problem in terms of the question: given all of the other boundary conditions of problem B, what surface pressure and normal stress values will result in the given surface values, $-u_z^A$ and $-V_z^A$, for the vertical displacement and velocity fields? First, define the sinc-like function

$$\mathrm{snc}_n\,(y) = \begin{cases} \frac{2}{M}\sum_{m=1}^{M}\cos(k_m y_n)\cos(k_m y) & n \neq 0 \\ \frac{1}{M}\sum_{m=1}^{M}\cos(k_m y) & n = 0 \end{cases} \tag{6.17}$$

where y_n is the y-coordinate of the $n^{\underline{\text{th}}}$ collocation point on the $z = 0$ axis,

$$y_n \equiv (n-1)/M\,. \tag{6.18}$$

(The use of the term "collocation point" will be come clearer in equations 6.22 below). The snc function has the property that

$$\mathrm{snc}_n\,(y_k) = \begin{cases} 1 & n = k \\ 0 & n \neq k \end{cases} \tag{6.19}$$

The pressure and (normal) stress basis coefficients may now be defined using the $\mathrm{snc}_n\,(y)$ function. The pressure basis coefficients, P_{ln}^m, are those values of the homogeneous solutions coefficients, c_l^m, for which (for a given value of M) the fields obey the boundary conditions ($\vec{J} = 0$)

$$\begin{aligned} p(y, z = 0) &= \mathrm{snc}_n(y) & s(y, 0) &= 0 & \sigma_{yz}(y, 0) &= 0 \\ u_y(y, -1) &= 0 & u_z(y, -1) &= 0 & V_z(y, -1) &= 0\,. \end{aligned} \tag{6.20}$$

The stress basis coefficients, S_{ln}^m, are defined analogously, with the roles of p and s reversed.

Note that any problem satisfying the boundary conditions of problem B with the conditions $u_z^*(y, z = 0, t) = -u_z^A(y, z = 0, t)$ and $V_z(y, z, t) = -V_z^A(y, z = 0, t)$ replaced by any two (consistent) boundary conditions can be solved using a superposition of the fields corresponding to the pressure and stress basis functions. By "solution", it is meant that the conditions hold at each of the

$$n_0 \equiv \lceil \frac{l_1}{l} M \rceil \tag{6.21}$$

collocation points in region I (*cf.* figure 6.3). In particular, there exist coefficients Π_n and Υ_n such that the n_0 collocation equations

$$\begin{aligned} -u_z^A(y_j, z = 0) &= \textstyle\sum_{n=1}^{n_0} \Pi_n \sum_{m=1}^{M} \cos(k_m y_j) \sum_{l=1}^{6} P_{ln}^m u_{zl}^m(z = 0) \\ & \textstyle\sum_{n=1}^{n_0} \Upsilon_n \sum_{m=1}^{M} \cos(k_m y_j) \sum_{l=1}^{6} S_{ln}^m u_{zl}^m(z = 0) \\ -V_z^A(y_j, z = 0) &= \textstyle\sum_{n=1}^{n_0} \Pi_n \sum_{m=1}^{M} \cos(k_m y_j) \sum_{l=1}^{6} P_{ln}^m V_{zl}^m(z = 0) \\ & \textstyle\sum_{n=1}^{n_0} \Upsilon_n \sum_{m=1}^{M} \cos(k_m y_j) \sum_{l=1}^{6} S_{ln}^m V_{zl}^m(z = 0) \end{aligned} \tag{6.22}$$

are satisfied for each $j = 1, \ldots, n_0$. From 6.20 and 6.19 it can be seen that

$$p^B(y, 0) = \sum_{n=1}^{n_0} \Pi_n \sum_{m=1}^{M} \cos(k_m y) \sum_{l=1}^{6} P_{ln}^m p_{yl}^m(z = 0)\,, \tag{6.23}$$

in which there is no contribution from the Υ_n terms. Moreover,

$$p^B(y_n, 0) = \Pi_n\,. \tag{6.24}$$

A similar equation holds for s^B with the Π_n terms omitted.

It may now be seen in what manner the problem has been rephrased in terms of which pressure and stress fields produce the desired displacement and velocity at the boundary. By equations 6.22 and 6.24 it is evident that the values of the pressure and stress on region I can be chosen to obtain the desired displacements there. Furthermore, given the values of the $\mathcal{P}_{ln}^m$ and $\mathcal{S}_{ln}^m$, the number of unknowns in the problem has been reduced to $2n_0$, comprised of the Π_n and Υ_n. As long as $l_1 \leq l/2$, equation 6.21 shows that $2n_0 < M$. Thus the problem has been reduced to one that can be solved in $O(M^3)$ time. (If $l_1 > l$, then the roles of p and s and those of u_s and V_s may be reversed to adhere strictly to this time bound. Even if this is not done, the time will be at most $O(8M^3)$, a factor of 27 better than the brute force collocation method.) All that now remains is to show how the $\mathcal{P}_{ln}^m$ and $\mathcal{S}_{ln}^m$ may be obtained in a time $T \ll O(M^3)$, and the exact procedure for finding Π_n and Υ_n.

6.3.5 Solution for the Basis Functions and their Coefficients

Because the Fourier coefficients of the snc function are known from equation 6.17, $\mathcal{P}_{ln}^m$ and $\mathcal{S}_{ln}^m$ may be easily calculated. For a fixed n and m, equation 6.23 shows that the six coefficients $\mathcal{P}_{ln}^m$ must obey the equation

$$\begin{aligned}
\textstyle\sum_{l=1}^{6} \mathcal{P}_{ln}^m p_l^m(0) &= \frac{2}{M}\cos(k_m y_n) \\
\textstyle\sum_{l=1}^{6} \mathcal{P}_{ln}^m s_l^m(0) &= 0 \\
\textstyle\sum_{l=1}^{6} \mathcal{P}_{ln}^m \sigma_l^m(0) &= 0 \\
\textstyle\sum_{l=1}^{6} \mathcal{P}_{ln}^m u_{yl}^m(-1) &= 0 \\
\textstyle\sum_{l=1}^{6} \mathcal{P}_{ln}^m u_{sl}^m(-1) &= 0 \\
\textstyle\sum_{l=1}^{6} \mathcal{P}_{ln}^m V_{sl}^m(-1) &= 0\,,
\end{aligned} \tag{6.25}$$

where the values must be divided by two if $n = 0$. The equations for the $\mathcal{S}_{ln}^m$ are identical, except that the roles of p_l^m and s_l^m are reversed. The solution of these equations must be found for $m = 1, \ldots, M$, and $n = 1, \ldots, n_0$. However, because the coefficients of the P_{ln}^m on the left side are independent of n, the coefficients may be found from the value of, *e.g.*, P_{l1}^m *via*

$$P_{ln}^m = 2\cos(k_m y_n) P_{l1}^m \tag{6.26}$$

($y_1 = 0$, *cf.* 6.18). Thus, if T_6 is the time required to solve a six by six linear equation with complex coefficients, the P_{ln}^m and S_{ln}^m may be solved for in MT_6 time[1].

To determine the values of the Π_n and Υ_N, equations 6.22 are used. The values of u_s^A (and V_s^A) are determined by equations 6.10 with $j_m = 0$, and $c_l^m = c_l^{Am}$ using a fast Fourier inversion. This takes only $M \log M$ time for each of the two variables. Note that the symmetries in this problem (*cf.* page 130) allow the determination of M Fourier coefficients from M spacial values. The $2n_0$ equations 6.22 are then solved for the values of the pressure and normal stress at the collocation points, Π_n and Υ_n, respectively. As mentioned in the previous section, this step requires M^3 time.

The homogeneous coefficients which correspond to problem B, c_l^{Bm} may now be determined. Note that

$$\begin{aligned} (p^B(y_1, z=0), \ldots, p^B(y_M, 0)) &= (\Pi_1, \ldots, \Pi_{n_0}, \overbrace{0, \ldots, 0}^{M - n_0 \text{ terms}} \quad) \\ (s^B(y_1, z=0), \ldots, s^B(y_M, 0)) &= (\Upsilon_1, \ldots, \Upsilon_{n_0}, \underbrace{0, \ldots, 0}_{M - n_0 \text{ terms}} \quad) . \end{aligned} \tag{6.27}$$

By performing a fast Fourier transform of these values, the M values of p^{Bm} and s^{Bm} in

$$\begin{aligned} p(y, z=0) &= \textstyle\sum_{m=1}^M p^{Bm} \cos k_m y \\ s(y, z=0) &= \textstyle\sum_{m=1}^M s^{Bm} \cos k_m y \end{aligned} \tag{6.28}$$

---

[1] This fact was not realised until after the algorithm was implemented, and the results presented used direct solution of all $n_0 M$ equations. As this is still $O(M^2 T_6)$ time, the overall performance was not direly effected.

may be determined. Thus problem B has been reduced to the problem

$$\begin{aligned}
\textstyle\sum_{l=1}^{6} c_l^{Bm} p_l^m(0) &= p^{Bm} \\
\textstyle\sum_{l=1}^{6} c_l^{Bm} s_l^m(0) &= s^{Bm} \\
\textstyle\sum_{l=1}^{6} c_l^{Bm} \sigma_l^m(0) &= 0 \\
\textstyle\sum_{l=1}^{6} c_l^{Bm} u_{yl}^m(-1) &= 0 \\
\textstyle\sum_{l=1}^{6} c_l^{Bm} u_{zl}^m(-1) &= 0 \\
\textstyle\sum_{l=1}^{6} c_l^{Bm} V_{zl}^m(-1) &= 0 \,,
\end{aligned}$$

for $m = 1, \ldots, M$. As before, this step takes only MT_6 time, though the comments about use of the shortwave approximation on page 139 are again appropriate. The solution to the problem defined by boundary conditions 6.1, 6.2, and 6.3 is now given by equations 6.4, 6.7, and 6.10, with

$$c_l^m = c_l^{Am} + c_l^{Bm} \,.$$

6.4 Results

The algorithm described in the preceding section was used to determine the fields with the parameter values of equations 4.6 and 4.7. In addition, the values $l = 1$ and $l_1 = 0.5$ were used. Calculations were made for current stimulus frequencies of $f = 10^{-5}$ and 10^{-3} Hz. Values of the coefficients were calculated for various values of M (the number of Fourier modes kept in equation 6.10). The values of M ranged between 20 and 100 modes for the low-frequency ($f = 10^{-5}$), and between 20 and 120 for the mid-frequency ($f = 10^{-3}$). Because the Fourier series for some of the fields converge slowly, the coefficients j_m and c_l^m were passed through the Hamming window [46] before calculating the fields. In particular, the coefficients were transformed according to

$$C_m \rightarrow [a + b\cos(\pi \frac{k_m}{k_M})] C_m \,,$$

where C_m is one of j_m or c_l^m, $b = 1 - a$, and

$$a = 0.523 + \frac{0.076}{M} .$$

The convergence of the fields with increasing M is discussed in Section §6.5.

The magnitudes and phases of the fields were plotted as functions of y and z for the range $0 \leq y \leq 2l$ (one half-period in the horizontal direction) and $-1 \leq z \leq 0$. (Plots of all of the relevant fields may be found in Appendix A.3, while the maximum and minimum values of the field magnitudes and phases are in Table 6.1.) In figure 6.4 the horizontal displacement, $|\bar{u}_y|$, is shown for $f = 10^{-3}$. Note that it grows over the region in which current is injected (region I), and is nearly constant in y near region II. The profile looks very much the same for $f = 10^{-5}$. The magnitudes of the vertical displacement, $|\bar{u}_z|$, is shown for both frequencies in figure 6.5. The apparent cusp in $|u_z|$ on the line $y = l$ is due to the fact that u_z is asymmetric about this axis. Note that in the "static" case ($f = 10^{-5}$), the behavior is drastically different. Also, in both cases the boundary condition $u_z = 0$ on region I and on $z = -1$ are met. For $f = 10^{-3}$, the maximum of $|u_z|$ over region I is less than 10^{-4} its maximum over region II. Other boundary conditions were met with similar accuracy.

The fluid velocity fields have a singularity at the interface between regions I and II. The magnitude and phase of the relative horizontal velocity, $\bar{V}_y$ are shown for $f = 10^{-5}$ in figure 6.6. The magnitude of the field is similar for $f = 10^{-3}$, but the maximum along the symmetry axis $y = l$ is larger by a factor of about three. In both cases a phase lag develops in region I with frequency, whereas in region II and away from the top V_y is 180° out of phase with the input (J_z). Thus, near the surface there is a rapid phase change from across singularity. The boundary and the singularity influence a much shallower region for higher frequencies, as expected from previously mentioned interpretations of the diffusion boundary layer thickness

Variable	Maximum Amplitude	Minimum Phase	Maximum Phase	Modes, Samples
$\bar{u}_y$	$3.10 \cdot 10^{-2}$	1.00	1.37	100, 513
	0.103	$2.9 \cdot 10^{-2}$	$3.8 \cdot 10^{-2}$	100, 513
$\bar{u}_z$	$1.53 \cdot 10^{-2}$	−3.13	3.14	100, 129
	$1.27 \cdot 10^{-2}$	−3.09	3.13	100, 129
$\bar{V}_y$	1.33	−3.14	3.14	100, 513
	2.88	−3.14	3.14	100, 513
$\bar{V}_z$	1.75	−3.14	3.14	100, 513
	3.615	−3.14	3.14	100, 513
$\bar{p}$	0.255	−2.58	2.66	100, 513
	0.456	−3.12	$5.3 \cdot 10^{-2}$	100, 513
$\bar{s}$	$4.06 \cdot 10^{-2}$	−2.26	2.37	100, 513
	0.120	−3.11	$4.9 \cdot 10^{-2}$	100, 513
$\bar{\sigma}_{yz}$	$1.17 \cdot 10^{-2}$	−0.356	2.37	100, 129
	$5.02 \cdot 10^{-2}$	−3.08	0.048	100, 129
$\bar{\phi}$	0.546	−3.14	3.14	100, 129
	0.570	−3.14	3.14	100, 129
$\bar{J}_y$	1.07	π	π	100, 513
	↑	↑	↑	100, 513
$\bar{J}_z$	1	0	0	∞, ∞
	↑	↑	↑	↑

Table 6.1: Field values for mixed boundary condition forcing. These are the values of the extrema (over y and z) of the (non-dimensional) magnitudes and phases of the indicated field variables calculated using the parameters described in Section §6.4. The upper values refer to $f = 10^{-3}\ Hz$, the lower to $f = 10^{-5}\ Hz$. Plots of these fields may be found in Appendix A.3.

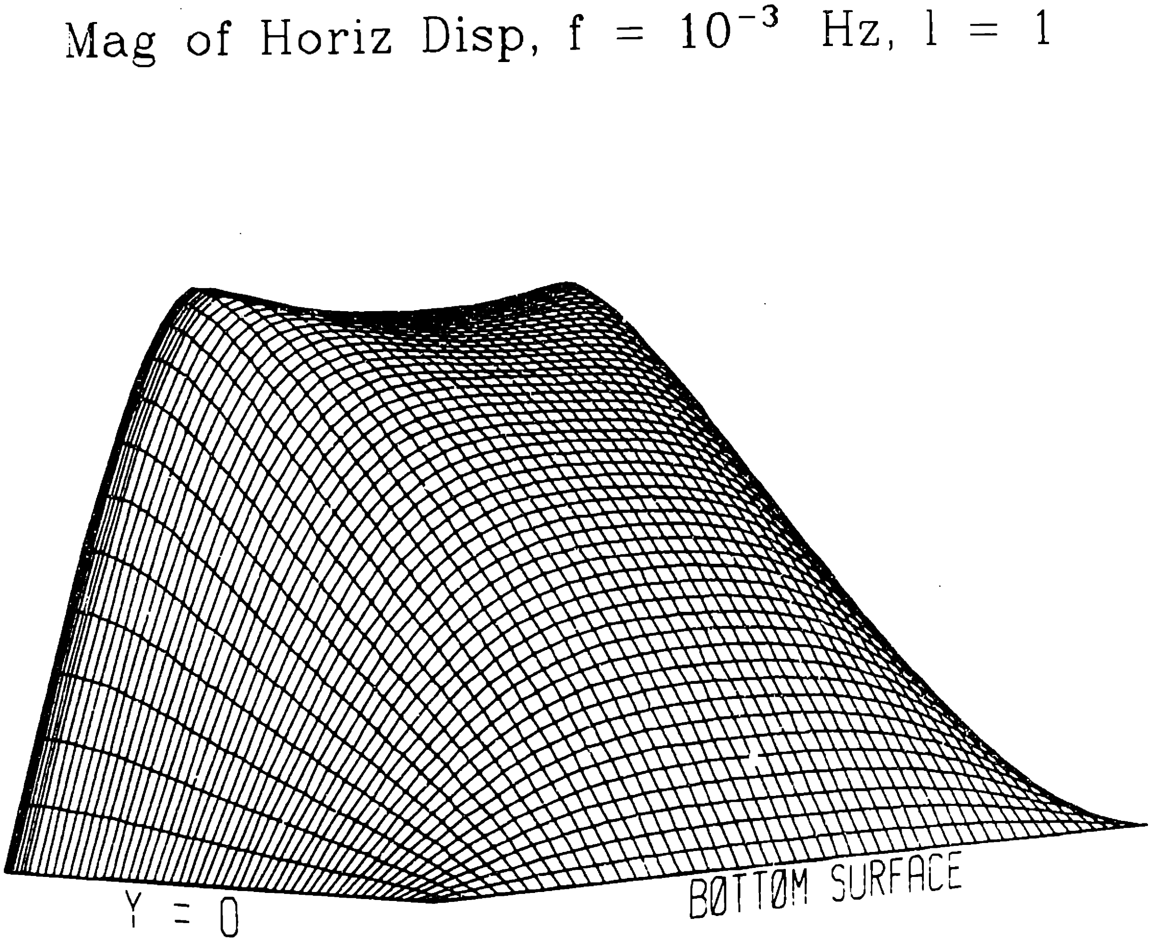

Figure 6.4: Magnitude of the horizontal displacement, $|\bar{u}_y|$, $f = 10^{-3}$ Hz, $M = 100$. The maximum non-dimensional value is 0.10.

Mag of Vert Disp, f = 10^{-5} Hz, l = 1

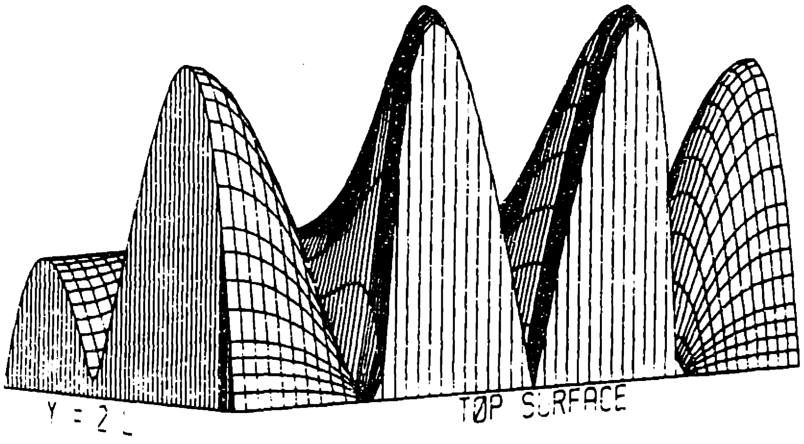

Mag of Vert Disp, f = 10^{-3} Hz, l = 1

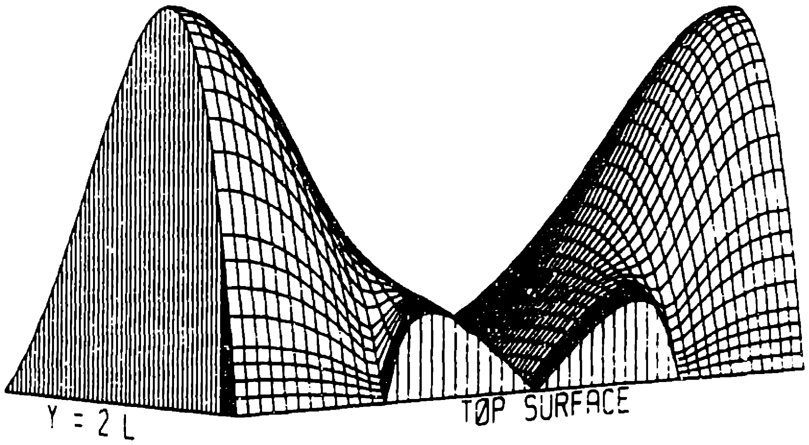

Figure 6.5: Magnitude of the Vertical Displacement, $|\bar{u}_z|$, $f = 10^{-5}$ and 10^{-3} Hz, $M = 60$ and 100, respectively (Differences are not due to the number of modes.). The maximum non-dimensional values are $1.3 \cdot 10^{-2}$ and $1.5 \cdot 10^{-2}$, respectively.

(*cf.* §3.3. The magnitude of the relative vertical velocity, $\bar{V}_z$ for both frequencies is in figure 6.7. Note that interior values of vertical velocity are also larger for $f = 10^{-3}$ here. The phase of the relative vertical velocity for $f = 10^{-3}$ is shown in figure 6.8. Note the transition of roughly 45° from region II into the interior, and the fact that V_z is in phase with J_z below the diffusion boundary layer thickness. For $f = 10^{-5}$, V_z is in phase with J_z everywhere.

The reason for the singularity in the velocity fields may seen in the pressure field. The magnitude of the pressure, $|\bar{p}|$ is shown in figure 6.9 for $f = 10^{-5}$. Note that the tangent to $|p|$ is nearly vertical at the boundary $y = l_1$ between regions I and II. (This is explained in §6.5. It is also seen in the real part of the pressure, and thus is not a manifestation of having taken the magnitude.) The coupling equation 2.6 indicates that the relative velocity can be calculated by adding the current density field and the gradient of the pressure. Because the current density is continuous at $y = l_1$, any discontinuity in the derivative or value of p would be expressed as a singularity of higher order in the relative velocity field. Thus, the singularity in the relative velocity fields is reasonable. Also, the of j_z is discontinuous at $y = l_1$, and it was considered possible that the singularity in the relative velocities was due to the consequent slow convergence of its (j_z's) Fourier series. This was disproven by demonstrating that the singularity exists even if the boundary conditions $J_z = \cos(k_1 y)\exp(-i\omega t)$ are used, *cf.* §6.5.

The magnitudes and phases of the three stress-related variables, p, s, and σ_{yz} have some striking similarities and differences. First, the profile of the pressure at $f = 10^{-3}$ looks very much like that shown for $f = 10^{-5}$ in figure 6.9. As might be expected from the velocity profiles and the diffusion boundary layer thickness, the magnitude decays more rapidly for $f = 10^{-3}$. Further, the maximum value at the latter frequency is roughly half that of the former. The maximum magnitude of the normal stress, s, however, is nearly 3 times as large for $f = 10^{-5}$ as for $f = 10^{-3}$.

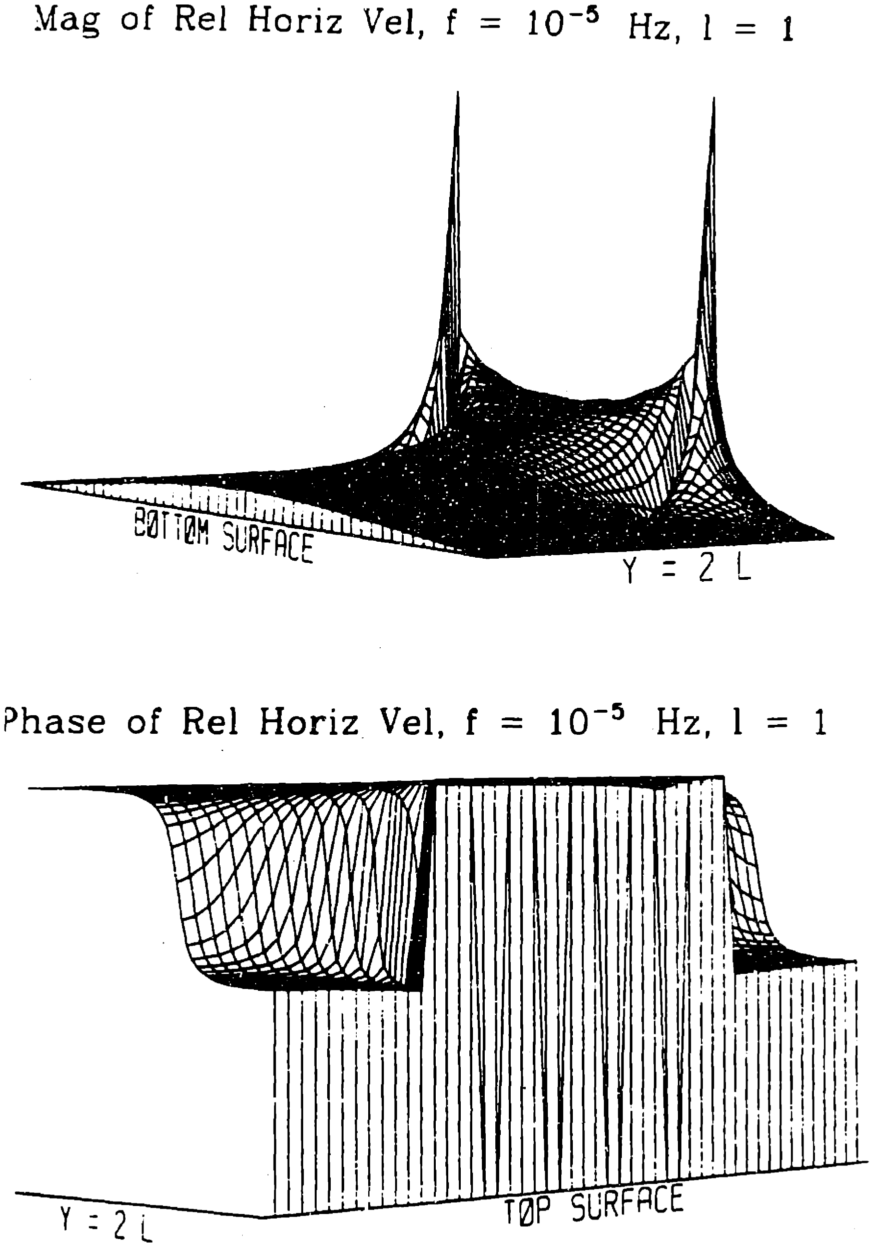

Figure 6.6: Magnitude and phase of the relative horizontal velocity, $\bar{V}_y$, $f = 10^{-5}$ Hz, $M = 100$. The maximum non-dimensional value of the magnitude is 1.8. The phase ranges between $-\pi$ and π. Values of the phase are not plotted for points at which the magnitude of the field is smaller than a specified fraction of the maximum value over the whole region. In this case that "cutoff fraction" was $5 \cdot 10^{-4}$.

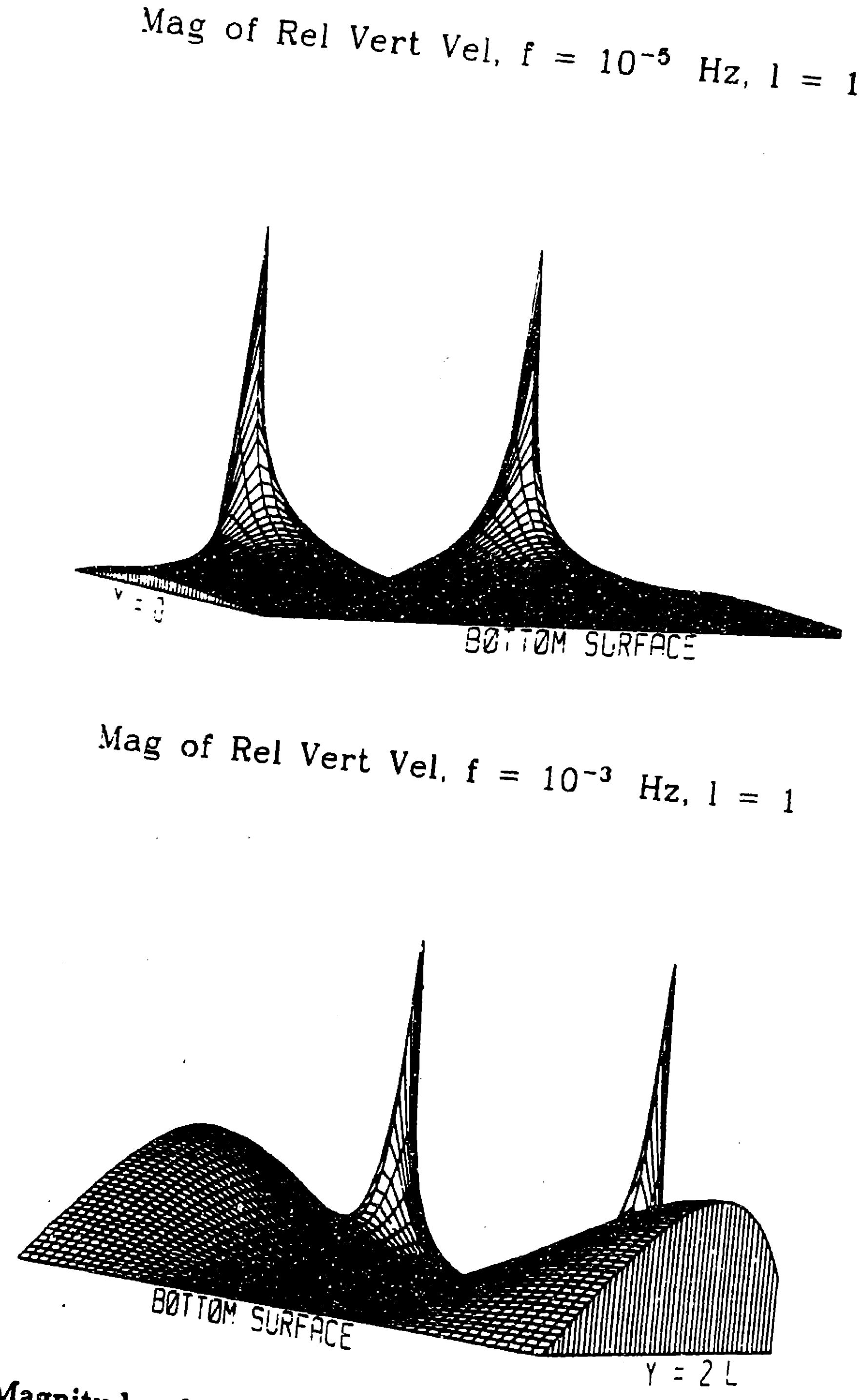

Figure 6.7: Magnitude of the relative vertical velocity, $|\bar{V}_z|$, for $f = 10^{-5}$ and 10^{-3} Hz, $M = 60$ and 100, respectively. The maximum values at the peaks are 1.8 in both cases.

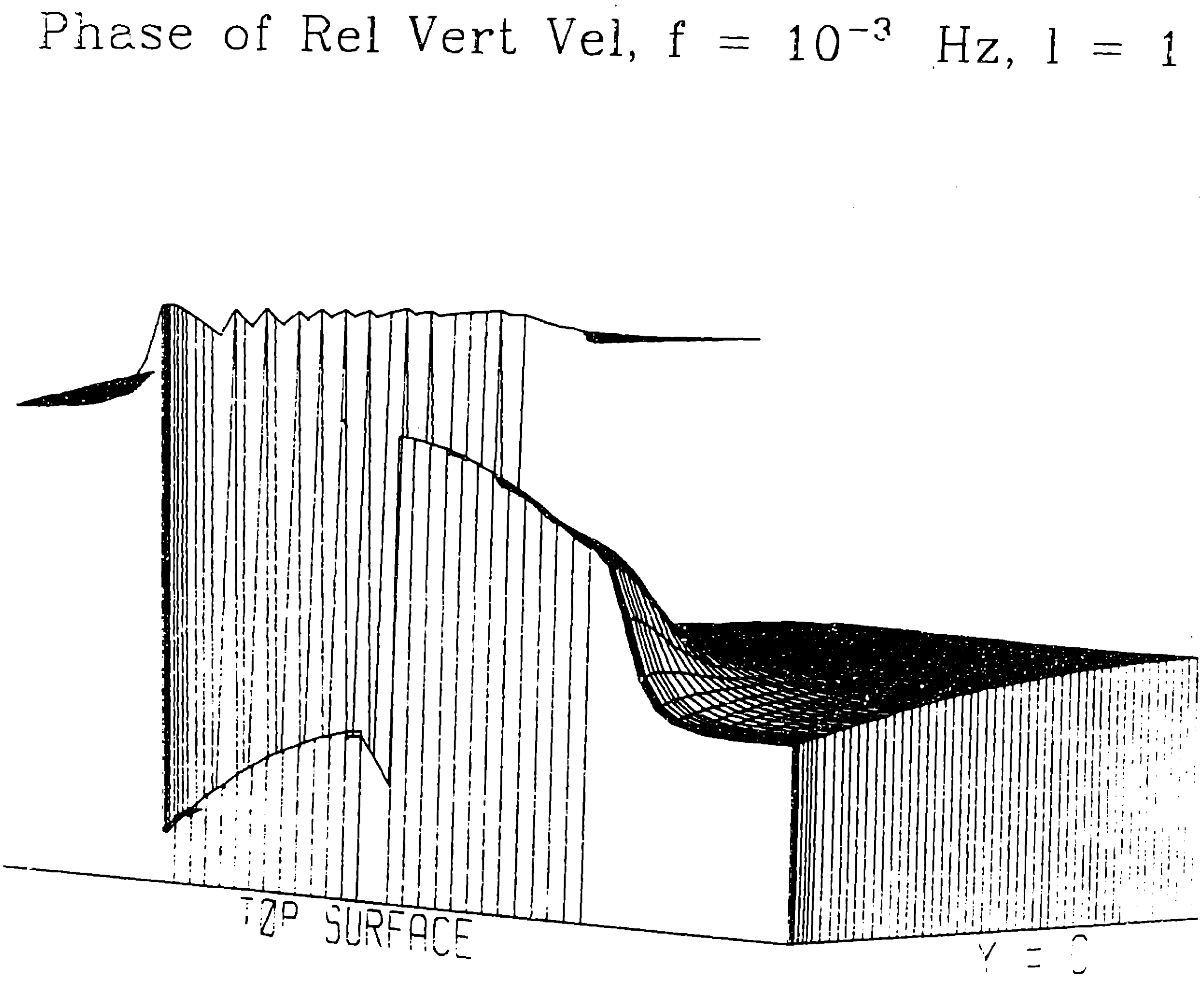

Figure 6.8: Phase of the relative vertical velocity, $\tilde{V}_z$, $f = 10^{-3}$, $M = 100$. The value ranges between $-\pi$ and π radians.

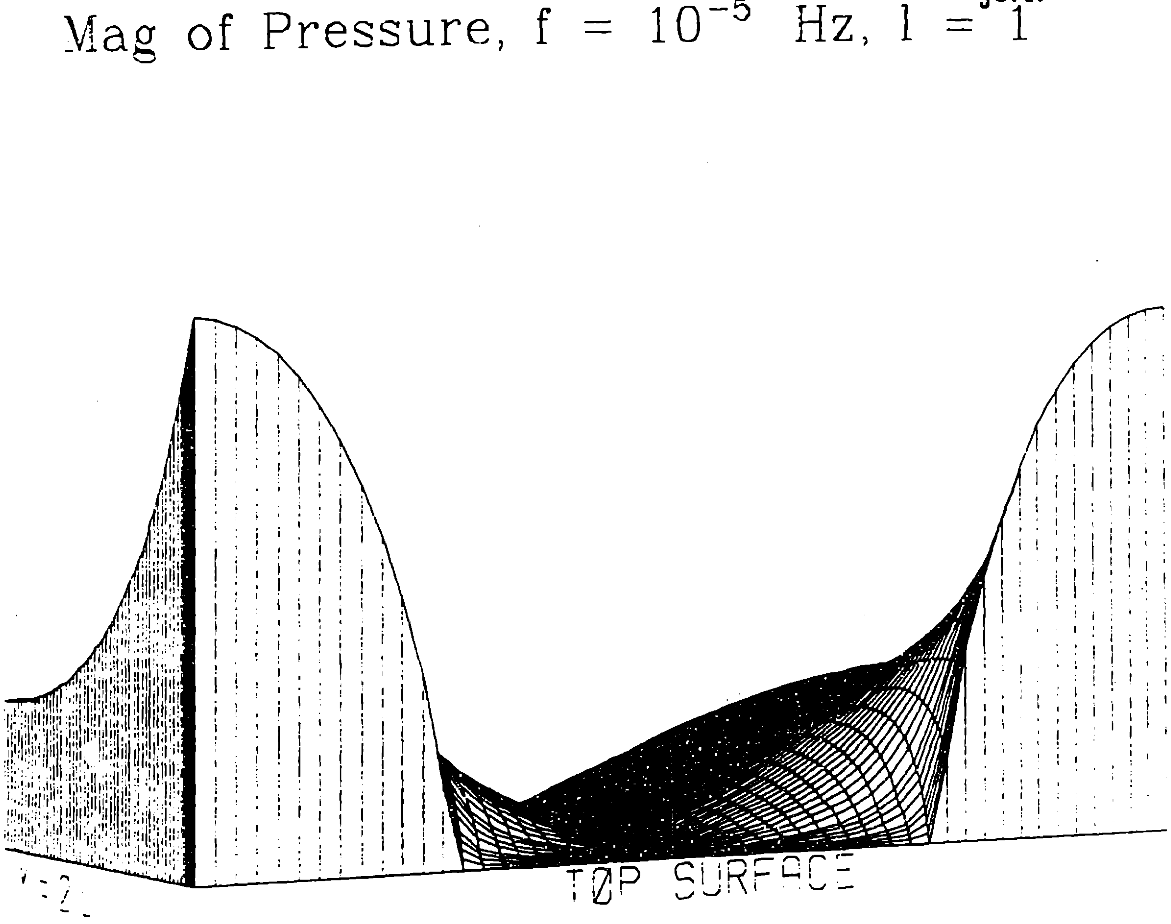

Figure 6.9: Magnitude of the pressure, $|\bar{p}|$, for $f = 10^{-5}$, M=60. The maximum value plotted is 0.454.

Since pressure stresses do not account for this, consideration of the constitutive equation 2.3 shows that the large difference must be due to a large change in either the magnitude of the elastic stresses or the relative phases of the elastic and pressure stresses (with the latter change resulting in cancellation). As with the pressure, the profile decays more rapidly (towards the bottom) for the higher frequency.

The phase profiles of the pressure and normal stress are also similar. For $f = 10^{-5}$, both variables are in phase with J_z, as they are real and positive for $0 \leq y < l$, and negative for $l < y \leq 2l$. In figure 6.10 it can be seen that, for $f = 10^{-3}$, s has a lag of $\pi/2$ over most of the volume, and a lag of $3\pi/4$ over a region within a diffusion layer thickness of region II. The lag for p is similar, with an average lag close to $3\pi/4$.

The behavior of the shear, σ_{yz}, shows the frequency dependence even more dramatically than p or s. In figure 6.11, the sharp maximum of $|\sigma_{yz}|$ which results from the change in boundary conditions propagates into the medium for almost one-third of its depth. Given the fact that the shear is zero at the surface, as required by the boundary conditions, the development of such narrow maxima just beneath the surface is somewhat surprising. This is especially true for the sharp peak present in the plot of the $f = 10^{-3}$ value in the same figure. In this case, however, the effect is spread over a wider region starting much closer to the surface, as would be expected. Further, the maximum value of $|\sigma_{yz}|$, which occurs at $(y, z) = (l, -1)$ is roughly four times as large for the lower frequency. This supports the idea that the mechanical stresses due to the solid matrix are stronger at lower frequencies, as mentioned above for the normal stress. Lastly, for both frequencies (especially $f = 10^{-5}$) the phases are relatively constant over the bottom 60% of the layer. The difference is that the low-frequency value is roughly zero, while that of $f = 10^{-3}$ is roughly $2\pi/5$. Thus there is a significant lag present for the higher frequency which is not for the lower one, as expected.

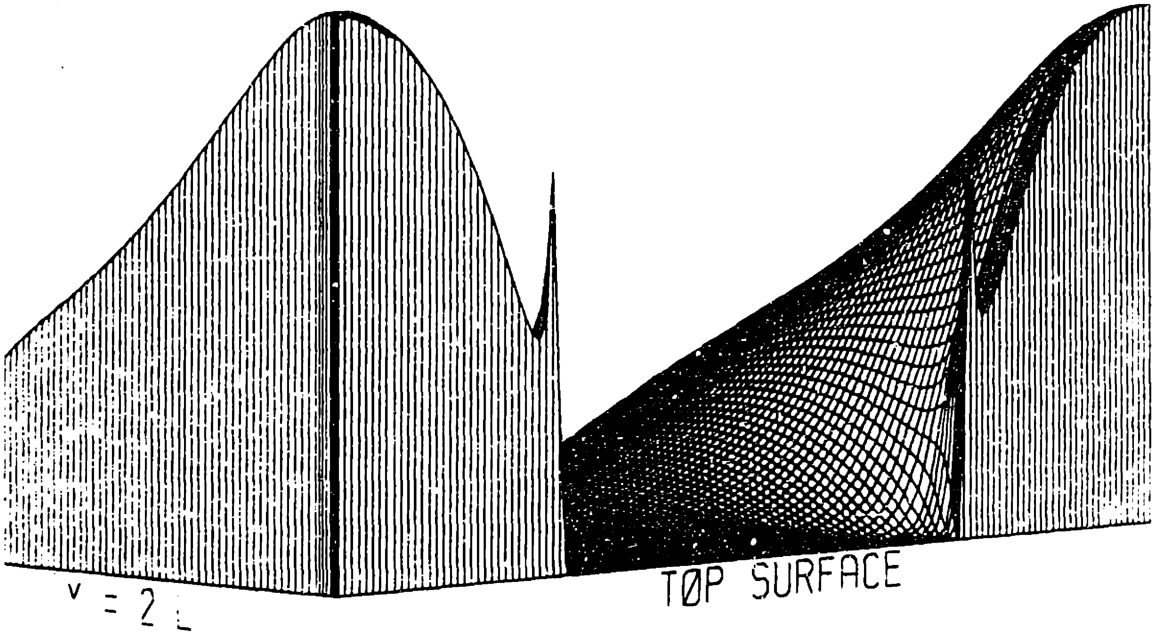

Figure 6.10: Magnitude of the normal stress, $|\bar{\mathbf{s}}|$, for $f = 10^{-3}$, $M = 100$. The value ranges from -2.26 to 2.37 with a cutoff frequency (*cf.* figure 6.6) of 0.01.

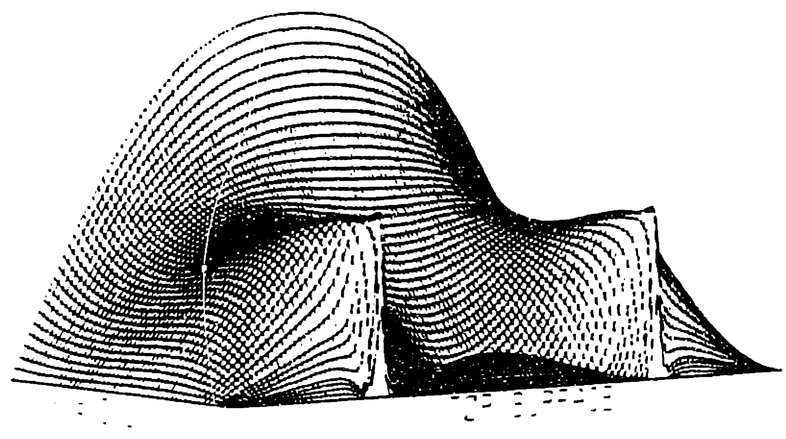

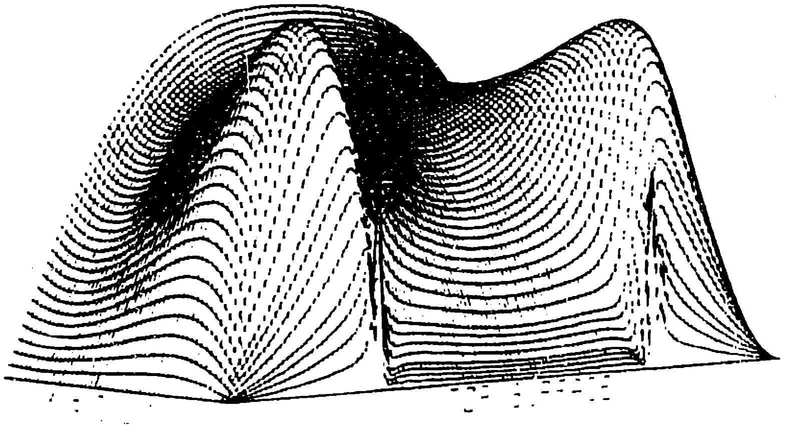

Figure 6.11: Magnitude of the shear stress, $|\tilde{\sigma}_{yz}|$, $f = 10^{-5}$ and 10^{-3}, $M = 60$, and 100, respectively. The maximum values are $5.02 \cdot 10^{-2}$ and $1.17 \cdot 10^{-2}$, respectively.

The potential fields for the two frequencies are surprisingly similar. The magnitude of the potential for $f = 10^{-3}$ is shown in figure 6.12. It is virtually indistinguishable from that of the lower frequency. The phases are also indistinguishable, and are 180° out of phase with J_z, as would be suspected from a purely conductive model (*cf.* §2.3.2. There is a difference in the maximum amplitude, though, as the maximum for $f = 10^{-5}$ is 4.5% higher than that at $f = 10^{-3}$. Since $\vec{J}$ is not frequency dependent, the change must be due to the change in amplitude and phase of the relative velocity field.

6.5 Discussion

This section addresses several points. First, the convergence of the fields as the number of modes kept (M) increases must be addressed before the results can be interpreted physically. Next, the results will be compared to those of the simpler boundary conditions used in previous chapters. In particular, the existence of the singularities in the relative velocity field, $\vec{V}$, will be discussed.

6.5.1 Convergence

The convergence of the fields as $M \to \infty$ was examined in three ways. First, the magnitude of several fields at a given depth, z, were plotted as a function of y for $M = 36$, 70, and 120. These plots are shown for the pressure and vertical current density at the surface, p and V_y in figures 6.13 and 6.14. For these plots, the fields have been calculated using the forcing $J_z = \cos(k_1 y)\exp(-i\omega t)$ mentioned on page 149 instead of that given in equations 6.1 and 6.2. Note that the values of p change very little except in the vicinity of the boundary $y = l_1$ between regions I and II.

As the resolution improves with M, it is clear the tangent to $p(y = l_1, z = 0)$ is

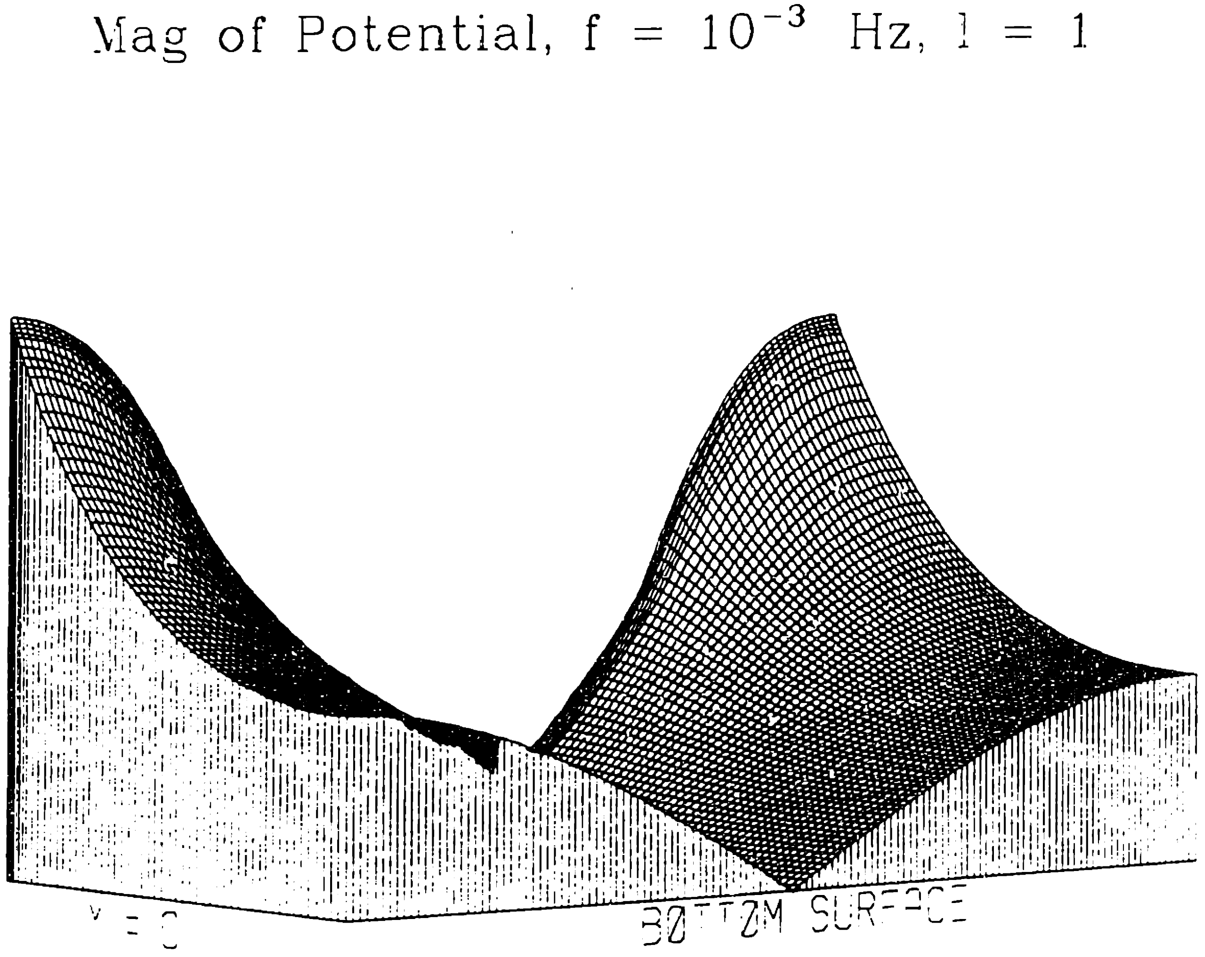

Figure 6.12: Magnitude of the potential, $|\bar{\phi}|$, $f = 10^{-3}$, $M = 100$. The maximum is 0.570.

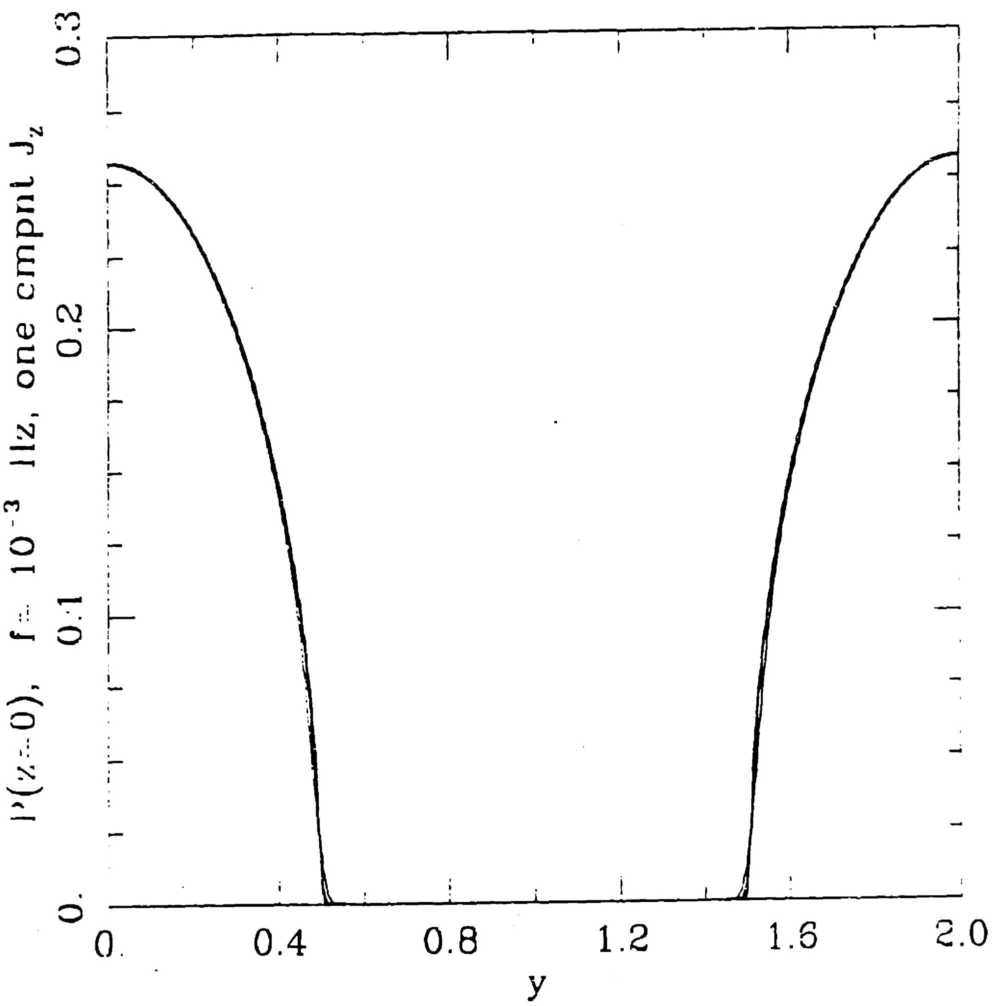

Figure 6.13: Magnitude of the pressure, $|\tilde{p}|$, $f = 10^{-3}$, M = 36, 70, and 120. The boundary condition $J_z = \cos(k_1 y)\exp(-i\omega t)$ was used.

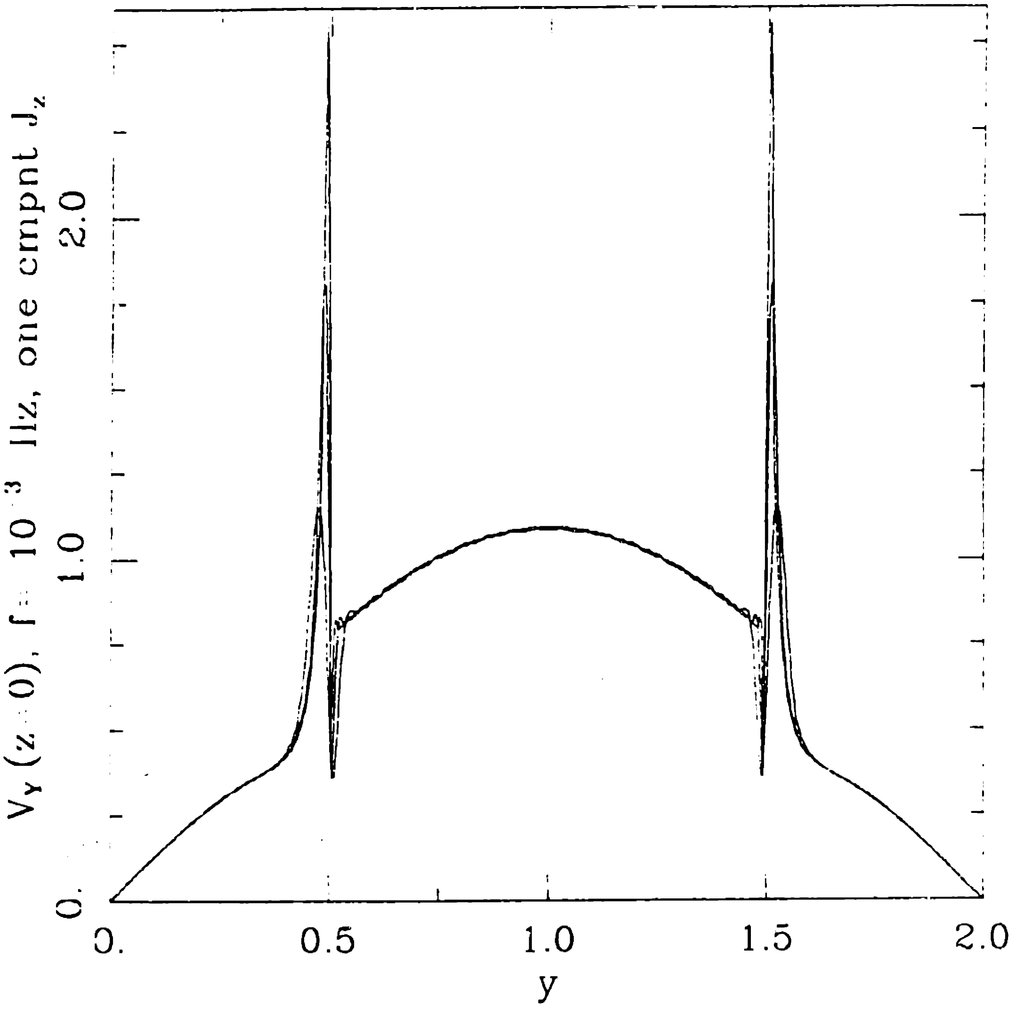

Figure 6.14: Magnitude of the relative horizontal velocity, $|\tilde{V}_y|$, $f = 10^{-3}$, $M = 36$, 70, and 120. The boundary condition $J_z = \cos(k_1 y)\exp(-i\omega t)$ was used.

becoming more and more vertical. In figure 6.14 it can be seen that, as expected from the y-component of the coupling equation 2.6a, the singularity in V_y at $y = l_1$ becomes better defined as the gradient of p in that neighborhood increases. In any region not containing the point $(y = l_1, z = 0)$, however, it appears that the values of this field are also converging. It is also important to note that even though the vertical current density profile is infinitely smooth in this case (as opposed to having the discontinuous derivative implicit in equations 6.1 and 6.2), there is still a singularity in V_y and V_z. The singularity is thus, as will be discussed further below, due to the mechanical boundary conditions, and not just the singularity in the chosen current density profile.

The second test for convergence examines the differences between successive approximations to the fields. The analysis involved in such a test is as follows. Assume that a complex number X is being successively approximated by the sequence $x_1, x_2, \ldots$. The first differences $d_n \equiv \Delta x_n$ are defined by $\Delta x_n = x_n - x_{n-1}$. Note that

$$x_m = \sum_{n=1}^{m} d_n \, , \tag{6.29}$$

where d_1 has been defined as x_1. Thus if the sequence x_m is to converge as $M \to \infty$, the d_n must decay sufficiently rapidly. In particular, if the slope of a plot of $\log |d_n|$ versus $\log n$ is (asymptotically) linear and has a slope $-b < -1$, then the sequence x_m converges absolutely at with an error on the order of $m^{-(b-1)}$. In figure 6.15, this procedure was performed using the maximum over y at $z = -0.5$ of each of the field variables u_y, u_z, V_y, V_z, p, s, j_y, and ϕ as a separate sequence x_n. It is evident that all but the last two converge like M^{-1}, and that the last two converge like M^{-3} or faster. In applications where more than a few digits of accuracy are needed, the convergence may thus be accelerated *via* a Richardson-Aitken or other, similar transformation [5].

At the surface ($z = 0$), however, the values of V_y and V_z converge only condi-

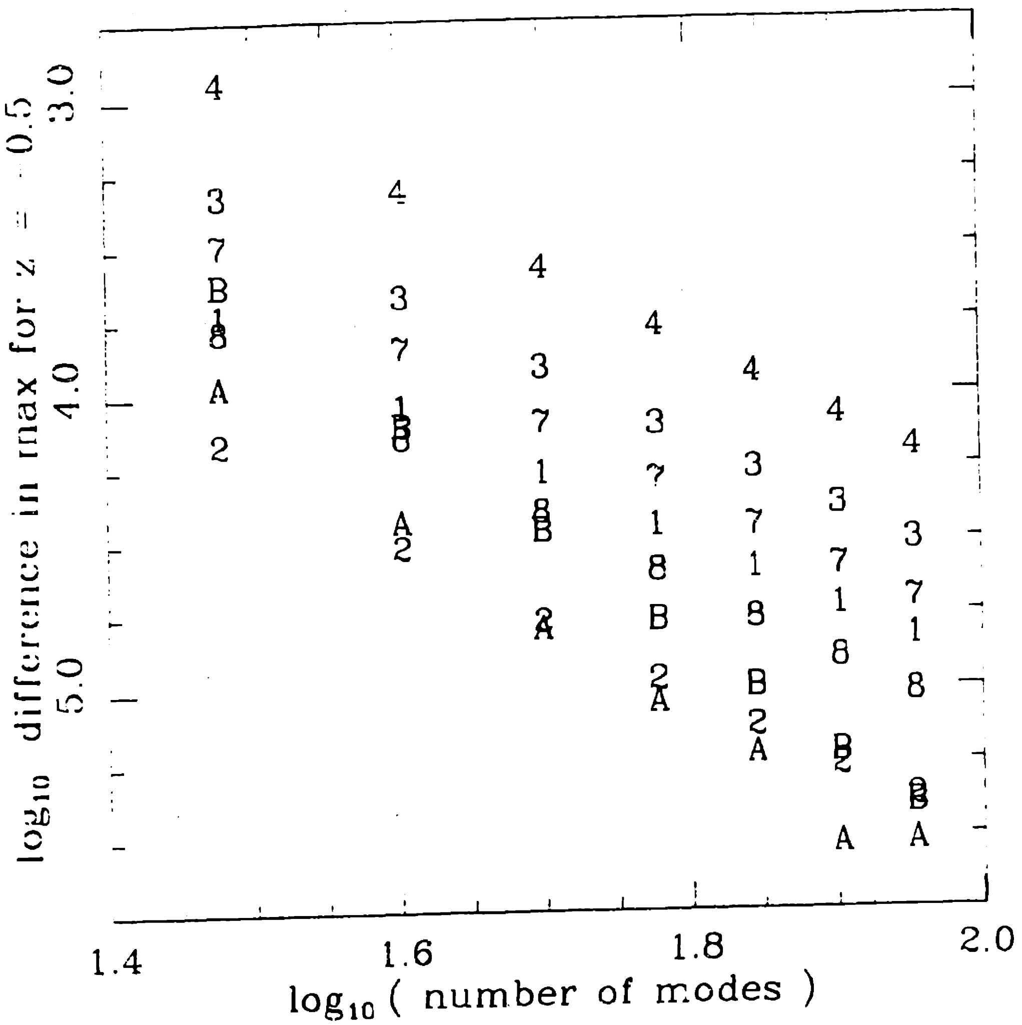

Figure 6.15: Convergence rate for the field maxima at $z = -0.5$, $f = 10^{-3}$, $l = 1$, $l_1 = 0.5$. The values correspond to the differences in the values of the maximum amplitudes of the fields over y at $z = -0.5$ for successive values of the number of modes used in the calculations, M. The symbols 1, 2, 3, 4, 7, 8 correspond to values for $|\tilde{a}_y|$, $|\tilde{a}_z|$, $|\tilde{V}_y|$, $|\tilde{V}_z|$, $|\tilde{p}|$, $|\tilde{s}|$, $|\tilde{j}_y|$, and $|\tilde{\phi}|$, respectively. For example, the upper-left-hand "4" represents the log of the difference between the value of $\max|\tilde{V}_z(y, z = -0.5)|$ ($0 \leq y \leq l$) evaluated for $M = 30$ and $M = 20$ modes. The values of M used are 30, 40, 50, 60, 70, 80, and 90.

tionally. To see this, observe that in figure 6.16 the values of the differences between the successive approximations to $V_y(y = 1, z = 0)$ are decaying only like $M^{-1/4}$. The other plot in this figure, however, shows that the values are converging in an oscillatory manner, and (from the previous observation) with an envelope of $M^{-1/4}$. These oscillations may be damped out to give more accurate values.

6.5.2 Comparison with Previous Results

There are several similarities between the behaviors associated with mixed boundary conditions, and those associated with non-mixed electrical or mechanical forcing. The first of these is the phase lag which develops at higher frequencies for virtually all of the variables. For current forcing, for example, in figure 4.6 it was seen that the phase of the horizontal displacement rises by a little more than one radian (on the average) as the frequency goes from 10^{-5} to 10^{-3}. In the mixed case this also happens, as the phase of u_y is nearly constant at zero for $f = 10^{-5}$, and ranges between 1.00 and 1.37 for $f = 10^{-3}$. In this sense the mixed problem is acting like the current forced one.

This similarity between the current forced response under mixed and non-mixed boundary conditions is also seen in the displacement amplitude. The horizontal displacement is much smaller at higher frequencies for both cases. If longer wavelengths are considered in the non-mixed case, it can be seen that the amplitude of the responses for both cases decrease roughly in proportion to the frequency. This makes sense in that the solid and fluid can not, given the frictional interaction between them, react instantaneously to the driving current. Thus at a higher frequency the solid matrix will not have time to move as far before the phase of the driving reverses. This argument also explains why there is a phase lag for the higher frequencies.

Note, however, that the vertical displacement actually increases slightly with frequency. This is probably due to the increase in vertical velocity (and conse-

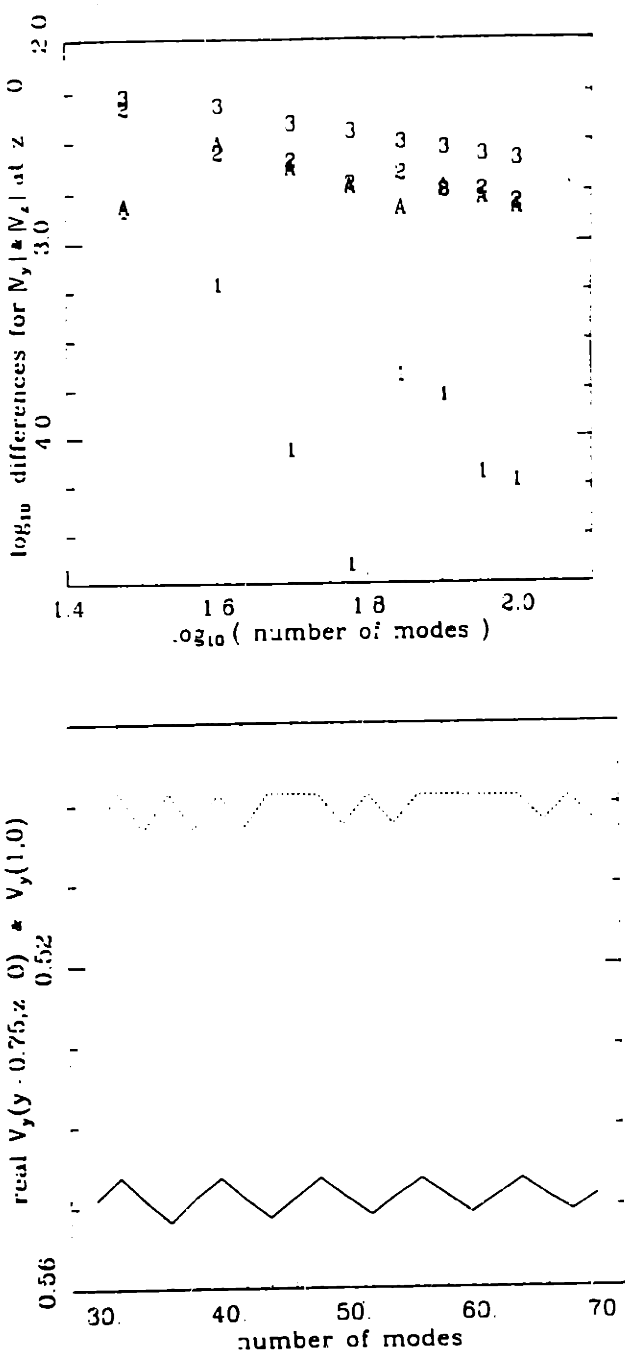

Figure 6.16: Convergence of the relative velocity fields, V_y, and V_z at $z = 0$, $f = 10^{-3}$, $l = 1$, $l_1 = 0.5$. Above: As in figure 6.15, but with the symbols 1, 2, 3, and A representing the differences for $|\bar{V}_y(y = 0.25, z = 0)|$, $|\bar{V}_y(0.75, 0)|$, $|\bar{V}_y(1, 0)|$, and $|\bar{V}_z(0.75, 0)|$. Below: Values of the real parts of $|\bar{V}_y(0.75, 0)|$ (solid line) and $|\bar{V}_y(1, 0)|$ for $M = 30, 32, \ldots, 70$. The break in the pattern is only due to missing data points at $M = 46$, 58, and 62.

quent drag on the matrix) in the interior where the vertical displacement is not constrained. The relative lack of change of amplitude is similar to that noted for the mechanically forced case. Also, the concentration of the vertical displacement field near the center of the layer seems related to the lack of equilibration time mentioned above. In the "static" case ($f = 10^{-5}$), the displacement has time to move all the way up to the spaces between the electrodes.

The latter effect is also responsible for the relative sizes of the normal and shear stresses, s and σ_{yz}, at $f = 10^{-5}$ and 10^{-3}. It was noted (in §6.4) that the pressure changes by a factor of only about two, whereas s changes by a factor of three, and σ_{yz} by one of four. The fact that, for lower frequencies, the displacement fields have time to develop large gradients. means that the stress fields will also be larger at these frequencies. Similarly, the stress and shear fields develop significant phase lags at the higher frequencies.

The relative velocity fields also appear to lack equilibration time. In the current driven case, the magnitudes of the relative velocities increased slightly with a two decade frequency change. If the region away from the singularity is considered, this is also true for the mixed boundary value problem as well. The increase is, most likely, due to a scaling effect. Namely, at higher frequencies, one expects proportionally higher velocities. This might be true for these two cases if the frequencies were in the static range ($f < 10^{-5}$), but here again the drag interaction with the solid matrix results in a certain time delay before the fluid can obtain its equilibrium (static) amplitude.

The two most outstanding features of the previous four non-mixed cases can be seen here as well. First, the influence of the diffusion boundary layer thickness has also been seen in this mixed boundary value problem. This is seen in the shear profile of figure 6.11, where the profile is smoothed at a much shallower depth for the case at the higher frequency (and, thus, lower diffusion boundary layer thickness).

Further, the singularities in the velocities are smoothed out closer to the surface for higher frequencies.

Finally, the penetration depth is still proportional to the input wavelength. Thus any information contained in harmonics with short wavelengths is lost beyond one wavelength below the surface. This can be seen in the smoothness of even the singular profiles of V_y and V_z (figures 6.6 and 6.7, respectively) for $z < -0.1$. In this manner it may be said that even though the singularities near the change in boundary conditions would not be physically realized, the values of the field away from the boundary would not be significantly altered if these singularities were not present.

6.5.3 The Nature of the Singularity

This section will demonstrate that the singularities, which may at first seem to be an extreme response the given change in boundary conditions, are to be expected in the present model. Consider, first, the vicinity of the point $p_0 = (y = l_1, z = 0)$ on a local yet macroscopic scale. That is to say, consider figure 6.17, in which the point p_0 is the origin of a stretched y, z-coordinate system. The scale of these coordinates is sufficiently stretched that all other boundaries in the problem are insignificant, yet not so much that the electrochemistry at the surface of the electrodes needs to be considered. (This coordinate scale is only considered for mathematical purposes, and does not necessarily exist in practice). An analysis of the singularity will be carried out on this coordinate scale using the classical potential theory for the irrotational flow of an incompressible fluid.

First, note that, in the static limit $f \to 0$, the relative velocity behaves like an incompressible and is also irrotational. In this limit, the relative and absolute fluid

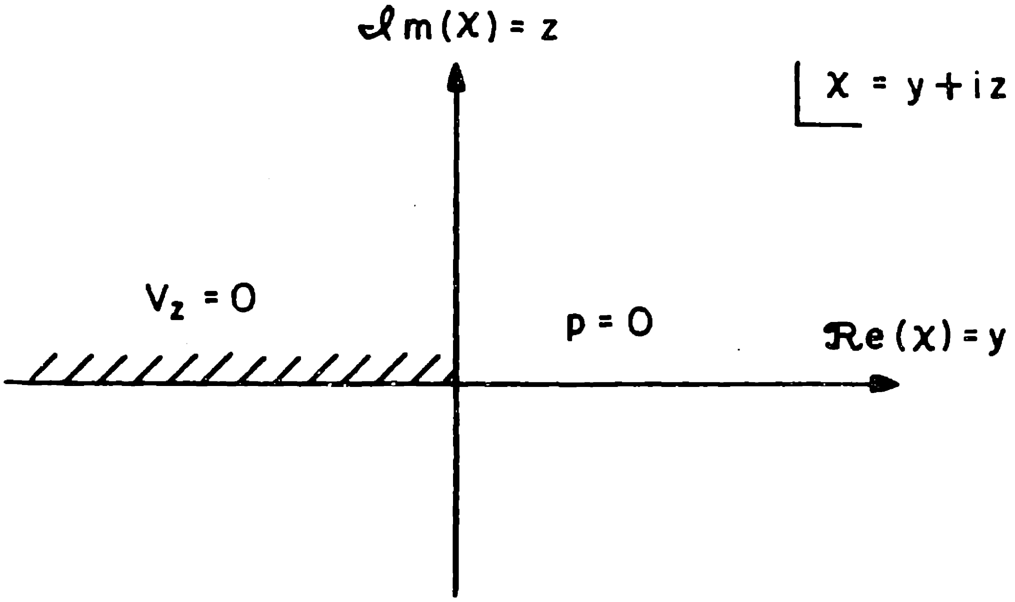

$\mathcal{I}m(X) = z$
$X = y + iz$
$V_z = 0$
$p = 0$
$\mathcal{R}e(X) = y$

Figure 6.17: Local coordinate system and boundary conditions for analysis of the singularity. The pressure is zero for $z = 0$, $y > 0$, which is the positive real axis if this plane is considered to be the complex $x = y + iz$ plane.

velocities, $\vec{V}$ and $\vec{v}$, are equal. By considering equation 2.1 or 3.8, it is evident that

$$\vec{\nabla} \cdot \vec{V} = 0\,, \tag{6.30}$$

which is the equation of conservation of mass for an incompressible flow. In addition, equation 2.7 ($\vec{\nabla} \times \vec{V} = \vec{0}$) shows that this flow is irrotational. Thus the relative velocity may be set equal to the gradient of a function φ

$$\vec{V} = \vec{\nabla}\varphi\,,$$

which is harmonic,

$$\vec{\nabla}^2\varphi = 0$$

The function $\varphi(y, z)$ is necessarily the real part of a function $\mathcal{F} = \varphi + i\psi$ of the complex variable $\chi = y + iz$. In terms of this complex potential, we wave

$$d_\chi \mathcal{F} = V_y - iV_z\,, \tag{6.31}$$

where d_χ is the derivative with respect to the complex variable χ.

The boundary conditions relevant to this potential flow problem are taken from equations 6.1 and 6.2 to be

$$\begin{aligned} p &= 0 \quad y > 0 \\ V_z &= 0 \quad y < 0\,. \end{aligned} \tag{6.32}$$

To convert the pressure equation into a velocity condition, the steady, constant density, irrotational form of Bernoulli's law is used. Substitution of 6.31 gives (assuming unit density)

$$p = c - |\vec{V}|^2 = c - |d_\chi \mathcal{F}|^2\,, \tag{6.33}$$

where c is an arbitrary constant, taken here as zero. Thus it is required that $|d_\chi \mathcal{F}|$ be constant on the positive real-χ axis. This condition may be generaly restated as

$$d_\chi \mathcal{F}\,|_{\chi=y>0} = e^{if(\chi)}\,|_{\chi=y>0} = e^{if(y)}\,, \tag{6.34}$$

for some real function $f(y)$ defined on $y > 0$. The other boundary condition simply requires that $d_\chi \mathcal{F}$ be real on the negative real axis.

Since one of the given equations 6.33 is non-linear, a general solution may not be obtainable. However, a very broad class of solutions is available in the form

$$d_\chi \mathcal{F} = e^{O(\sqrt{\chi})}\,, \tag{6.35}$$

where $O(\chi)$ is an "odd" function which is analytic in the vicinity of the origin, and real on the real χ-axis. By odd, it is meant that O has the Taylor series

$$O(\chi) = \sum_{j=1}^{\infty} a_j \chi^{2j-1}\,.$$

If O is also positive for χ real and $\chi < 0$, and negative for $\chi > 0$, then conditions 6.34 and $d_\chi \mathcal{F}$ real for $\chi < 0$, χ real, are clearly satisfied.

The simplest example function O satisfying these conditions is $O = -\chi$. This function gives $p = -|\exp(2\sqrt{-\chi})|$. Note that this function has a vertical tangent at the origin (approaching along the negative real χ-axis). This is exactly what is seen in figures 6.9 and 6.13. In fact, this property is shared by any solution of the above form if $a_1 \neq 0$. Thus it can be seen that the vertical tangent of the pressure field at p_0 is a natural consequence of the irrotationality (and, at low frequencies, incompressibility) of the flow. From the coupling equations 2.6 and the continuity of $\vec{J}$ it is clear that such a tangent would cause a singularity in the relative velocity field. It is this singularity which is observed.

There are at least two ways this analysis could be supported by other results. The first is to perform a numerical analysis of a series of problems having boundary conditions 6.3 on the bottom, and obeying

$$\begin{aligned} J_x &= \text{(as given above)} \\ f(y;l_t)u_x(y,0) + (1-f)s(y,0) &= 0 \\ f(y;l_t)V_x(y,0) + (1-f)p(y,0) &= 0 \end{aligned} \tag{6.36}$$

at the top. Here f is a smoothing function which changes from one for $y = 0$ to zero for $y = l$. Most of the change should take place within a transition region of length l_t on either side of the point $p_0 = (l_1, 0)$. One such function is

$$f = a(1 - \tanh(\frac{y - l_1}{l_t})) + b\,,$$

where

$$a = [\tanh(\frac{l_1}{l_t}) + \tanh(\frac{l - l_1}{l_t})]^{-1}$$

and

$$b = [\tanh(\frac{l - l_1}{l_t}) - 1]a\,.$$

The idea is to smoothly simulate the transition between the region I and II boundary conditions. By solving a series of problems with decreasing l_t, the development of the singularities in the velocity fields should be observed.

The second method is similar to that used in this section. By modifying the potential theory of poroelastic media proposed by McNamee and Gibson [80] to include the effects of the electrokinetic coupling, it is possible to express the mixed boundary value problem of this chapter strictly in terms of harmonic and biharmonic functions. By considering only the vicinity of the point p_0 (*i.e.* , taking an infinitely deep layer with region I extending to $y = -\infty$ and region II to $y = \infty$), it may be possible to find the exact analytic nature of the singularities in all of the variables. This could be compared in more detail with the present numerical results.

In both of the clarification methods it is clear that the physical limitations of the material being studied must be taken into account. More considerations would be necessary to determine the effects that the large velocities and stresses could have on a sample being tested. It is yet to be determined to what extent the the assumptions of linearity and uniform material property would breakdown, and to what extent there could be damage to the material being probed.

Chapter 7

Conclusion

A new, three-dimensional model of an electromechanically coupled poroelastic medium has been proposed in this thesis. The assumptions of the model have been considered in terms of the biophysical properties of articular cartilage, which was the material used as an example in this work. Further, some of the mathematical assumptions, such as linearity, have also been discussed. General solutions to the model equations have been given, and their physical implications have been examined. When properly superposed, these solutions yield the answers to a variety of three-dimensional problems.

The model has been used to predict the behavior of several types of surface probes which, it is proposed, could be used to measure the electromechanical properties of a charged biphasic medium. The first of these, examined in Chapter 4, is a surface probe which would supply a sinusoidal current density to the top surface of a finite-thickness layer. (By rescaling the solutions, the results of a potential, rather than current, input may be found.) Next, in Chapter 5, the response of this layer to mechanical stimulation was considered. The boundaries were assumed to be electrically insulating, and the top surface was considered in turn to be either impermeable or else infinitely permeable to fluid flow. Lastly, in Chapter 6, the response to a mixed boundary condition was investigated by simulating a probe which injects current into some regions along the surface of the material, and yet where the mechanical boundary conditions prevent vertical displacement and velocity. The adjacent regions were imagined to be bounded by an insulating fluid (*e.g.* low ionic-strength water), but were otherwise unconstrained mechanically (*i.e.* there was no pressure or normal stress).

The behavior of the model was determined through the use of numerics and asymptotics. For the current-stimulated case, the main findings are:

- the penetration depth of a surface disturbance is proportional to the wavelength of the stimulus;
- at short wavelengths the field amplitudes are independent of frequency, except for the velocities, which are proportional to f;
- there is an increase in the change of phase over the penetration depth as the diffusion boundary layer thickness, $\Delta \propto f^{-1/2}$, becomes small;

and,

- for wavelengths on the order of or greater than the thickness, the frequency strongly influences the phase lag between stimulus and response, and affects the locations of field amplitude maxima.

For the mechanically stimulated case, we found in addition that:

- the overall amplitude of the displacement fields is independent of the frequency of the surface disturbance;

and,

- the amplitude of the relative velocity in the bulk is strongly affected by the boundary conditions: it is greatest in the direction normal to a permeable boundary, and minimum normal to an impermeable one.

Asymptotic solutions were found for both the electrically and mechanically driven cases. In particular, the short-wave (infinite-depth) and long-wave limits of the model were examined using these asymptotic solutions. There is excellent agreement between the numerics and the asymptotics, and the results of both solution methods agree with physical interpretations of the model. Using parameter values from the literature, the long-wave limit of the model agrees well with data obtained from experiments using uniaxial geometries. Further experimentation is needed, however, to test the model fully under conditions of finite wavelength.

Results for the mixed boundary value problem were generated using a Fourier collocation algorithm which was shown to be approximately 216 times faster than the most straightforward algorithm. The results of the numerical studies using this algorithm were:

- there is a violent singularity in the relative velocity field at the boundary between the two kinds of boundary conditions – this singularity arises from an infinite derivative of the pressure which may be explained in terms of the potential theory of incompressible irrotational fluid flow;

- the behavior is consistent with that of the non-mixed problems – the short-wave phenomena are damped out rapidly as one moves into the layer, and a phase lag develops in most field variables as the frequency of the driving current is increased;

- at higher frequencies the field profiles cannot attain their equilibrium amplitudes, so that, overall, displacements and stresses decrease with frequency, whereas the magnitudes of the relative velocities change relatively little;

and,

- as the imposed frequency is varied, there is a significant change in directly measurable quantities such as the normal surface force, s, and potential ϕ: for

> the former variable the changes include both amplitude and phase, whereas for the latter they are only in the amplitude.

Nevertheless, if this approach is used to model the outcome of an actual experiment, the assumptions of linearity and homogeneity of material properties should be reexamined in light of the nature of the singularities present in the results.

The results of the model motivate the use of a surface probe for the measurement of electromechanical properties of charged biphasic media. For the mixed boundary value problem, there is a significant change in the response of the medium with frequency despite the fact that the current density field is frequency-independent. This suggests that all of the coupling parameters, (b_{ij}) make significant contributions to the values of the fields. A measurement protocol similar to that suggested in Section 4.4 could thus be effective. The sensitivity and accuracy of the measurements depend on the variation of the surface stress and potential with the parameters to be measured. Further studies should be undertaken to determine the extent of these variations.

Appendix A

Plots

A.1 Current-Forced Fields

A.1.1 Numerical Results

This section presents the results for the current forced case (case one) presented in Chapter 4. The results are presented as plots of non-dimensional transform variables, as before. First the current density magnitudes are presented (*cf.* equations 4.5) *versus* depth, z, and wavelength, λ. Then the magnitudes and phases of the fields are presented for the parameter values:

1. $\lambda = 10\ mm, f = 10^{-3}$ to $0.1\ Hz$ logarithmically,
2. $\lambda = 1\ mm, f = 10^{-3}$ to $0.1\ Hz$ logarithmically,
3. $\lambda = 0.1\ mm, f = 10^{-3}$ to $0.1\ Hz$ logarithmically,
4. $f = 10^{-3}\ Hz, \lambda = 0.1$ to $10\ mm$ logarithmically,

and

5. $f = 0.1\ Hz, \lambda = 0.1$ to $10\ mm$ logarithmically.

The magnitude and phase of the fields are presented in the order u_y (horizontal displacement), u_z (vertical displacement), V_y (horizontal relative velocity), V_z (vertical relative velocity), p (pressure), ϕ (potential), and (for some cases) $|j_y|$ and $|j_z|$ (current densities). Field magnitudes may be obtained from Table 4.1, and the ranges of arguments (complex phases) are listed in the captions. The arguments have been linearized (in z) whenever there was an apparent discontinuity due to numerical error in the vicinity of a relatively small field magnitude. The phases were linearized whenever the difference in the phases at two consecutive grid points (in z) exceeded a specified tolerance. The tolerance was chosen by eye using the overall smoothness and integrity of the data as criteria.

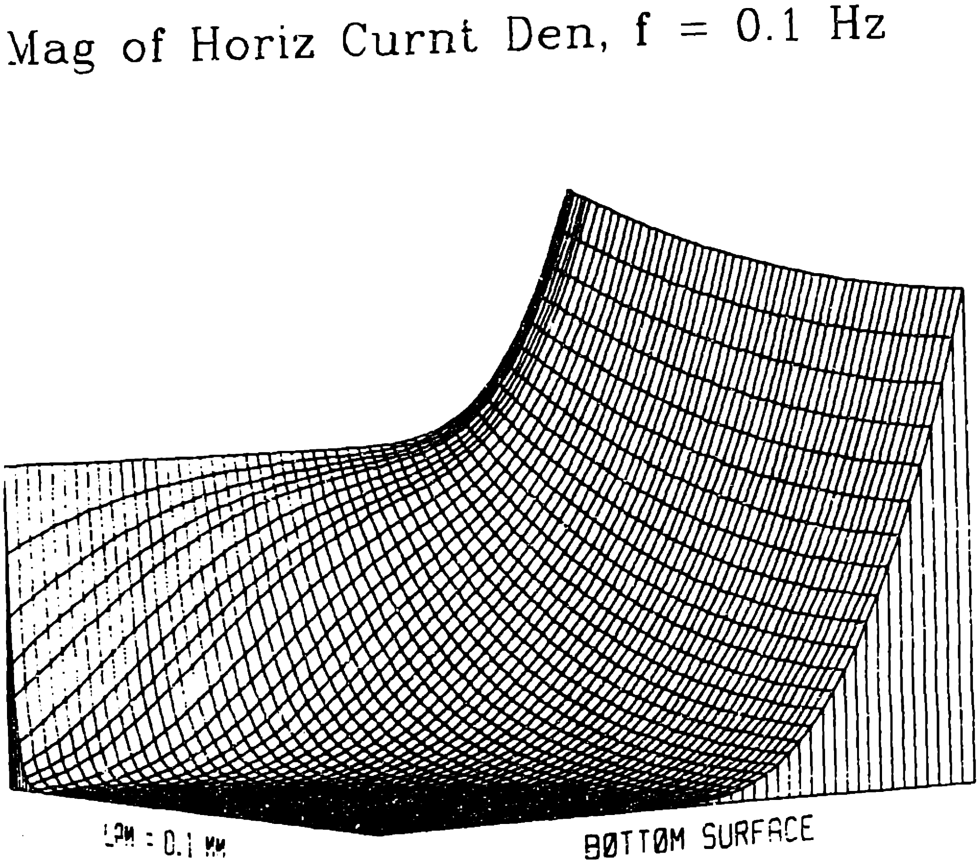

$|j_y|$, $\lambda = 0.1$ to 10.0 mm logarithmically. $|j_y|$ is independent of f. The maximum depicted value of $|j_y|$ is 1.80.

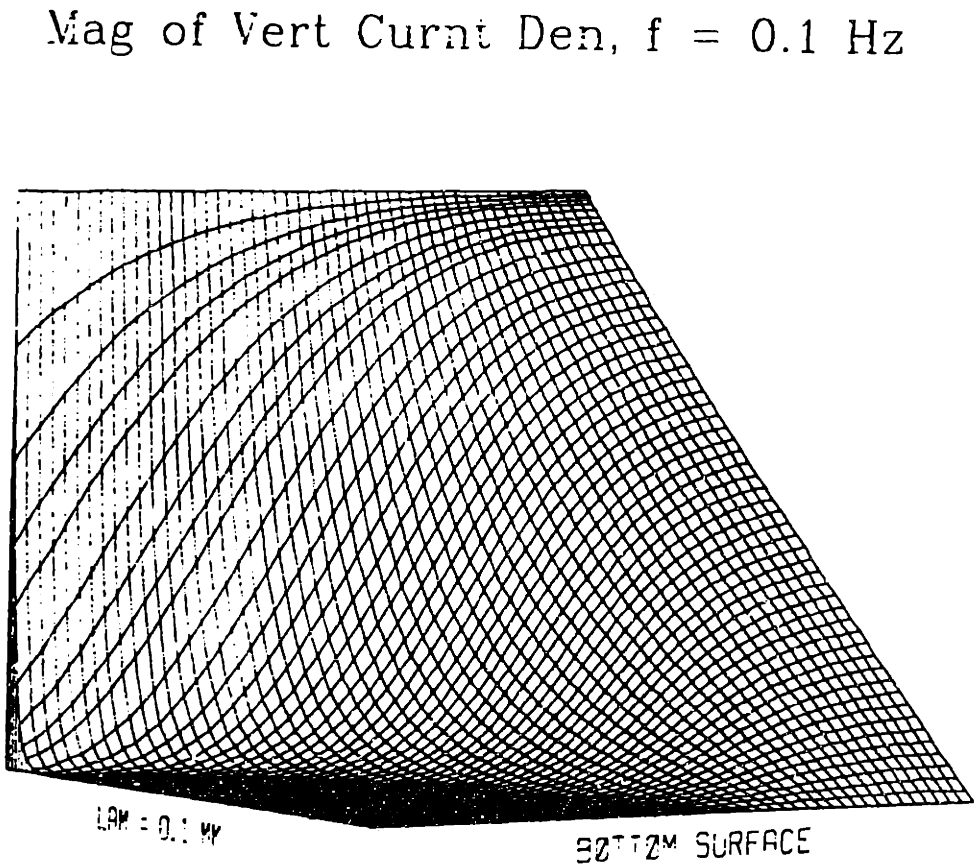

Mag of Vert Curnt Den, f = 0.1 Hz

$|j_z|$, $\lambda = 0.1$ to 10.0 *mm* logarithmically. $|j_z|$ is independent of f. The maximum depicted value of $|j_z|$ is 1 (*cf.* equations 4.1).

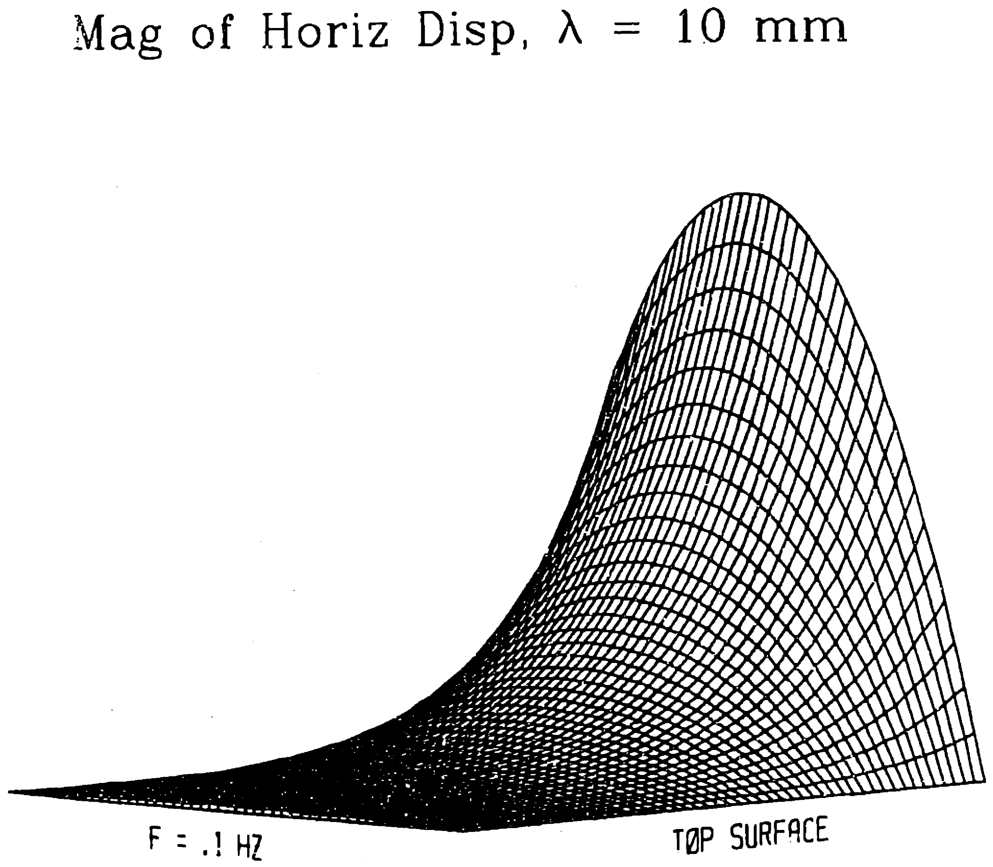

$|u_y|$, $\lambda = 10\ mm$, $f = 10^{-3}$ to 0.1 Hz logarithmically.

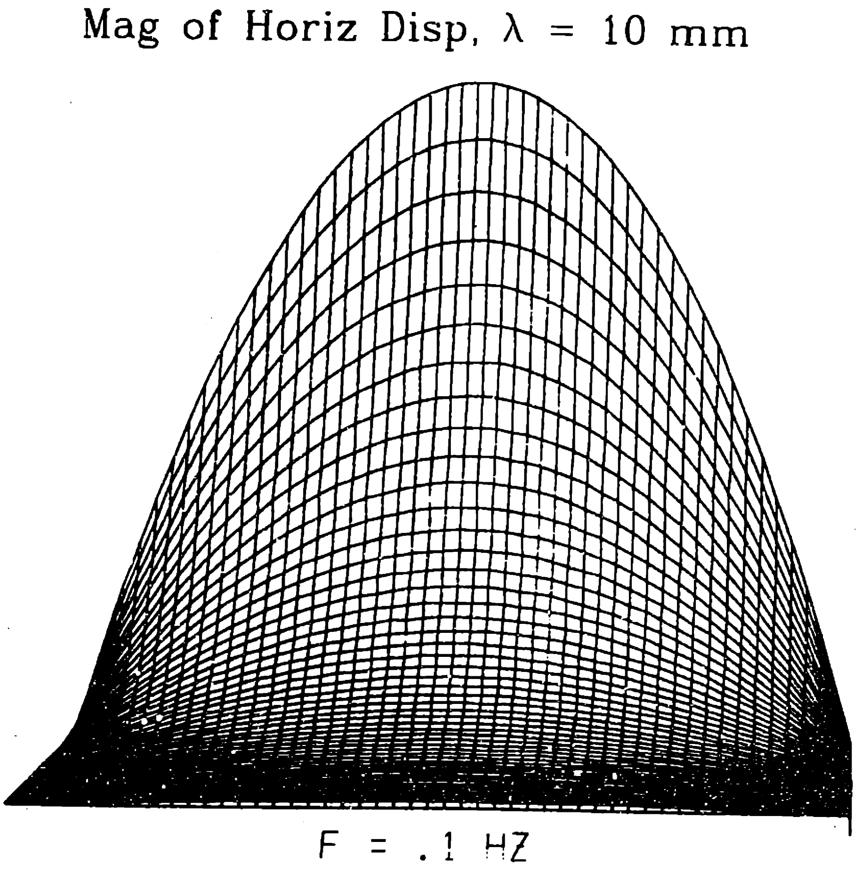

$|u_y|$, $\lambda = 10\,mm$, $f = 10^{-3}$ to 0.1 Hz logarithmically.

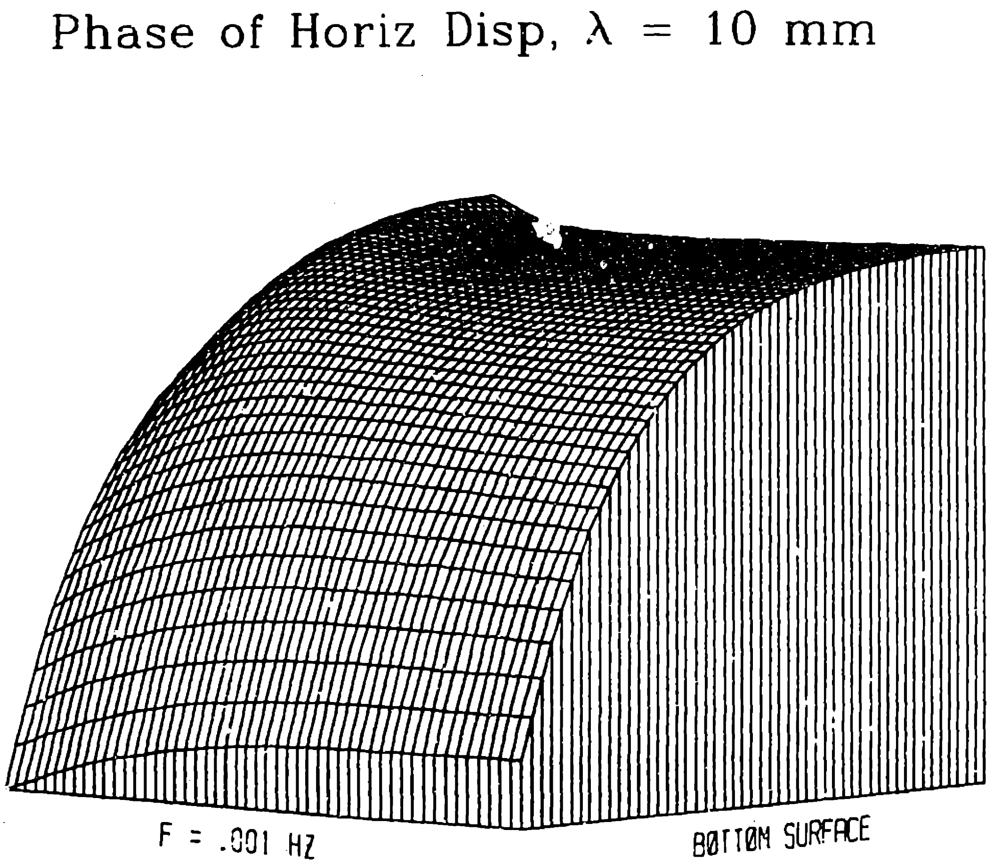

$-0.170 < \arg u_y < 1.08 \cdot 10^{-2}$; $\lambda = 10\ mm$, $f = 10^{-3}$ to 0.1 Hz logarithmically.

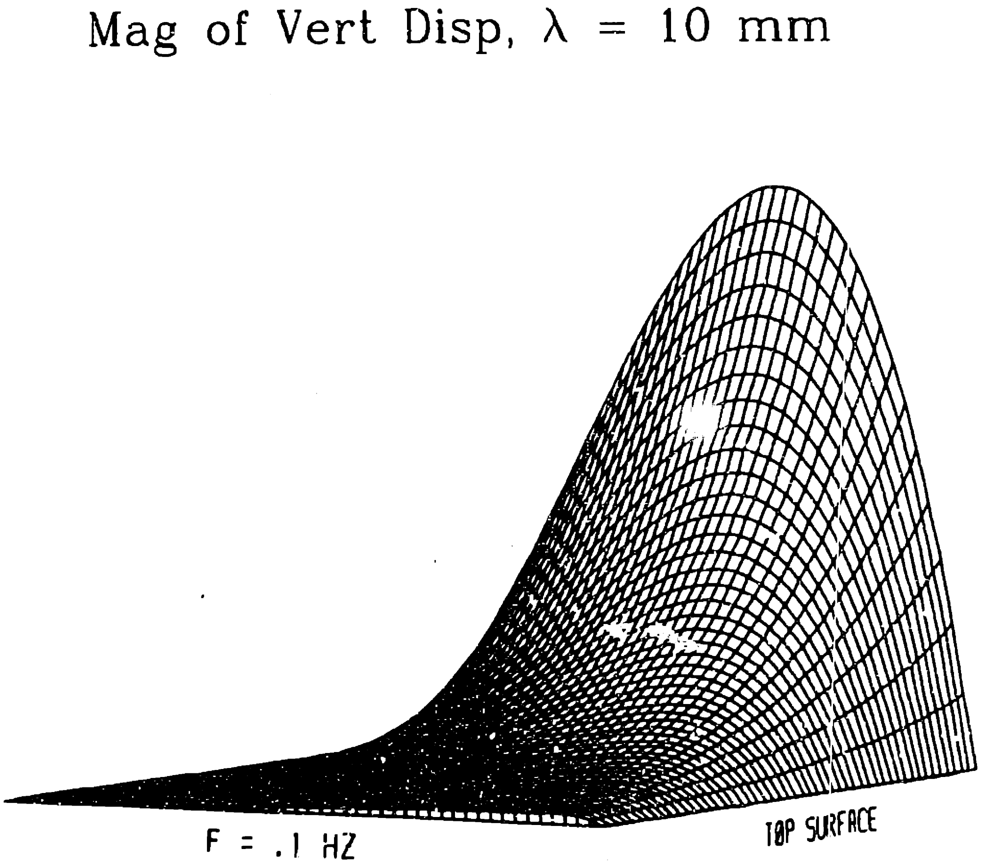

$|u_z|$, $\lambda = 10\,mm$, $f = 10^{-3}$ to 0.1 Hz logarithmically.

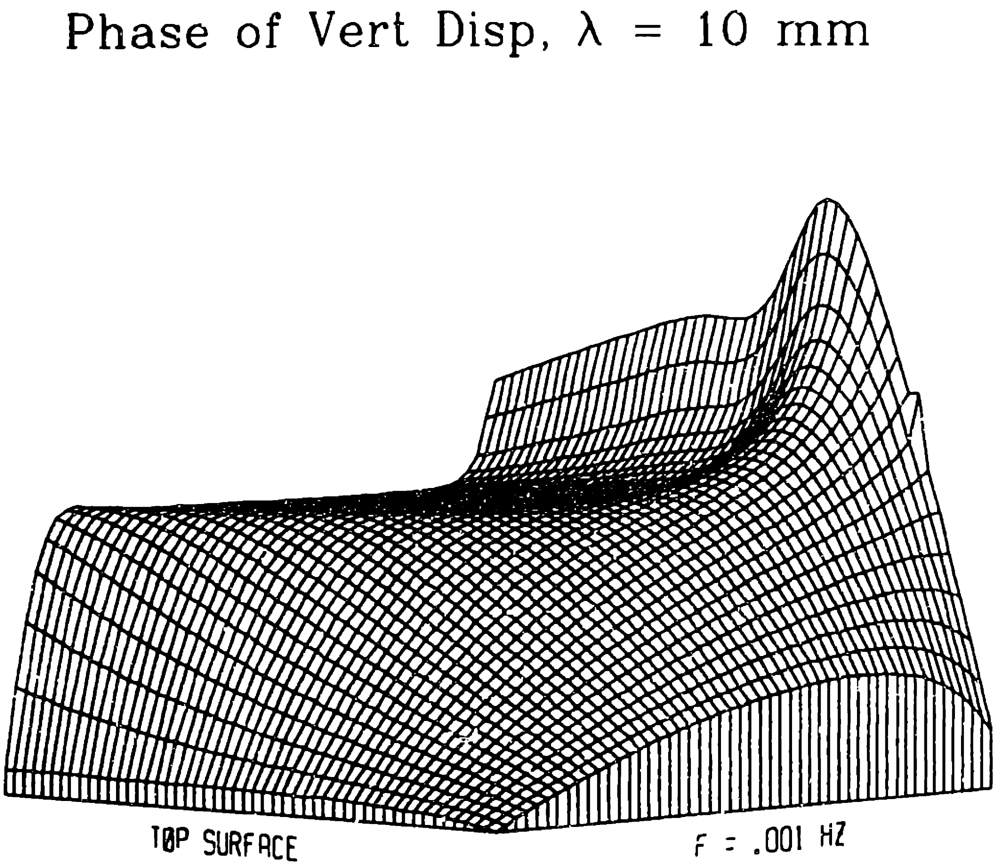

$-2.43 < \arg u_z < -0.614$, $\lambda = 10\ mm$, $f = 10^{-3}$ to 0.1 Hz logarithmically.

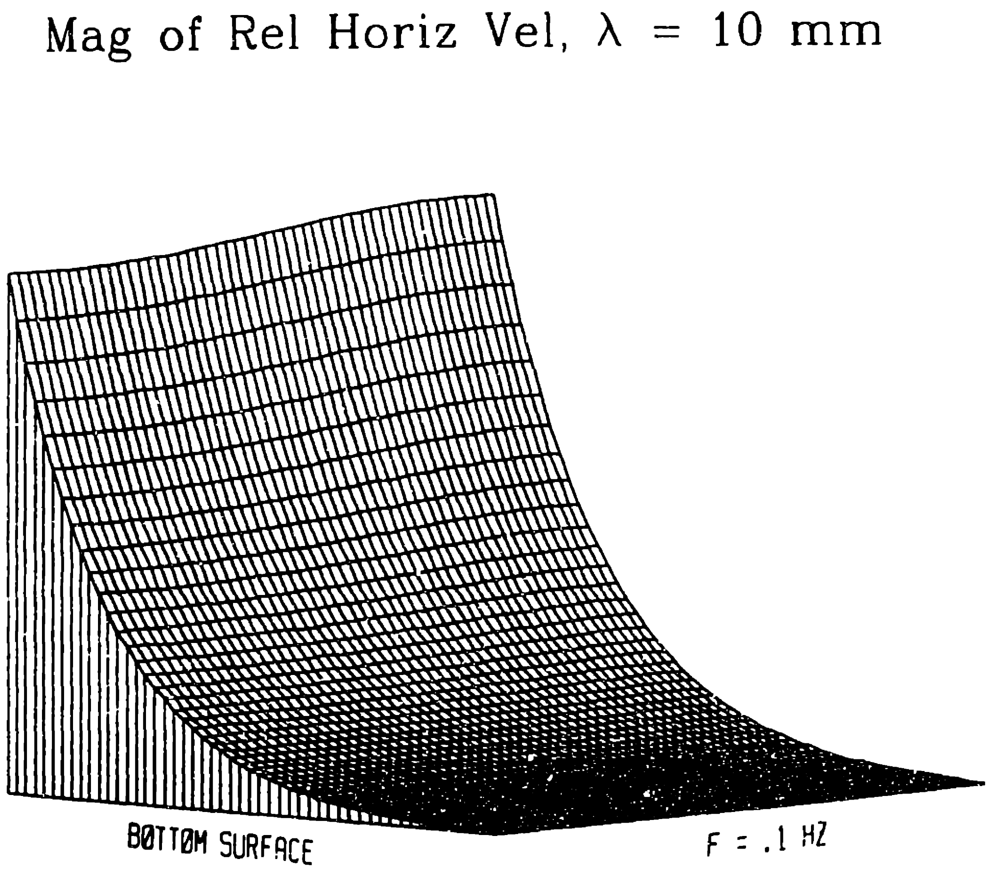

$|V_y^*/\omega a_J|$, $\lambda = 10\ mm$, $f = 10^{-3}$ to 0.1 Hz logarithmically.

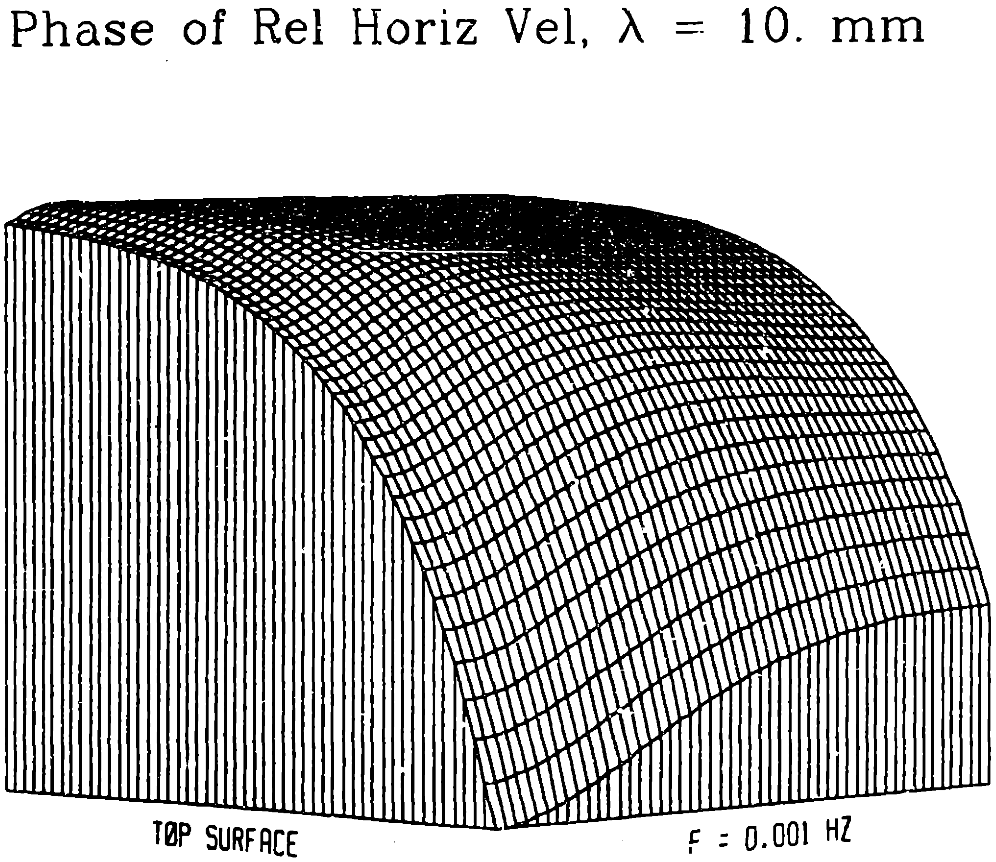

$1.38 < \arg V_y < 1.57$, $\lambda = 10\ mm$, $f = 10^{-3}$ to 0.1 Hz logarithmically.

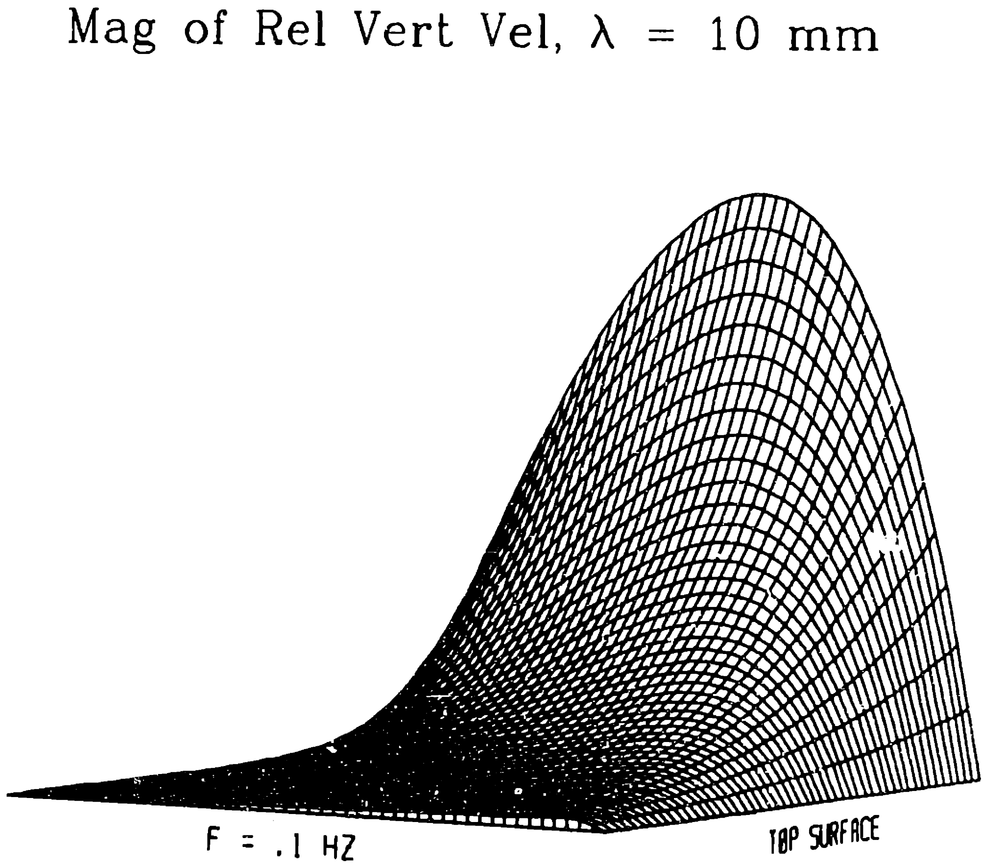

$|V_z^*/\omega a_J|$, $\lambda = 10\ mm, f = 10^{-3}$ to 0.1 Hz logarithmically.

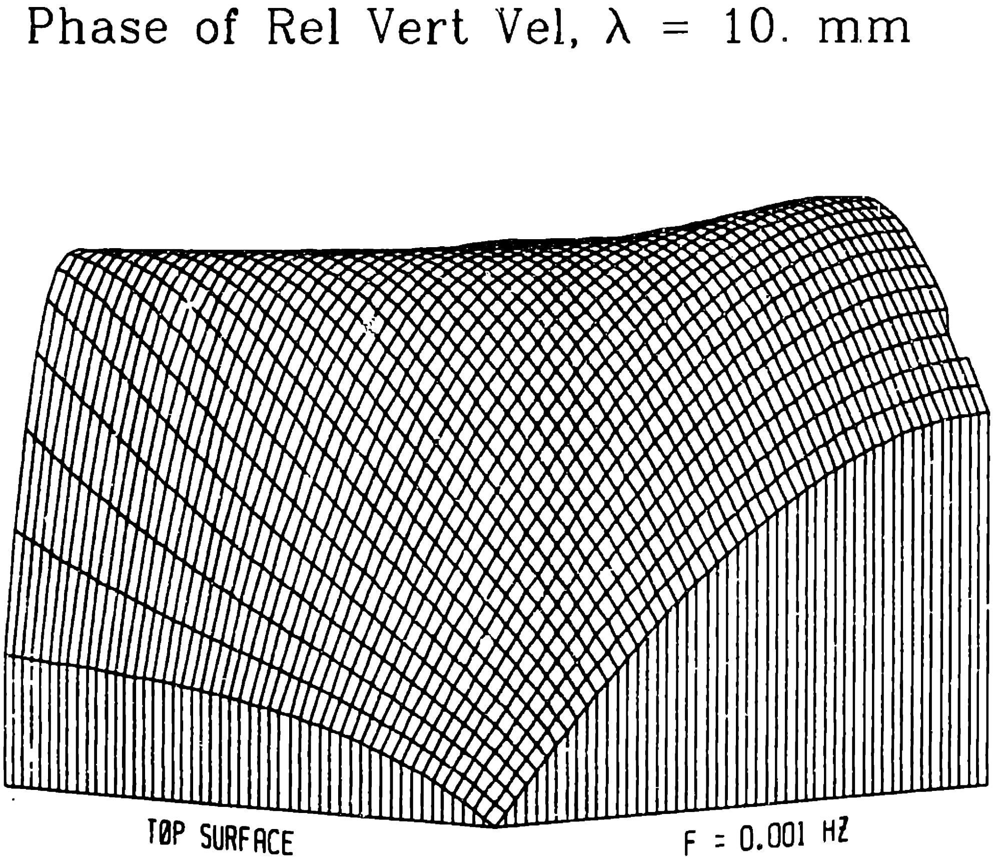

$-1.07 < \arg V_z < 0.122$, $\lambda = 10$ *mm*, $f = 10^{-3}$ to 0.1 *Hz* logarithmically.

Mag of Pressure, λ = 10 mm

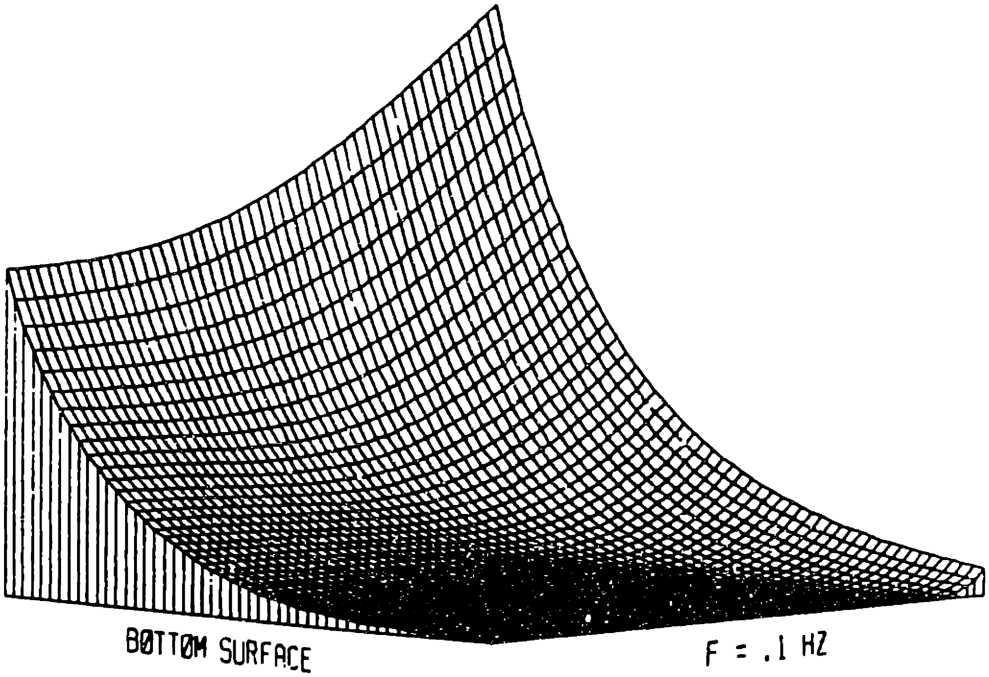

$|p|$, $\lambda = 10\ mm$, $f = 10^{-3}$ to 0.1 Hz logarithmically.

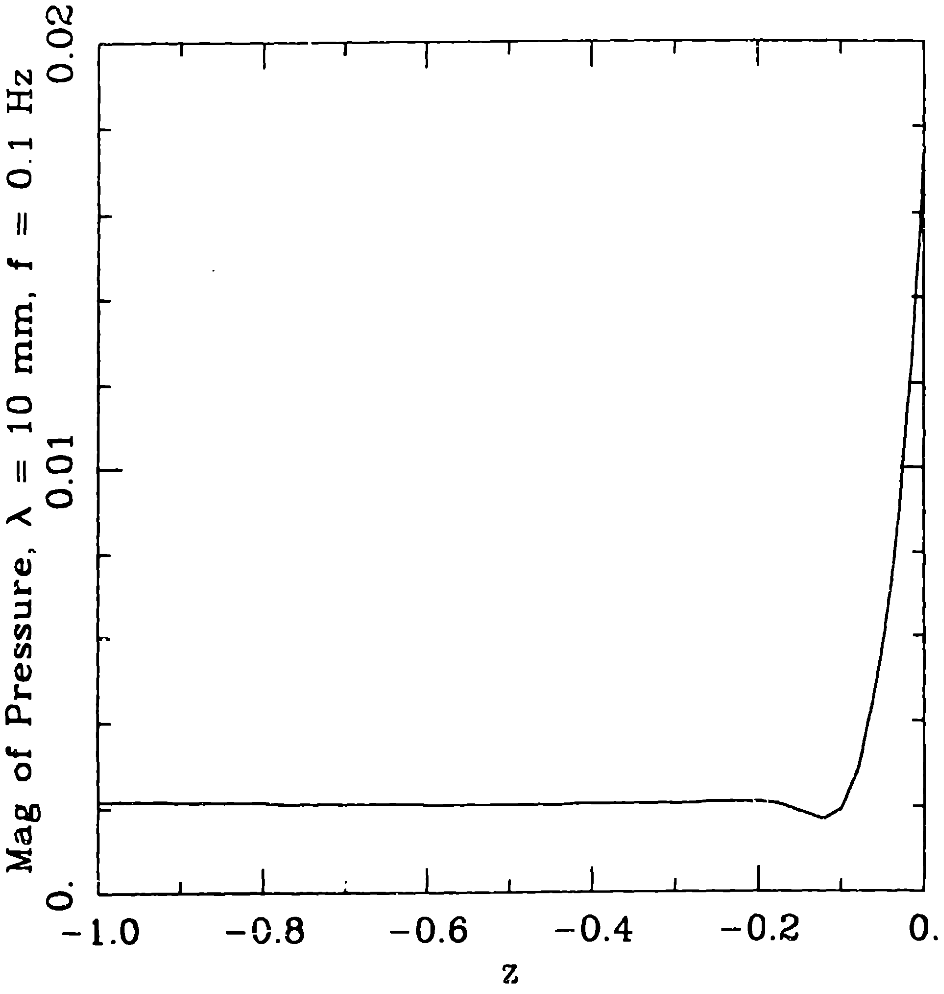

$|p|$, $\lambda = 10\ mm$, $f = 0.1\ Hz$.

Phase of Pressure, λ = 10 mm

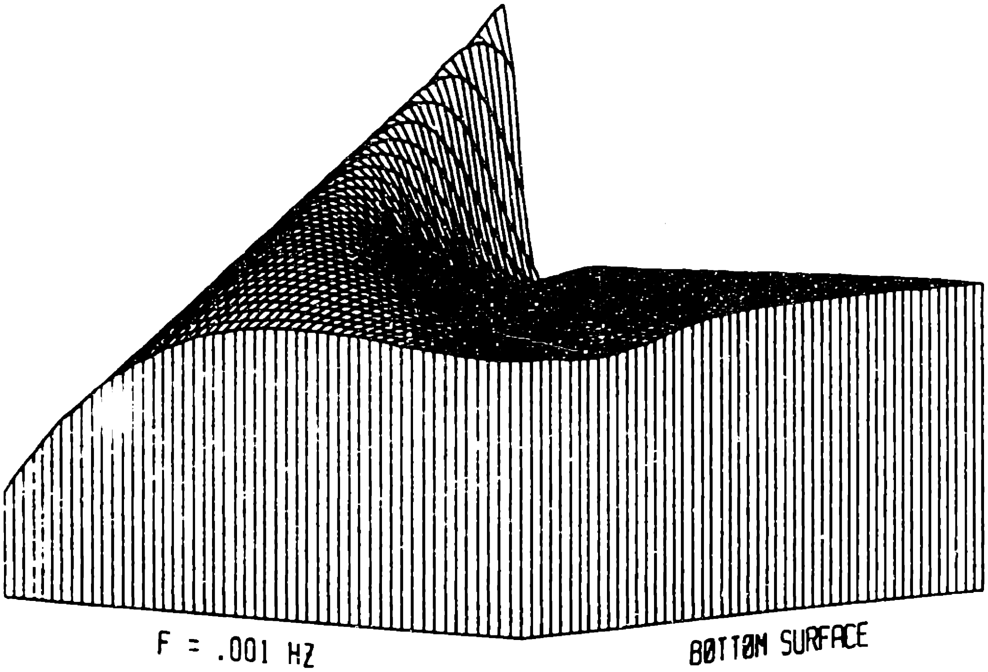

$0.873 < \arg p < 2.17$, $\lambda = 10\ mm$, $f = 10^{-3}$ to $0.1\ Hz$ logarithmically.

Phase of Pressure, λ = 10 mm

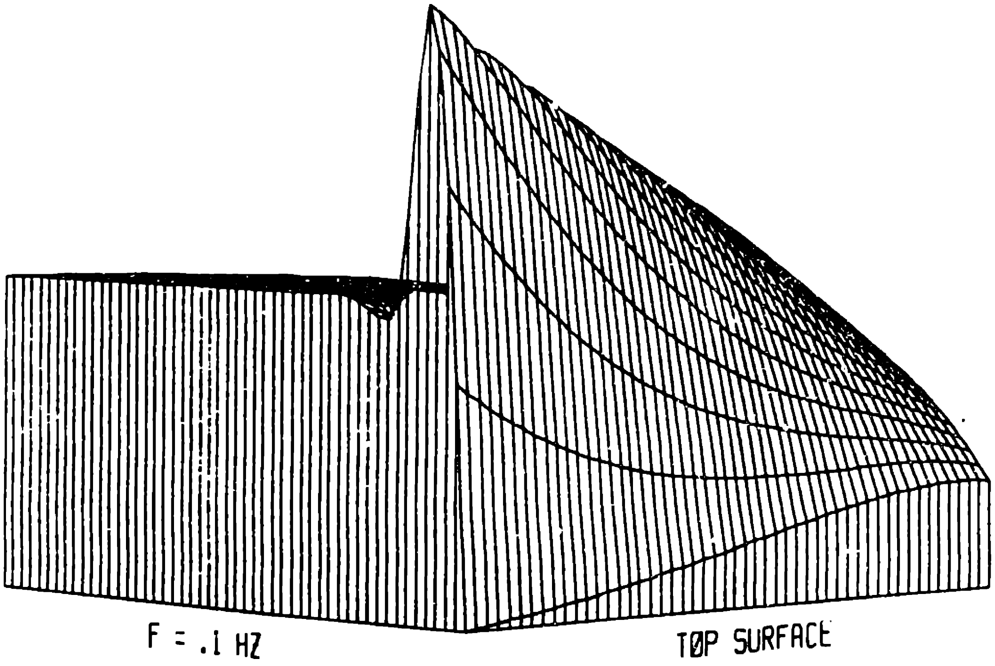

$0.873 < \arg p < 2.17$, $\lambda = 10\ mm$, $f = 10^{-3}$ to 0.1 Hz logarithmically.

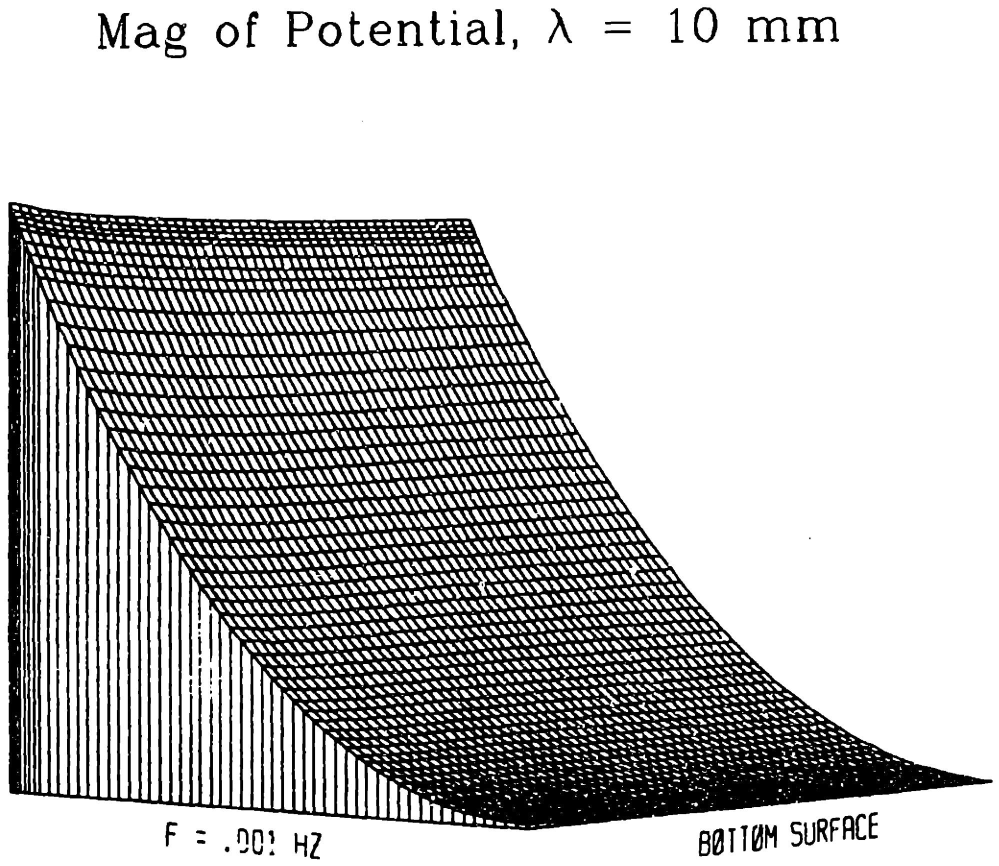

$|\phi|$, $\lambda = 10\ mm, f = 10^{-3}$ to 0.1 Hz logarithmically.

Phase of Potential, $\lambda = 10$ mm

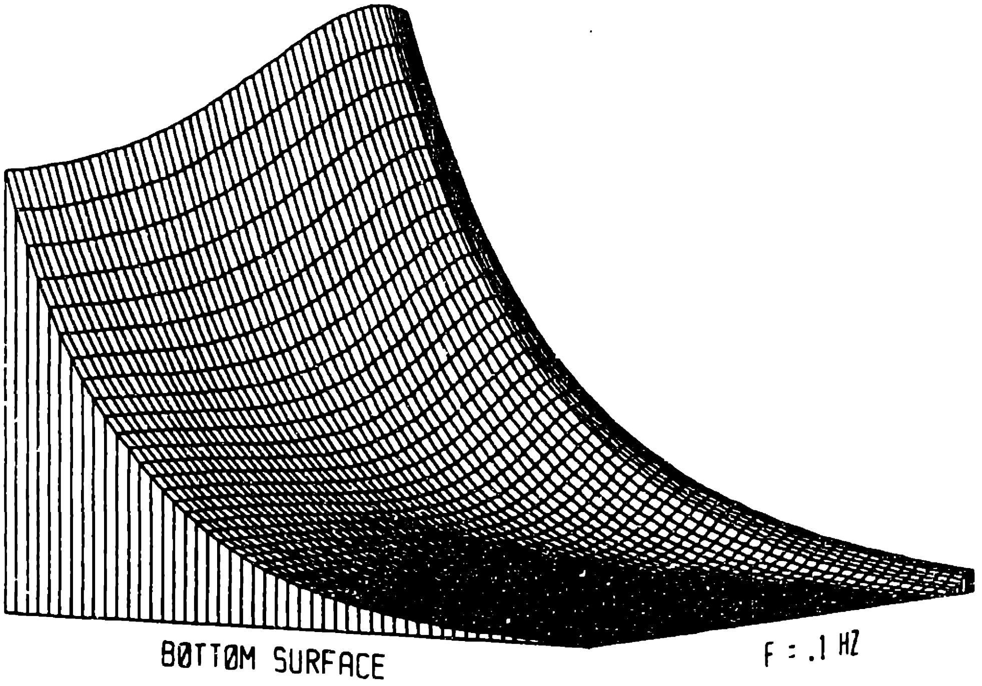

$-3.14 < \arg\phi < -3.12$, $\lambda = 10\ mm$, $f = 10^{-3}$ **to 0.1** Hz **logarithmically.**

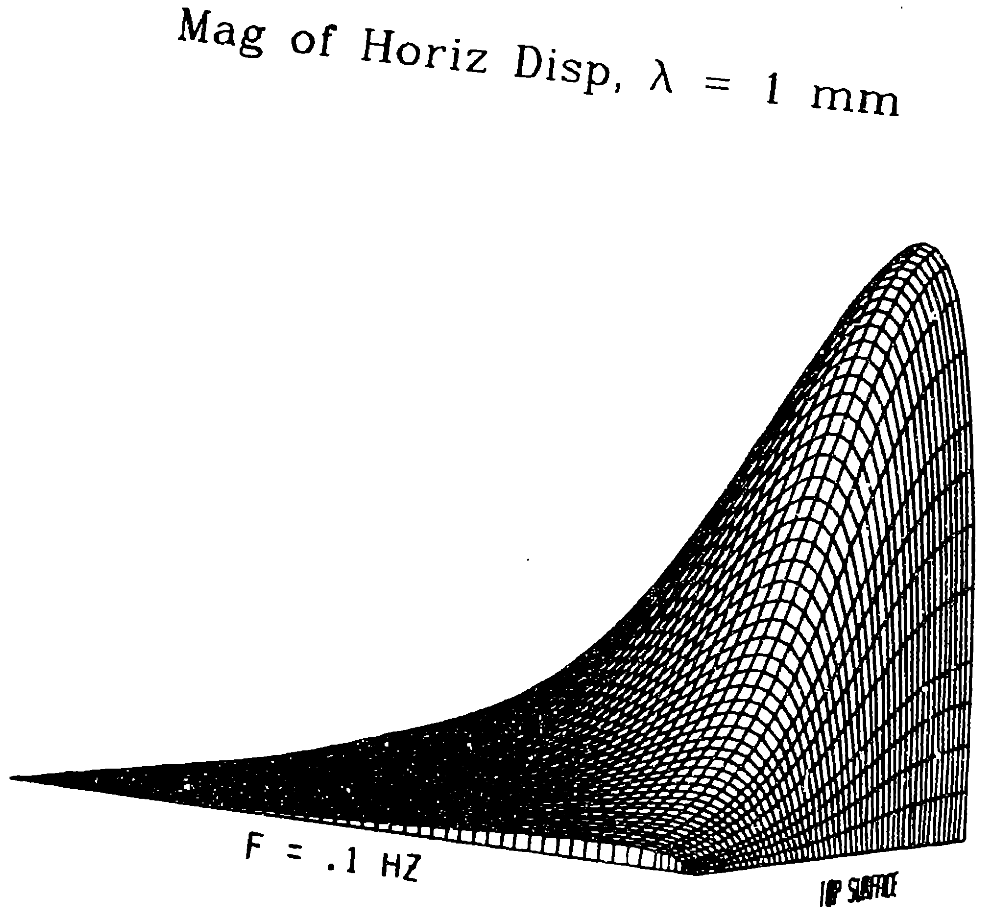

$|u_y|$, $\lambda = 1\ mm$, $f = 10^{-3}$ to 0.1 Hz logarithmically.

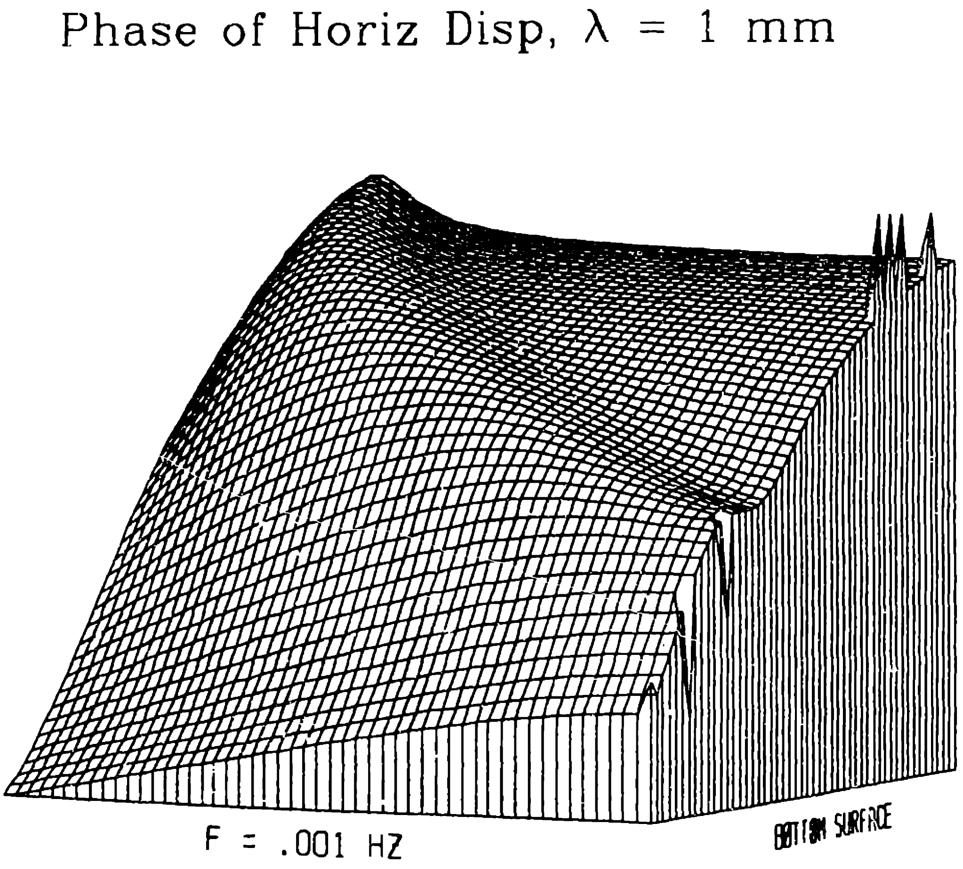

$-1.32 < \arg u_y < 0.0790 \cdot 10^{-2}$, $\lambda = 1\ mm, f = 10^{-3}$ to 0.1 Hz logarithmically.

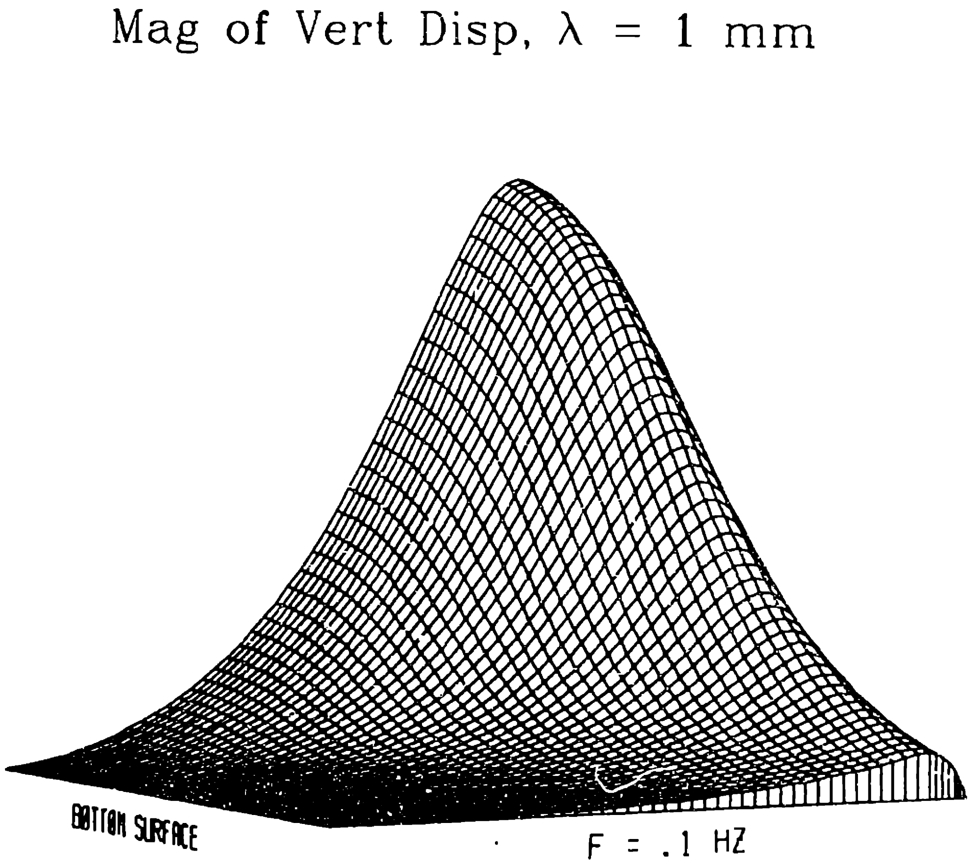

$|u_z|$, $\lambda = 1\ mm, f = 10^{-3}$ to 0.1 Hz logarithmically.

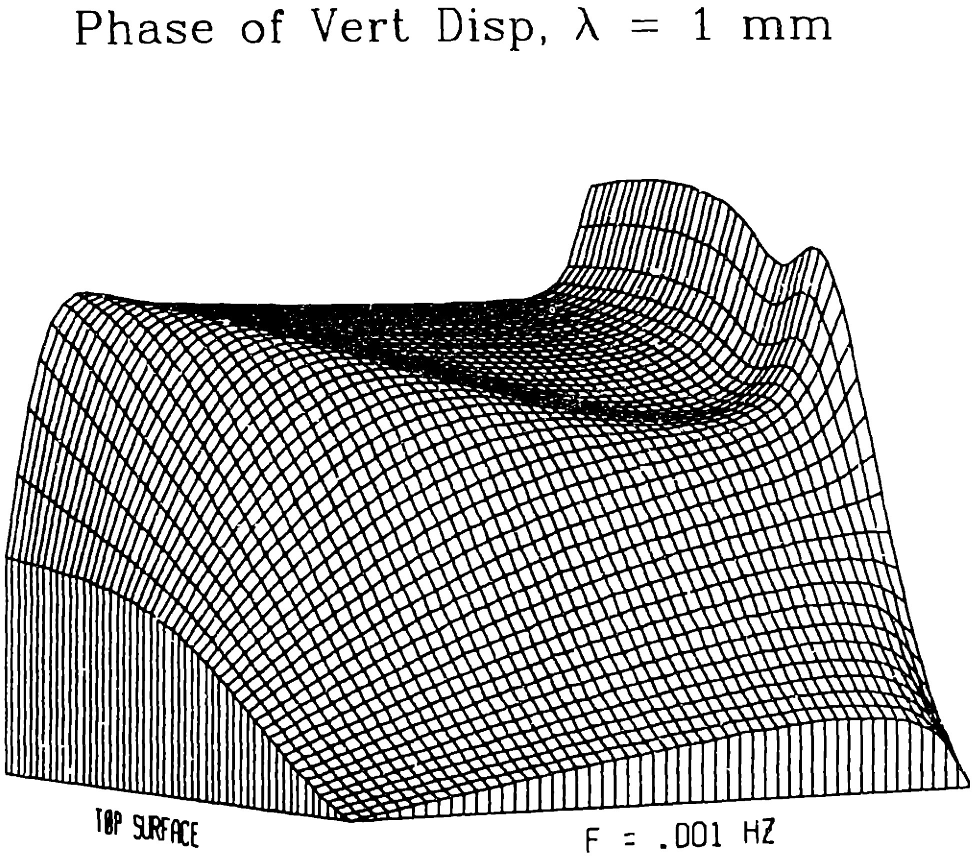

$-2.99 < \arg u_z < -1.31$, $\lambda = 1\ mm$, $f = 10^{-3}$ to $0.1\ Hz$ logarithmically.

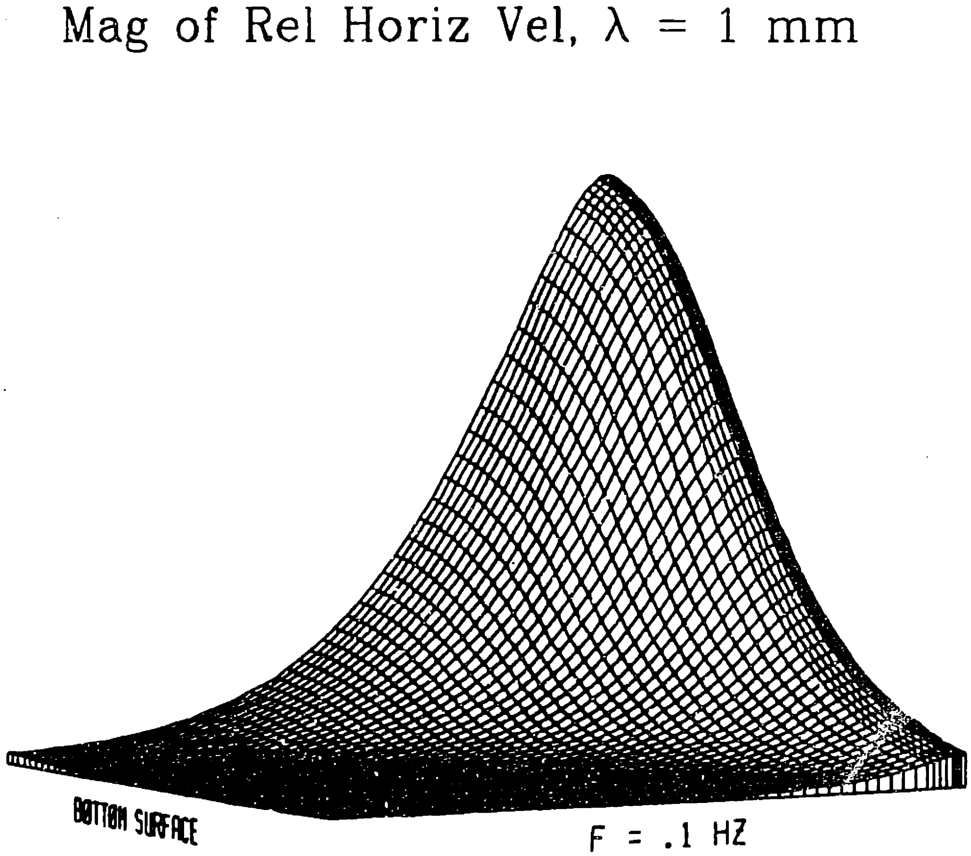

$|V_y^*/\omega a_J|$, $\lambda = 1\ mm, f = 10^{-3}$ to 0.1 Hz logarithmically.

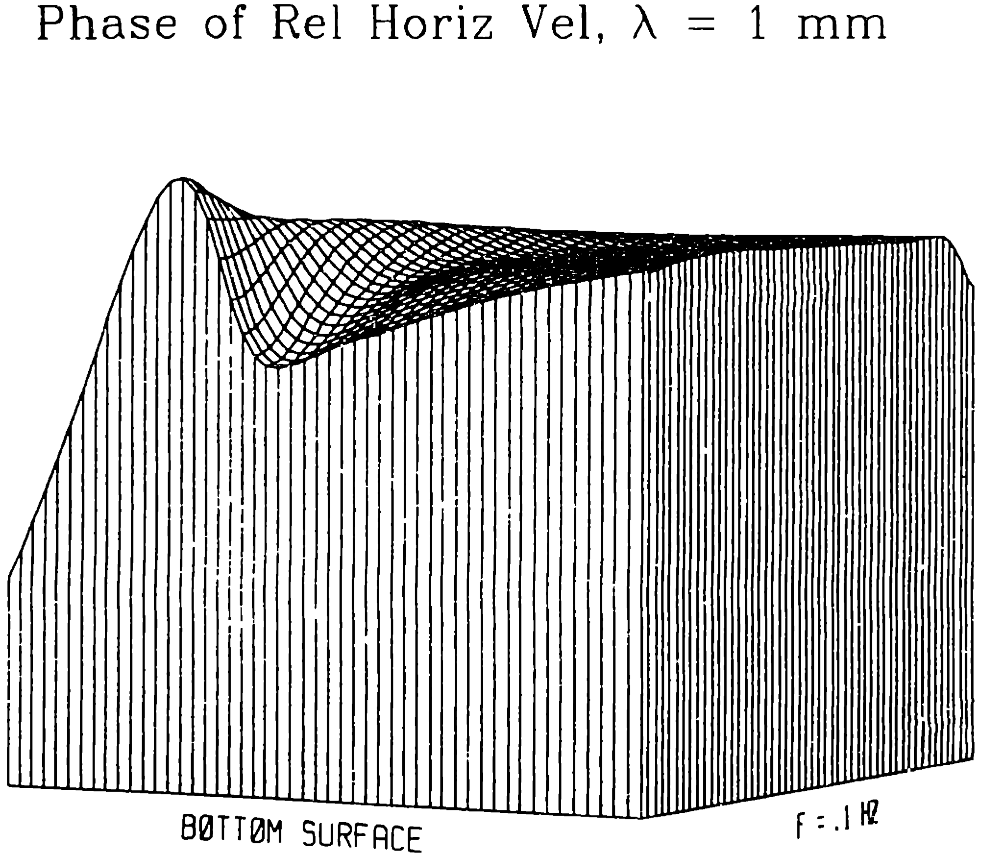

$0.247 < \arg V_y < 1.73$, $\lambda = 1$ mm, $f = 10^{-3}$ to 0.1 Hz logarithmically.

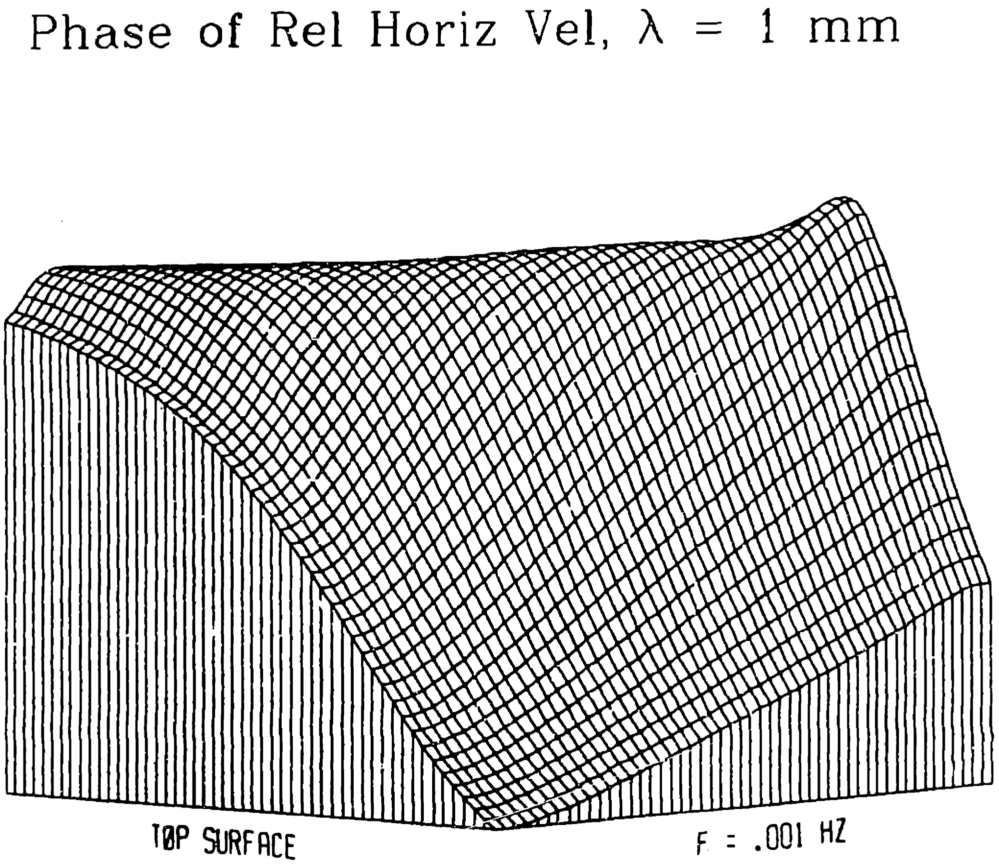

$0.247 < \arg V_y < 1.73$, $\lambda = 1\ mm$, $f = 10^{-3}$ to 0.1 Hz logarithmically.

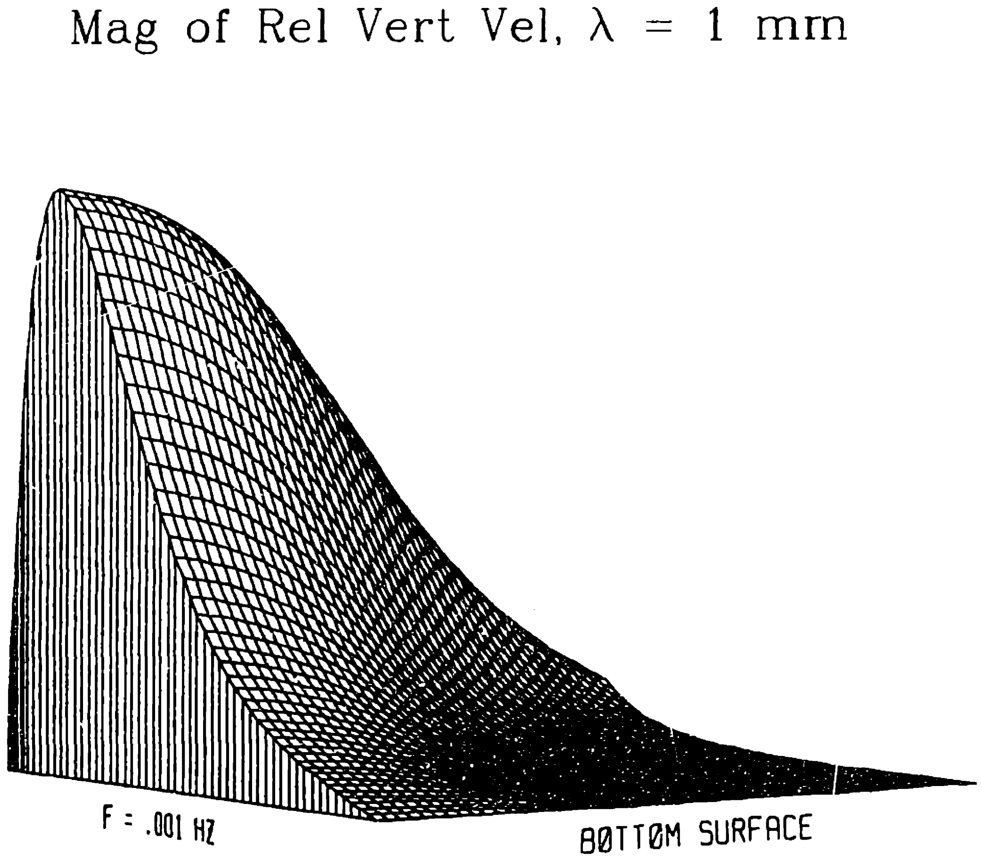

$|V_z^*/\omega a_J|$, $\lambda = 1\ mm, f = 10^{-3}$ to 0.1 Hz logarithmically.

Phase of Rel Vert Vel, $\lambda = 1$ mm

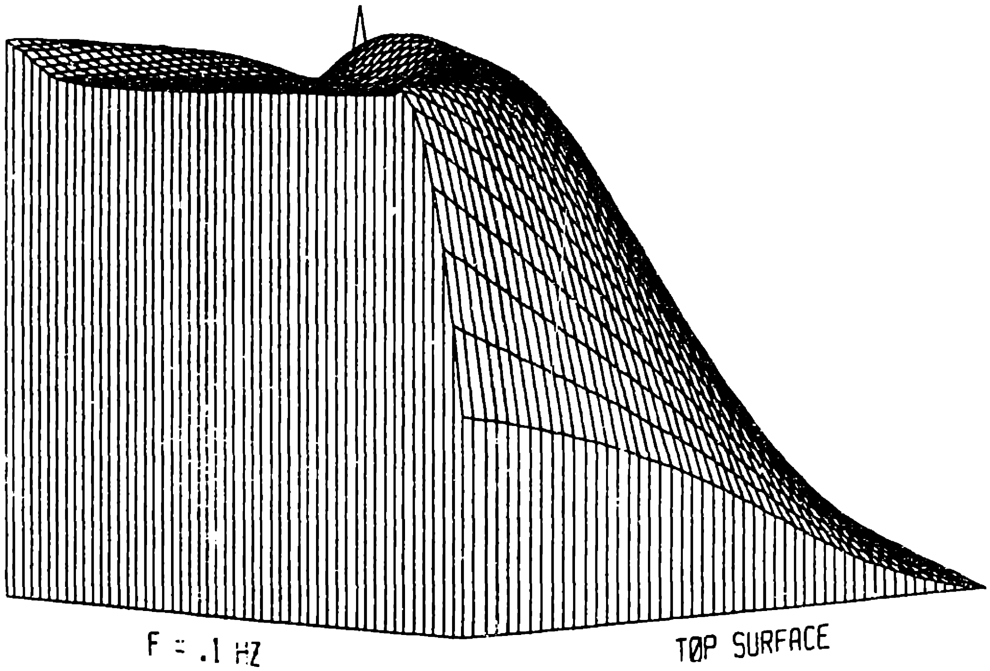

$-1.51 < \arg V_z < 0.218$, $\lambda = 1\ mm$, $f = 10^{-3}$ to $0.1\ Hz$ logarithmically.

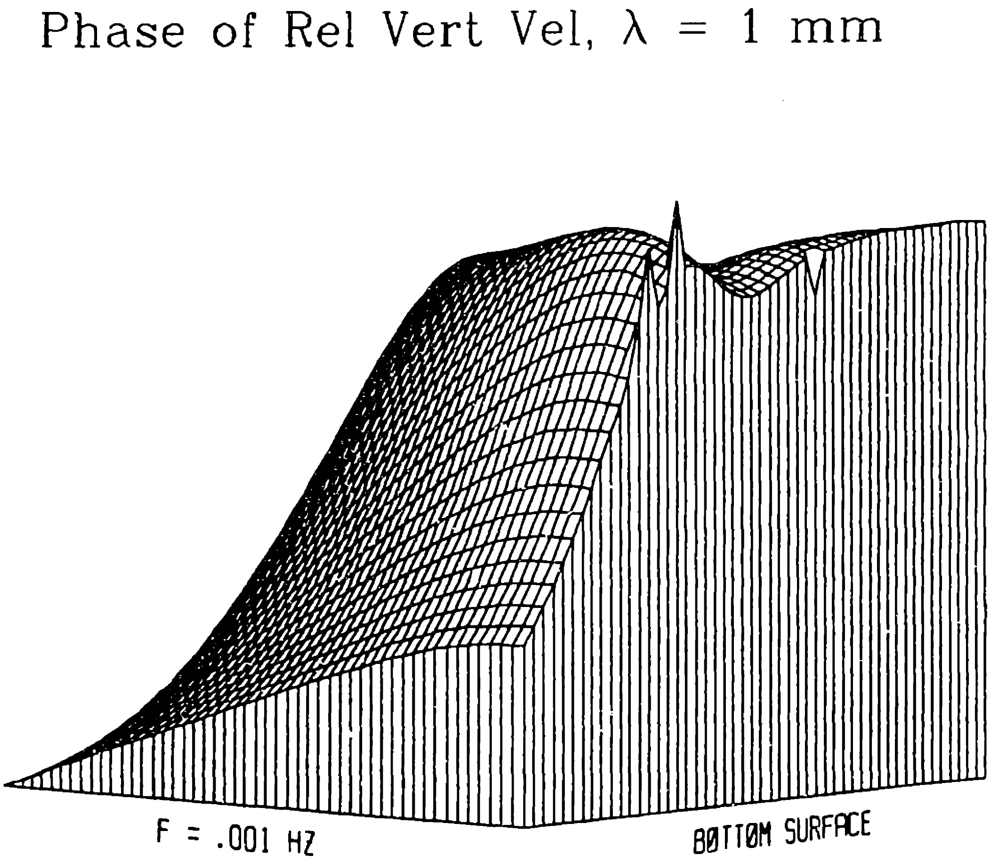

$-1.51 < \arg V_z < 0.218$, $\lambda = 1\ mm, f = 10^{-3}$ to 0.1 Hz logarithmically.

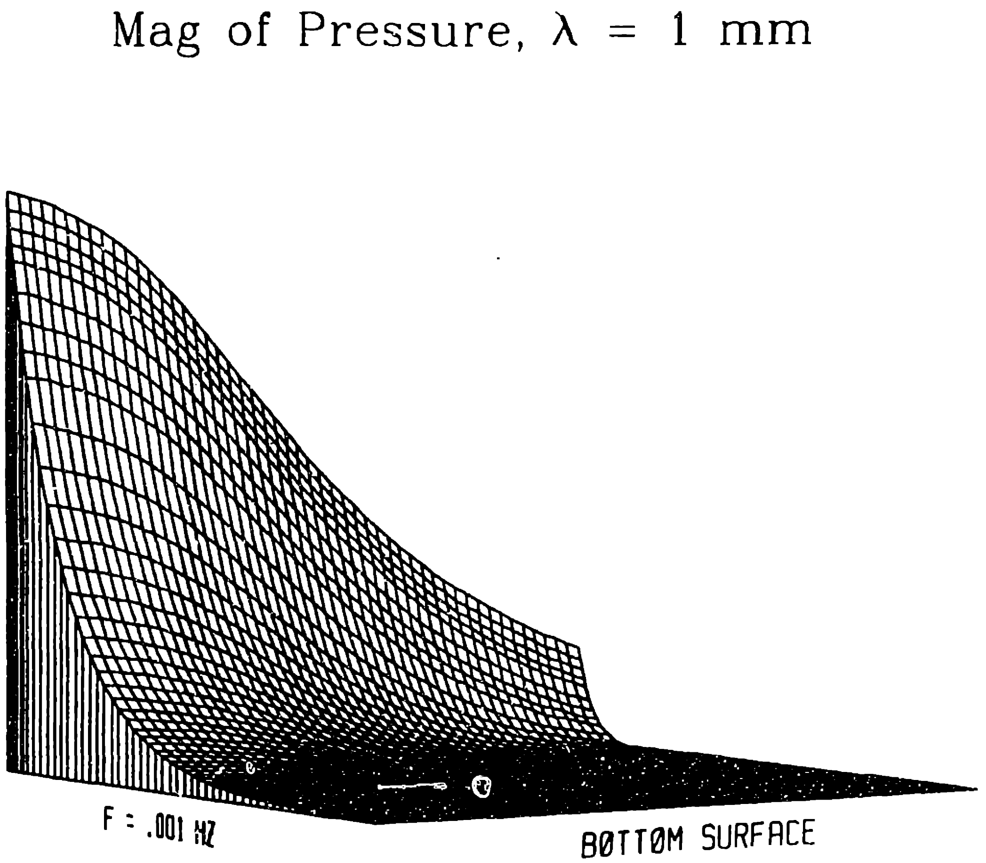

$|p|$, $\lambda = 1\ mm$, $f = 10^{-3}$ to 0.1 Hz logarithmically.

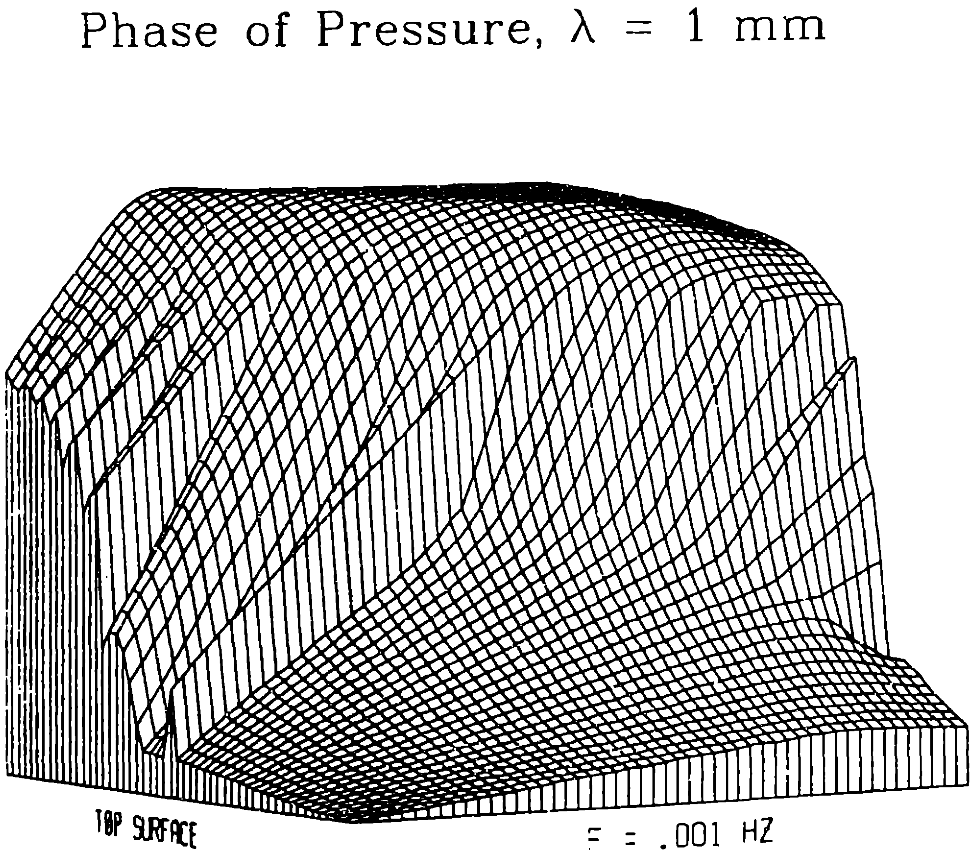

< 7.75, $\lambda = 1\ mm, f = 10^{-3}$ to 0.1 Hz logarithmically.

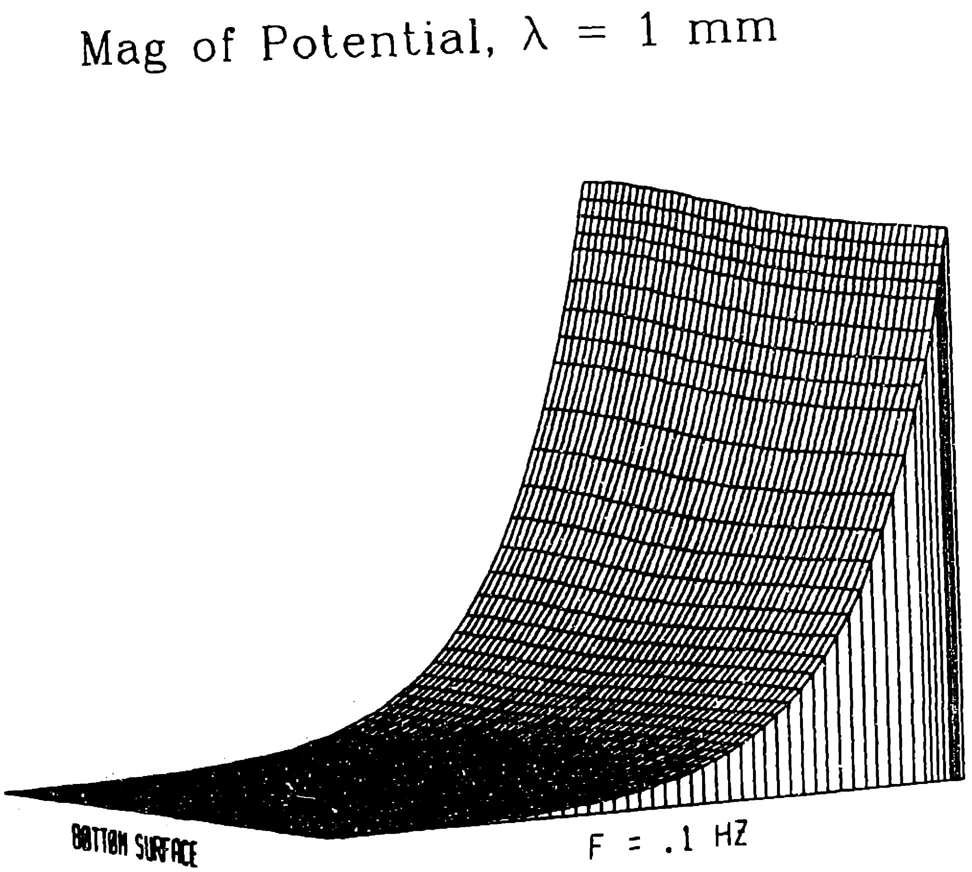

$|\phi|$, $\lambda = 1\ mm$, $f = 10^{-3}$ to 0.1 Hz logarithmically.

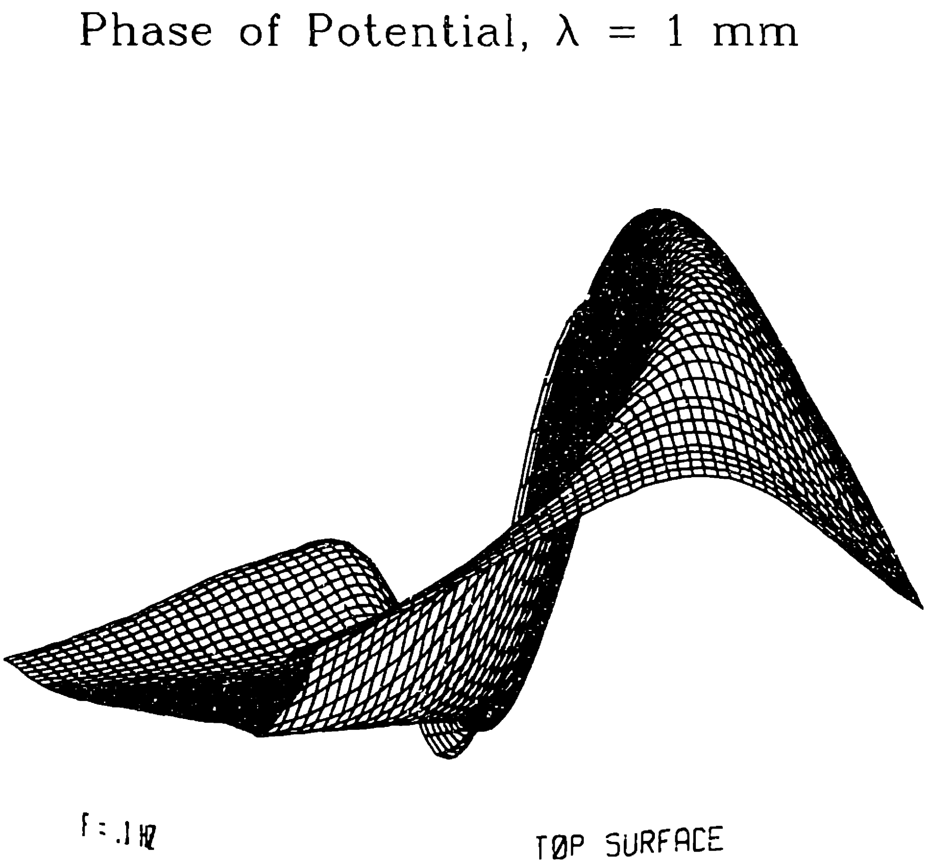

$-3.16 < \arg\phi < -3.065$, $\lambda = 1\ mm$, $f = 10^{-3}$ to 0.1 Hz logarithmically.

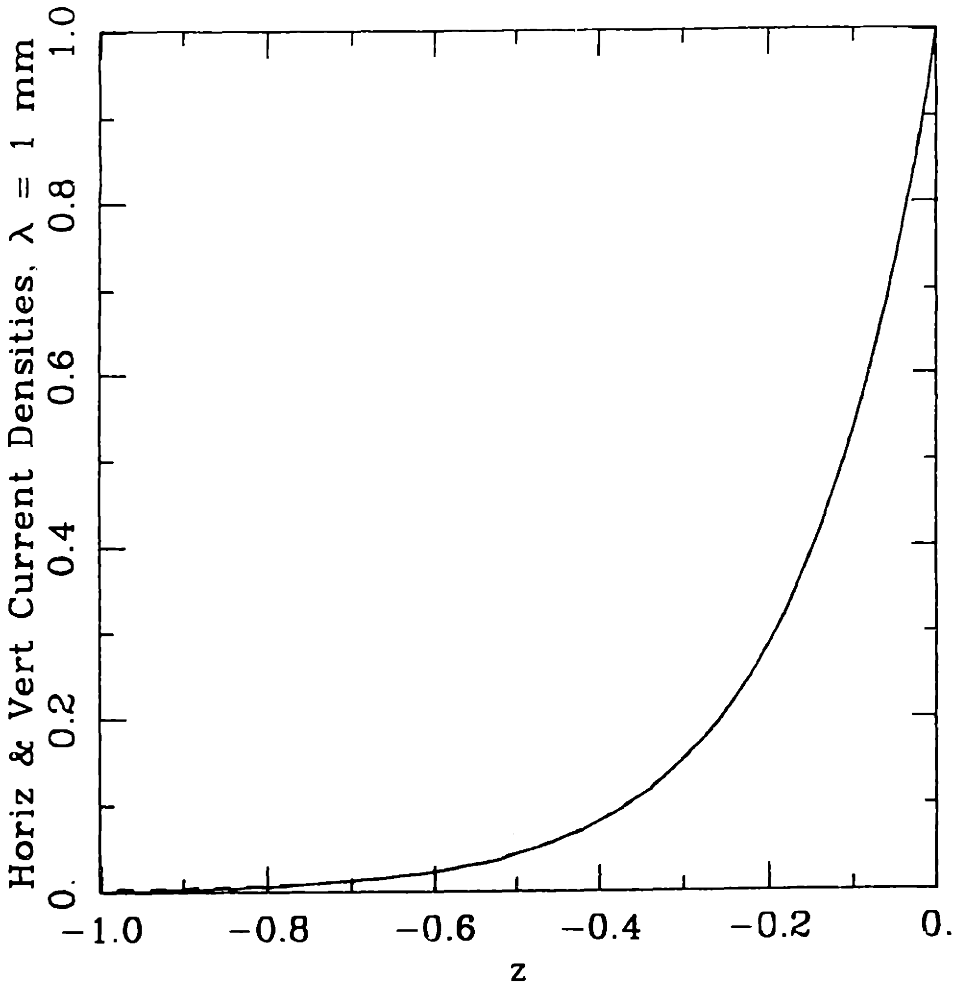

$|j_y|$ and $|j_z|$, $\lambda = 1\ mm$ (**frequency independent**).

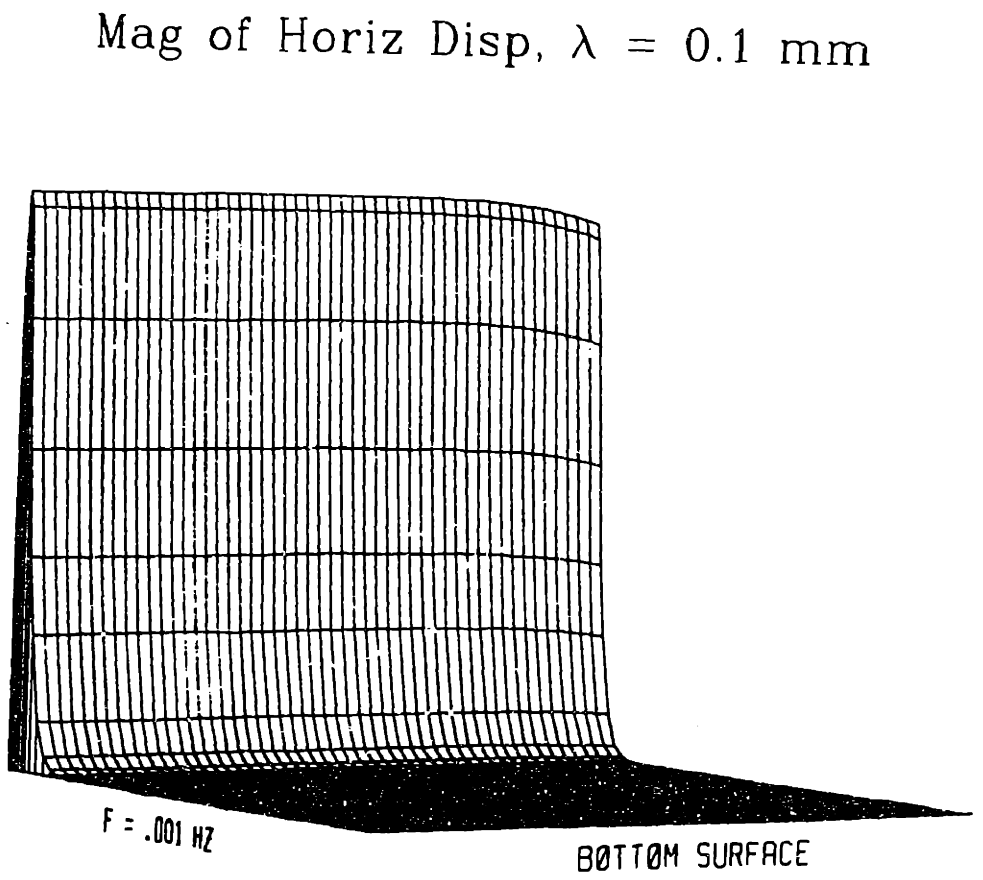
Mag of Horiz Disp, λ = 0.1 mm

$|u_y|$, $\lambda = 0.1\ mm, f = 10^{-3}$ to 0.1 Hz logarithmically. $|u_x|$ and $|V_x^*/\omega a_J|$ look the same.

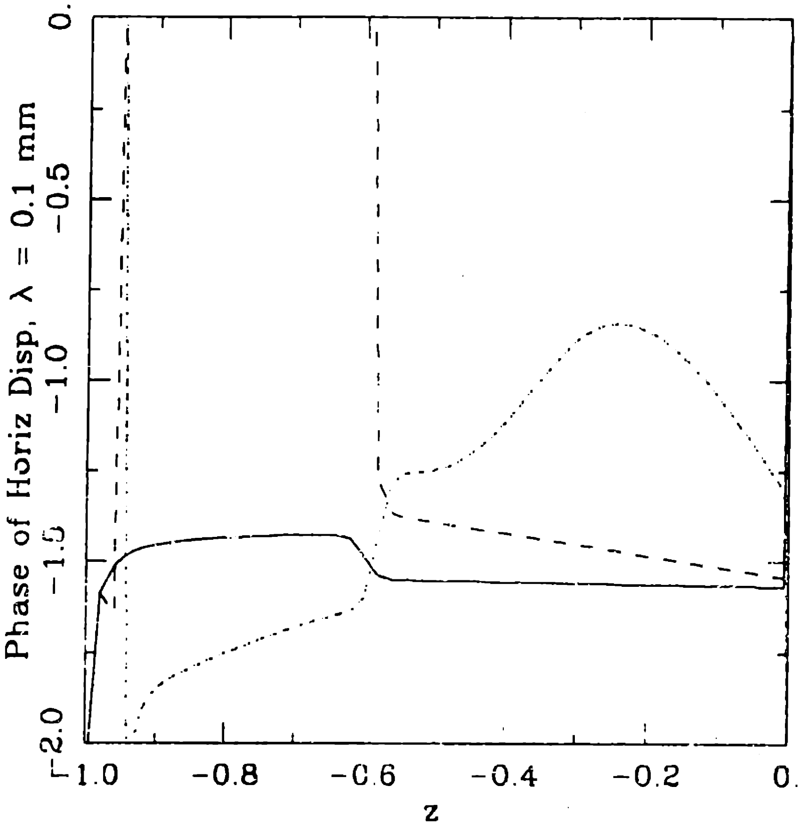

arg u_y, $\lambda = 0.1$ *mm*, $f = 10^{-3}$, $f = 10^{-2}$ (— —), and $f = 0.1$ *Hz* (- - - -).

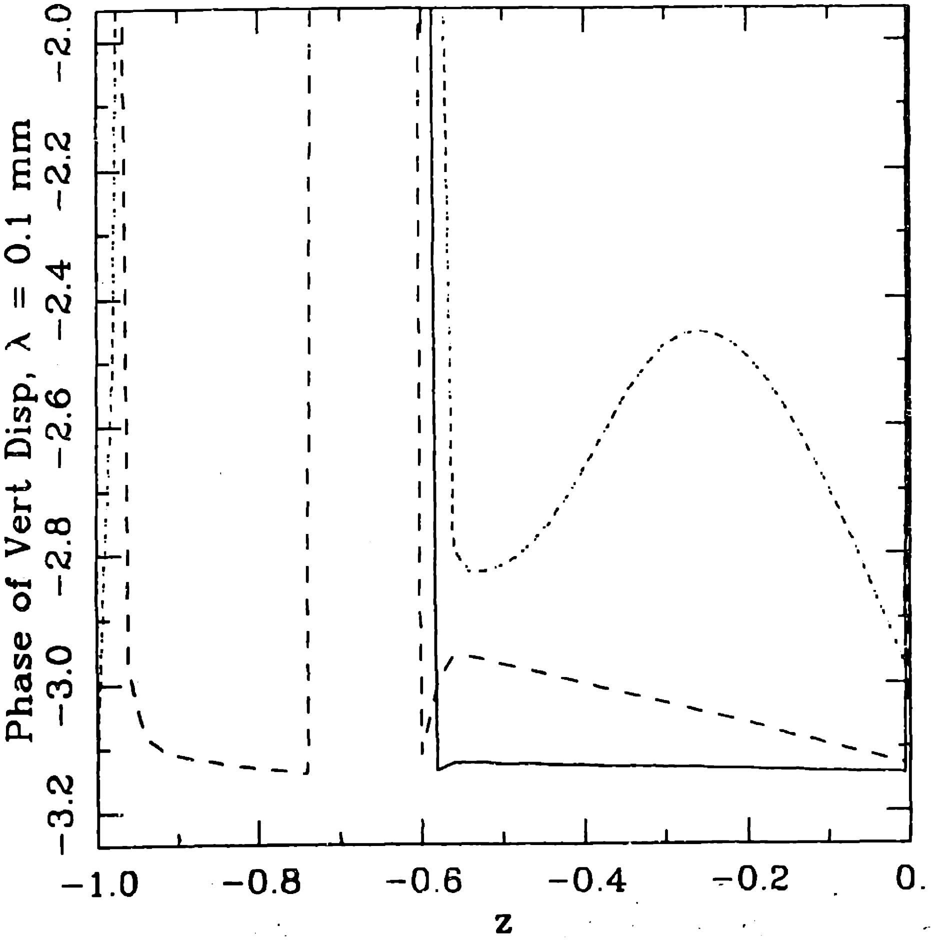

arg u_z, $\lambda = 0.1\ mm, f = 10^{-3}$, $f = 10^{-2}$ (— —), and $f = 0.1\ Hz$ (- - - -).

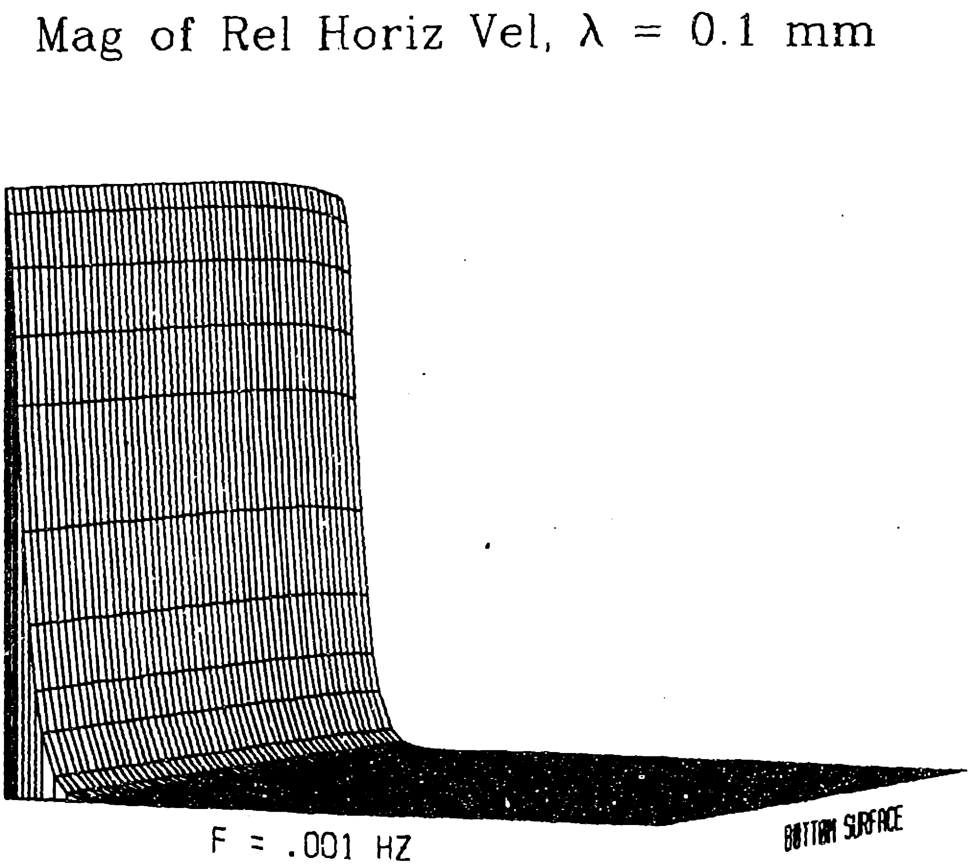

$|V_y^*/\omega a_J|$, $\lambda = 0.1\ mm, f = 10^{-3}$ to 0.1 Hz logarithmically. $|p|$ and $|\phi|$ look the same.

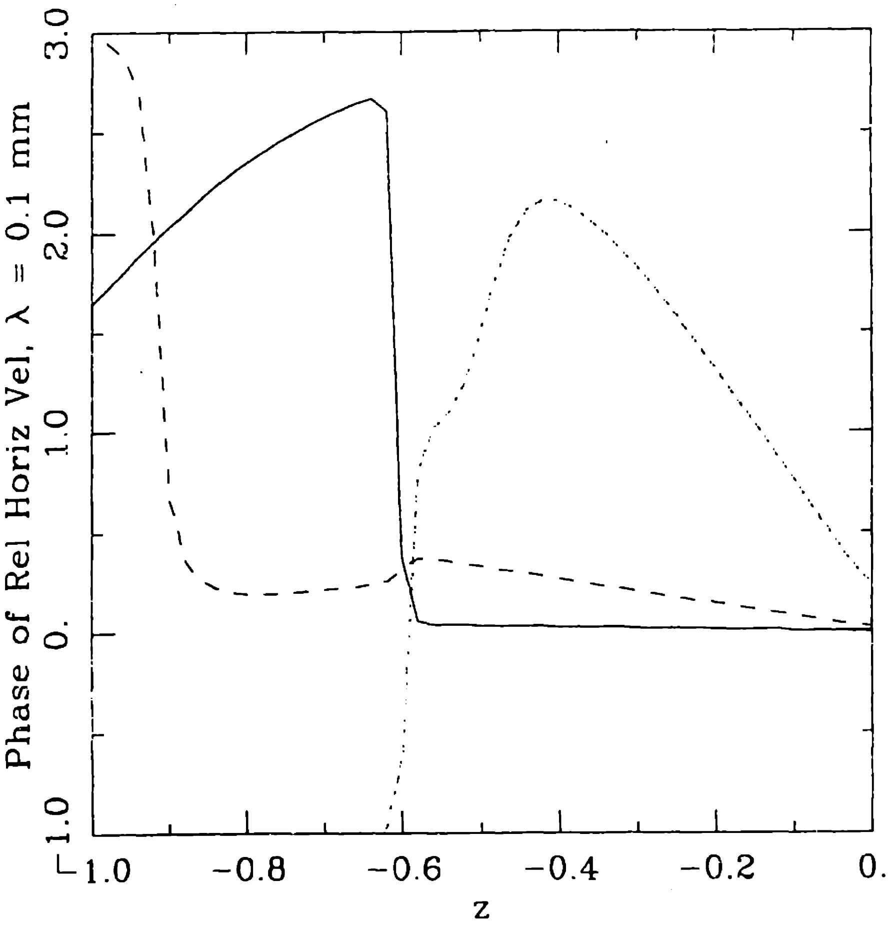

arg V_y, $\lambda = 0.1$ *mm*, $f = 10^{-3}$, $f = 10^{-2}$ (— —), and $f = 0.1$ *Hz* (- - - -).

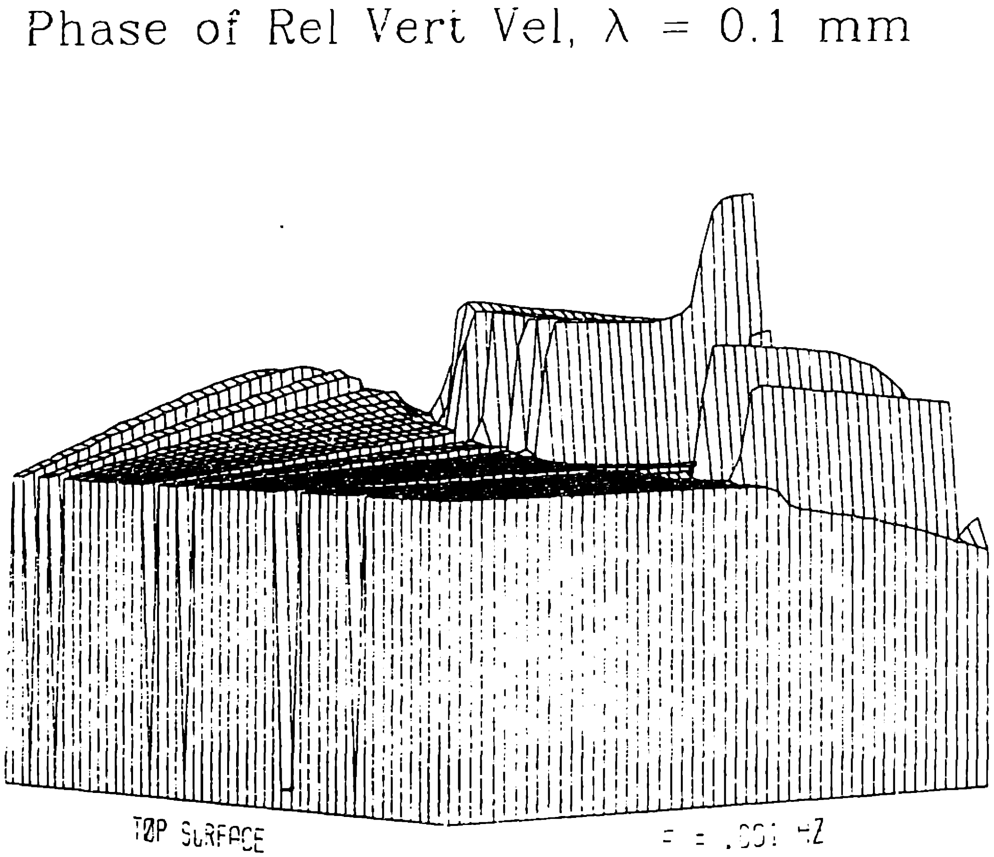

$-8.27 < \arg V_z < 4.56$, $\lambda = 1\ mm$, $f = 10^{-3}$ to $0.1\ Hz$ logarithmically.

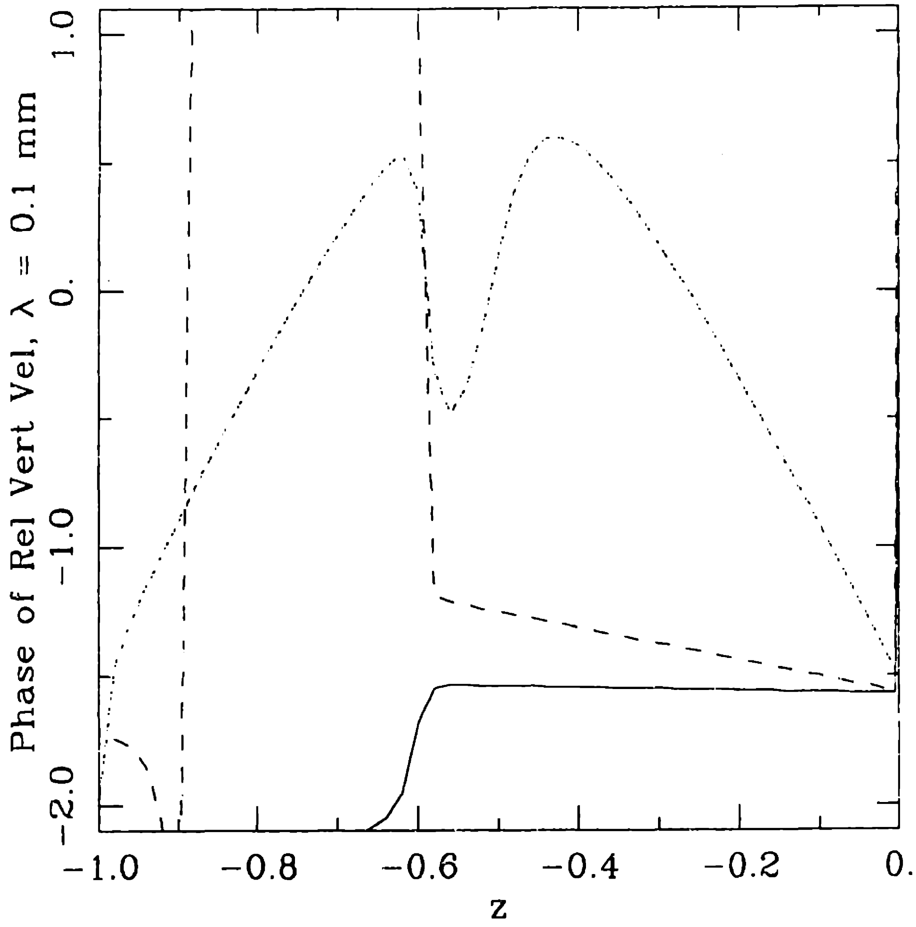

arg V_z, $\lambda = 0.1\ mm, f = 10^{-3}$, $f = 10^{-2}$ (— —), and $f = 0.1\ Hz$ (- - - -).

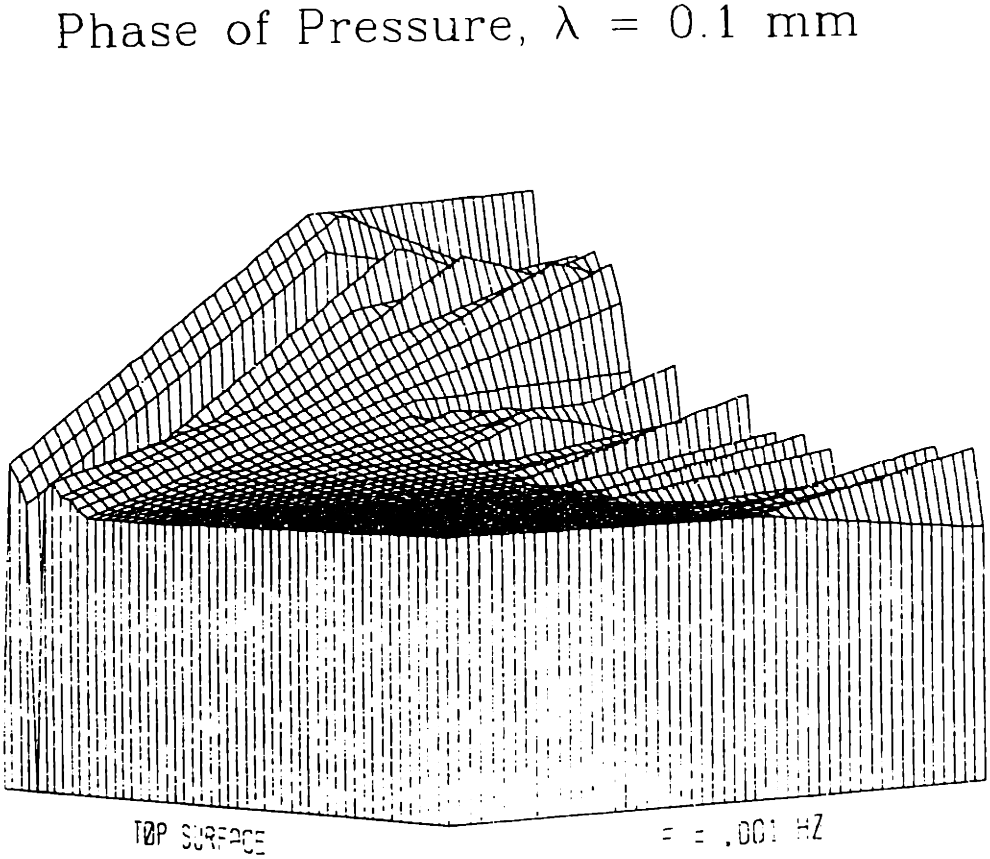
Phase of Pressure, λ = 0.1 mm

$-5.94 < \arg p < 6.88$, $\lambda = 1\ mm$, $f = 10^{-3}$ to 0.1 Hz logarithmically.

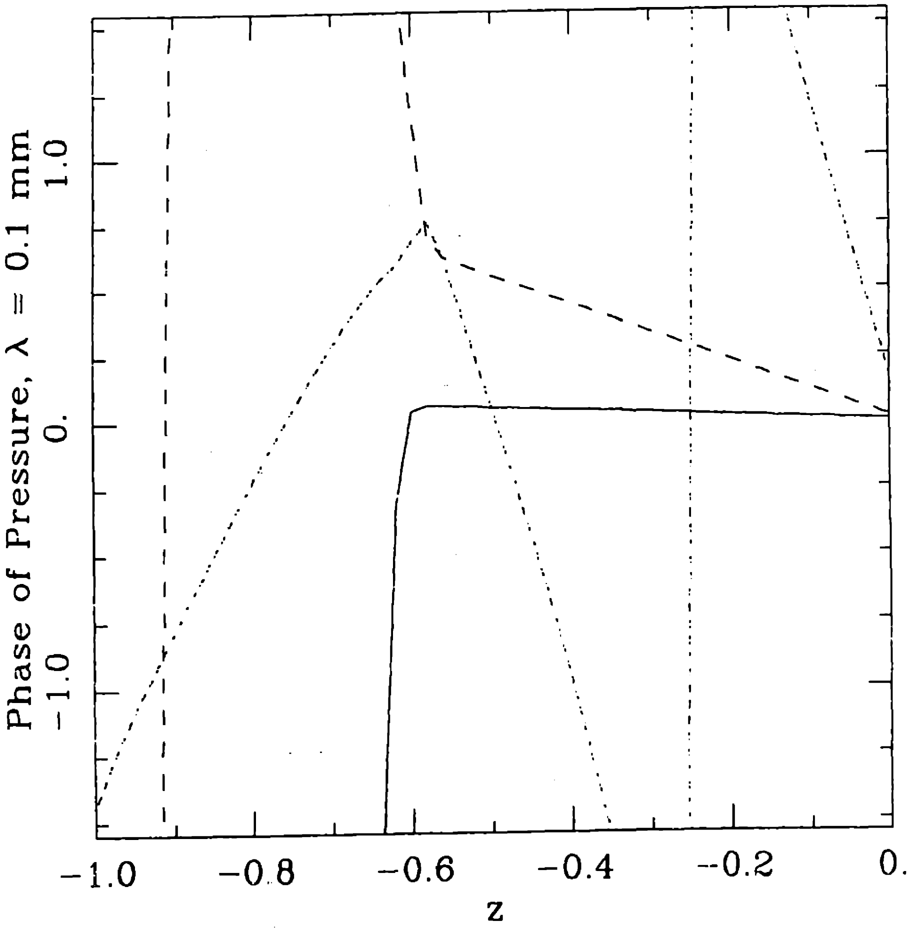

arg p**,** λ **= 0.1** *mm*, f **=** 10^{-3}**,** f **=** 10^{-2} **(— —), and** f **= 0.1** *Hz* **(- - - -).**

logarithmically.

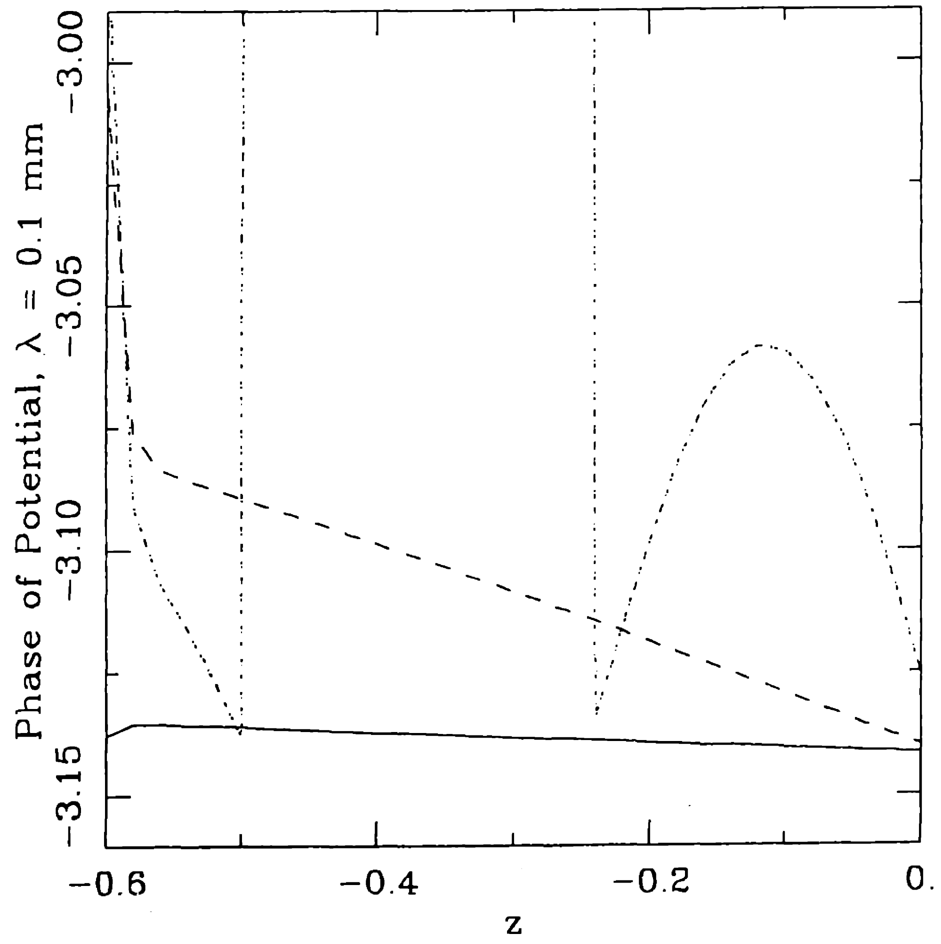

arg ϕ, $\lambda = 0.1$ mm, $f = 10^{-3}$, $f = 10^{-2}$ (— —), and $f = 0.1$ Hz (- - - -).

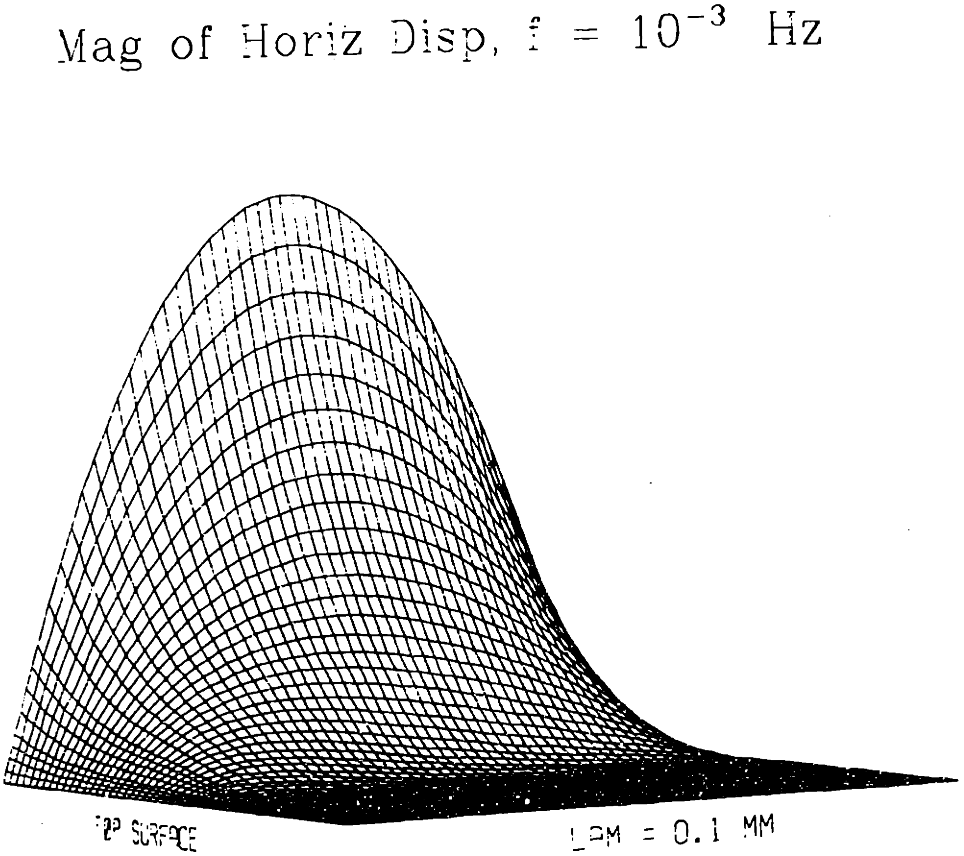

$|u_y|$, $f = 10^{-3}$ *Hz*, $\lambda = 0.1$ to 10.0 *mm* logarithmically.

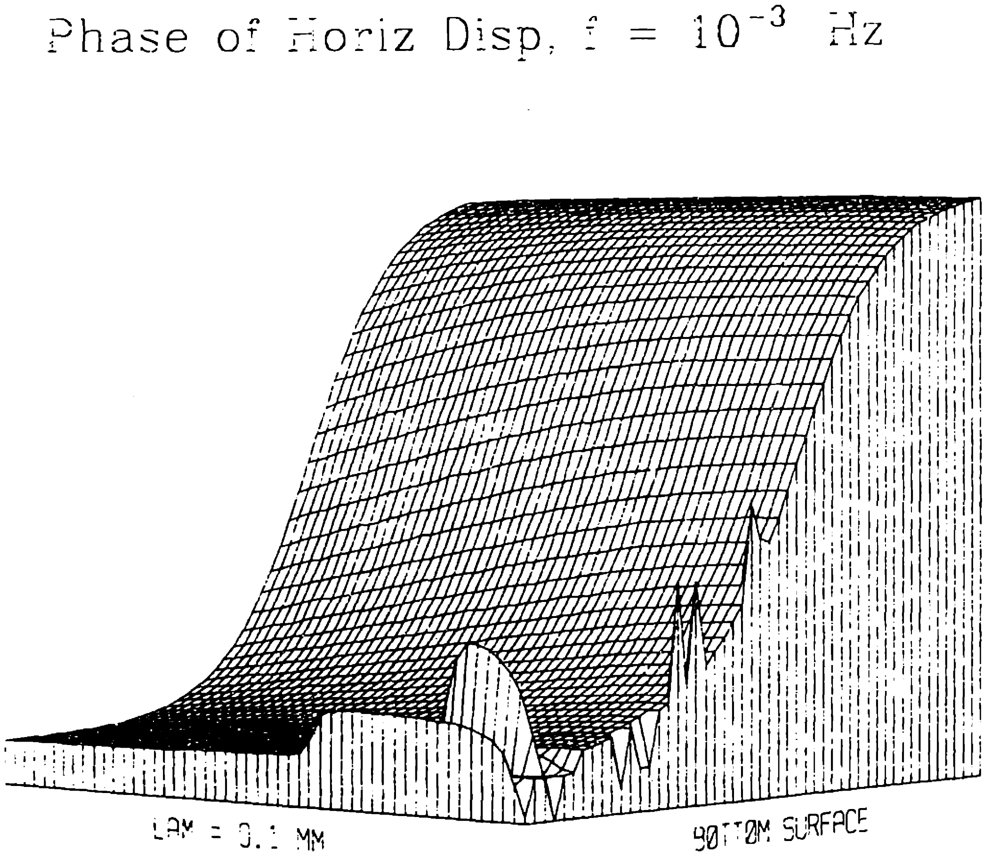

$-1.68 < \arg u_y < -0.150 \cdot 10^{-2}$, $f = 10^{-3}$ *Hz*, $\lambda = 0.1$ to 10.0 *mm* logarithmically.

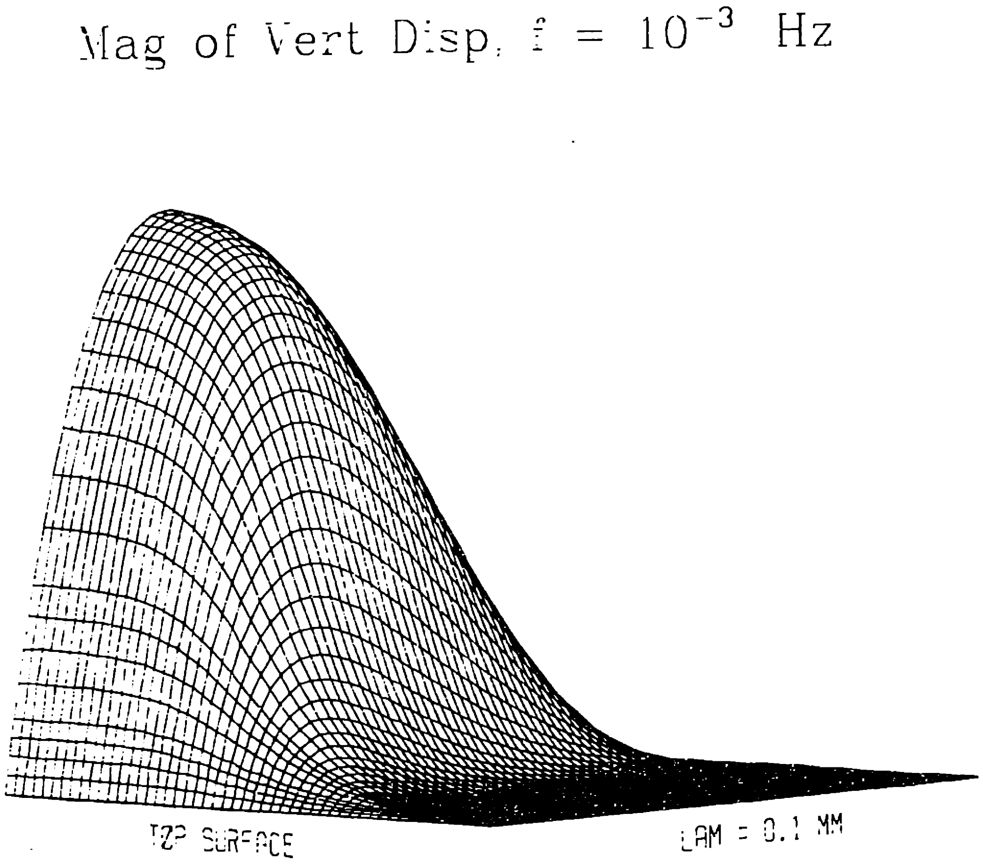

$|u_z|$, $f = 10^{-3}\ Hz$, $\lambda = 0.1$ to $10.0\ mm$ logarithmically.

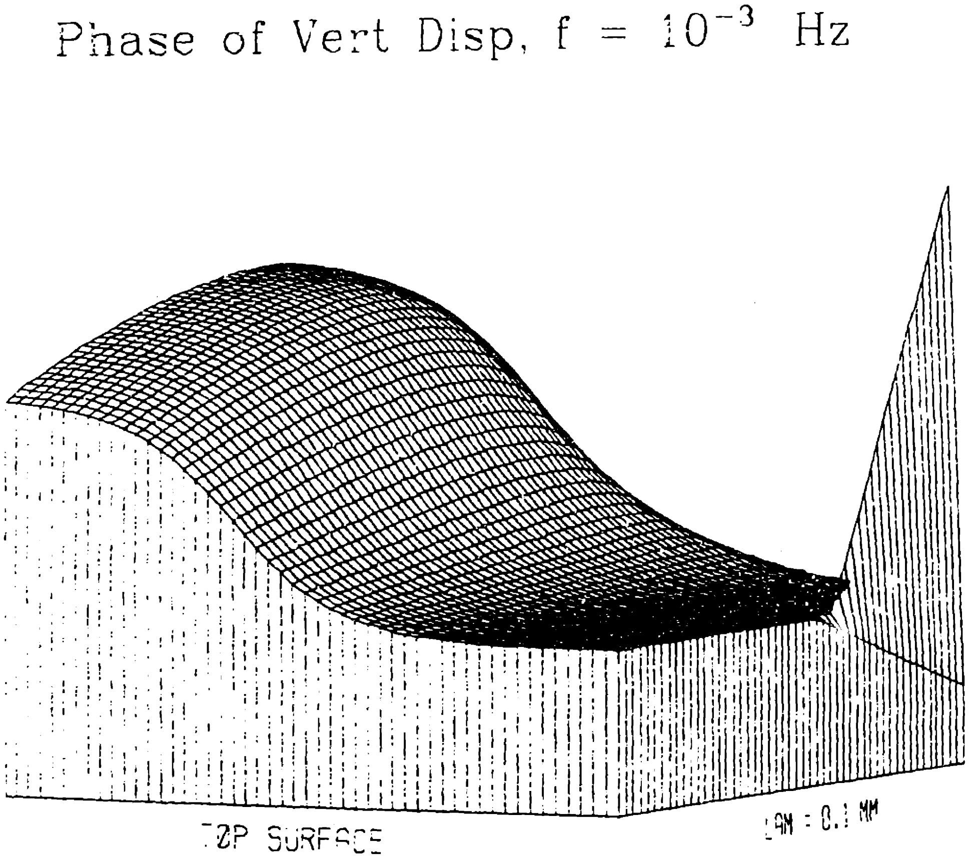

$-3.63 < \arg u_z < -1.82$, $f = 10^{-3}$ Hz, $\lambda = 0.1$ to 10.0 *mm* logarithmically.

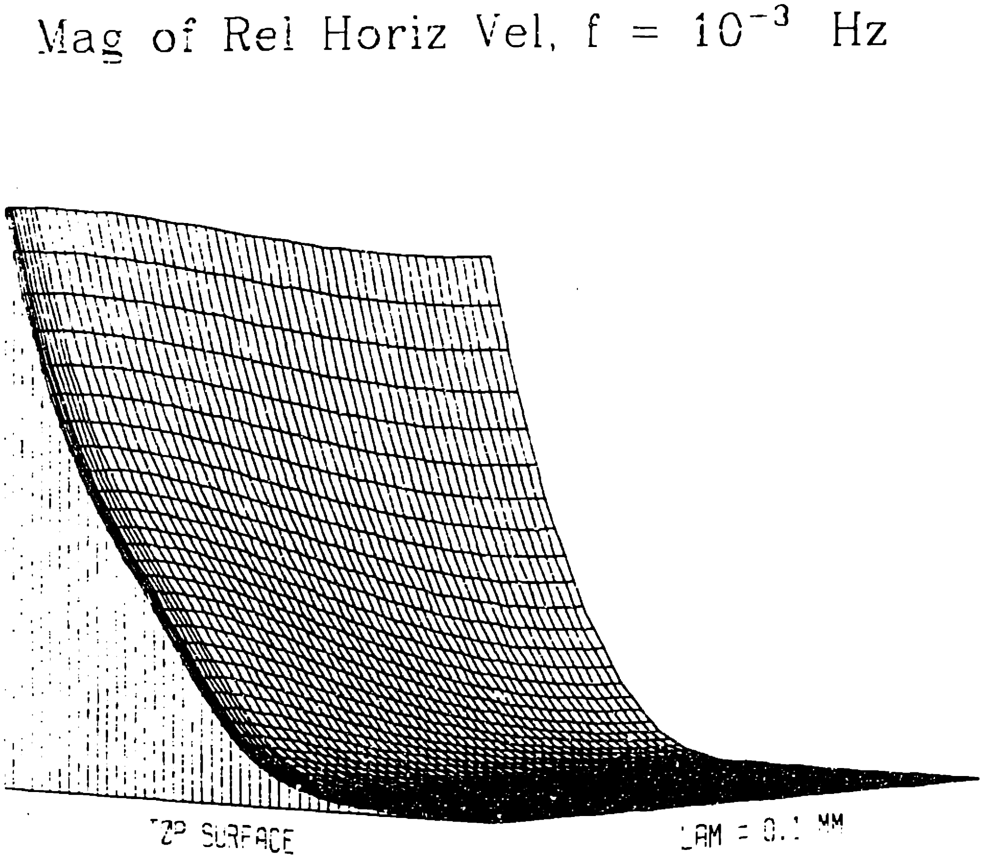

$|V_y|$, $f = 10^{-3}$ Hz, $\lambda = 0.1$ to 10.0 *mm* logarithmically.

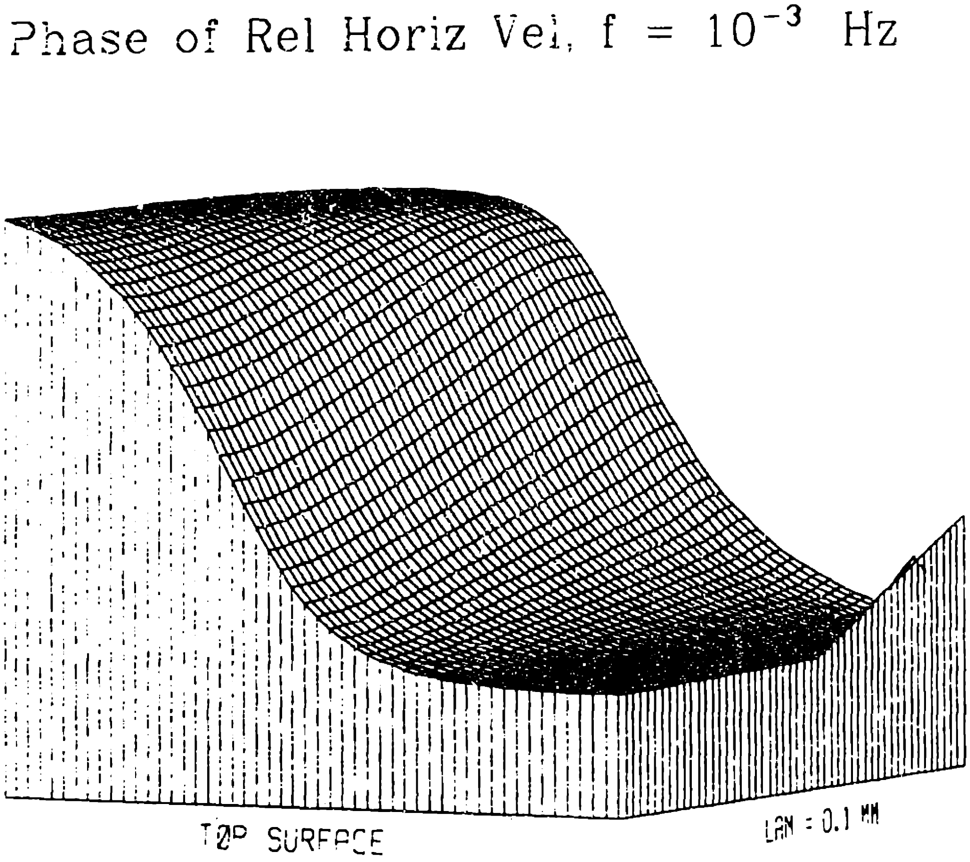

$-0.357 < \arg V_y < 1.44$, $f = 10^{-3}$ *Hz*, $\lambda = 0.1$ to 10.0 *mm* logarithmically.

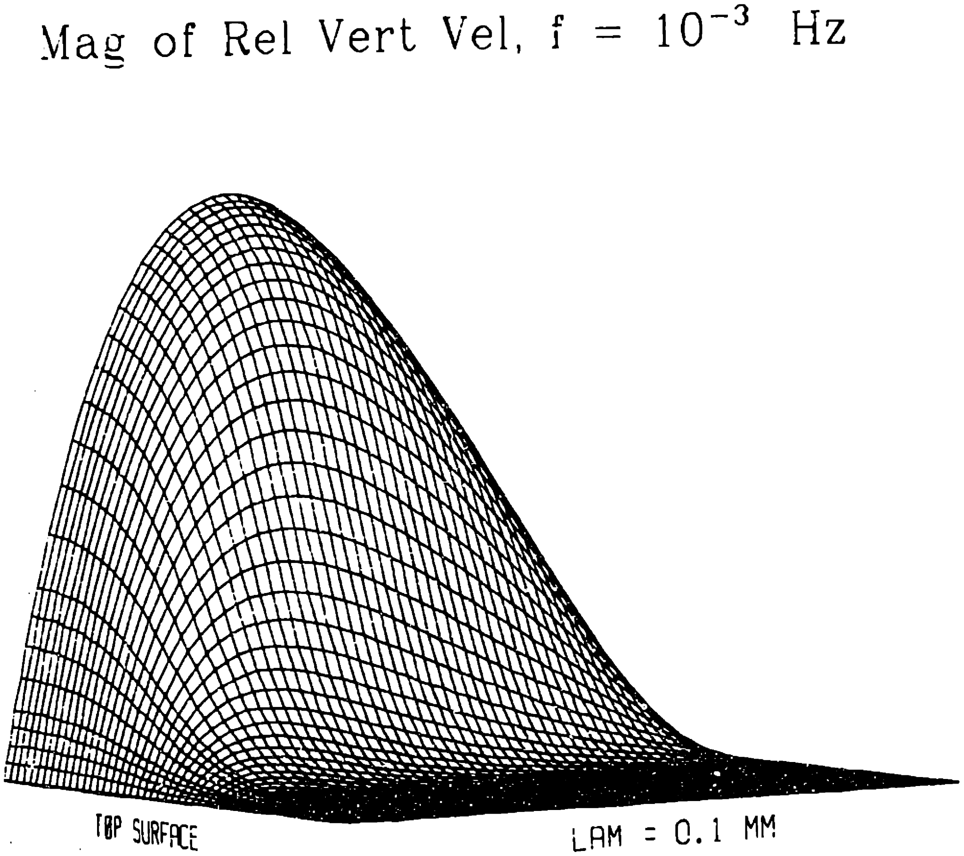

$|V_z|$, $f = 10^{-3}$ Hz, $\lambda = 0.1$ to 10.0 mm logarithmically.

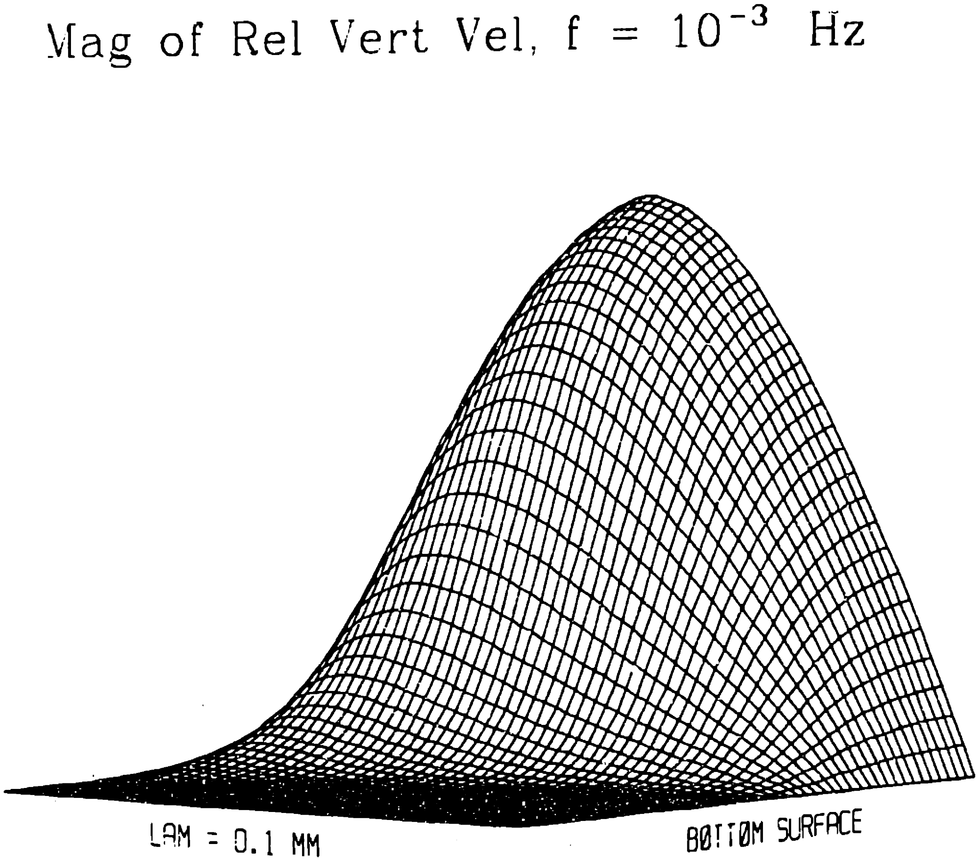

$|V_z|$, $f = 10^{-3}$ *Hz*, $\lambda = 0.1$ to 10.0 *mm* logarithmically.

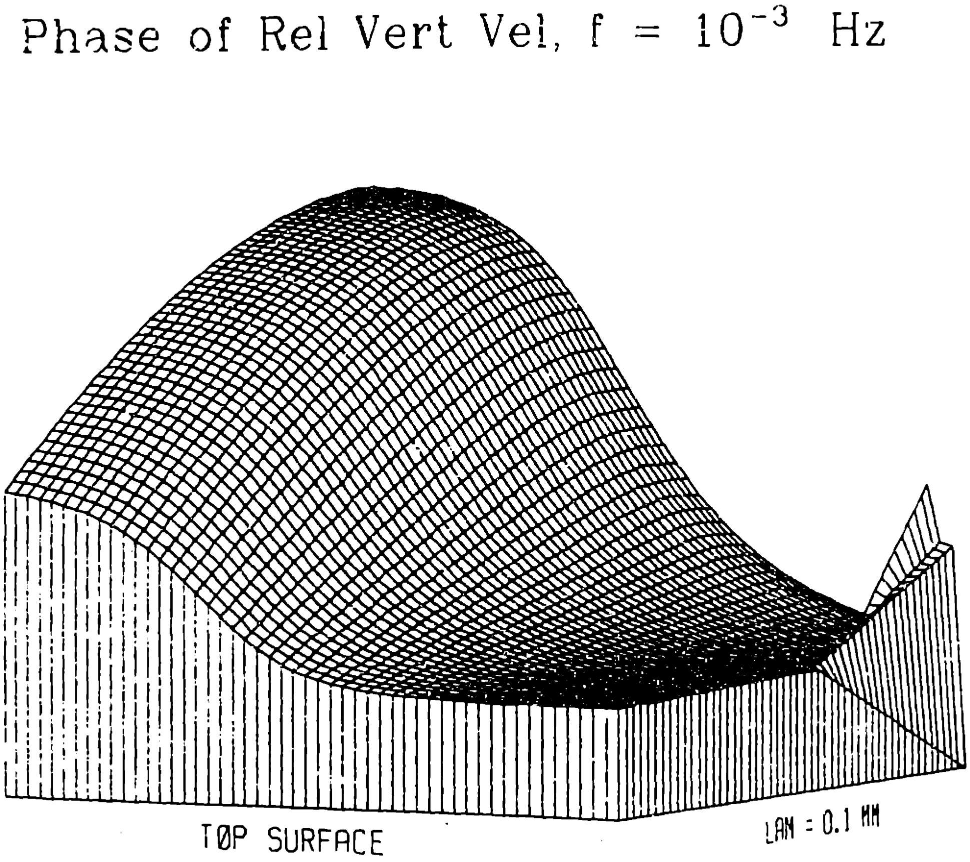

$-1.85 < \arg V_z < -0.312$, $f = 10^{-3}$ *Hz*, $\lambda = 0.1$ to 10.0 *mm* logarithmically.

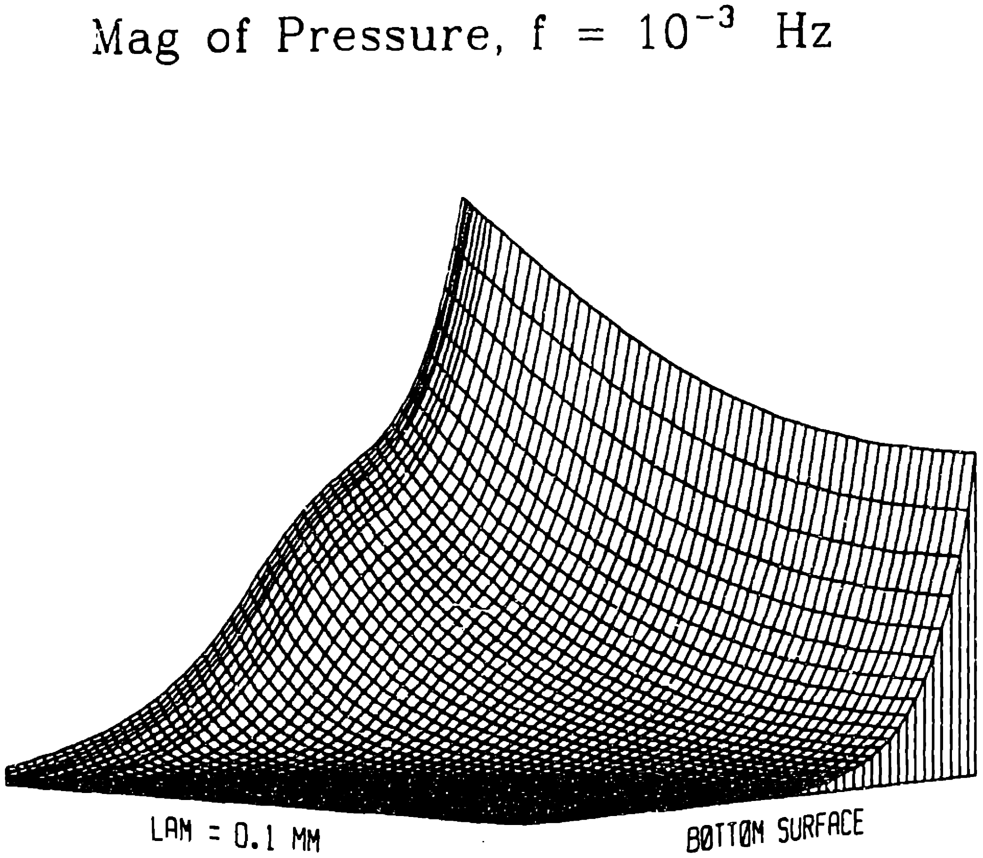

$|p|$, $f = 10^{-3}$ *Hz*, $f = 10^{-3}$ *Hz*, $\lambda = 0.1$ to 10.0 *mm* logarithmically.

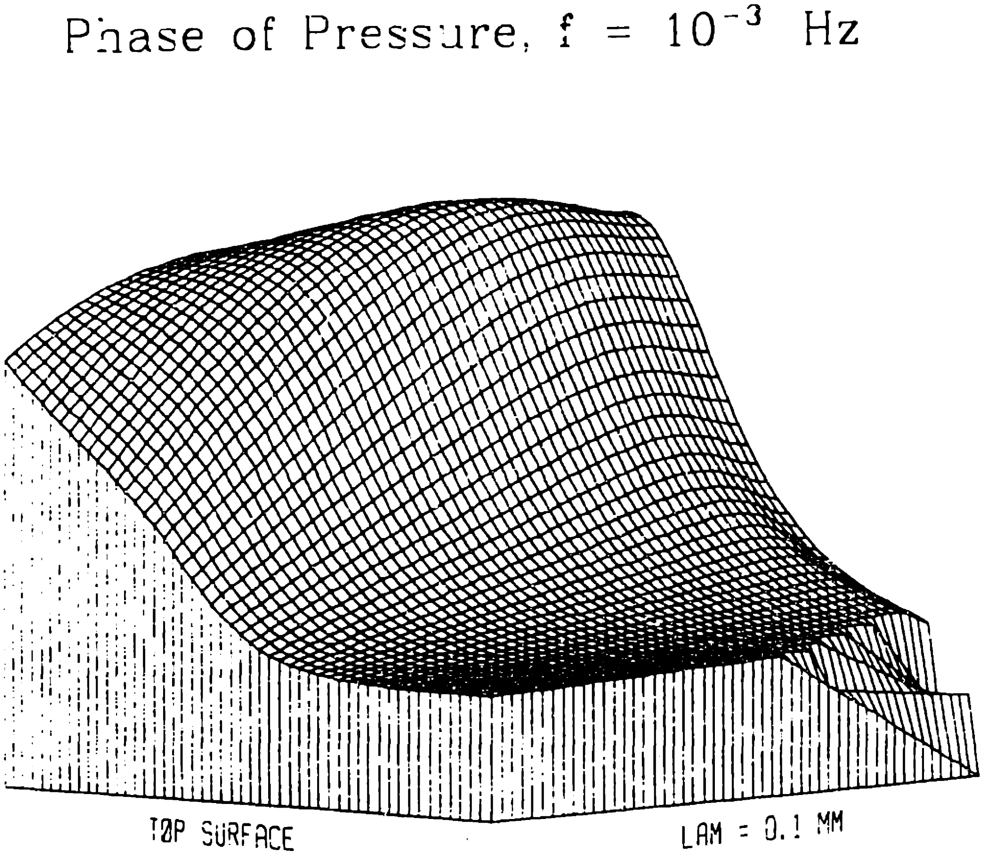

$-0.430 < \arg p < 1.67$, $f = 10^{-3}$ *Hz*, $\lambda = 0.1$ to 10.0 *mm* logarithmically.

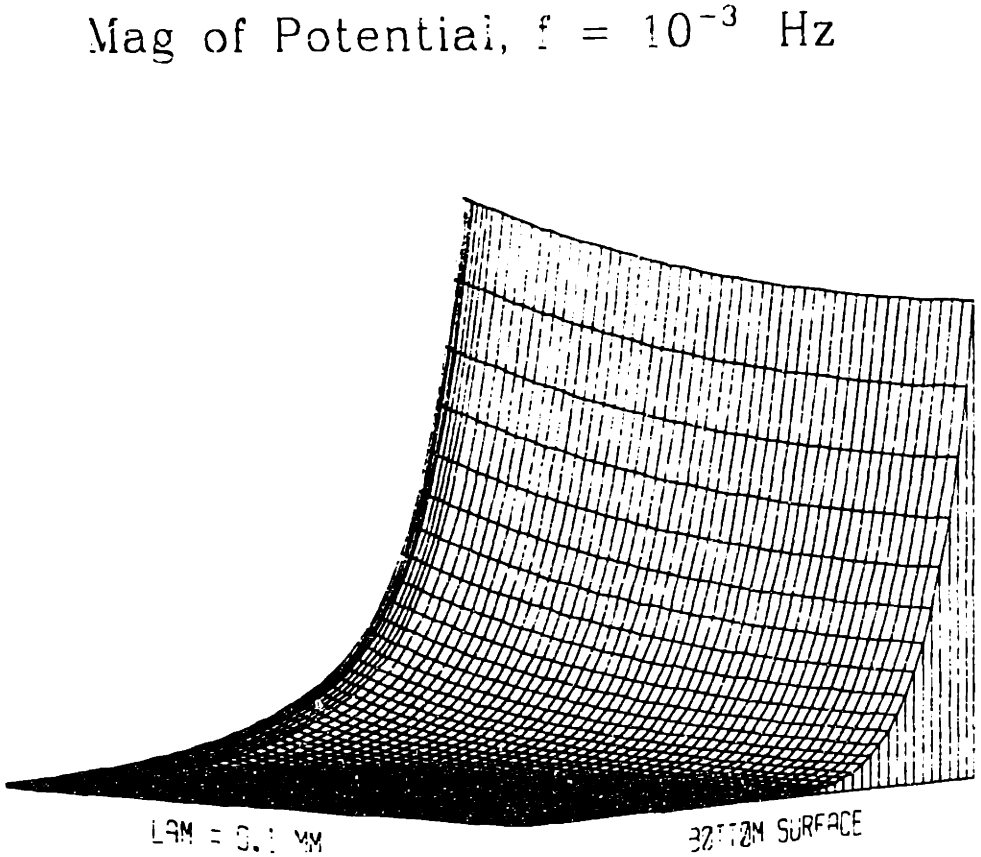

$|\phi|$, $f = 10^{-3}$ Hz, $f = 10^{-3}$ Hz, $\lambda = 0.1$ to 10.0 mm logarithmically.

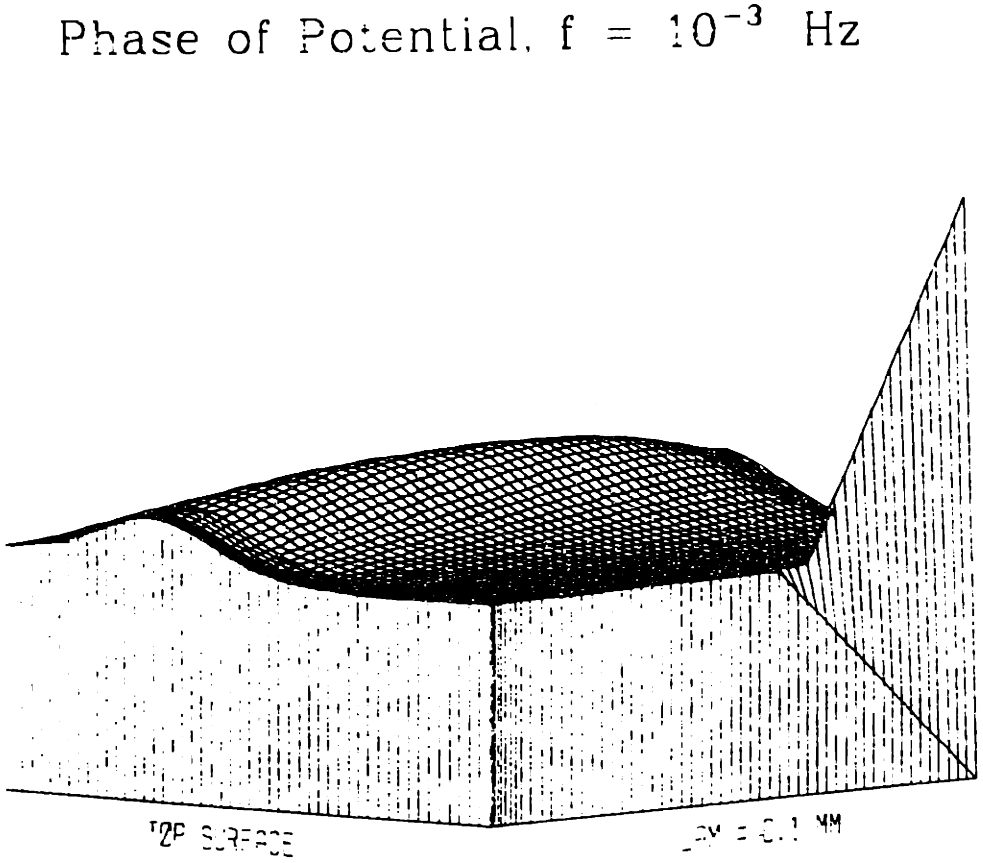

$-3.257 < \arg\phi < -2.936$, $f = 10^{-3}$ Hz, $\lambda = 0.1$ to 10.0 *mm* logarithmically.

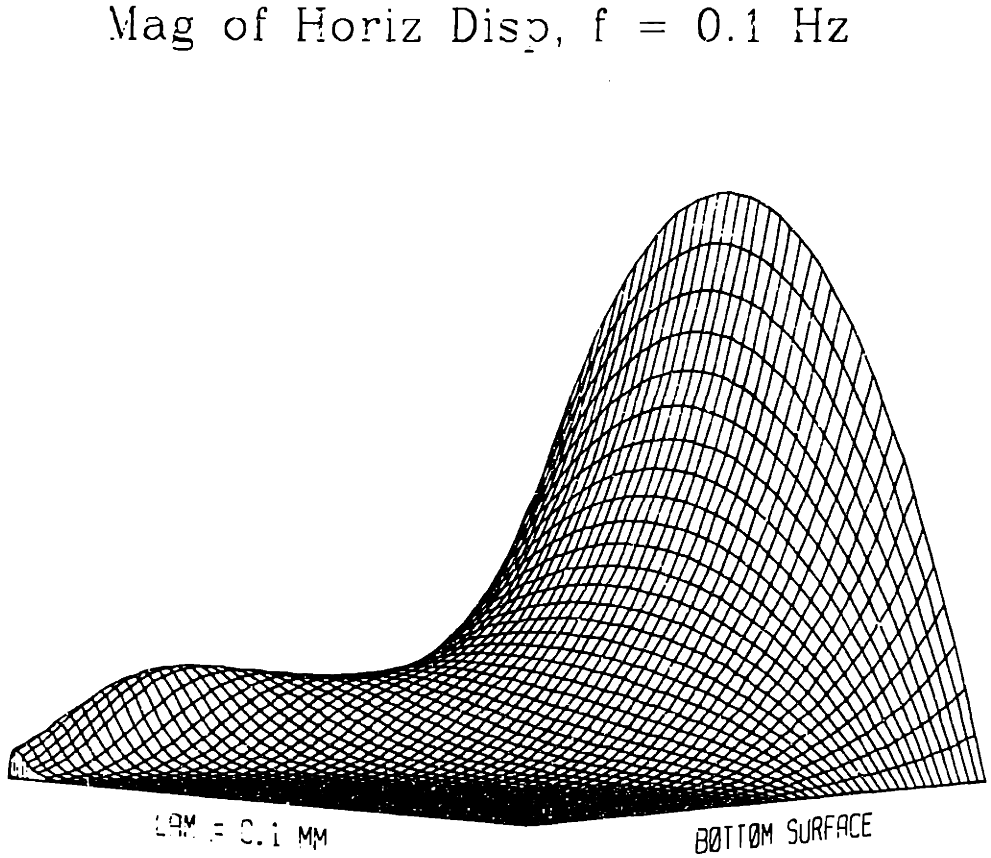

$|u_y|$, $f = 0.1\ Hz$, $\lambda = 0.1$ to $10.0\ mm$ **logarithmically.**

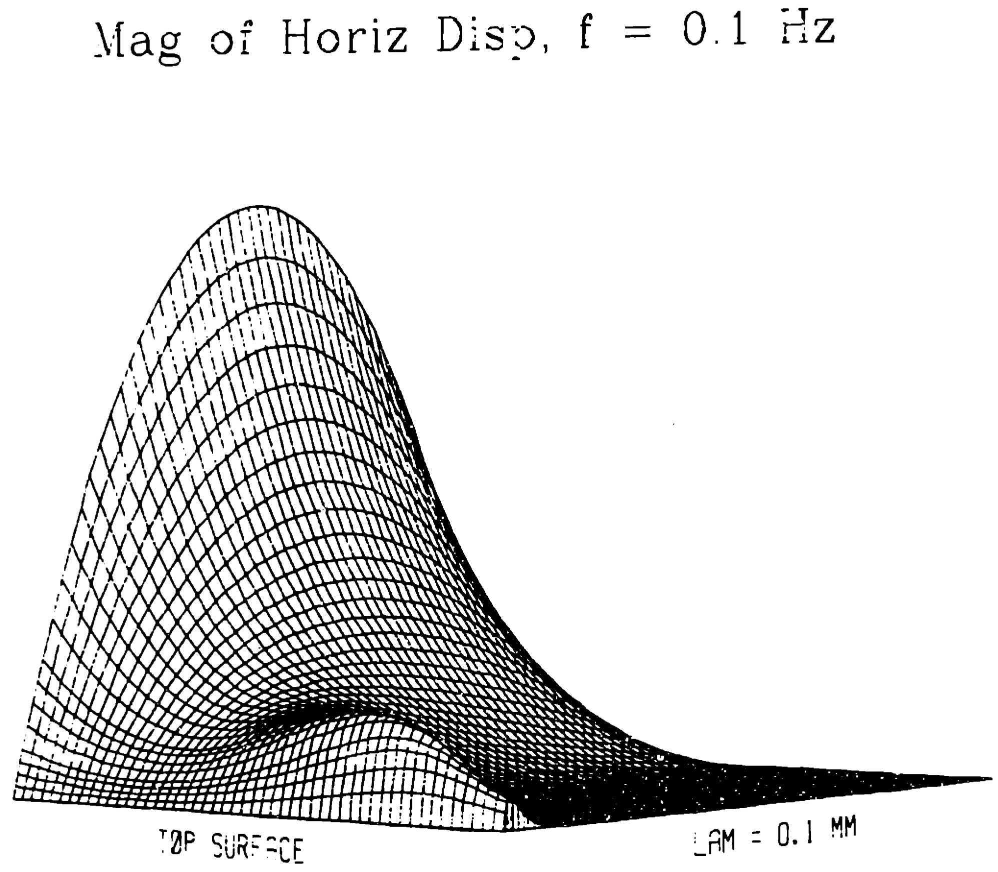

$|u_y|$, $f = 0.1\ Hz$, $\lambda = 0.1$ to 10.0 mm logarithmically.

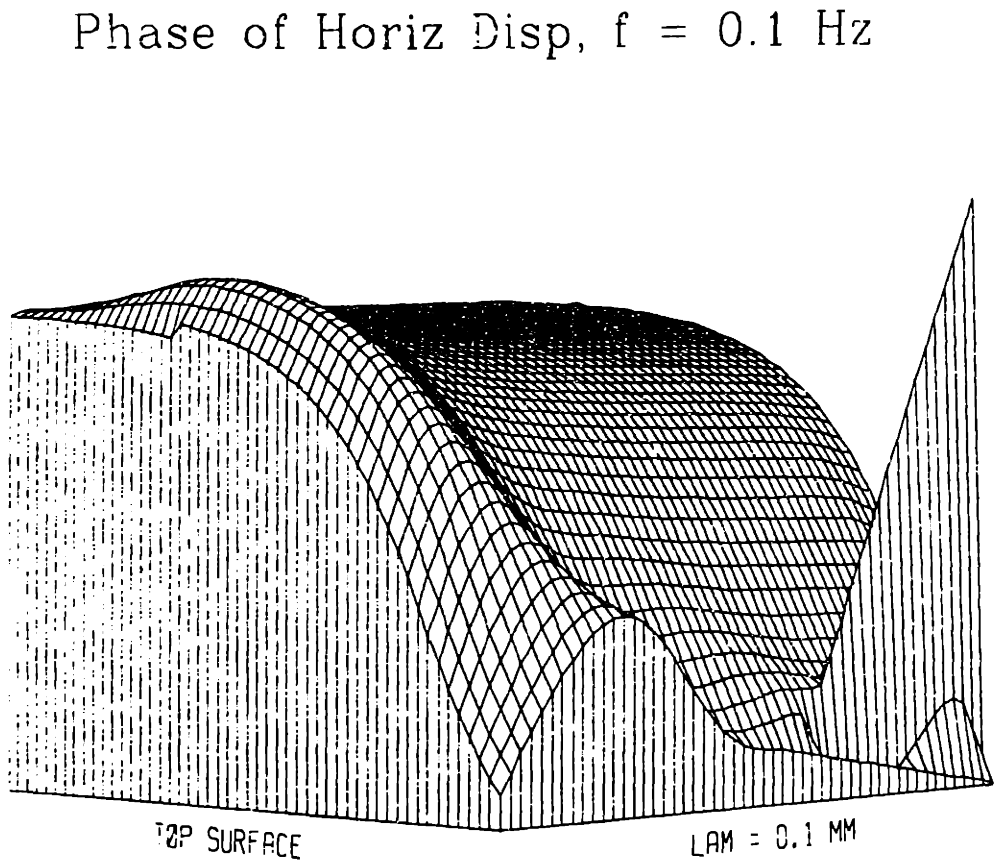

$-1.42 < \arg u_y < 0.333 \cdot 10^{-2}$, $f = 0.1\ Hz$, $\lambda = 0.1$ to $10.0\ mm$ logarithmically.

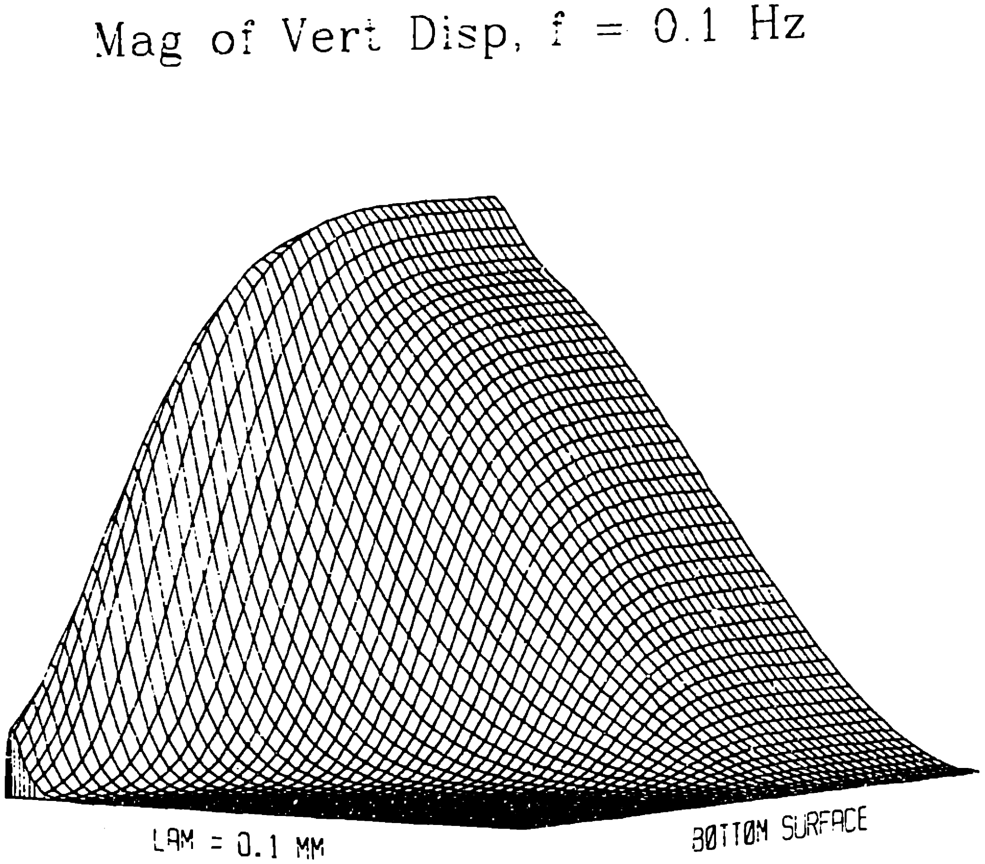

$|u_z|$, $f = 0.1\ Hz$, $\lambda = 0.1$ to 10.0 mm logarithmically.

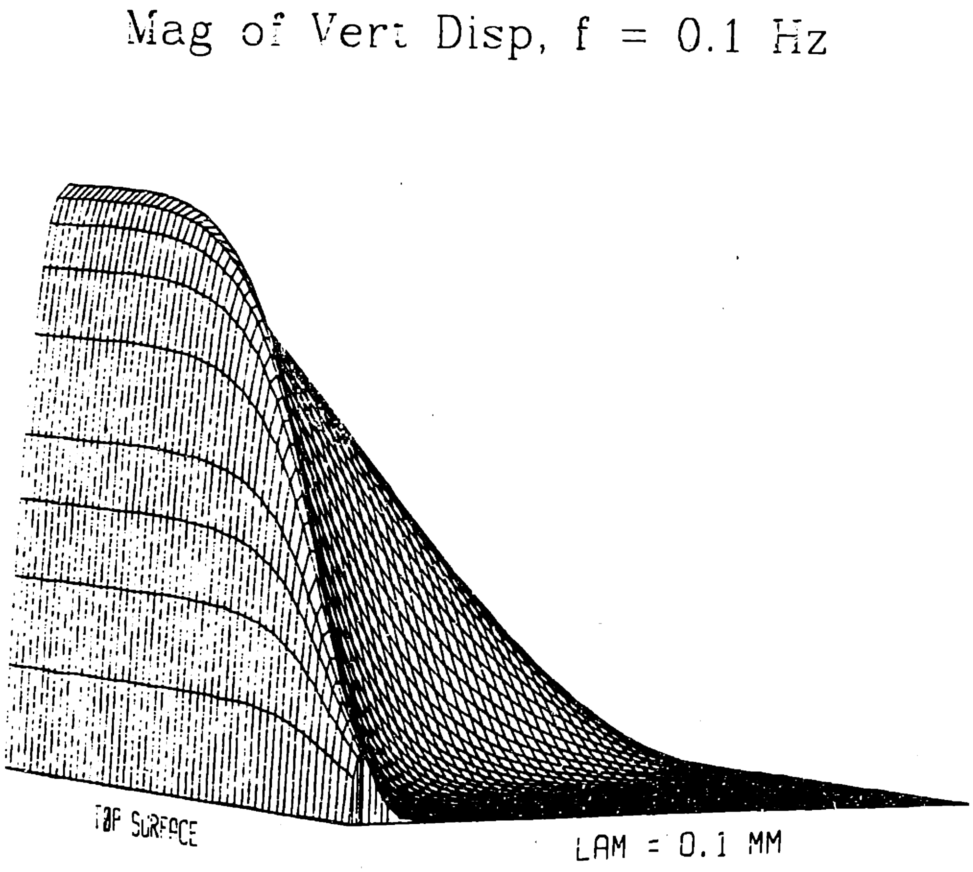

$|u_z|$, $f = 0.1\ Hz$, $\lambda = 0.1$ to $10.0\ mm$ logarithmically.

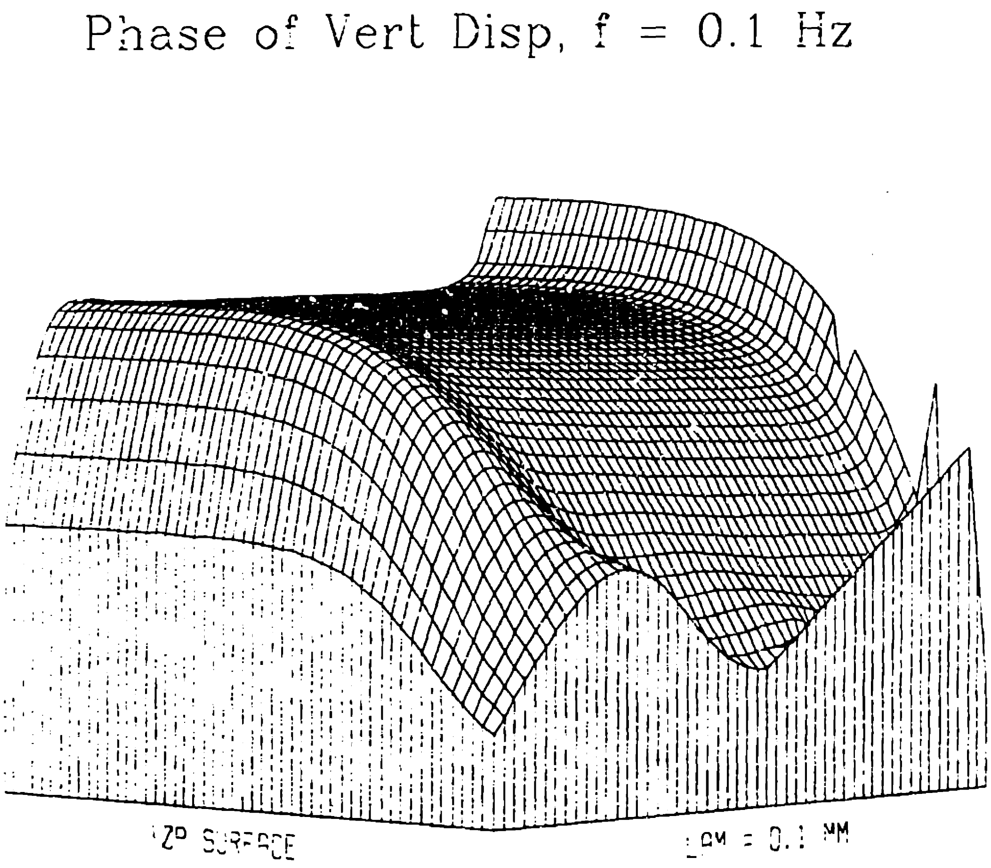

$-3.31 < \arg u_z < -1.22$, $f = 0.1\ Hz$, $\lambda = 0.1$ to $10.0\ mm$ logarithmically.

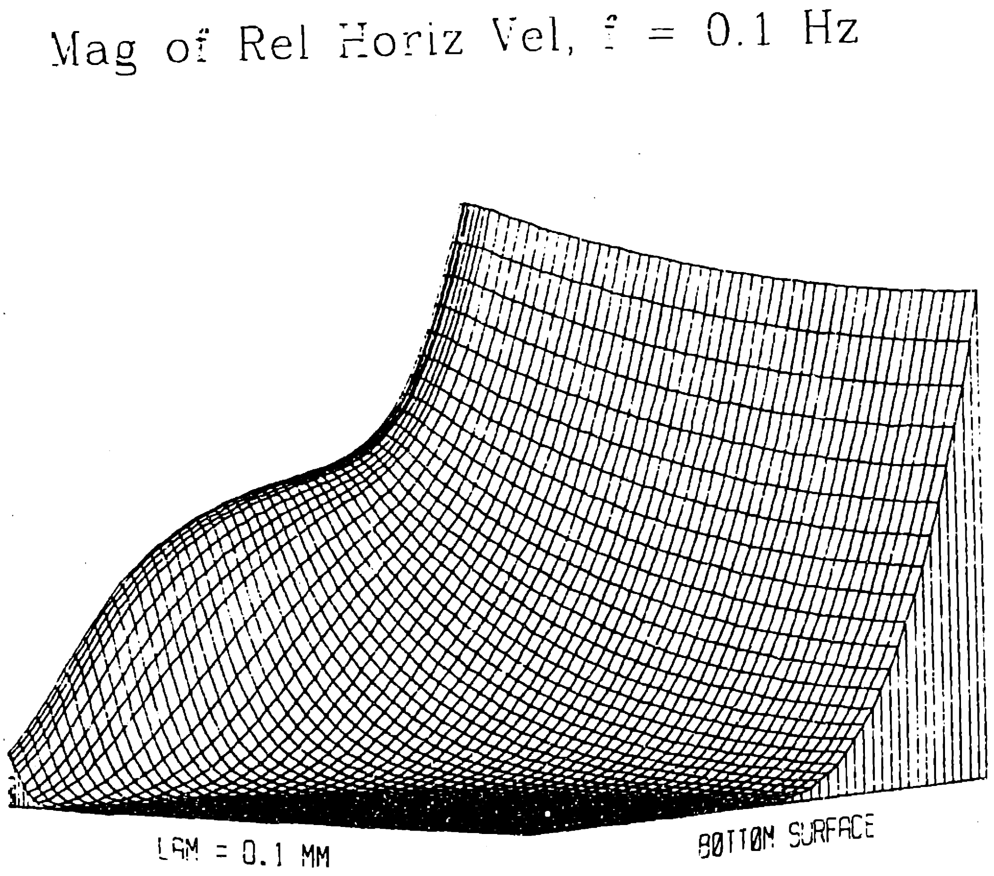

$|V_y|$, $f = 0.1\ Hz$, $\lambda = 0.1$ to 10.0 mm logarithmically.

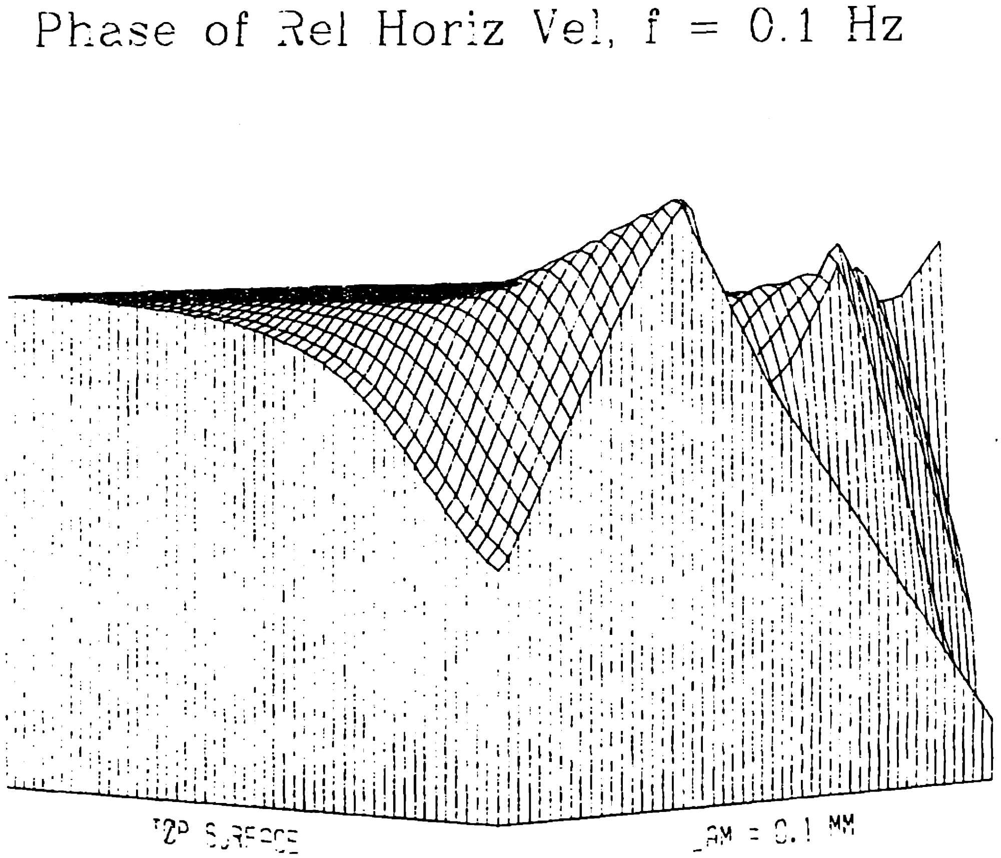

$-1.03 < \arg V_y < 2.09$, $f = 0.1\ Hz$, $\lambda = 0.1$ to $10.0\ mm$ logarithmically.

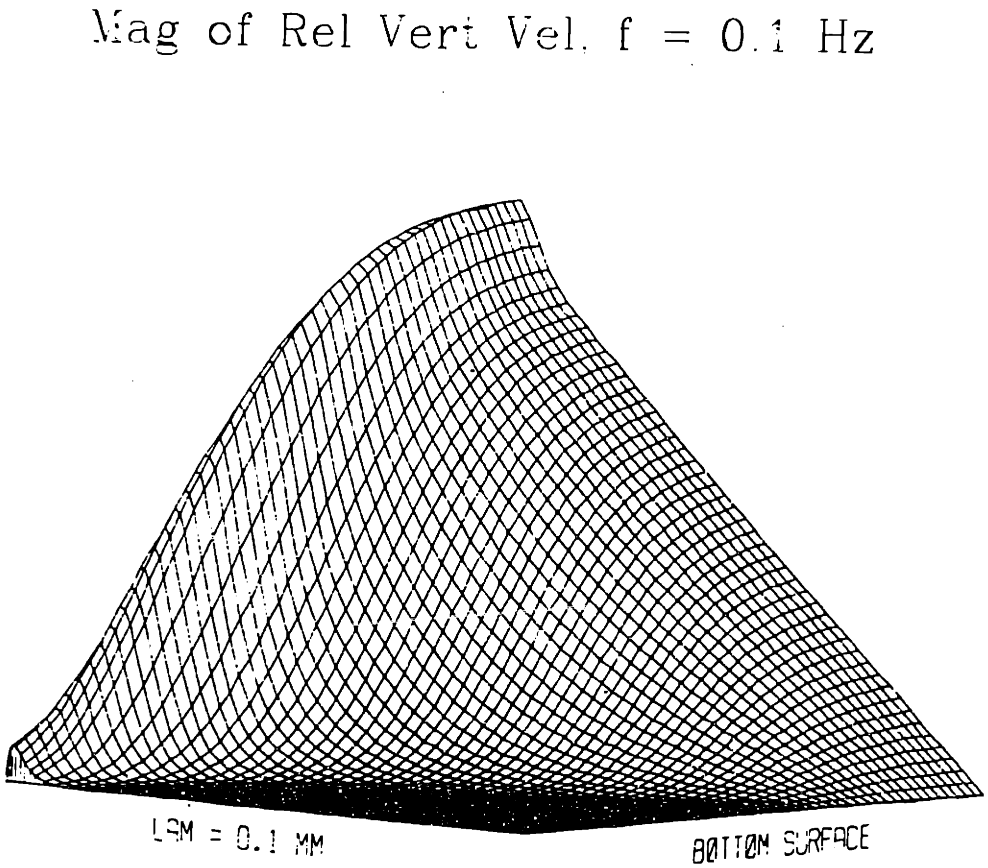

$|V_z|$, $f = 0.1\ Hz$, $\lambda = 0.1$ to $10.0\ mm$ logarithmically.

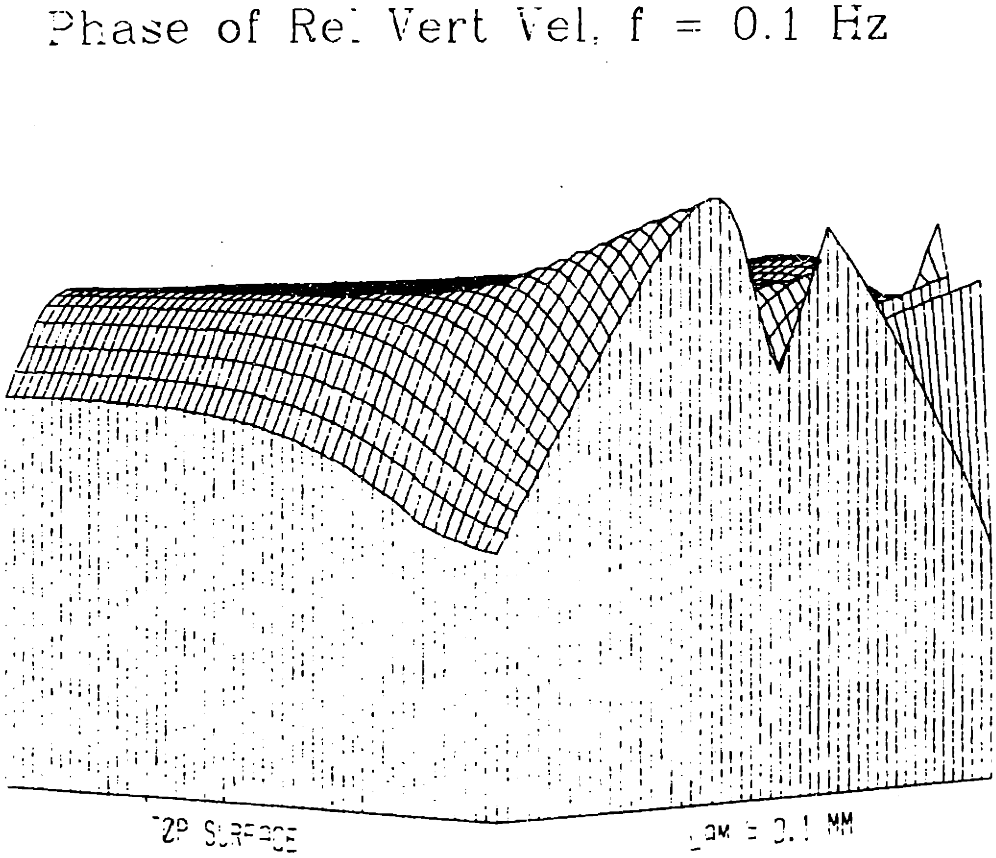

$-3.12 < \arg V_z < 0.599$, $f = 0.1$ *Hz*, $\lambda = 0.1$ to 10.0 *mm* logarithmically.

Mag of Pressure, f = 0.1 Hz

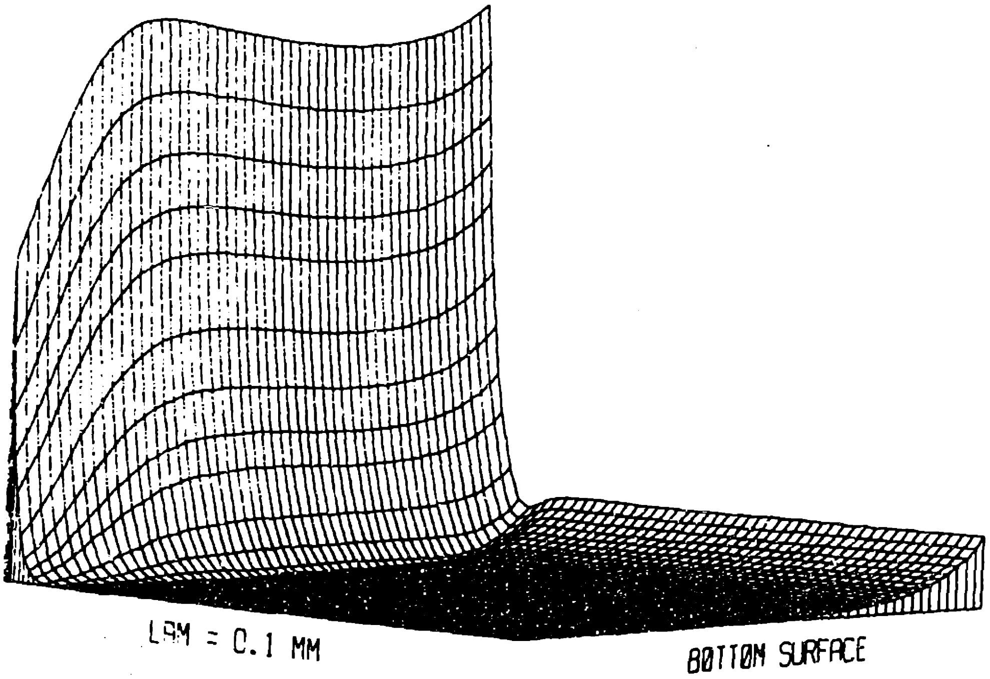

$|\lambda p|$, $f = 0.1\ Hz$, $f = 0.1\ Hz$, $\lambda = 0.1$ to $10.0\ mm$ logarithmically.

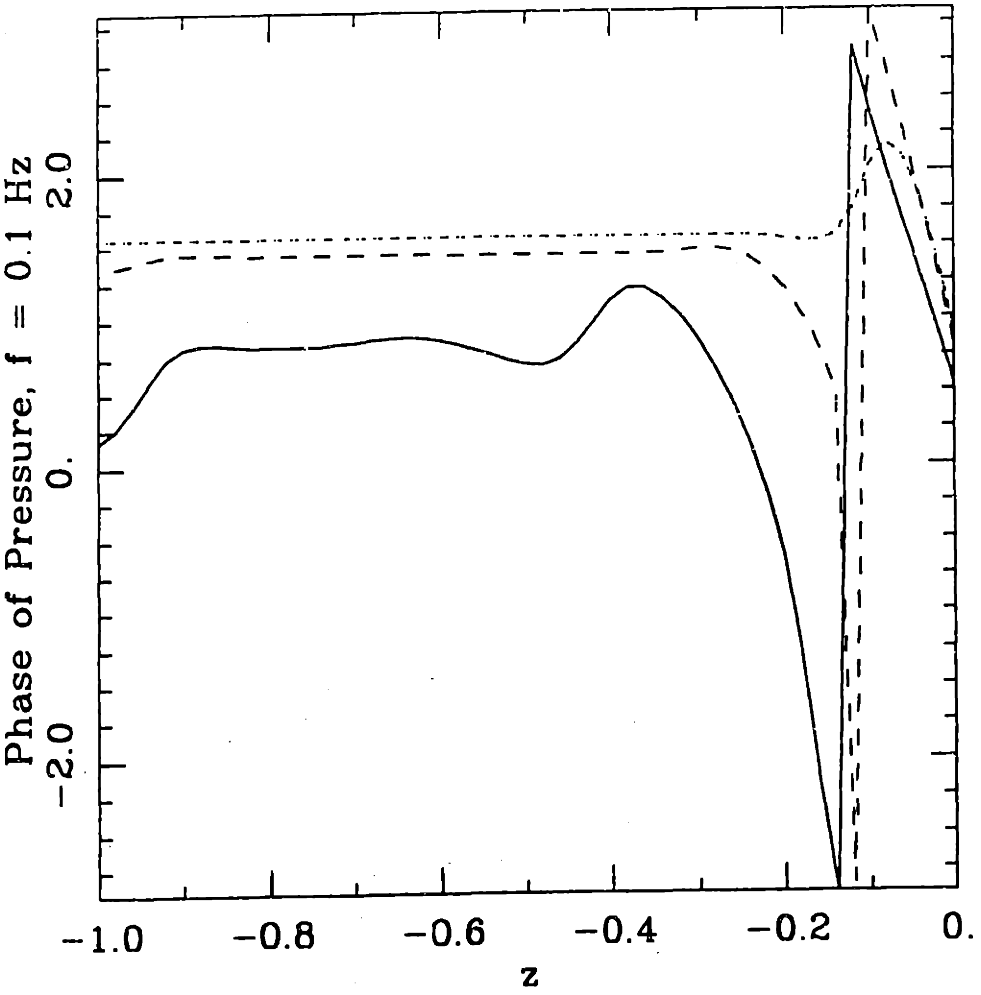

arg p, $f = 0.1\ Hz$, $\lambda \sim 0.25$, $\lambda = 1$ (— —), and $\lambda = 10\ mm$ (- - - -).

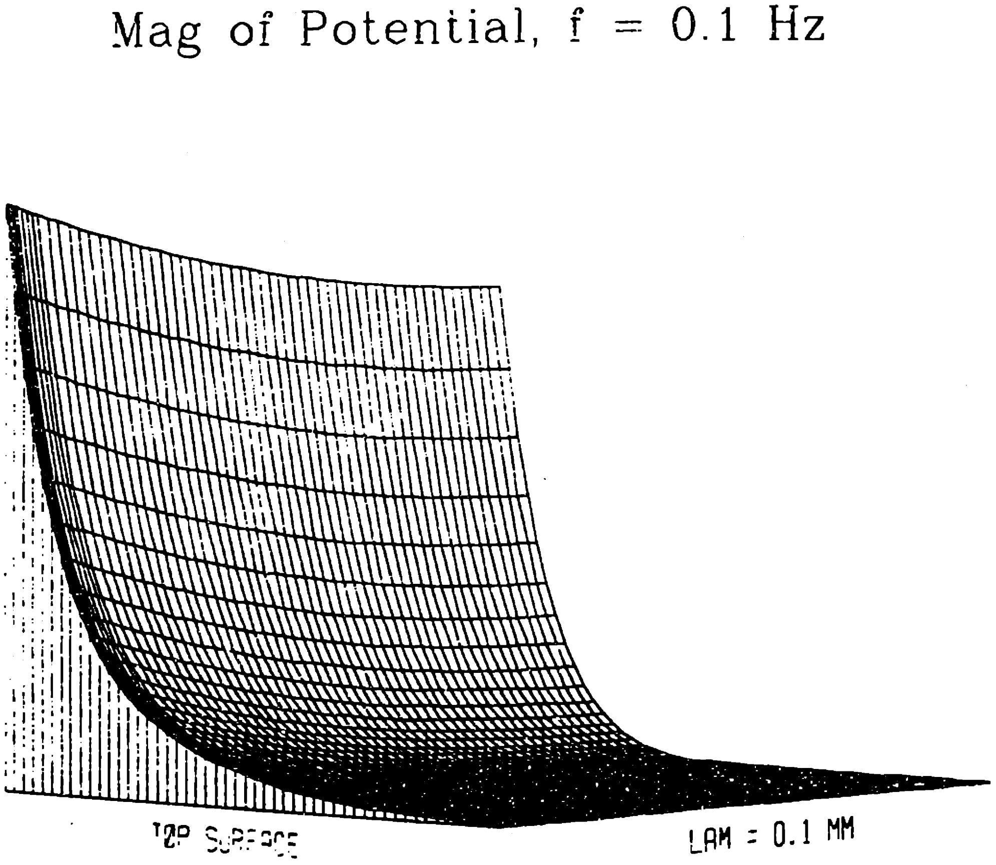

$|\phi|$, $f = 0.1\ Hz$, $f = 0.1\ Hz$, $\lambda = 0.1$ to $10.0\ mm$ logarithmically. $\arg\phi \sim -\pi$.

A.1.2 Asymptotic Results

This section presents graphs comparing the results of the asymptotic expansions in sections 4.2.2 and 4.2.2 with the appropriate numerics. The numerical calculations (*àla* §4.2.1) are plotted with solid curves, while the asymptotics with which they are being compared are plotted with “+”’s, “×”’s, “.”’s, or dashed lines. Short-wave results (equations 4.11 are presented for:

1. $f = 10^{-3}\,Hz$, $\lambda = 0.1\,mm$,
2. $f = 0.1\,Hz$, $\lambda = 0.1\,mm$,
3. $f = 10^{-3}\,Hz$, $\lambda = 1.0mm$,

and

4. $f = 0.1\,Hz$, $\lambda = 1.0mm$.

The short-wave and numerical magnitude and phase of the normal surface stress, s, are presented for $\lambda = 0.1$ and 1.0, with f varying from 10^{-3} to $10^{-1}\,Hz$. Long-wave results are presented for $f = 10^{-3}$, and $f = 0.1\,Hz$, both with $\lambda = 10\,mm$. The magnitudes and phases of the fields are presented in the order u_y, u_z, V_y, V_z, p, and ϕ.

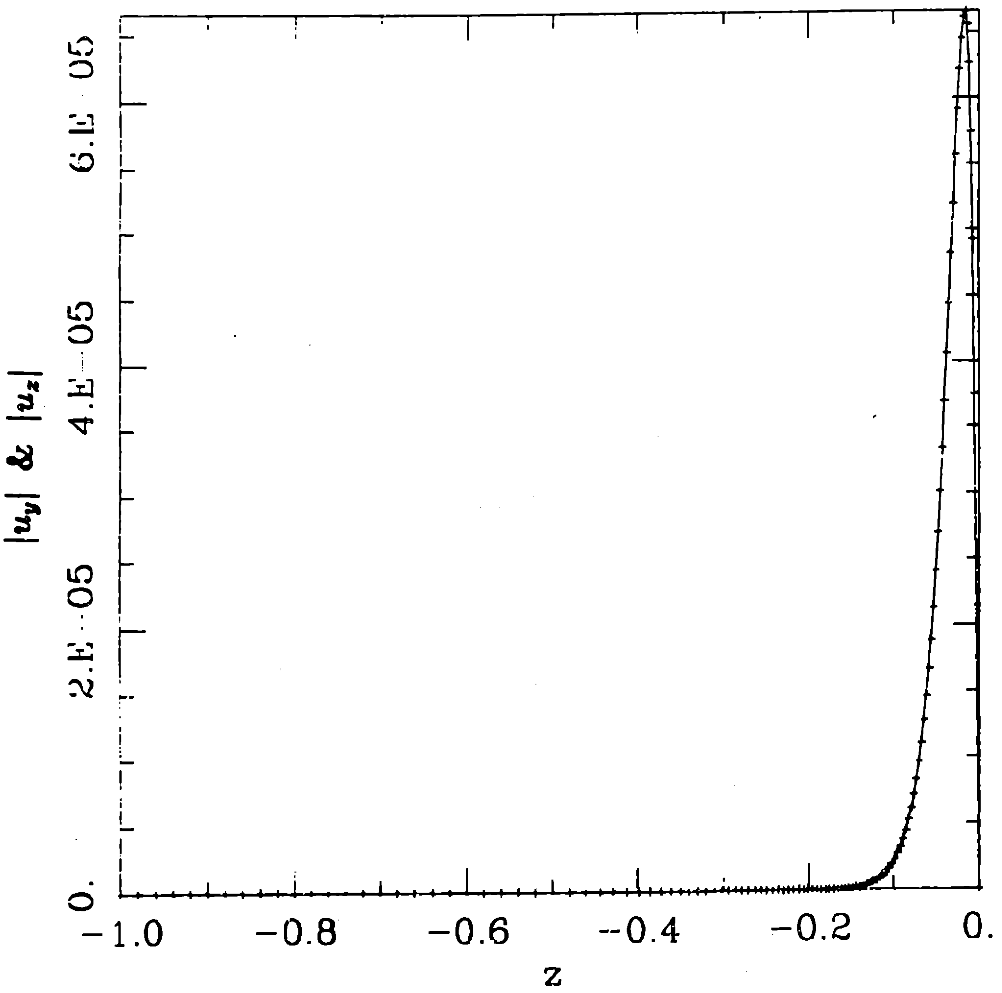

$|u_y|$ & $|u_z|$, $f = 10^{-3}$ Hz, $\lambda = 0.1$ mm. The four curves are not distinguishable.

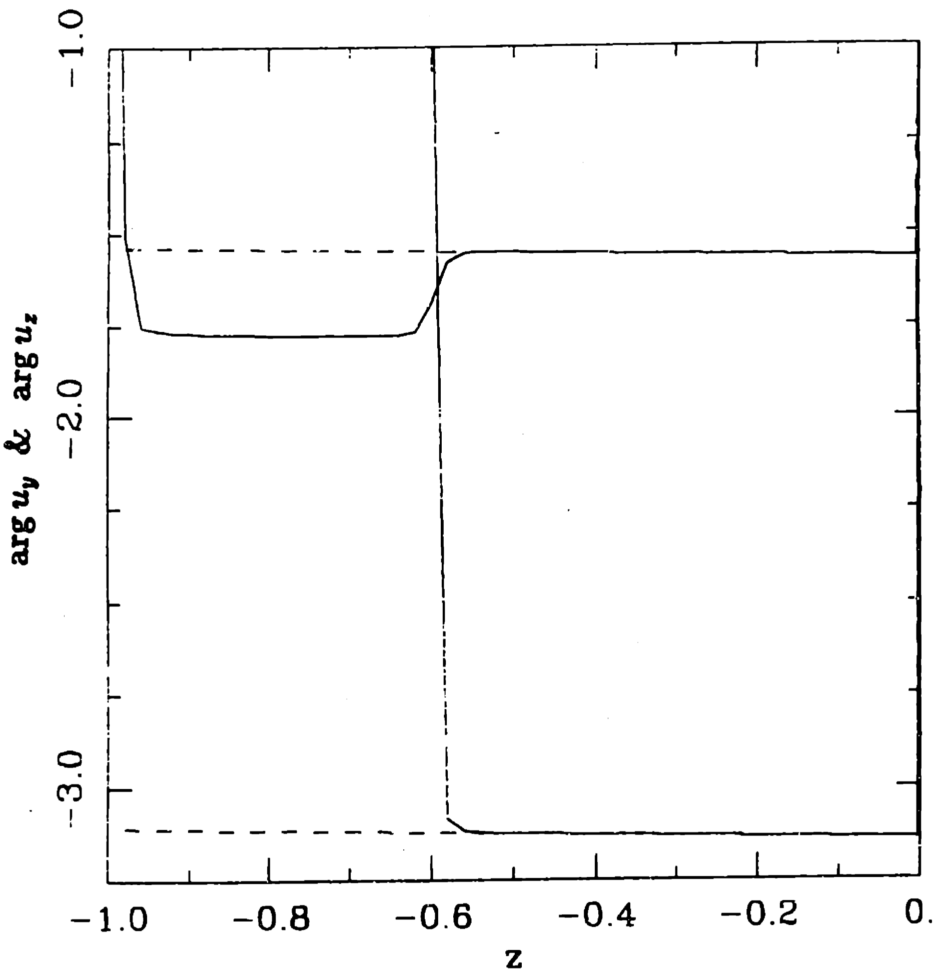

arg u_y & arg u_z, $f = 10^{-3}\ Hz$, $\lambda = 0.1\ mm$, arg u_z is lower.

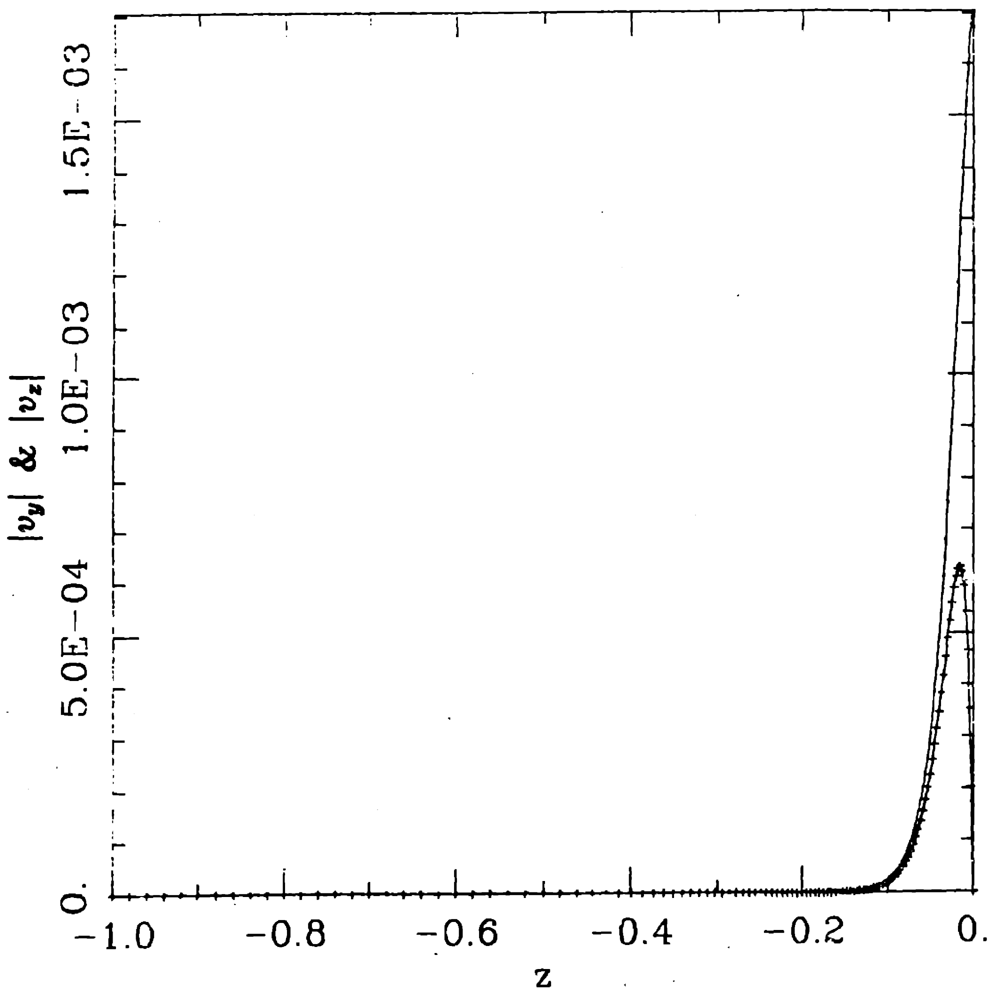

$|V_y|$ & $|V_z|$, $f = 10^{-3}\ Hz$, $\lambda = 0.1\ mm$, $|V_z|$ is lower.

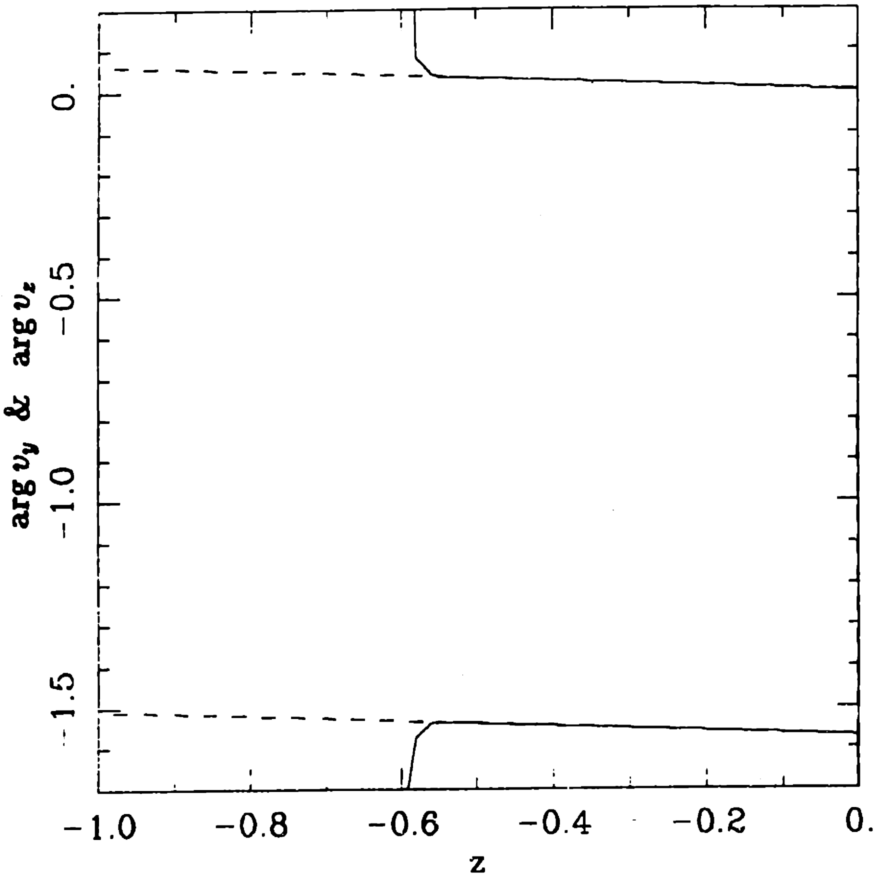

arg V_y & arg V_z, $f = 10^{-3}\ Hz$, $\lambda = 0.1\ mm$, arg V_z is lower.

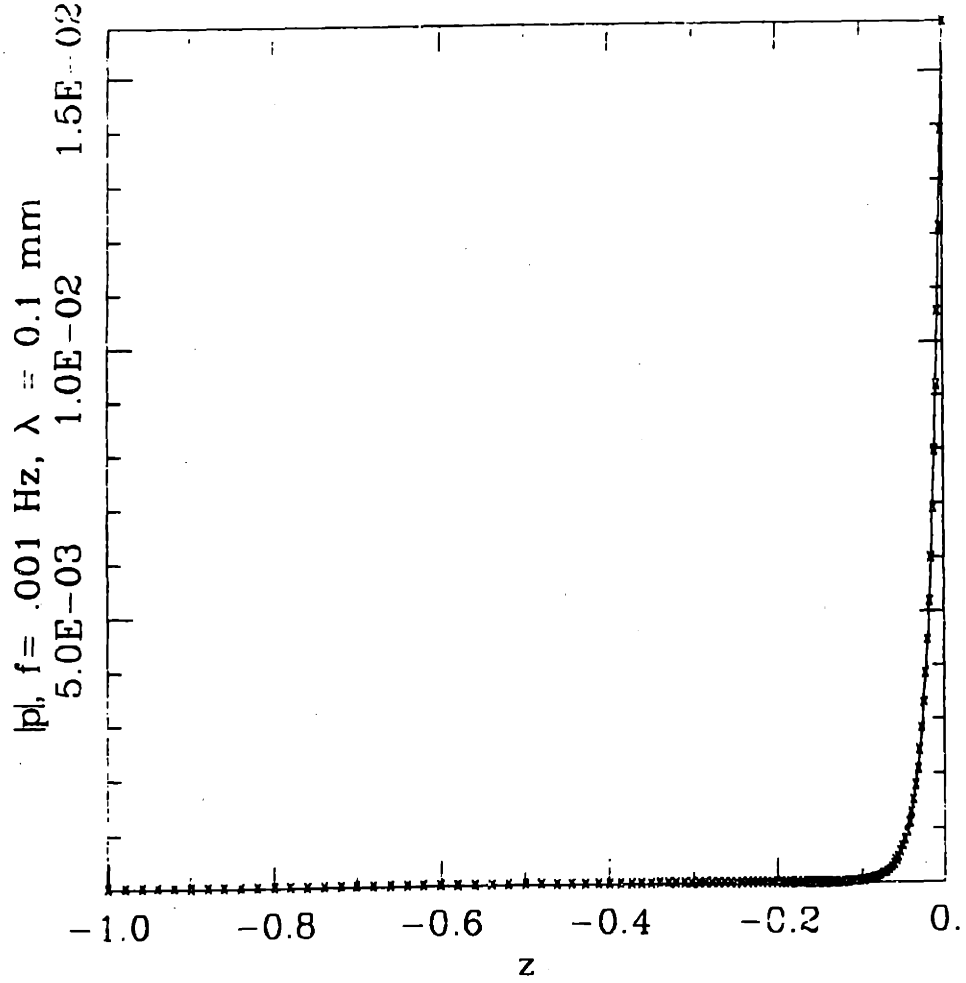

$|p|$, $f = 10^{-3}\ Hz$, $\lambda = 0.1\ mm$.

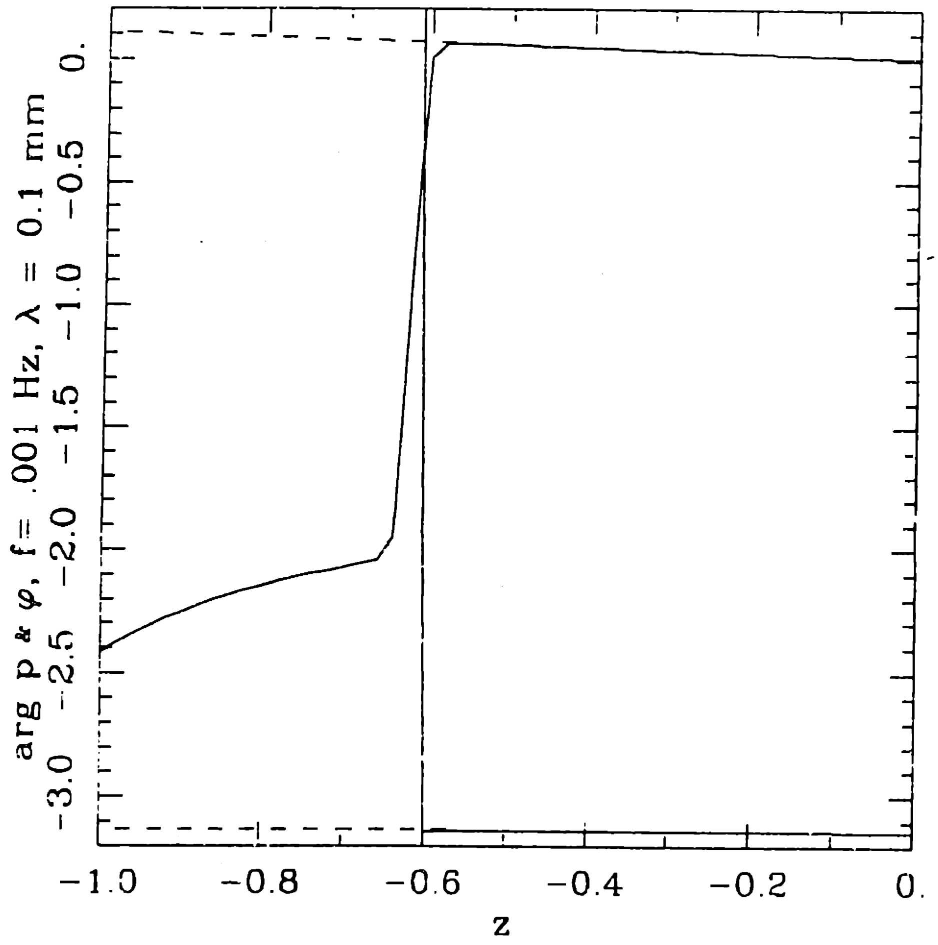

arg p & arg ϕ, $f = 10^{-3}$ Hz, $\lambda = 0.1$ mm, arg ϕ is lower.

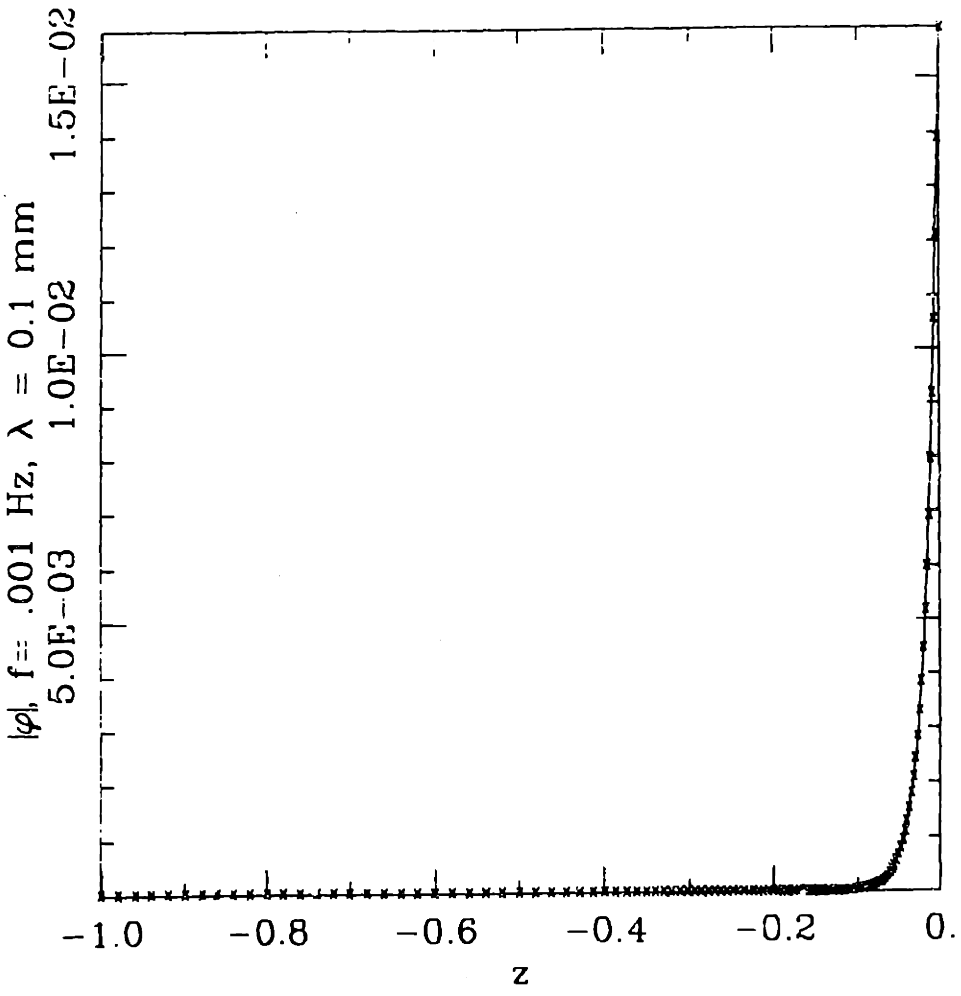

$|\phi|$, $f = 10^{-3}\ Hz$, $\lambda = 0.1\ mm$.

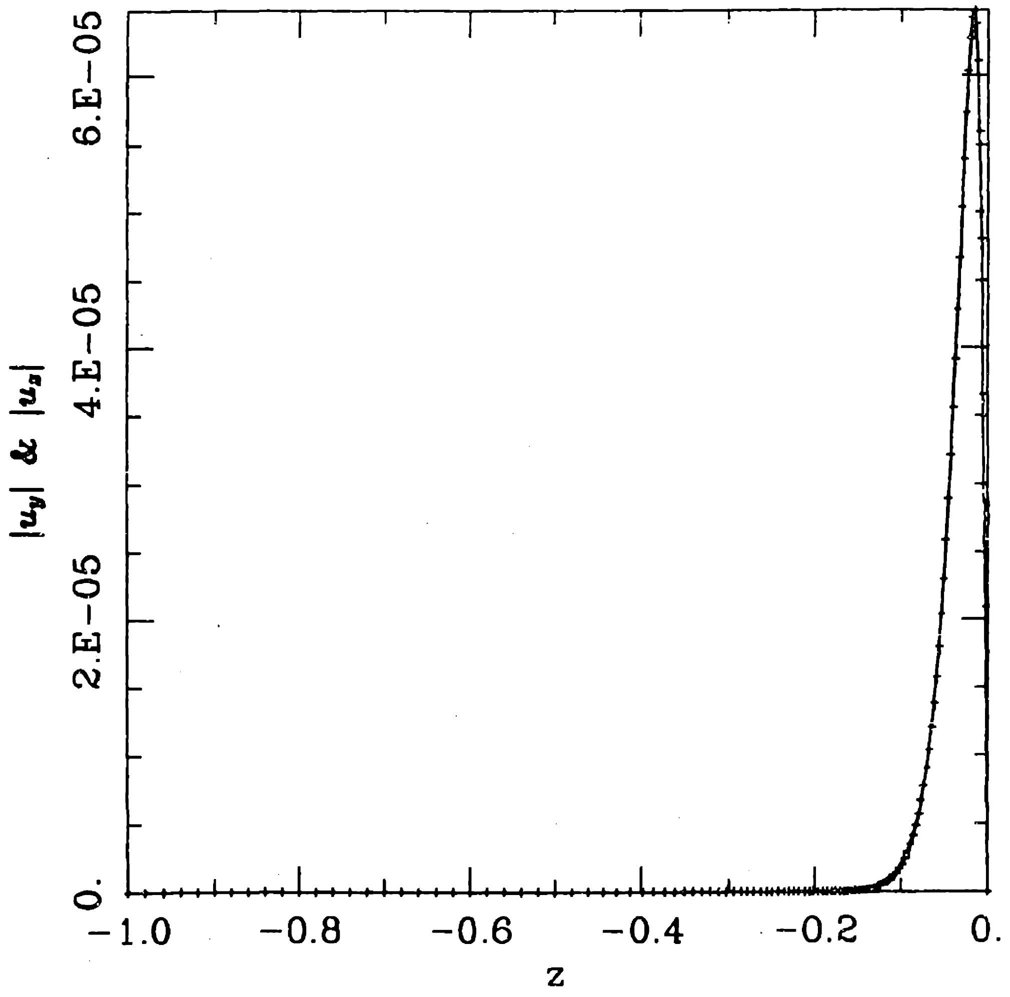

$|u_y|$ & $|u_z|$, $f = 0.1\ Hz$, $\lambda = 0.1\ mm$.

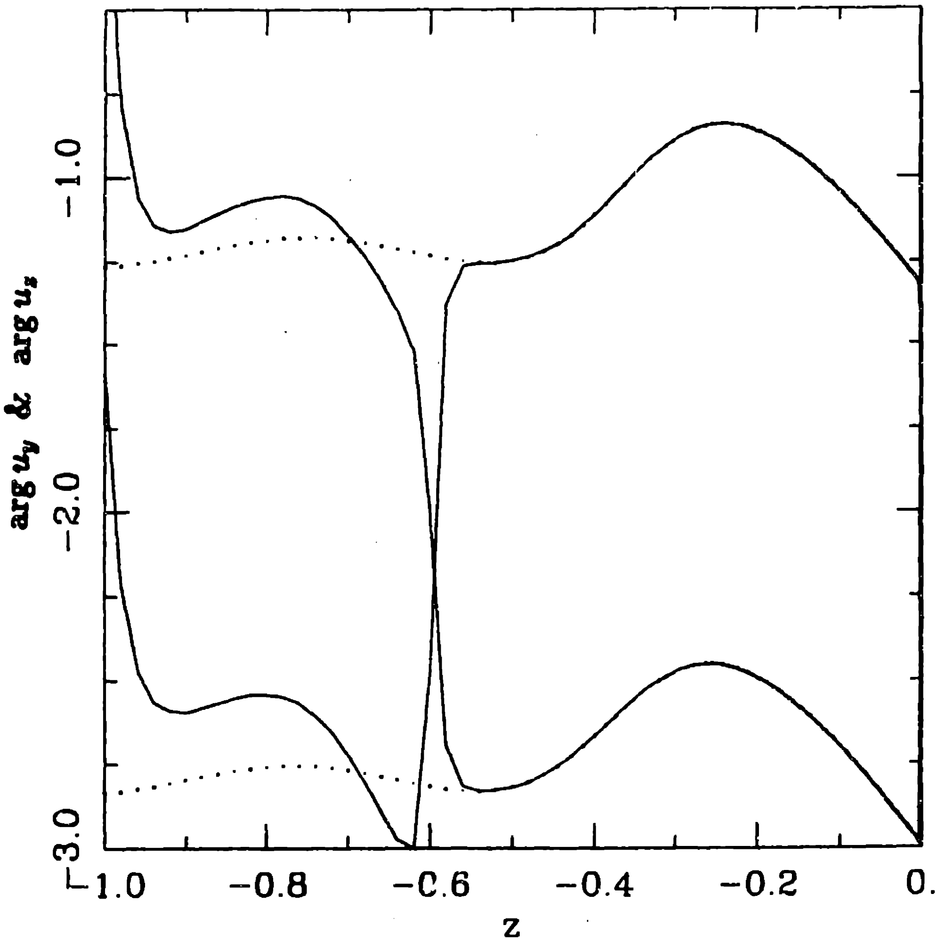

arg u_y & arg u_z, $f = 0.1\ Hz$, $\lambda = 0.1\ mm$, arg u_z is lower.

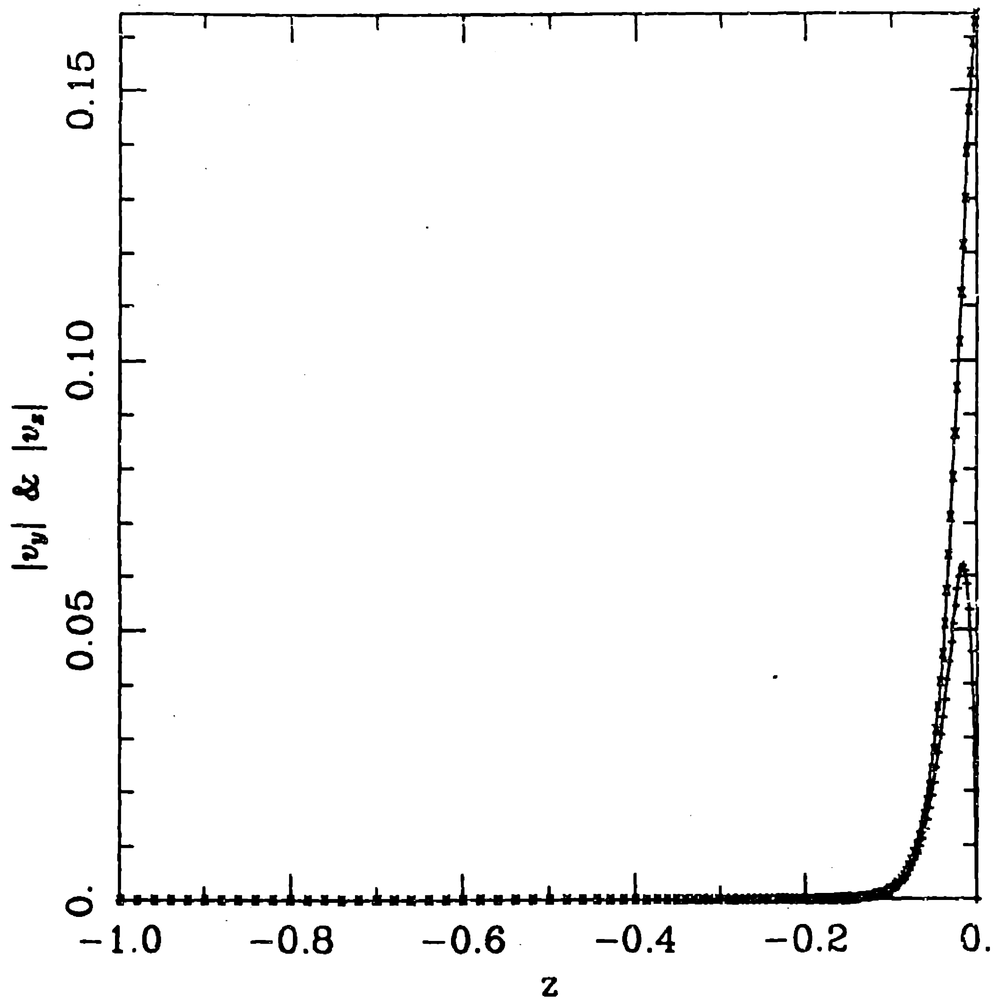

$|V_y|$ & $|V_z|$, $f = 0.1\ Hz$, $\lambda = 0.1\ mm$, $|V_z|$ is lower.

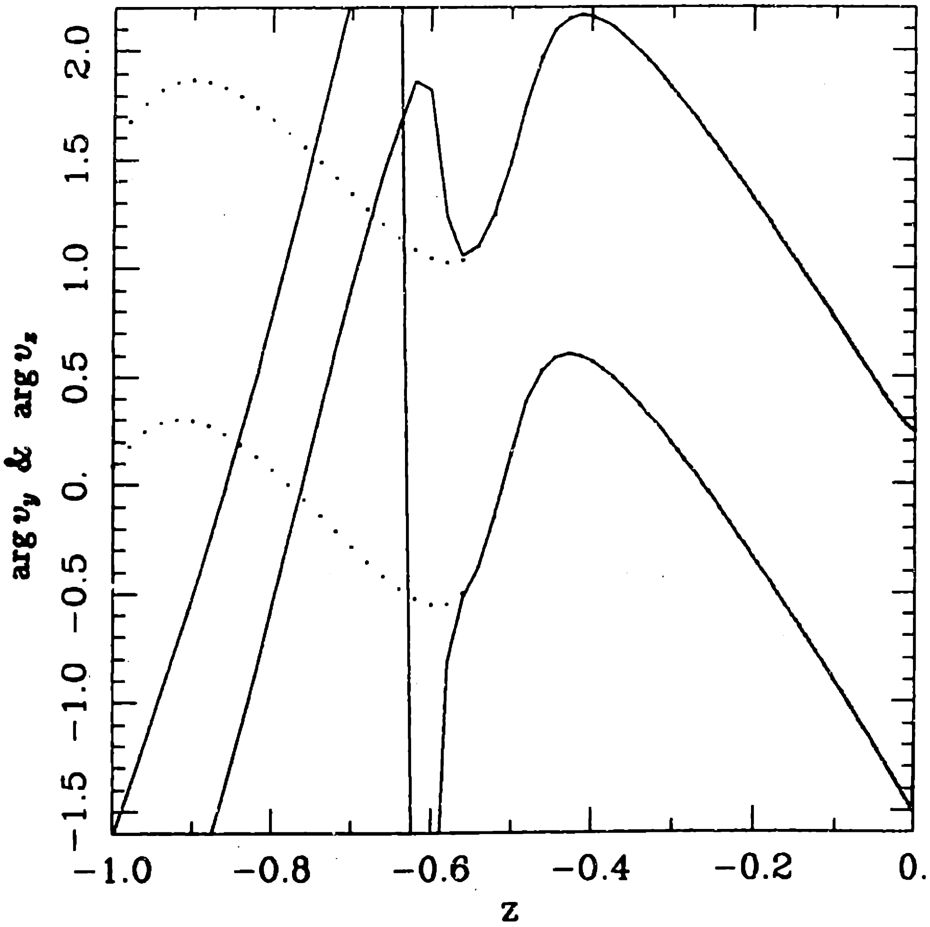

$\arg V_y$ & $\arg V_z$, $f = 0.1\ Hz$, $\lambda = 0.1\ mm$, $\arg V_z$ is lower.

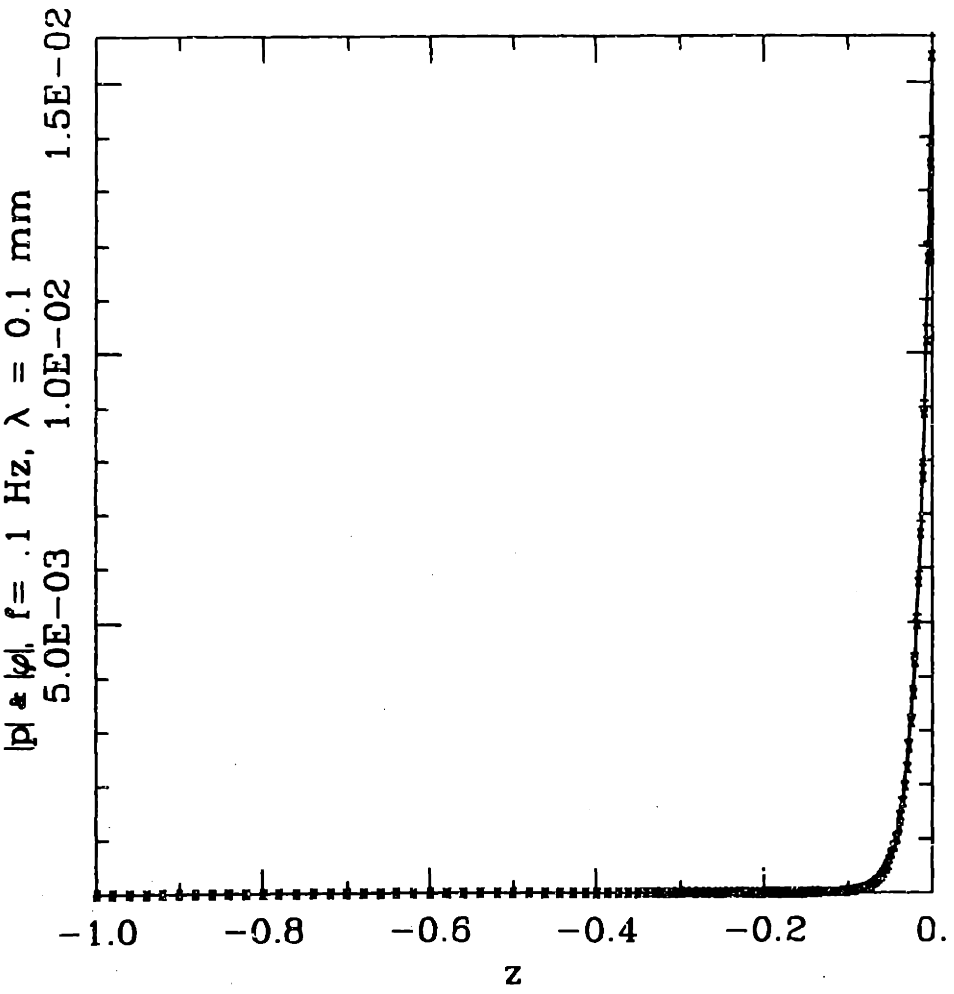

$|p|$ & $|\phi|$, $f = 0.1$ Hz, $\lambda = 0.1$ mm. The four curves are all but indistinguishable.

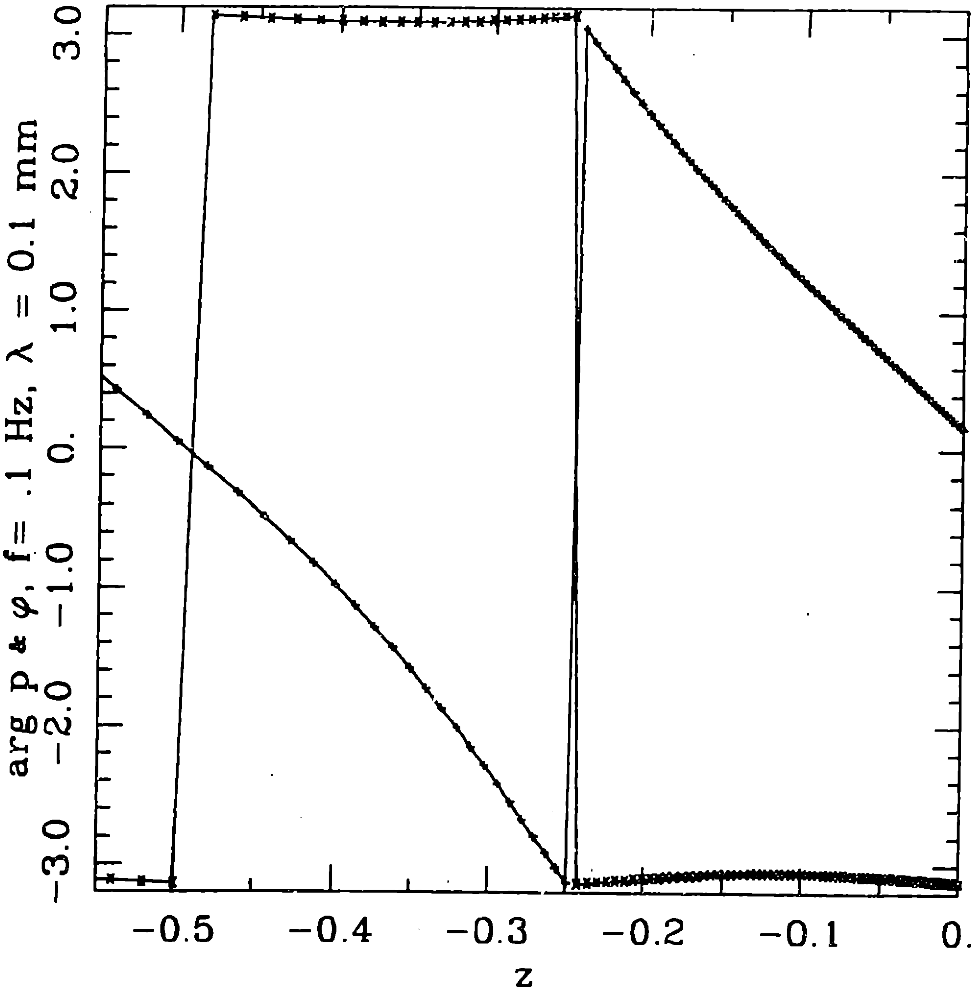

arg p & arg ϕ, $f = 0.1\ Hz$, $\lambda = 0.1\ mm$, arg ϕ is lower.

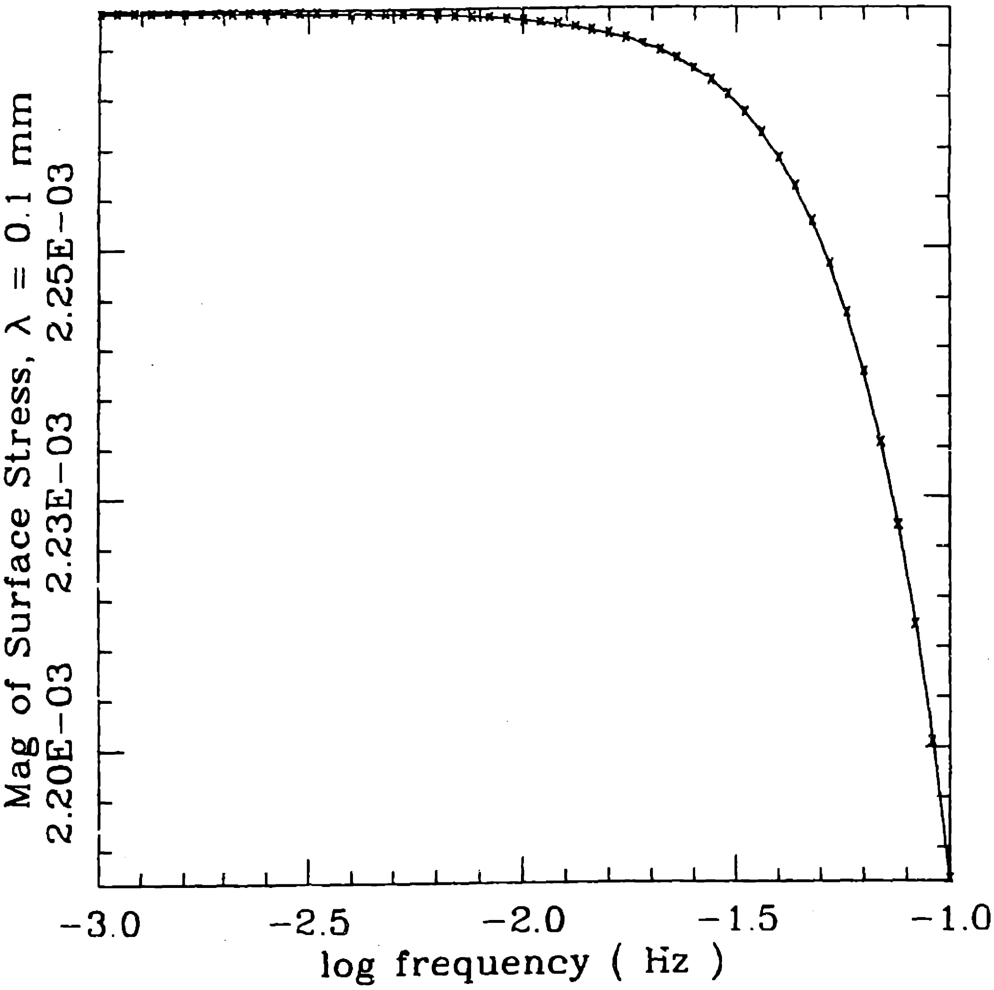

$|s|$, $\lambda = 0.1$ *mm*, $f = 10^{-3}$ to 0.1 *Hz*.

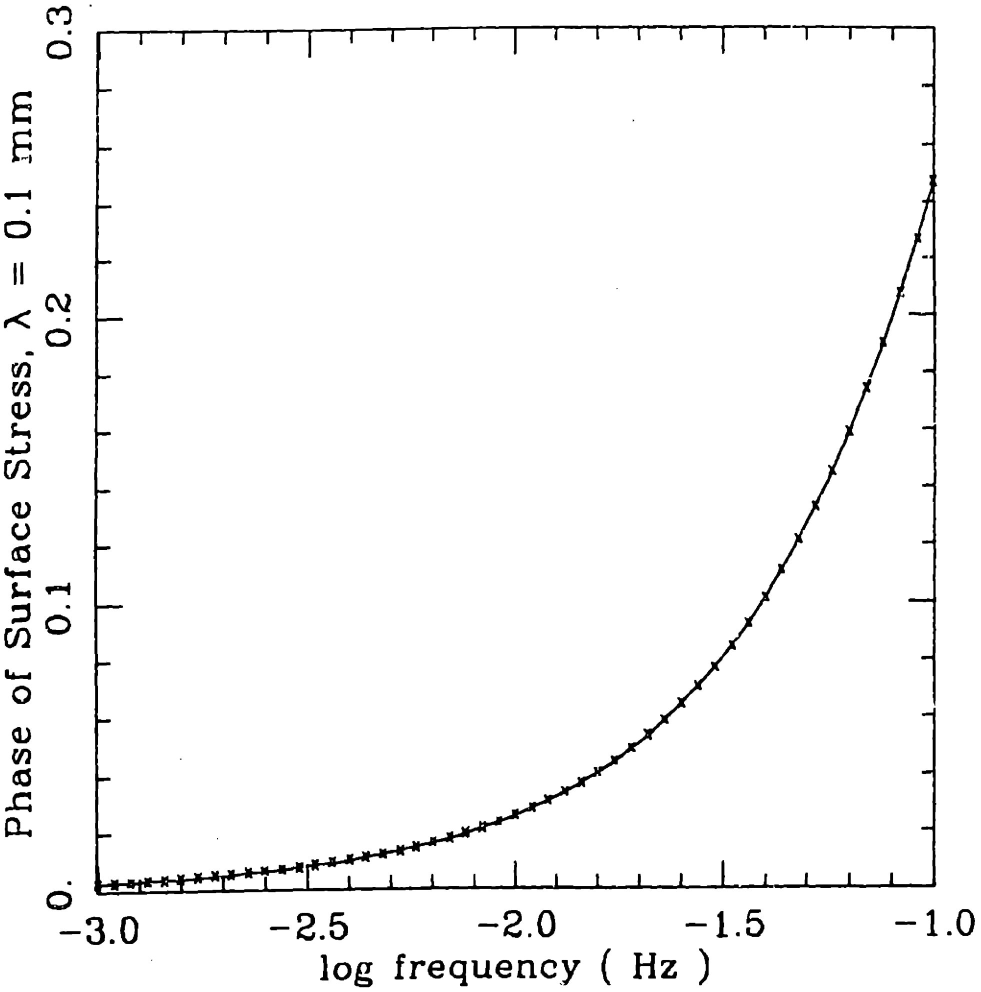

arg s, $\lambda = 0.1$ *mm*, $f = 10^{-3}$ to 0.1 *Hz*.

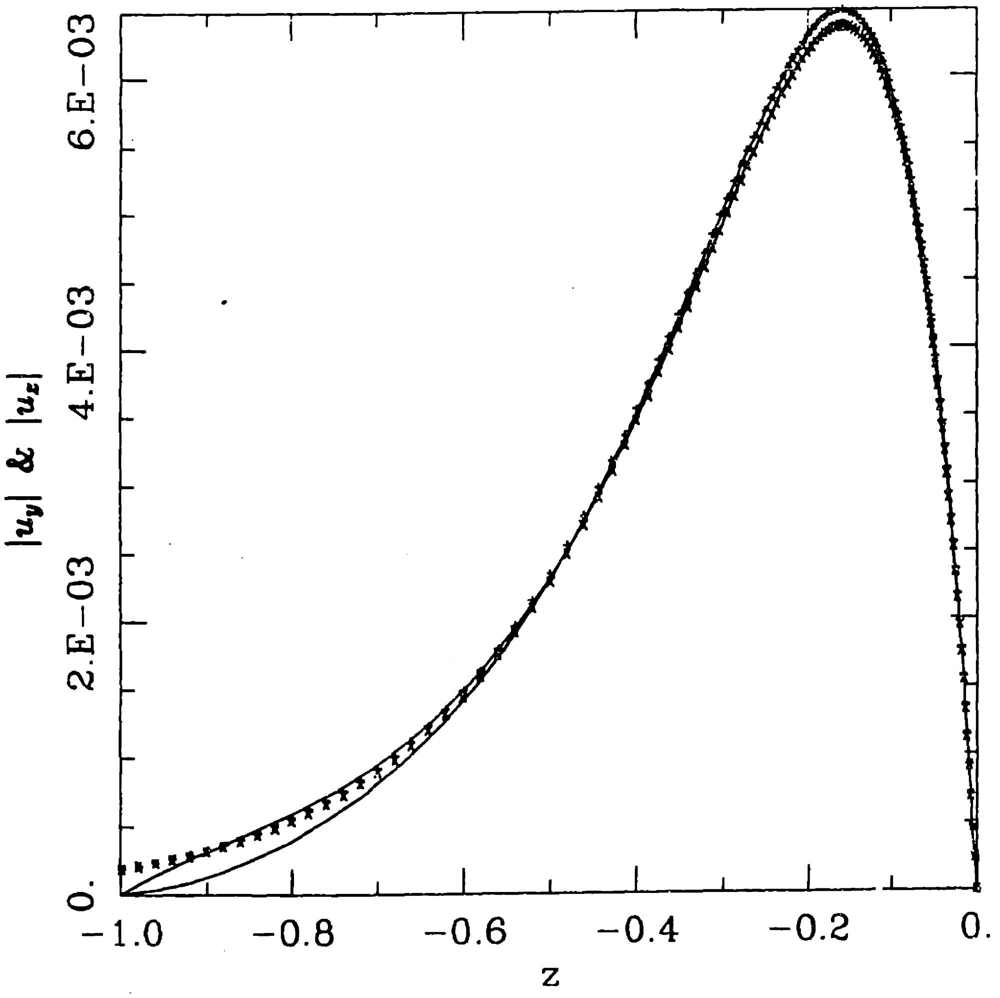

$|u_y|$ & $|u_z|$, $f = 10^{-3}$ Hz, $\lambda = 1.0$ mm, $|u_z|$ has the greater maximum.

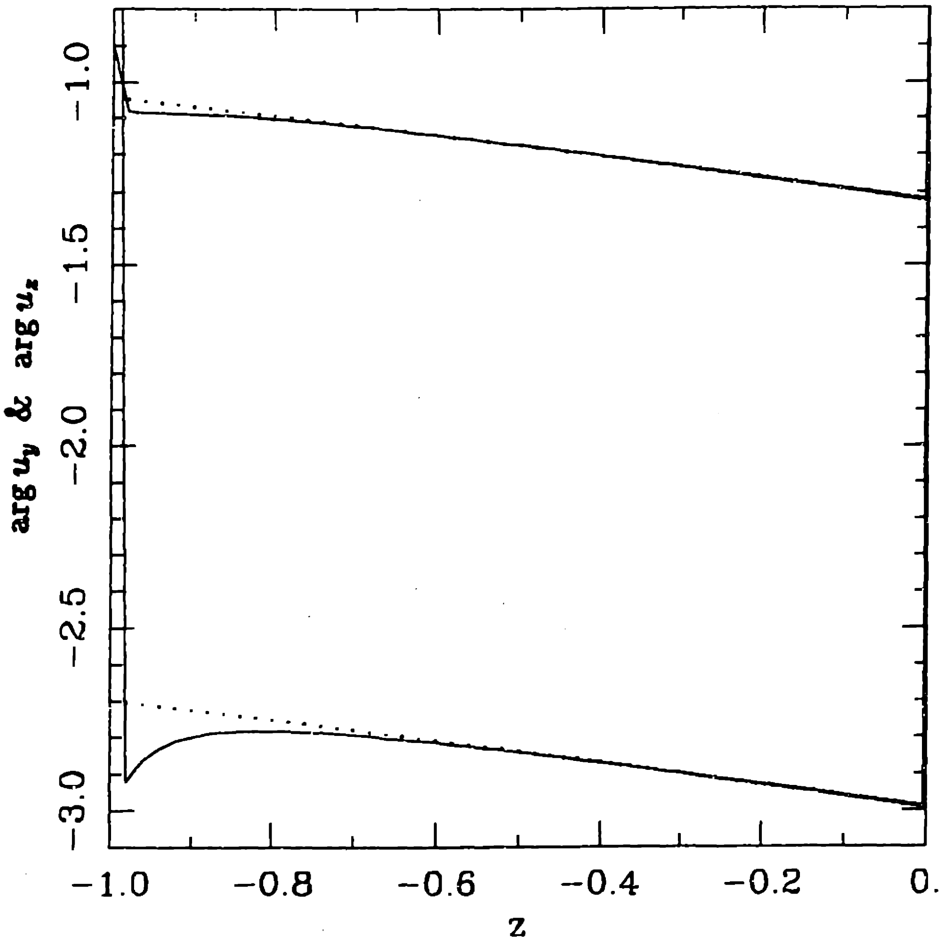

arg u_y & arg v_z, $f = 10^{-3}$ Hz, $\lambda = 1.0$ mm, arg u_z is lower.

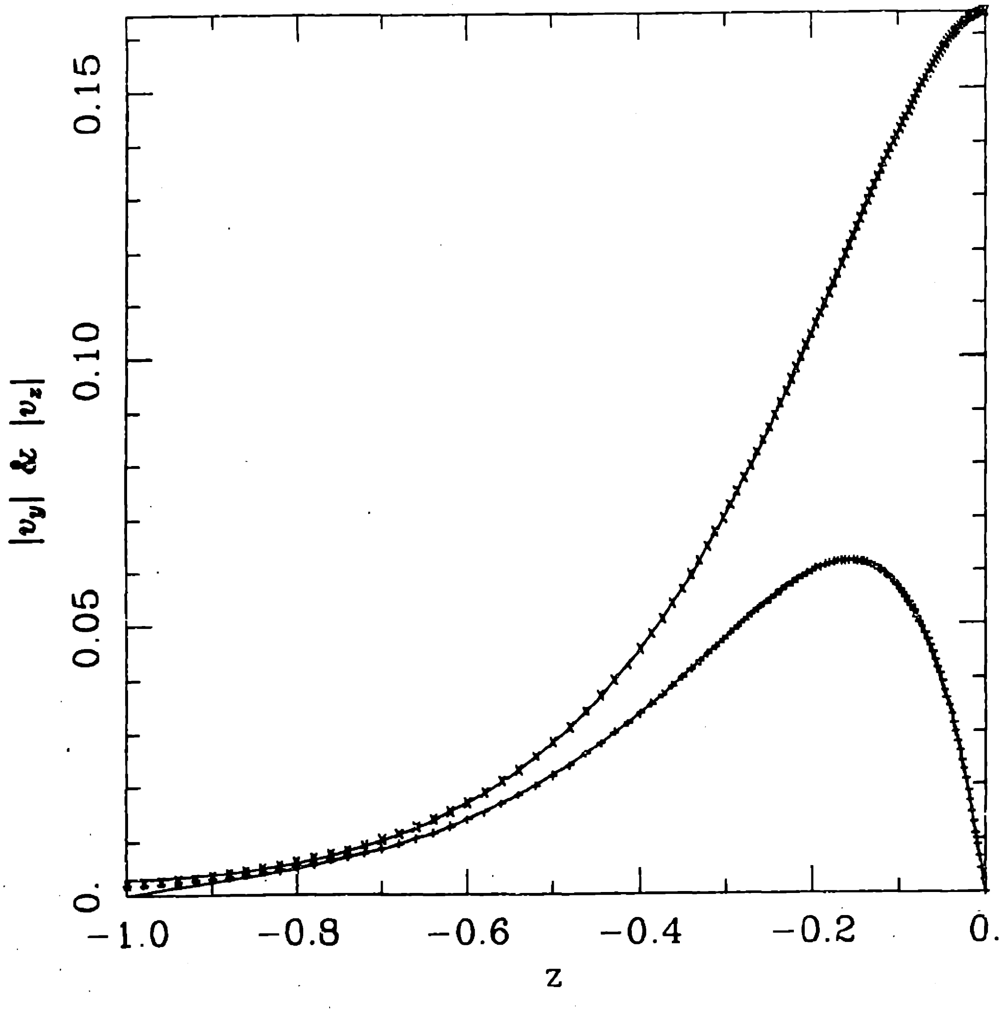

$|V_y|$ & $|V_z|$, $f = 10^{-3}\,Hz$, $\lambda = 1.0\,mm$, $|V_z|$ is lower.

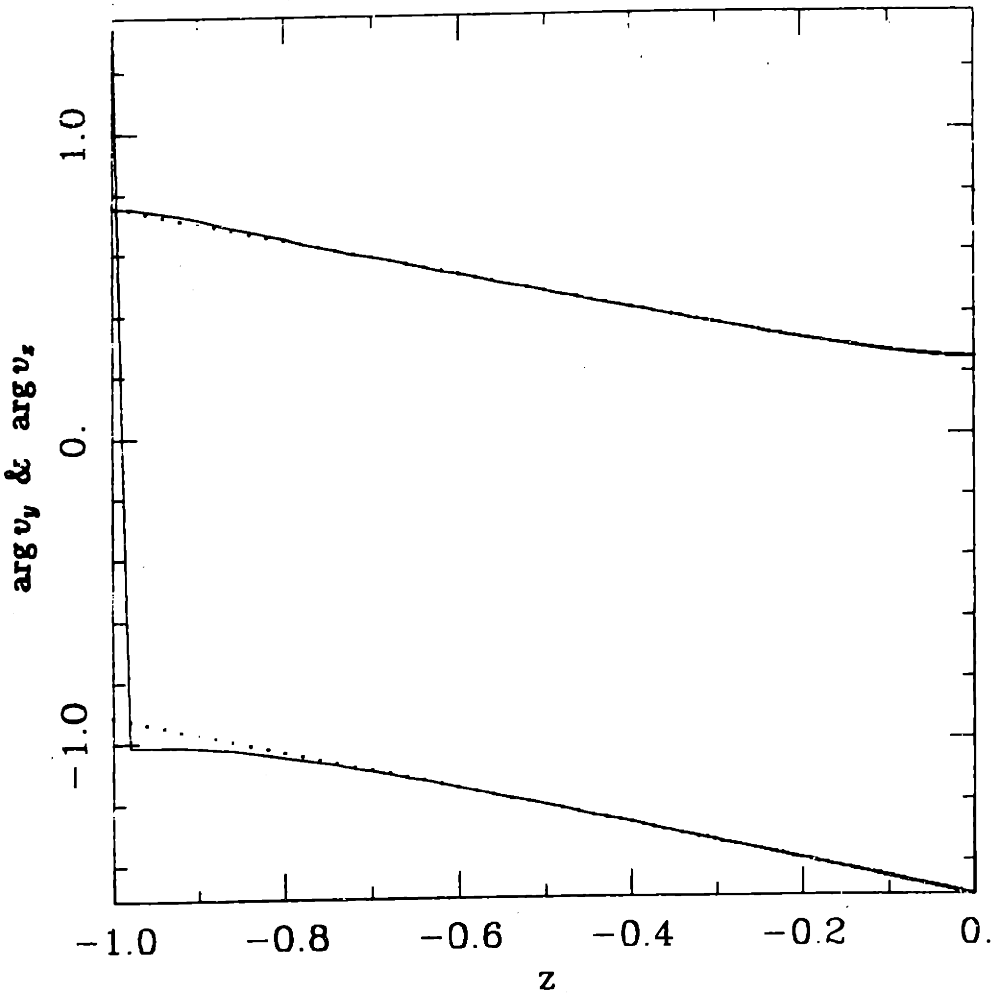

arg V_y & arg V_z, $f = 10^{-3}$ Hz, $\lambda = 1.0$ mm, arg V_z is lower.

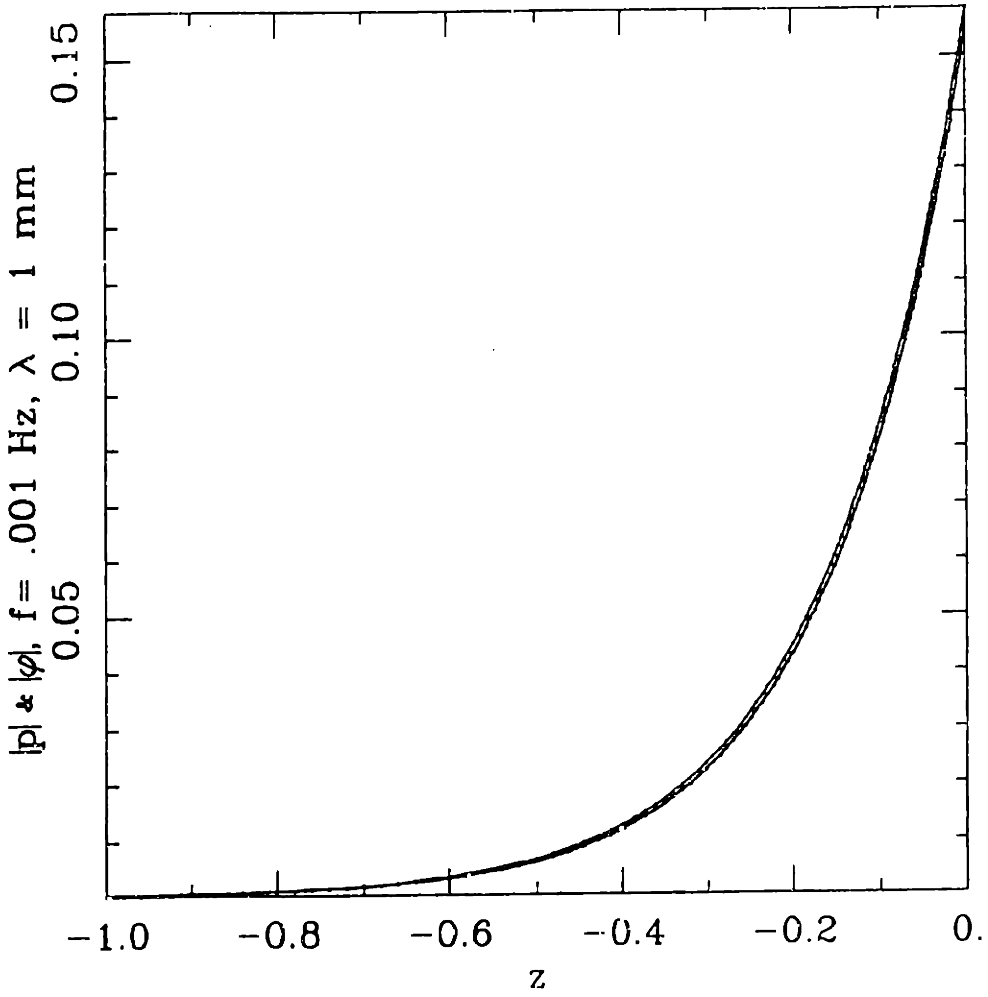

$|p|$ & $|\phi|$, $f = 10^{-3}\ Hz$, $\lambda = 1.0\ mm$.

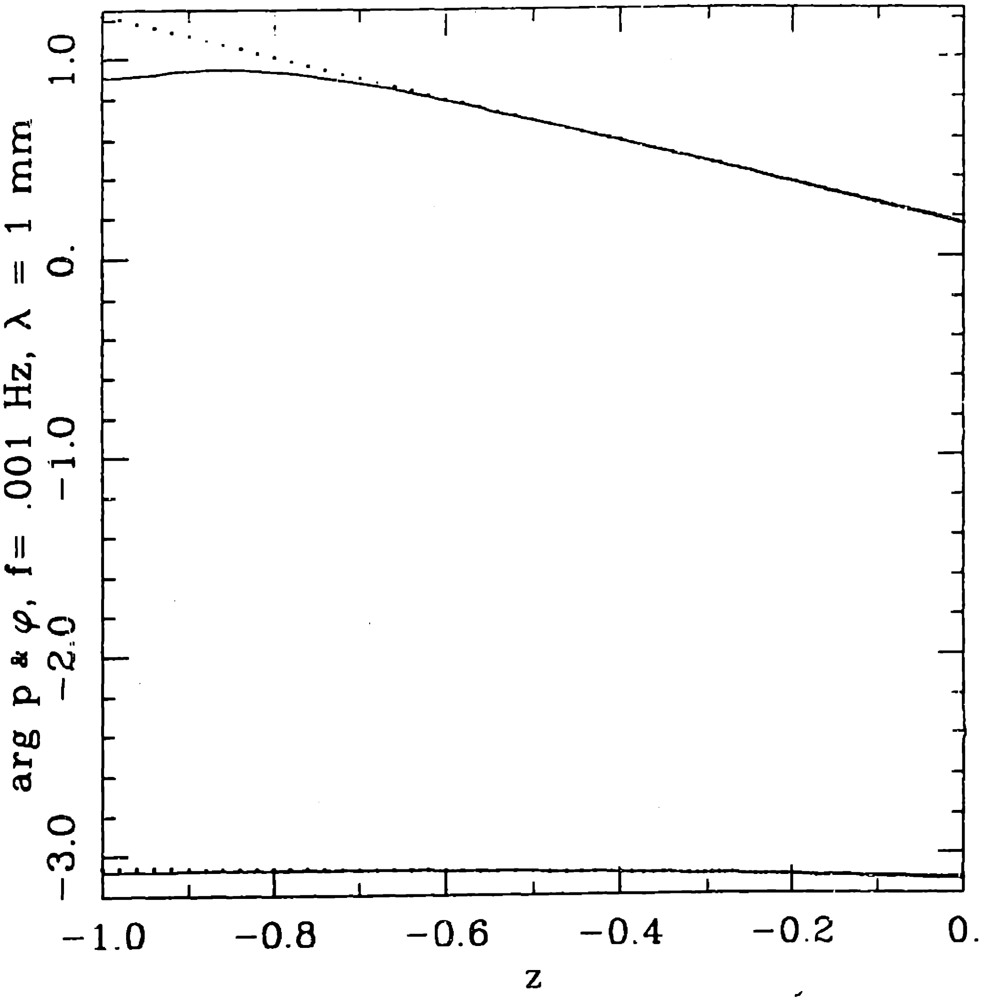

arg p & arg ϕ, $f = 10^{-3}$ Hz, $\lambda = 1.0$ mm, arg ϕ is lower.

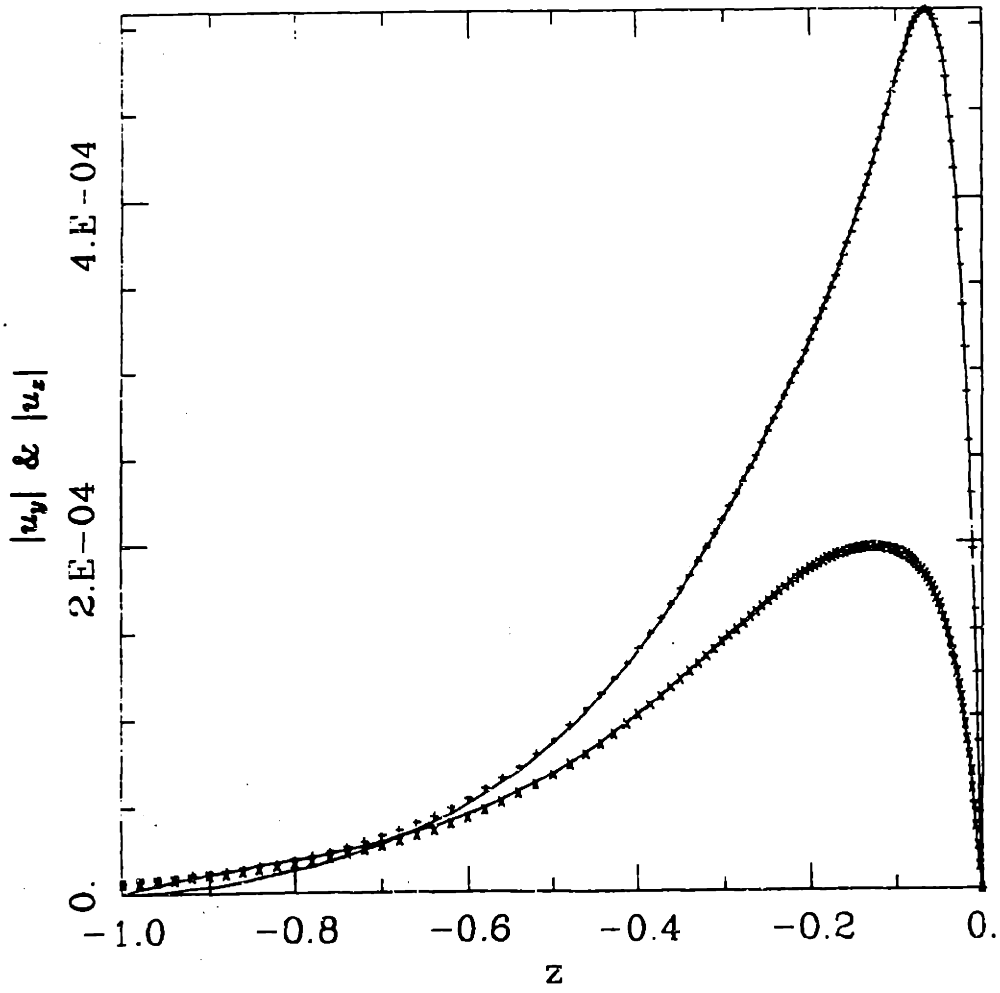

$|u_y|$ & $|u_z|$, $f = 0.1\ Hz$, $\lambda = 1.0\ mm$, $|u_z|$ has the greater maximum.

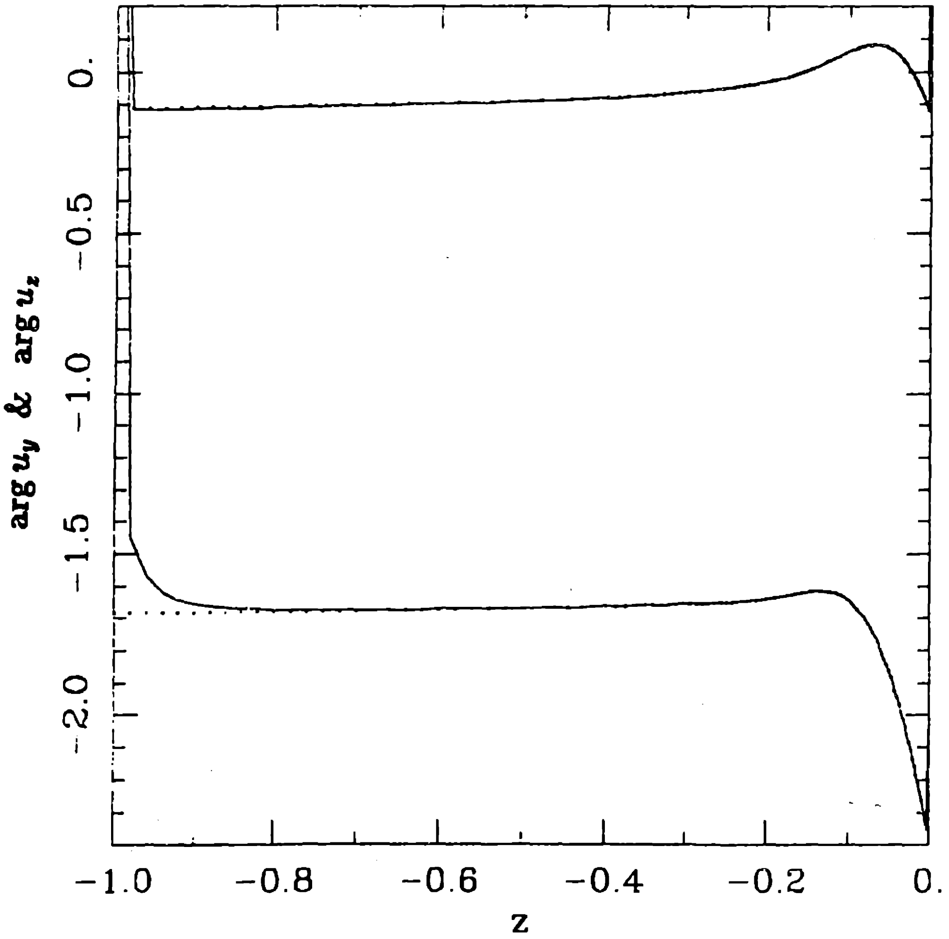

arg u_y & arg u_z, $f = 0.1\ Hz$, $\lambda = 1.0\ mm$, arg u_z is lower.

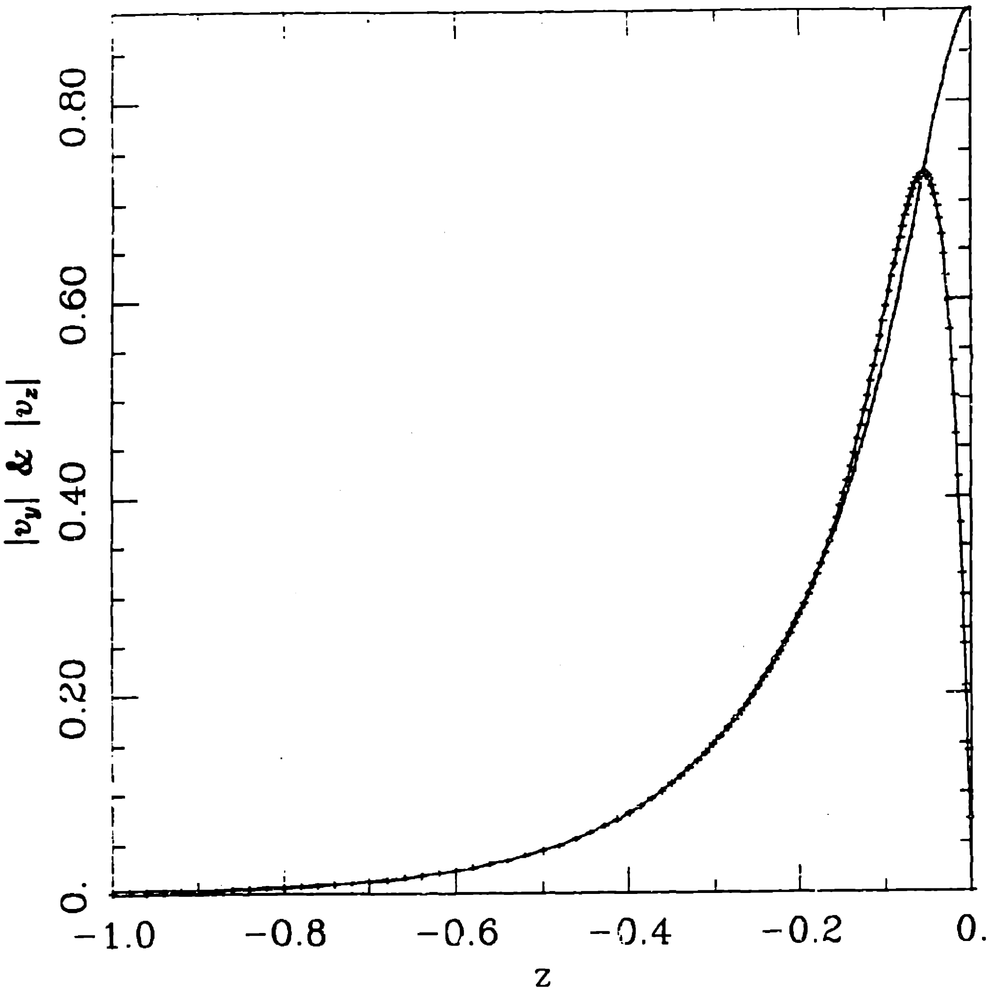

$|V_y|$ & $|V_z|$, $f = 0.1\ Hz$, $\lambda = 1.0\ mm$, $|V_z|$ is lower.

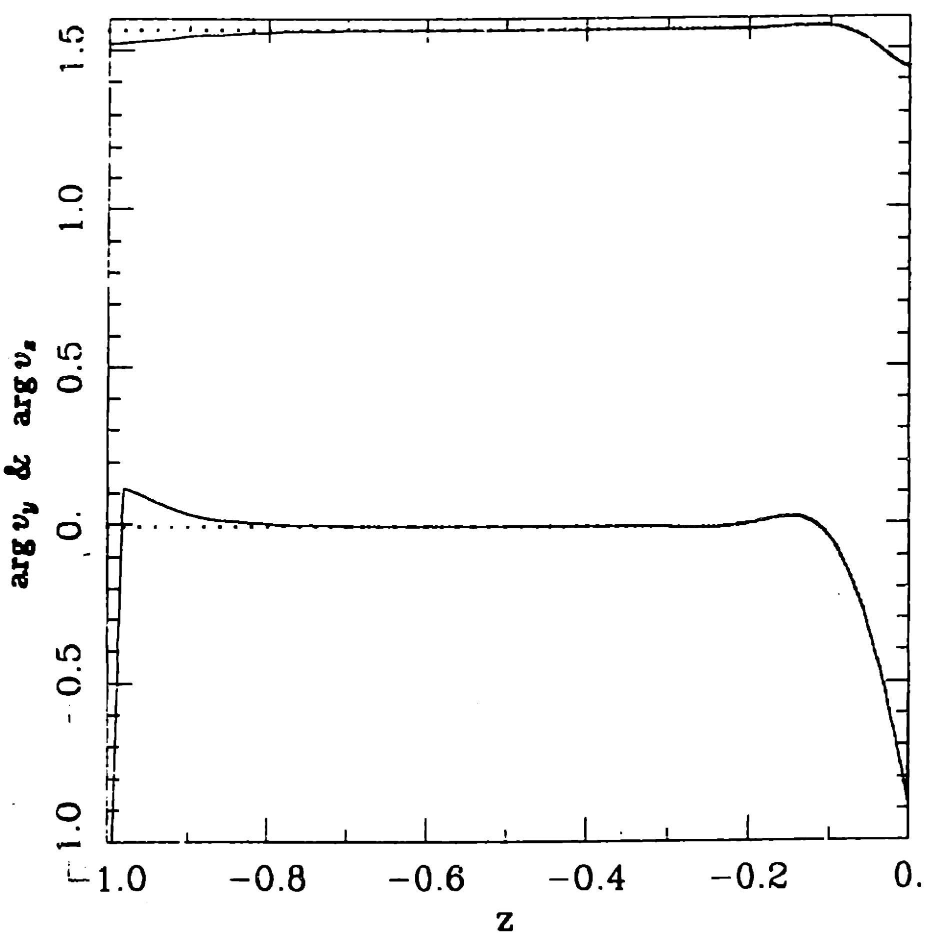

$\arg V_y$ & $\arg V_z$, $f = 0.1\ Hz$, $\lambda = 1.0\ mm$, $\arg V_z$ is lower.

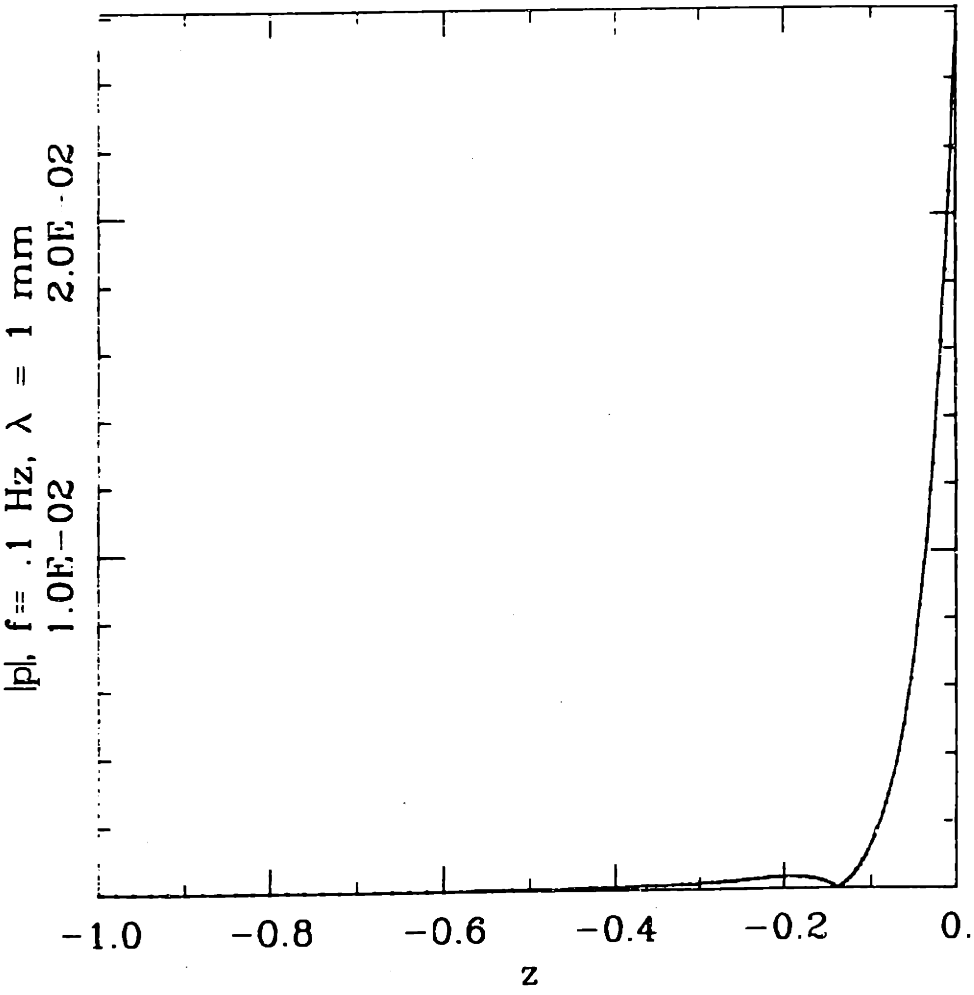

$|p|$, $f = 0.1\ Hz$, $\lambda = 1.0\ mm$.

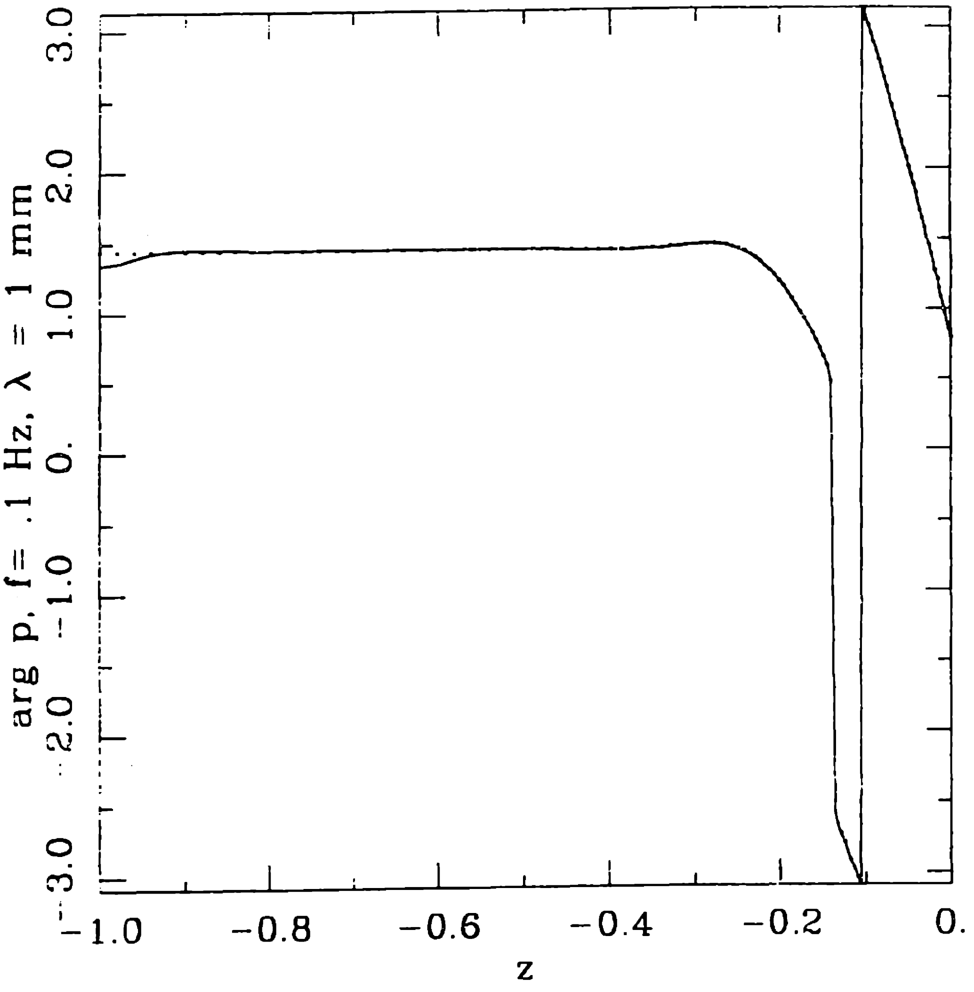

arg p, $f = 0.1\ Hz$, $\lambda = 1.0\ mm$.

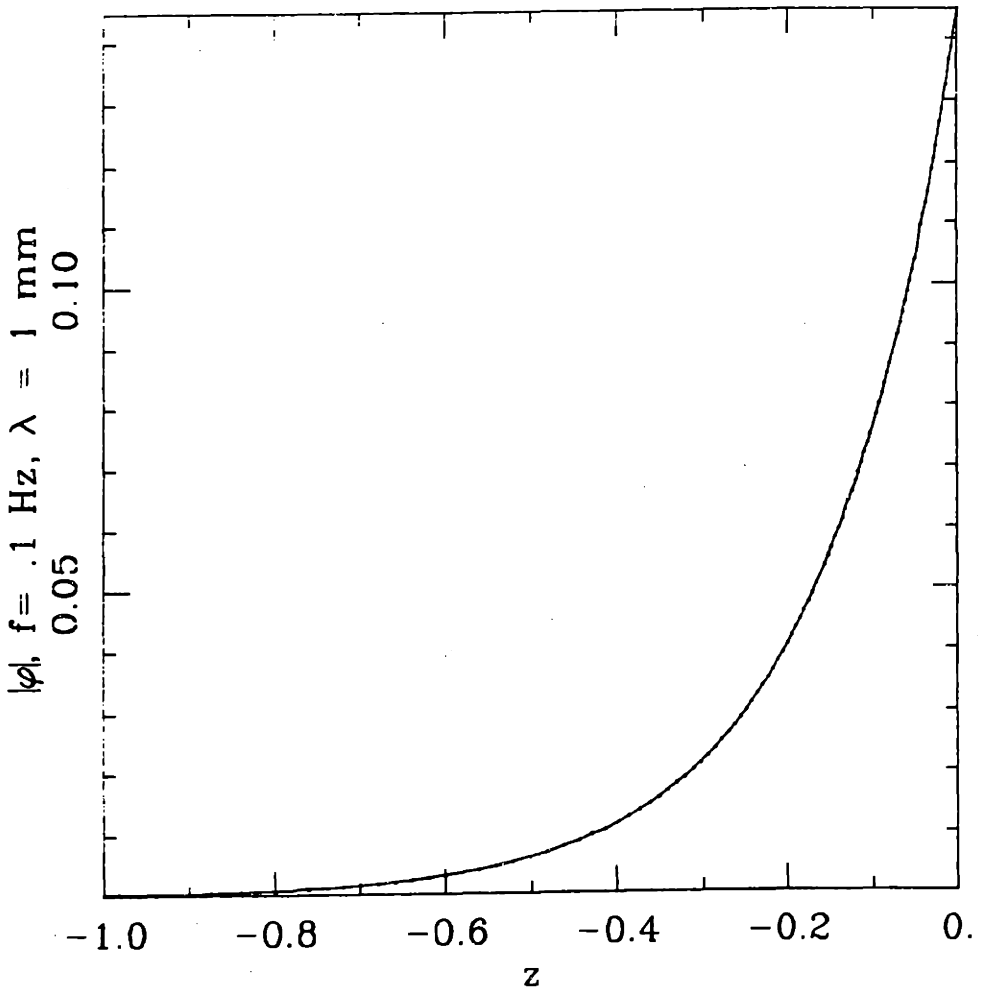

$|\phi|$, $f = 0.1\ Hz$, $\lambda = 1.0\ mm$.

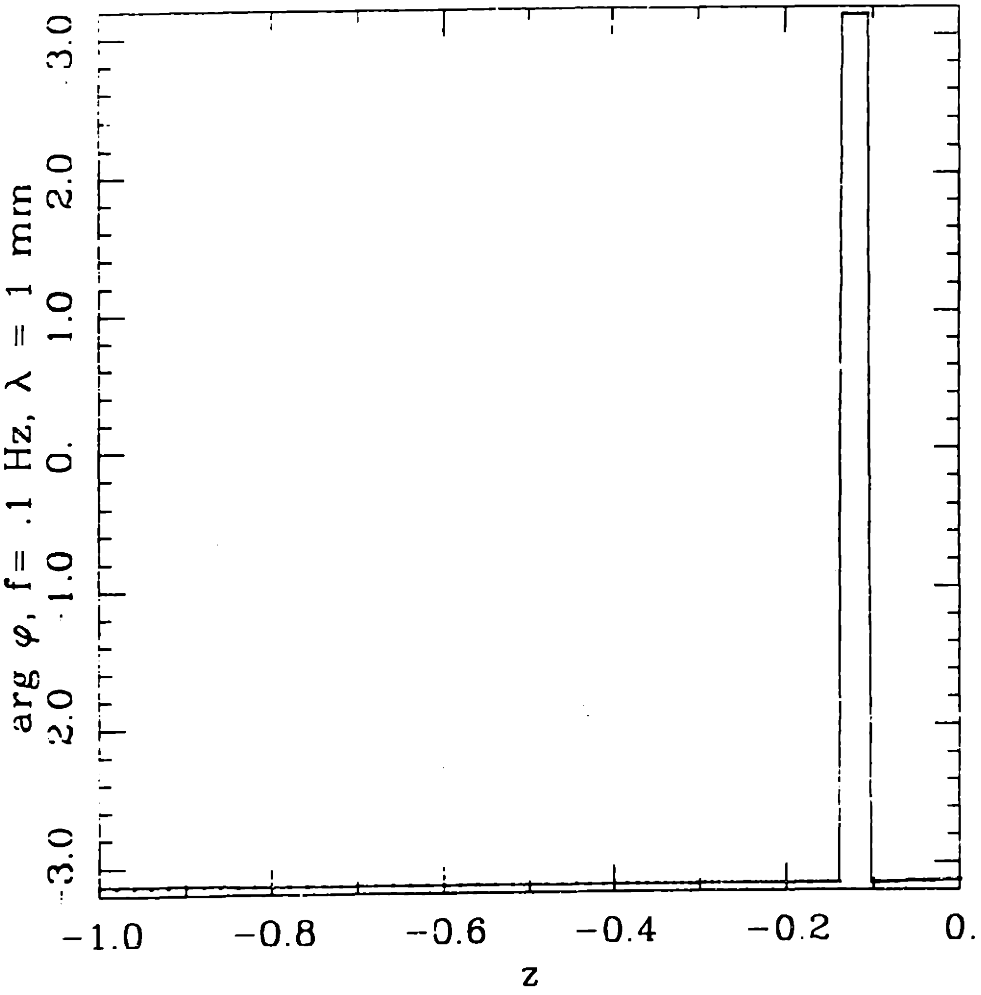

arg ϕ, $f = 0.1$ *Hz*, $\lambda = 1.0$ *mm*.

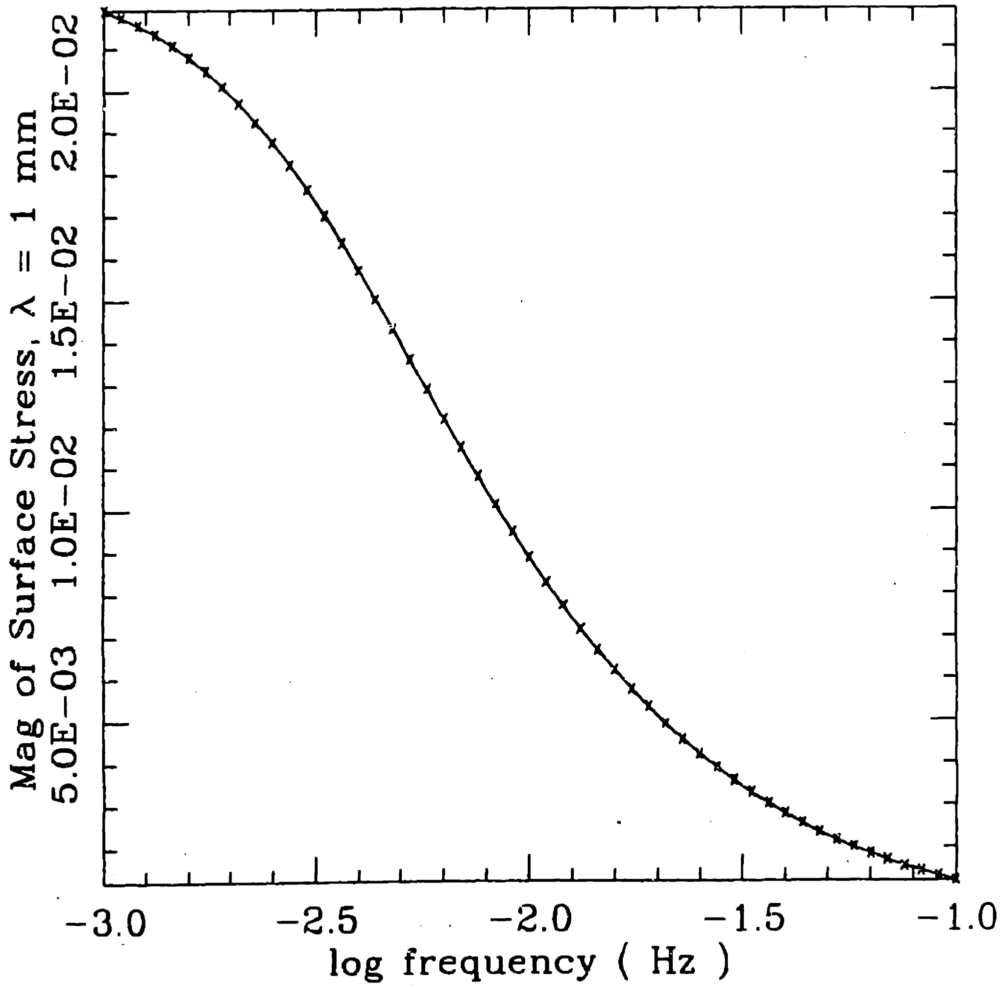

$|s|$, $\lambda = 1.0\,mm$, $f = 10^{-3}$ to $0.1\,Hz$.

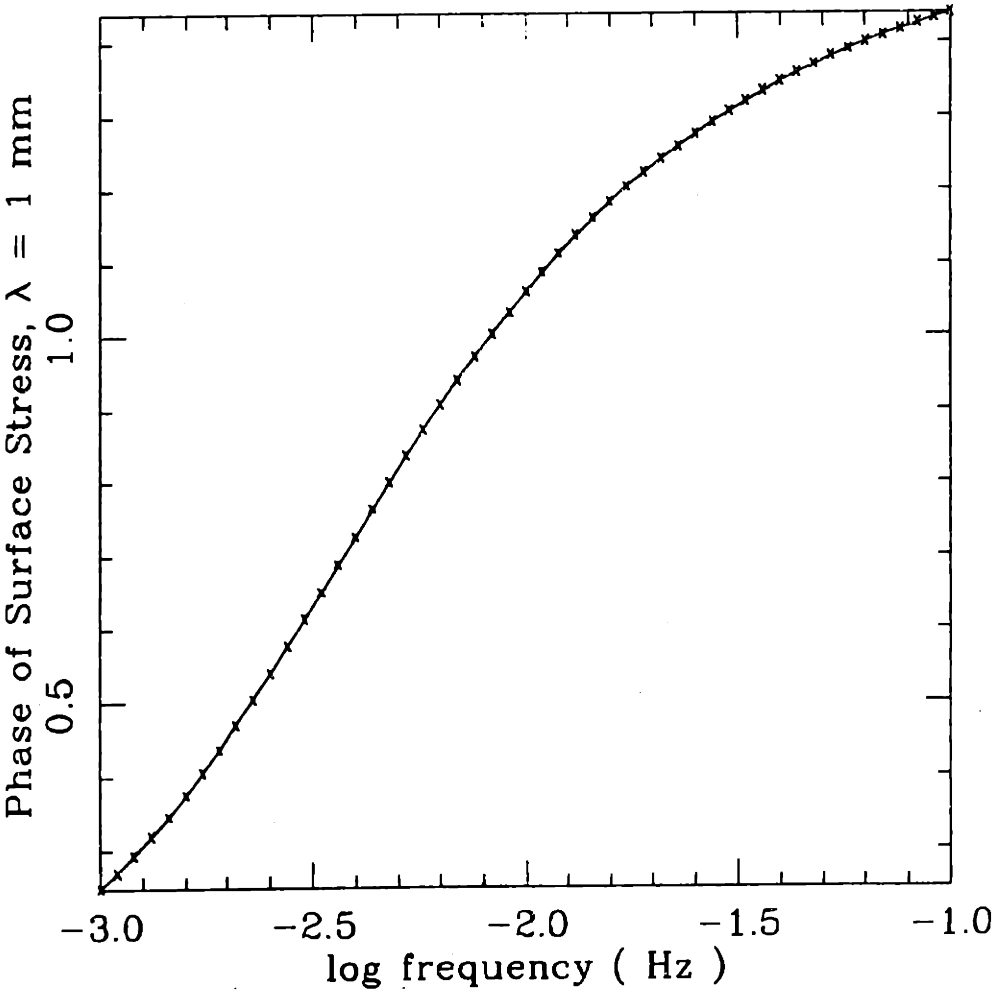

arg s, $\lambda = 1.0\ mm$, $f = 10^{-3}$ to 0.1 Hz.

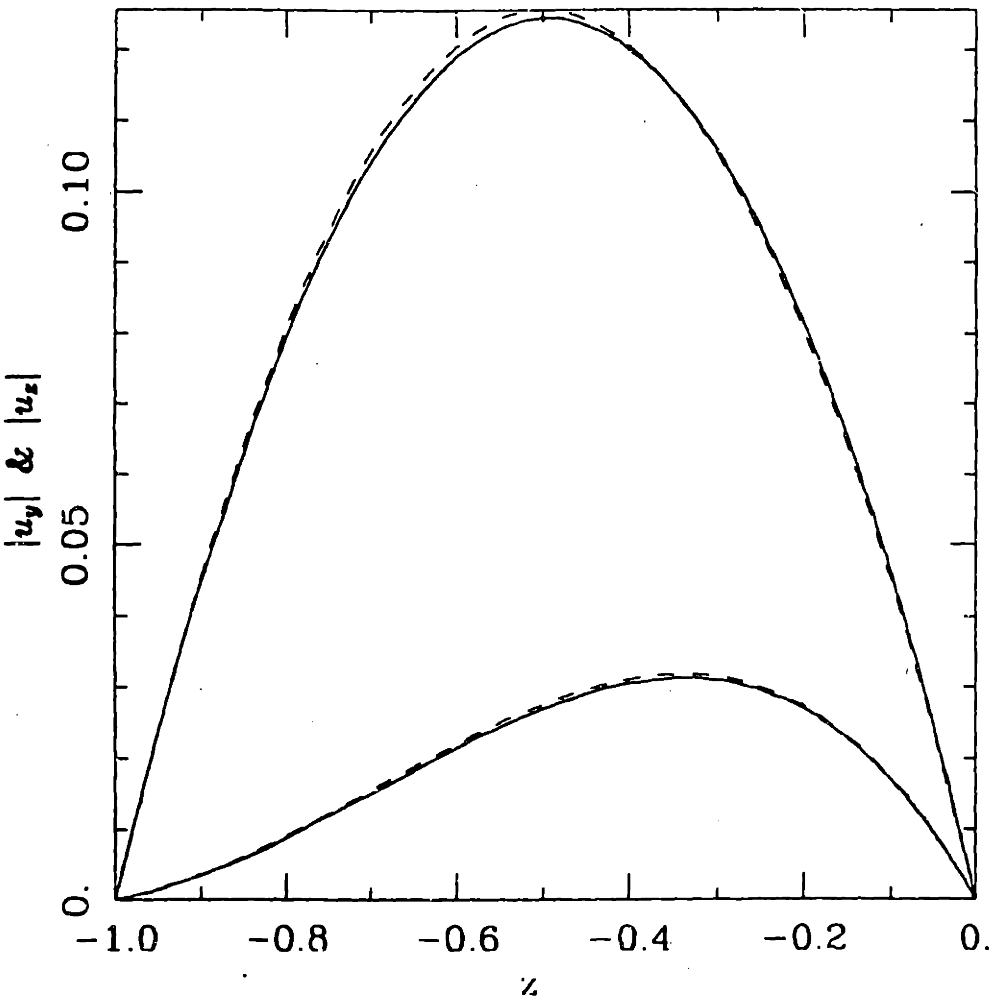

$|u_y|$ & $|u_z|$, $f = 10^{-3}\ Hz$, $\lambda = 10.0\ mm$, $|u_y|$ **has the greater maximum.**

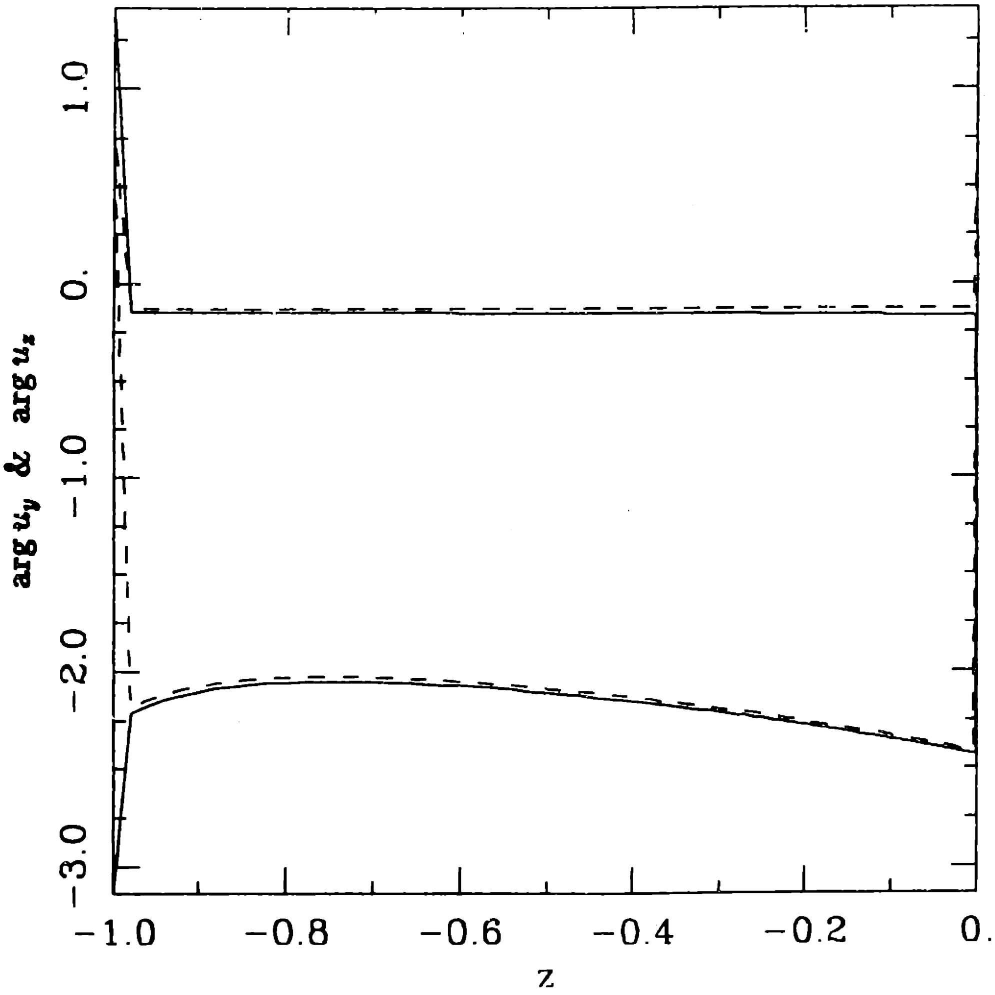

arg u_y & arg u_z, $f = 10^{-3}\,Hz$, $\lambda = 10.0\,mm$.

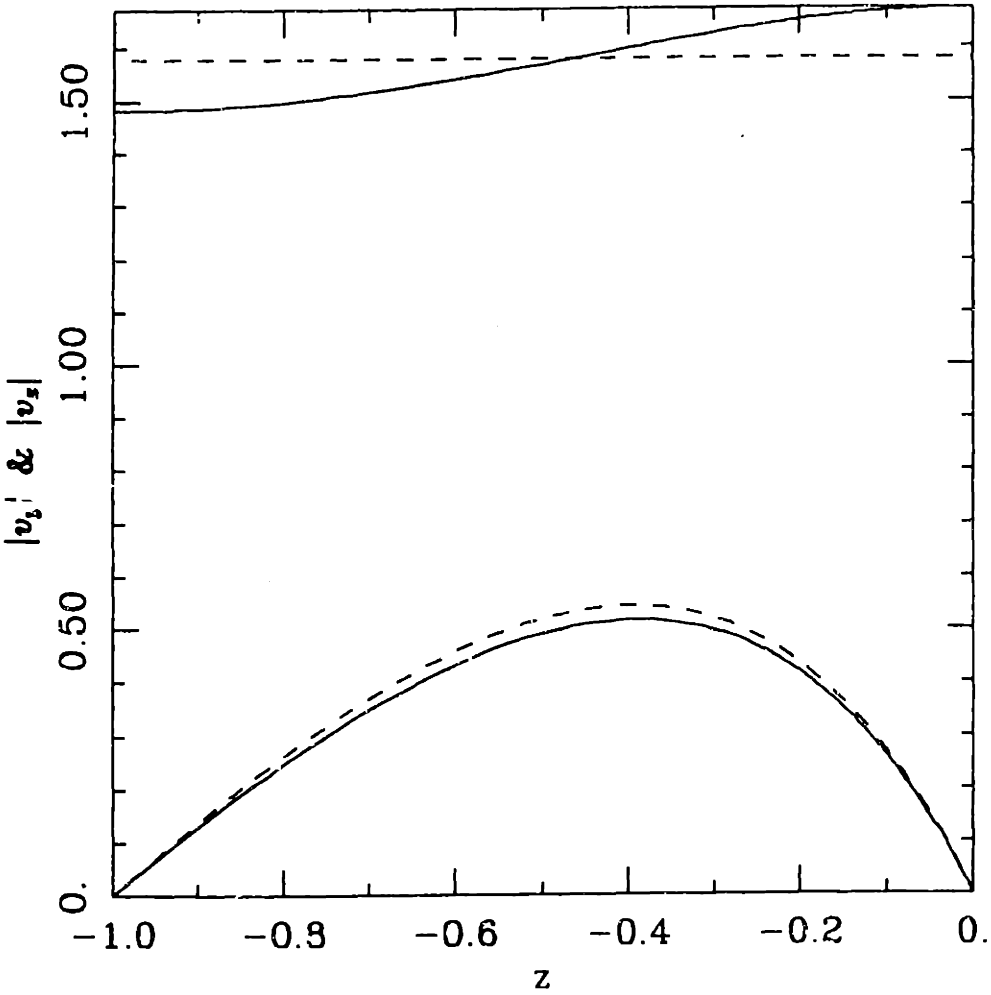

$|V_y|$ & $|V_z|$, $f = 10^{-3}$ *Hz*, $\lambda = 10.0$ *mm*. Note that an average value is obtained for $|V_y|$.

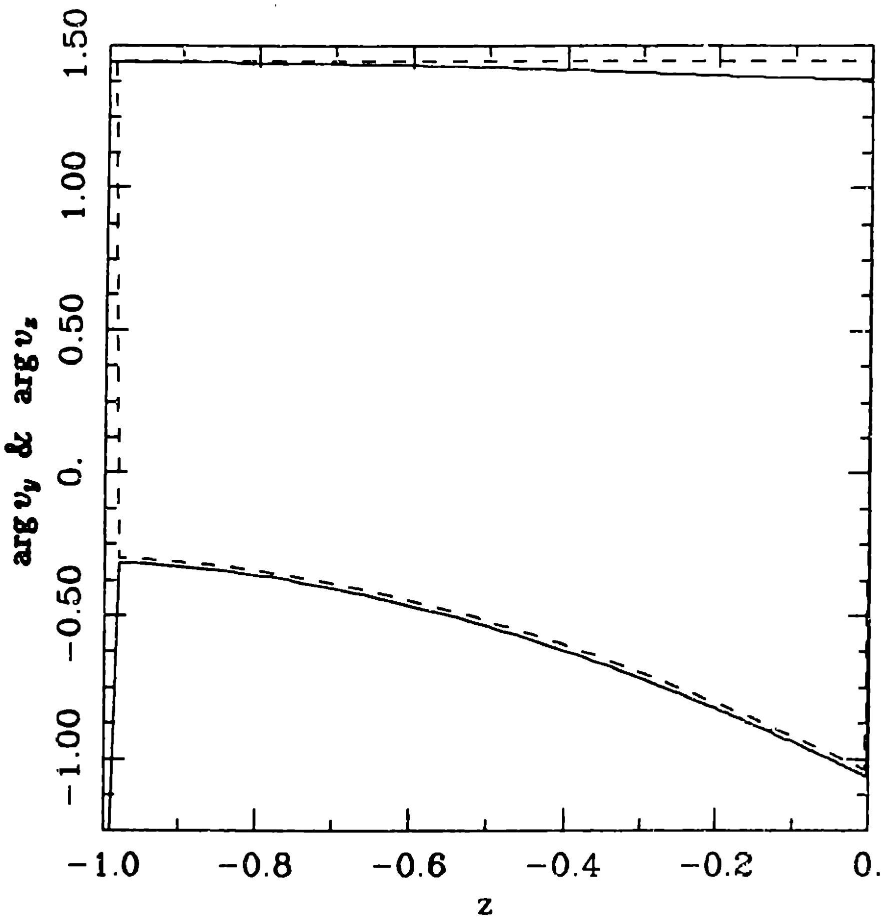

$\arg V_y$ & $\arg V_z$, $f = 10^{-3}\ Hz$, $\lambda = 10.0\ mm$,

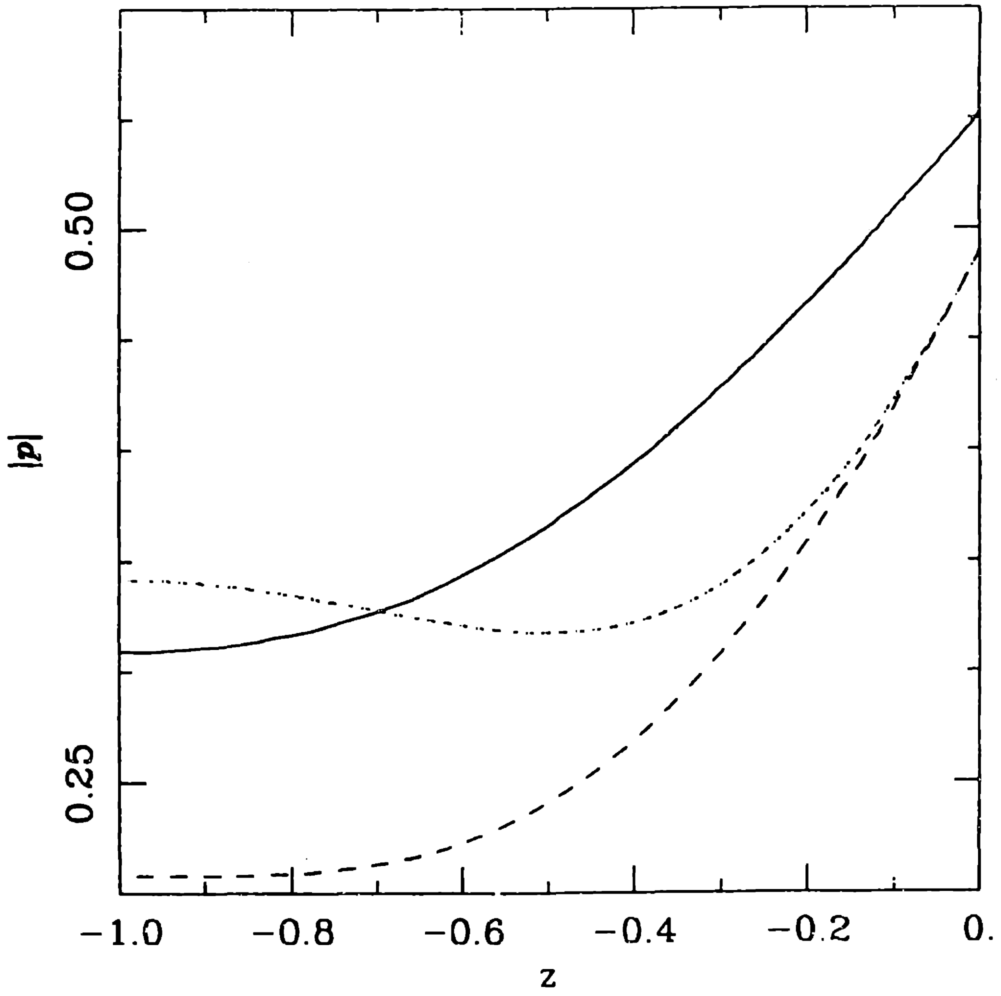

$|p|$, $f = 10^{-3}$ Hz, $\lambda = 1.0\,mm$. Numerical solution, equation 4.18 (- - - -), and equation 4.19 (— —).

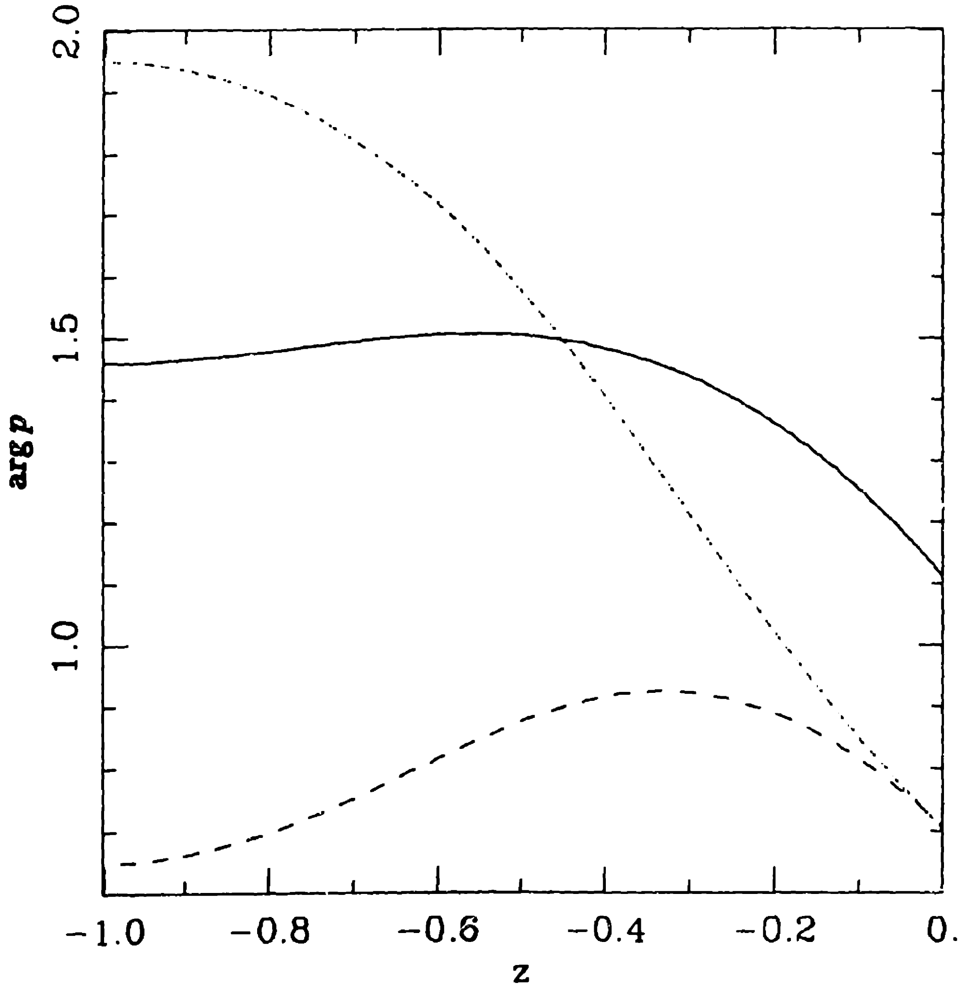

arg p, $f = 10^{-3}$ Hz, $\lambda = 1.0$ mm. Numerical solution, equation 4.18 (- - - -), and equation 4.19 (— —).

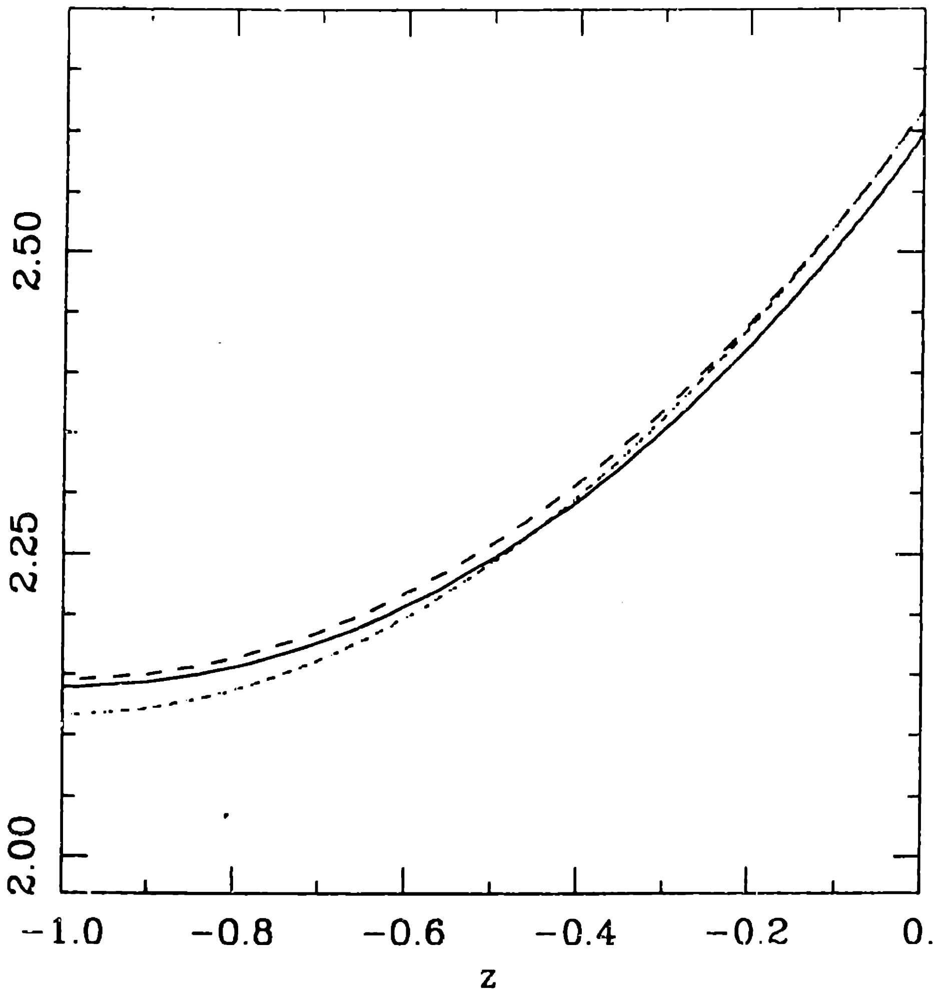

|ϕ|, $f = 10^{-3}$ Hz, $\lambda = 1.0$ mm. Numerical solution, equation 4.18 (- - - -), and equation 4.19 (— —).

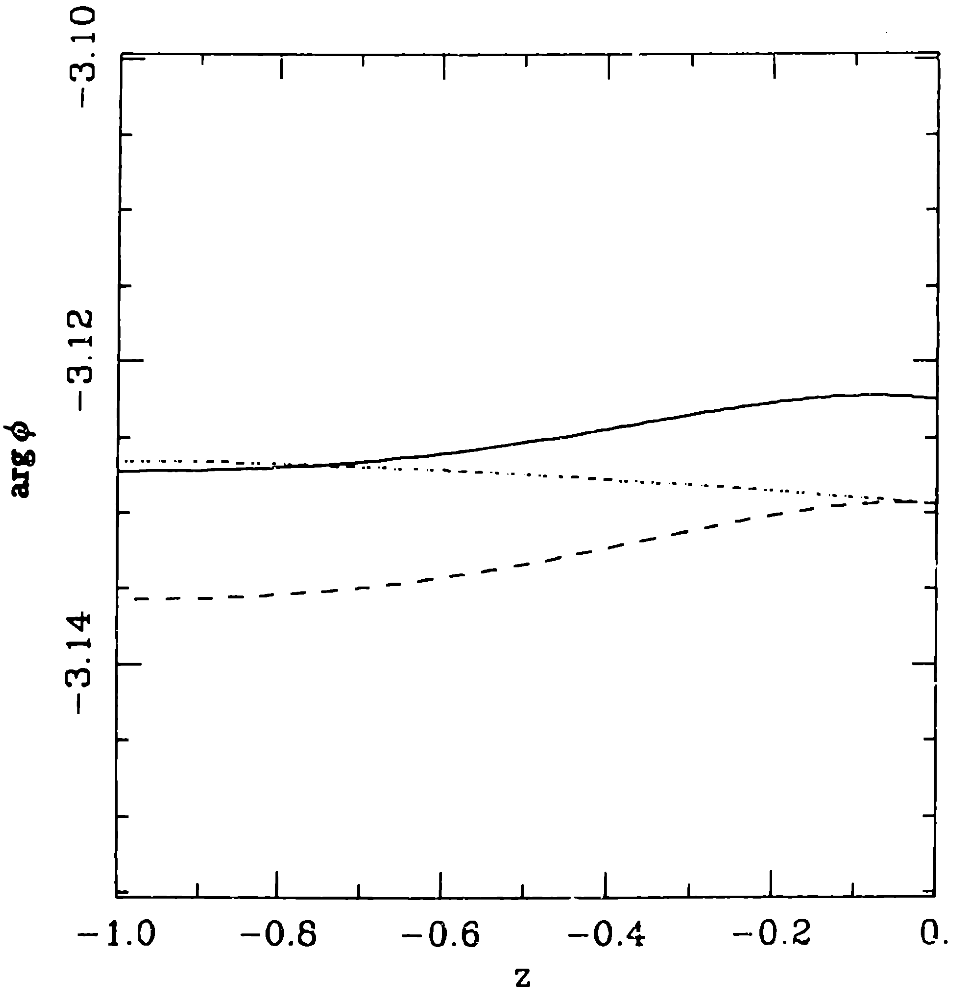

arg ϕ, $f = 10^{-3}$ Hz, $\lambda = 1.0$ mm. Numerical solution, equation 4.18 (- - - -), and equation 4.19 (— —).

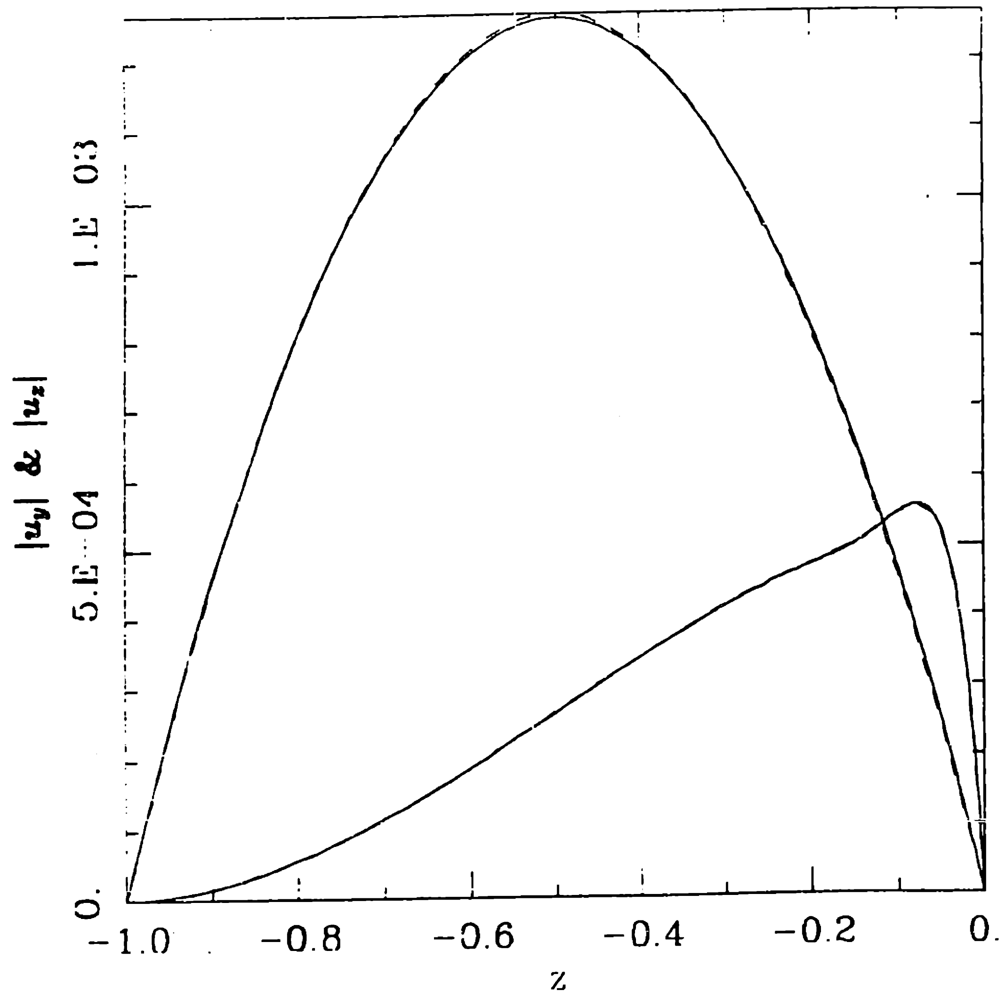

$|u_y|$ & $|u_z|$, $f = 0.1\ Hz$, $\lambda = 10.0\ mm$, $|u_y|$ has the greater maximum.

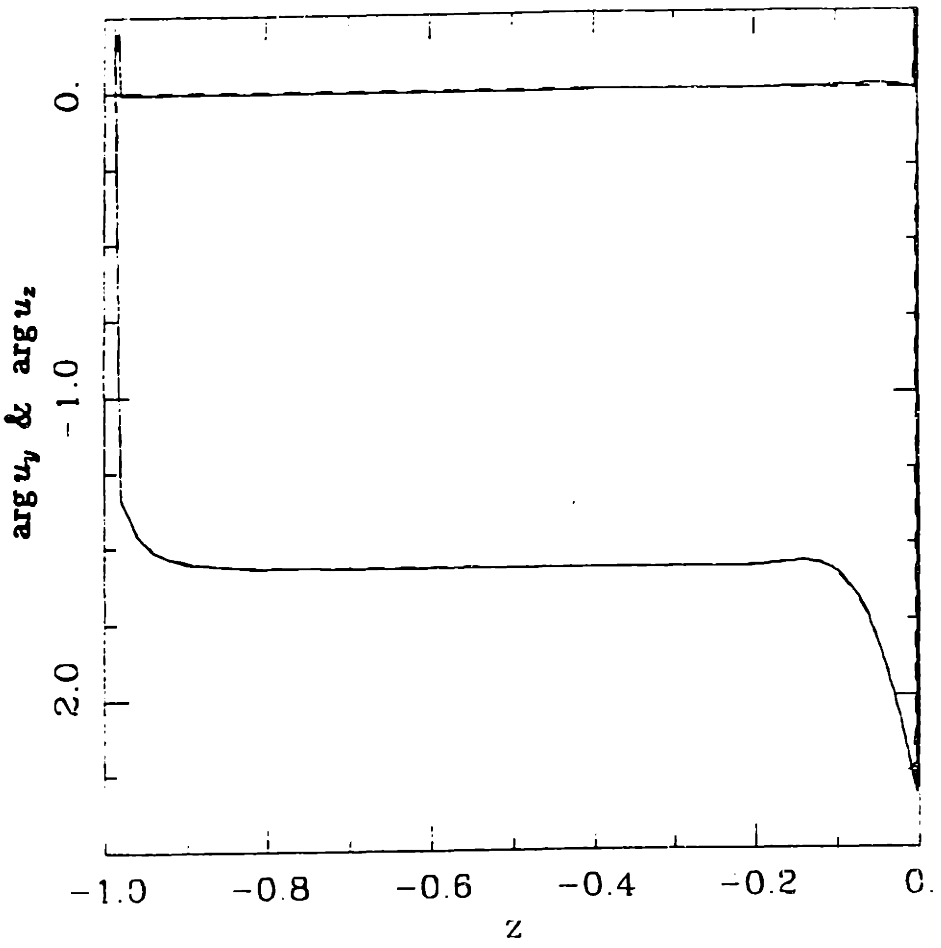

arg u_y & arg u_z, $f = 0.1\ Hz$, $\lambda = 10.0\ mm$.

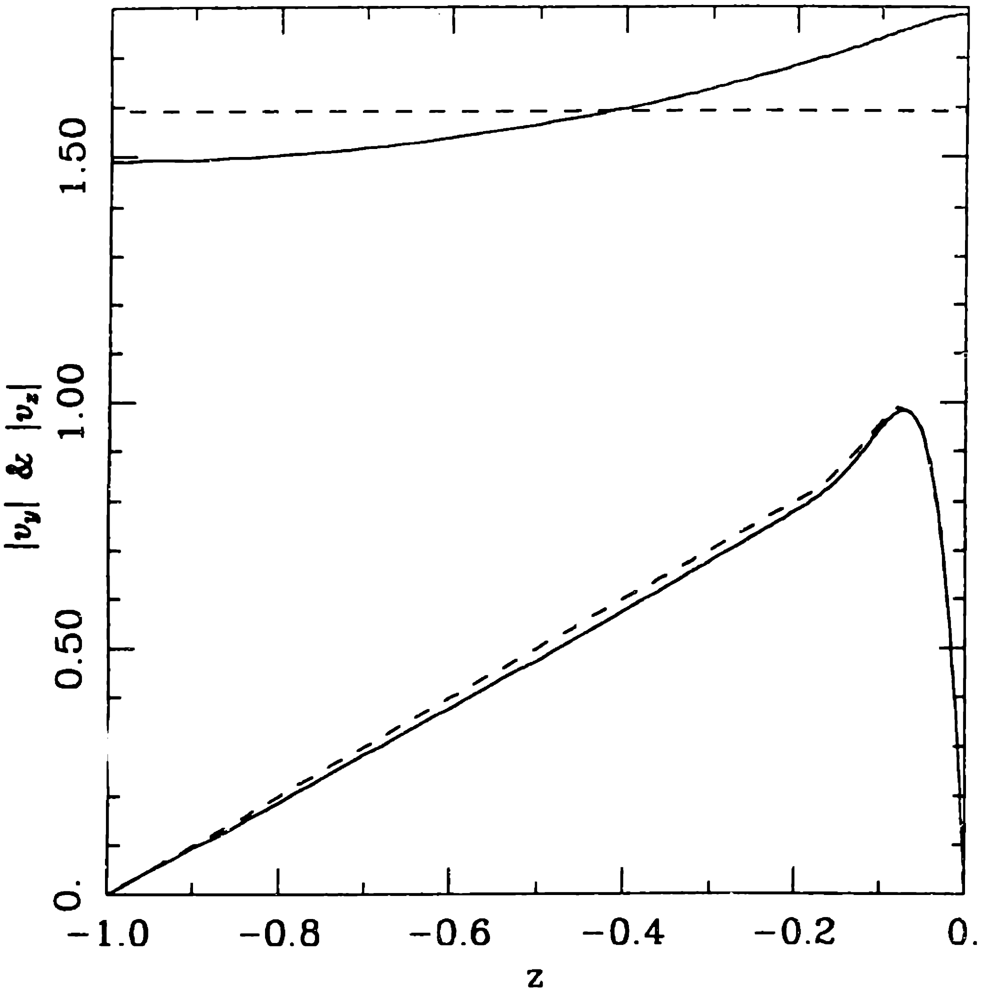

$|V_y|$ & $|V_z|$, $f = 0.1$ *Hz*, $\lambda = 10.0$ *mm*. Note that an average value is obtained for $|V_y|$.

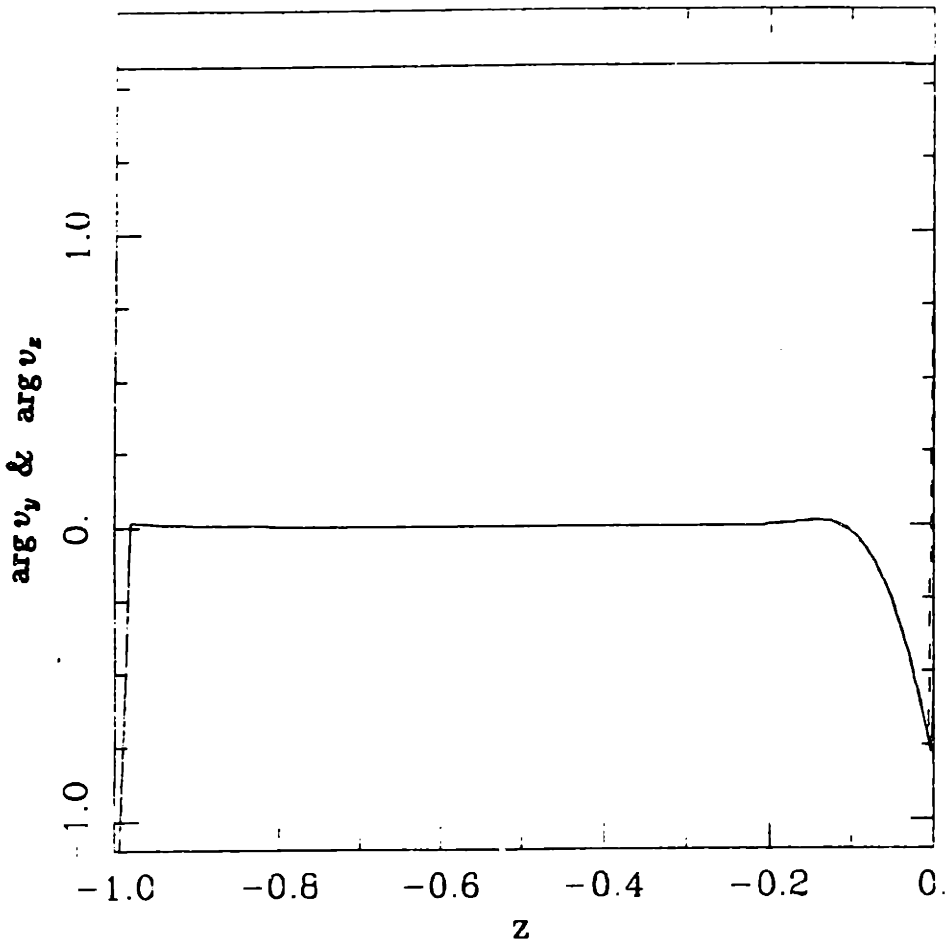

arg V_y & arg V_z, $f = 0.1$ Hz, $\lambda = 10.0$ mm.

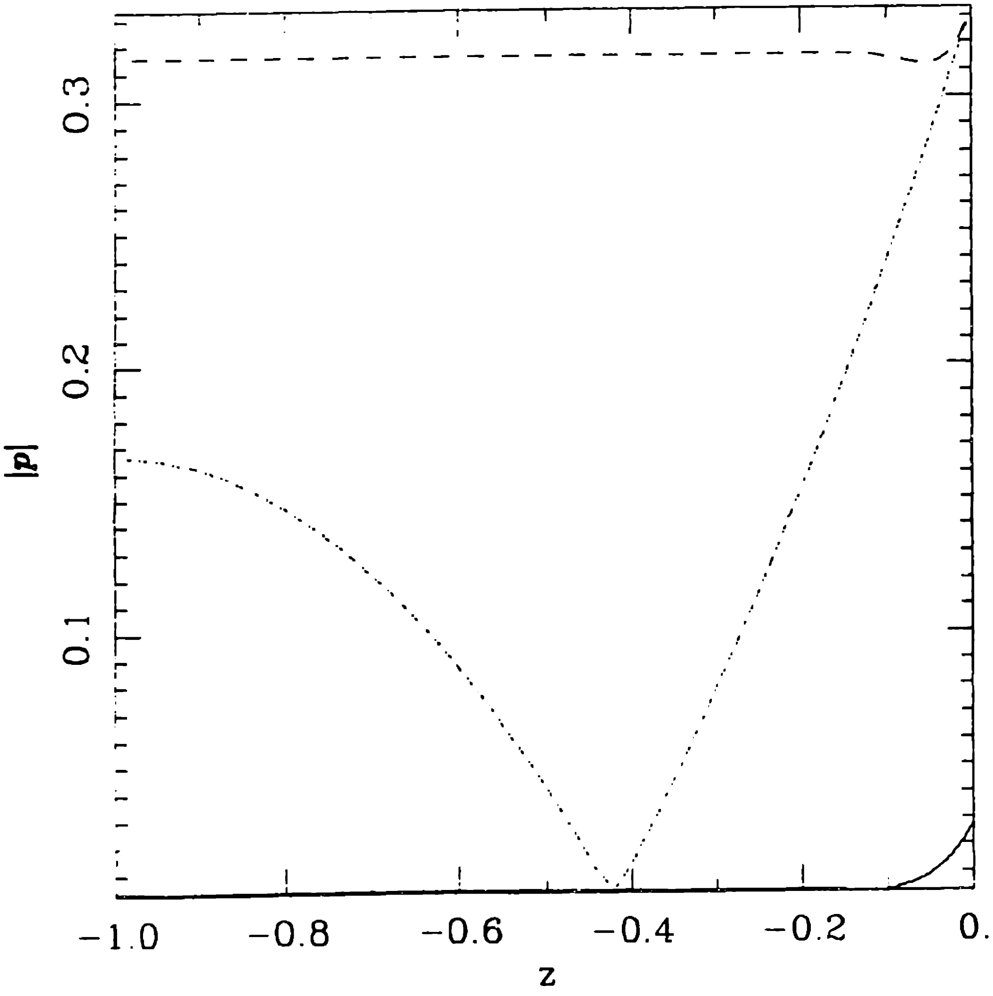

$|p|$, $f = 0.1\ Hz$, $\lambda = 10.0\ mm$. Numerical solution, equation 4.18 (- - - -), and equation 4.19 (— —).

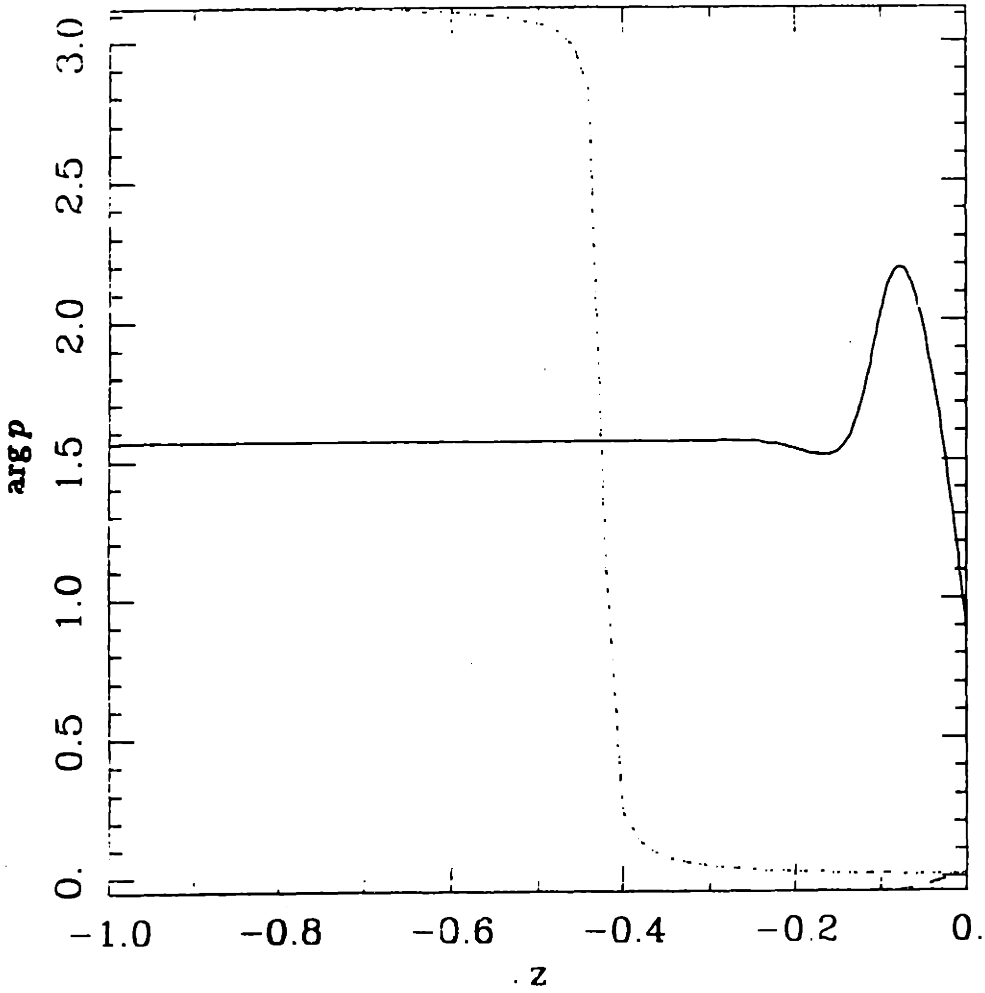

arg p, $f = 0.1$ Hz, $\lambda = 10.0$ mm. Numerical solution, equation 4.18 (- - - -), and equation 4.19 (— —).

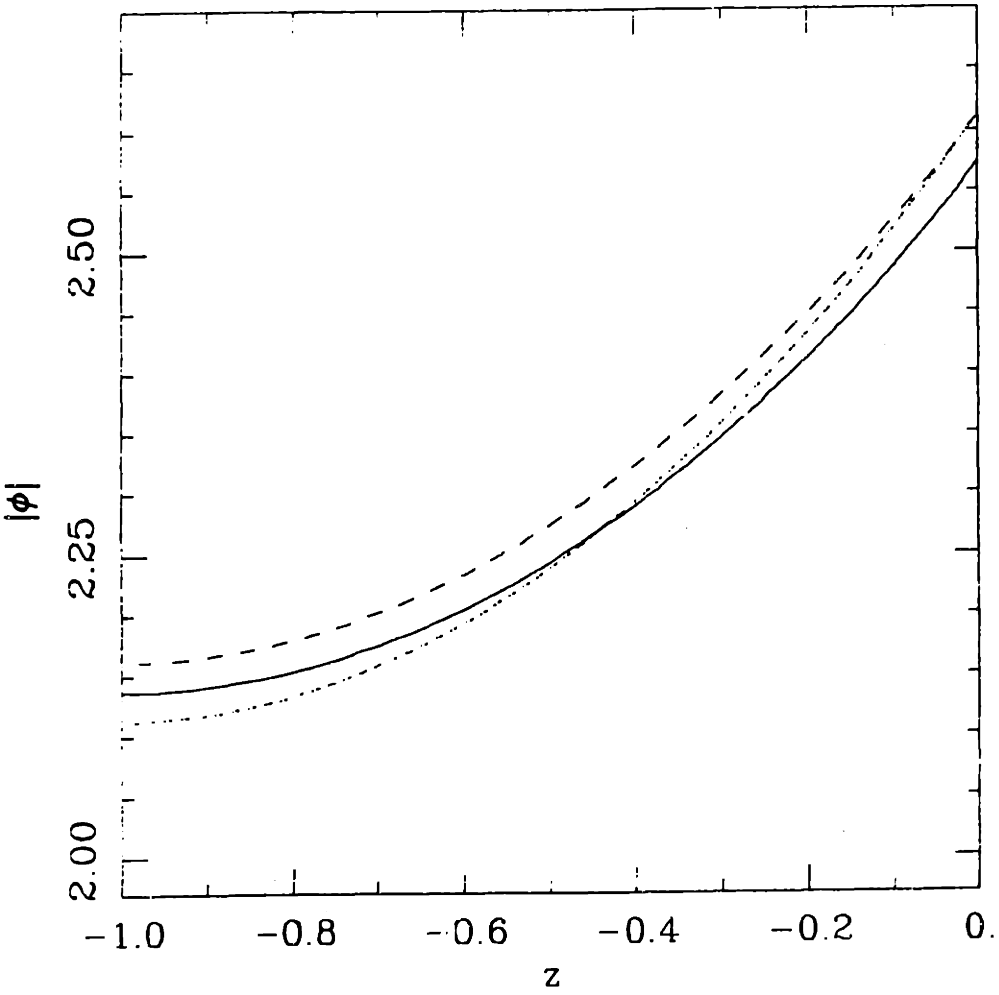

$|\phi|$, $f = 0.1\ Hz$, $\lambda = 10.0\ mm$. Numerical solution, equation 4.18 (- - - -), and equation 4.19 (— —).

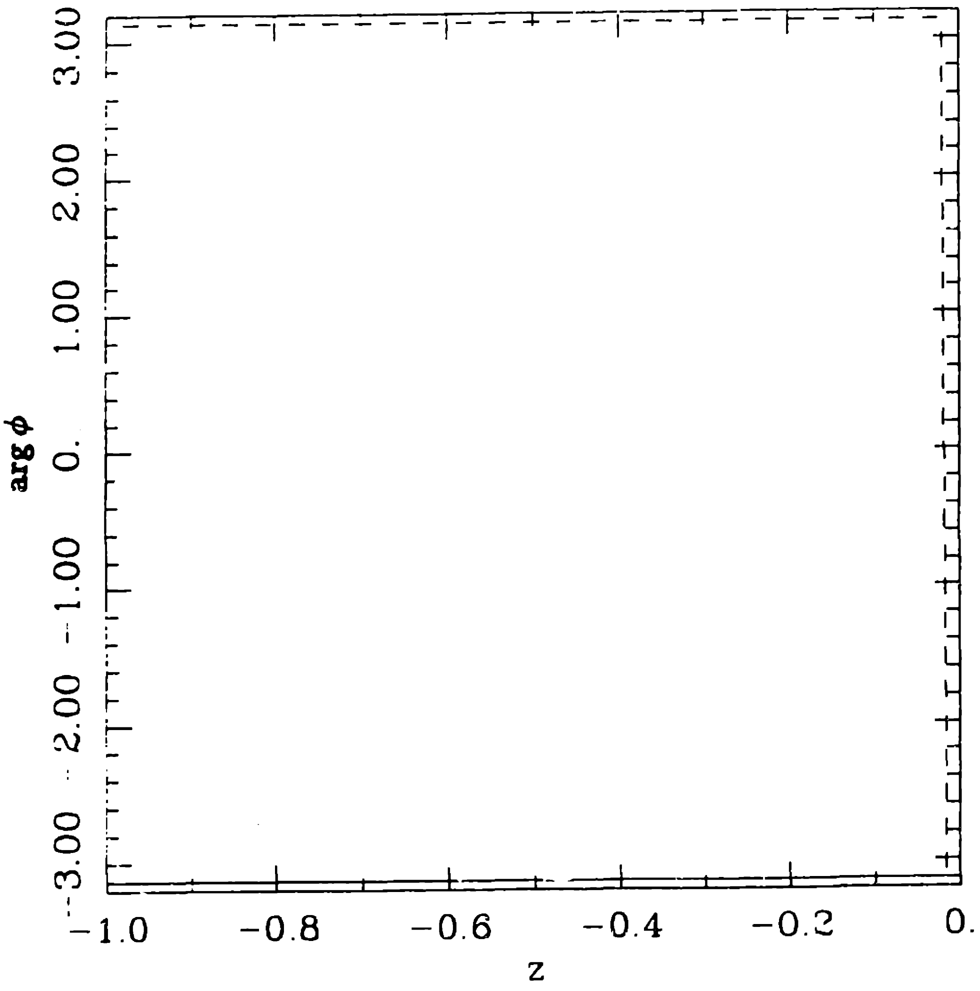

arg ϕ, $f = 0.1\ Hz$, $\lambda = 10.0\ mm$. Numerical solution and equation 4.19 (— —).

A.1.3 Development of Long-Wave Behavior in Section 4.3

This section contains graphs which exemplify the fact that the fields of §4.3 approach a one-dimensional limit as the wavelength, λ, is increased. Magnitudes of u_y (horizontal displacement), u_z (vertical displacement), V_y (horizontal relative velocity), and V_z (vertical relative velocity) are shown as functions of z for $\lambda = 10$ to 10^3 mm, with $f = 0.7$ Hz. (Because of the decrease in the diffusion boundary layer thickness, one-dimensional behavior should require longer wavelenghths at higher frequencies. Thus a relatively high frequency is used to provide a more stringent test.) Also, $|s(0)|$, and $args(0)$ are plotted *versus* ϕ_0 for $\lambda = 10^3$ mm, $f = 0.1$ Hz.

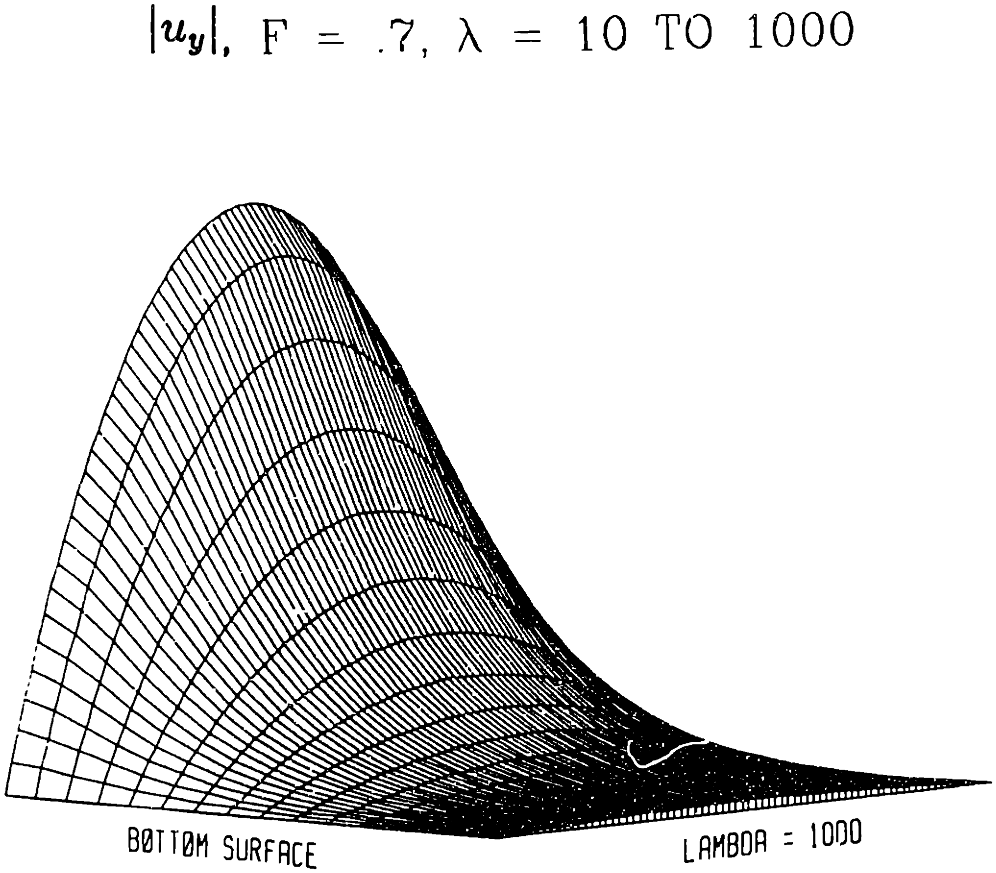

$|u_y|$, $f = 0.7$, $\lambda = 10$ to 10^3 mm logarithmically. $|u_y| < 1.50 \cdot 10^{-3}$.

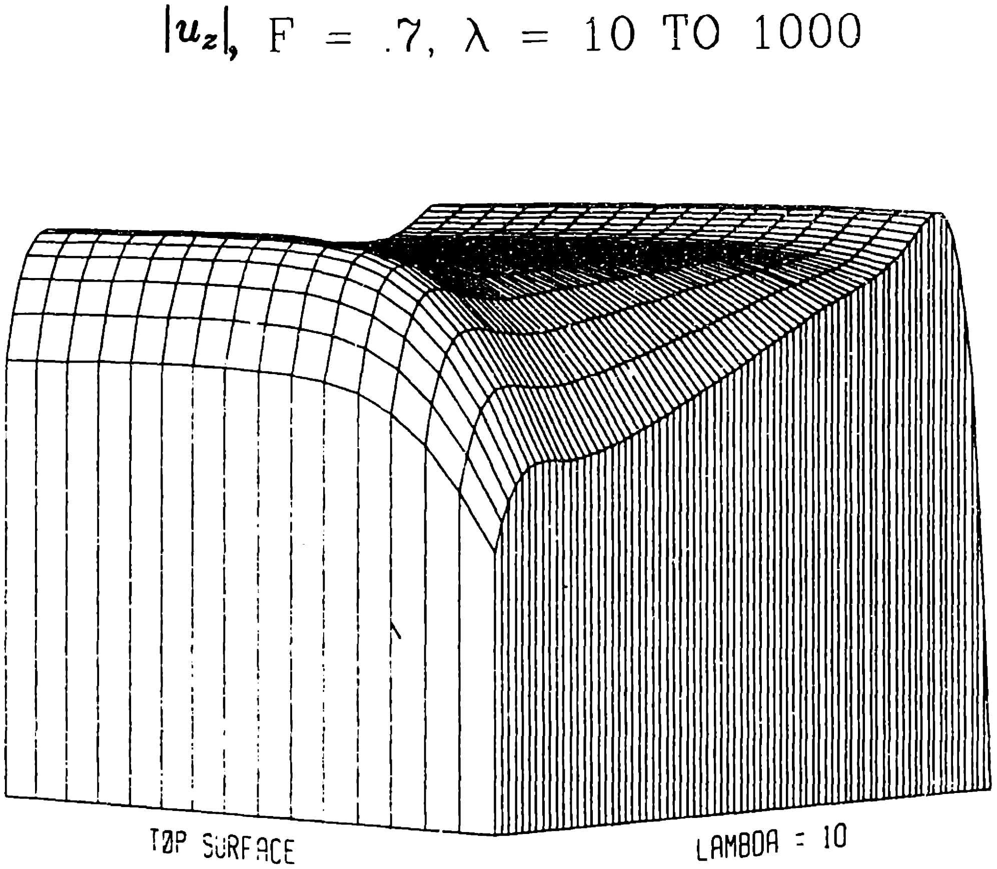

$|u_z|$, $f = 0.7$, $\lambda = 10$ to 10^3 *mm* logarithmically. $|u_z| < 1.16 \cdot 10^{-3}$.

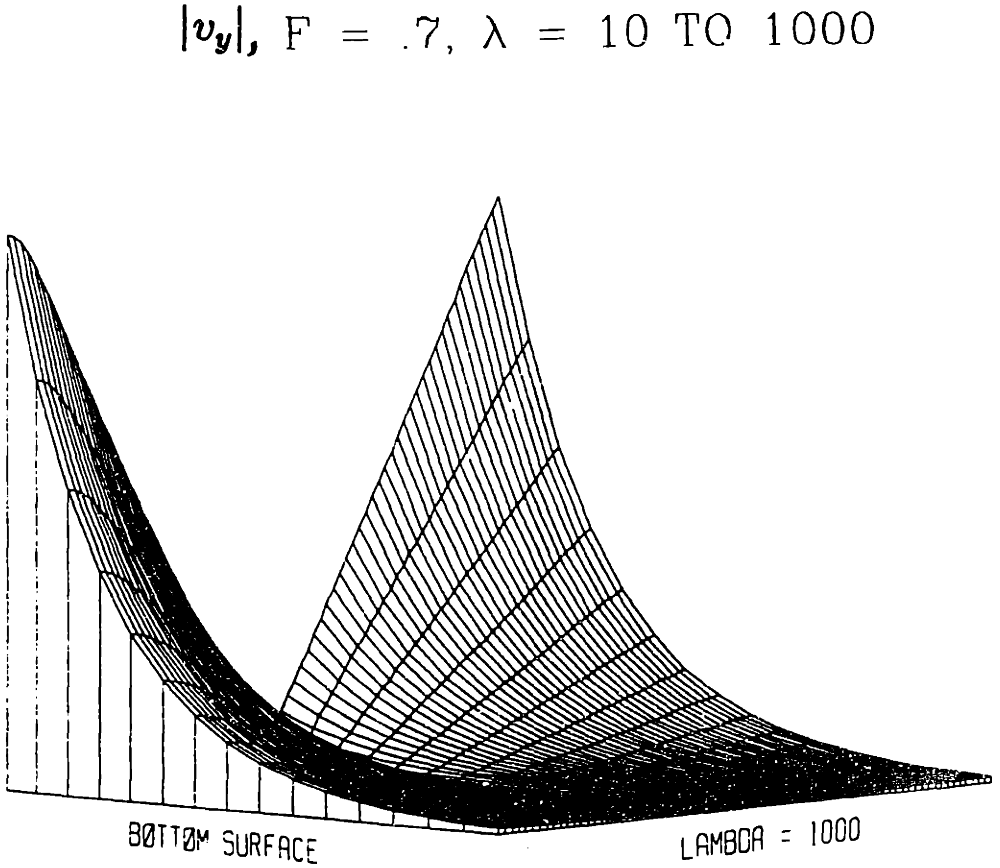

$|V_y|$, $f = 0.7$, $\lambda = 10$ to 10^3 *mm* logarithmically. $|V_y| < 0.210$.

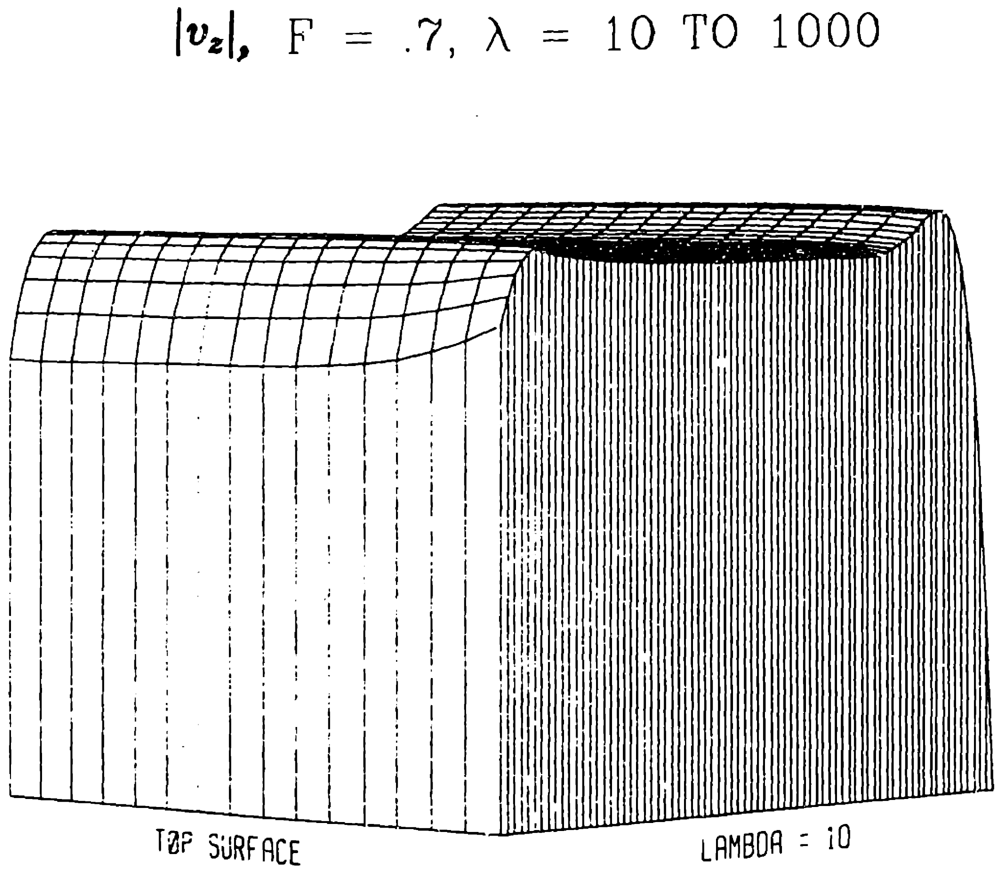

$|v_z|$, F = .7, λ = 10 TO 1000

$|V_z|$, $f = 0.7$, $\lambda = 10$ to 10^3 *mm* logarithmically. $|V_z| < 1.07$.

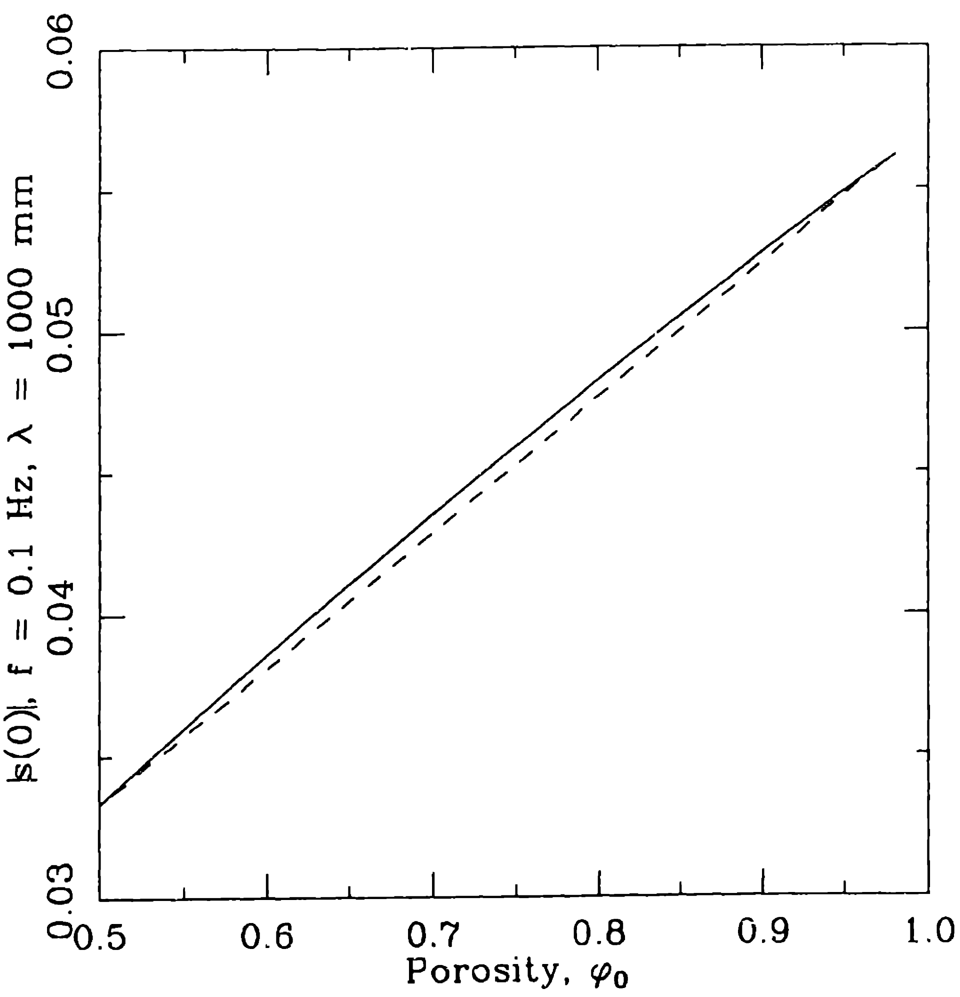

$|s(0)|$ *versus* ϕ_0; $\lambda = 10^3$ *mm*, $f = 0.1$ *Hz*. The dashed line is a straight line put in for comparison.

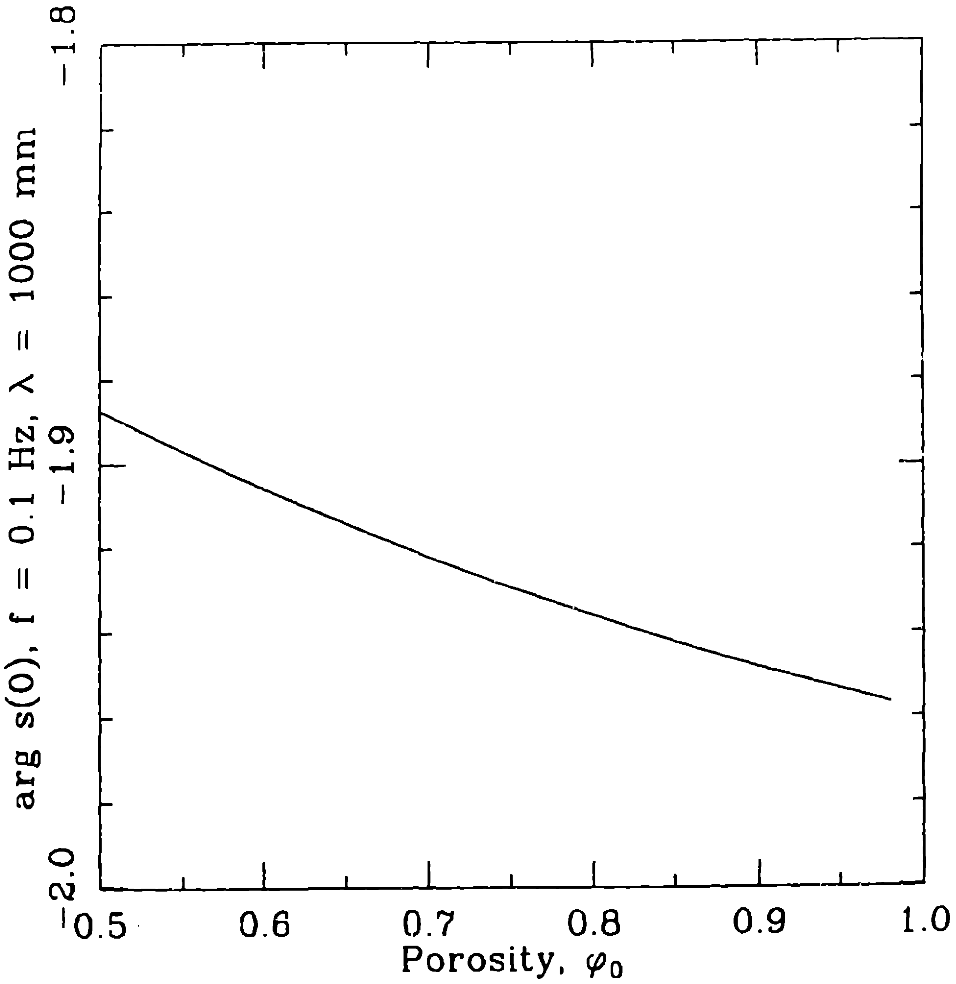

arg $s(0)$ *versus* ϕ_0, $\lambda = 10^3$ *mm*, $f = 0.1$ *Hz*.

A.2 Mechanically Forced Fields

A.2.1 Case Three: Impermeable Surface

This section presents the results for case three (mechanical driving with an impermeable surface) presented in Chapter 5. The results are presented as plots of non-dimensional transform variables as before. The magnitudes and phases of the fields are presented for the parameter values:

1. $\lambda = 10\, mm, f = 10^{-3}$ to $0.1\, Hz$ logarithmically,

2. $\lambda = 1\, mm, f = 10^{-3}$ to $0.1\, Hz$ logarithmically,

3. $\lambda = 0.1\, mm, f = 10^{-3}$ to $0.1\, Hz$ logarithmically,

4. $f = 10^{-3}\, Hz, \lambda = 0.1$ to $10\, mm$ logarithmically,

and

5. $f = 0.1\, Hz, \lambda = 0.1$ to $10\, mm$ logarithmically.

The magnitude and phase of the fields are presented in the order u_y (horizontal displacement), u_z (vertical displacement), V_y (horizontal relative velocity), V_z (vertical relative velocity), p (pressure), and ϕ (potential). Physical values for V_y and V_z are presented for $\lambda = 10$. Field magnitudes may be obtained from Table 5.1, and the ranges of arguments (complex phases) are listed in the captions. The arguments have been linearized (in z) whenever there was an apparent discontinuity due to numerical error in the vicinity of a relatively small field magnitude. The phases were linearized whenever the difference in the phases at two consecutive grid points (in z) exceeded a specified tolerance. The tolerance was chosen by eye using the overall smoothness and integrity of the data as criteria.

NOTE:

The axies in this section are scaled as follows: length by a_J, velocity by ωa_J, and pressure by $2\pi a_J(G + \lambda_L)/\lambda$.

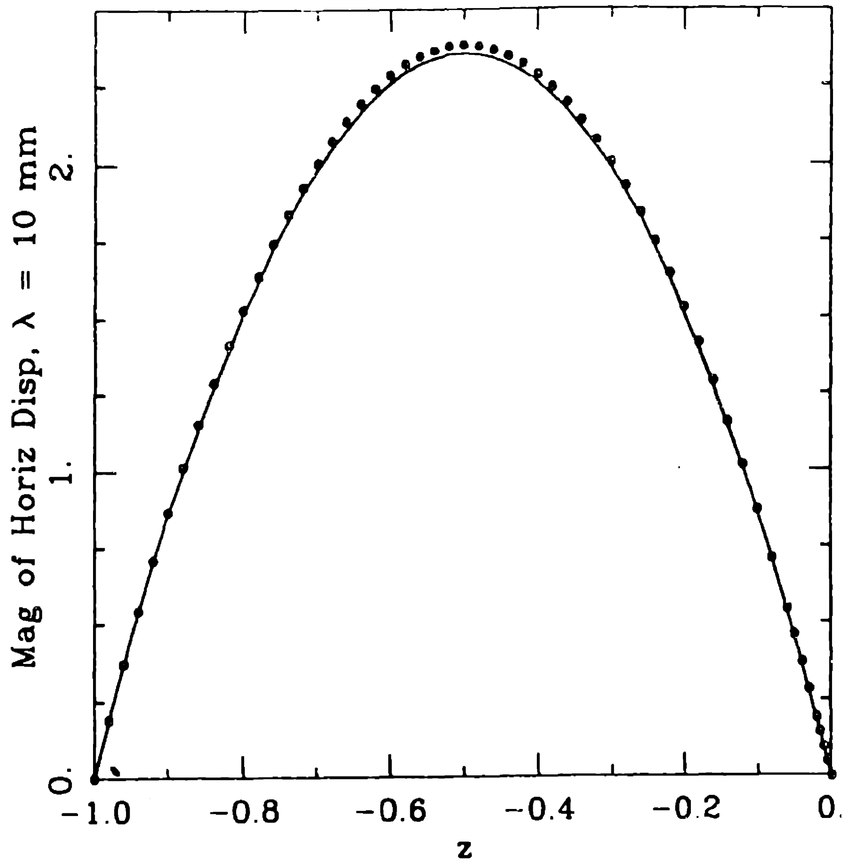

$|u_y|$, $\lambda = 10\, mm, f = 10^{-3}$ to 0.1 Hz logarithmically.

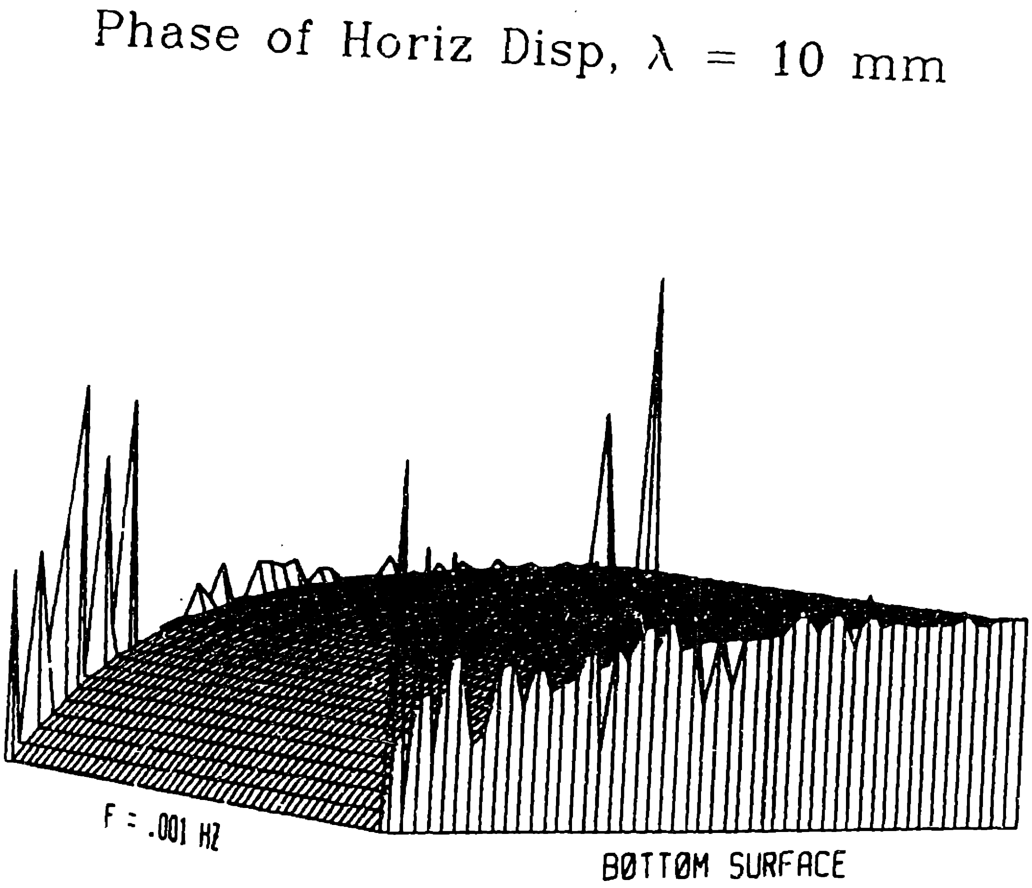

$1.44 < \arg u_v < 1.79$, $\lambda = 10\ mm$, $f = 10^{-3}$ to 0.1 Hz logarithmically.

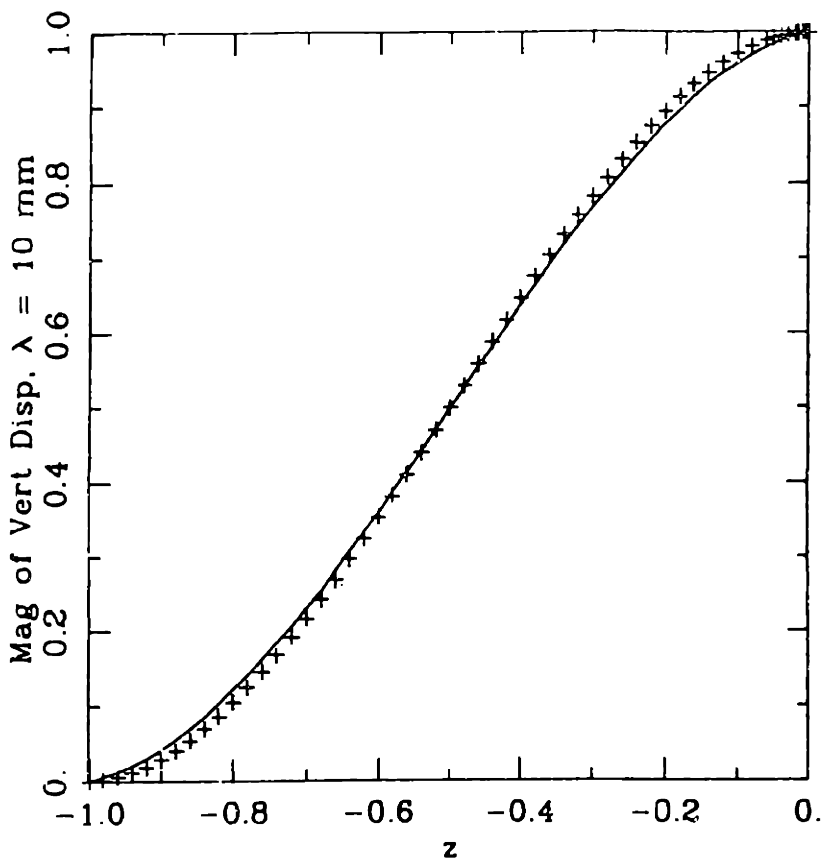

$|u_z|$, $\lambda = 10\,mm, f = 10^{-3}$ and 0.1 Hz ("+") logarithmically.

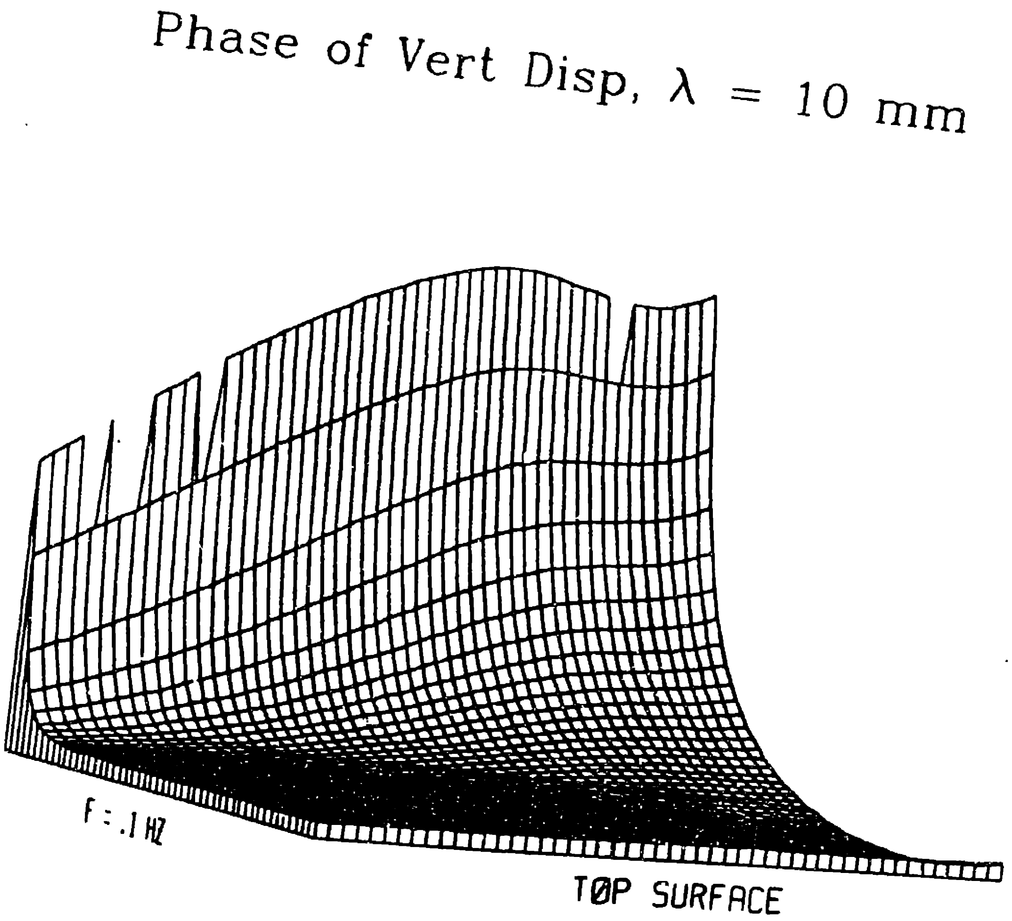

$-0.02 < \arg u_z < 0.66$, $\lambda = 10\ mm$, $f = 10^{-3}$ to 0.1 Hz logarithmically.

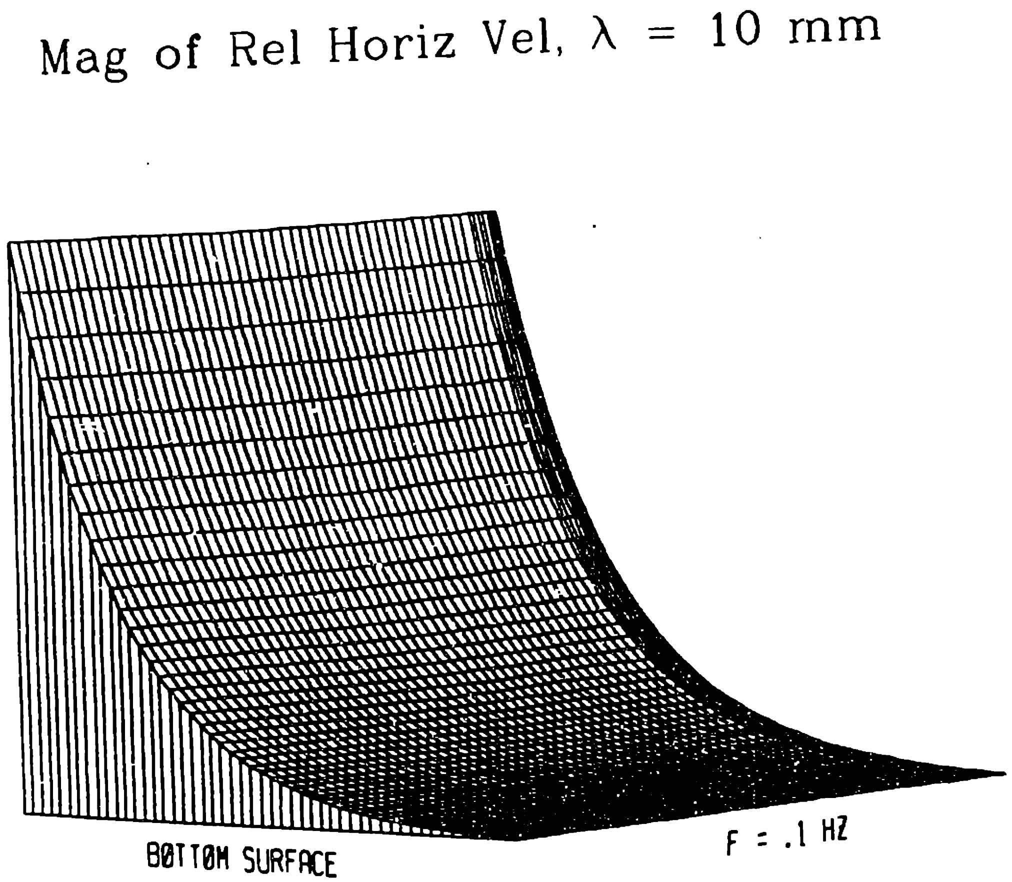

$|V_y^*/\omega a_J|$, $\lambda = 10\ mm, f = 10^{-3}$ to 0.1 Hz logarithmically.

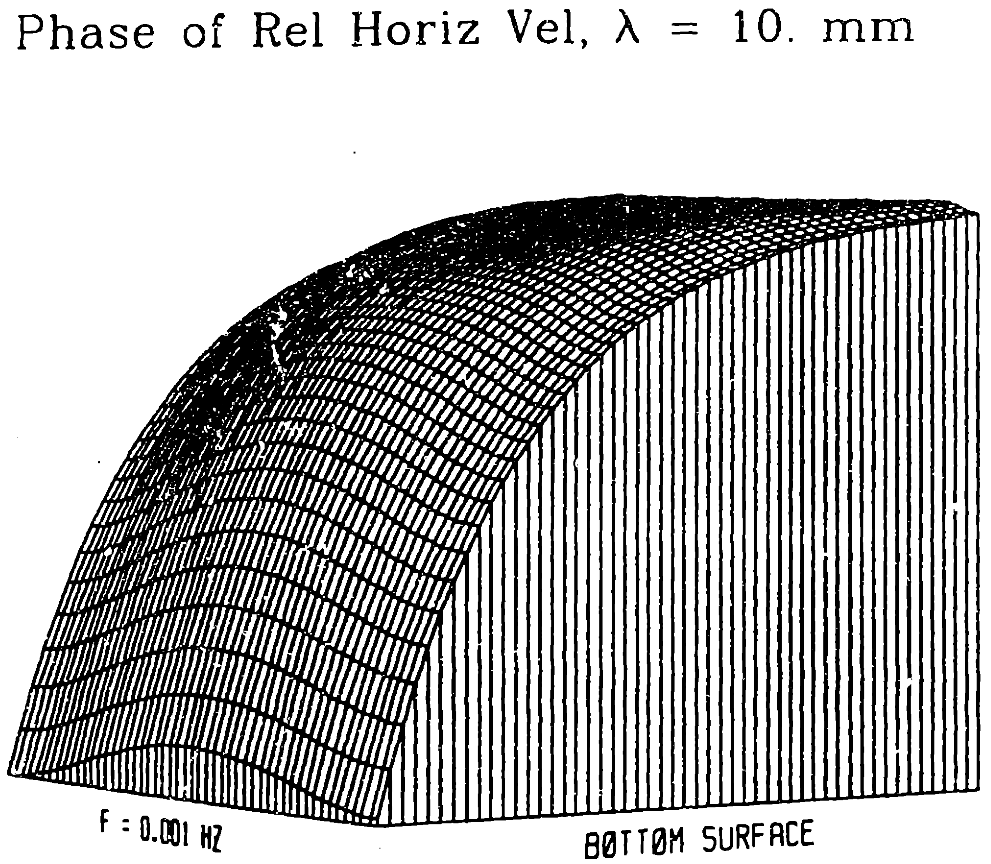

$1.409 < \arg V_y < 1.57$, $\lambda = 10\ mm$, $f = 10^{-3}$ to 0.1 Hz logarithmically.

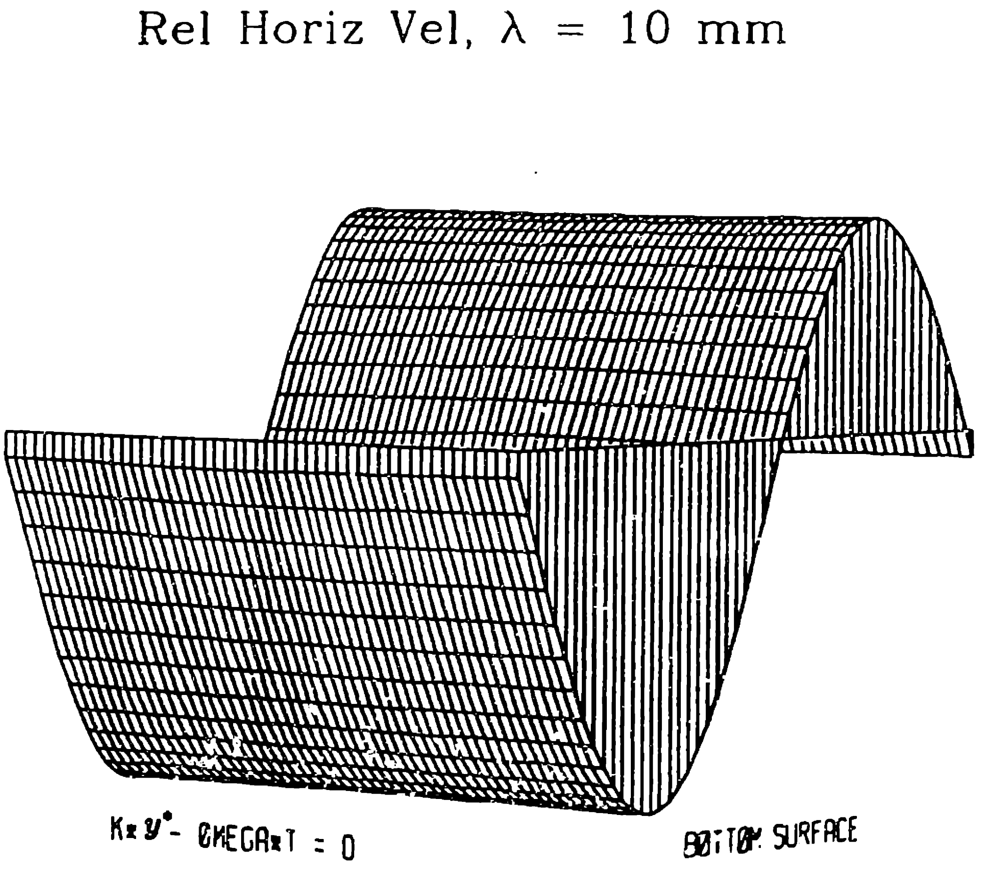

V_y versus z and $ky^* - \omega t$, $0 \le ky^* - \omega t \le 2\pi$, $\lambda = 10\ mm, f = 10^{-3}$. Note the contrast with V_z, below.

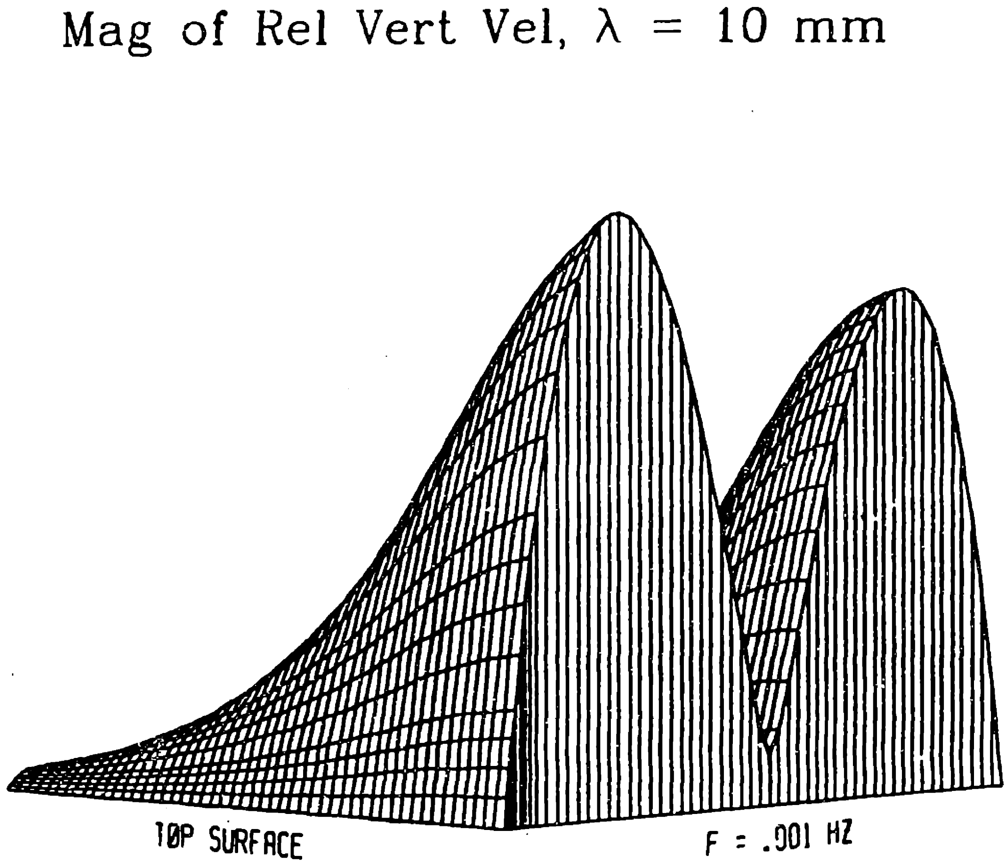
Mag of Rel Vert Vel, λ = 10 mm

$|V_z^*/\omega a_J|$, $\lambda = 10\,mm, f = 10^{-3}$ to 0.1 Hz logarithmically.

Phase of Rel Vert Vel, λ = 10. mm

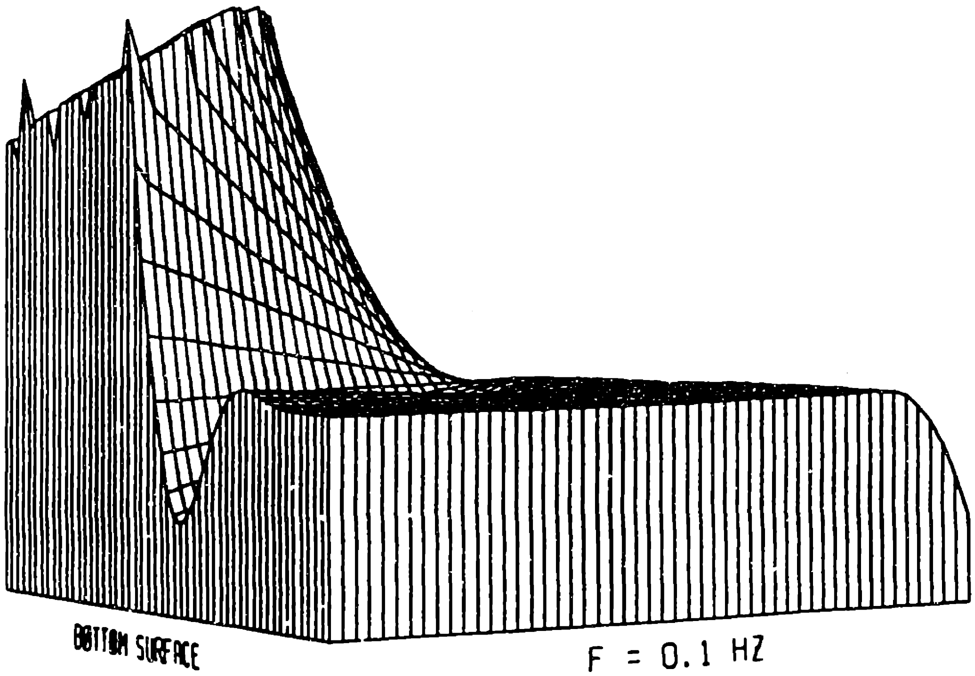

$-1.43 < \arg V_z < 2.58$, $\lambda = 10$ *mm*, $f = 10^{-3}$ to 0.1 *Hz* logarithmically.

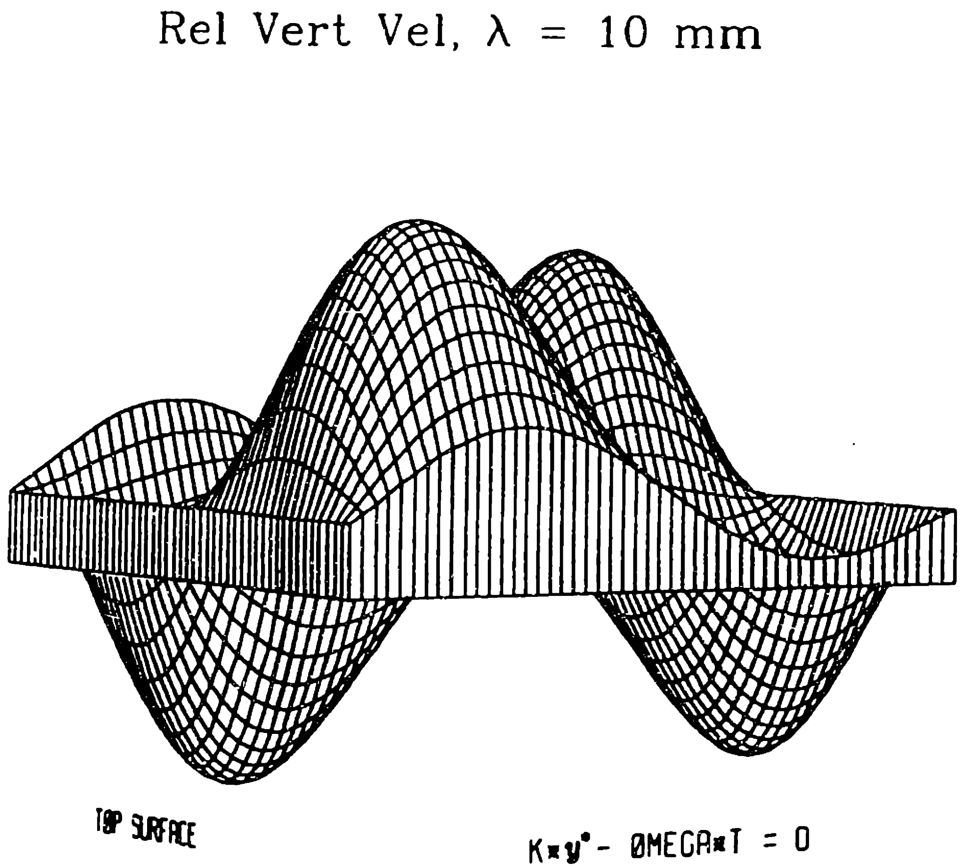

V_z *versus* z and $ky^* - \omega t$, $0 \le ky^* - \omega t \le 2\pi$, $\lambda = 10\ mm, f = 10^{-3}$. Note the contrast with V_y, above.

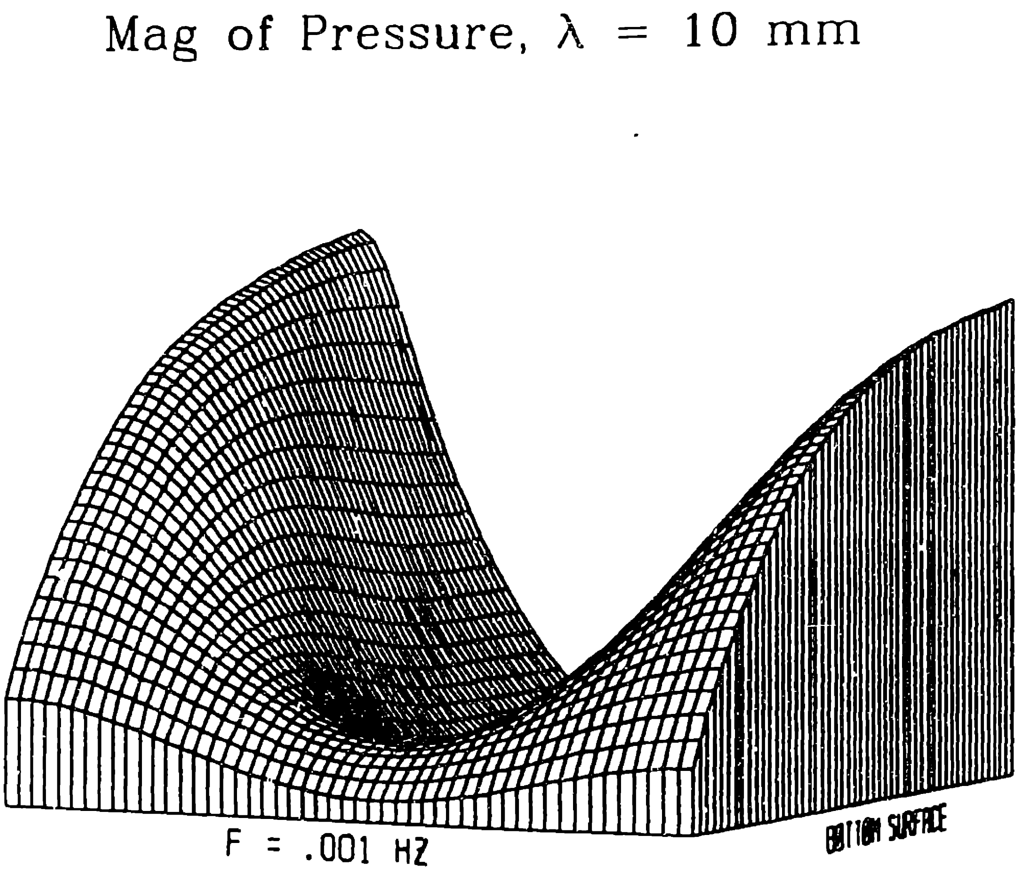

$|p|$, $\lambda = 10\ mm, f = 10^{-3}$ to 0.1 Hz logarithmically. The variation depicted is actually only 6%. Here $\arg p = \arg V_y + \pi/2$.

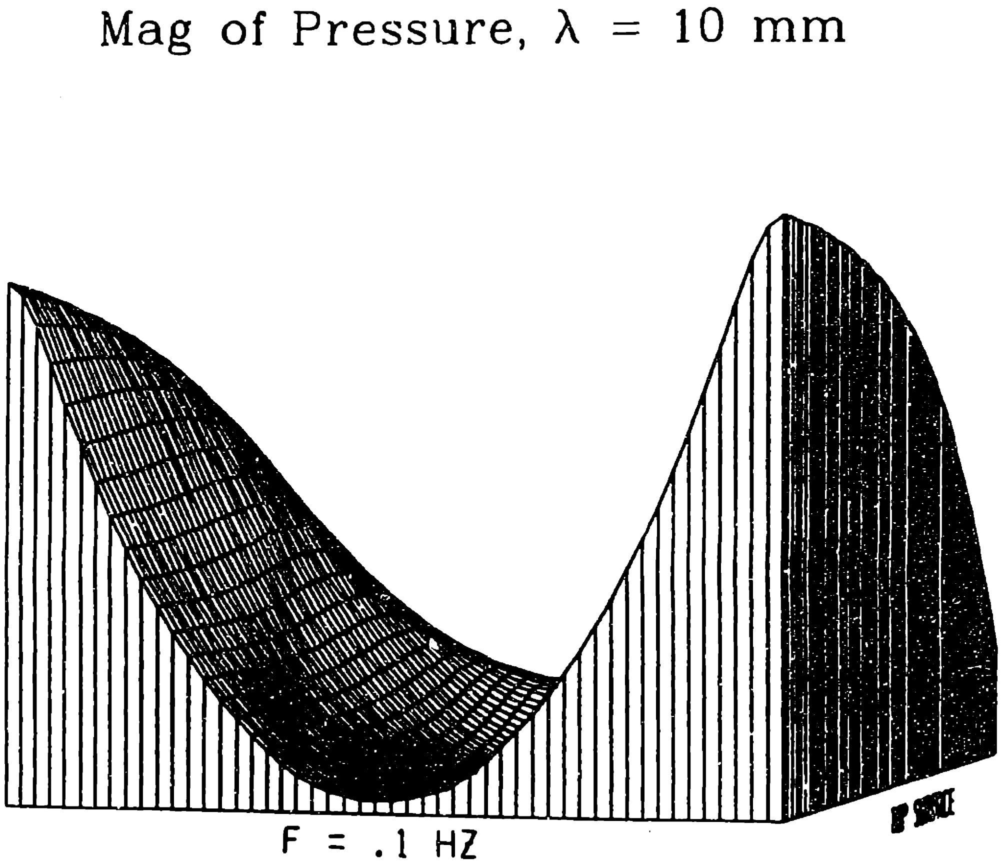

$|p|$, $\lambda = 10\ mm, f = 10^{-3}$ to 0.1 Hz logarithmically. The variation depicted is actually only 6%. Here $\arg p = \arg V_y + \pi/2$.

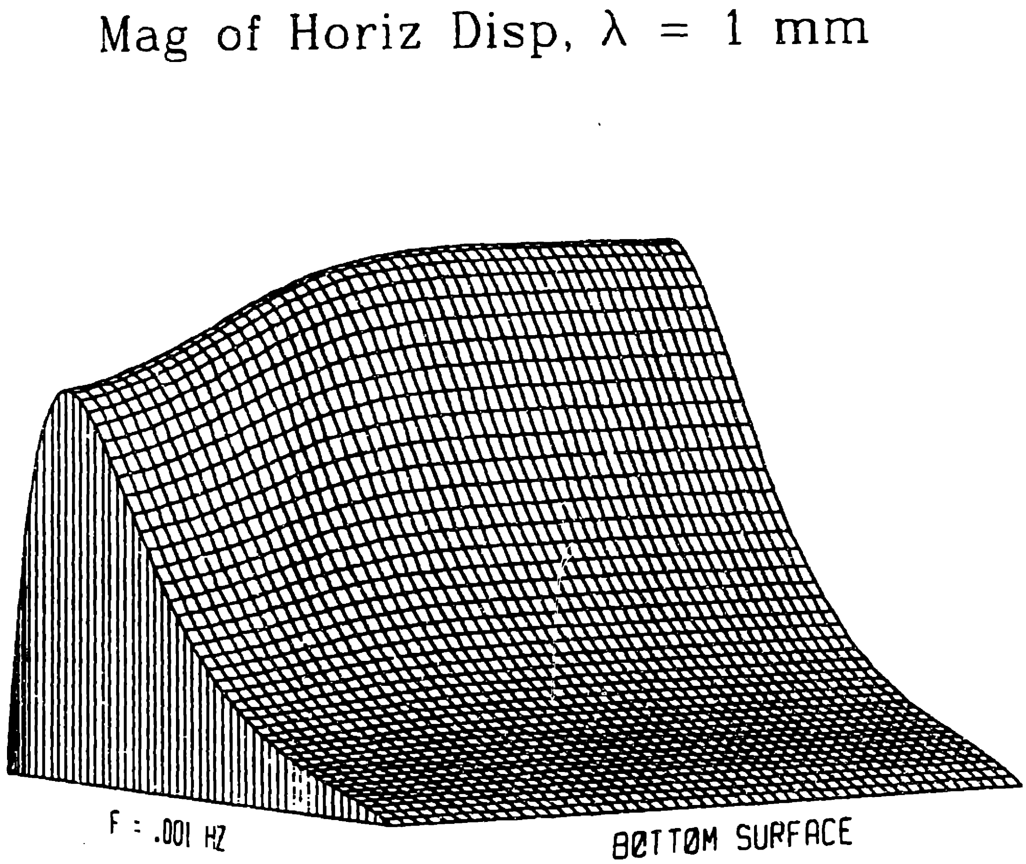

$|u_y|$, $\lambda = 1\ mm, f = 10^{-3}$ to 0.1 Hz logarithmically.

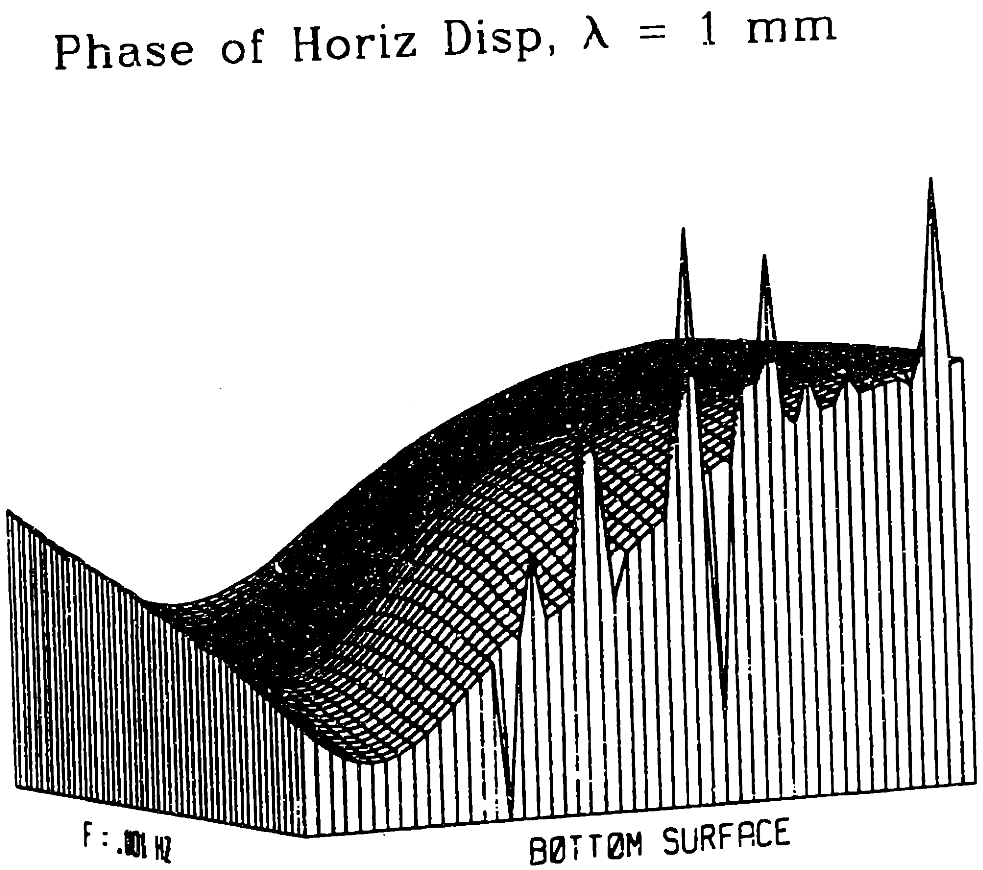

$1.31 < \arg u_y < 1.66 \cdot 10^{-2}$, $\lambda = 1\ mm, f = 10^{-3}$ to 0.1 *Hz* logarithmically.

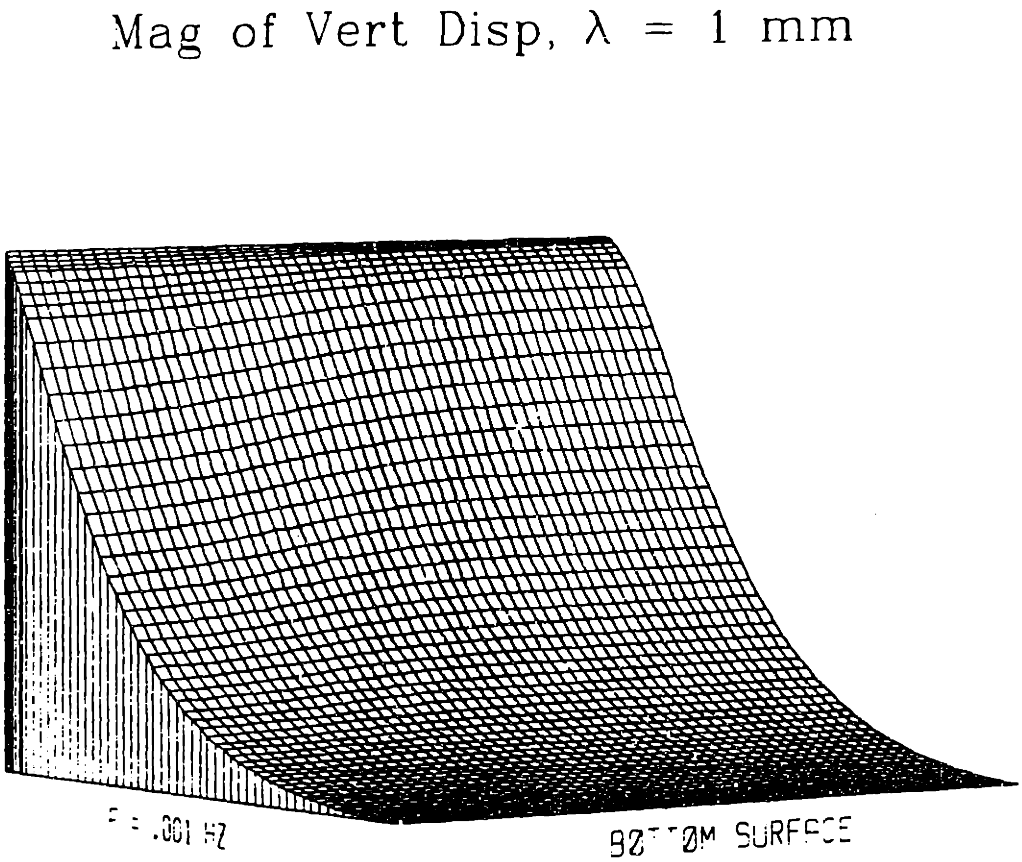

$|u_z|$, $\lambda = 1\ mm$, $f = 10^{-3}$ to 0.1 Hz logarithmically.

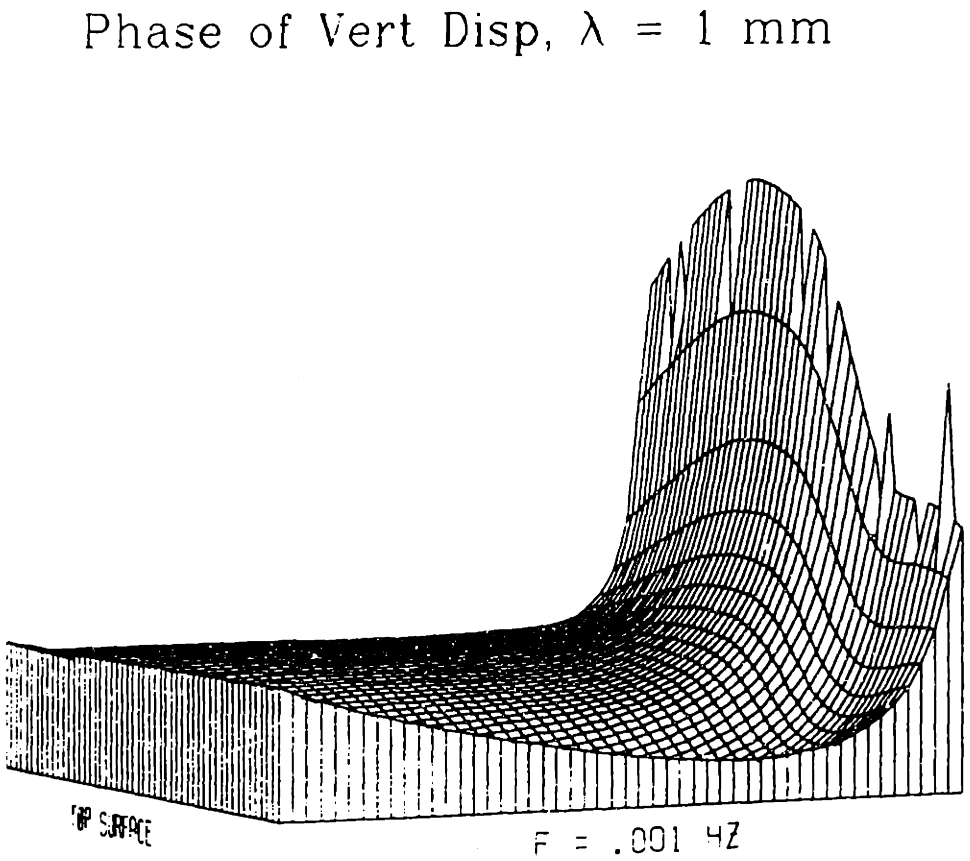

$-0.124 < \arg u_s < 0.453$, $\lambda = 1\ mm, f = 10^{-3}$ to 0.1 Hz logarithmically.

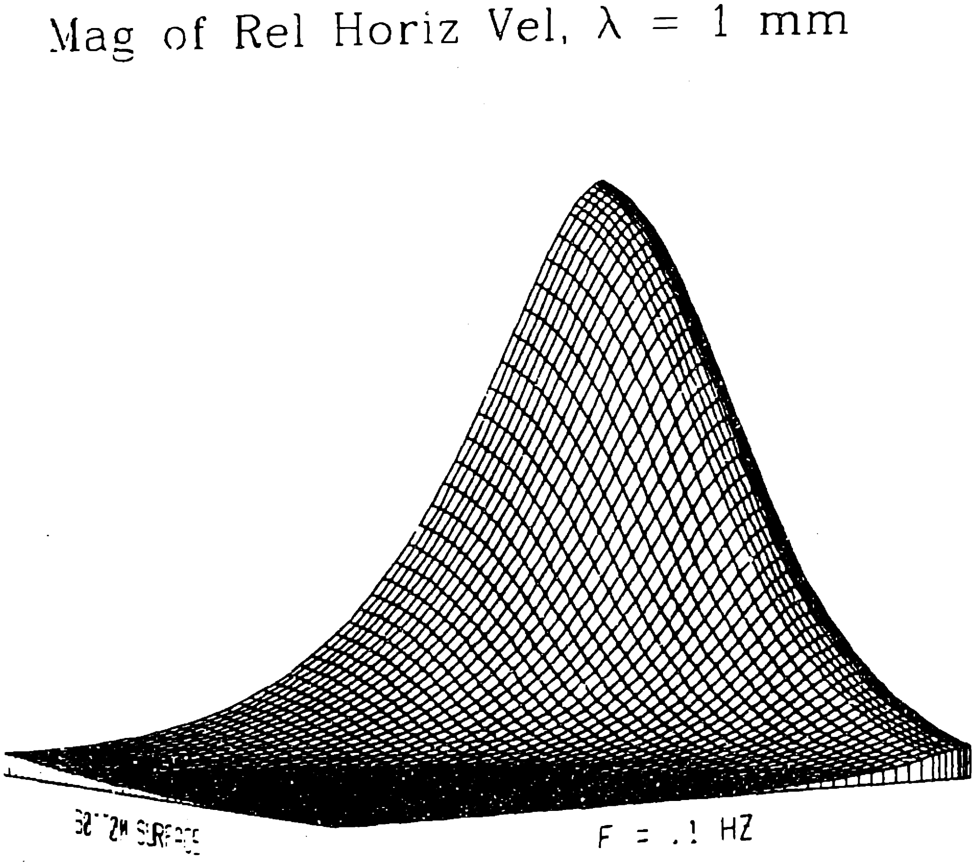

$|V_y^*/\omega a_J|$, $\lambda = 1$ *mm*, $f = 10^{-3}$ **to 0.1** *Hz* **logarithmically.**

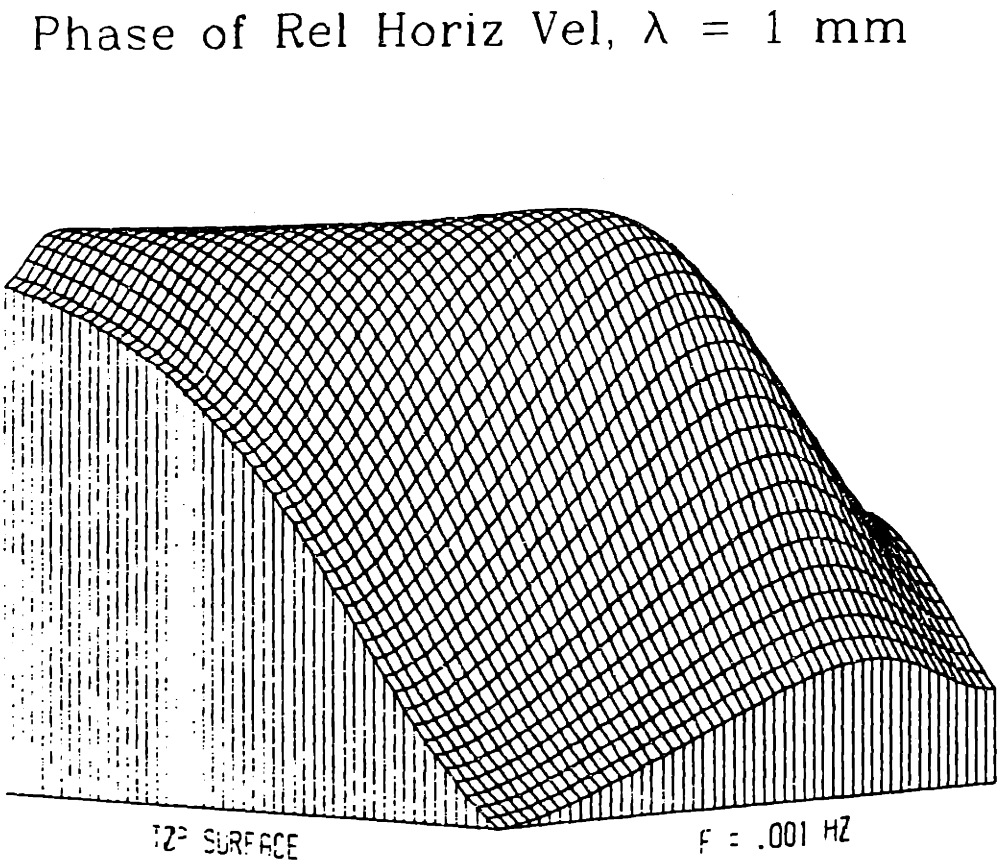

$0.247 < \arg V_y < 1.61$, $\lambda = 1$ *mm*, $f = 10^{-3}$ to 0.1 *Hz* logarithmically.

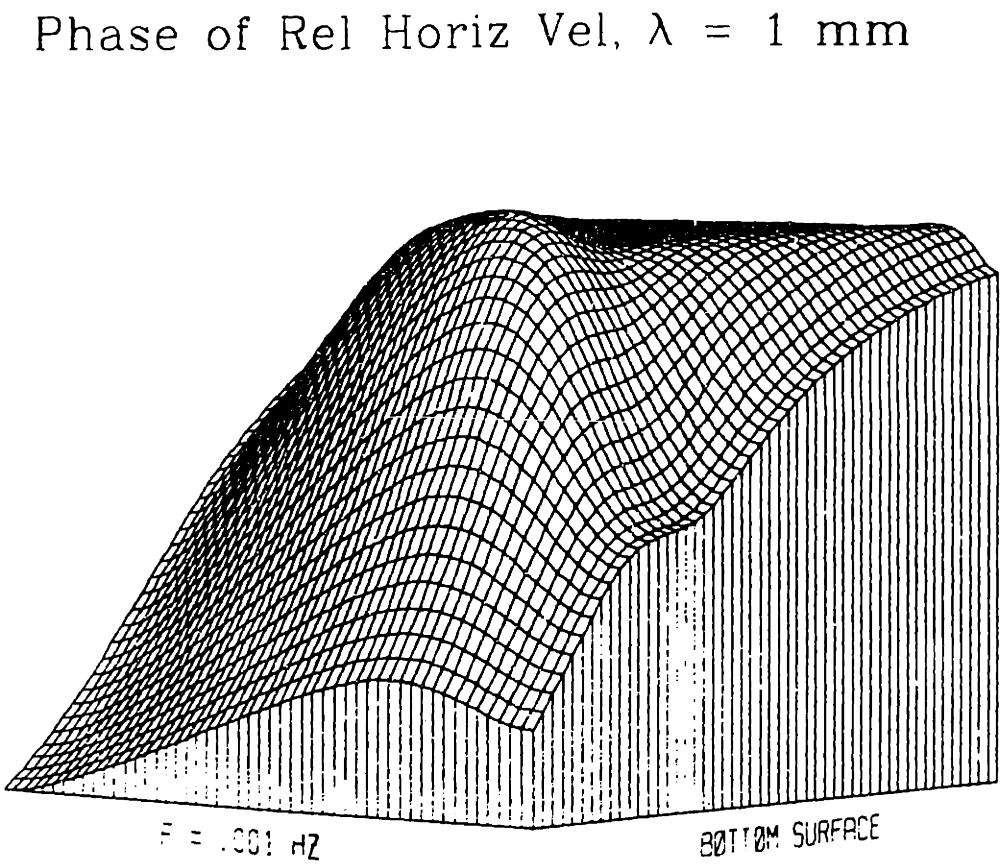

$0.247 < \arg V_y < 1.61$, $\lambda = 1\ mm$, $f = 10^{-3}$ to $0.1\ Hz$ logarithmically.

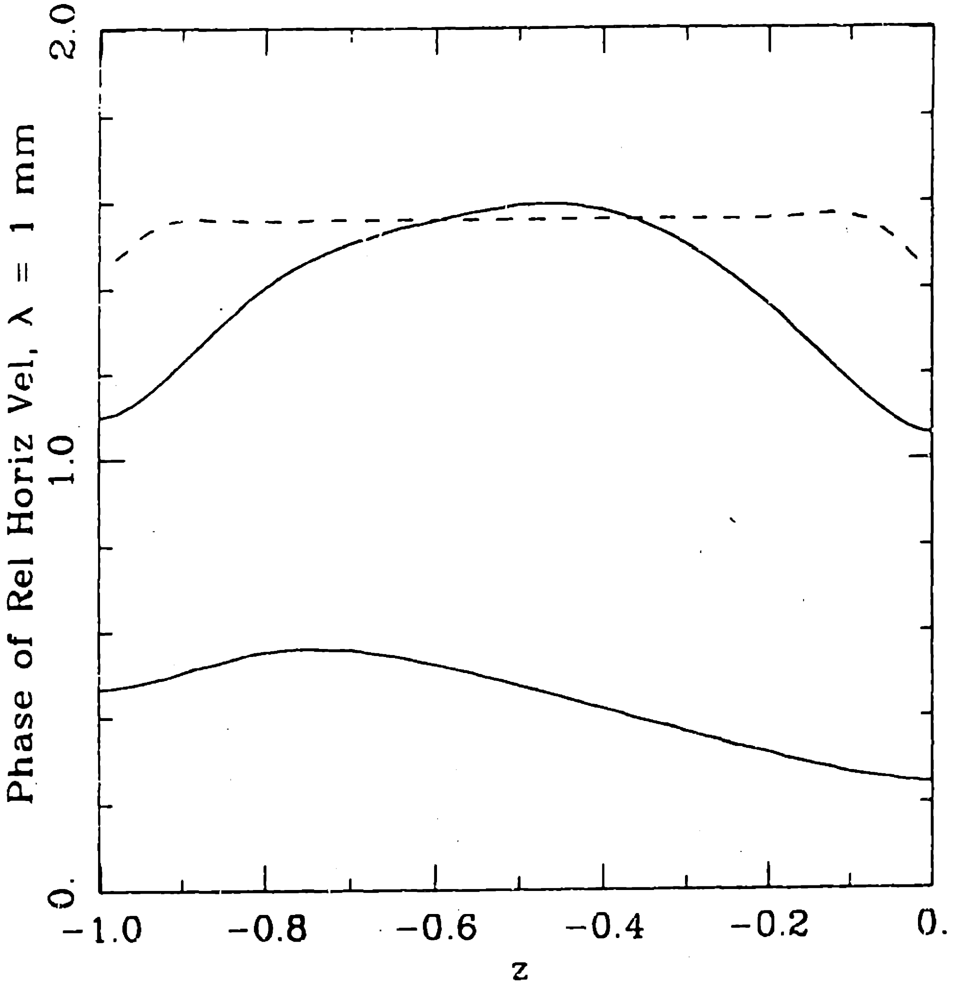

$\arg V_y$ *versus* z, $\lambda = 1$, $f = 10^{-3}, 10^{-2}, 10^{-1}$ (– –).

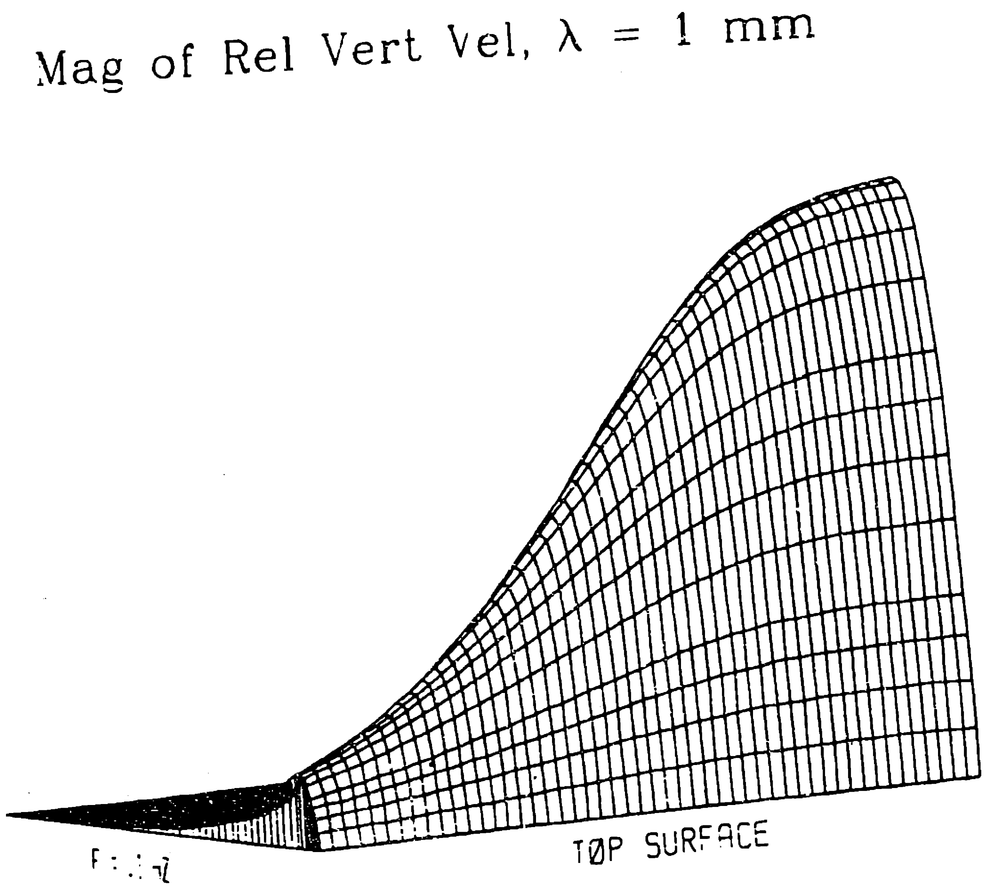

$|V_z^*/\omega a_J|$, $\lambda = 1\ mm$, $f = 10^{-3}$ to 0.1 Hz logarithmically.

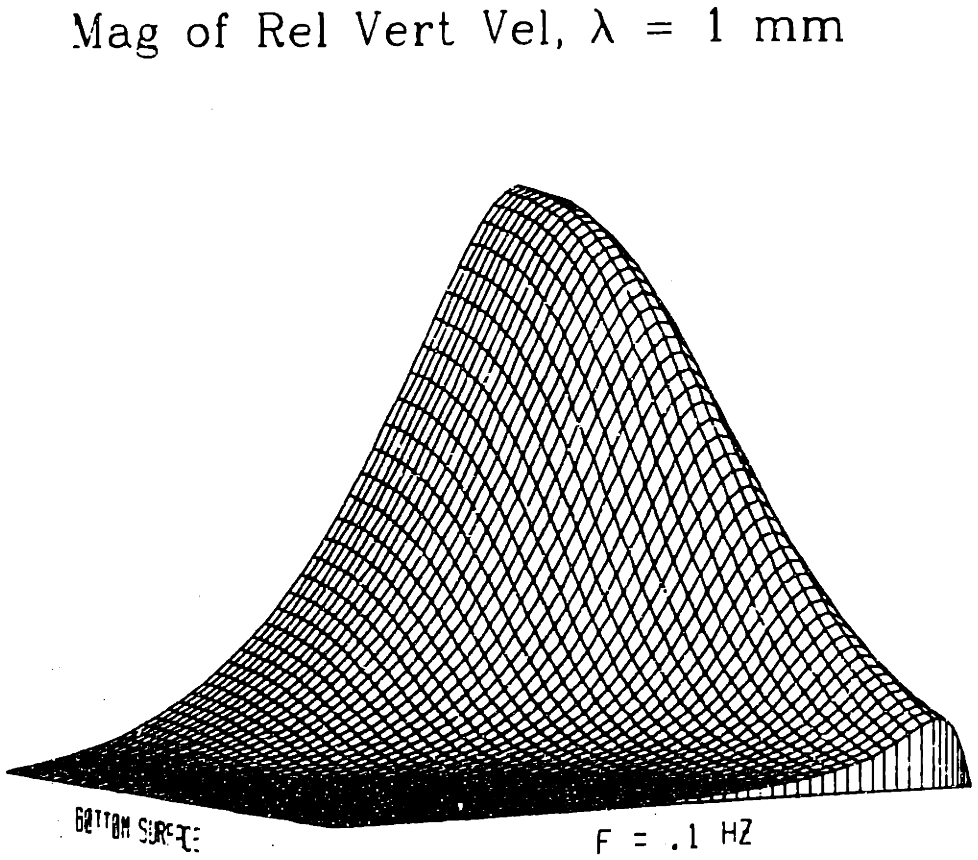

$|V_z^*/\omega a_J|$, $\lambda = 1\ mm, f = 10^{-3}$ to 0.1 Hz logarithmically.

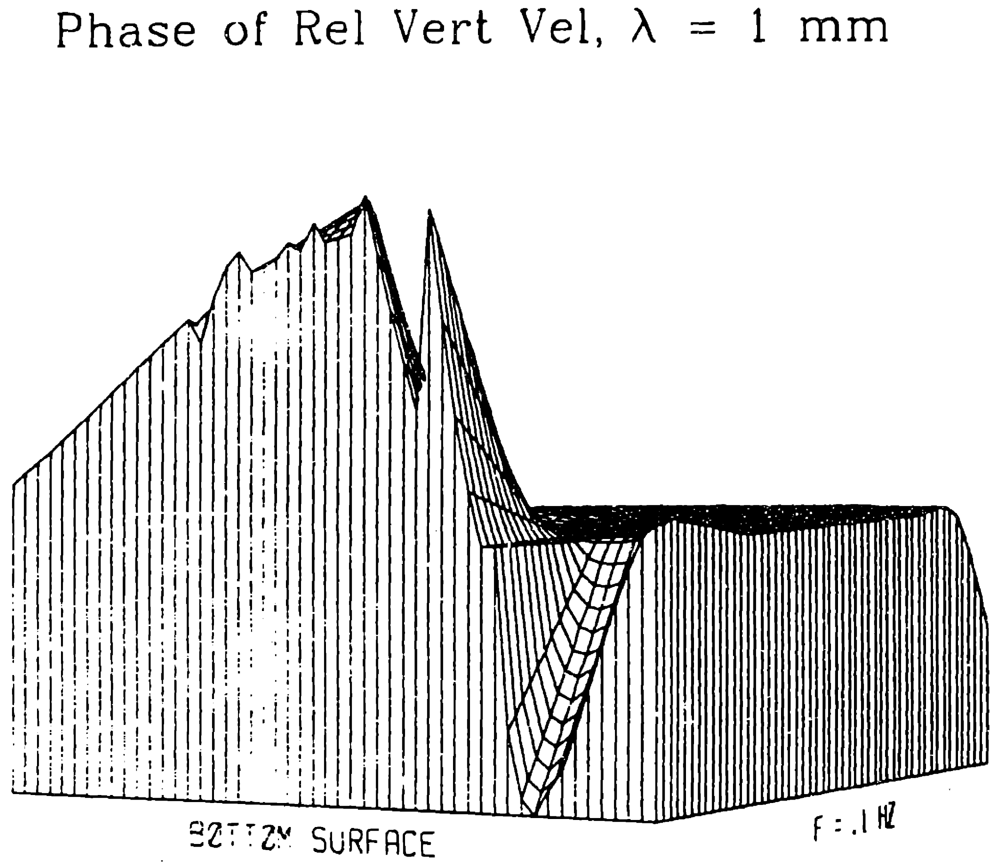

$-1.67 < \arg V_z < 2.10$, $\lambda = 1\ mm$, $f = 10^{-3}$ to 0.1 Hz logarithmically.

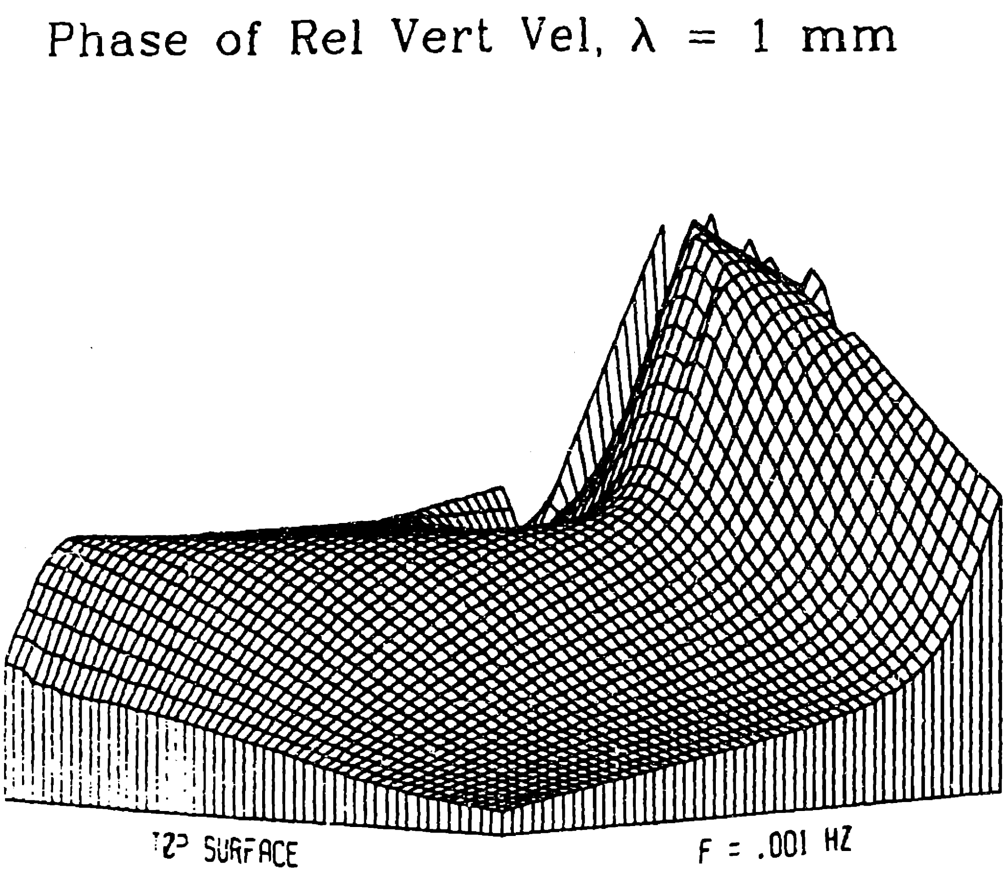

$-1.67 < \arg V_z < 2.10$, $\lambda = 1$ *mm*, $f = 10^{-3}$ to 0.1 *Hz* logarithmically.

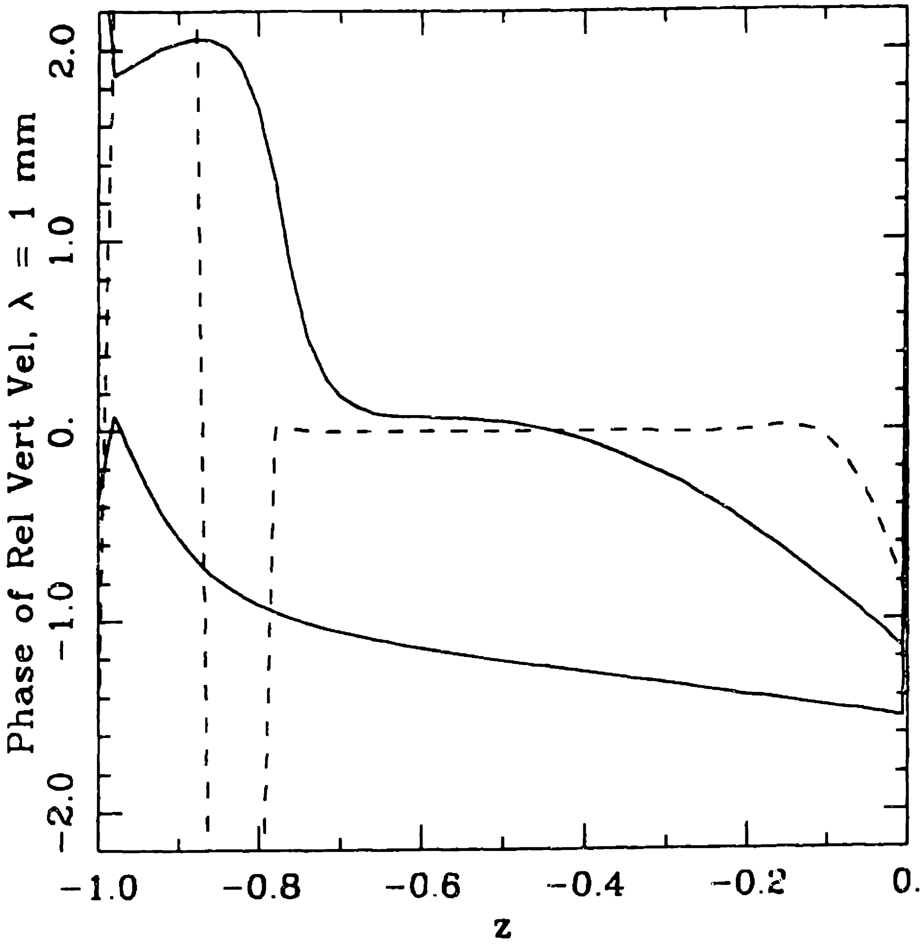

arg V_z *versus* z, $\lambda = 1$, $f = 10^{-3}, 10^{-2}, 10^{-1}$ (– –).

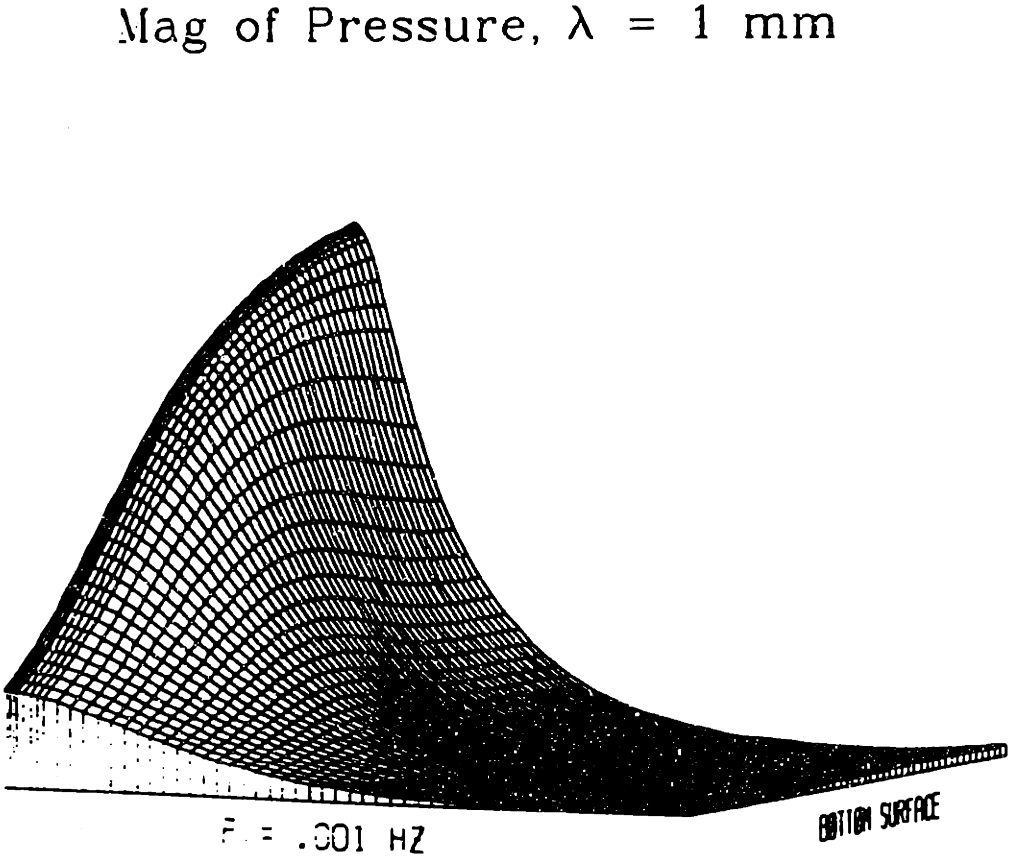

Mag of Pressure, λ = 1 mm

$|p|$, $\lambda = 1\ mm, f = 10^{-3}$ to 0.1 Hz logarithmically.

Phase of Pressure, λ = 1 mm

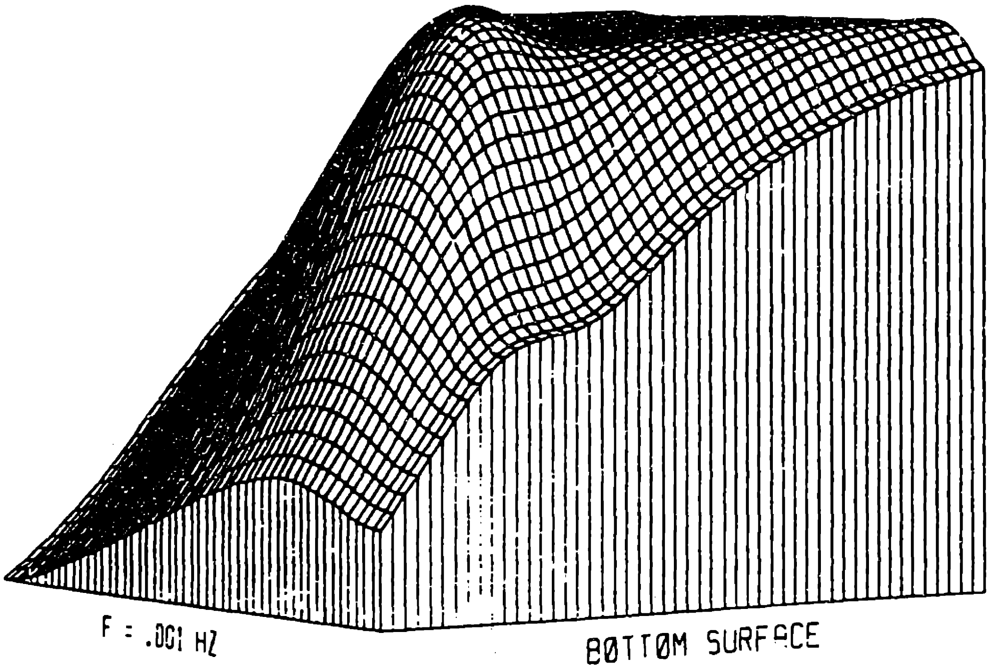

$1.82 < \arg p < 3.18$, $\lambda = 1\ mm$, $f = 10^{-3}$ to $0.1\ Hz$ logarithmically.

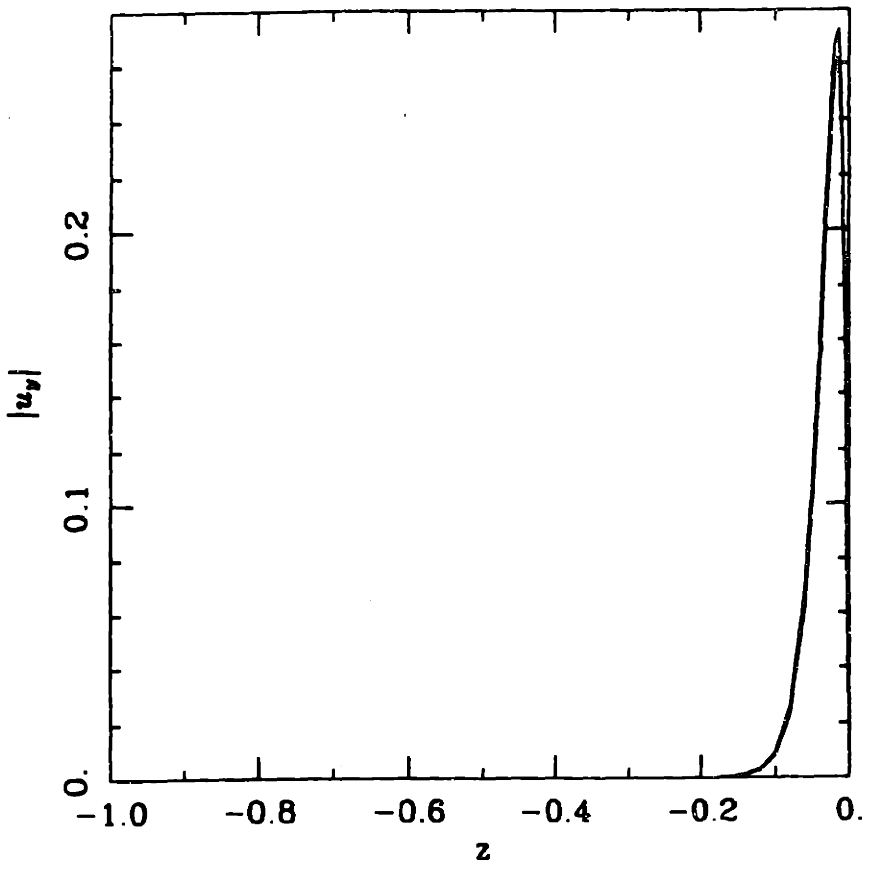

$|u_y|$, $\lambda = 0.1\ mm, f = 10^{-3}$ and 0.1 *Hz* (0.1 has the higher maximum)

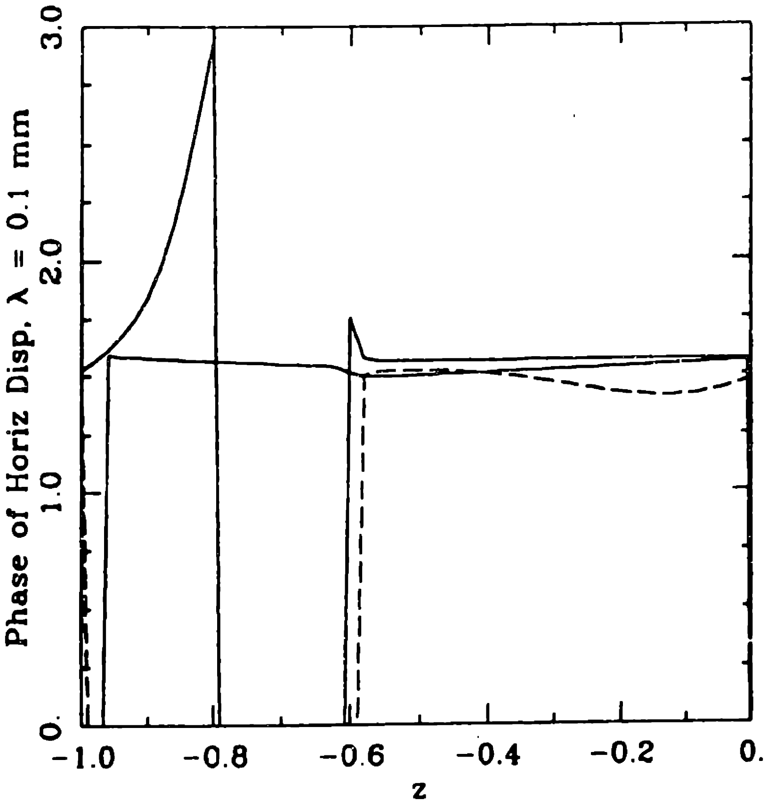

arg u_y, $\lambda = 0.1\ mm, f = 10^{-3}$, $f = 10^{-2}$, and $f = 0.1\ Hz$ (— —).

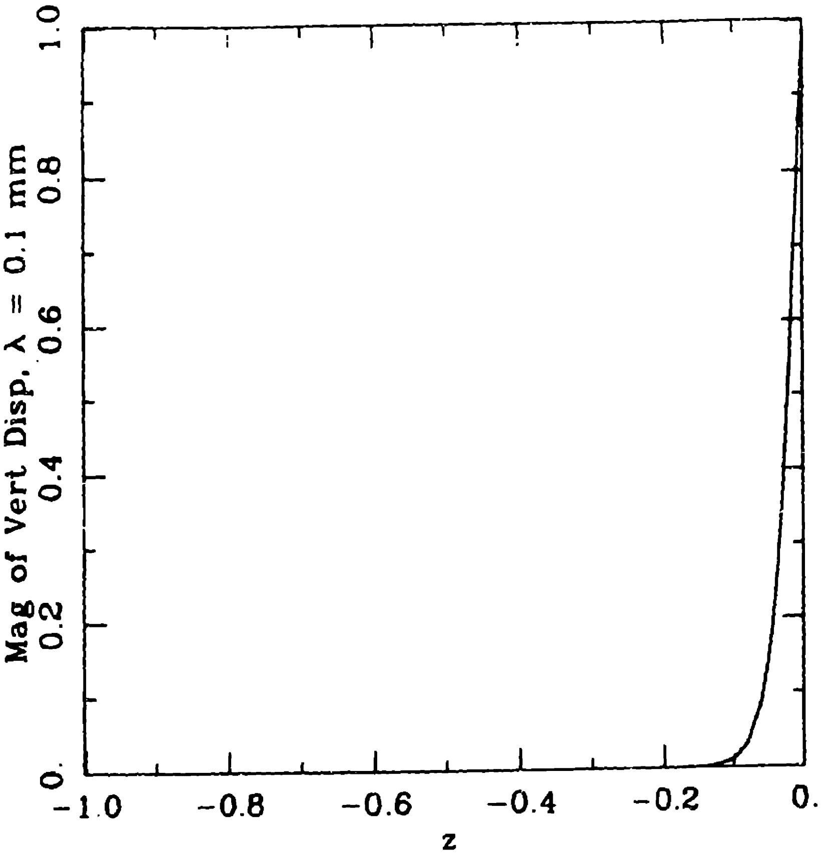

$|u_z|$, $\lambda = 0.1\, mm, f = 10^{-3}$ and $0.1\, Hz$.

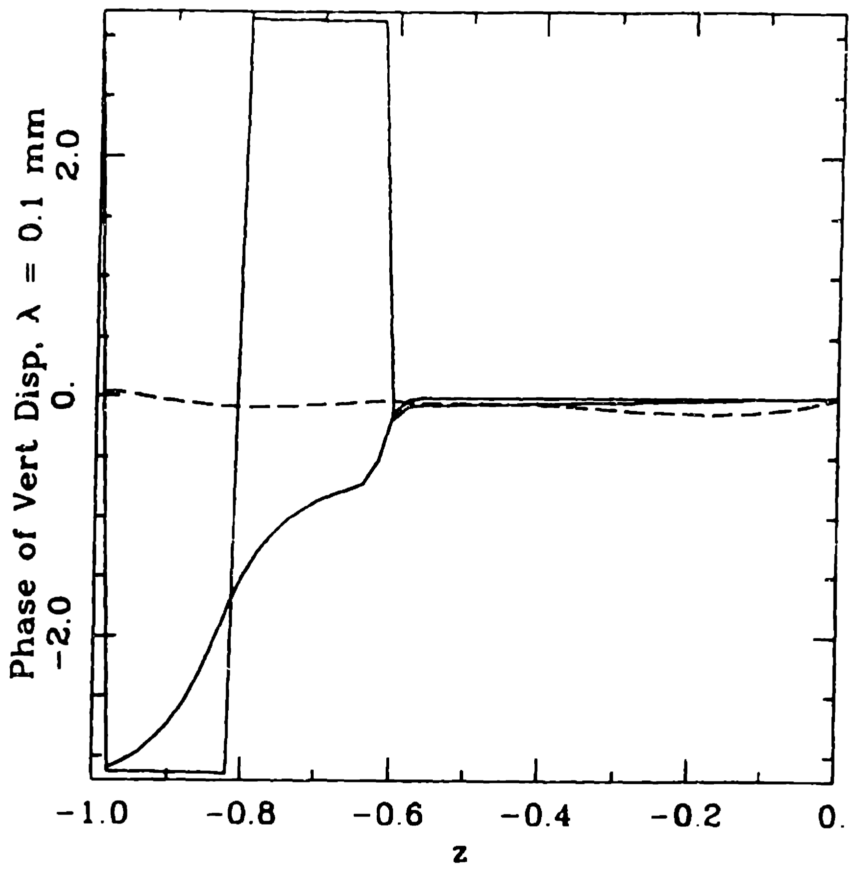

arg u_z, $\lambda = 0.1\ mm$, $f = 10^{-3}$, $f = 10^{-2}$, and $f = 0.1\ Hz$ (— —).

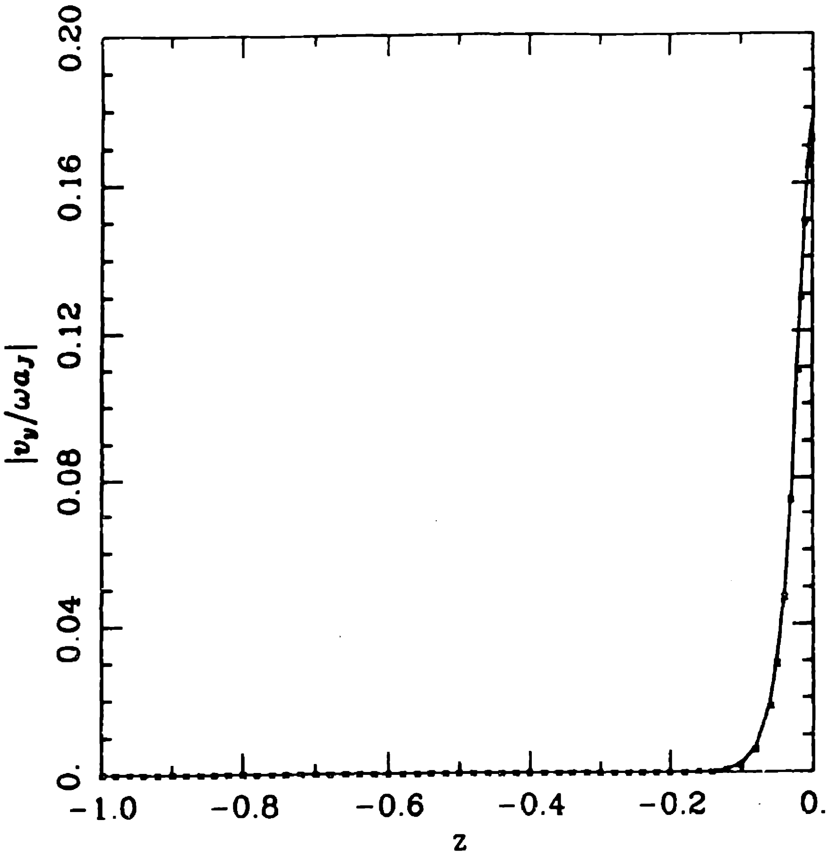

$|V_y^*/\omega a_J|$, $\lambda = 0.1$ *mm*, $f = 10^{-3}$ (solid) and 0.1 *Hz* ("*").

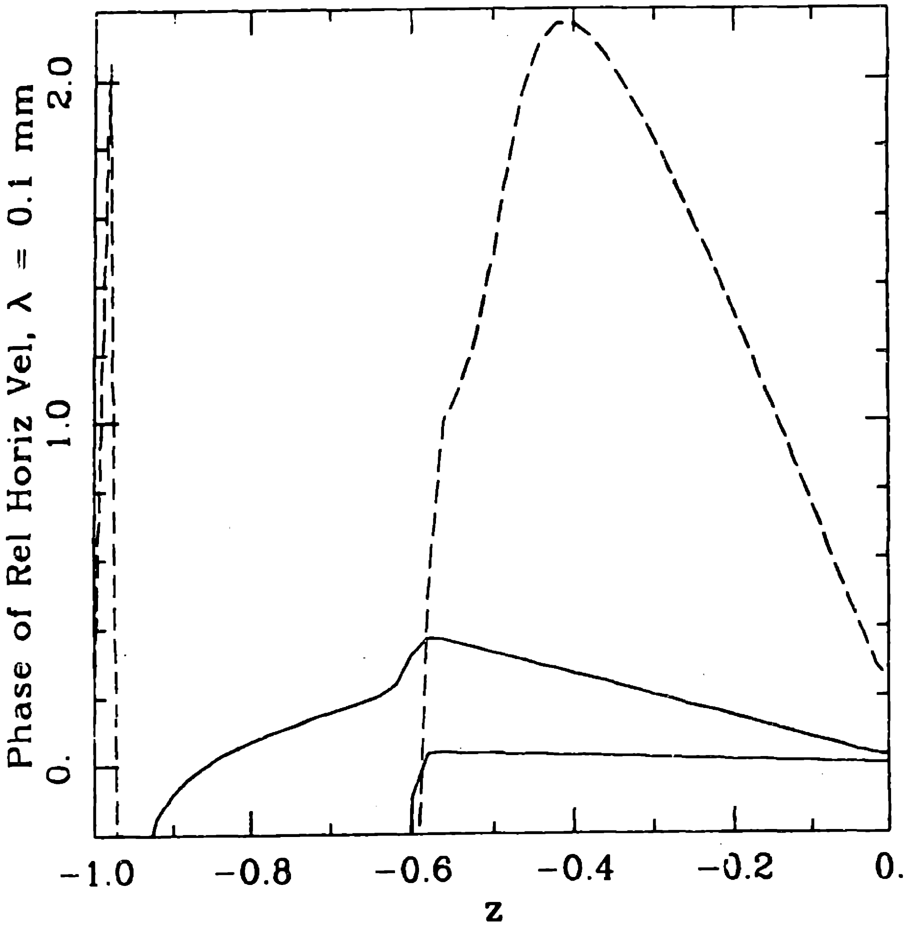

$\arg V_y$, $\lambda = 0.1\ mm$, $f = 10^{-3}$, $f = 10^{-2}$ and $f = 0.1\ Hz$ (— —).

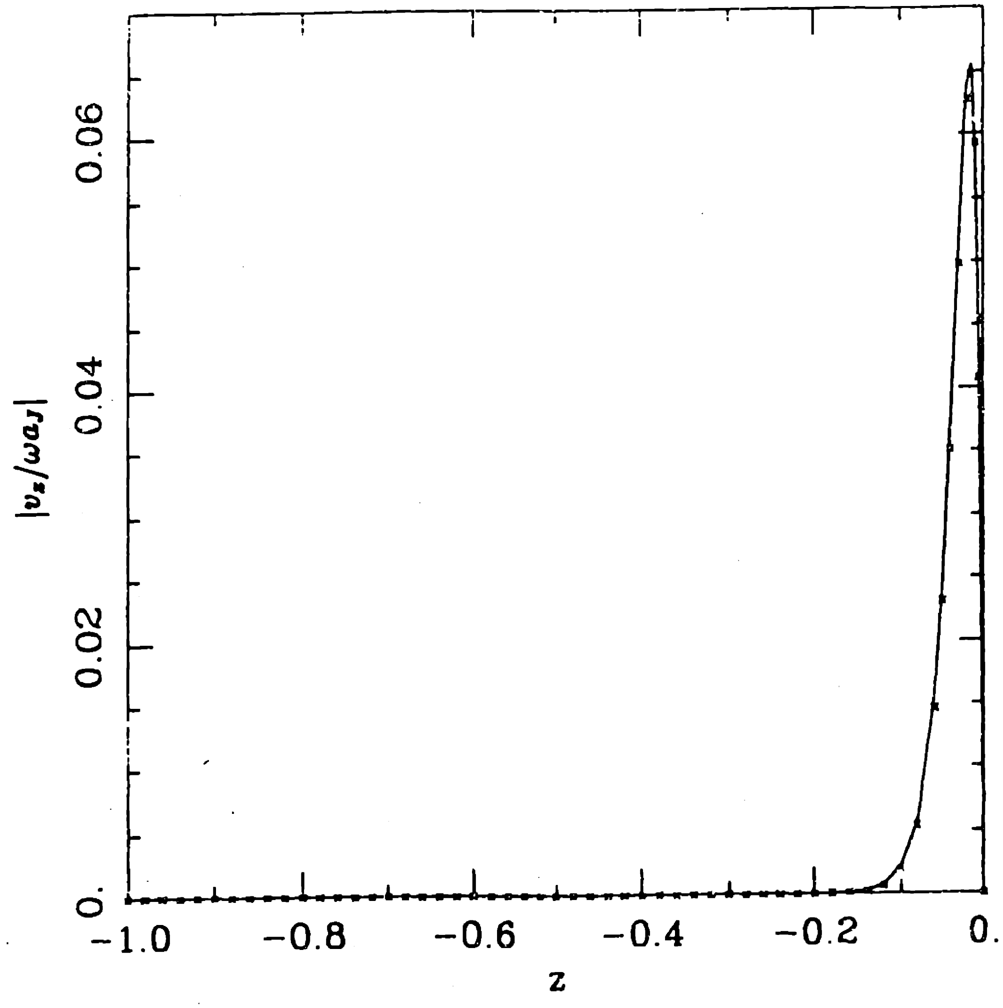

$|V_z^*/\omega a_J|$, $\lambda = 0.1\ mm$, $f = 10^{-3}$ (solid) and 0.1 Hz ("x").

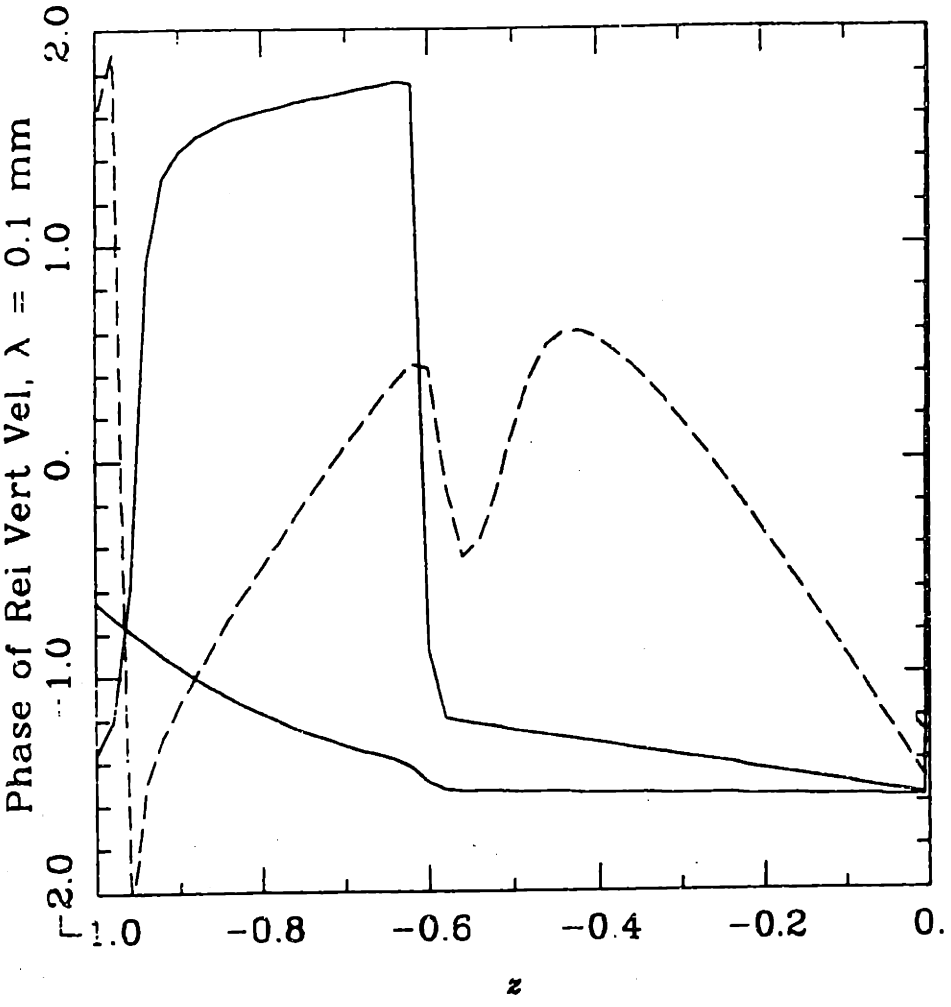

arg V_z, $\lambda = 0.1\ mm$, $f = 10^{-3}$, $f = 10^{-2}$ and $f = 0.1\ Hz$ (— —).

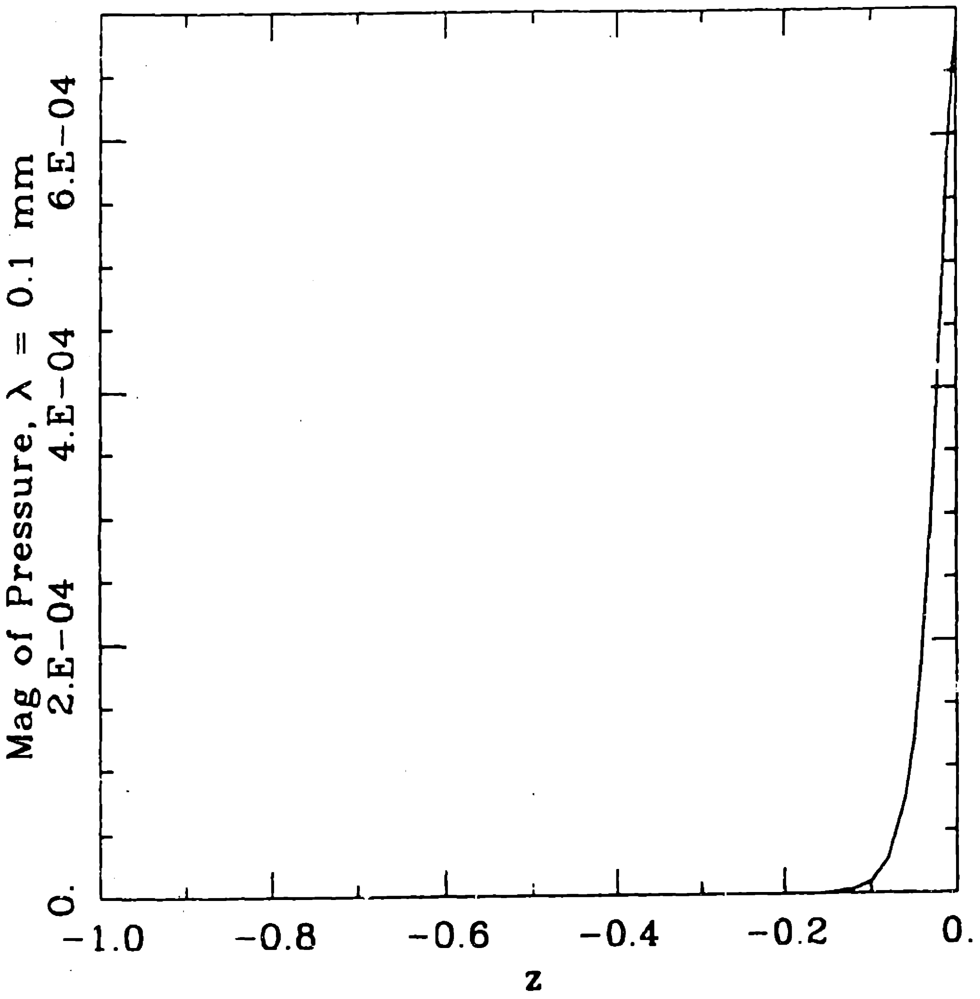

$|\frac{p}{\epsilon\pi + \jmath(\mathcal{G} + \lambda_{\mathcal{L}})/\lambda}$, $\lambda = 0.1\, mm$, $f = 10^{-3}\, Hz$.

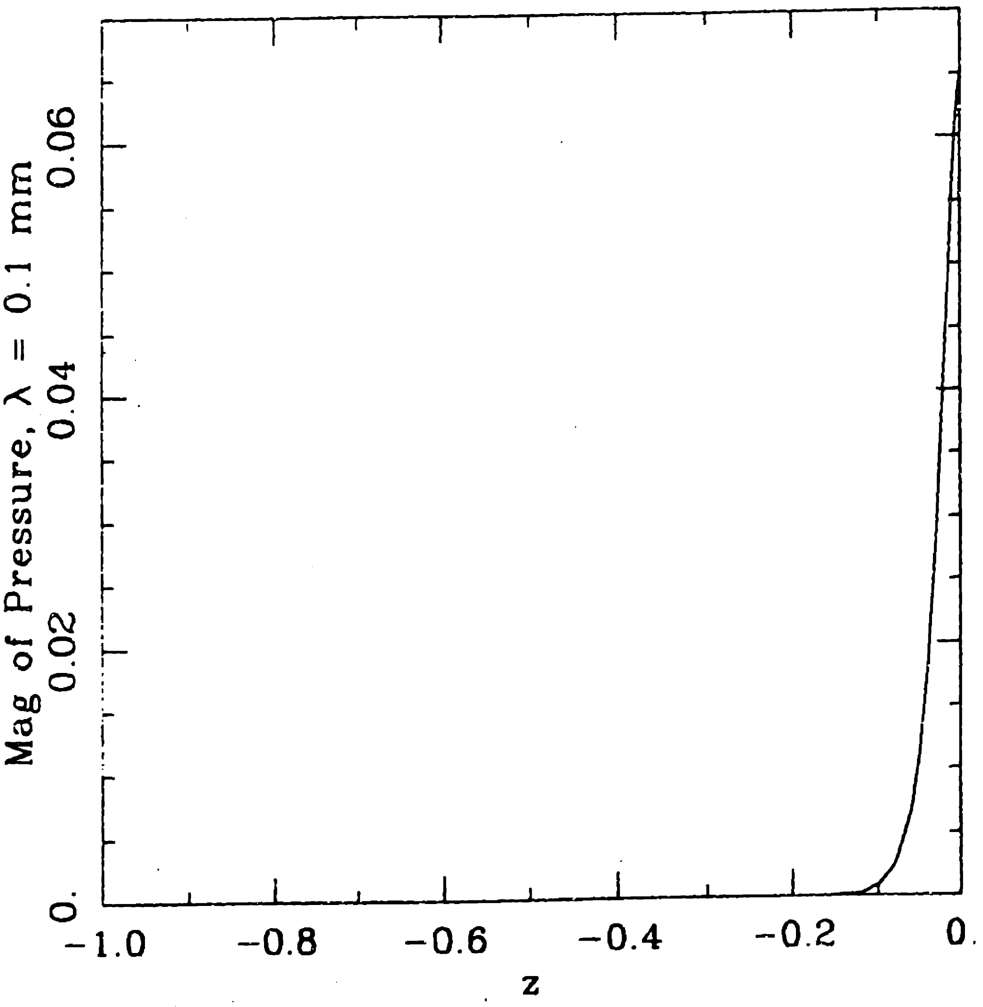

$\left|\frac{p}{\epsilon\pi + j(\mathcal{G} + \lambda_{\mathcal{L}})/\lambda}\right.$, $\lambda = 0.1\ mm$, $f = 0.1\ Hz$.

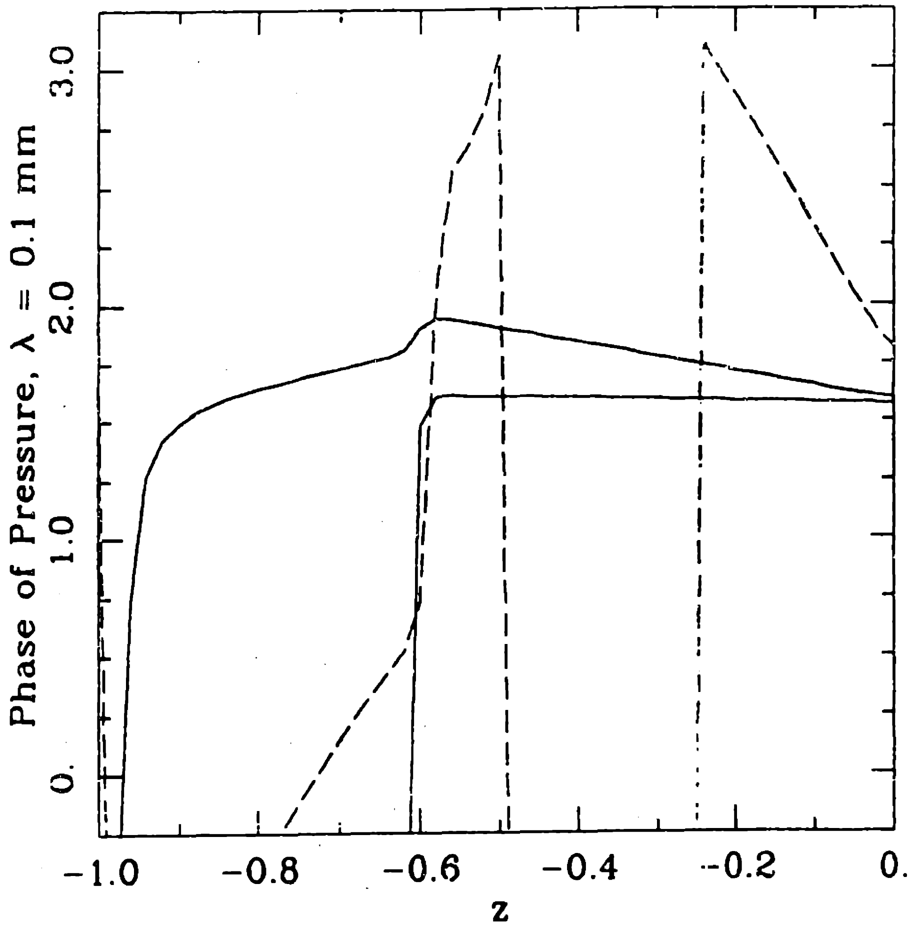

arg p, $\lambda = 0.1\ mm, f = 10^{-3}$, $f = 10^{-2}$ **and** $f = 0.1\ Hz$ **(— —).**

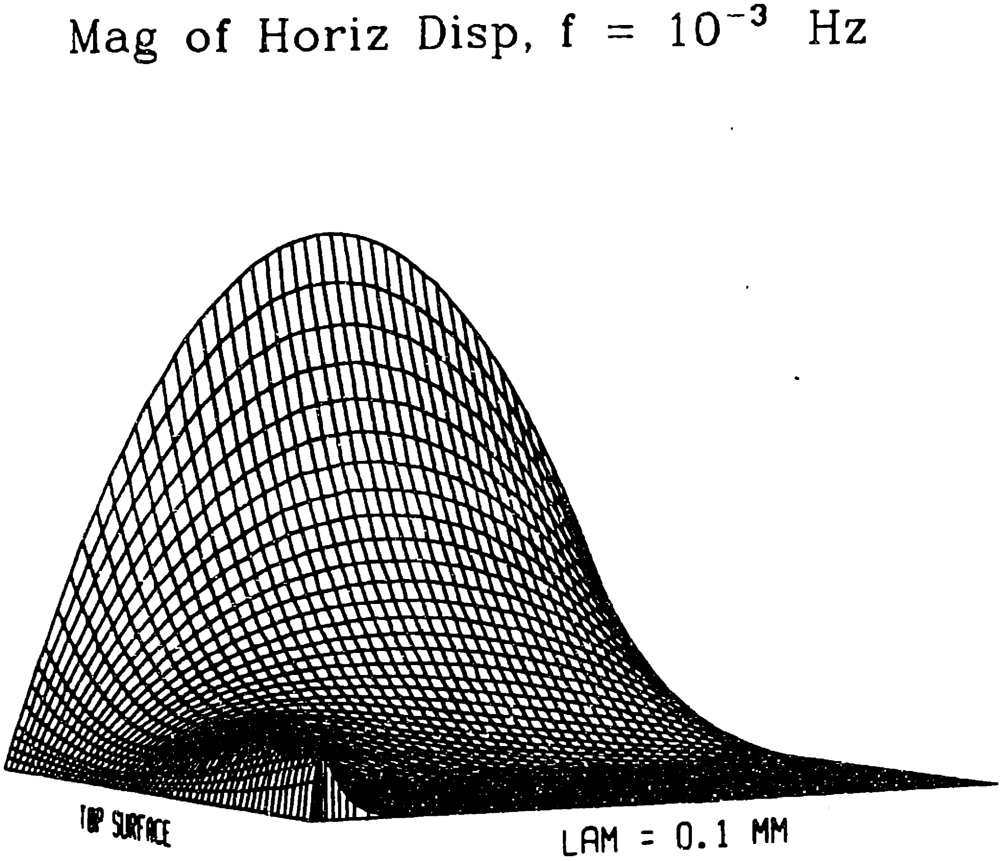

$|u_y|$, $f = 10^{-3}$ Hz, $\lambda = 0.1$ to 10.0 mm logarithmically.

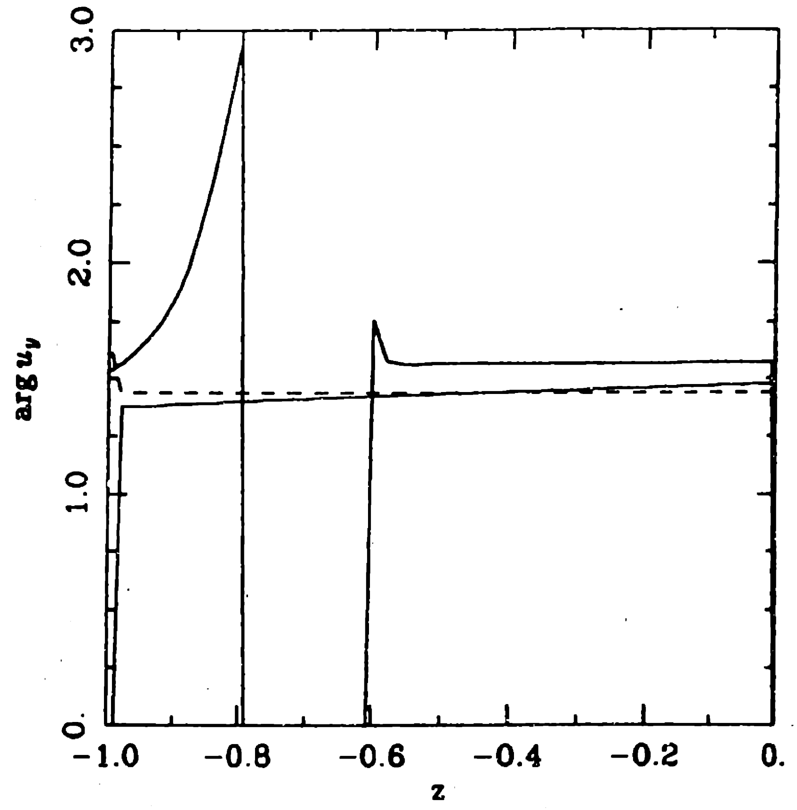

arg u_y, $f = 10^{-3}$ Hz, $\lambda = 0.1$, 1.0, and 10.0 *mm* (— —).

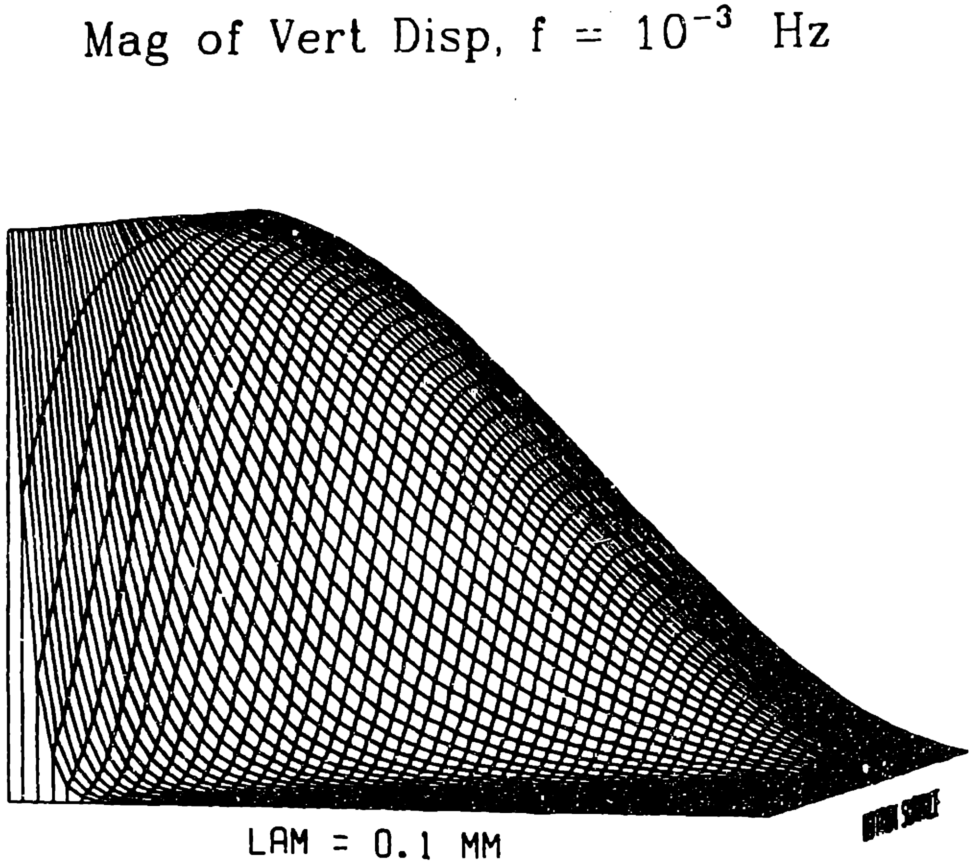

$|u_z|$, $f = 10^{-3}\ Hz$, $\lambda = 0.1$ to $10.0\ mm$ logarithmically.

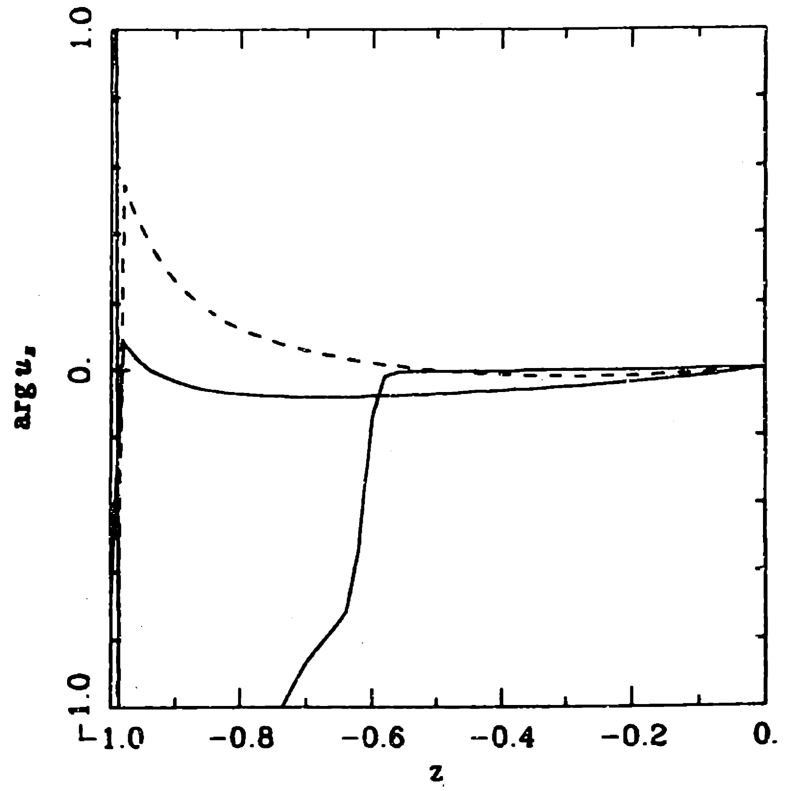

arg u_z, $f = 10^{-3}$ Hz, $\lambda = 0.1$, 1.0, and 10.0 mm (— —).

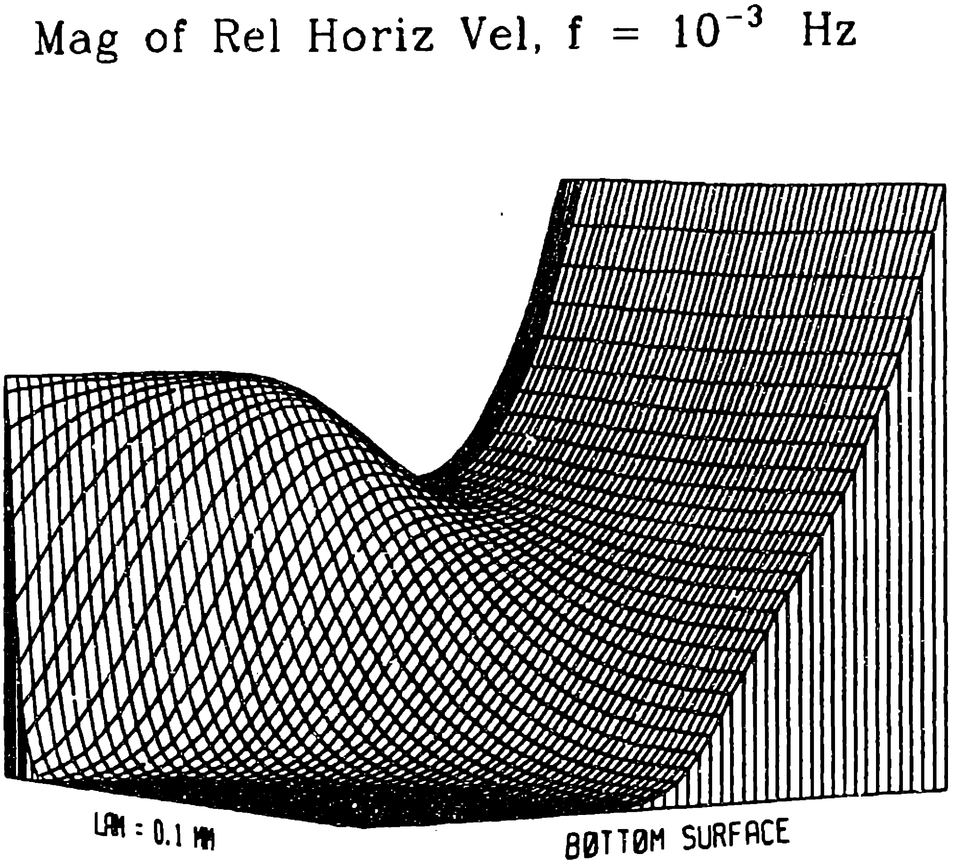

$|V_y|$, $f = 10^{-3}$ Hz, $\lambda = 0.1$ to 10.0 mm logarithmically.

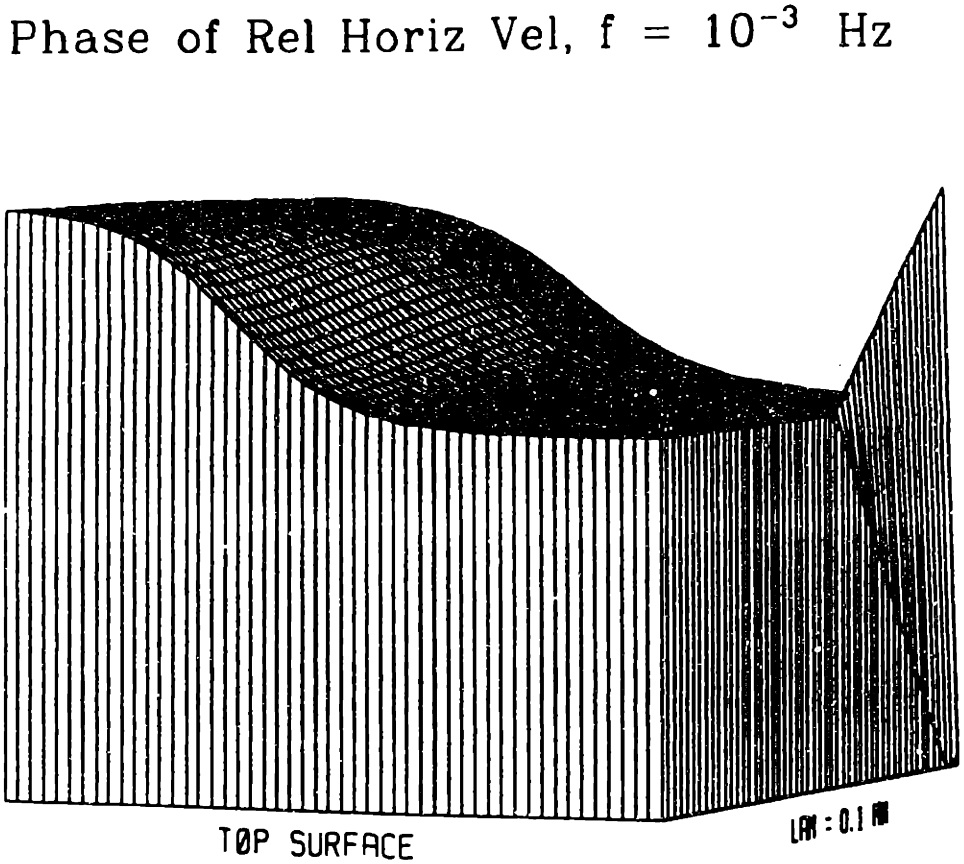

$-2.34 < \arg V_y < 1.47$, $f = 10^{-3}$ Hz, $\lambda = 0.1$ to 10.0 mm logarithmically.

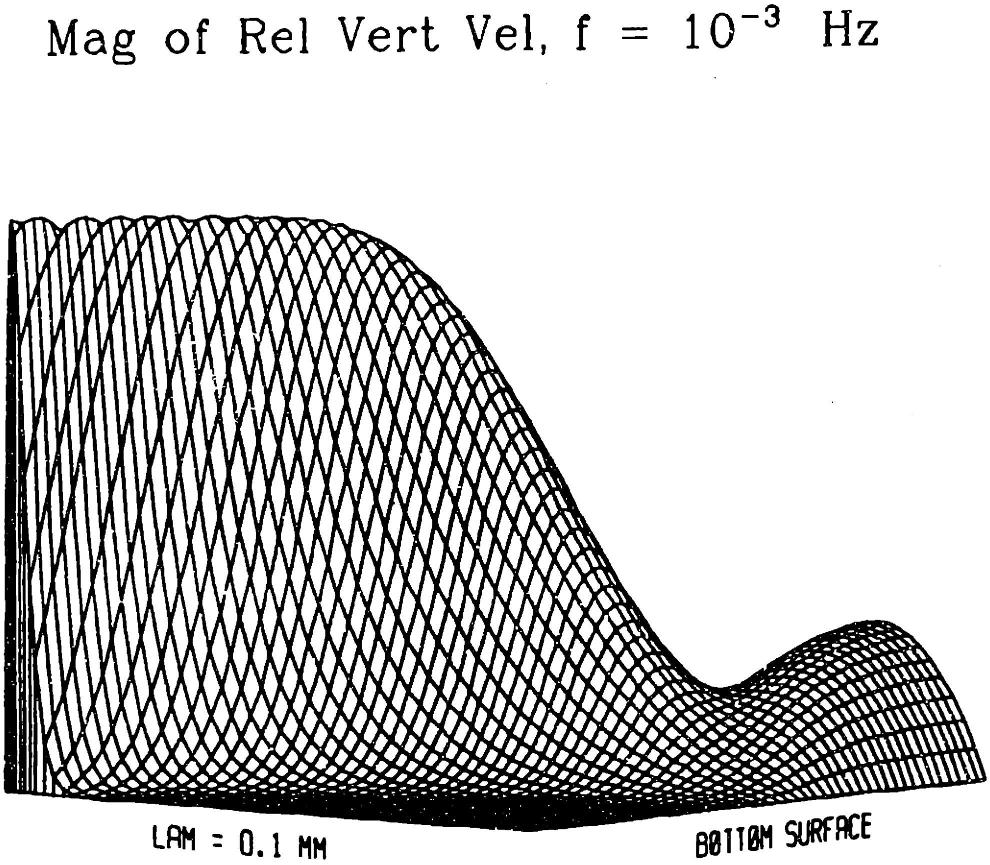

$|V_z|$, $f = 10^{-3}\ Hz$, $\lambda = 0.1$ to $10.0\ mm$ logarithmically.

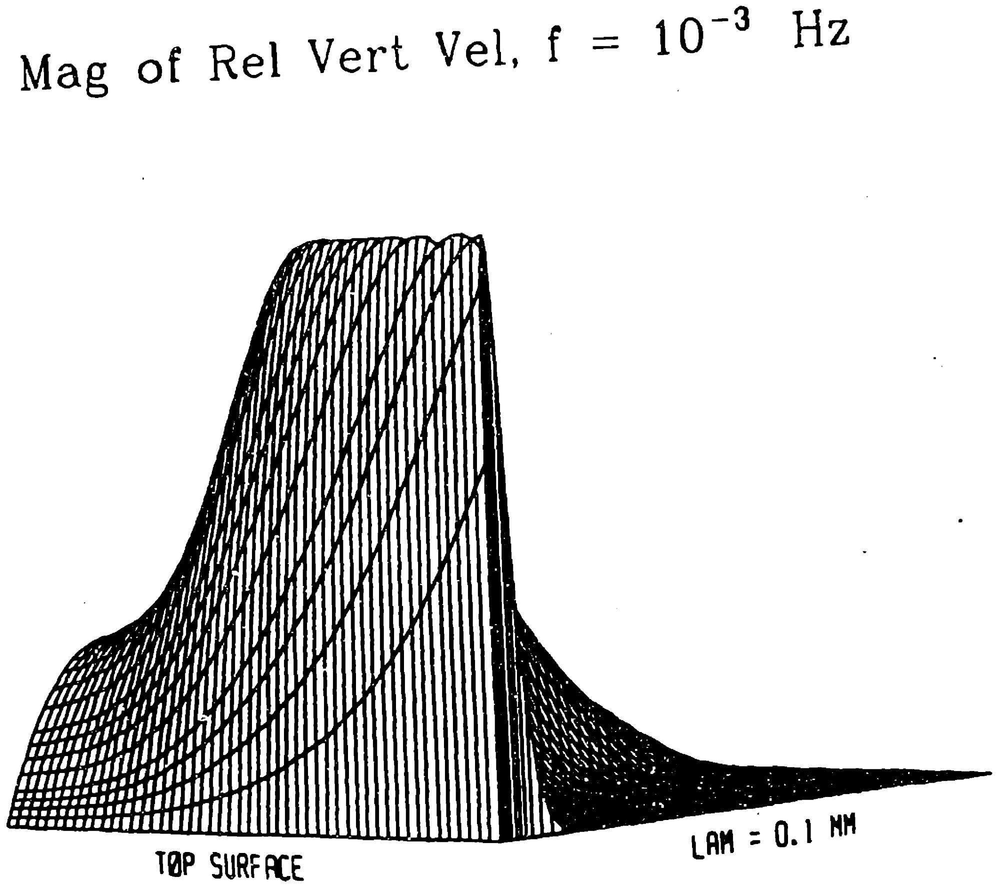

$|V_z|$, $f = 10^{-3}\ Hz$, $\lambda = 0.1$ to $10.0\ mm$ logarithmically.

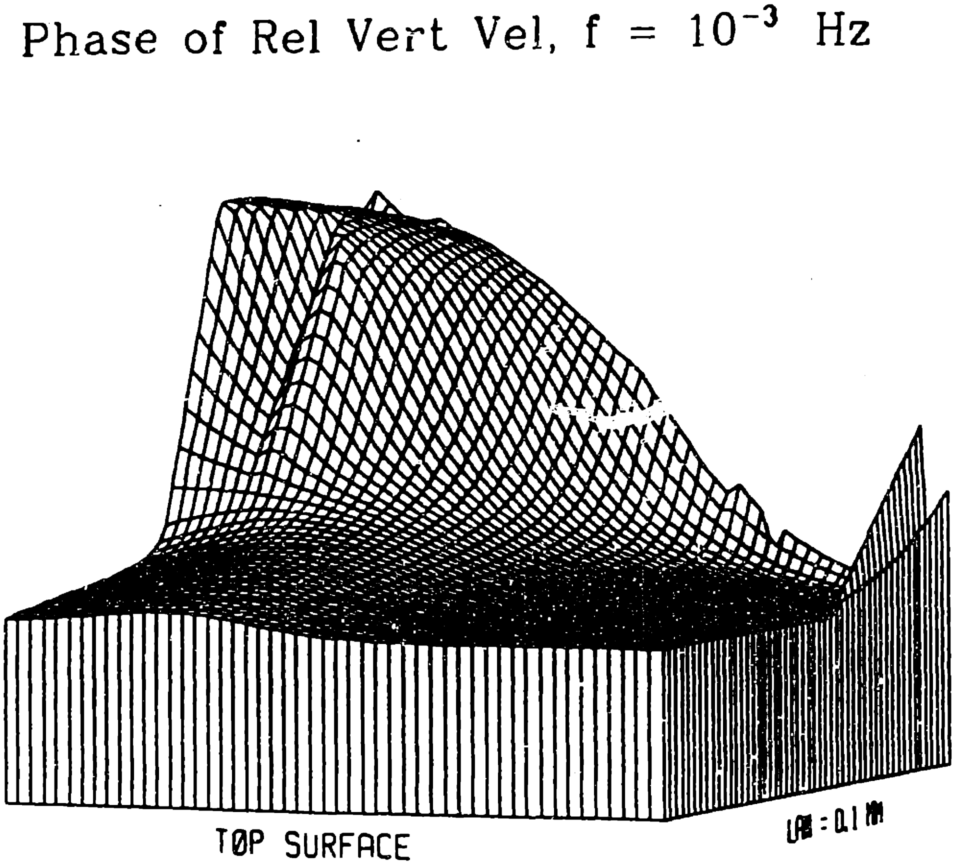

$-2.9 < \arg V_z < 1.78$, $f = 10^{-3}\ Hz$, $\lambda = 0.1$ to $10.0\ mm$ logarithmically.

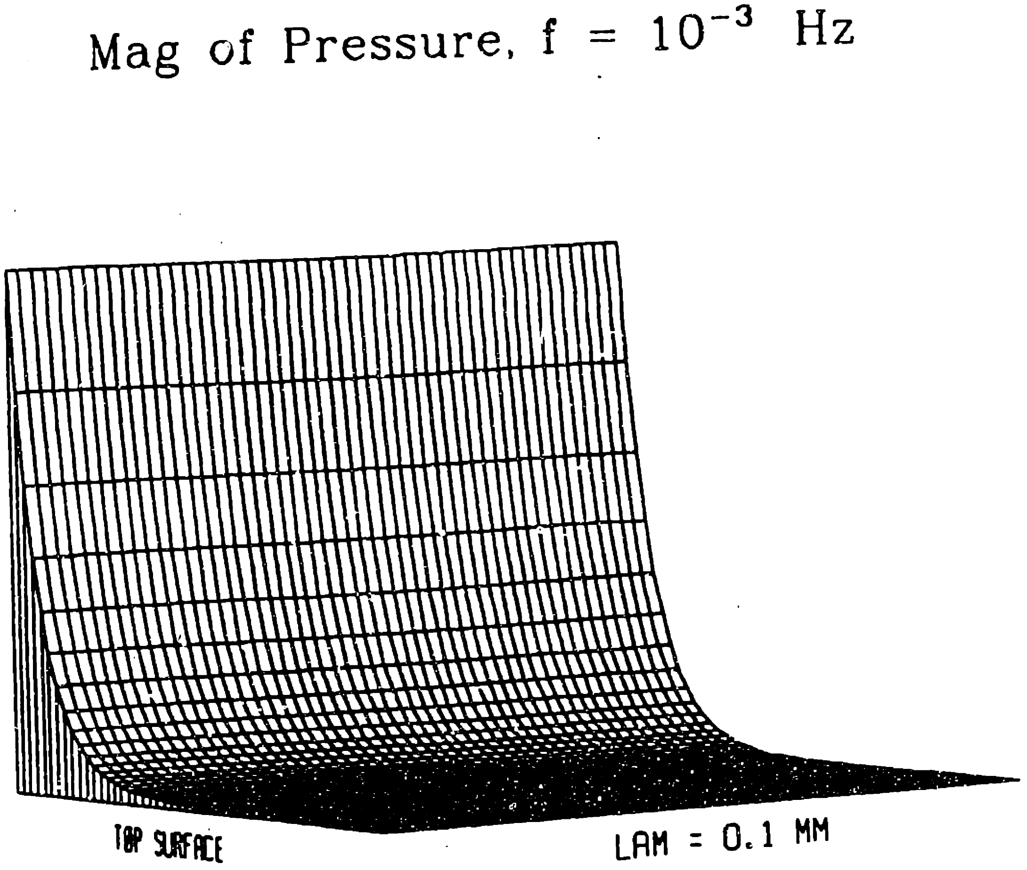

$|\lambda p|$, $f = 10^{-3}\ Hz$, $f = 10^{-3}\ Hz$, $\lambda = 0.1$ to $10.0\ mm$ logarithmically.

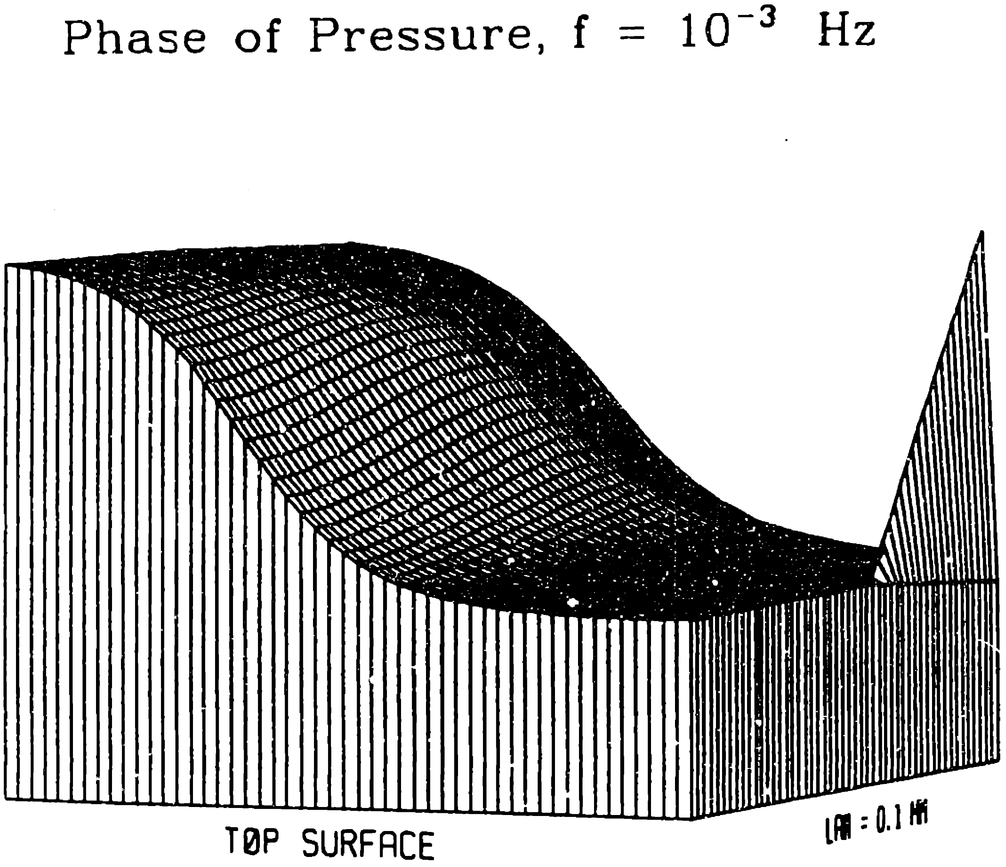

$0.784 < \arg p < 3.04$, $f = 10^{-3}\ Hz$, $\lambda = 0.1$ to 10.0 *mm* logarithmically.

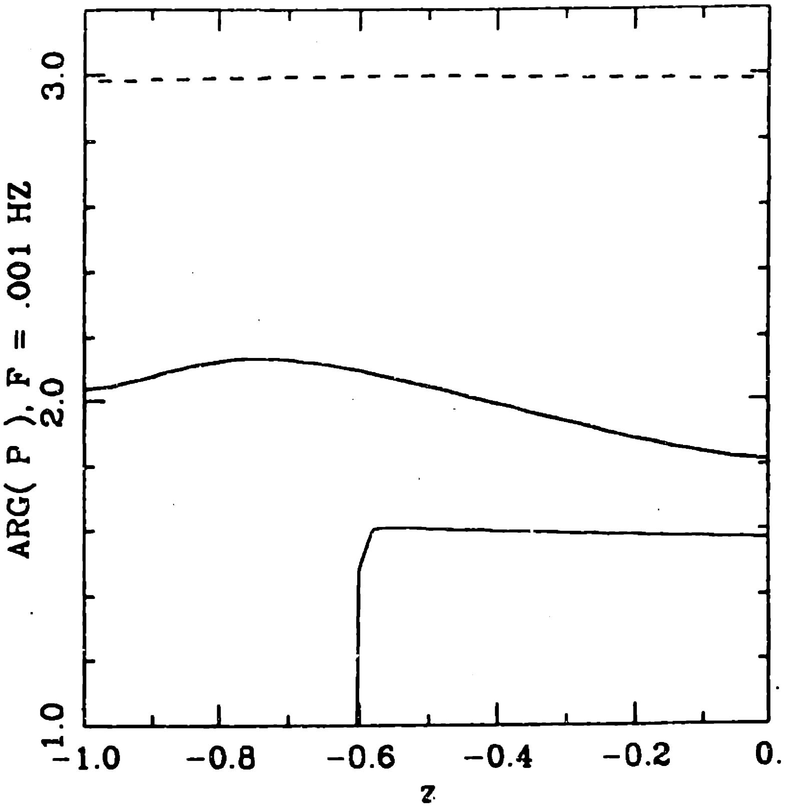

$\arg p$, $f = 10^{-3}$ Hz, $\lambda = 0.1$, 1.0, and 10.0 mm (— —).

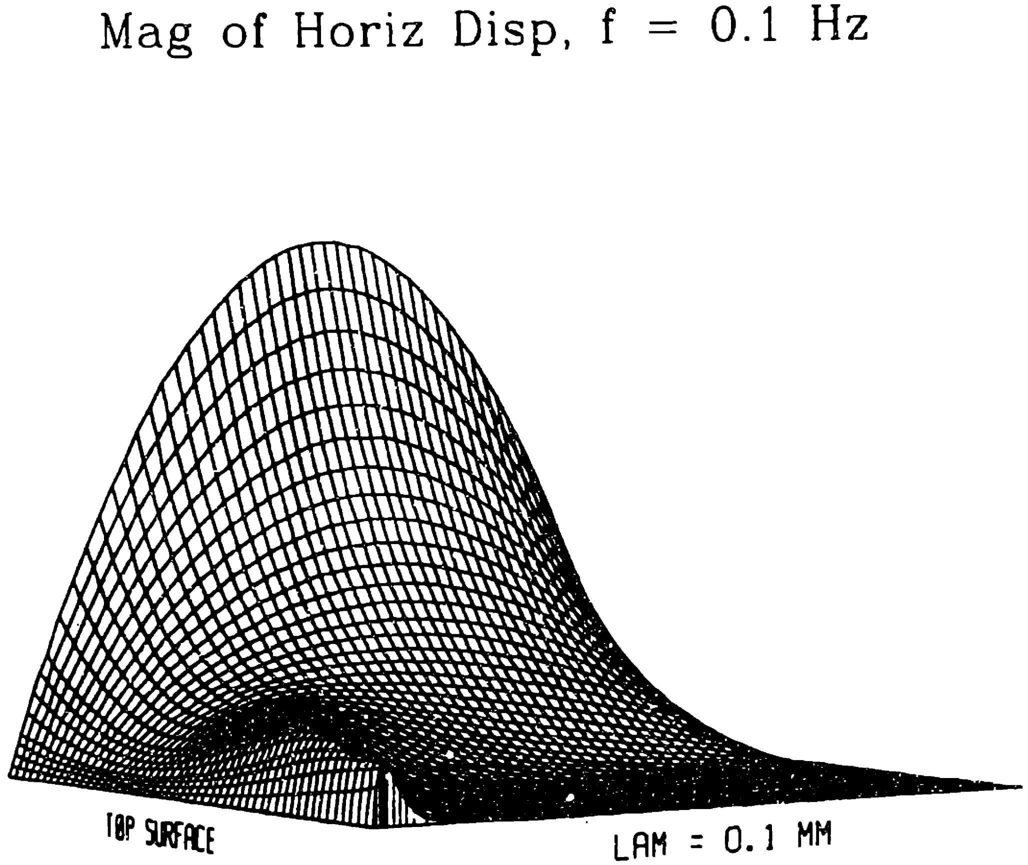

$|u_y|$, $f = 0.1\ Hz$, $\lambda = 0.1$ to $10.0\ mm$ logarithmically.

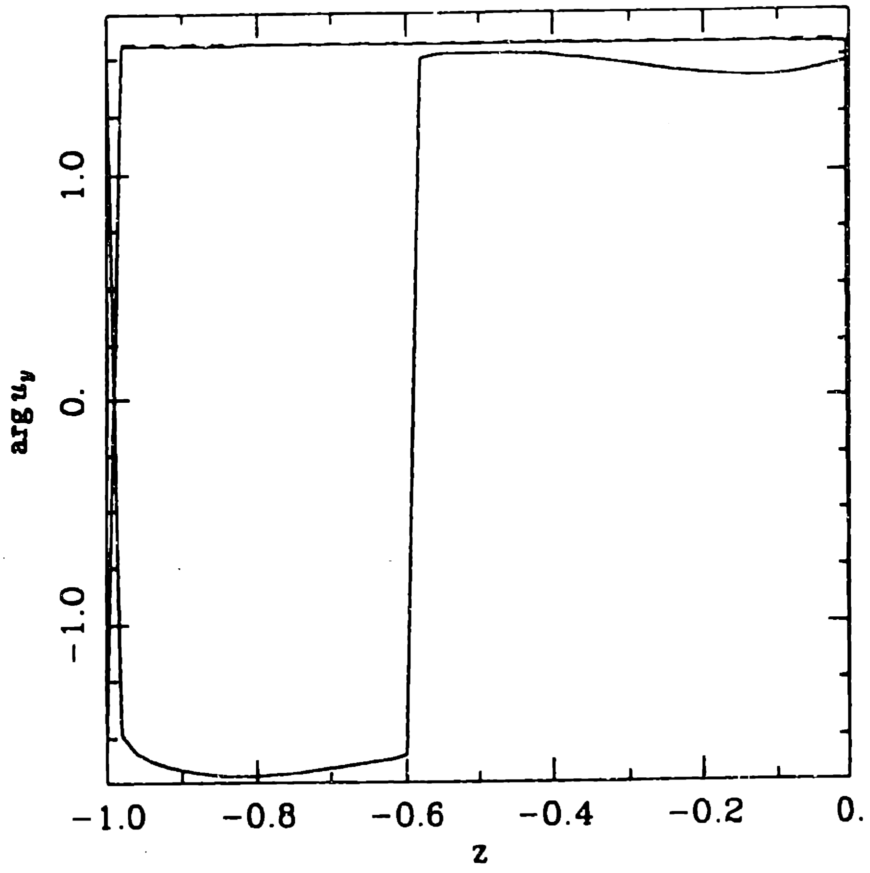

arg u_y, $f = 0.1\ Hz$, $\lambda = 0.1$, 0.759, and 10.0 mm (— —).

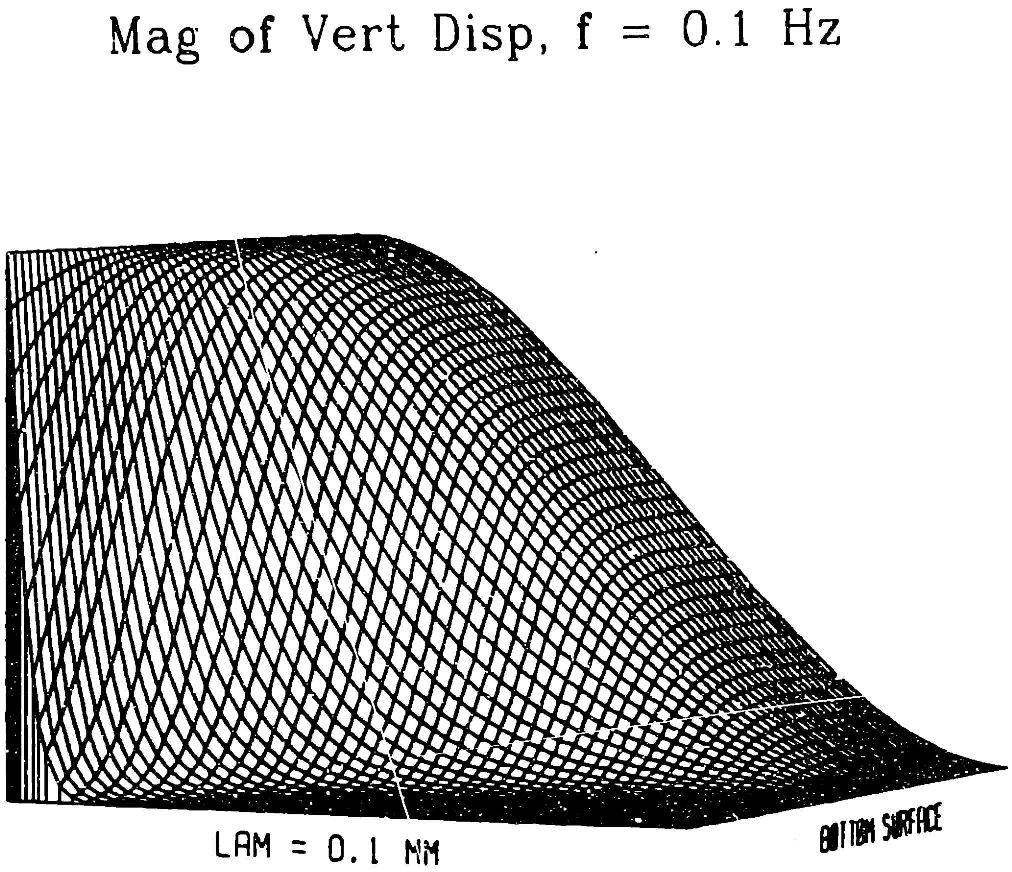

$|u_z|$, $f = 0.1\ Hz$, $\lambda = 0.1$ to $10.0\ mm$ logarithmically.

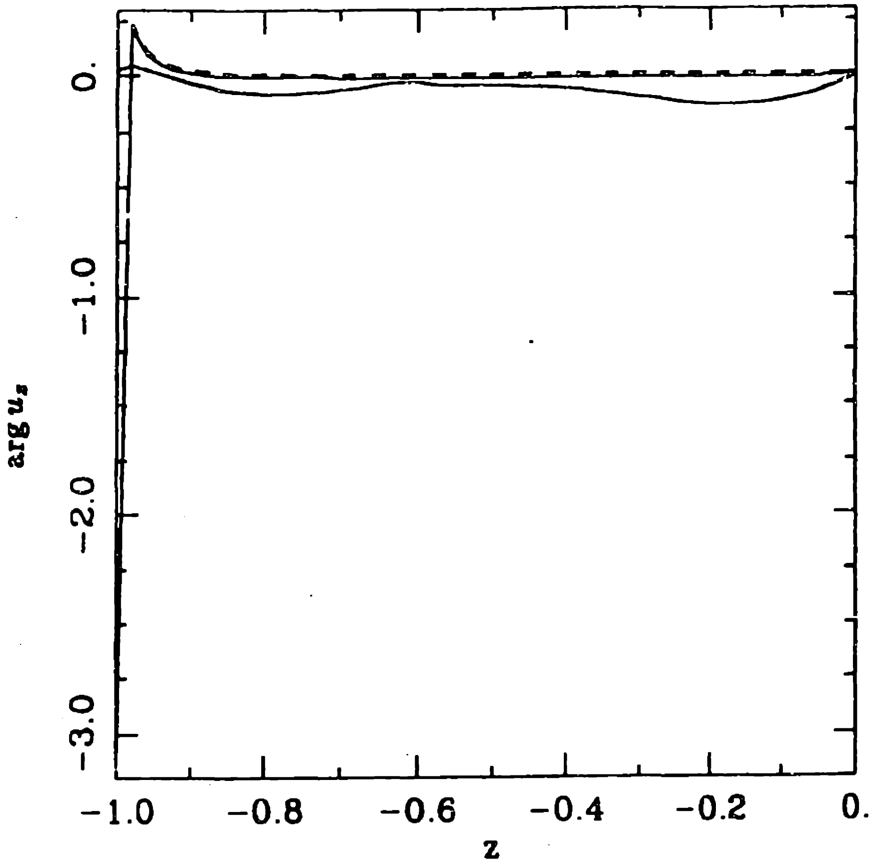

arg u_z, $f \doteq 0.1\ Hz$, $\lambda = 0.1$, 1.0, and 10.0 *mm* (— —).

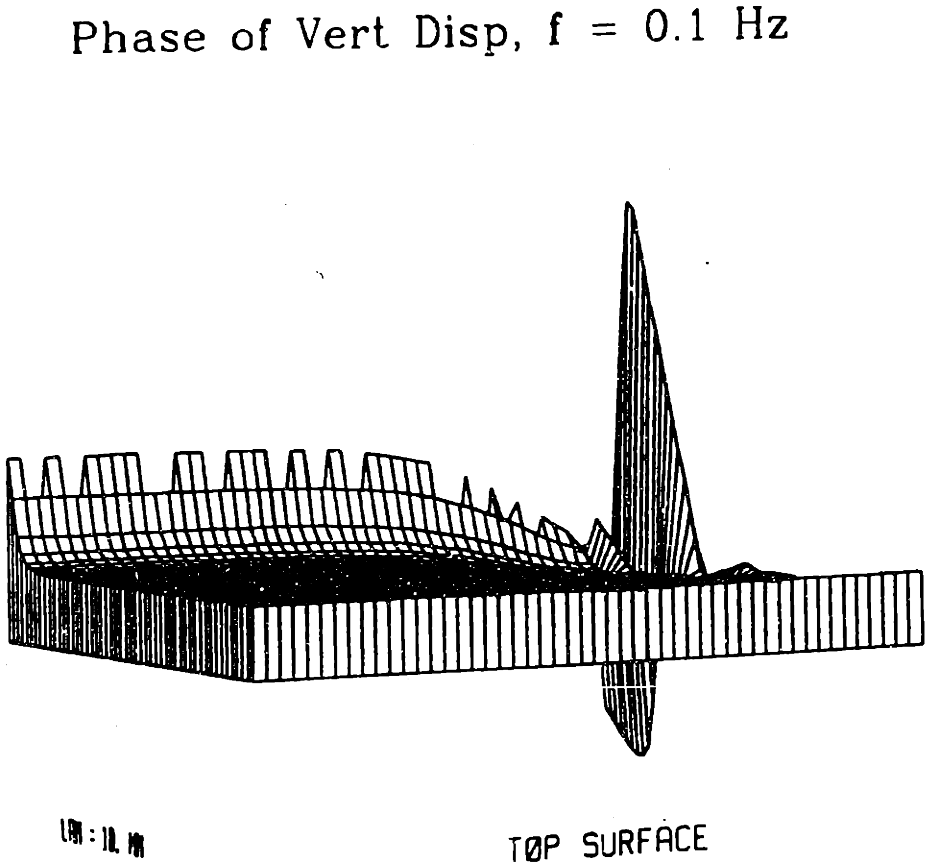

arg u_z, $f = 0.1$ *Hz*, $\lambda = 0.1$ to 10.0 *mm* logarithmically: range unknown – *cf.* previous page.

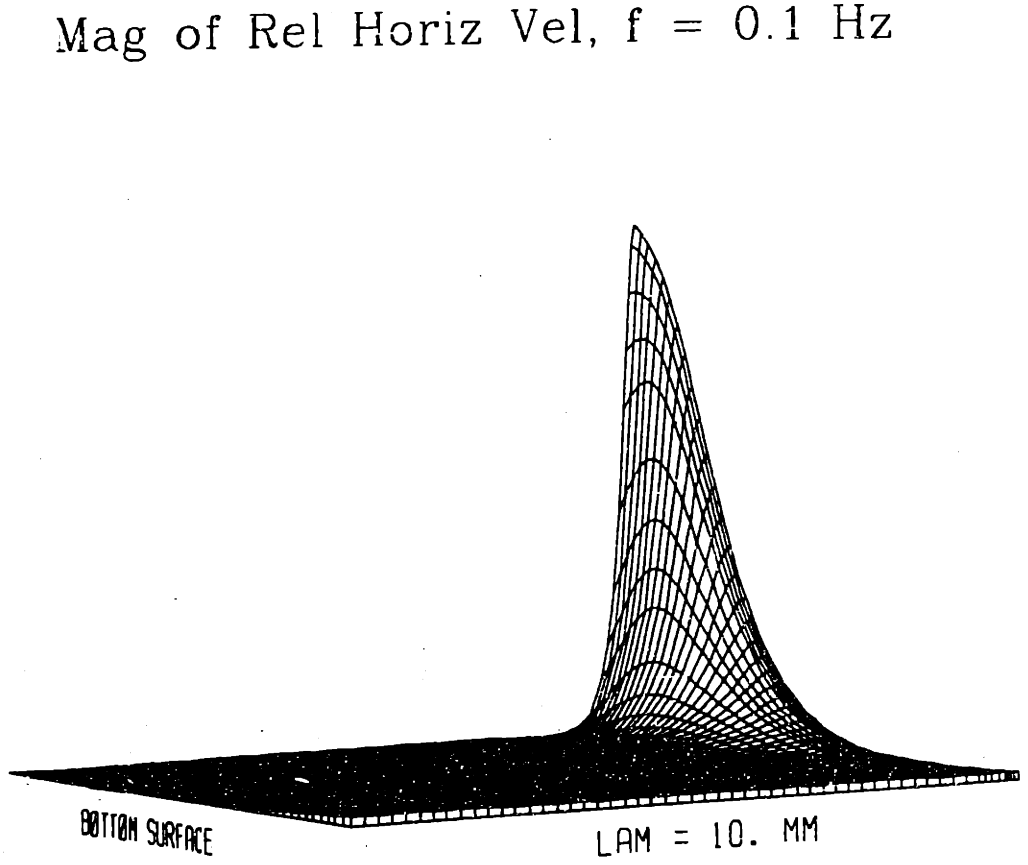

$|V_y|$, $f = 0.1$ *Hz*, $\lambda = 0.1$ to 10.0 *mm* logarithmically.

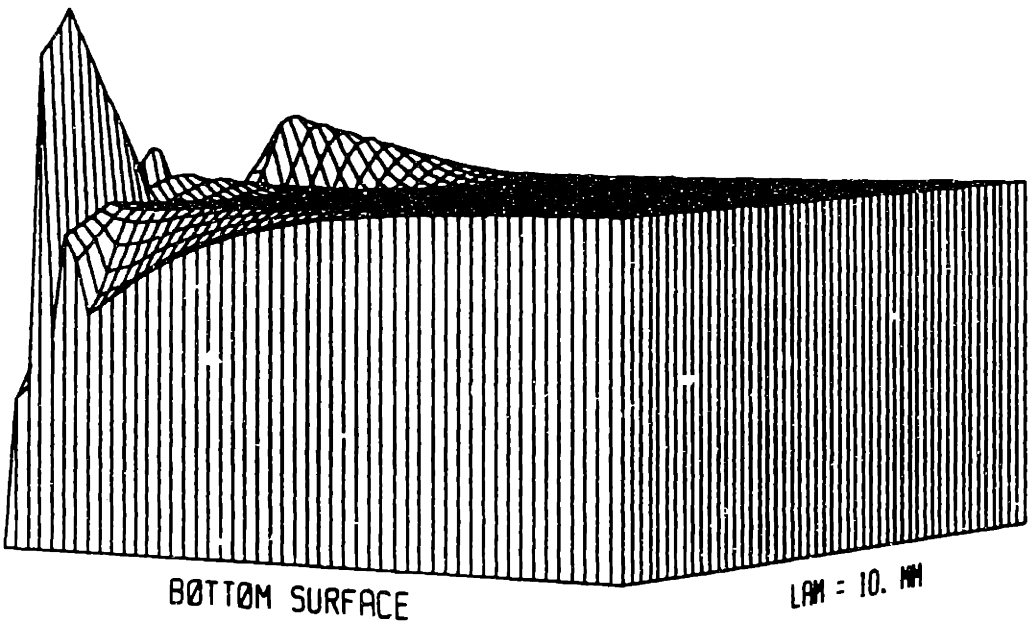

Phase of Rel Horiz Vel, f = 0.1 Hz

$-1.22 < \arg V_y < 3.08$, $f = 0.1\ Hz$, $\lambda = 0.1$ to $10.0\ mm$ logarithmically.

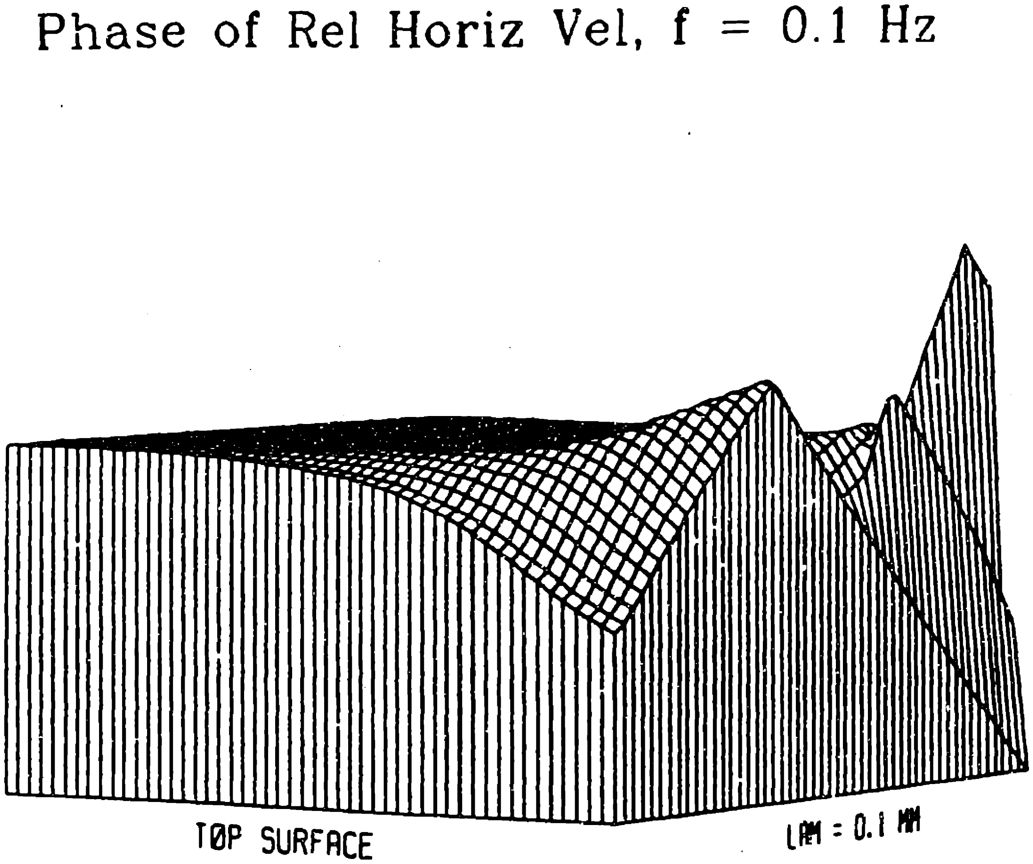

$-1.22 < \arg V_y < 3.08$, $f = 0.1$ *Hz*, $\lambda = 0.1$ to 10.0 *mm* logarithmically.

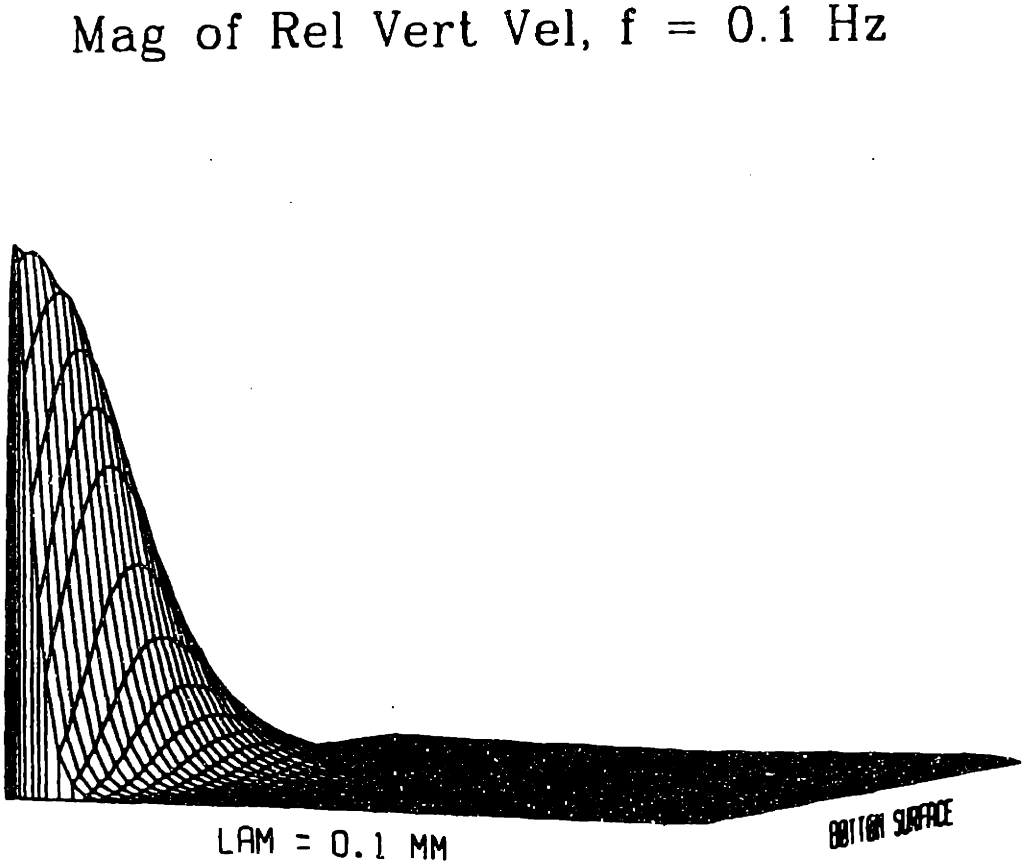

$|V_z|$, $f = 0.1\ Hz$, $\lambda = 0.1$ to $10.0\ mm$ logarithmically.

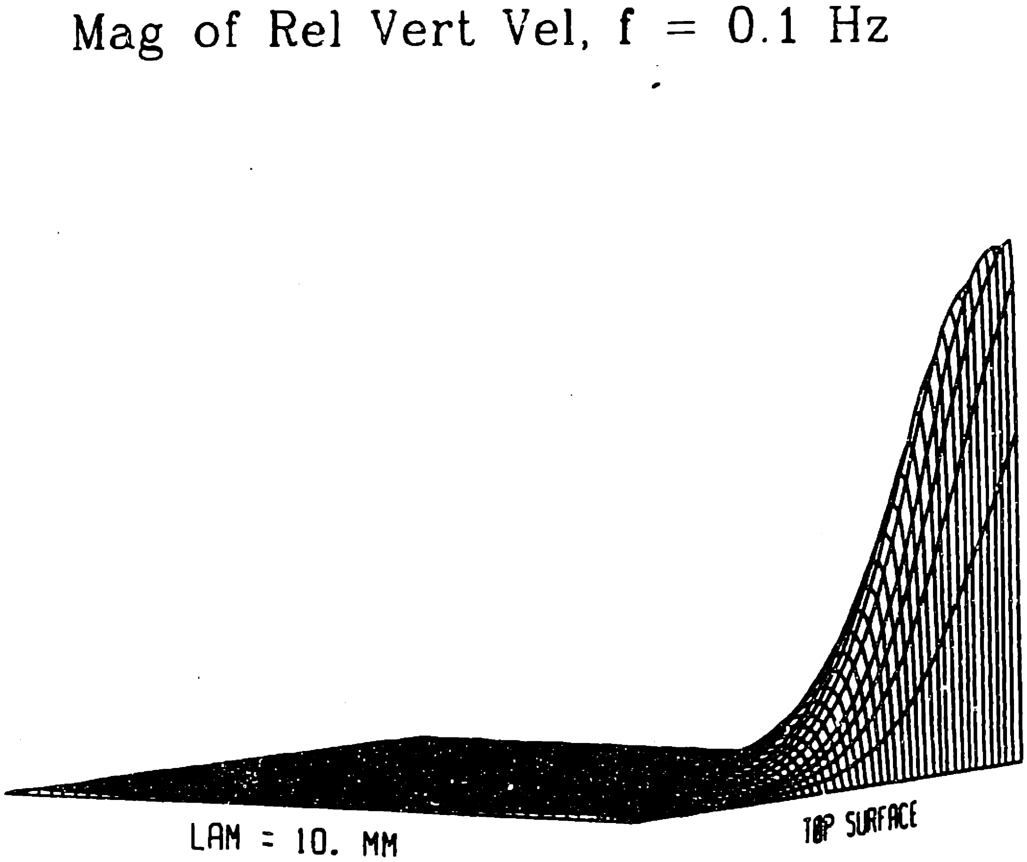

$|V_z|$, $f = 0.1\ Hz$, $\lambda = 0.1$ to $10.0\ mm$ logarithmically.

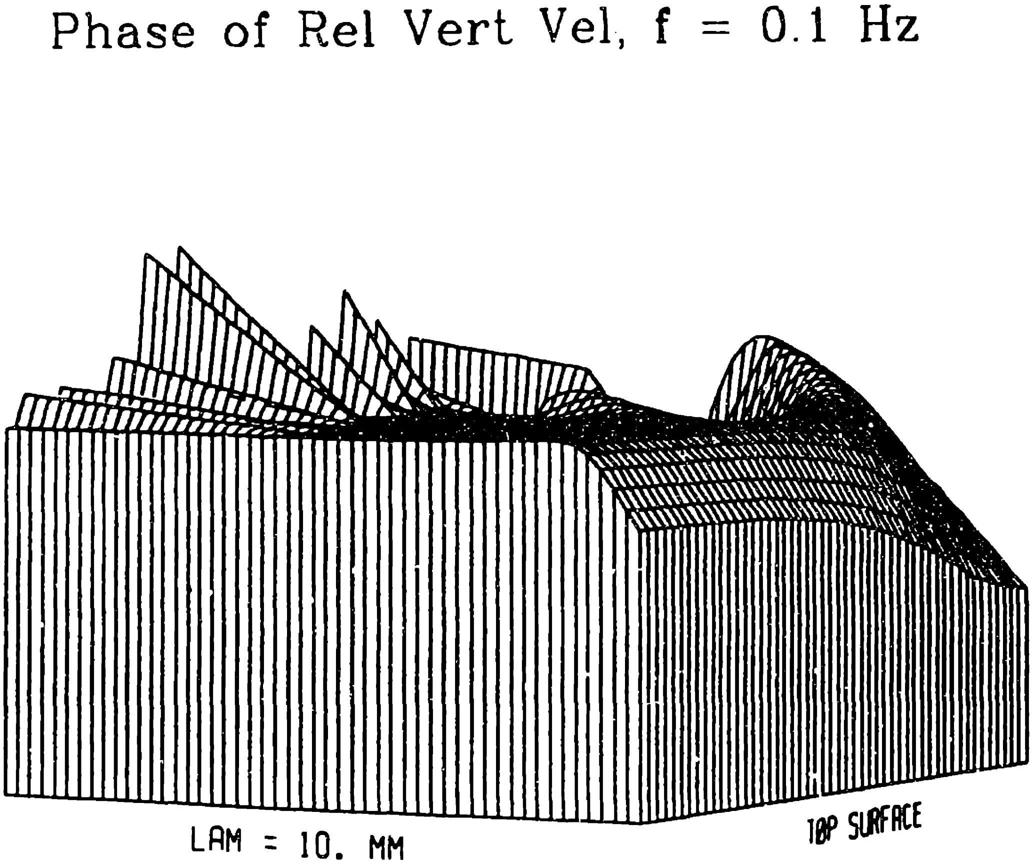

$-3.00 < \arg V_z < 1.44$, $f = 0.1\ Hz$, $\lambda = 0.1$ to 10.0 mm logarithmically.

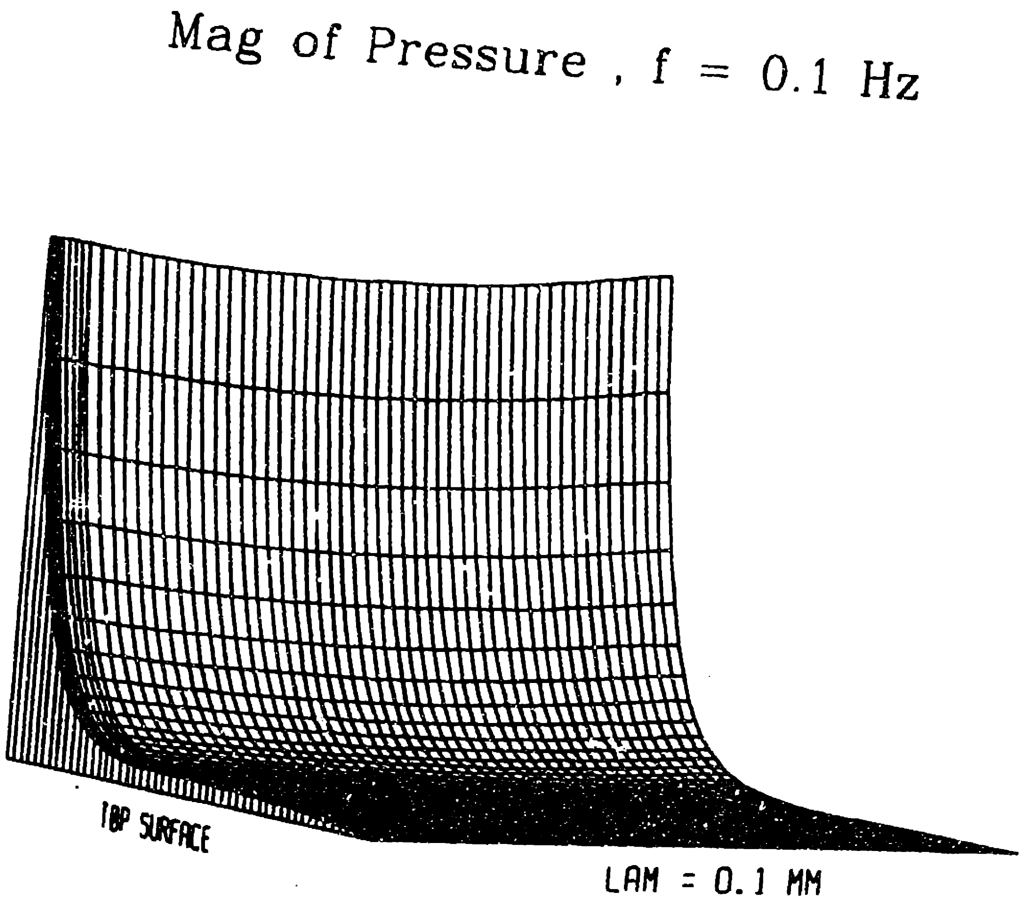

$|\lambda\, p|$, $f = 0.1\ Hz$, $f = 0.1\ Hz$. $\lambda = 0.1$ to 10.0 mm logarithmically.

Phase of Pressure, f = 0.1 Hz

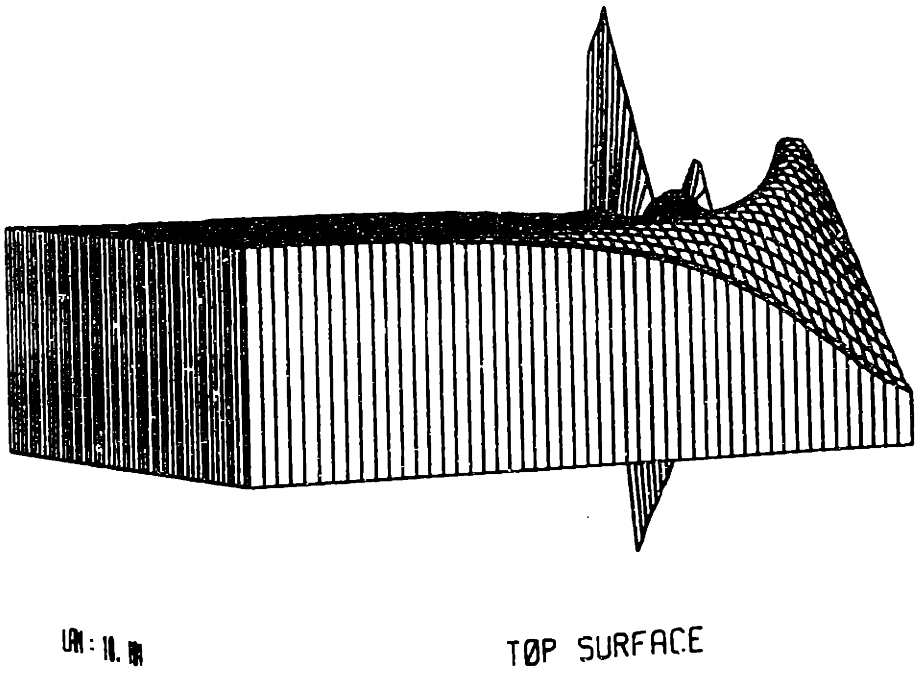

$0.350 < \arg < p4.65$, $f = 0.1\ Hz$, $\lambda = 0.1$ to $10.0\ mm$ logarithmically.

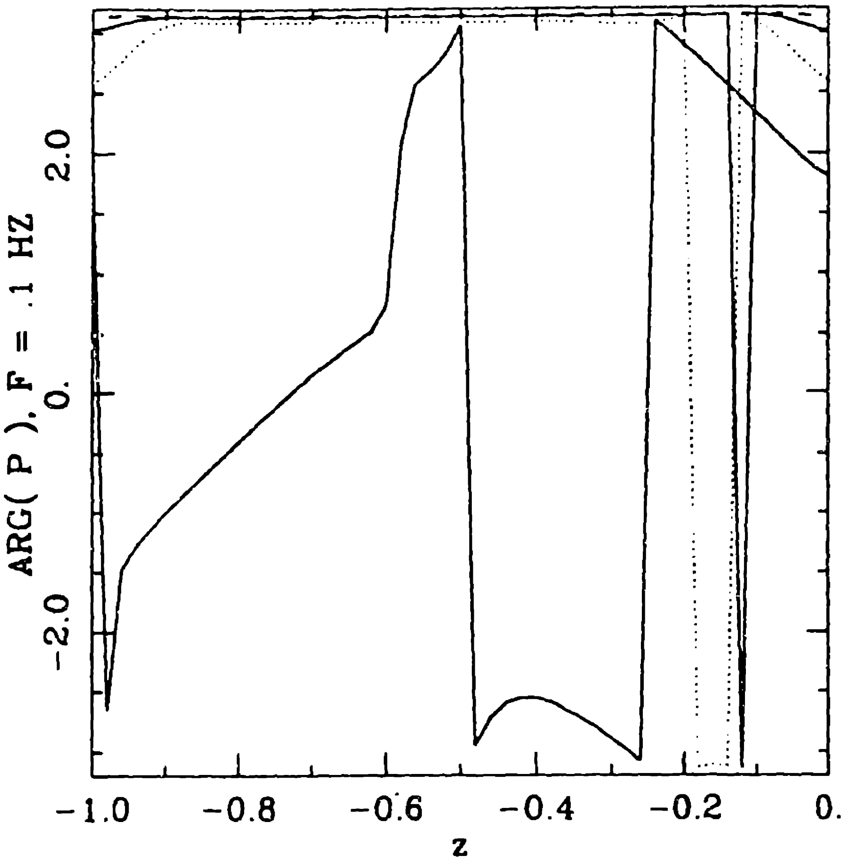

arg p, $f = 0.1\ Hz$, $\lambda = 0.1, 0.302$ (- - -), 1.0, and 10 mm (— —).

A.2.2 Case Four: Infinitely Permeable Surface

This section presents the results of for case four (mechanical driving with an infinitely permeable surface) presented in Chapter 5. The results are presented as plots of non-dimensional transform variables as before. The magnitudes and phases of the fields are presented for the parameter values:

1. $\lambda = 10\, mm, f = 10^{-3}$ to 0.1 Hz logarithmically,

2. $\lambda = 0.1\, mm, f = 0.001$ to 0.101 Hz by steps of 0.002,

3. $f = 10^{-3}\, Hz, \lambda = 0.1$ to 10.1 mm by 0.2,

and

4. $f = 0.1\, Hz, \lambda = 0.1$ to 10.1 mm by 0.2.

The magnitude and phase of the fields are presented in the order u_y (horizontal displacement), u_z (vertical displacement), V_y (horizontal relative velocity), V_z (vertical relative velocity), p (pressure), and ϕ (potential). Physical values for V_y and V_z are presented for $\lambda = 10$. Field magnitudes may be obtained from Table 5.1, and the ranges of arguments (complex phases) are listed in the captions. The arguments have been linearized (in z) whenever there was an apparent discontinuity due to numerical error in the vicinity of a relatively small field magnitude. The phases were linearized whenever the difference in the phases at two consecutive grid points (in z) exceeded a specified tolerance. The tolerance was chosen by eye using the overall smoothness and integrity of the data as criteria.

NOTE:

The axies in this section are scaled as follows: length by a_J, velocity by ωa_J, and pressure by $2\pi a_J(G + \lambda_L)/\lambda$.

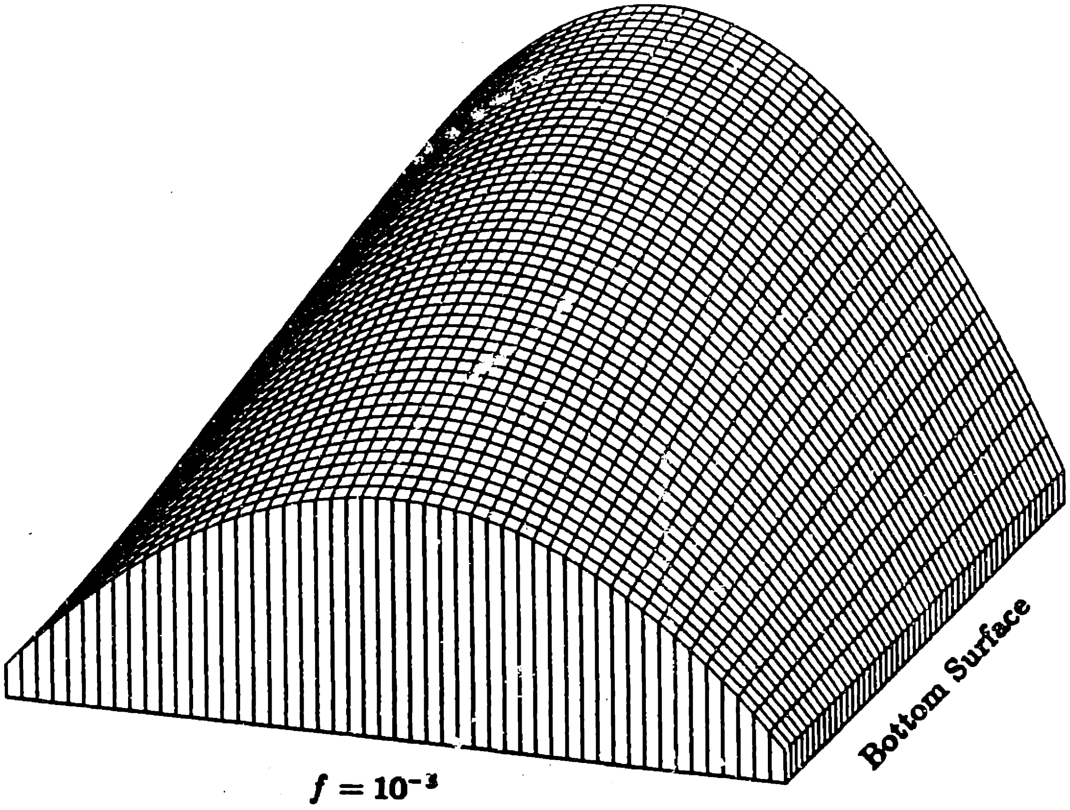

$|u_y|$, $\lambda = 10\,mm$, $f = 10^{-3}$ to 0.1 Hz logarithmically.

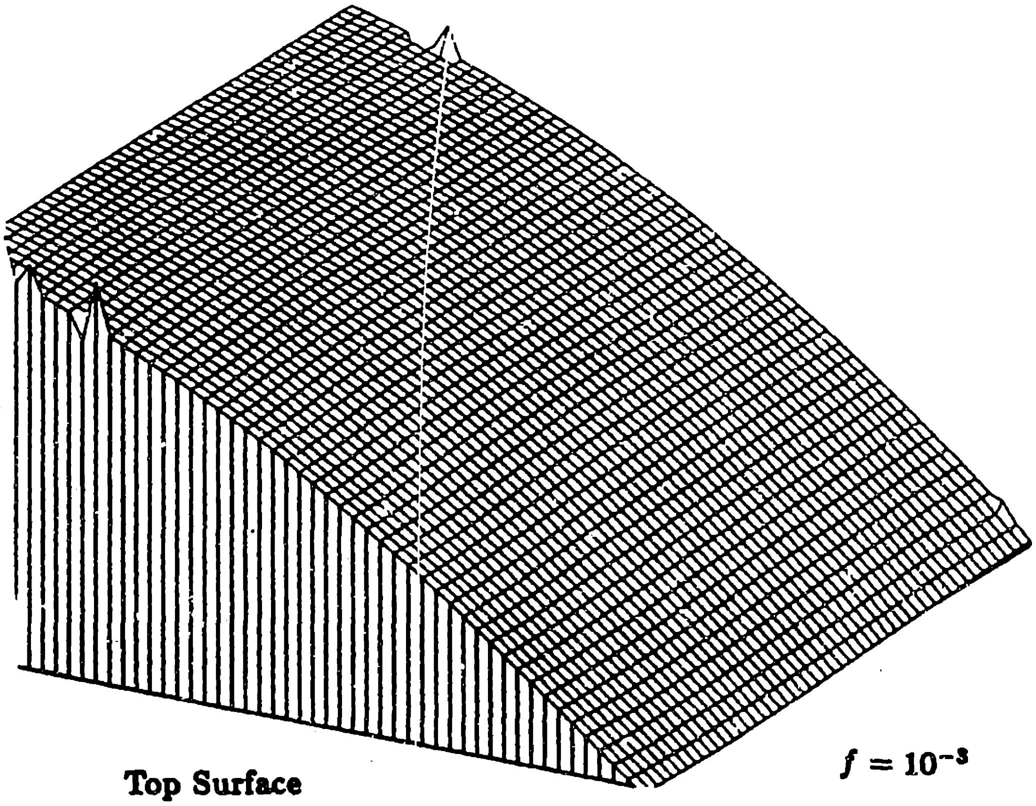

$1.06 < \arg u_y < 1.50$, $\lambda = 10\,mm$, $f = 10^{-3}$ to $0.1\ Hz$ logarithmically.

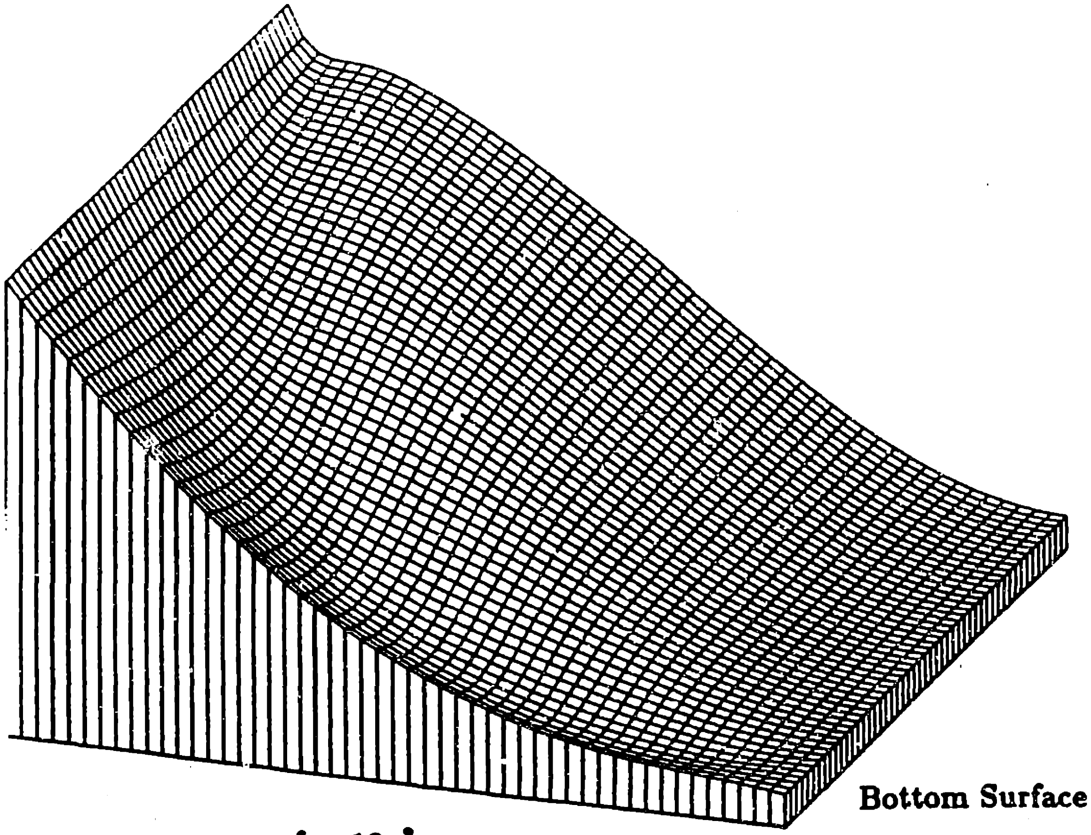

$f = 10^{-3}$

$|u_z|$, $\lambda = 10\,mm, f = 10^{-3}$ and 0.1 Hz ("+") logarithmically.

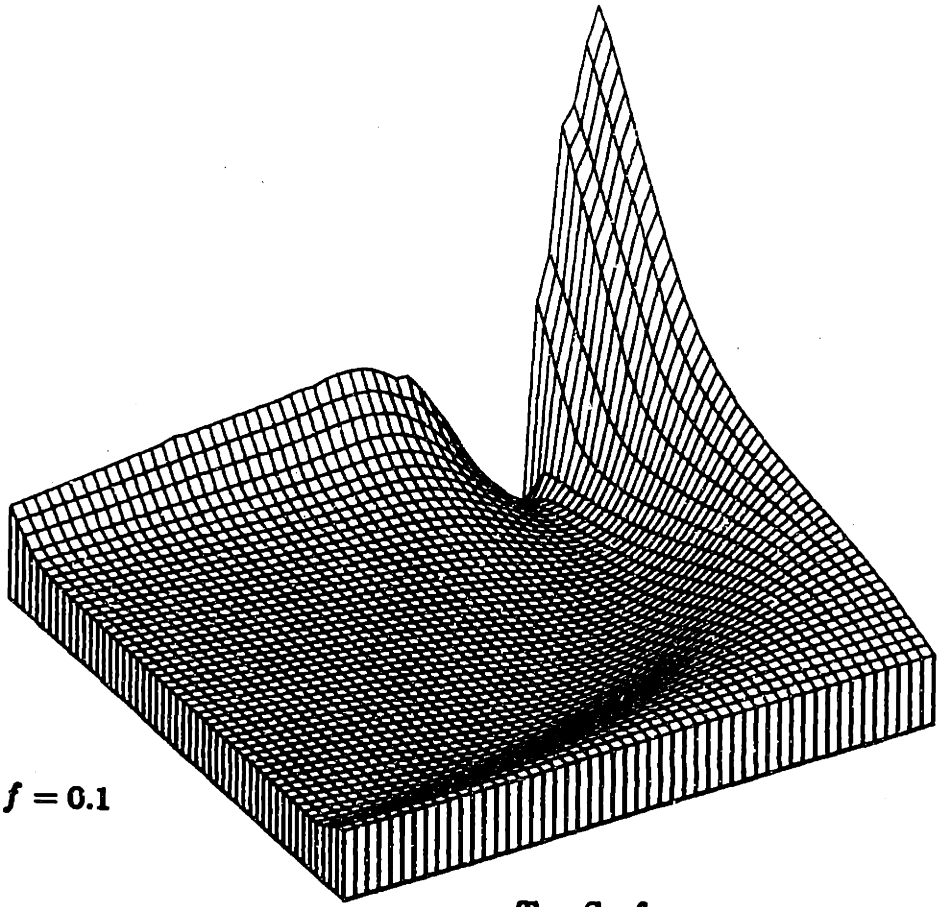

$-0.72 < \arg u_s < 1.9$, $\lambda = 10\ mm$, $f = 10^{-3}$ to $0.1\ Hz$ logarithmically.

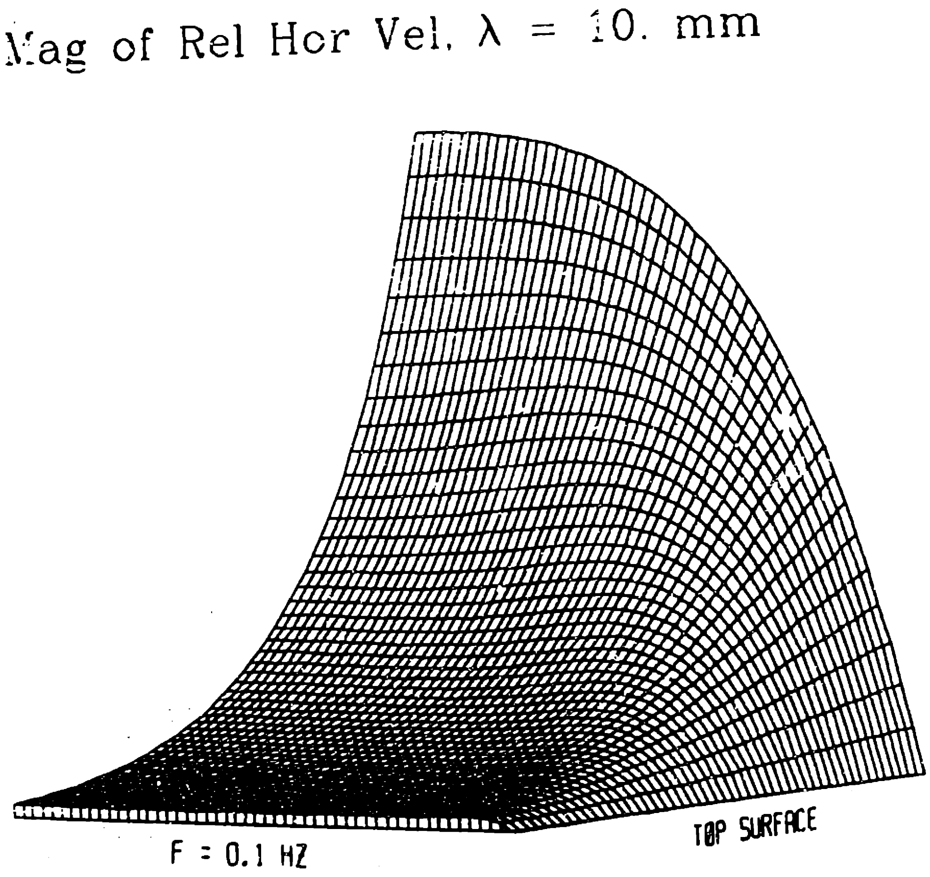

$|V_y^*/\omega a_J|$, $\lambda = 10\ mm, f = 10^{-3}$ to 0.1 Hz logarithmically.

Phase of Rel Hor Vel, λ = 10. mm

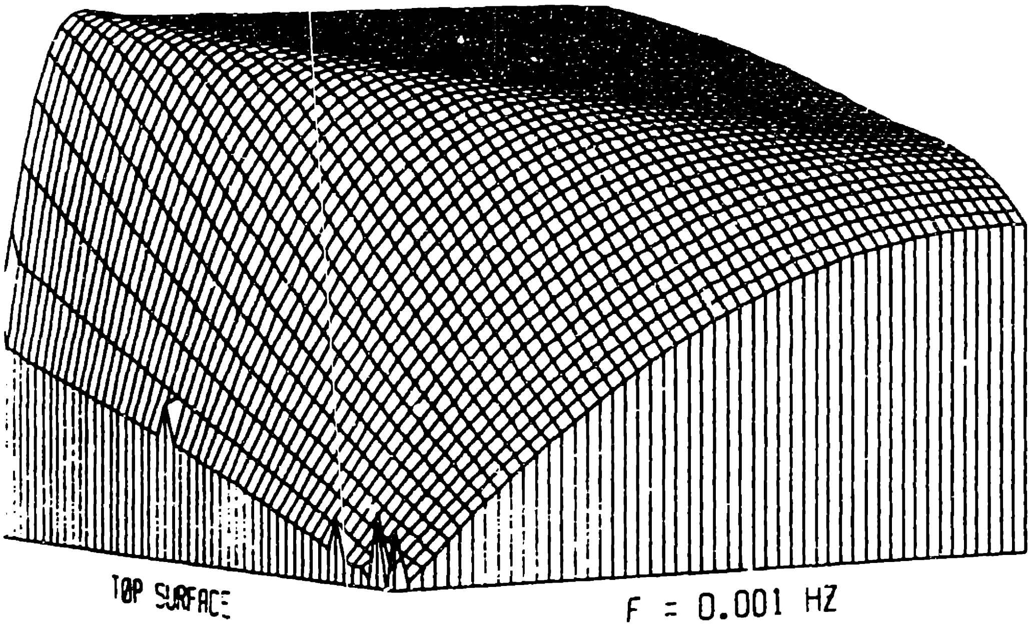

$0.309 < \arg V_y < 1.50$, $\lambda = 10\ mm$, $f = 10^{-3}$ to $0.1\ Hz$ logarithmically.

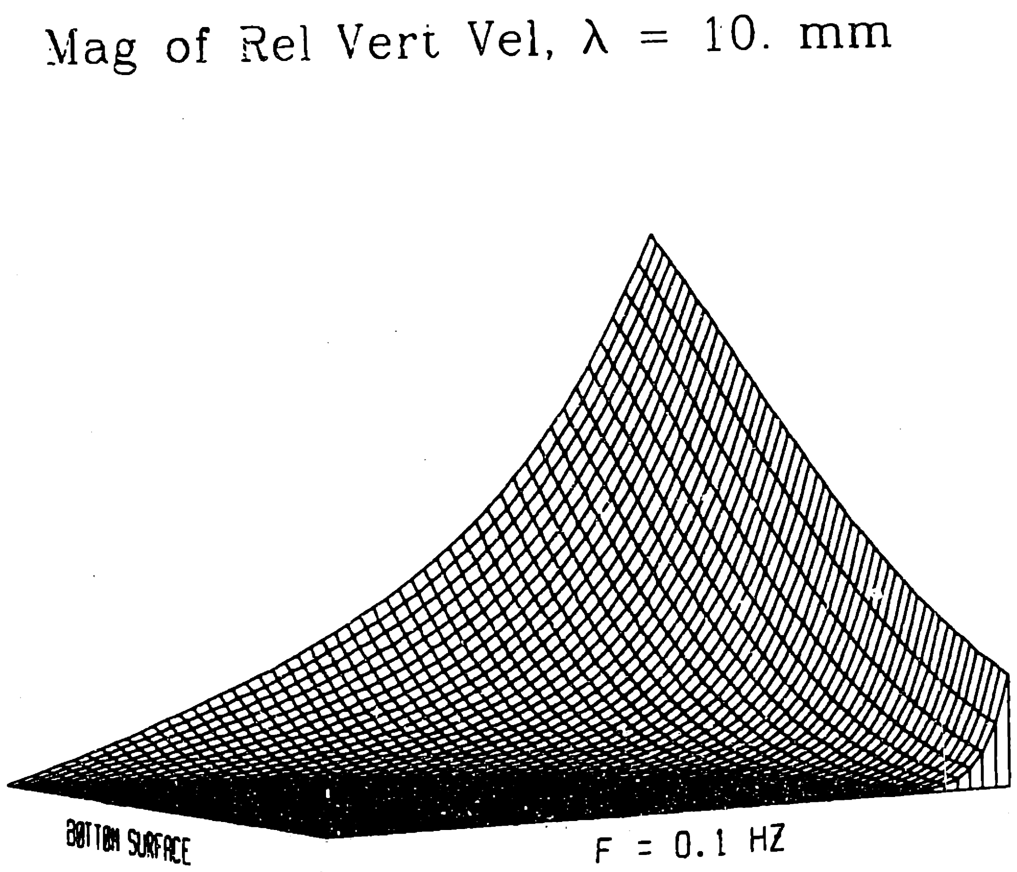

$|V_z^*/\omega a_J|$, $\lambda = 10\,mm$, $f = 10^{-3}$ to 0.1 Hz logarithmically.

Phase of Rel Vert Vel, λ = 10. mm

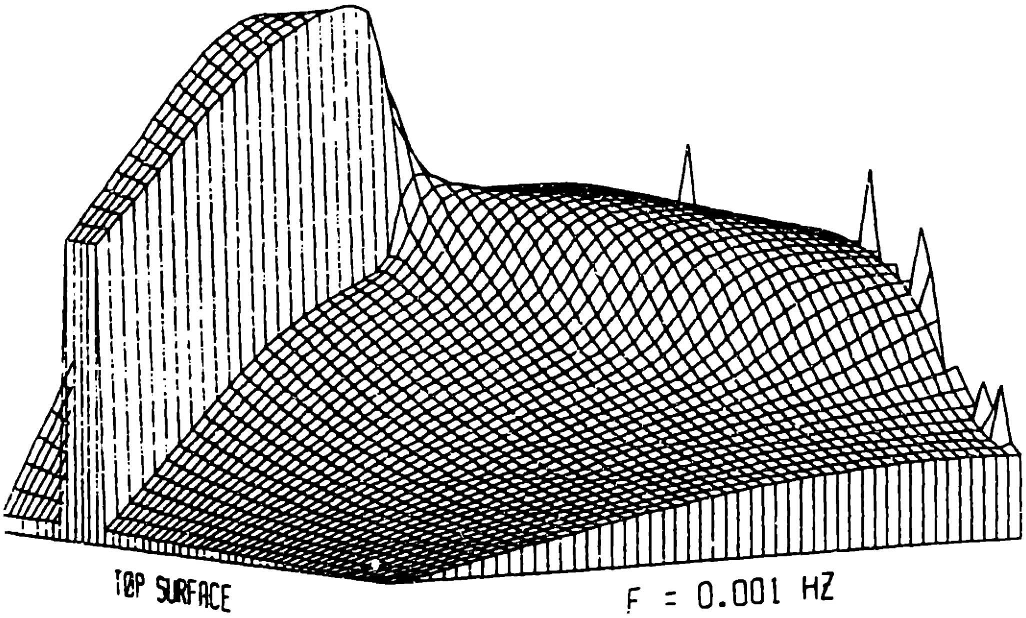

$1.87 < \arg V_z < 13.59$, $\lambda = 10\ mm$, $f = 10^{-3}$ to $0.1\ Hz$ logarithmically.

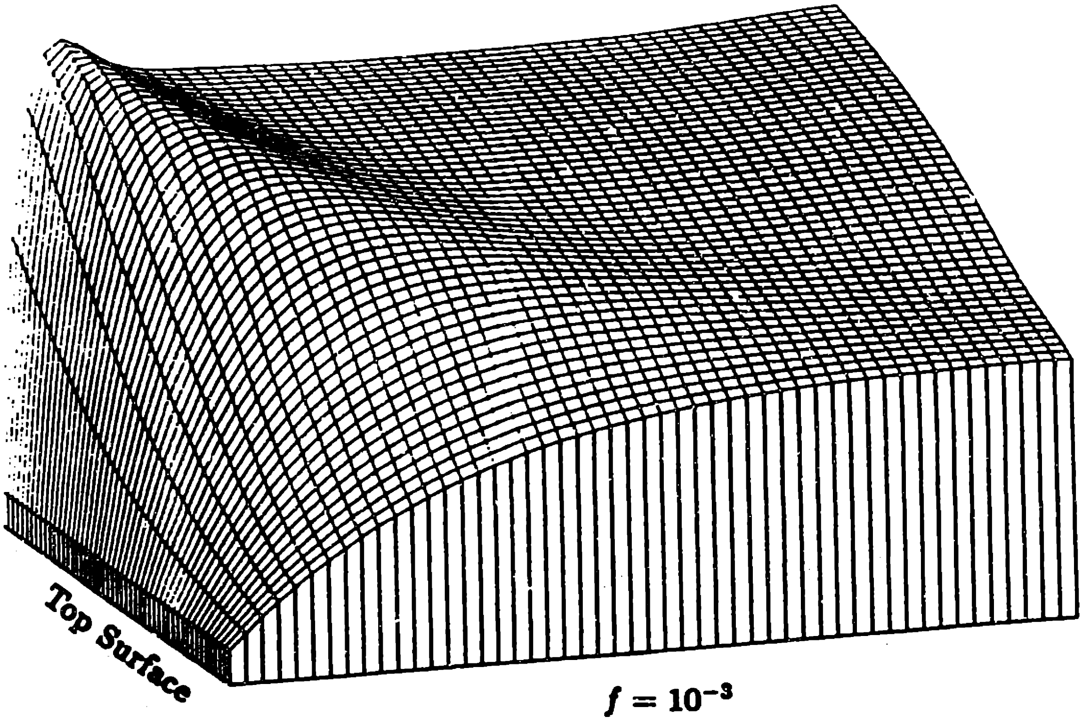

$|p|$, $\lambda = 10\ mm$, $f = 10^{-3}$ to 0.1 Hz logarithmically.

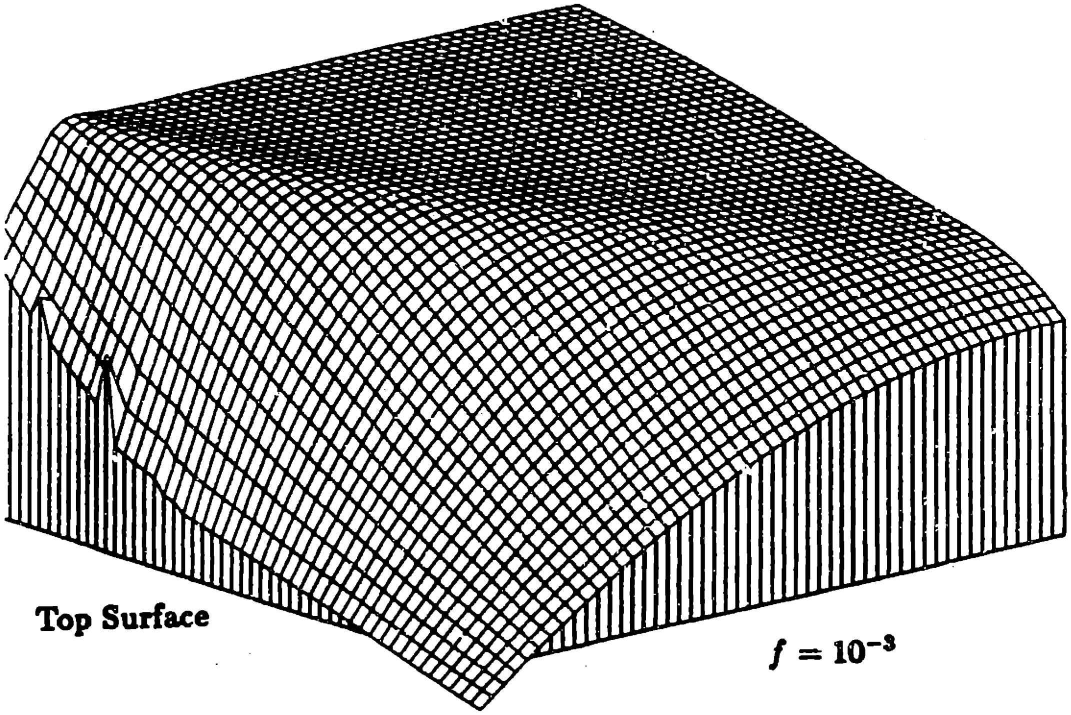

$1.87 < \arg p < 3.07$, $\lambda = 10\ mm$, $f = 10^{-3}$ to $0.1\ Hz$ logarithmically.

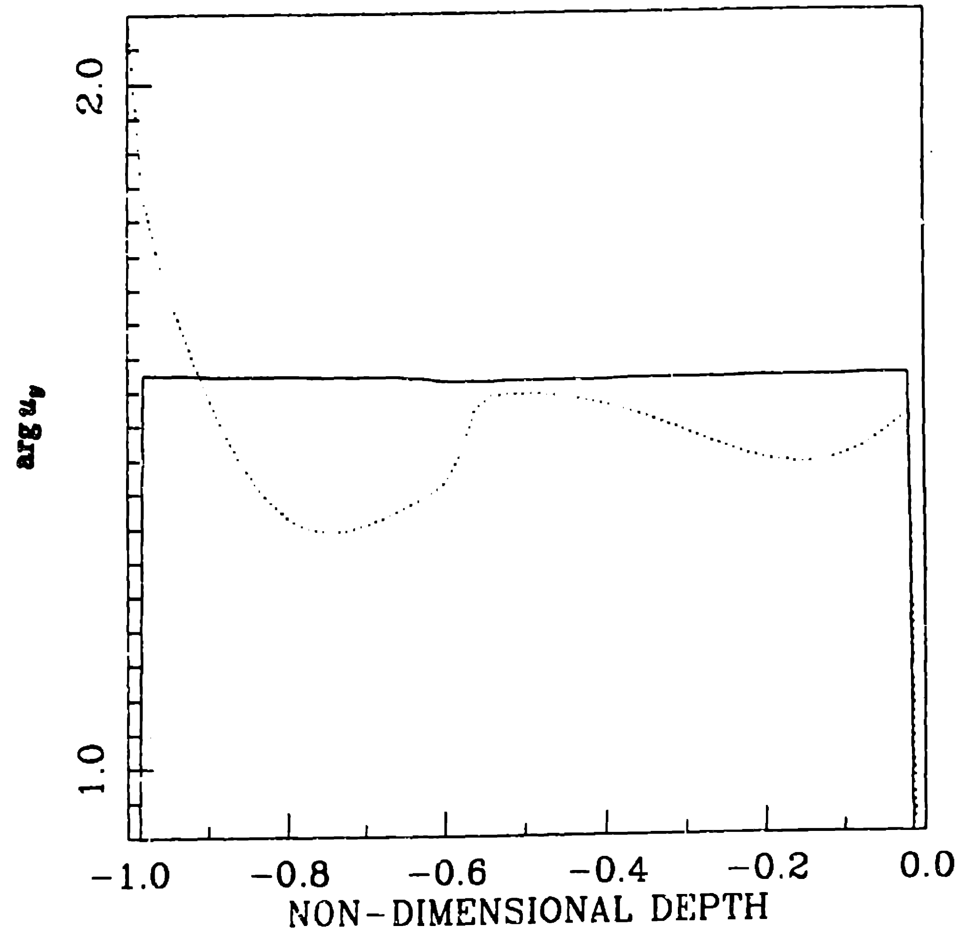

arg u_y, $\lambda = 0.1$ *mm*, $f = 0.001$ and $f = 0.101$ *Hz* (- - -).

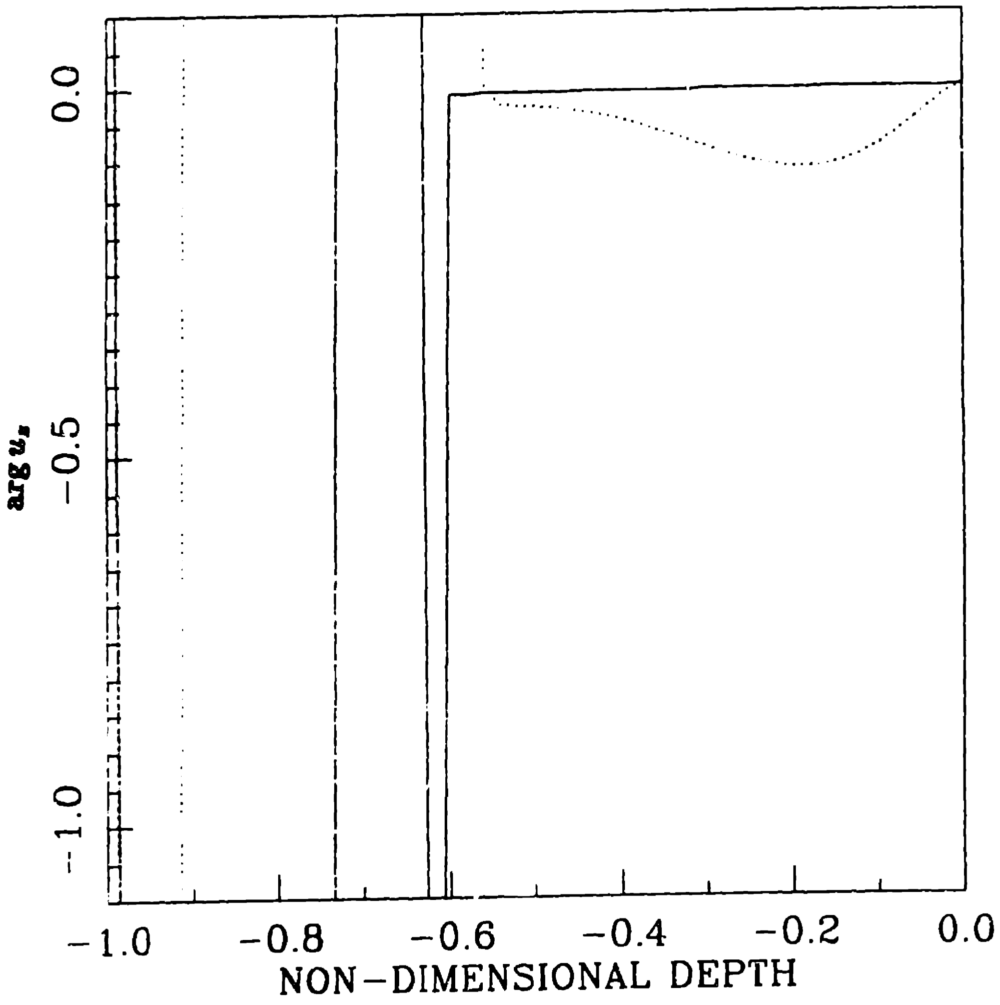

arg u_s, $\lambda = 0.1$ mm, $f = 0.001$ and $f = 0.101$ Hz (- - -).

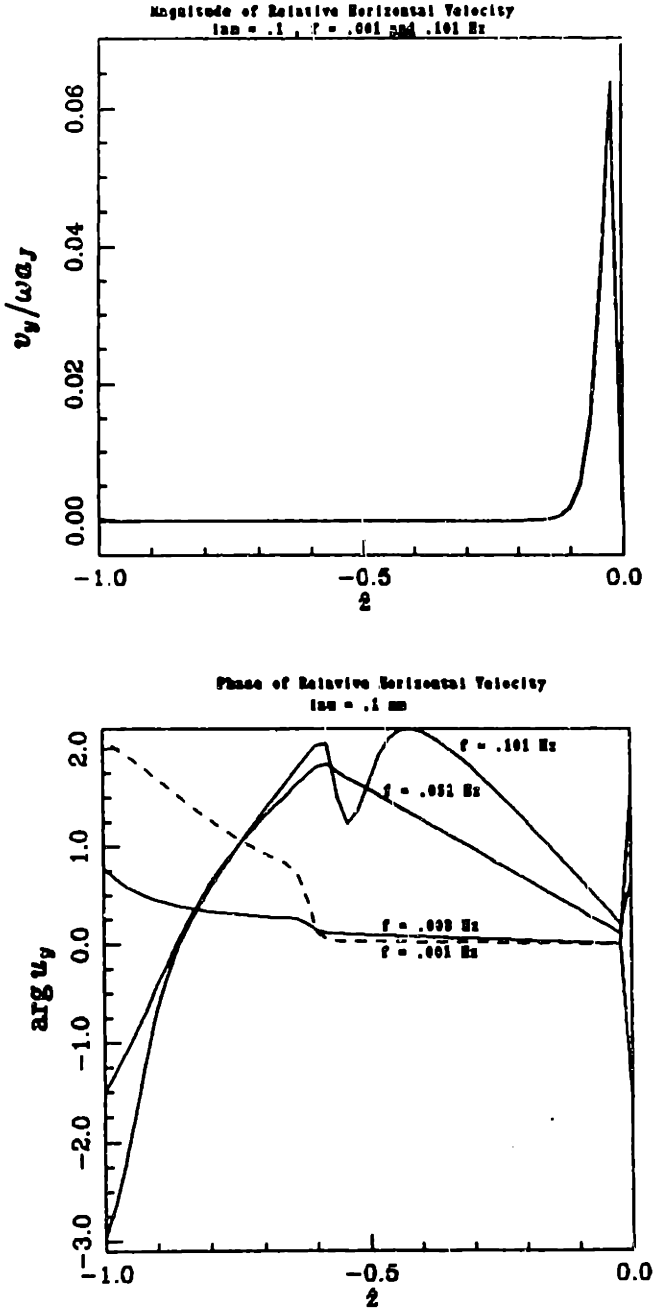

Magnitude and phase of $|V_y^*/\omega a_J|$, $f = 0.1\ Hz$, $\lambda = 0.1$ to $10.1\ mm$ by 0.2.

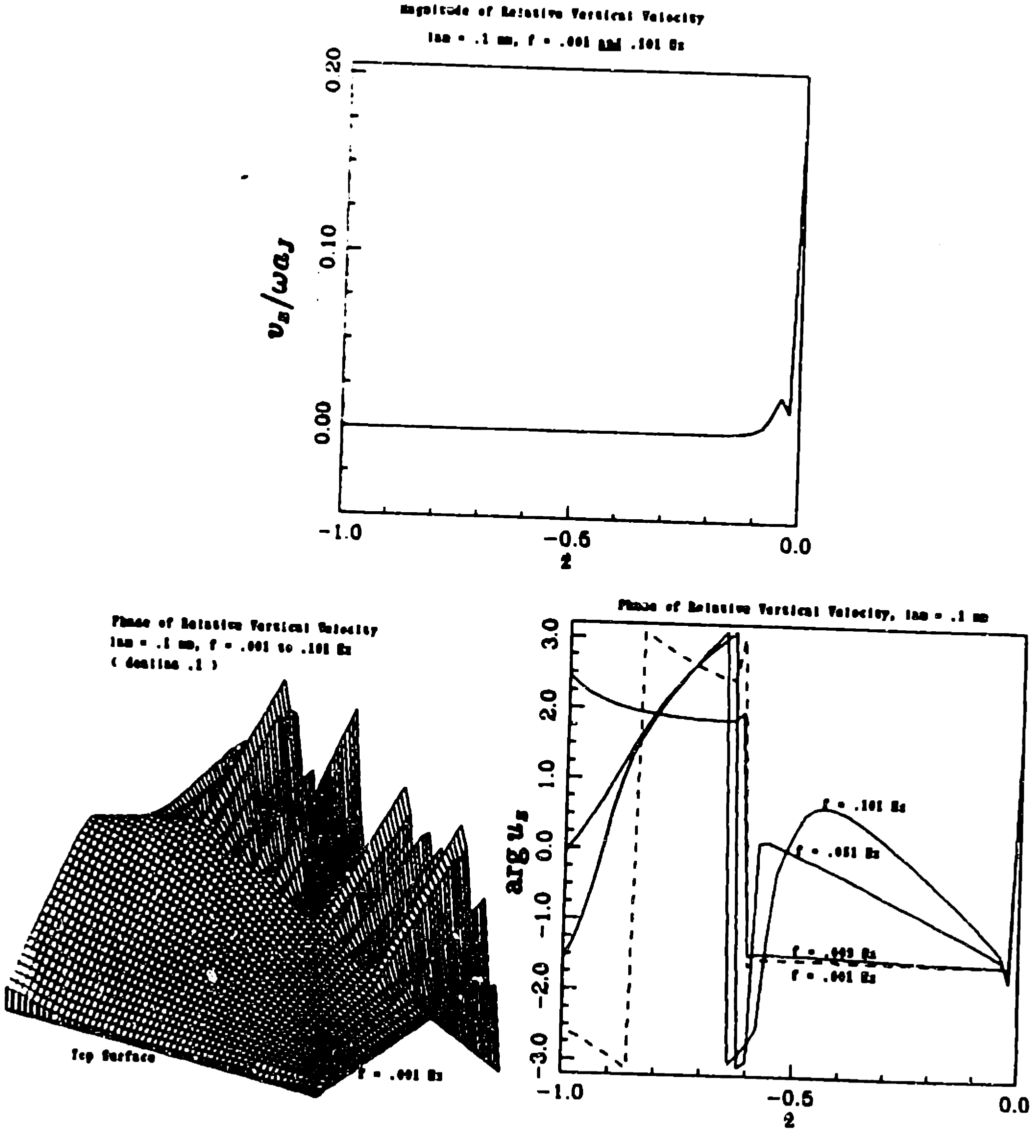

Magnitude and phase of $|V_z^*/\omega a_J|$, $f = 0.1\ Hz$, $\lambda = 0.1$ to $10.1\ mm$ by 0.2.

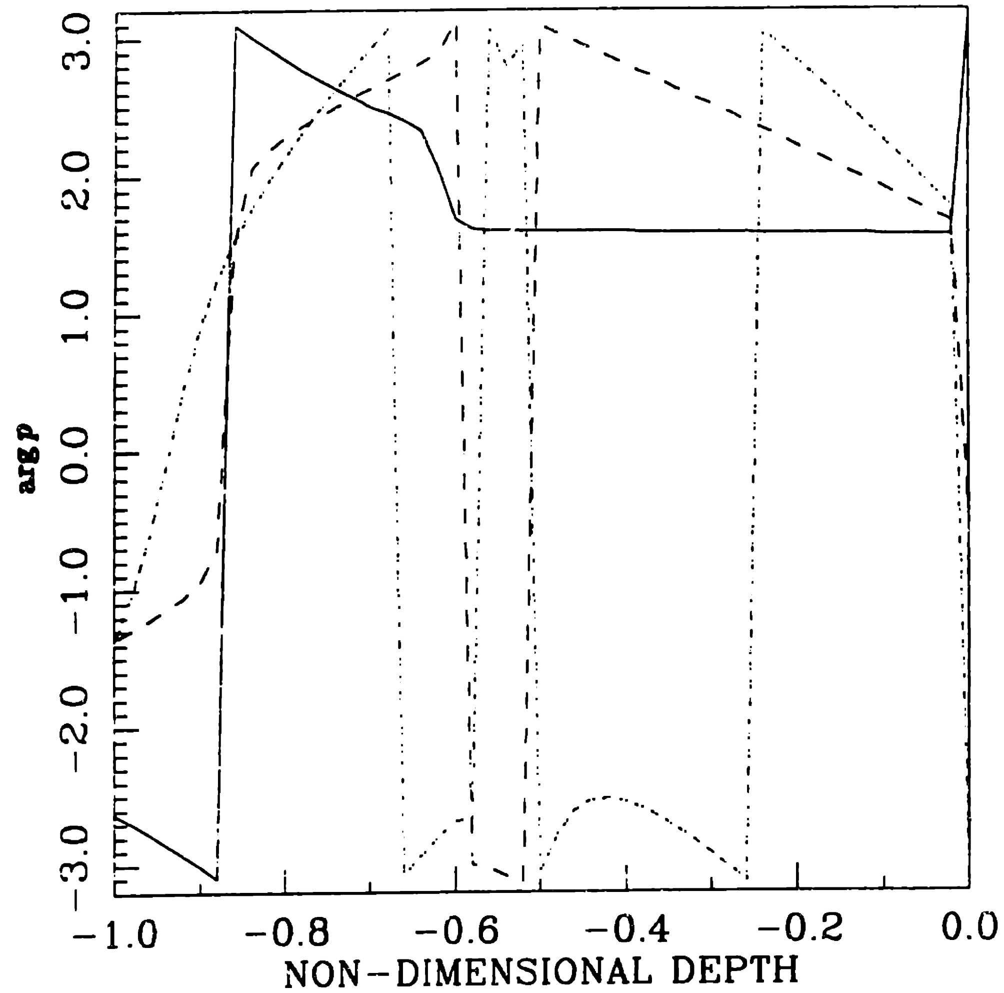

$\arg p$, $\lambda = 0.1\ mm$, $f = 0.001$, $f = 9\cdot 10^{-3}$ (— —) and $f = 0.101\ Hz$ (- — - —).

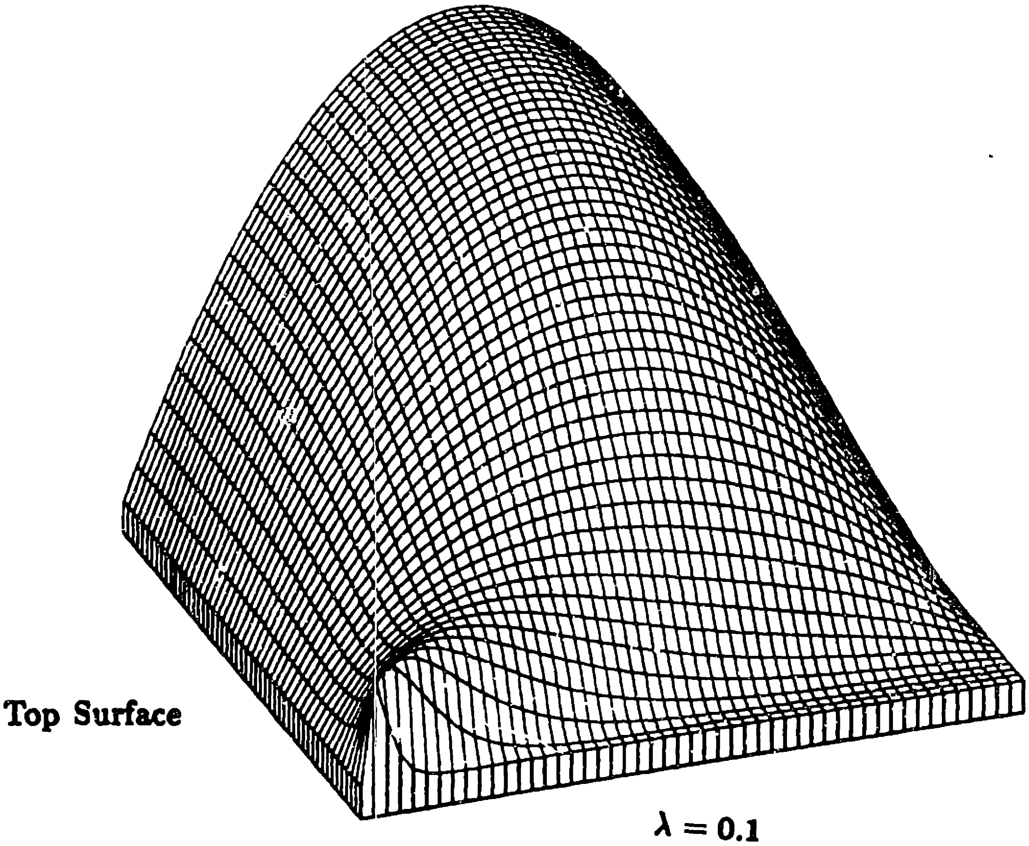

$|u_y|$, $f = 10^{-3}\ Hz$, $\lambda = 0.1$ to $10.1\ mm$ by 0.2.

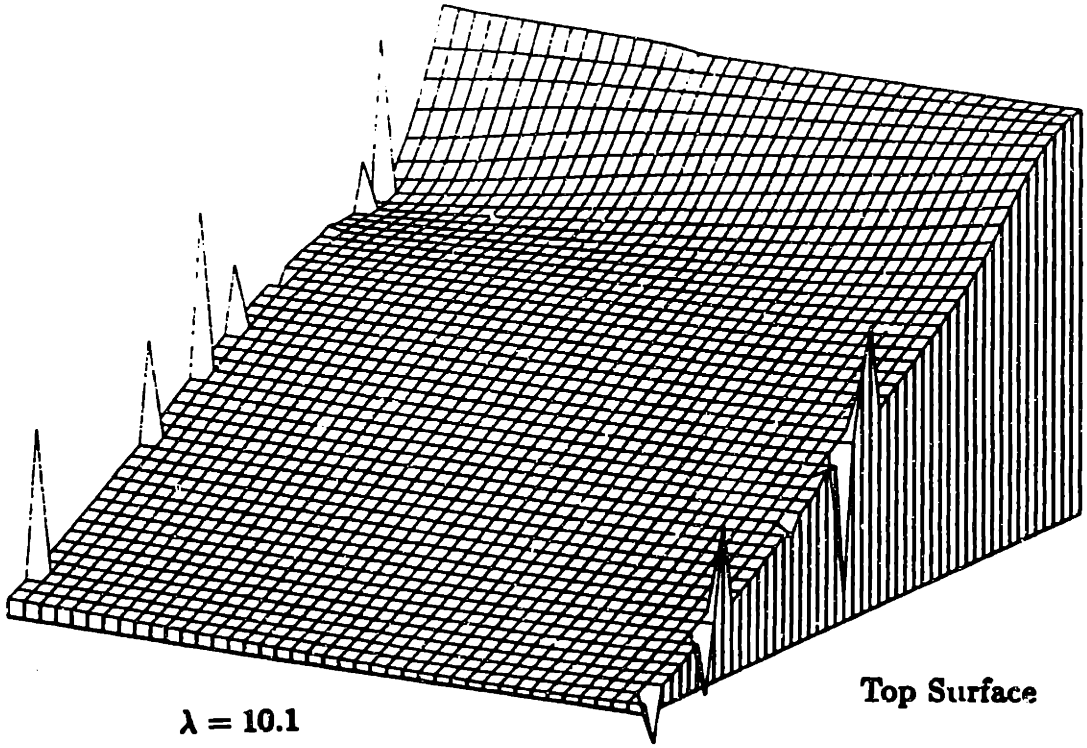

$1.00 < \arg u_y < 1.577$, $f = 10^{-3}\ Hz$, $\lambda = 0.1$ to $10.1\ mm$ by 0.2.

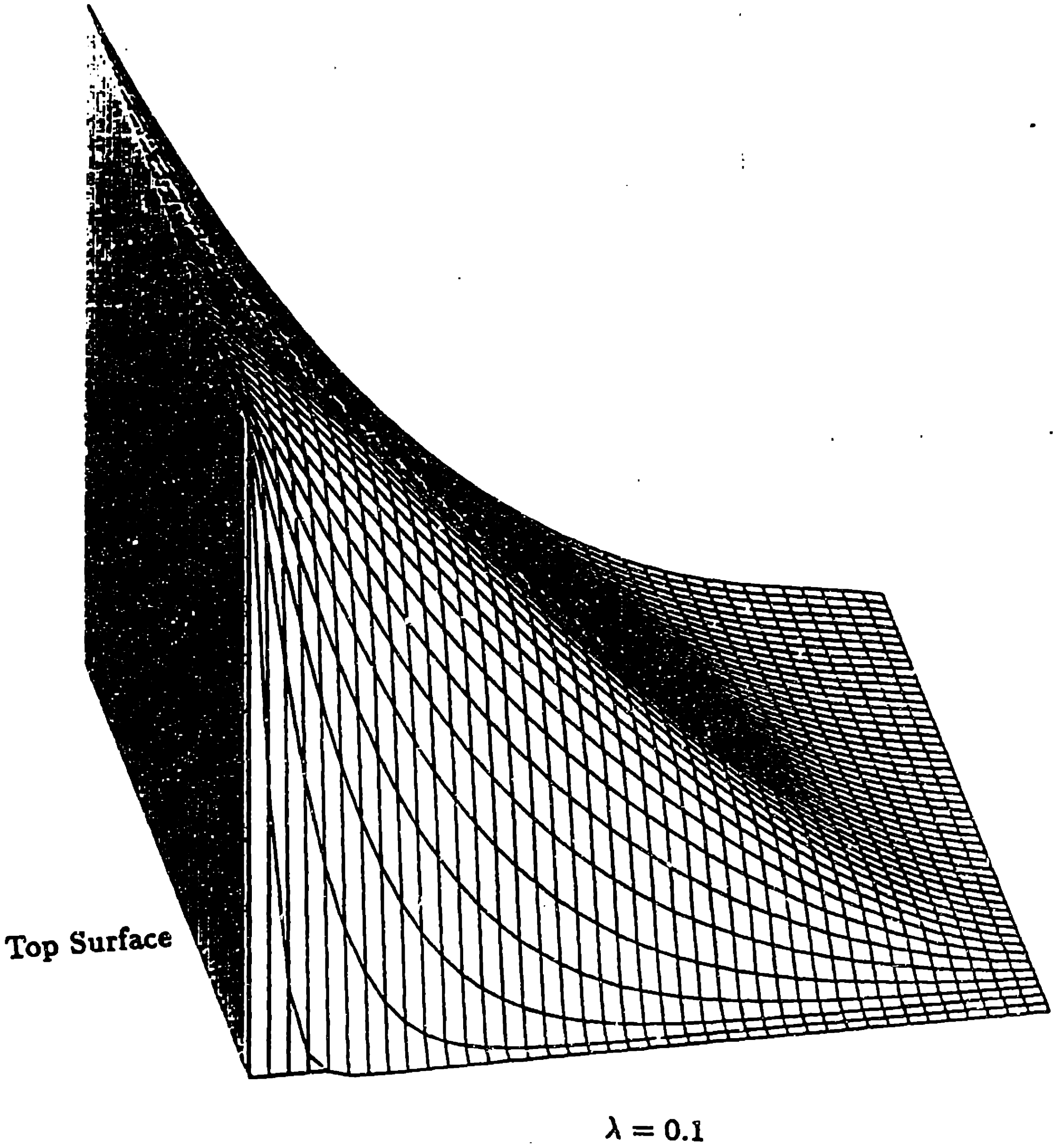

$|u_z|$, $f = 10^{-3}\ Hz$, $\lambda = 0.1$ to $10.1\ mm$ by 0.2.

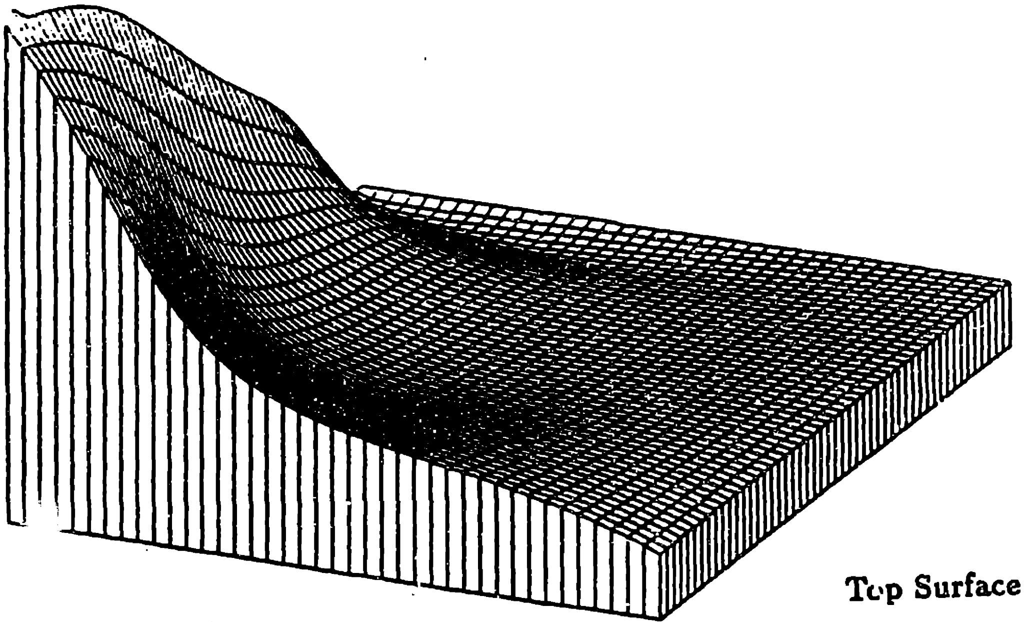

$-5 \cdot 10^{-2} < \arg u_z < 1.96$, $f = 10^{-3}$ Hz, $\lambda = 0.1$ to 10.1 mm by 0.2.

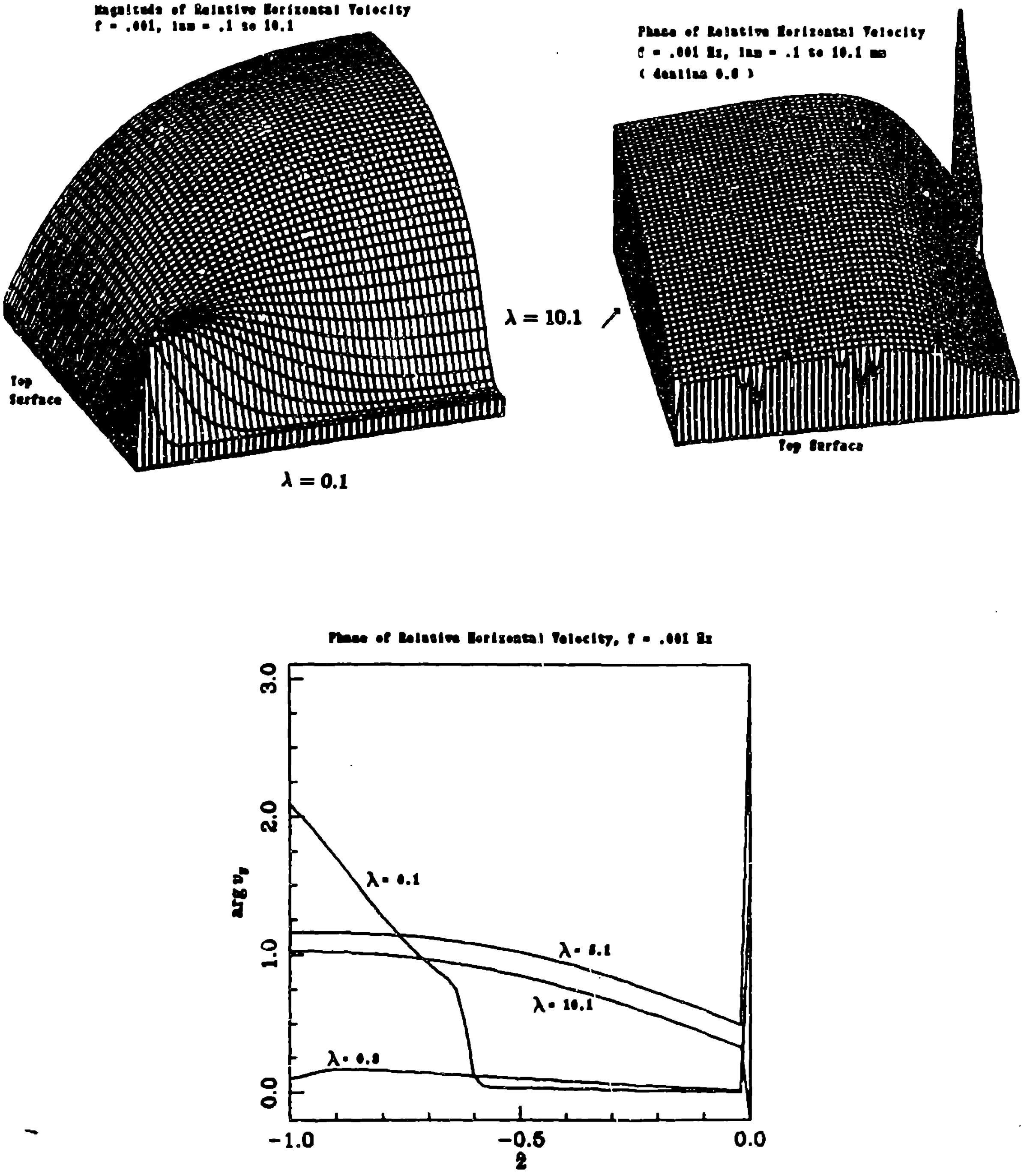

Magnitude and phase of $|V_y^*/\omega a_J|$, $f = 0.1\ Hz$, $\lambda = 0.1$ to $10.1\ mm$ by 0.2.

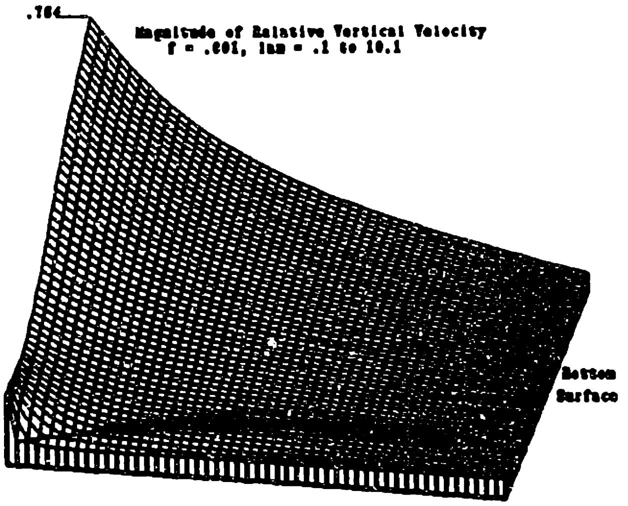

$\lambda = 0.1$

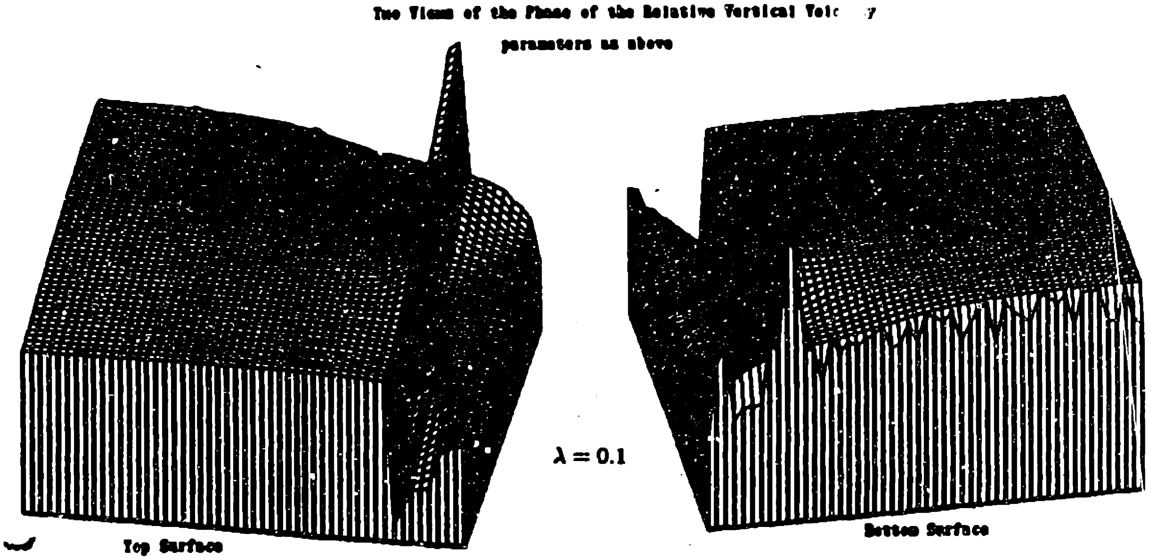

Magnitude and phase of $|V_z^*/\omega a_J|$, $f = 0.1\ Hz$, $\lambda = 0.1$ to $10.1\ mm$ by 0.2.

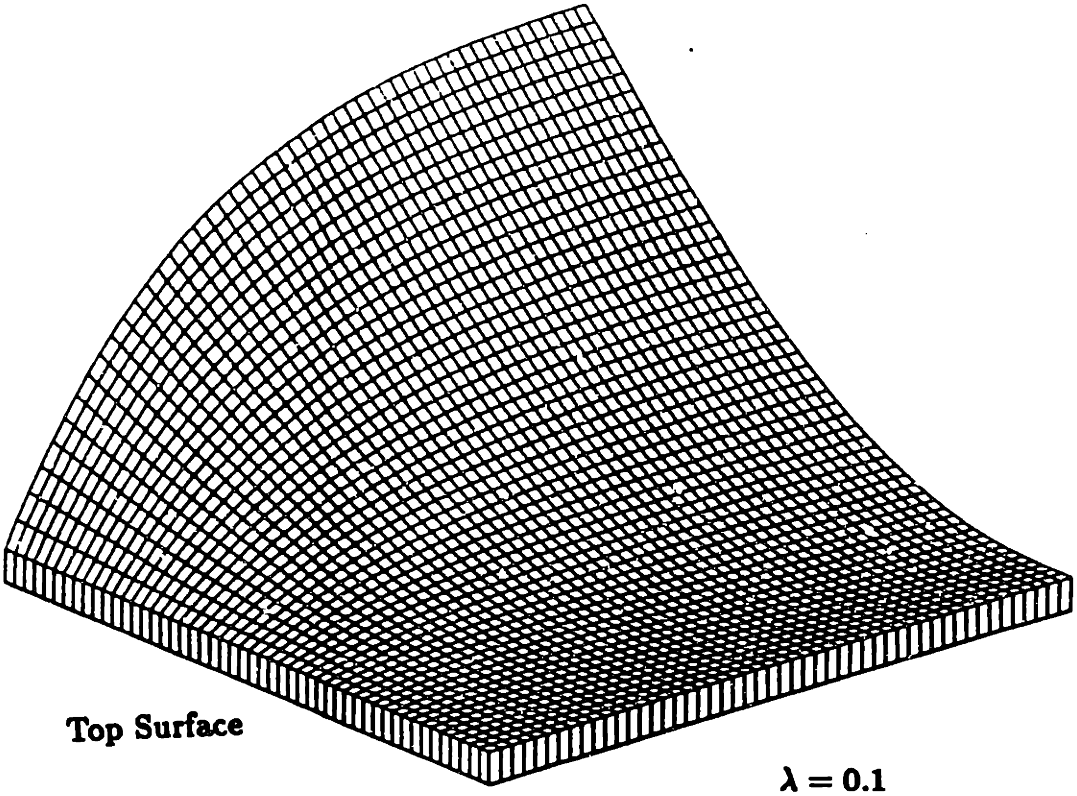

$|\lambda\, p|$, $f = 10^{-3}$ Hz, $\lambda = 0.1$ to 10.1 mm by 0.2.

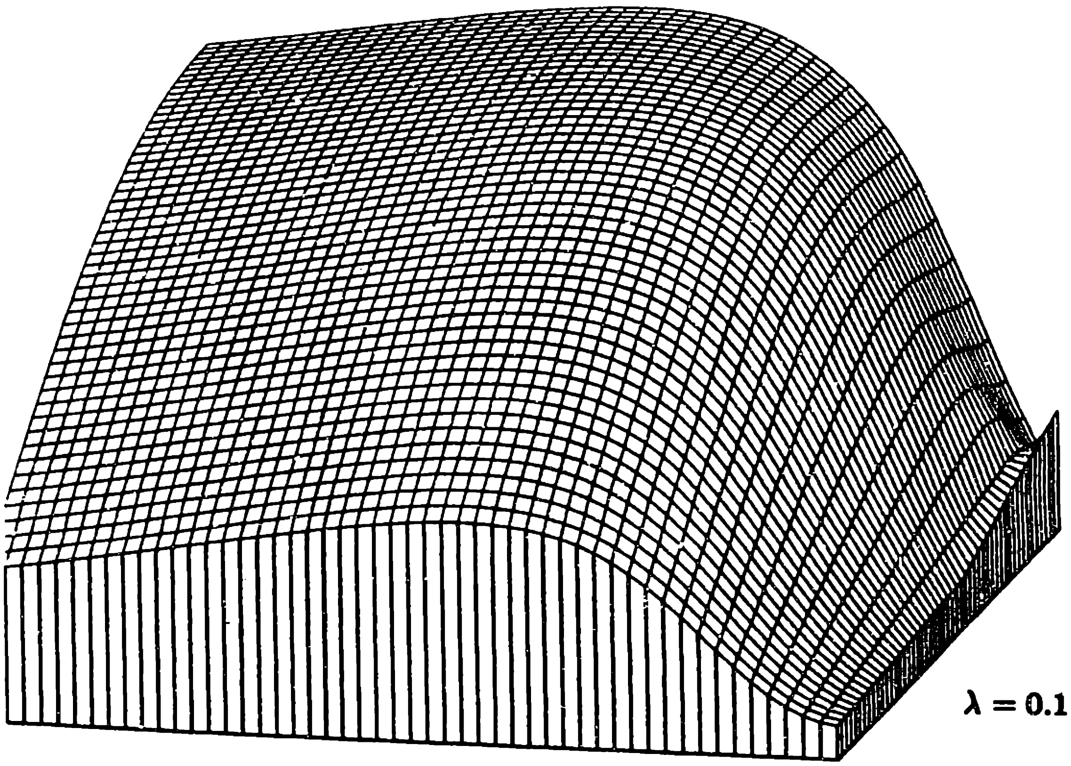

$1.57 < \arg p < 2.7$, $f = 10^{-3}\ Hz$, $\lambda = 0.1$ to $10.1\ mm$ by 0.2.

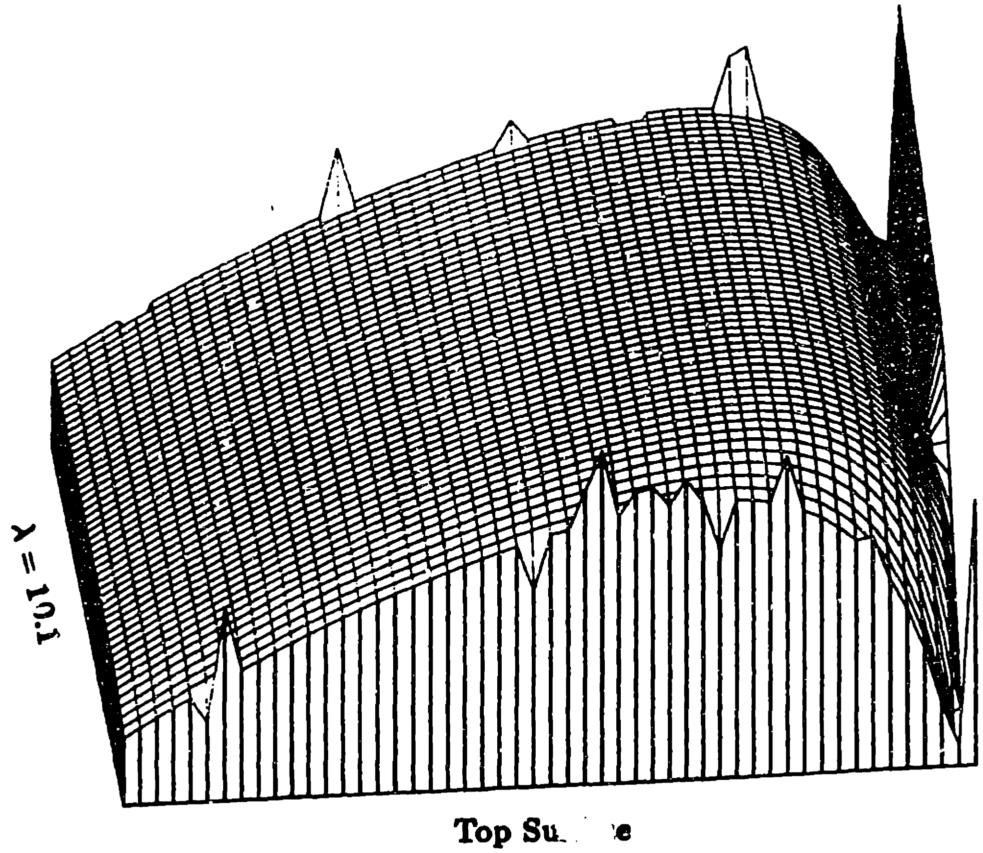

arg u_y, $f = 0.1$ *Hz*, $\lambda = 0.1$ to 10.1 *mm* by 0.2. The corresponding graph for $|u_y|$ looks like that for $f = 10^{-3}$.

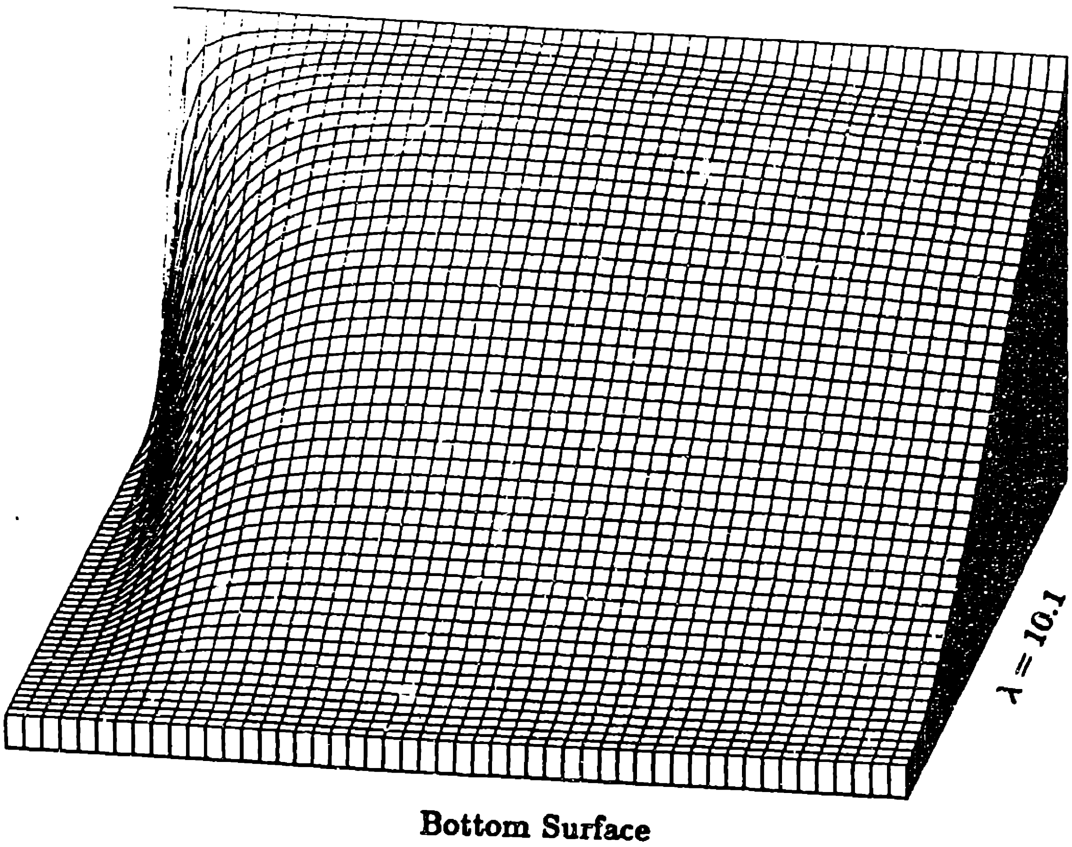

$|u_z|$, $f = 0.1\ Hz$, $\lambda = 0.1$ to $10.1\ mm$ by 0.2. $|\arg u_z| <\sim 0.1$ in this range.

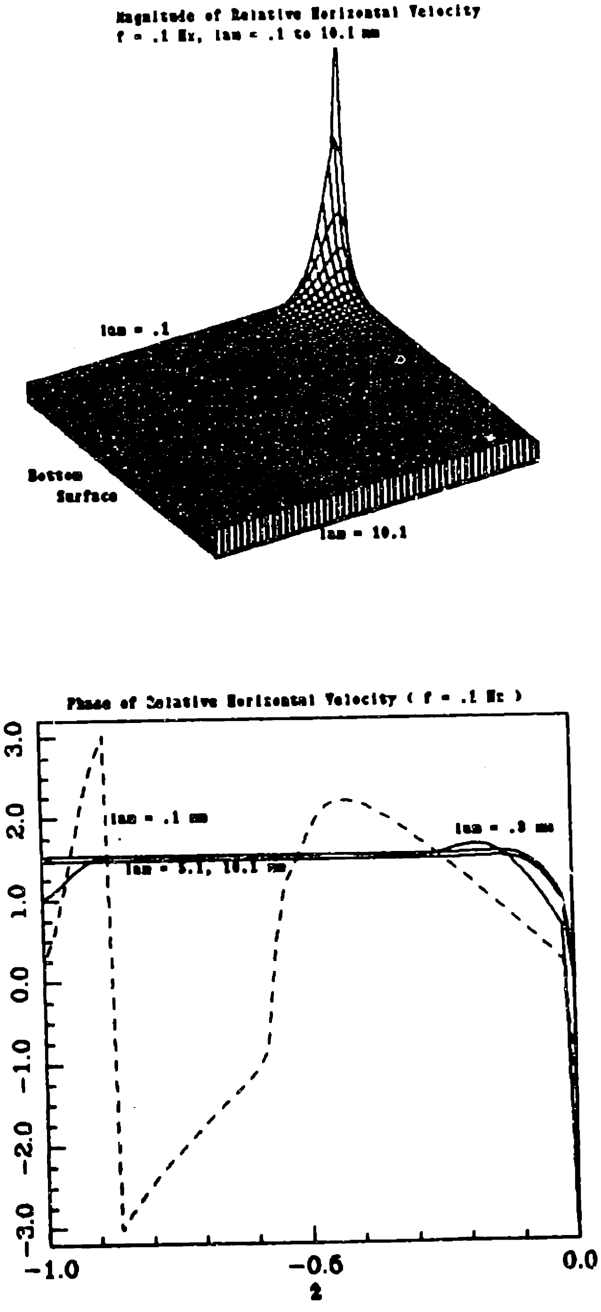

Magnitude and phase of $|V_y^*/\omega a_J|$, $f = 0.1$ *Hz*, $\lambda = 0.1$ to 10.1 *mm* by 0.2.

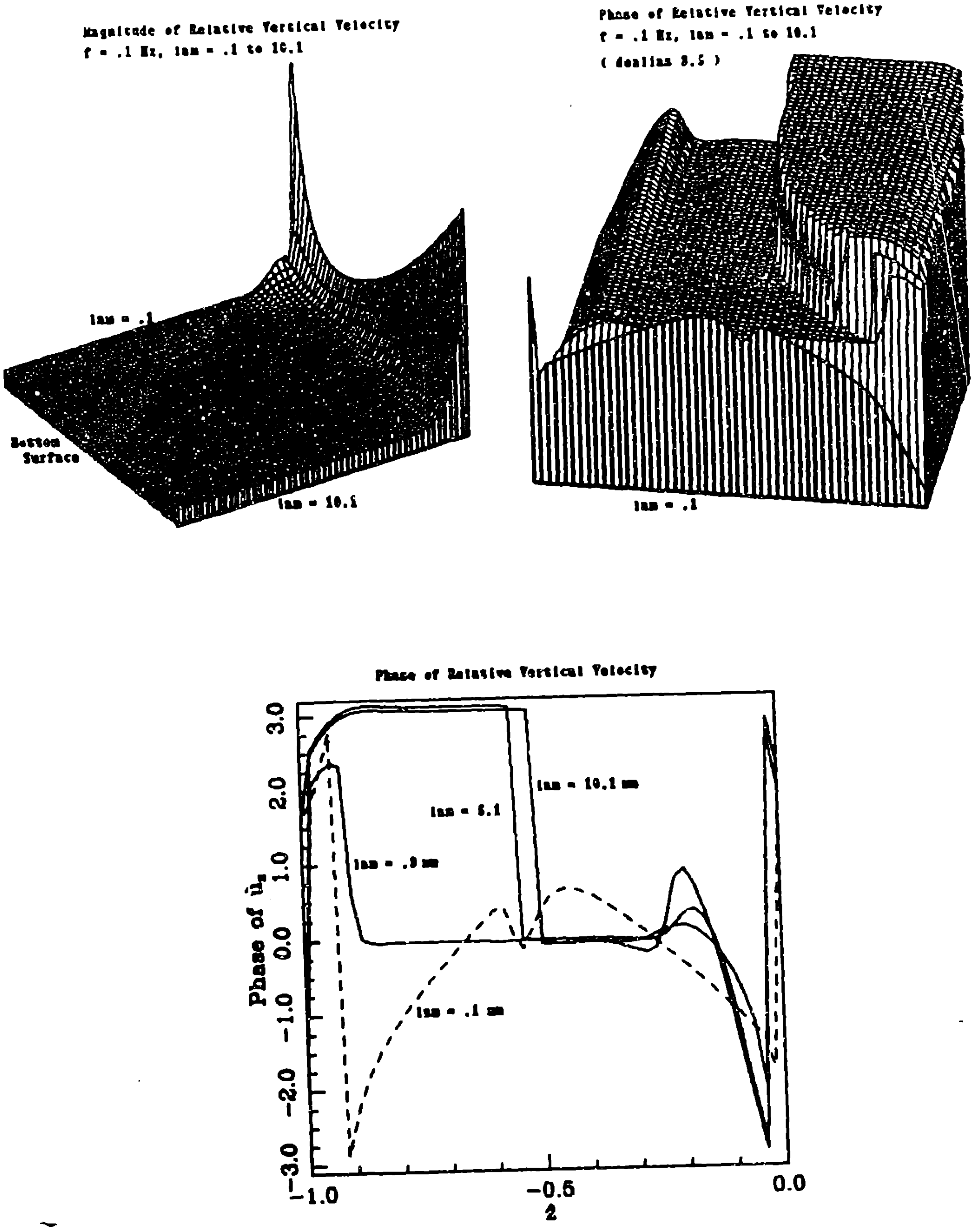

Magnitude and phase of $|V_z^*/\omega a_J|$, $f = 0.1$ Hz, $\lambda = 0.1$ to 10.1 mm by 0.2.

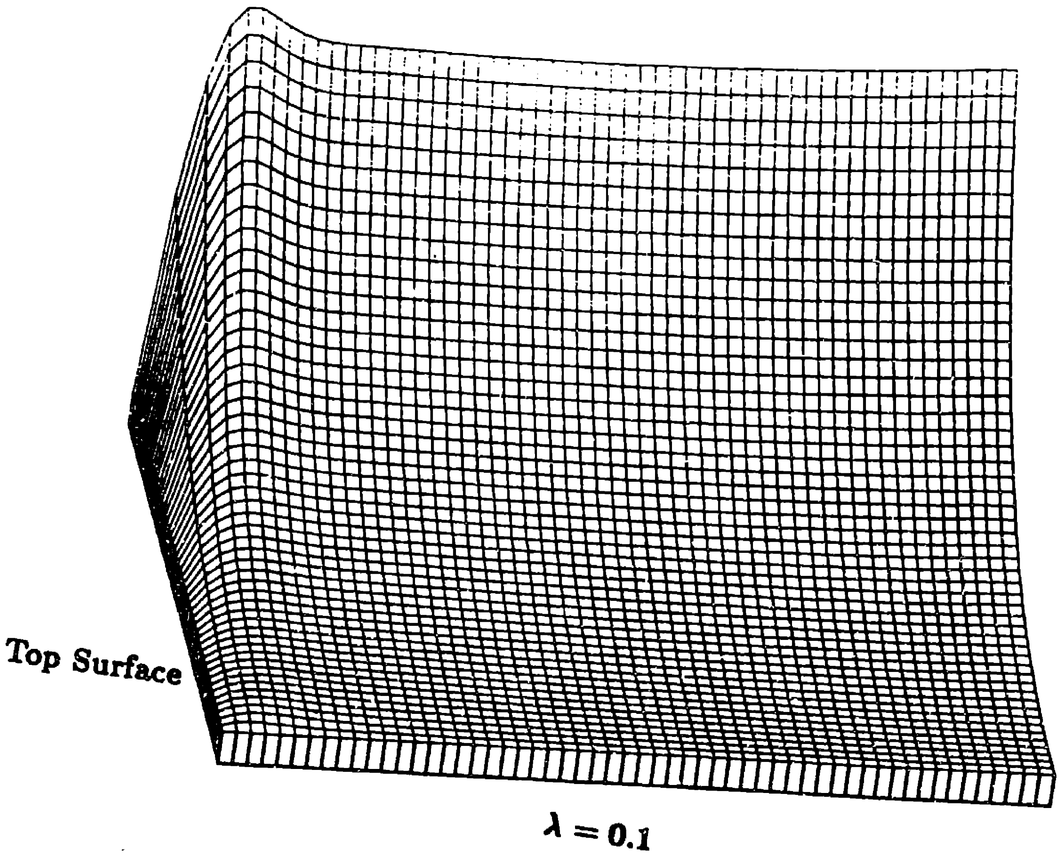

$|\lambda\, p|$, $f = 0.1\ Hz$, $f = 0.1\ Hz$, $\lambda = 0.1$ to $10.1\ mm$ by 0.2. $\arg p = \pi \pm 0.2$.

A.3 Fields Resulting from Mixed Boundary Conditions

This section presents plots of the values of the field variables for the mixed boundary value problem of Chapter 6. Magnitudes of the horizontal and vertical current densities, j_y and j_z, are plotted as functions of y and z for one half of the period in the y-direction. Then the same is done for the magnitudes and phases of u_y (horizontal displacement), u_z (vertical displacement), V_y (horizontal relative velocity), V_z (vertical relative velocity), p (pressure), s (normal stress), σ_{yz} (shear stress), and ϕ (potential) for frequencies of $f = 10^{-5}$ and $f = 10^{-3}$ Hz. (Values of the other parameters are given in §6.4.) If, at a given point, the magnitude of a variable is less than a specified fraction (generally about $2 \cdot 10^{-3}$) of its maximum magnitude, its phase is not plotted at that point. Extrema of the magnitudes and phases are given in Table 6.1. Because of differences in resolution (number of samples on $[0, 1]$) or number of modes (M), there are some differences between the extrema in the table and those of the plots.

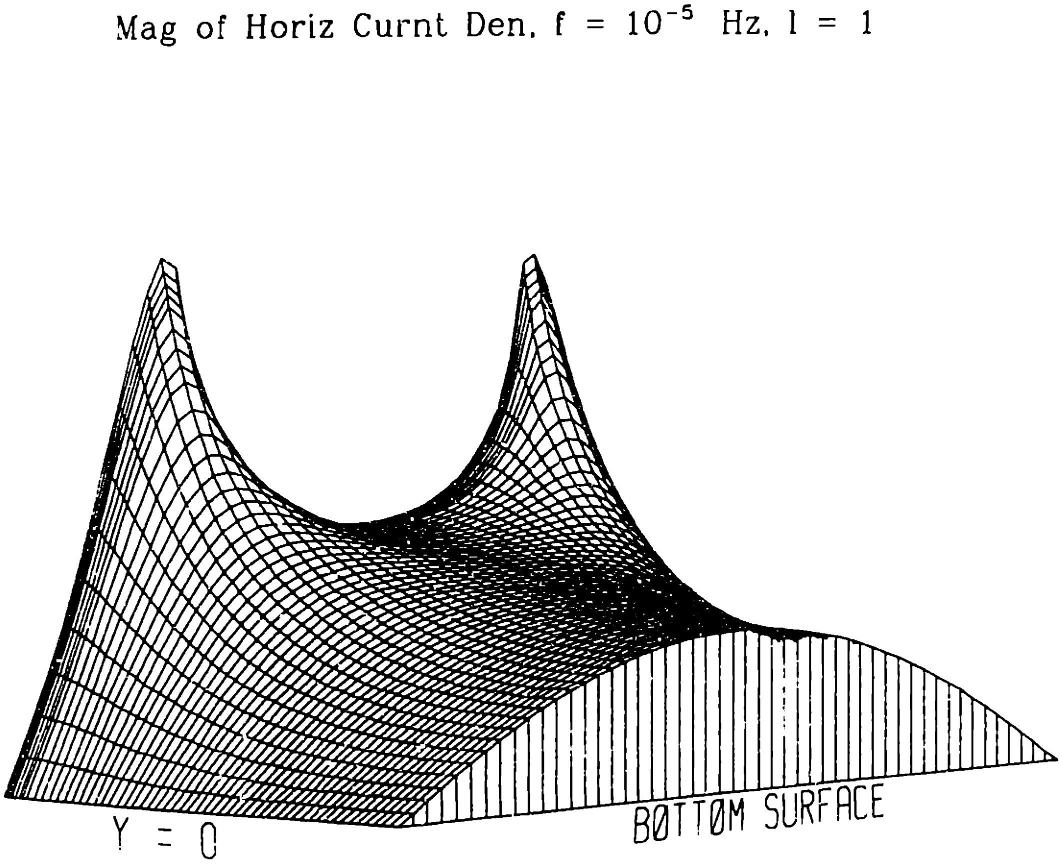

$|j_y|$, $f = 10^{-5}$ *Hz*.

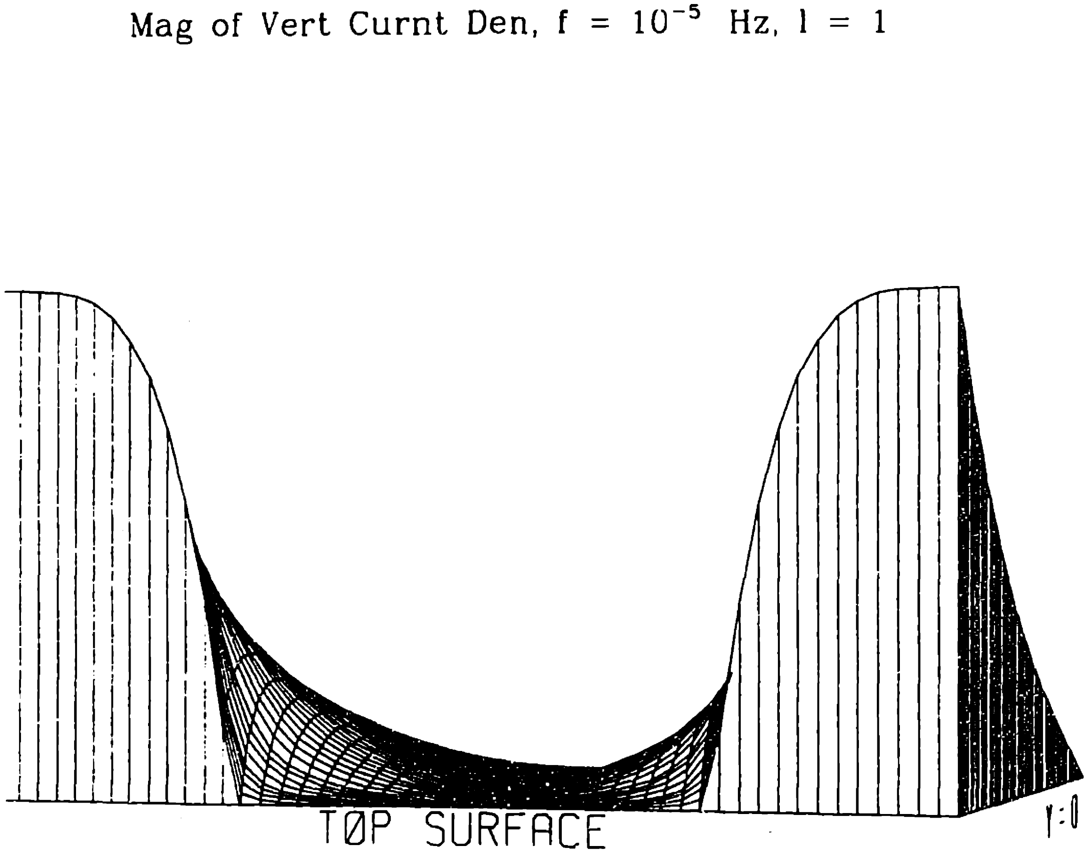

$|j_z|$, $f = 10^{-5}$ *Hz.*

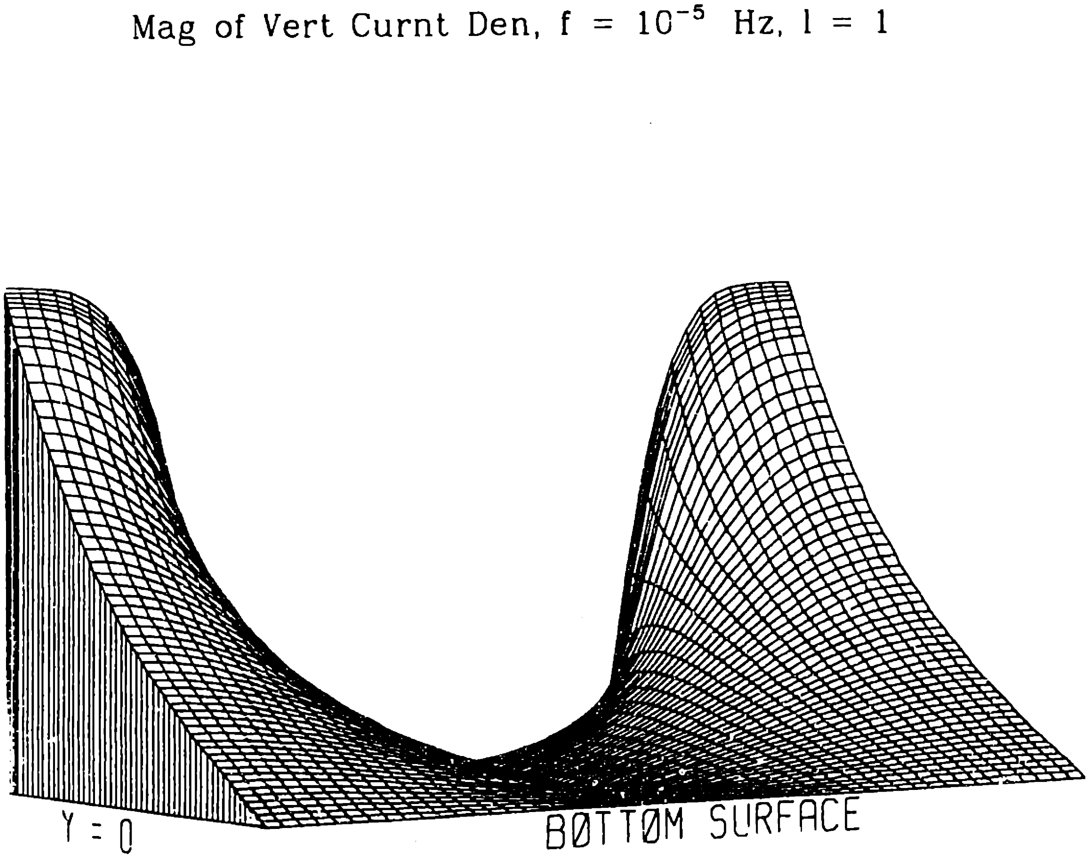

$|j_z|$, $f = 10^{-5}$ Hz.

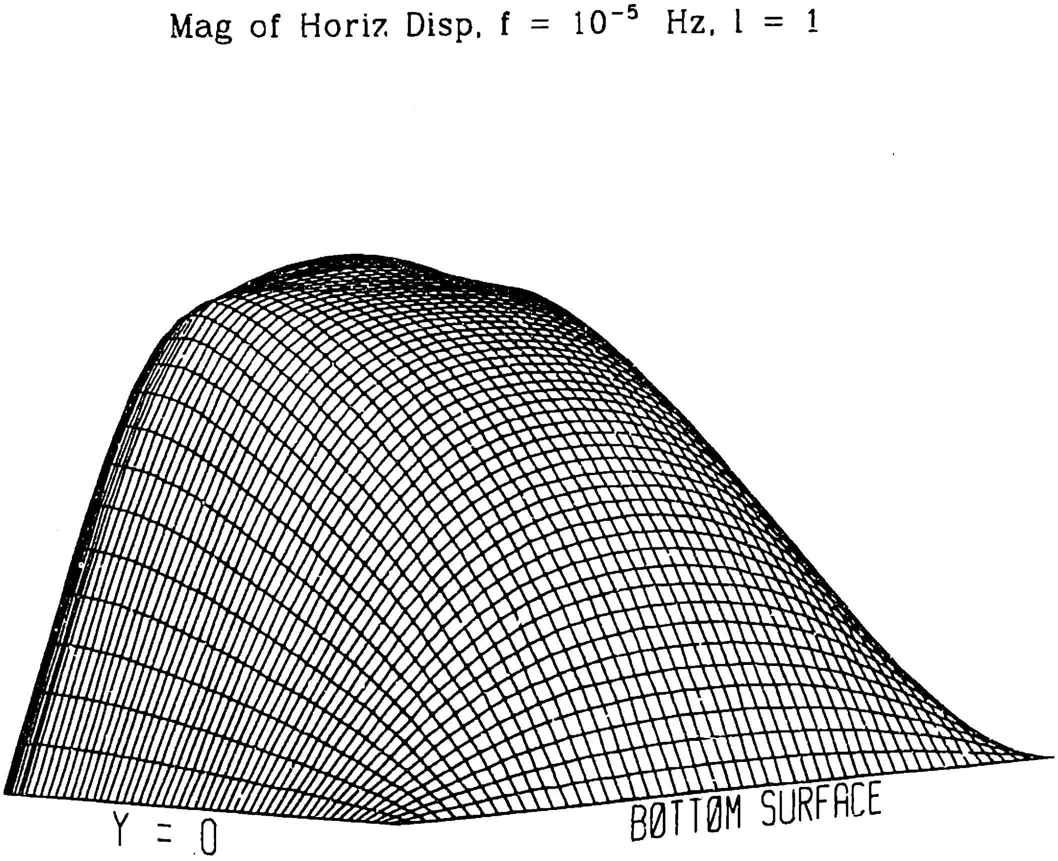

$|u_y|$, $f = 10^{-5}$ Hz. $\arg u_y \sim 3 \cdot 10^{-2}$.

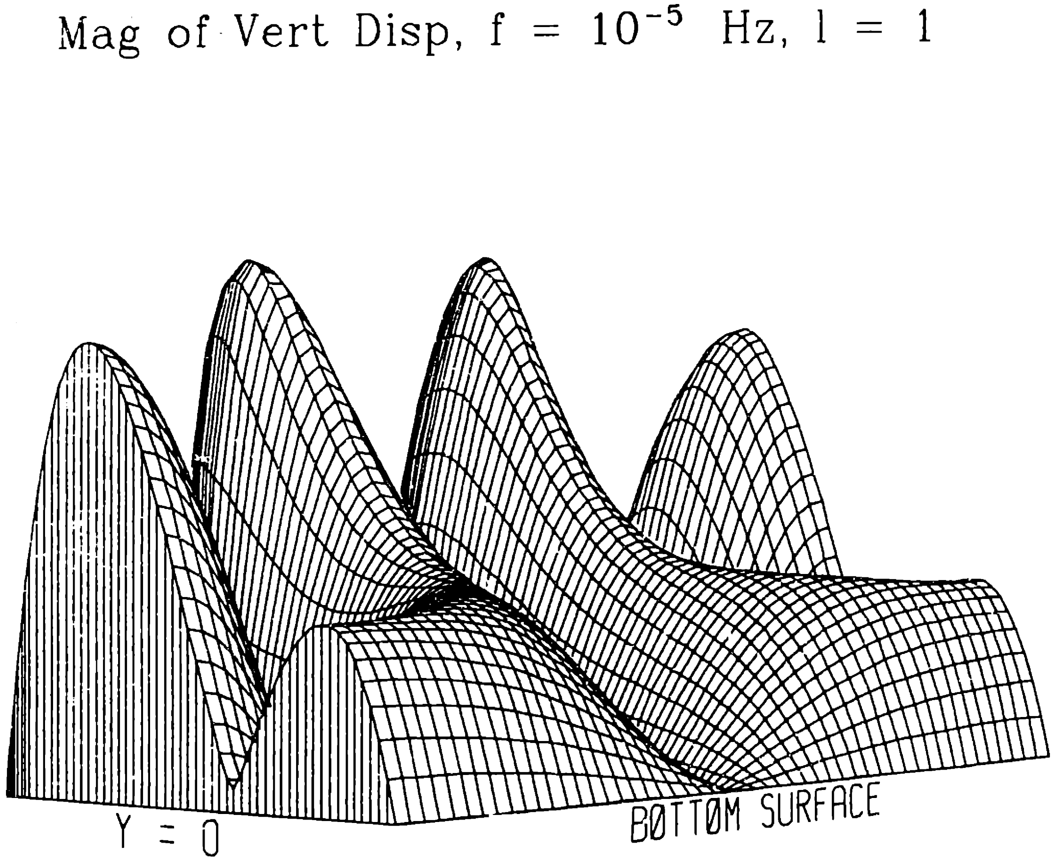

$|u_z|$, $f = 10^{-5}$ Hz.

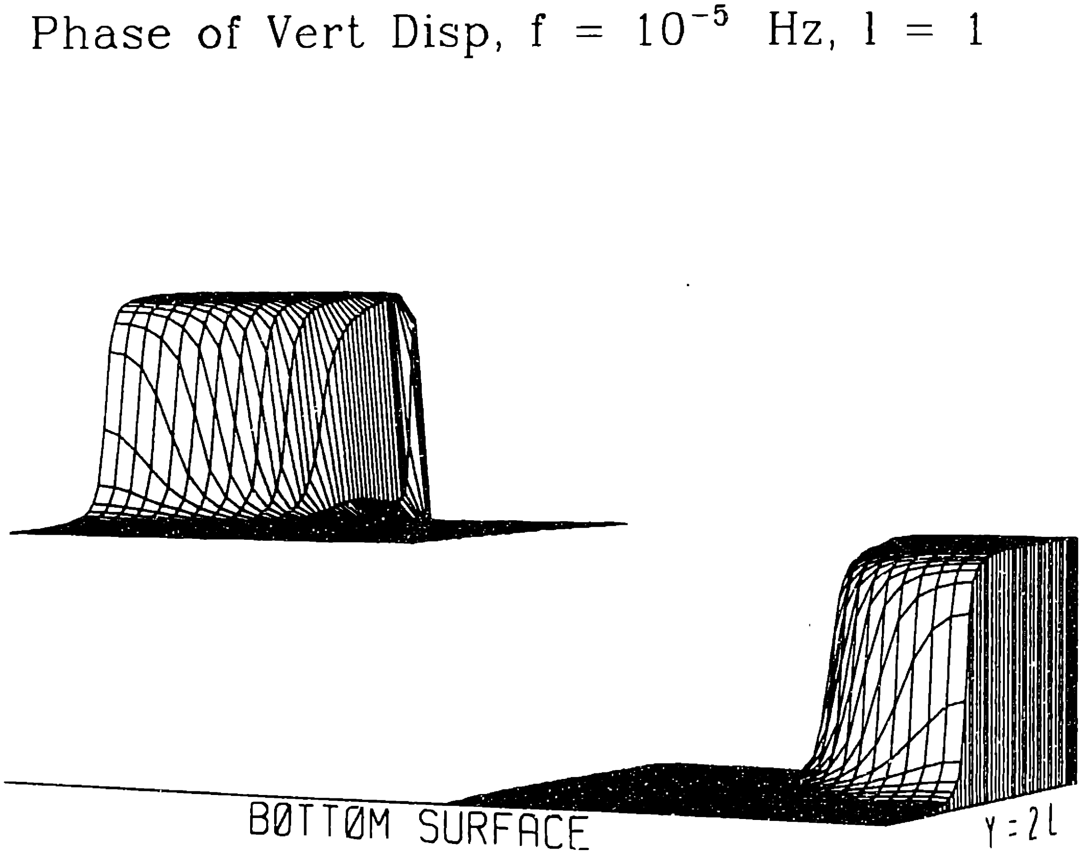

arg u_z, $f = 10^{-5}$ Hz.

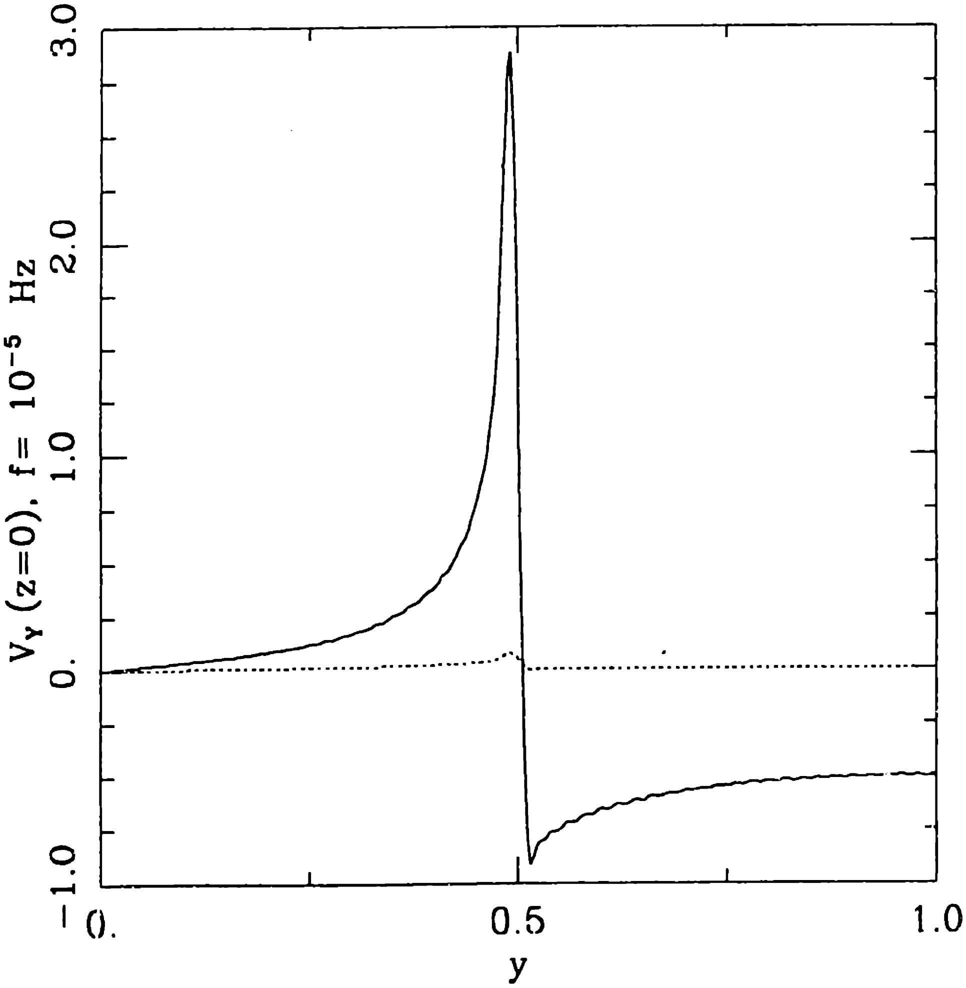

Real (solid curve) and imaginary (dashed) parts of $v_y(y, z = 0)$, $f = 10^{-5}$ Hz.

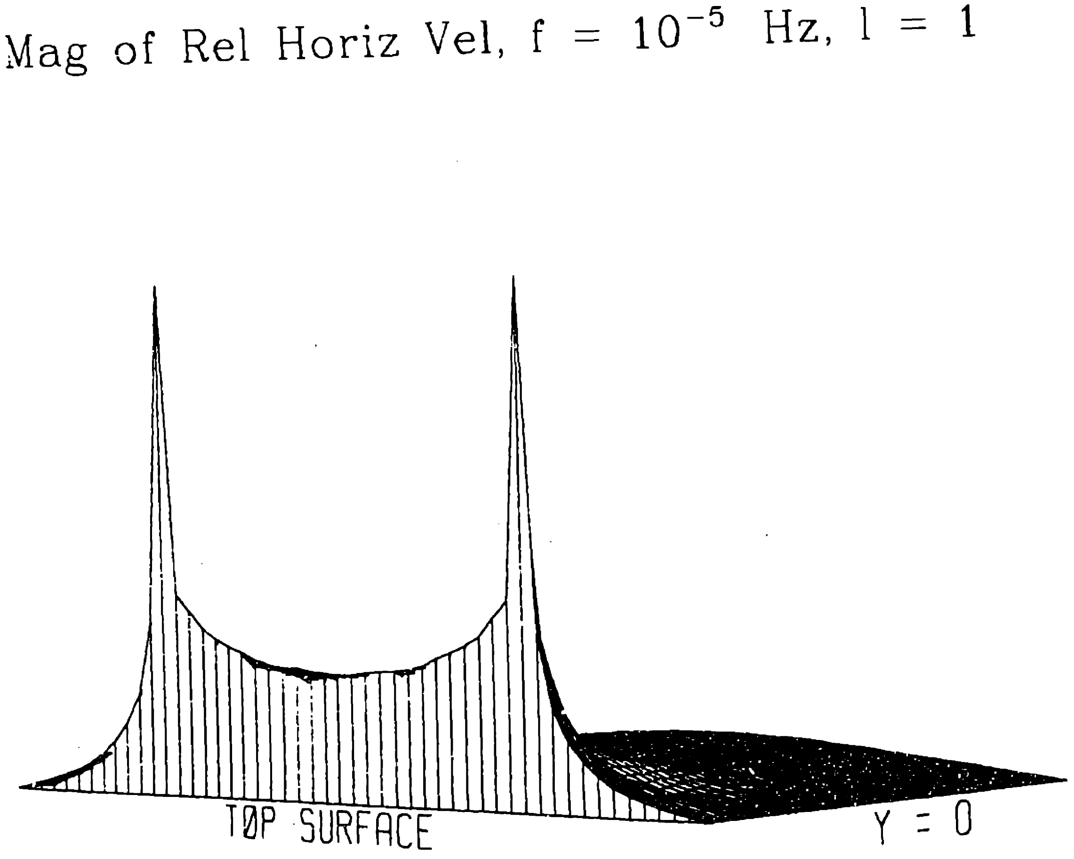

$|V_y|$, $f = 10^{-5}$ *Hz*.

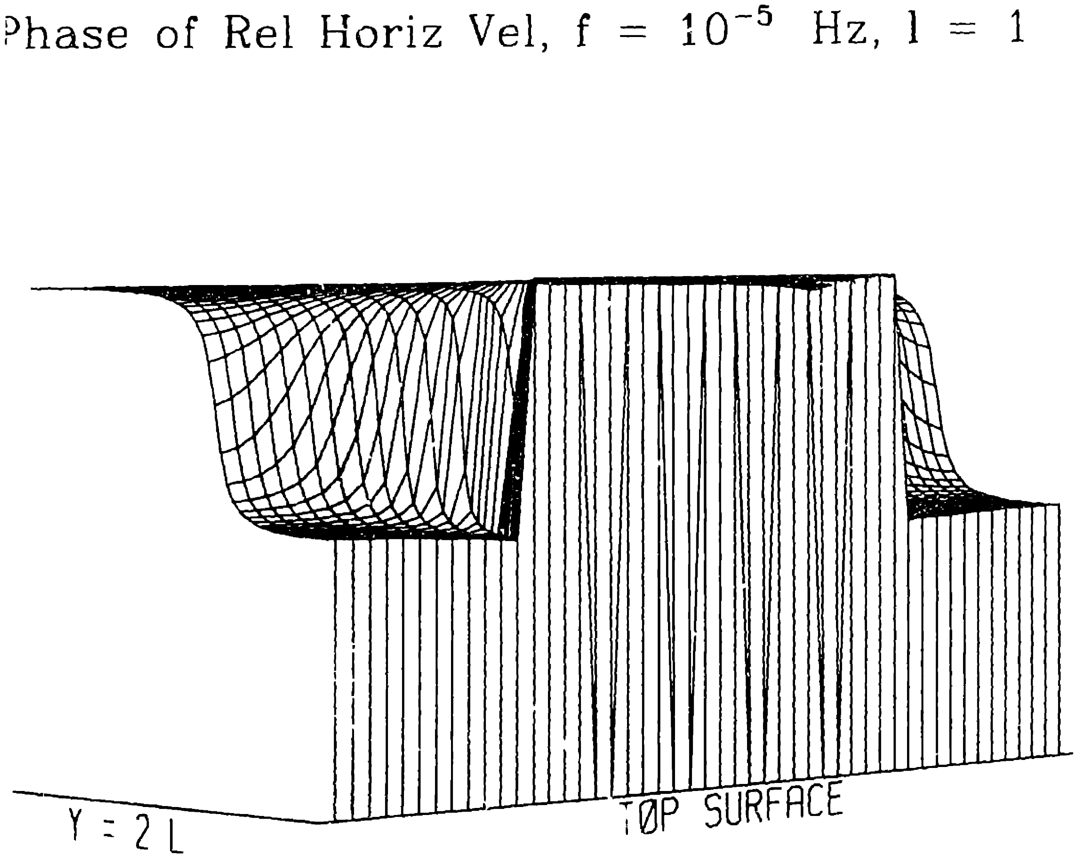

arg V_y, $f = 10^{-5}\ Hz.$

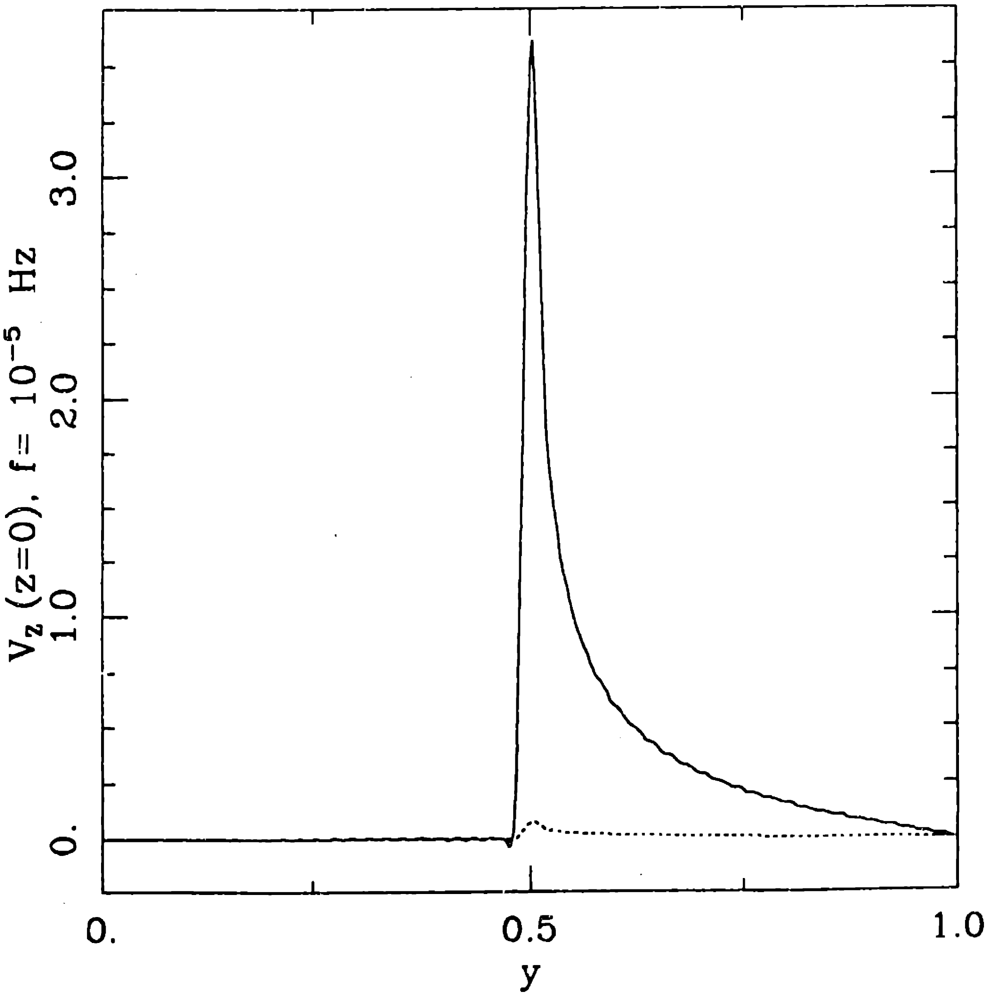

Real (solid curve) and imaginary (dashed) parts of $V_z(y, z = 0)$, $f = 10^{-5}$ Hz.

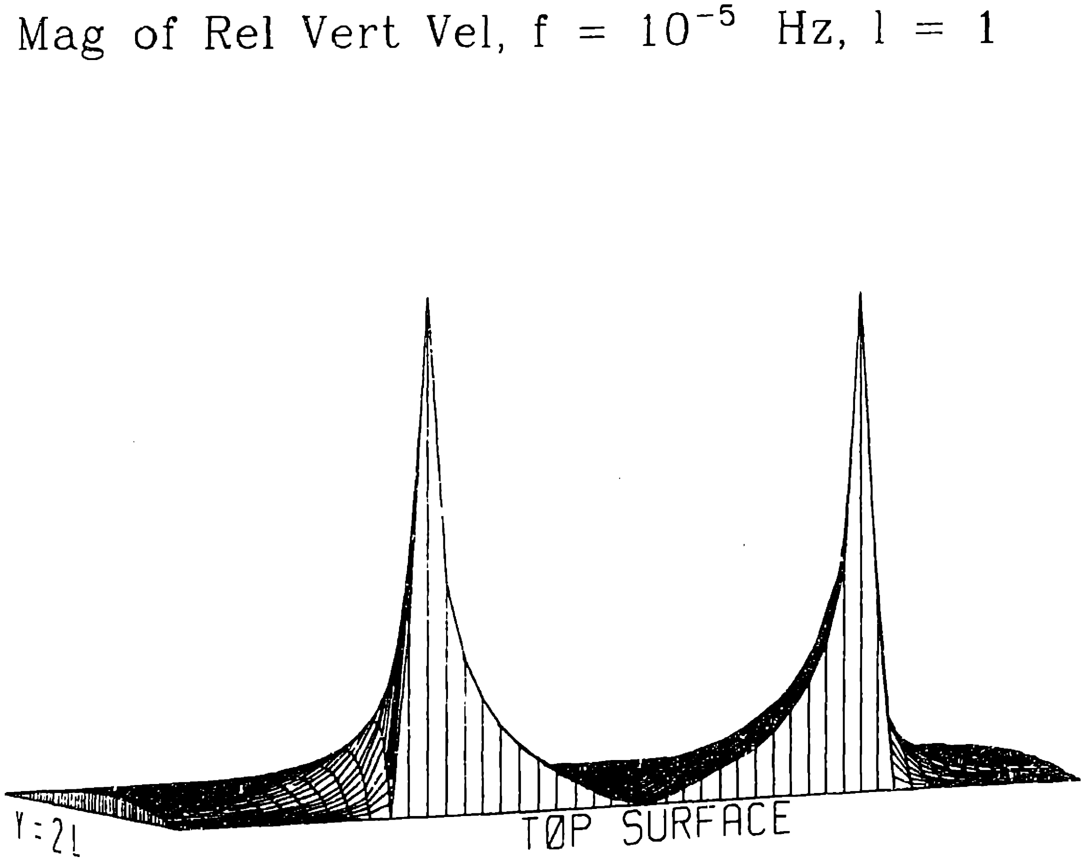

$|V_z|$, $f = 10^{-5}$ Hz.

Phase of Rel Vert Vel, f = 10^{-5} Hz, l = 1

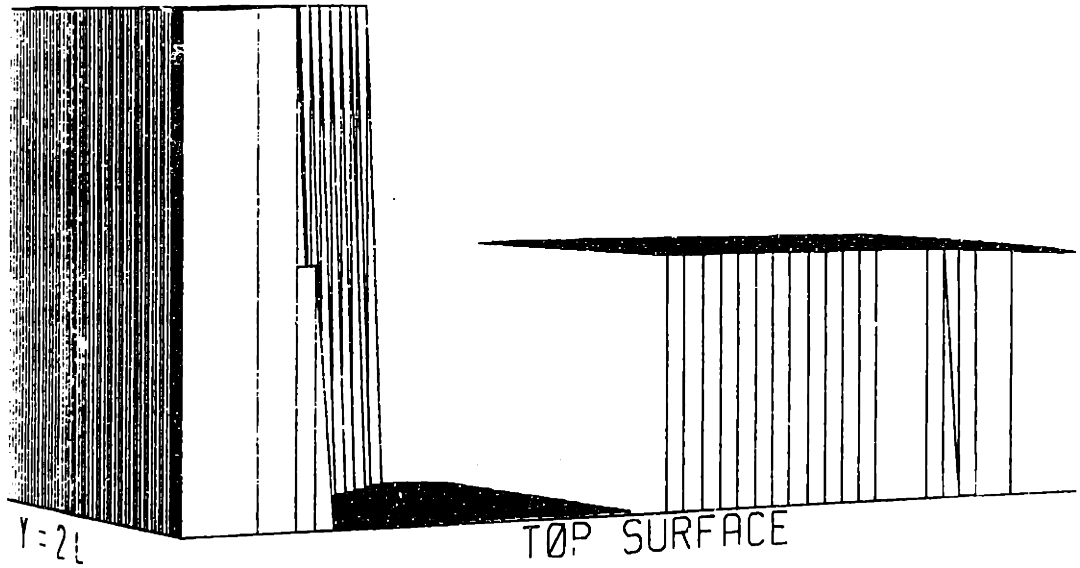

arg V_z, $f = 10^{-5}$ Hz.

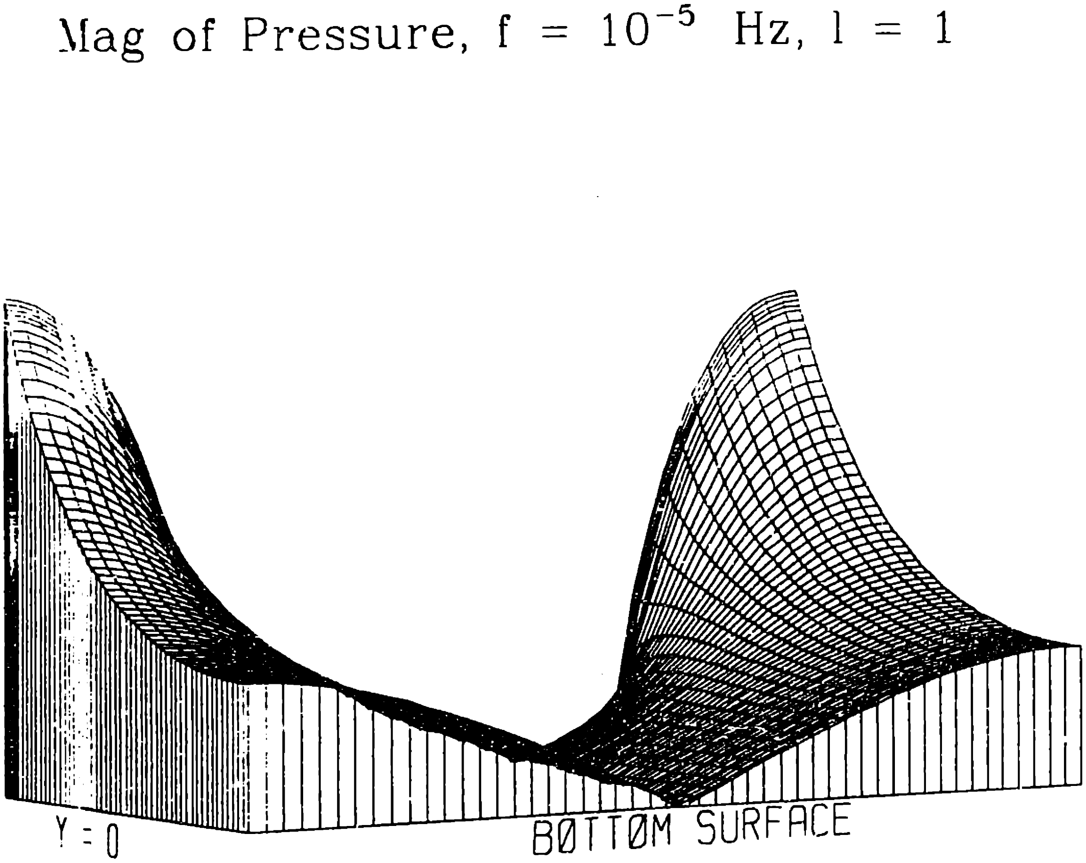

$|p|$, $f = 10^{-5}\ Hz$.

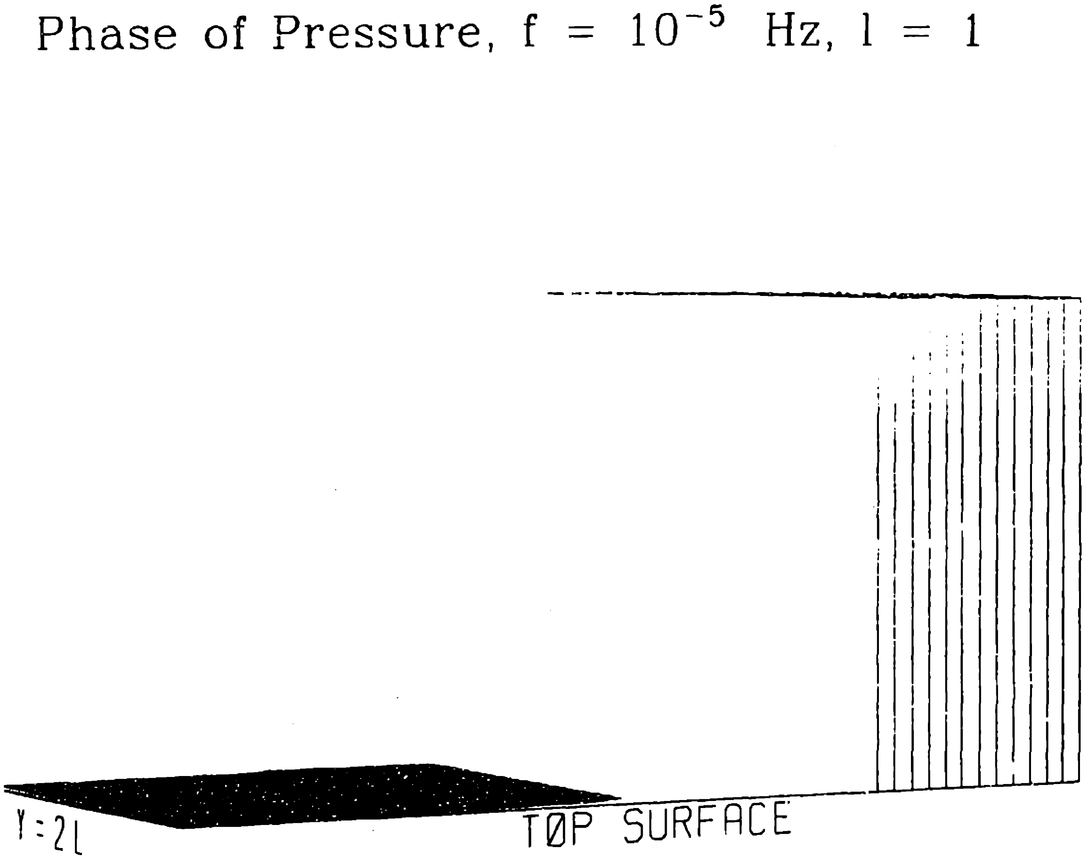

$\arg p$, $f = 10^{-5}$ Hz.

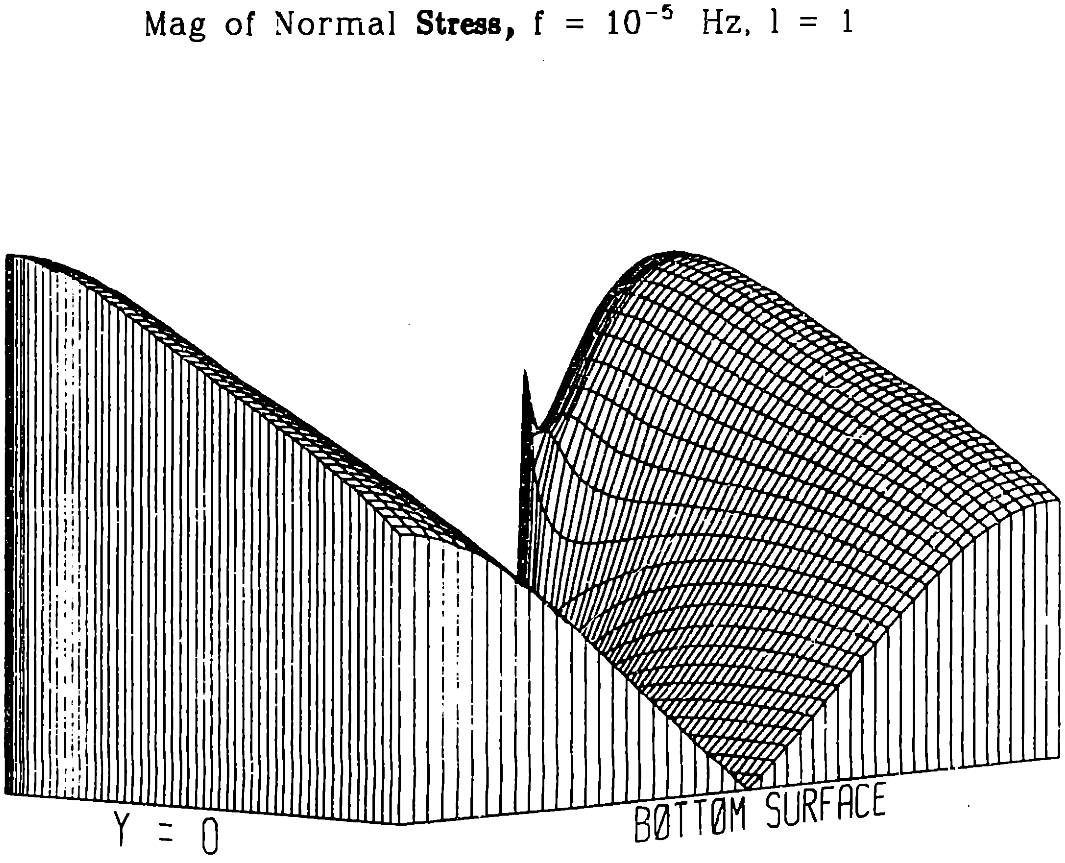

$|s|$, $f = 10^{-5}$ Hz.

Phase of Normal **Stress,** f = 10^{-5} Hz, l = 1

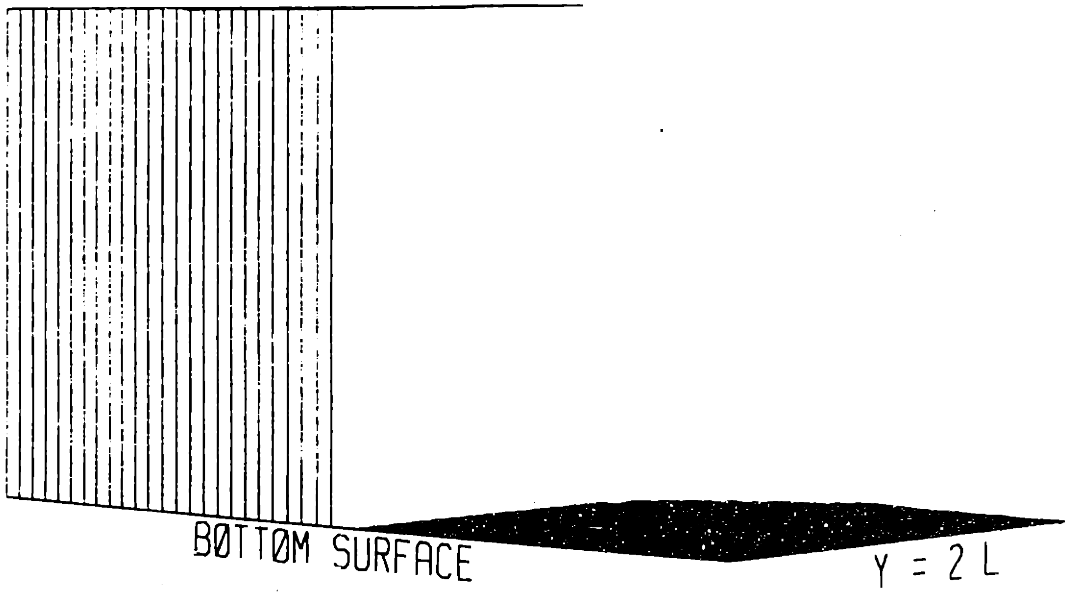

arg s, $f = 10^{-5}$ Hz.

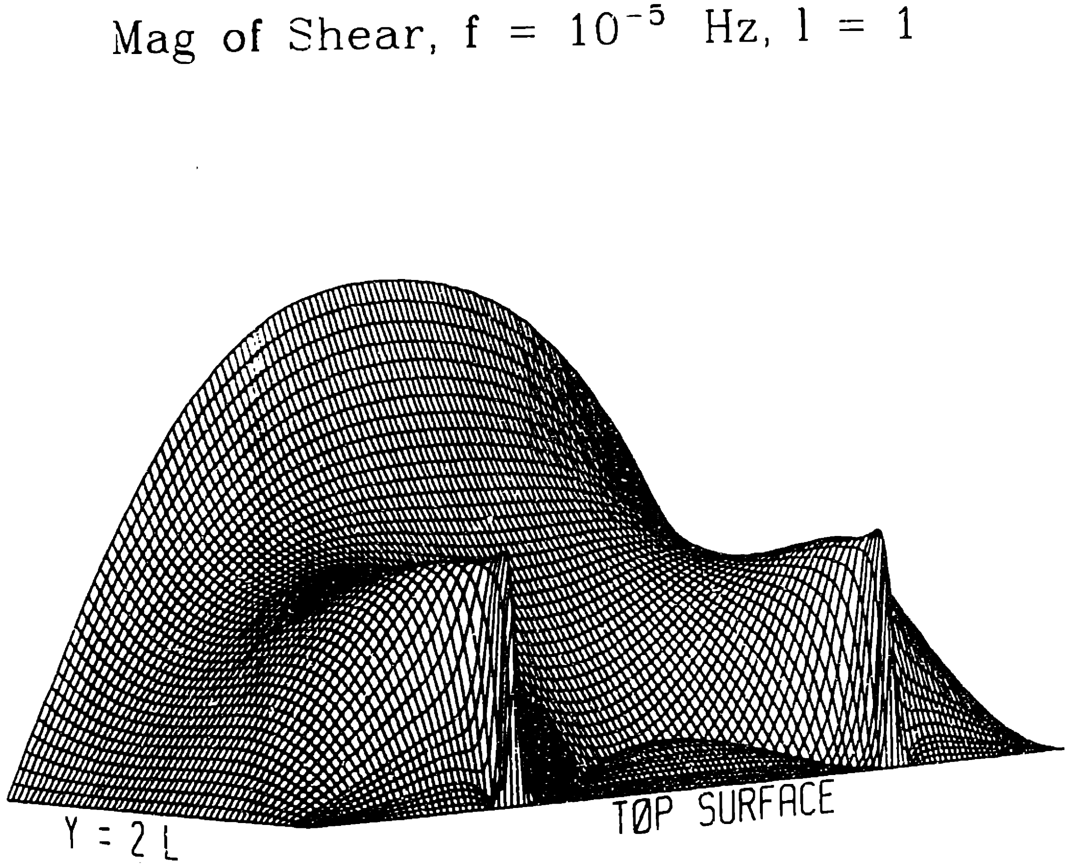

$|\sigma_{yz}|$, $f = 10^{-5}$ *Hz*.

Phase of Shear, $f = 10^{-5}$ Hz, l = 1

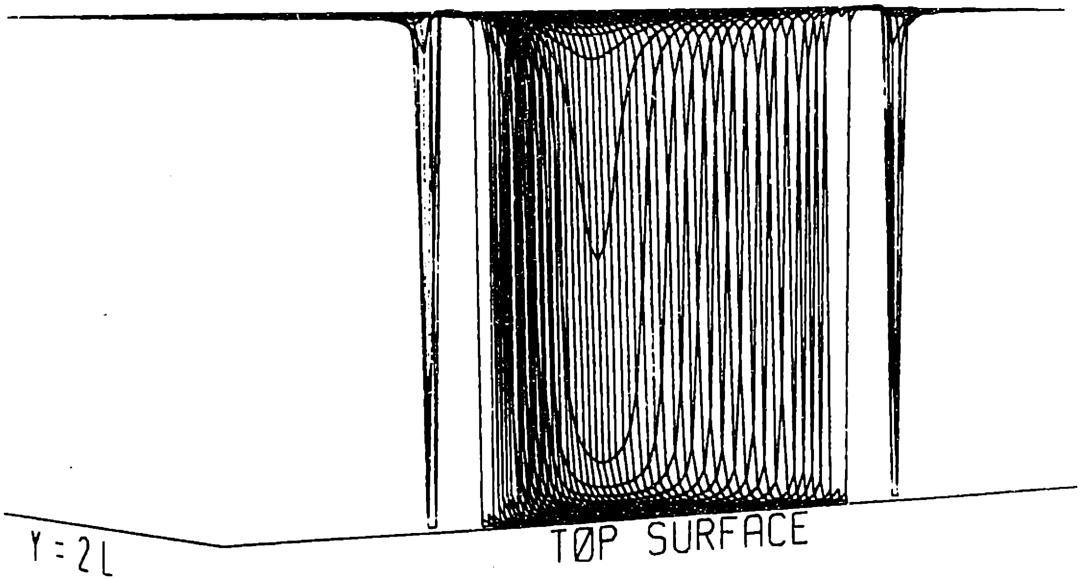

arg σ_{yz}, $f = 10^{-5}$ Hz.

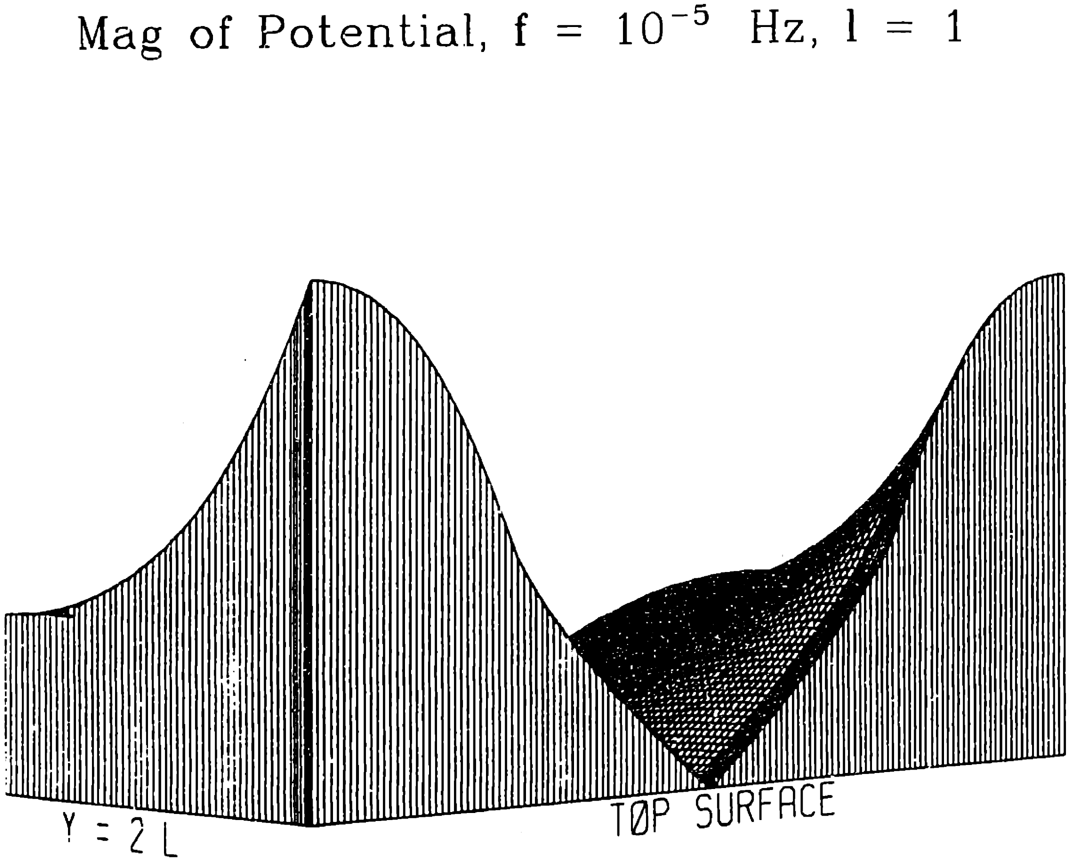

$|\phi|$, $f = 10^{-5}$ Hz.

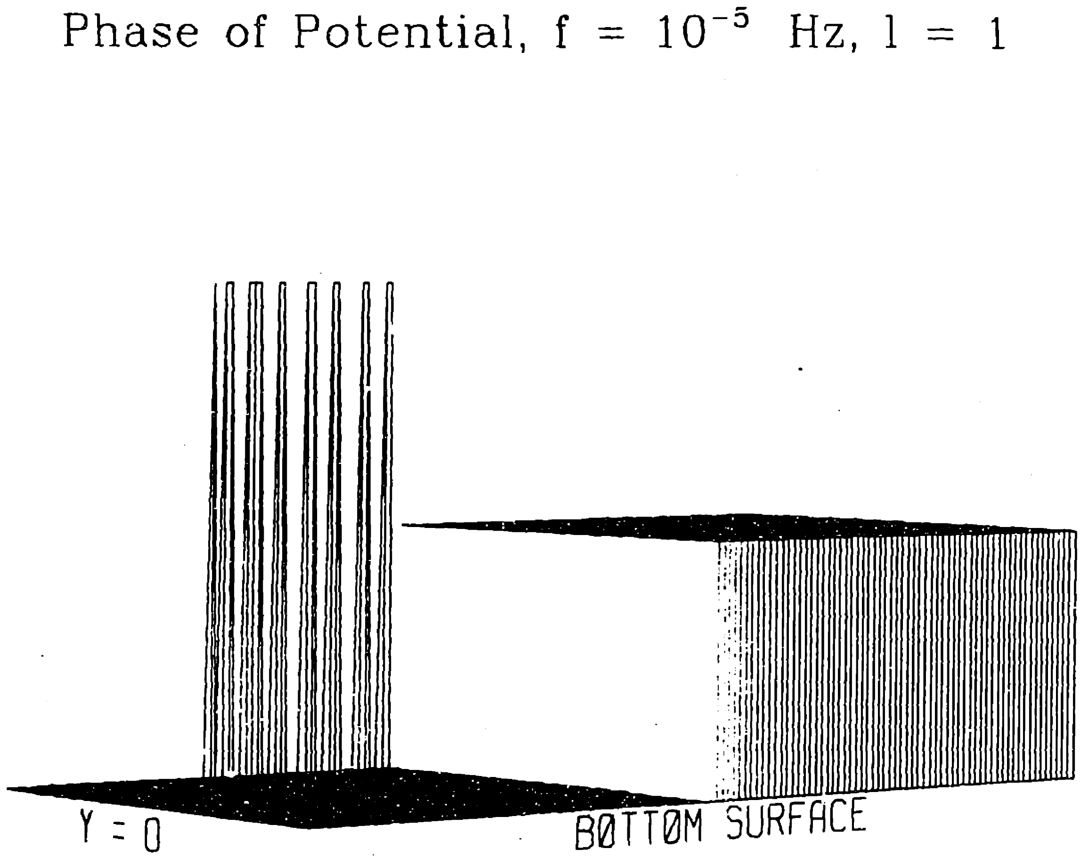

arg ϕ, $f = 10^{-5}$ Hz.

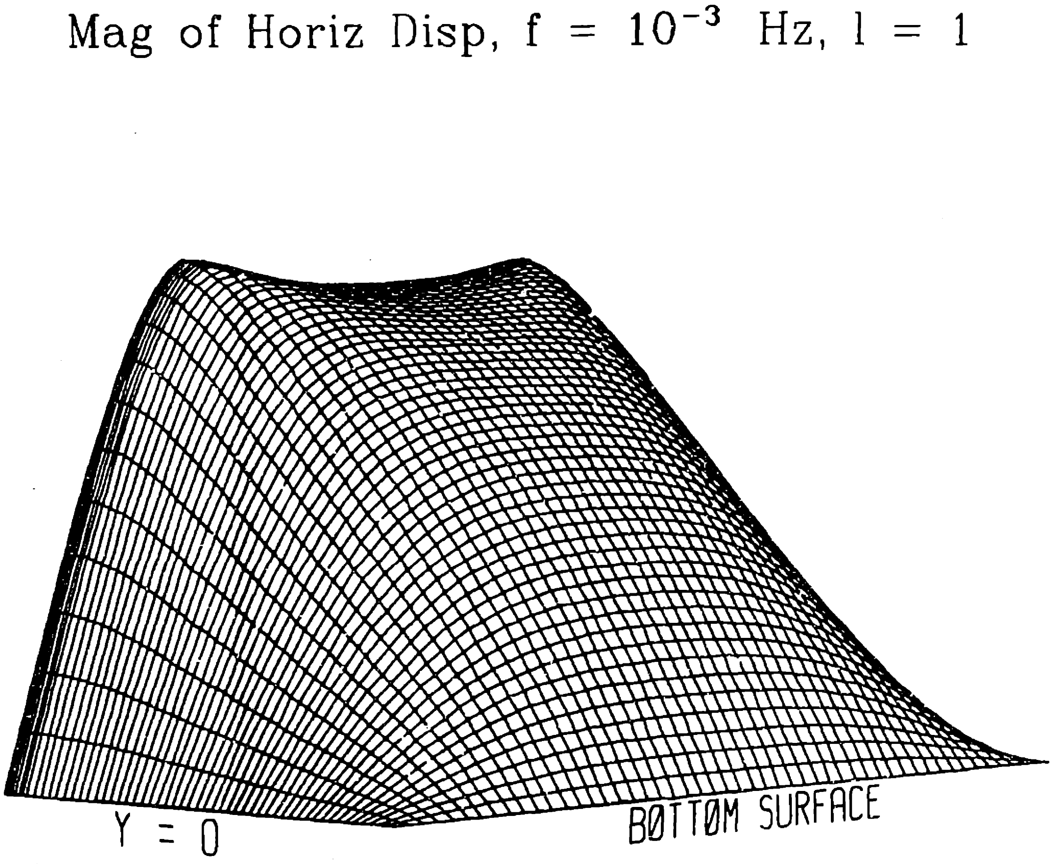

$|u_y|$, $f = 10^{-3}$ Hz.

Phase of Horiz Disp, f = 10^{-3} Hz, l = 1

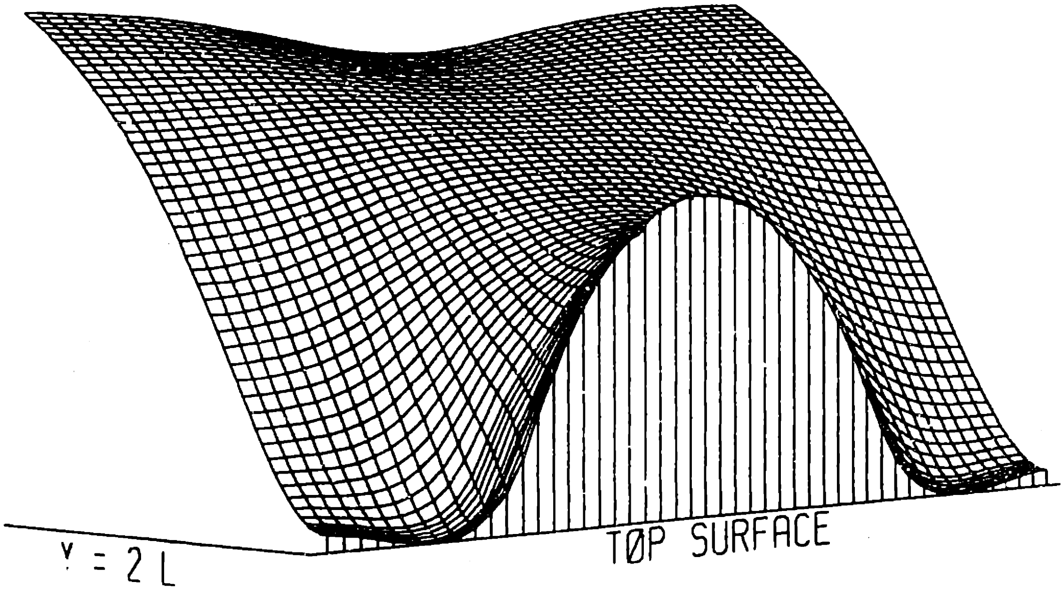

arg u_y, $f = 10^{-3}$ Hz.

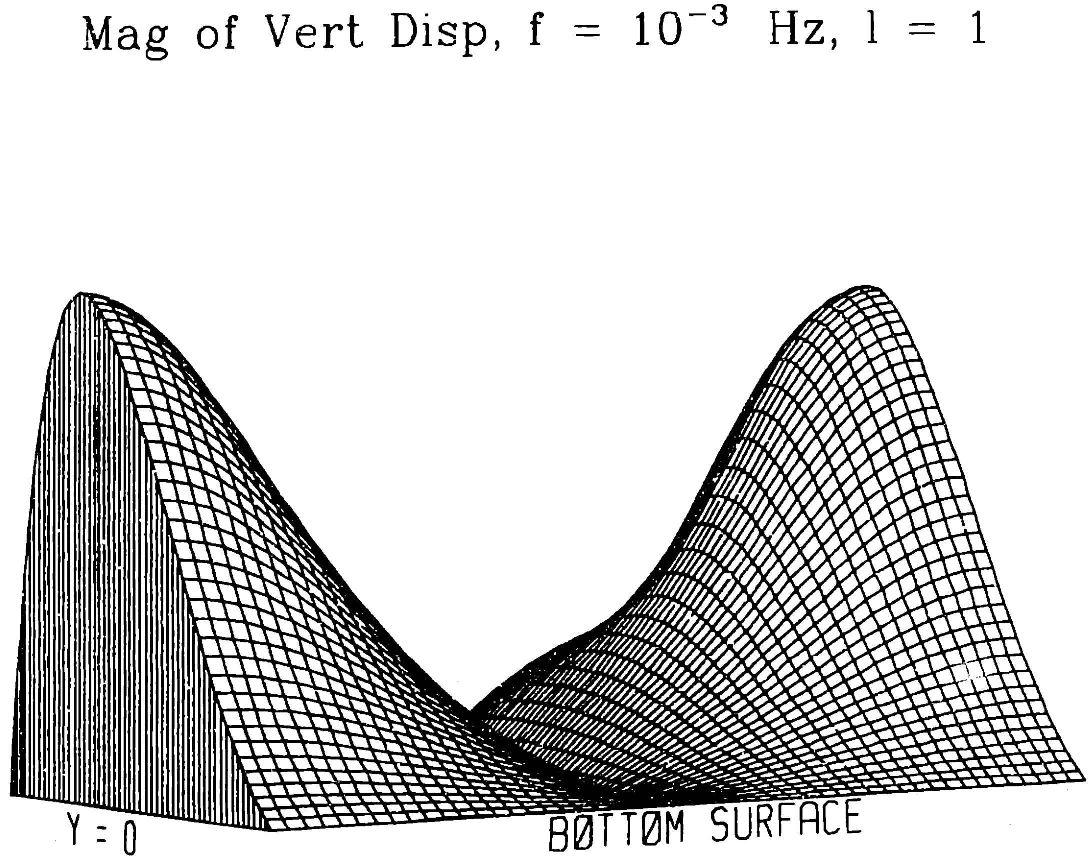

$|u_z|$, $f = 10^{-3}$ Hz.

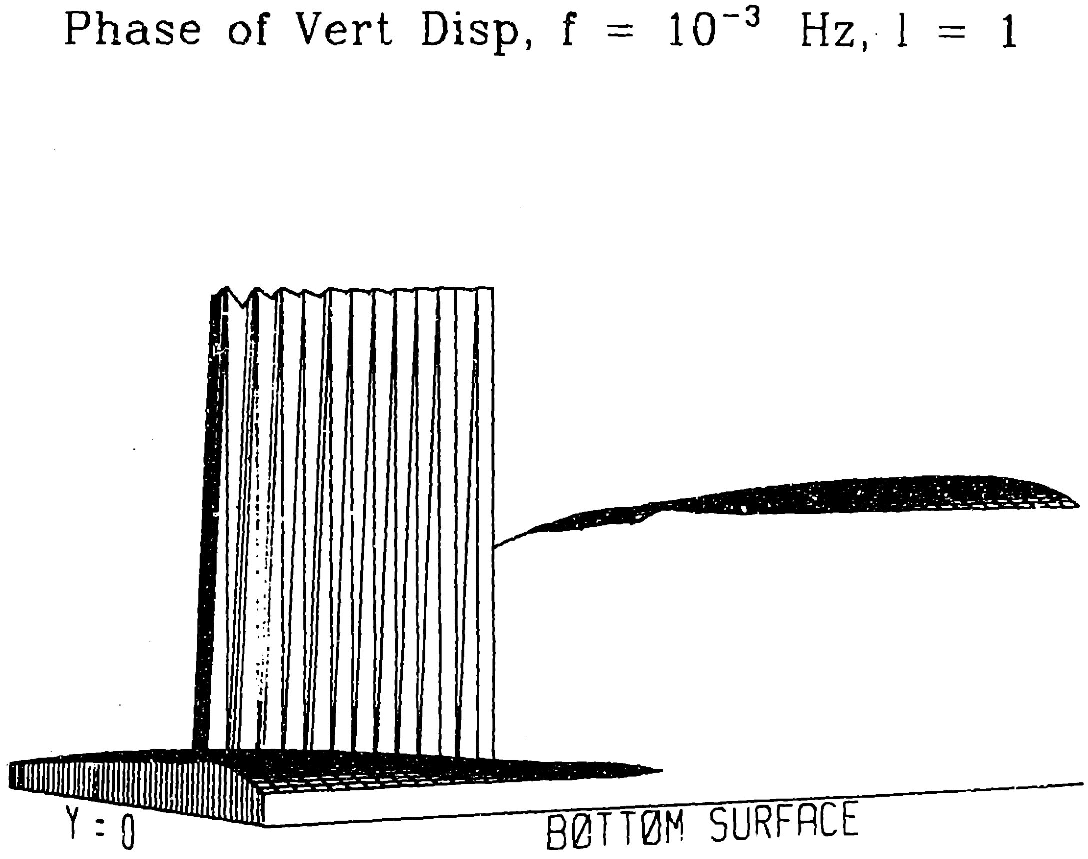

arg u_z, $f = 10^{-3}$ *Hz*.

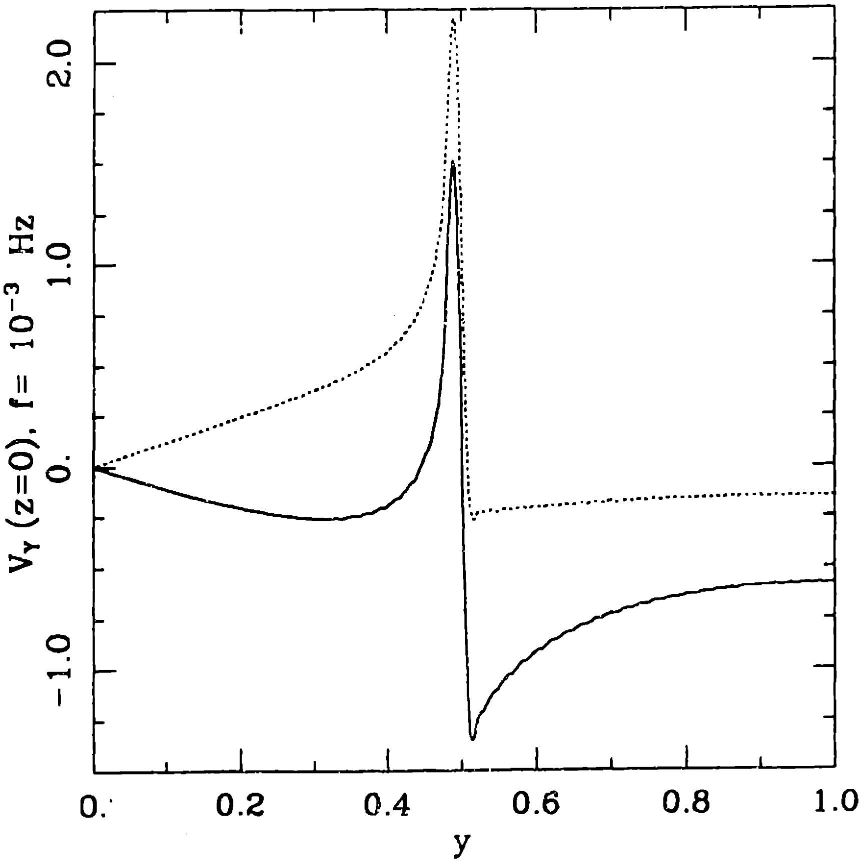

Real (solid curve) and imaginary (dashed) parts of $V_y(y, z = 0)$, $f = 10^{-3}$ Hz.

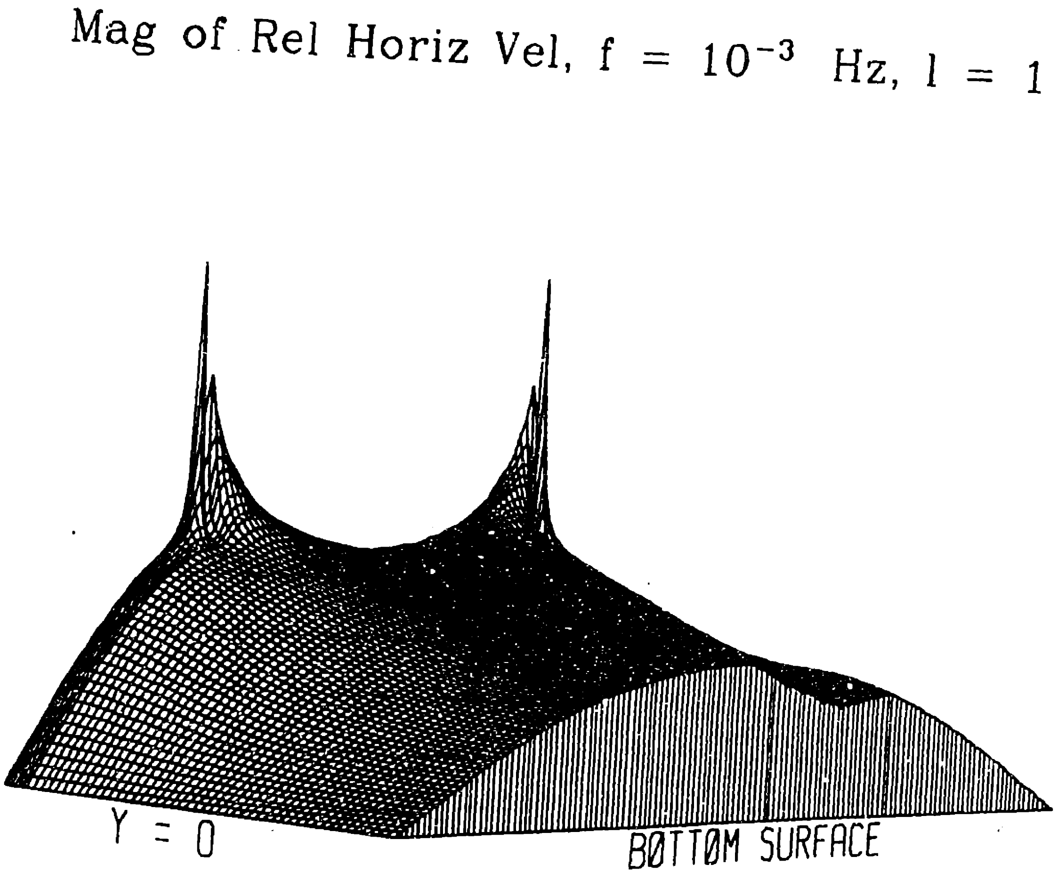

$|V_y|$, $f = 10^{-3}$ Hz. Maximum shown is 1.25.

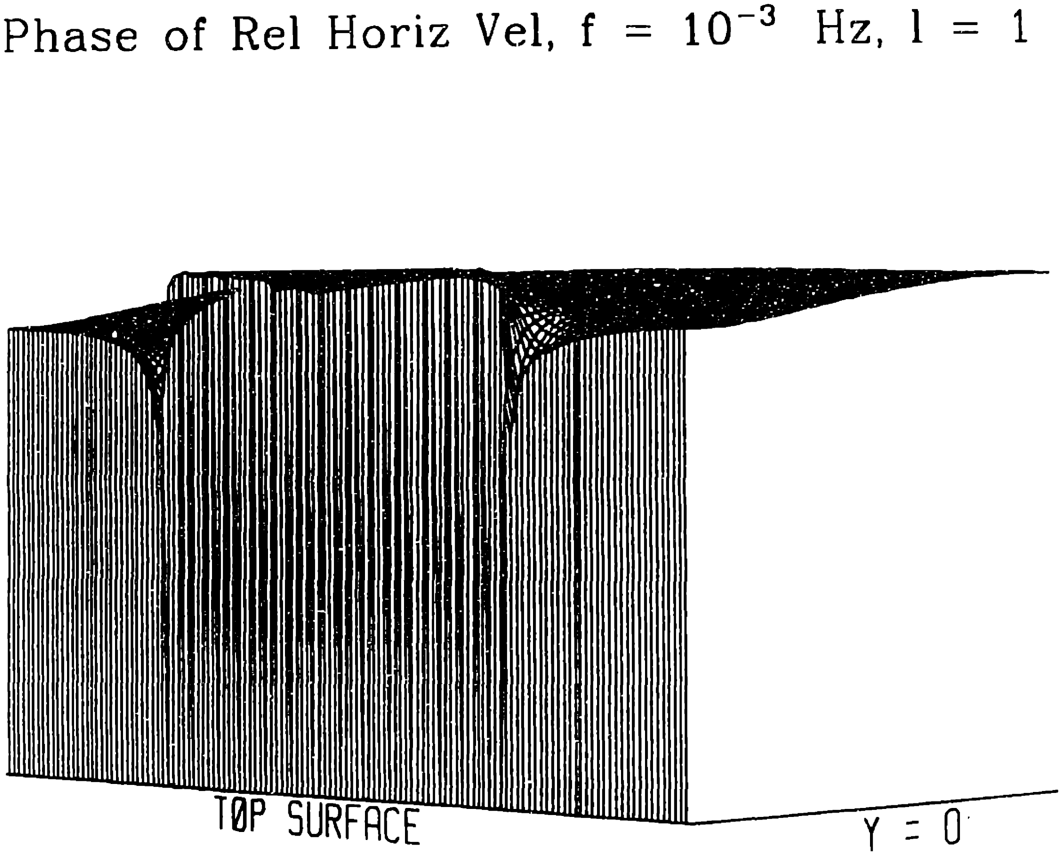

arg V_y, $f = 10^{-3}$ Hz.

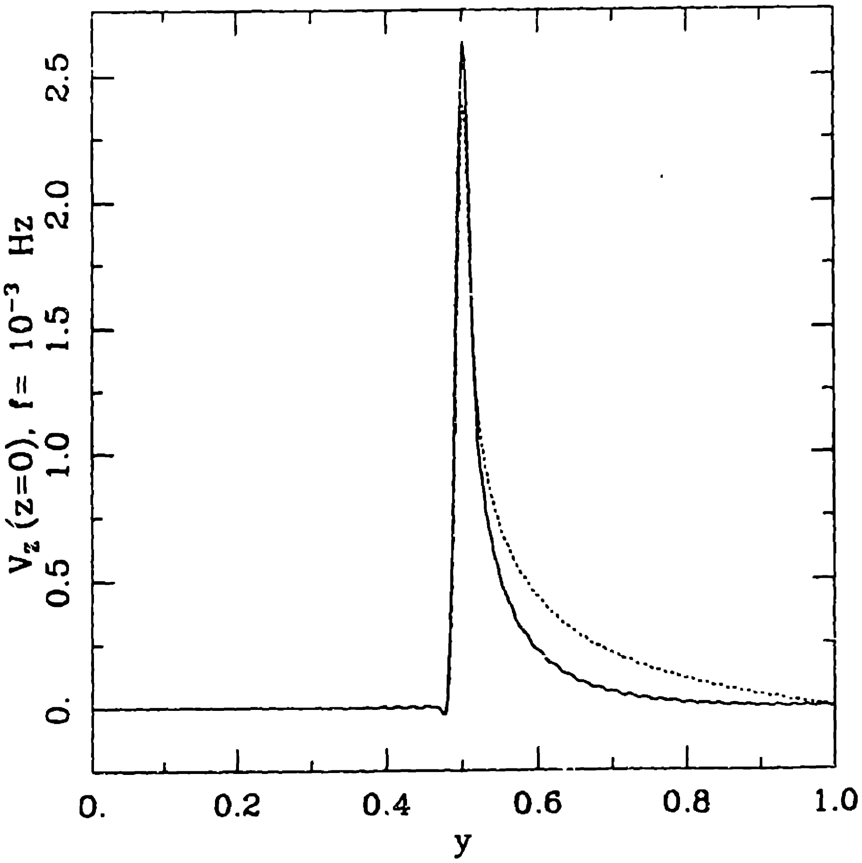

Real (solid curve) and imaginary (dashed) parts of $V_z(y, z = 0)$, $f = 10^{-3}$ Hz.

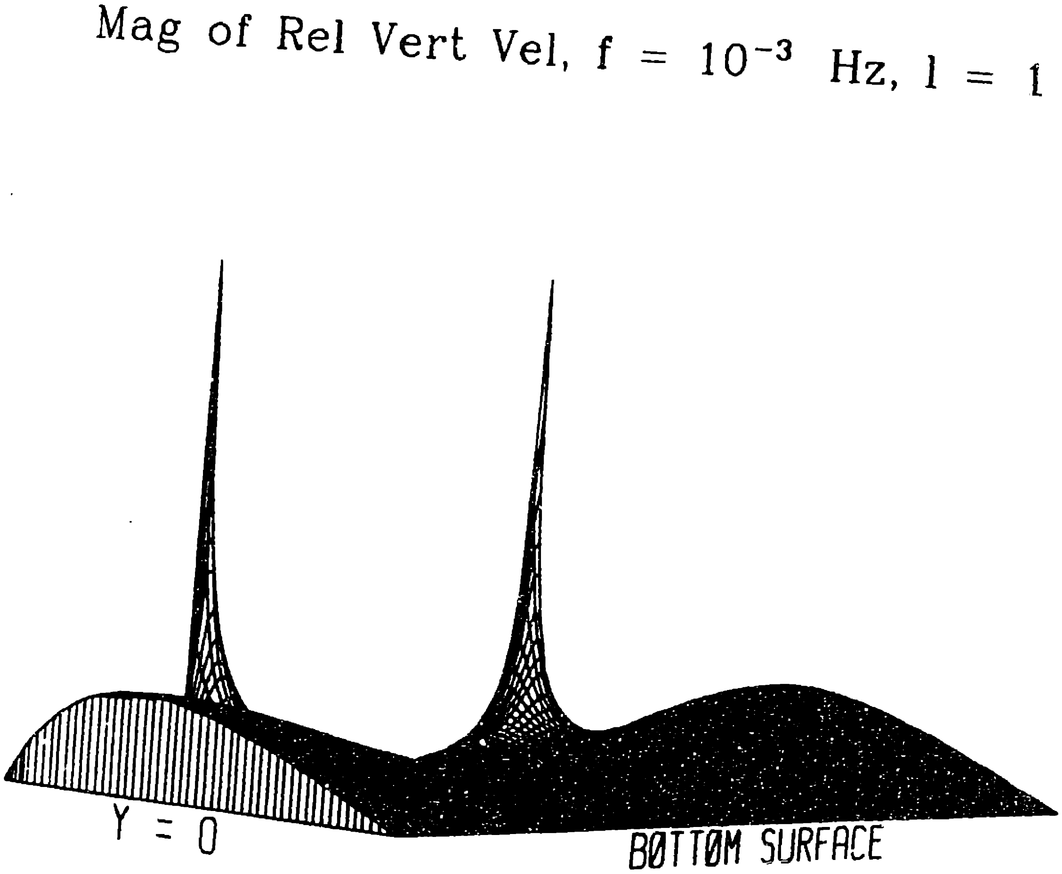

$|V_z|$, $f = 10^{-3}$ Hz. Maximum shown is 1.71.

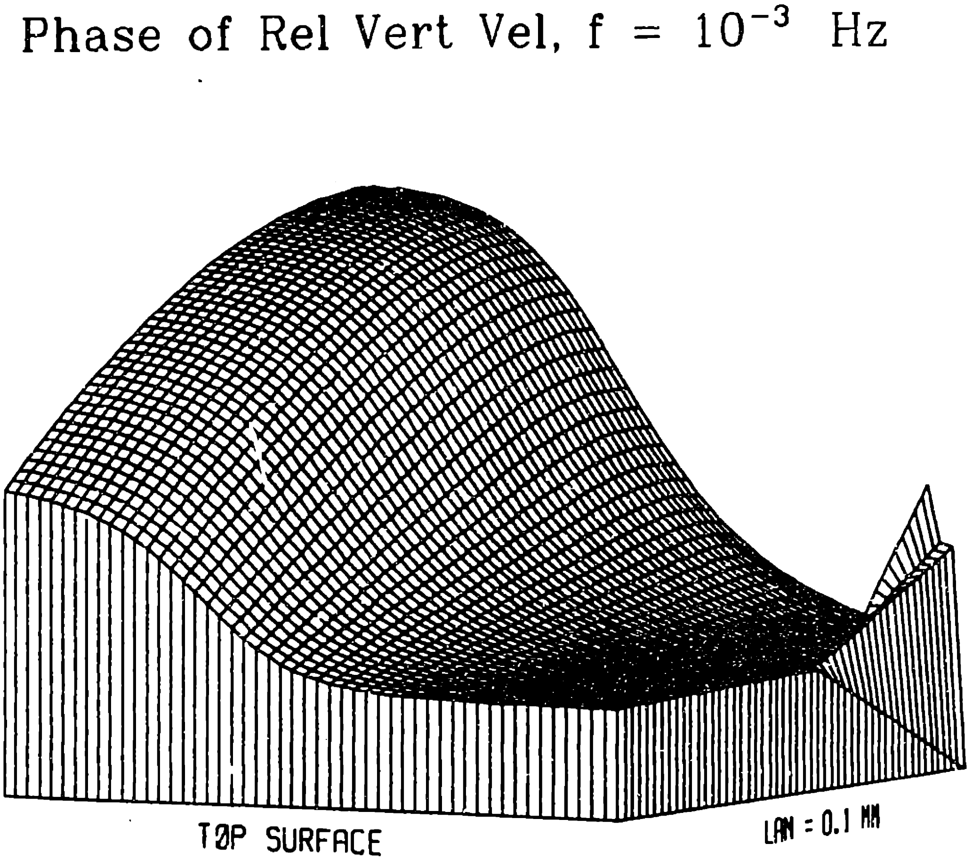

arg V_z**,** $f = 10^{-3}$ Hz**.**

Mag of Pressure, f = 10^{-3} Hz, l = 1

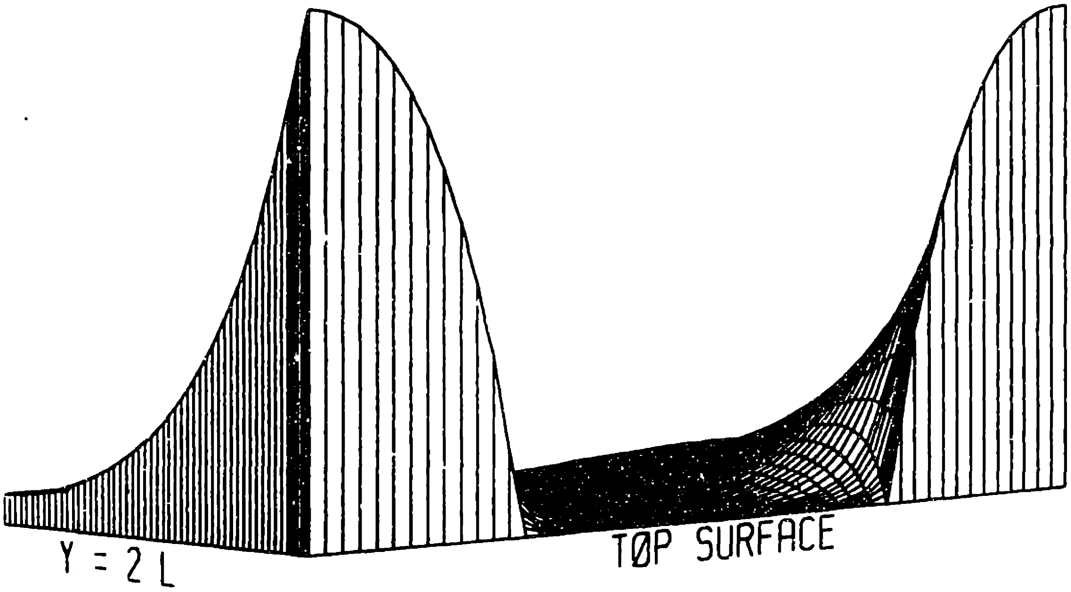

$|p|$, $f = 10^{-3}\ Hz$.

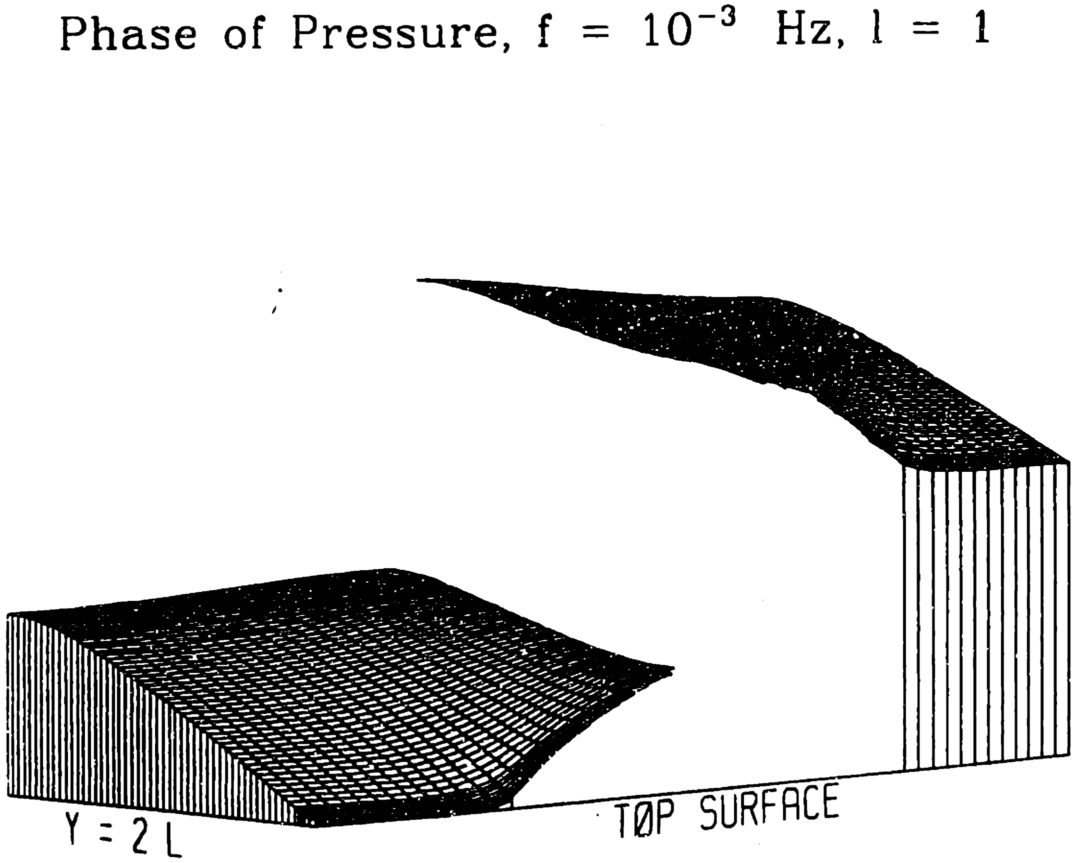

arg p, $f = 10^{-3}$ Hz.

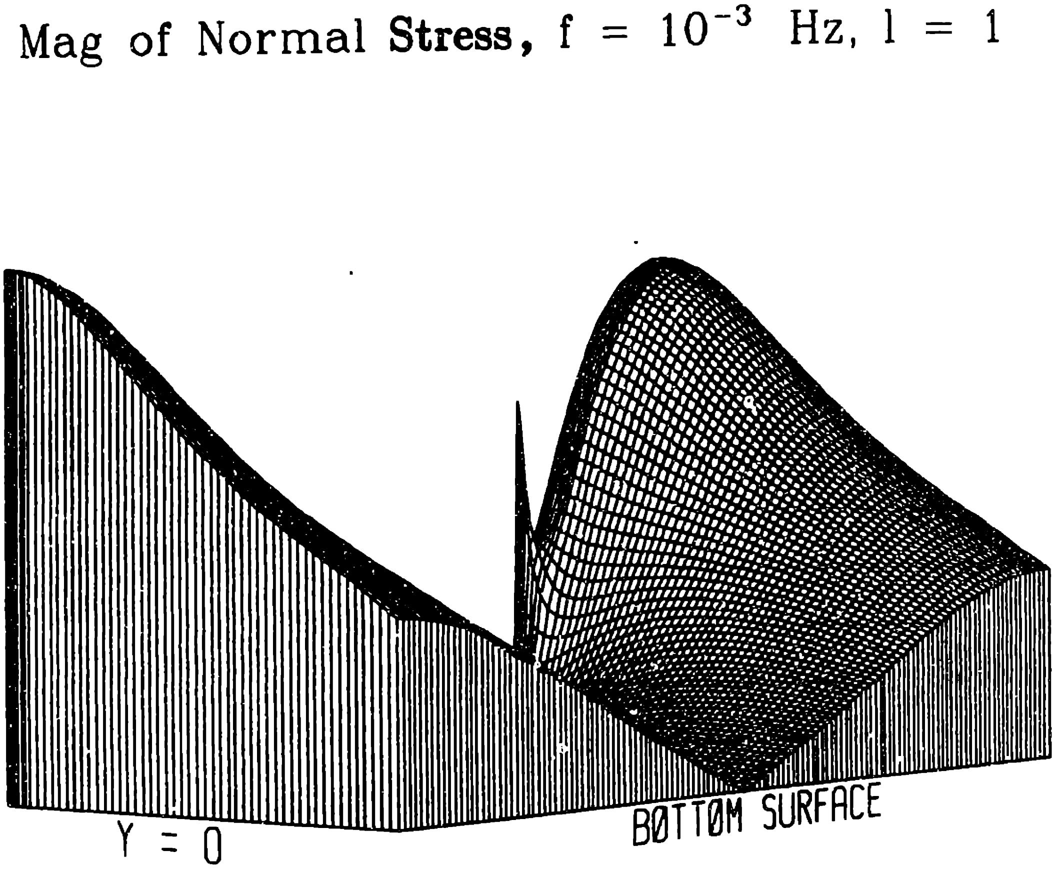

$|s|$, $f = 10^{-3}$ *Hz*.

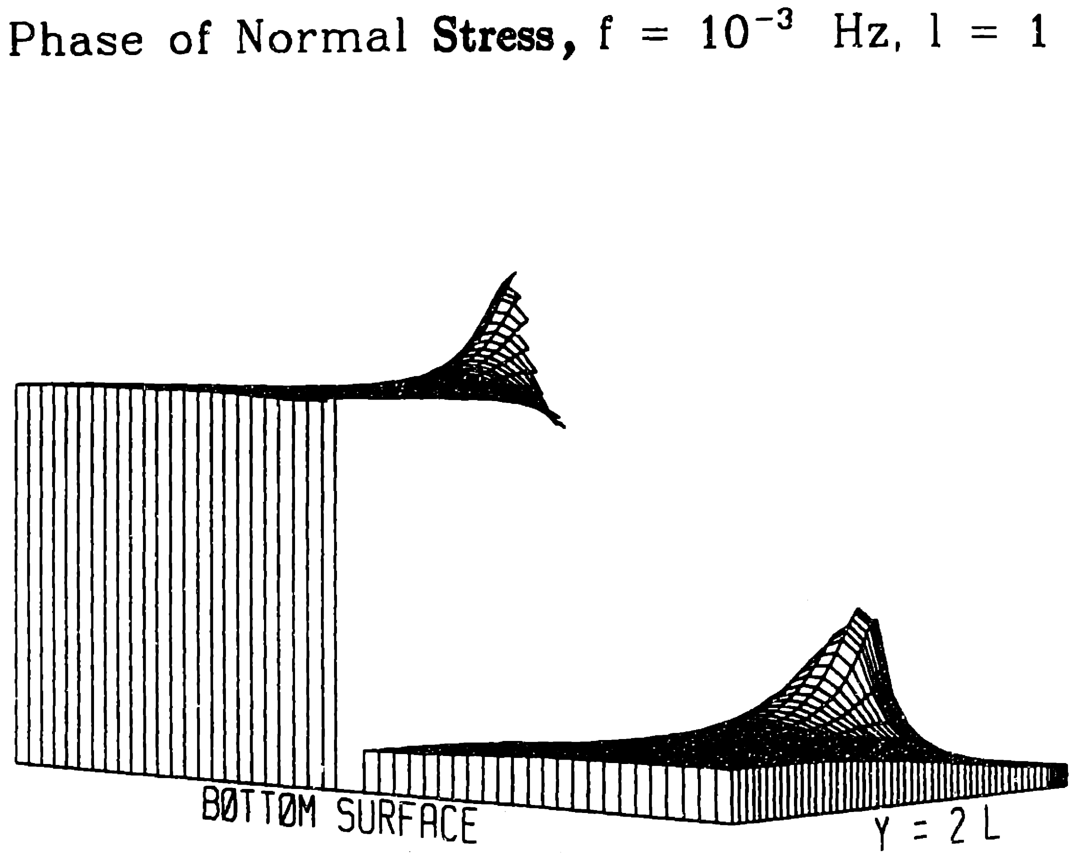

arg s, $f = 10^{-3}$ Hz.

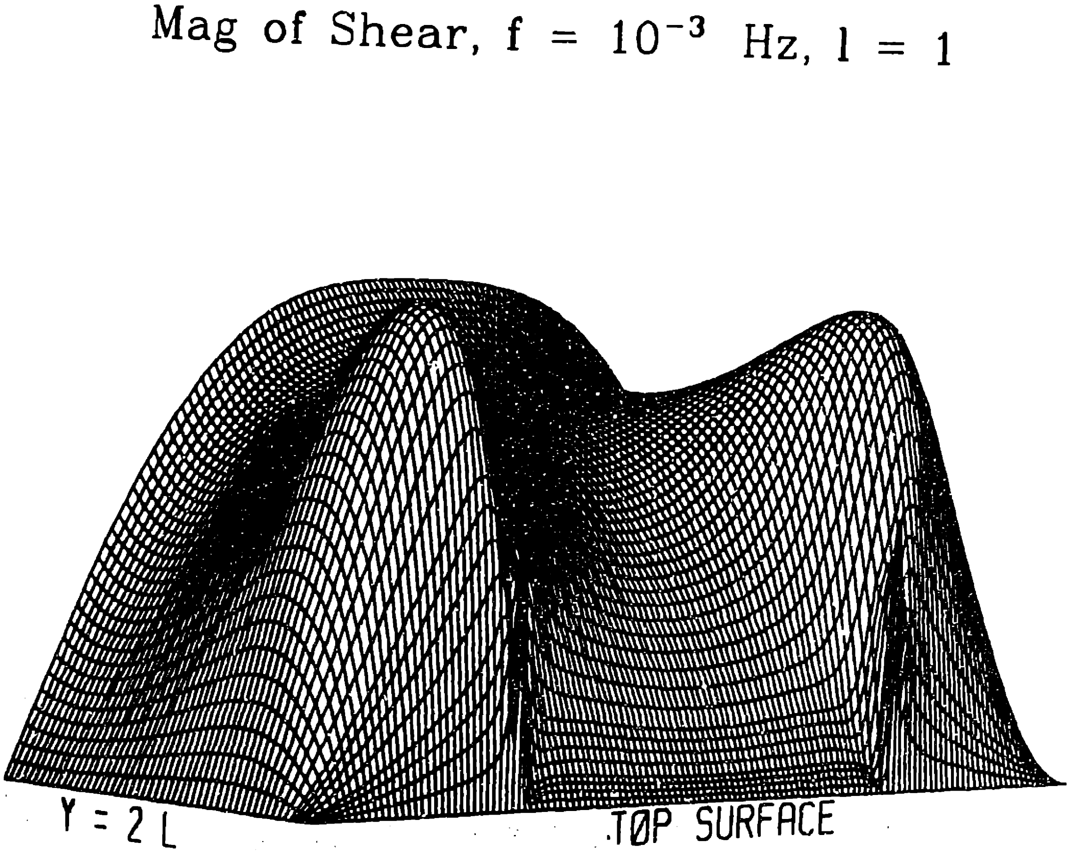

$|\sigma_{yz}|$, $f = 10^{-3}$ *Hz*.

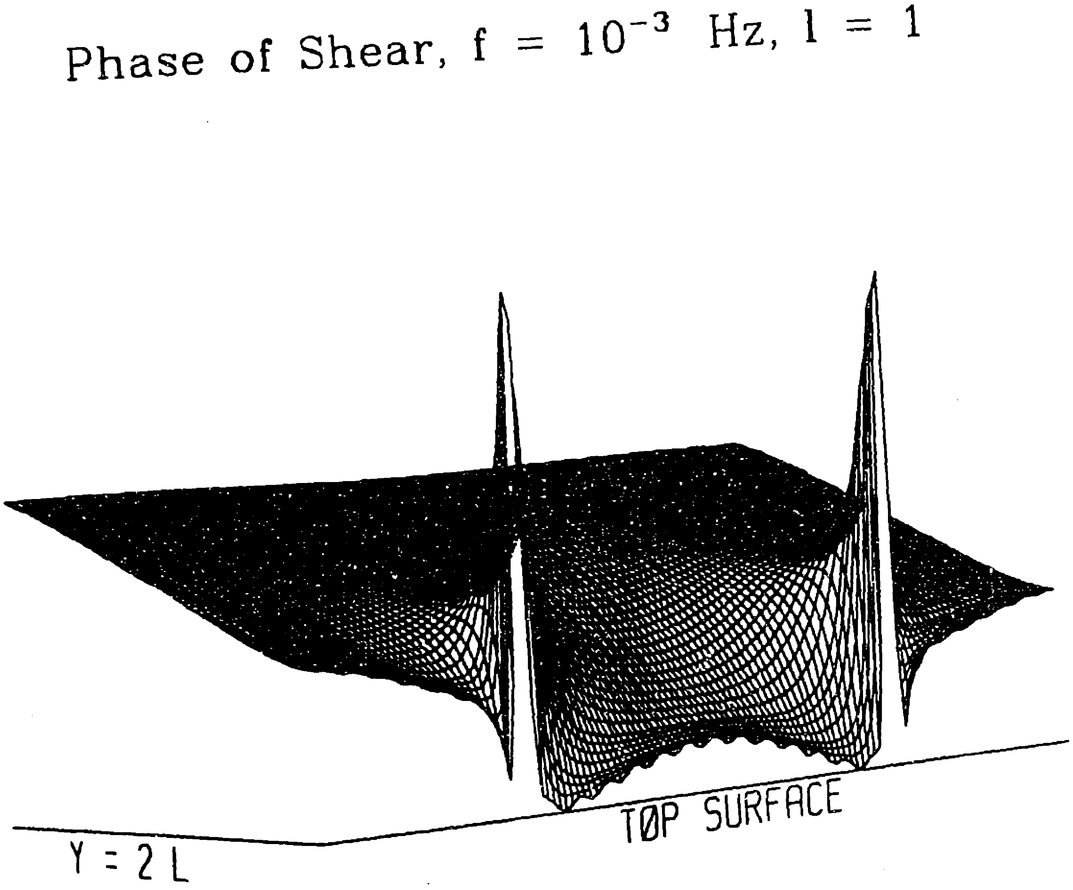

$\arg \sigma_{yz}$, $f = 10^{-3}$ Hz.

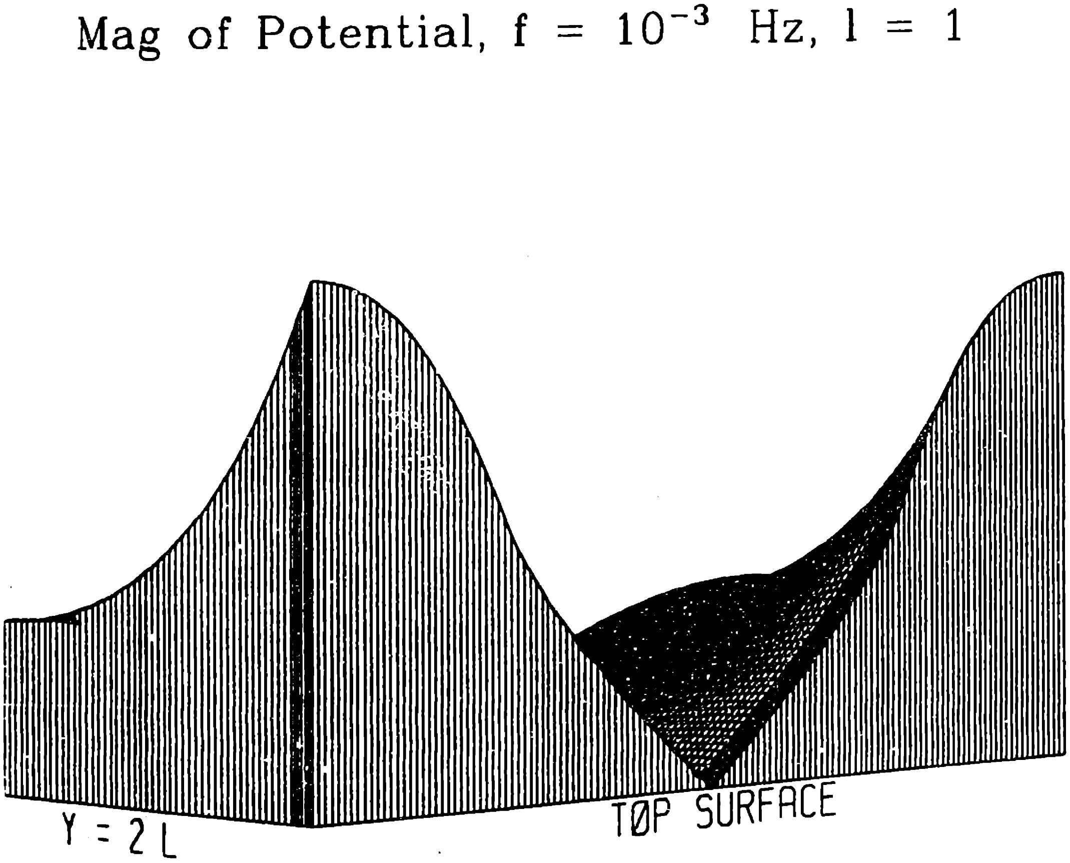
Mag of Potential, f = 10^{-3} Hz, l = 1
Y = 2 L
TOP SURFACE

$|\phi|$, $f = 10^{-3}$ Hz.

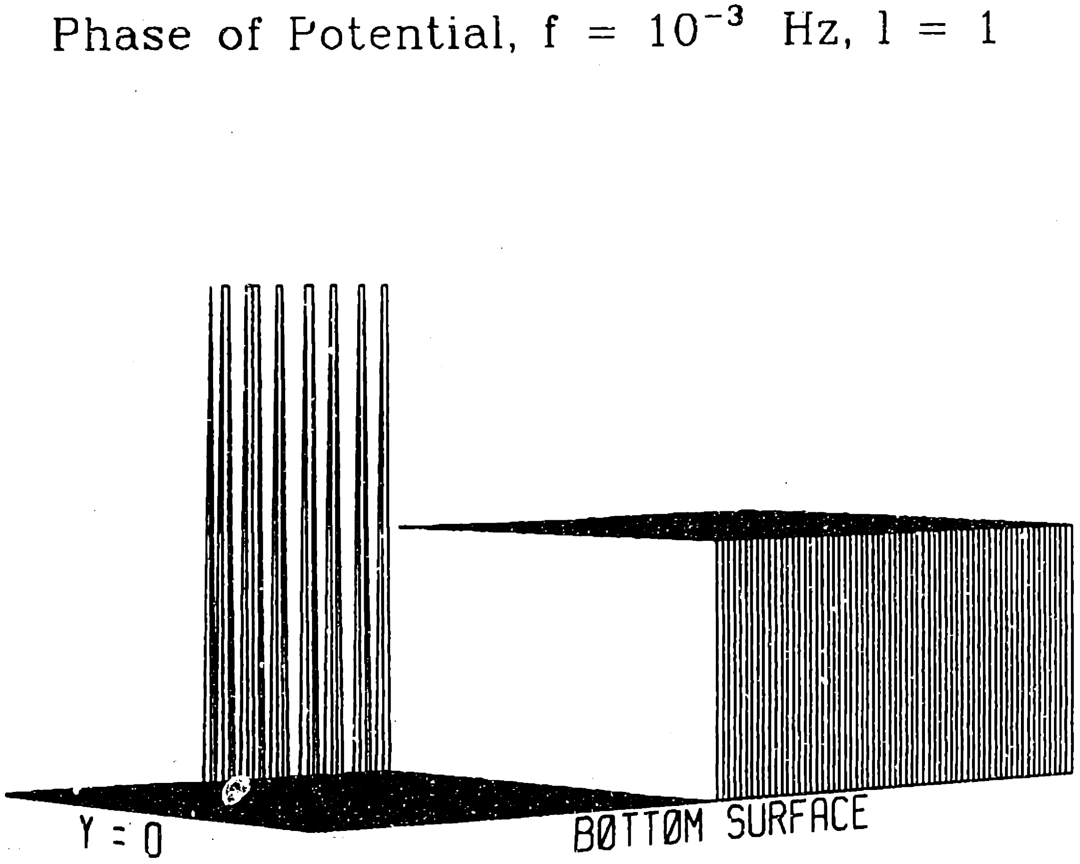

arg ϕ, $f = 10^{-3}$ *Hz.*

Appendix B

Fortran Code for the Mixed Boundary Value Problem

The code for the fortran programs which produced the solutions seen in Chapter 6 follow. In addition to the explanations given in Chapter 6, the program and subroutines are documented internally. The order of the programs and suboutines are as follows:

1. **SOLV8JS**: Main routine for solving the mixed boundary value problem;
2. **HMG6** : evaluates homogeneous solutions;
3. **PRTSLN**: evaluates particular solutions;
4. **MRESET**: restores matrix values;
5. **CSET**: sets coefficients of the homogeneous solutions;
6. **FFTCOS**: performs a fast fourier cosine transform using NAGLIB routine C06FCF;

7. COSUM: performs an inverse fast fourier cosine transform using NAGLIB routine C06FCF;

8. FFTST: tests programs FFTCOS and COSUM;

9. MULTZ8: evaluates the non-dimensional solutions on a grid of y and z values given the coefficients of the homogeneous solutions (c_l^m);

and

10. MONEZ: as for MULTZ8, but for a single value of z.

```
      PROGRAM SOLV8JS
c
c version 1, 6/13/87
c version 2, 6/20/87, number of modes up to 100 on 7/23, 120 on 7/28
c*****************************************************************
c
c     This code solves the mixed boundary value problem of section VIII.
c The steps are as follows ( T is the time for a 6by6 cplx system soln ):
c                1)  solve the forced, non-mixed problem with shear, pressure,
c                  normal stress =0 at top, v, w, uz zero at bottom. =>ca(l,m)
c                  This is called PROBLEM A
c modes*T time
c
c                2)  solve for coefficients of pressure and stress basis funs:
c                  fill matrix cp(j,l,m) and cs(j,l,m) from mth coef of Pj (Sj)
c                  known, that of shear(0), stress(0), v(-1), w(-1), uz(-1) = 0
c
c modes*T*leftn
c                3) solve for coefs of pressure and stress basis funs (=values)
c                   of pressure and stress.
c
c leftn*modes*log(modes) time: leftn fft inverses
c                                                  LEFTN = # left sub-interval
c                                                  collocation points
c                                                       = ceiling( ll/l * modes )
c leftn^3:  leftn by leftn linear equations, one right hand side.
c
c                4) solve for the coefs cb(j,l,m) using the ca(l,m) to get the
c                   displacement and velocity forcing at z=0.  PROBLEM B
c modes*T time
c
c The values ( at z=0 ) of the homogeneous and particular solutions, for
c the coef matrix and rhs ( forcing ), resp., are obtained from the subroutines
c
c      SUBROUTINE HMG6( z, c1,c2,c3,c4,c5,c6,v,w,vy,vz,uy,uz,p,s,shear )
c and
c      SUBROUTINE PRTSLN( z, v, w, vy, vz, p, s, shear, phi, jy, jz)
c
c the selection of c1,c2...c6 is done by subroutine
c
c      SUBROUTINE CSET( whichc, c1, c2, c3, c4, c5, c6 )
c
c Fast fourier inversion of a complex cosine series with the symmetry of
c this system is performed by
c
c      SUBROUTINE COSUM( coefs, vals, modes ),
c
c while fast transformation ( the inverse ) is performed by
c
c      SUBROUTINE FFTCOS( vals, coefs, modes ).
c
c  The solution of the linear eqns is found by the naglib routine F04ADF, and
c the error checking is presumably done through examination of the function
c values.  Because F04ADF changes the matrix,
c
c      SUBROUTINE MRESET( matrix, savmtx )
c
c which sets matrix = savmtx, is used to put values back for next round when
c necessary.
c
```

```
C*****************************************************************
c
      IMPLICIT UNDEFINED ( a - z )
c
      INTEGER NMODES, HLFMDS, NMDSP2
      PARAMETER ( NMODES = 120, NMDSP2 = NMODES+2, HLFMDS = NMODES/2+1 )
c
c NMODES is the maximum number of fourier components that may be kept in
c               the calculations -- the equations will be 3*NMODES by 3*NMODES
c               if 11/1 = 2
c
c
      DOUBLE PRECISION B11, B12,  B21, B22, BC, UNIAXM, THIKNS
      PARAMETER  ( b11 = 1.0d15, B12 = 1.0d7, B21 = 1.0d7, B22 = 1.0d0 )
      PARAMETER  (  BC = B12 * B21 / ( B11 * B22 )  )
      PARAMETER  ( UNIAXM = 5.0d5  )
      PARAMETER  ( THIKNS = 1.0d-3 )
c
c L1OVRL is the ratio L1 / L of electrode to open space on the surface
c                    -- note that "names" must be changed if this parm is...
c Bij are the coupling coefs in MKS units: Ns/m^4, Vs/m^2, N/Am,and Ohm m
c BC is the electrokinetic coupling coefficient.
c UNIAXM = the uniaxial modulus 2 G + lambda in N/m^2.
c THIKNS = the thickness of the layer in meters.
c
      DOUBLE PRECISION 1, l1ovrl
      DOUBLE COMPLEX  ca(6, NMODES), cb(6,NMODES)
      DOUBLE COMPLEX  cp(HLFMDS,6,NMODES), cs(HLFMDS,6,NMODES)
c
c 1 is the ratio of the length of the QUARTER period to the depth.
c l1ovrl is the duty cycle ratio of l1/l: left to right length ratio
c
c ca(l,m) holds the coef of the type 1 soln, wavelength k(m) of the type A
c                              unmixed problem, cf step 1 above
c cb is like ca, but is the golden nugget here : final solution is ca+cb
c
c cp(j,l,m) is the solution to the current=0 problem forced by zero bc's all
c               around EXCEPT for the jth coll. point where the pressure = 1
c cs is like cp except for normal stress instead of pressure.
c
c
      INTEGER modes, leftn,  wavnum, ptnum, ynum
      INTEGER whichc
c
c modes = number of modes to be kept on this try...max = NMODES
c wavnum is the wave number such that the coef of y above is k(n) = k(wavnum)
c                                                          (see kn below)
c ptnum = number of current collocation point
c ynum = the number of the point at which a value is given ( forced at
c                                          ptnum_th collocation point )
c
c column is the column of the matrix being filled in, sim for row
c whichc is the number of the mode whose coefficients are being considered
c
      DOUBLE COMPLEX v, w, vy, vz, uy, uz, p, s, shear, phi, jy, jz
      DOUBLE COMPLEX vsave(6,NMODES), wsave(6,NMODES), uzsave(6,NMODES)
      DOUBLE COMPLEX shrsav(6,NMODES), psave(6,NMODES), ssave(6,NMODES)
      DOUBLE COMPLEX wsavt(6, NMODES), uzsavt( 6, NMODES )
      DOUBLE PRECISION jn( NMODES ), thisjn
c
```

```
c v, w = horiz and vertical solid matrix displacement
c vy, vz = horiz and vert lab-frame velocity
c uy, uz =  horiz and vert relative velocity
c s = normal compressive force assuming
c shear = sigma( y,z )
c phi = electrical potential ( not used here, but appears in PRTSLN call )
c jy, jz = horiz and vert current density
c
c the save variables save the values of the homogeneous solutions at the
c                appropriate boundaries so they don't have to be re-calculated
c                first subscript is for solution number, second for wavenumber
c
c jn( n ) = the  nth coefficient of the Fourier series for vert current density
c
      DOUBLE COMPLEX  wscof( NMODES ),  wpcof( NMODES )
      DOUBLE COMPLEX uzscof( NMODES ), uzpcof( NMODES )
      DOUBLE COMPLEX  wsval( NMODES ),  wpval( NMODES )
      DOUBLE COMPLEX uzsval( NMODES ), uzpval( NMODES )
      DOUBLE COMPLEX  wvalz( NMODES ), uzvalz( NMODES )
      DOUBLE COMPLEX  wcofz( NMODES ), uzcofz( NMODES )
      DOUBLE COMPLEX   svec( NMODES ),   pvec( NMODES )
      DOUBLE COMPLEX scoefs( NMODES ), pcoefs( NMODES )
c
cccc      EQUIVALENCE ( wscof, wsval, wvalz, wcofz )
cccc      EQUIVALENCE ( uzscof, uzsval, uzvalz, uzcofz )
cccc      EQUIVALENCE ( wpcof, wpval, pvec, pcoefs )
cccc      EQUIVALENCE ( uzpcof, uzpval, svec, scoefs )
c
c wscof/val(n) is the Fourier coef/value of w at wavenumber n/collocation
c                        point n due to the current stress basis function
c wpcof/val is the same, but for pressure instead of stress
c uzscof/val and uzpcof/val are the  same, but for uz instead of w
c wcofz/valz is the coef/value of w at z=0 due to the solution of problem A
c uzcofz/valz are the same but for uz instead of w
c scoefs/svec are the coefs/values of stress at z=0 from problem A
c pcoefs/pvec are those of pressure.
c
c NOTE that the above variables are not used simultaneously, and the storage
c required could be reduced by a factor of 4, while keeping mnemonic names,
c except the equivalences seem to screw up the basis functions.
c
      DOUBLE PRECISION  f, omega, delt, nu, phi0, alpha0, n, r, dltinv
      DOUBLE COMPLEX    lambda
      DOUBLE PRECISION  kn(NMODES), kninv(NMODES), thiskn
      DOUBLE COMPLEX    lambdn(NMODES)
c
c f = frequency for which calculations are performed ( user specified )
c omega = 2*pi*f
c delt = y-wavenumber * thickness ( "delta-hat" ),  = ( 2*wavnum-1)*pi/( 2*1 )
c deltinv = 1/delt
c n = 1 - 2 nu
c nu = Poisson's ratio
c phi0 = porosity
c alpha0 = solid volume fraction = 1/phi0   - 1
c r = frequency paramater, prop to omega, ( diffn bdry lyr thick ) **-2...
c lambda = dynamic decay parameter ("LAMBDA2") of homogeneous solutions
c
c kn = nth y-wavenumber * thickness ( "delt" ),  = ( 2*n -1)*pi/( 2*1 )
c kninv = 1/kn
c lambdn(n) is the value of lambda that corresponds to wavenumber kn
```

```
c
      DOUBLE PRECISION  shd, chd, cothd, shkn(NMODES), chkn(NMODES)
      DOUBLE COMPLEX    shld, chld, chlkn(NMODES), shlkn(NMODES)
c
c       chd =  cosh( delt ), chkn( n ) = chd( delt = kn(n) )
c       shd =  sinh(kn)
c       shld =   sinh( lambda*kn )
c       chld =   cosh( lambda*kn )
c
      DOUBLE COMPLEX matrix(NMDSP2, NMDSP2), rhs(NMDSP2, 1)
      DOUBLE COMPLEX cvec(NMDSP2, 1), c1, c2, c3, c4, c5, c6
      DOUBLE COMPLEX cvec6(6,2), rhs6(6,2), matrx6(6,6), savmtx(6,6)
c
c matrix = matrix of linear eqns to be solved
c rhs = right hand side of eqn to be solved, rhs6 = version for small problems
c cvec = solution of current problem, cvec6 = version for small problems
c matrx6 = for 6 by 6 problems
c savmtx = used to save values so matrix can be reused after calls to F04ADF
c
      DOUBLE PRECISION  temp, hold, csh, snh, work( NMDSP2 ), dy
      CHARACTER*200 header
      CHARACTER*20 outfil
c
c header = file headers
c outfil = file name for output of c values
c
      INTEGER ifail
c
      DOUBLE PRECISION pi, pi6
      DOUBLE COMPLEX i, zero
c
      PARAMETER (   pi = 3.1415926535897932384d0, pi6 = 6.0d0 * pi )
      PARAMETER (    i = ( 0.0d0, 1.0d0 ) )
      PARAMETER ( zero = ( 0.0d0, 0.0d0 ) )
c
      COMMON / prtcom /  shd, chd, cothd
      COMMON / homcom /  delt, dltinv, lambda, n, nu, phi0, alpha0, r
c
c----------------------------------------------------------------
c
c set up default param values
c
      phi0 = 0.8
      alpha0 = 1.0d0/phi0 - 1.0d0
      nu = 0.4
      n = 1 - 2.0*nu
c
c find out if current or mechanically forced, i/o names
c
  1   WRITE(6,*)"number of modes to try? must be even and < ", NMODES
      READ( 5, * ) modes
      IF( modes .eq. 0 .or. mod(modes,2) .ne. 0 )stop
      WRITE(6,*)"frequency, in Hertz?"
      READ( 5, * ) f
      WRITE(6,*)'quarter-period to depth ratio ( "l" )?'
      READ( 5, * ) l
      WRITE(6,*)"duty cycle ll/l (< 50%, unless HLFMDS changed )?"
      READ( 5, * ) llovrl
      leftn = llovrl * dfloat( modes )
c
```

```
c now take ceiling of  the rhs in that def...
c
      IF( dfloat( leftn ) / dfloat( modes )  .lt. llovrl - .01 )
     ~                               leftn = leftn + 1
      WRITE( 6, * ) leftn, "colloc. points on left,",
     ~              modes-leftn, " on the right"
c
      WRITE(6,*)"name of output file for c vectors?"
      READ(5,"(a)") outfil
      OPEN(1,file=outfil,form="unformatted",status="new",err=1)
      WRITE( header, * )modes, f, LlovrL, l, " = # modes, freq., ll/l "
     ~              //   "cl,c2,...c6; fast j forced algorithm"
      WRITE(1)header
c
c calculate parameter values for each of the wavenumbers, so it only has
c to be done once... cf. eqns V-44 and VIII-15, 33, 43, 47, 48, note that
c
      omega = 2.0d0 * pi * f
      temp = omega * ( B11 * THIKNS*THIKNS / UNIAXM ) / phi0
      r = temp * 2.0d0* (1.0d0 - nu )    * phi0
c
      DO 1001 wavnum = 1, modes
         delt = dfloat( 2* wavnum - 1 ) * pi / ( 2.0d0 * l )
         kn( wavnum ) = delt
         kninv( wavnum ) = 1.0d0 / delt
         hold =  LLOVRL * delt
         csh = dcos( hold )
         snh = dsin( hold )
         hold = 1.0d0 / hold
         jn(wavnum) = - 8.0d0* (          hold*csh/delt
     ~                          - 3.0d0*hold*hold*snh/delt
     ~                          - 6.0d0*hold**3  *csh/delt
     ~                          + 6.0d0*hold**4  *snh/delt )
         lambda = cdsqrt( 1.0d0 - i * temp / ( delt*delt ) )
         lambdn( wavnum ) = lambda
         shkn( wavnum ) = ( dexp(delt) - dexp(-delt) ) / 2.0d0
         chkn( wavnum ) = ( dexp(delt) + dexp(-delt) ) / 2.0d0
         shlkn( wavnum ) = ( cdexp(lambda*delt) - cdexp(-lambda*delt) )
     ~                    / 2.0d0
         chlkn( wavnum ) = ( cdexp(lambda*delt) + cdexp(-lambda*delt) )
     ~                    / 2.0d0
 1001 CONTINUE
c
c*****************************************************************
c
c set up and solve part A problem one mode at a time, save values of the
c homogeneous solutions to be used later.  set up rhs so prt slns CANCELLED!!
c
      rhs6( 6, 1 ) = zero
      DO 101 wavnum = 1, modes
         delt   = kn( wavnum )
         dltinv = kninv( wavnum )
         lambda = lambdn( wavnum )
         shd = shkn( wavnum )
         chd = chkn( wavnum )
         cothd = chd/shd
         shld = shlkn( wavnum )
         chld = chlkn( wavnum )
         thisjn = jn( wavnum )
         IF( delt .lt. pi6 ) THEN
```

```
            DO 102 whichc = 1, 6
               CALL cset( whichc, c1, c2, c3, c4, c5, c6 )
               CALL HMG6( 0.0d0, c1, c2, c3, c4, c5, c6,
     ~                       v, w, vy, vz, uy, uz, p, s, shear )
               matrx6( 1, whichc ) = shear
               matrx6( 2, whichc ) = p
               matrx6( 3, whichc ) = s
               shrsav( whichc, wavnum ) = shear
               psave ( whichc, wavnum ) = p
               ssave ( whichc, wavnum ) = s
               wsavt ( whichc, wavnum ) = w
               uzsavt( whichc, wavnum ) = uz
c
               CALL HMG6( -1.0d0, c1, c2, c3, c4, c5, c6,
     ~                       v, w, vy, vz, uy, uz, p, s, shear )
               matrx6( 4, whichc ) = v
               matrx6( 5, whichc ) = w
               matrx6( 6, whichc ) = uz
               vsave( whichc, wavnum ) = v
               wsave( whichc, wavnum ) = w
               uzsave(whichc, wavnum ) = uz
  102       CONTINUE
            CALL prtsln( 0.0d0, v, w, vy, vz, p, s, shear, phi, jy, jz)
            rhs6( 1, 1 ) = - shear * thisjn
            rhs6( 2, 1 ) = - p * thisjn
            rhs6( 3, 1 ) = - s * thisjn
            CALL prtsln( -1.0d0, v, w, vy, vz, p, s, shear, phi, jy, jz)
            rhs6( 4, 1 ) = - v * thisjn
            rhs6( 5, 1 ) = - w * thisjn
cccc        rhs6( 6, 1 ) = zero,      cf beginning of wavnum loop
c
c              solve system at this mode, put solution into appropriate place
c
c
            CALL F04ADF( matrx6, 6, rhs6, 6, 6, 1, cvec6,
     ~                                  6, work, ifail )
            DO 103 whichc = 1, 6
               ca( whichc, wavnum ) = cvec6( whichc, 1 )
  103       CONTINUE
c
        ELSE
c                  SHORT WAVE APPROACH HERE for delt > 6 pi
c              note that only the top bc's are imposed, and c1,c3,c5 solved for
c
            DO 1025 whichc = 1, 3
               CALL cset( 2*whichc-1, c1, c2, c3, c4, c5, c6 )
               CALL HMG6( 0.0d0, c1, c2, c3, c4, c5, c6,
     ~                       v, w, vy, vz, uy, uz, p, s, shear )
               matrx6( 1, whichc ) = shear
               matrx6( 2, whichc ) = p
               matrx6( 3, whichc ) = s
               shrsav( 2*whichc-1, wavnum ) = shear
               psave ( 2*whichc-1, wavnum ) = p
               ssave ( 2*whichc-1, wavnum ) = s
               wsavt ( 2*whichc-1, wavnum ) = w
               uzsavt( 2*whichc-1, wavnum ) = uz
c
 1025       CONTINUE
            CALL prtsln( 0.0d0, v, w, vy, vz, p, s, shear, phi, jy, jz)
            rhs6( 1, 1 ) = - shear * thisjn
            rhs6( 2, 1 ) = - p * thisjn
            rhs6( 3, 1 ) = - s * thisjn
c
c              solve system at this mode, put solution into appropriate place
c
c
            CALL F04ADF( matrx6, 6, rhs6, 6, 3, 1, cvec6,
     -                               6, work, ifail )
            DO 1035 whichc = 1, 3
               ca( 2*whichc-1, wavnum ) = cvec6( whichc, 1 )
 1035       CONTINUE
            ca( 2, wavnum ) = zero
            ca( 4, wavnum ) = zero
            ca( 6, wavnum ) = zero
c
         ENDIF
c
         IF( mod( wavnum, 16 ) .eq. 0)
     -             write(6,*)"part A complete thru wavenumber", wavnum
 101  CONTINUE
      WRITE(6,*)"part A solution complete"
c
c*****************************************************************
c
c now solve for the pressure and stress basis function coefficients.
c note that the cosine expansion of a fun odd about y = 1  which is 1 at
c         L * ( j-1 )/modes = j_th coll pt = "dy  * (ptnum-1)" below
c has coefs
c
c          2 / modes *  SUM( m=1, modes )  cos( kn(m)* y(j) ) * cos( kn * y )
c
c unless j = 1, in which case the leading of SUM coef is 1/modes.
c
      dy = 1 / dfloat( modes )
      hold = 2.0d0 * dy
      rhs6( 2, 1 ) = zero
      rhs6( 3, 1 ) = zero
      rhs6( 4, 1 ) = zero
      rhs6( 5, 1 ) = zero
      rhs6( 6, 1 ) = zero
      rhs6( 1, 2 ) = zero
      rhs6( 3, 2 ) = zero
      rhs6( 4, 2 ) = zero
      rhs6( 5, 2 ) = zero
      rhs6( 6, 2 ) = zero
c
      DO 104 wavnum = 1, modes
         thiskn = kn( wavnum )
         IF( thiskn .lt. pi6 ) THEN
            DO 106 whichc = 1, 6
               matrx6( 1, whichc ) = ssave( whichc, wavnum )
               matrx6( 2, whichc ) = psave( whichc, wavnum )
               matrx6( 3, whichc ) = shrsav( whichc, wavnum )
               matrx6( 4, whichc ) = vsave( whichc, wavnum )
               matrx6( 5, whichc ) = wsave( whichc, wavnum )
               matrx6( 6, whichc ) = uzsave( whichc, wavnum )
               savmtx( 1, whichc ) = ssave( whichc, wavnum )
               savmtx( 2, whichc ) = psave( whichc, wavnum )
               savmtx( 3, whichc ) = shrsav( whichc, wavnum )
               savmtx( 4, whichc ) = vsave( whichc, wavnum )
               savmtx( 5, whichc ) = wsave( whichc, wavnum )
               savmtx( 6, whichc ) = uzsave( whichc, wavnum )
 106        CONTINUE
c
c  solve pressure and stress problems simultaneously, using 2 rhs feature of
c F04ADF. Note that matrix is changed by the routine, and must be reset after..
c
            DO 105 ptnum = 1, leftn
               rhs6( 1, 1 ) = hold * dcos( thiskn * dfloat( ptnum-1 ) * dy)
               IF( ptnum .eq. 1 ) THEN
                  rhs6( 1, 1 ) = rhs6( 1, 1 ) / 2.0d0
               ELSE
                  CALL mreset( matrx6, savmtx )
               ENDIF
               rhs6( 2, 2 ) = rhs6( 1, 1 )
c
               CALL F04ADF( matrx6, 6, rhs6, 6, 6, 2, cvec6,
                                           6, work, ifail )
               DO 107 whichc = 1, 6
                  cs(ptnum, whichc, wavnum) = cvec6( whichc, 1 )
                  cp(ptnum, whichc, wavnum) = cvec6( whichc, 2 )
 107           CONTINUE
 105        CONTINUE
c
         ELSE
c                 SHORT WAVE APPROACH: ONLY TOP BC'S IMPORTANT for delt > 6 pi
c              note that only the top bc's are imposed, and c1,c3,c5 solved for
c
            DO 1065 whichc = 1, 3
               matrx6( 1, whichc ) = ssave( 2*whichc-1, wavnum )
               matrx6( 2, whichc ) = psave( 2*whichc-1, wavnum )
               matrx6( 3, whichc ) = shrsav( 2*whichc-1, wavnum )
               savmtx( 1, whichc ) = ssave( 2*whichc-1, wavnum )
               savmtx( 2, whichc ) = psave( 2*whichc-1, wavnum )
               savmtx( 3, whichc ) = shrsav( 2*whichc-1, wavnum )
 1065       CONTINUE
c
c  solve pressure and stress problems simultaneously, using 2 rhs feature of
c F04ADF. Note that matrix is changed by the routine, and must be reset after..
c
            DO 1055 ptnum = 1, leftn
c
               rhs6( 1, 1 ) = hold * dcos( thiskn * dfloat( ptnum-1 ) * dy)
               IF( ptnum .eq. 1 ) THEN
                  rhs6( 1, 1 ) = rhs6( 1, 1 ) / 2.0d0
               ELSE
                  CALL mreset( matrx6, savmtx )
               ENDIF
               rhs6( 2, 2 ) = rhs6( 1, 1 )
c
               CALL F04ADF( matrx6, 6, rhs6, 6, 3, 2, cvec6,
                                           6, work, ifail )
               DO 1075 whichc = 1, 3
                  cs(ptnum, 2*whichc-1, wavnum) = cvec6( whichc, 1 )
                  cp(ptnum, 2*whichc-1, wavnum) = cvec6( whichc, 2 )
 1075          CONTINUE
               cs( ptnum, 2, wavnum ) = zero
               cs( ptnum, 4, wavnum ) = zero
               cs( ptnum, 6, wavnum ) = zero
               cp( ptnum, 2, wavnum ) = zero
               cp( ptnum, 4, wavnum ) = zero
               cp( ptnum, 6, wavnum ) = zero
 1055        CONTINUE
c
         ENDIF
c
         IF( mod( wavnum, 8 ) .eq. 0 )
     ~                WRITE(6,*)"basis coefs through wavenumber", wavnum
104   CONTINUE
c
      WRITE(6,*)"basis functions solutions are now complete"
c
c*****************************************************************
c
c     Now the only large system needing to be solved will be.  We now find
c the coefs of the basis functions which will cancel the w(0) and uz(0)
c resulting from the solution in part A.  The first leftn columns of the
c matrix are the coefficients of the stress solution, the next leftn are those
c of the pressure.  The first leftn equations ( rows ) are for vert
c displacement ( w ), the next are for vert velocity ( uz ).
c
c      Note that fast fourier cosine inversion (COSUM) is used
c to sum the contributions from the modes at the different points...
c this gives us more info than we need, but at a considerable time savings.
c ALSO, only 3 non-zero coefs after bl approach starts, so only do half
c the sum.
c
      DO 108 ptnum = 1, leftn
         DO 109 wavnum = 1, modes
            wpcof(wavnum) = zero
            wscof(wavnum) = zero
            uzpcof(wavnum) = zero
            uzscof(wavnum) = zero
            IF( kn( wavnum ) .lt. pi6 ) THEN
               DO 110 whichc = 1, 6
                  wscof( wavnum ) =  wscof(wavnum) +
     ~                 cs(ptnum,whichc,wavnum) * wsavt( whichc, wavnum )
                  wpcof( wavnum ) =  wpcof(wavnum) +
     ~                 cp(ptnum,whichc,wavnum) * wsavt( whichc, wavnum )
                  uzscof( wavnum ) =  uzscof(wavnum) +
     ~                 cs(ptnum,whichc,wavnum) * uzsavt( whichc, wavnum)
                  uzpcof( wavnum ) =  uzpcof(wavnum) +
     ~                 cp(ptnum,whichc,wavnum) * uzsavt( whichc, wavnum)
  110          CONTINUE
            ELSE
               DO 1105 whichc = 1, 5, 2
                  wscof( wavnum ) =  wscof(wavnum) +
     ~                 cs(ptnum,whichc,wavnum) * wsavt( whichc, wavnum )
                  wpcof( wavnum ) =  wpcof(wavnum) +
     ~                 cp(ptnum,whichc,wavnum) * wsavt( whichc, wavnum )
                  uzscof( wavnum ) =  uzscof(wavnum) +
     ~                 cs(ptnum,whichc,wavnum) * uzsavt( whichc, wavnum)
                  uzpcof( wavnum ) =  uzpcof(wavnum) +
     ~                 cp(ptnum,whichc,wavnum) * uzsavt( whichc, wavnum)
 1105          CONTINUE
            ENDIF
 109     CONTINUE
c
            CALL COSUM( wscof, wsval, modes )
            CALL COSUM( wpcof, wpval, modes )
            CALL COSUM( uzscof, uzsval, modes )
            CALL COSUM( uzpcof, uzpval, modes )
c
c The values of the funs at the different points are just written where the
c coeffs of the Fourier series were.
c
c now that the values of w, uz due to the forcing at this ptnum_th point are
c known at every value of y, put them in the matrix, at the position
c corresponding to the equation for w or uz to disappear at the ynum_th point.
c
         DO 111 ynum = 1, leftn
            matrix( ynum        , ptnum         ) =   wsval( ynum )
            matrix( ynum        , ptnum + leftn ) =   wpval( ynum )
            matrix( ynum + leftn, ptnum         ) =  uzsval( ynum )
            matrix( ynum + leftn, ptnum + leftn ) =  uzpval( ynum )
 111     CONTINUE
c
         IF( mod( ptnum, 8 ) .eq. 0)
     ~                   write(6,*)"matrix setup thru point", ptnum
c
108   CONTINUE
c
      WRITE(6,*)" matrix setup complete, now right hand side "
c
c   wvalz is the value of w( z=0 ) produced by solution to part A,
c   uzvalz is the value of uz( z = 0 ).  Both are obtained from the
c   appropriate Fourier coef sums ( from 1 to 6 ).  But in short wave
c   case, we only use c1, c3, c5
c
      DO 112 wavnum = 1, modes
         wcofz( wavnum ) = zero
         uzcofz( wavnum ) = zero
c
         IF( kn( wavnum ) .lt. pi6 ) THEN
            DO 113 whichc = 1, 6
               wcofz( wavnum ) = wcofz( wavnum )
     ~                    + ca( whichc, wavnum )*wsavt( whichc, wavnum )
               uzcofz( wavnum ) = uzcofz( wavnum )
     ~                   + ca( whichc, wavnum )*uzsavt( whichc, wavnum )
 113        CONTINUE
         ELSE
            DO 1135 whichc = 1, 5, 2
               wcofz( wavnum ) = wcofz( wavnum )
     ~                    + ca( whichc, wavnum )*wsavt( whichc, wavnum )
               uzcofz( wavnum ) = uzcofz( wavnum )
     ~                   + ca( whichc, wavnum )*uzsavt( whichc, wavnum )
1135        CONTINUE
         ENDIF
112   CONTINUE

c
      CALL COSUM( wcofz, wvalz, modes )
      CALL COSUM( uzcofz, uzvalz, modes )
      DO 114 ynum = 1, leftn
         rhs( ynum        , 1 ) =  wvalz( ynum )
         rhs( ynum + leftn, 1 ) = uzvalz( ynum )
 114  CONTINUE
c
      WRITE( 6, * )" setup complete, solving matrix eqns..."
c
```

```
c solve the system of eqns
c
            CALL F04ADF( matrix, NMDSP2, rhs, NMDSP2, 2*leftn, 1, cvec,
                                              NMDSP2, work, ifail )
c
      WRITE( 6, * )"matrix inversion completed. part B commencing"
c
c now find coefs c1 ... c6 at each M which satisfy pressure and stress fields
c calculated by that matrix inversion, and now held in cvec.
c
c first find fourier coefs of these fields using fast Fourier cosine tform.
c note: minus signs are so that values of fields are cancelled!!!
c
      DO 115 ptnum = 1, modes
         IF( ptnum .le. leftn ) THEN
            svec( ptnum ) = - cvec( ptnum        , 1 )
            pvec( ptnum ) = - cvec( ptnum + leftn, 1 )
         ELSE
            svec( ptnum ) = zero
            pvec( ptnum ) = zero
         ENDIF
115   CONTINUE
c
      CALL FFTCOS( svec, scoefs, modes )
      CALL FFTCOS( pvec, pcoefs, modes )
c
c now Fourier coefs are known, so solve for cb!!!!
c
      DO 118 wavnum = 1, modes
         rhs6( 3, 1 ) = zero
         rhs6( 4, 1 ) = zero
         rhs6( 5, 1 ) = zero
         rhs6( 6, 1 ) = zero
         IF( kn( wavnum ) .lt. pi6 ) THEN
            DO 116 whichc = 1, 6
               matrx6( 1, whichc ) = ssave( whichc, wavnum )
               matrx6( 2, whichc ) = psave( whichc, wavnum )
               matrx6( 3, whichc ) = shrsav( whichc, wavnum )
               matrx6( 4, whichc ) = vsave( whichc, wavnum )
               matrx6( 5, whichc ) = wsave( whichc, wavnum )
               matrx6( 6, whichc ) = uzsave( whichc, wavnum )
  116       CONTINUE
c
            rhs6( 1, 1 ) = scoefs( wavnum )
            rhs6( 2, 1 ) = pcoefs( wavnum )
c
c solve system at this mode, put solution into appropriate place
c
            CALL F04ADF( matrx6, 6, rhs6, 6, 6, 1, cvec6,
                                             6, work, ifail )
            DO 117 whichc = 1, 6
               cb( whichc, wavnum ) = cvec6( whichc, 1 )
 117        CONTINUE
c
         ELSE
c                SHORT WAVE APPROACH: ONLY TOP BC'S IMPORTANT for delt > 6 pi
c              note that only the top bc's are imposed, and c1,c3,c5 solved for
c
            DO 1165 whichc = 1, 3
               matrx6( 1, whichc ) = ssave( 2*whichc-1, wavnum )
```

```
              matrx6( 2, whichc ) = psave( 2*whichc-1, wavnum )
              matrx6( 3, whichc ) = shrsav( 2*whichc-1, wavnum )
 1165      CONTINUE
c
           rhs6( 1, 1 ) = scoefs( wavnum )
           rhs6( 2, 1 ) = pcoefs( wavnum )
c
c solve system at this mode, put solution into appropriate place
c
           CALL F04ADF( matrx6, 6, rhs6, 6, 3, 1, cvec6,
     ~                                6, work, ifail )
           DO 1175 whichc = 1, 3
              cb( 2*whichc-1, wavnum ) = cvec6( whichc, 1 )
 1175      CONTINUE
           cb( 2, wavnum ) = zero
           cb( 4, wavnum ) = zero
           cb( 6, wavnum ) = zero
        ENDIF
        IF( mod( wavnum, 16 ) .eq. 0)
     ~                write(6,*)"part b thru wavenumber",wavnum
c
 118  CONTINUE
c
c give some idea of the convergence... assume nmode >= 8
c
c output to file
c
      WRITE(1)( ( ca( whichc,wavnum ) + cb( whichc,wavnum ),
     ~                 whichc = 1, 6 ),  wavnum = 1, modes )
      CLOSE(1)
c
      WRITE(6,*) " For modes, f, 11/1, and 1 =", modes, f, llovrl, 1
c
      WRITE(6,99)( ( whichc, wavnum,
     ~               ca( whichc,wavnum ) + cb( whichc,wavnum ) ,
     ~                  whichc = 1, 6 ),  wavnum = 1, 2  )
      WRITE(6,99)  ( whichc,    8,
     ~               ca( whichc,  8    ) + cb( whichc,  8 ) ,
     ~                  whichc = 1, 6 )
99    FORMAT( 6( "c(", i1, ",", i1, ") = ",
     ~             1pg12.5, " + i * ", 1pg12.5, / ), / )
      GO TO 1
      END
      SUBROUTINE HMG6( z, c1, c2, c3, c4, c5, c6,
                       v, w, vy, vz, uy, uz, p, s, shear )
c
c version 1, 6/9/87
c version 2, 7/31: shear fixed
c*****************************************************************
c
c   This calculates the values of the field variables corresponding to
c the homogeneous solutions of equations VIC-11 to 15 using symmetric versions
c of the solutions in paper1...od variables are multiplied by i, even ones
c by 1.
c
c*****************************************************************
c
      IMPLICIT UNDEFINED ( a - z )
c
      DOUBLE PRECISION z
      DOUBLE COMPLEX    c1, c2, c3, c4, c5, c6
      DOUBLE COMPLEX v, w, vy, vz, uy, uz, p, s, shear
c
c z = depth at which to evaluate: 0> z > -1
c c1, ..., c6 -- the coefficients of the six solns
c v, w, vy, vz, uy, uz, p = horiz and vert disp, horiz and vert abs velocity
c               horiz and vert relative velocity, and pressure
c
      DOUBLE PRECISION   delt, n, nu, phi0, alpha0, r, dltinv
c
c delt = y-wavenumber * thickness ( "Kn" )
c n = 1 - 2 nu
c nu = Poisson's ratio
c phi0 = porosity
c alpha0 = solid volume fraction = 1/phi0   - 1
c r = frequency paramater, prop to omega, ( diffn bdry lyr thick ) **-2...
c rstuff = r / ( n*delt*phi0 )
c
      DOUBLE COMPLEX lambda
c
c another frequency parameter: expnential decay factor
c
      DOUBLE PRECISION expdz, expmdz, dz
      DOUBLE COMPLEX   expdlz, expmdl, i
c
      COMMON / homcom /  delt, dltinv, lambda, n, nu, phi0, alpha0, r
c
      PARAMETER  ( i = ( 0.0d0, 1.0d0 )  )
c
c_________________________________________________________________
c
```

```
c
      dz = delt * z
      expdz = exp( dz )
      expmdz = 1.0d0 / expdz
      expdlz = cdexp( lambda * dcmplx( dz, 0.0d0 ) )
      expmdl = ( 1.0d0, 0.0d0 ) / expdlz
c
     _v = -( ( dltinv + z )* c3  + c1 )* expdz
     ~    + ( c2 + ( z - dltinv ) * c4   )* expmdz
     ~    -c5 * expdlz + c6 * expmdl
c
     _w =  ( c1 + c3 * z ) * expdz  + ( c2 + c4 * z ) * expmdz
     ~    + lambda * ( c5 * expdlz + c6 * expmdl )
c
     _vy = i*r*( (  c1 + ( dltinv + z - 2.0d0*i*n*delt/r ) * c3 )*expdz
     ~          +( -c2 + ( dltinv - z - 2.0d0*i*n*delt/r ) * c4 )*expmdz
     ~          + alpha0 * ( c6 * expmdl - c5 * expdlz ) )
c
     _vz = i*r*( ( -c1 + (  2.0d0*i*n*delt/r - z ) * c3 )*expdz
     ~          -(  c2 + (  2.0d0*i*n*delt/r + z ) * c4 )*expmdz
     ~          + alpha0 * lambda * ( c5 * expdlz + c6 * expmdl ) )
c
      uy = vy + i * r * v
c
      uz = vz + i * r * w
c
      p = uy / delt
c
     _s = -2.0d0 * n * delt *
     ~           (  ( c1 + c3 * z ) * expdz - ( c2 + c4 * z ) * expmdz
     ~             + c5 * expdlz - c6 * expmdl )
c
     _shear= - 2.0d0*n*delt* (  (c1 + (  dltinv + z ) * c3 ) * expdz
     ~                         + (c2 + ( -dltinv + z ) * c4 ) * expmdz
     ~                         + lambda * ( c5 * expdlz + c6 * expmdl ) )
c
      RETURN
      END
```

```
        SUBROUTINE PRTSLN( z, v, w, vy, vz, p, s,shear,phi,jy,jz)
c
c version 1 4/26/87;  vs. 2, 7/31: shear fixed, sinh and cosh put in explicitly
c*****************************************************************
c
c calculates the particular solutions to VIII-11
c uses VIII - 20, ...
c
c*****************************************************************
c
      IMPLICIT UNDEFINED ( a - z )
c
      DOUBLE PRECISION z
      DOUBLE COMPLEX  v, w, vy, vz, p, phi, s, shear, jy, jz
c
c z = depth at which to evaluate
c v,w = horiz, vert displacements
c vy, vz = horiz, vert lab-fram fluid velocities
c p = pressure
c s = normal compressive stress
c shear = shear stress sig( y,z )
c phi = potential
c jy = horiz current density
c jz = vert current density
c
      DOUBLE  PRECISION delt, dltinv, n, nu, phi0, alpha0, r
      DOUBLE  PRECISION gamma, shgam, chgam, tmp
      DOUBLE PRECISION shd, chd, cothd
c
c n = 1 - 2 * nu, nu = Poisson's ratio
c sinh( delt ), cosh( delt ), coth( delt ) , delt = wavenumber*thickness
c
      DOUBLE COMPLEX lambda, i
      COMMON / prtcom /  shd, chd, cothd
      COMMON / homcom /  delt, dltinv, lambda, n, nu, phi0, alpha0, r
      PARAMETER  ( i = ( 0.0d0, 1.0d0 )  )
c
c-----------------------------------------------------------------
c
      gamma = delt*(z+1.0d0)
      tmp = dexp( gamma )
      shgam = ( tmp - 1.0d0/tmp ) / 2.0d0
      chgam = ( tmp + 1.0d0/tmp ) / 2.0d0
      tmp   =  2.0d0*n*delt*delt*shd
c
      jz = dcmplx( shgam / shd, 0.0d0 )
      jy = dcmplx( - chgam / shd, 0.0d0 )
      p = -jy / delt
      phi = - p
     _v = dcmplx( -(chgam*(1.0d0 - delt*cothd) + gamma*shgam) / tmp
                , 0.0d0 )
      w = dcmplx(  ( gamma*chgam - delt*cothd*shgam ) / tmp, 0.0d0 )
      vy = -i*r*v
      vz = -i*r*w
      s = p + 2.0d0 * delt * n * v
     _shear = dcmplx( -( (1.0d0-delt*cothd)*shgam + gamma*chgam )
     ~                                                /( delt*shd )
                  , 0.0d0 )
      RETURN
      END
      SUBROUTINE MRESET( matrix, savmtx )
c
c version 1, 6/19/87
c****************************************************************
c
c resets the values in matrix to those in savmts
c
c****************************************************************
c
      IMPLICIT UNDEFINED ( a - z )
c
      DOUBLE COMPLEX matrix( 6,6 ), savmtx( 6,6 )
c
      INTEGER i, j
c
      DO 2 i = 1, 6
         DO 1 j = 1, 6
            matrix( i, j ) = savmtx( i, j )
  1      CONTINUE
2     CONTINUE
      RETURN
      END
      SUBROUTINE CSET( whichc, c1, c2, c3, c4, c5, c6 )
c
c version 1, 6/13/87
c
c This prog. sets up the coefs of the homogeneous solutions for matrix filling
c
      IMPLICIT UNDEFINED ( a - z )
c
      INTEGER                  whichc
      DOUBLE COMPLEX   c1, c2, c3, c4, c5, c6
c
      GO TO ( 1, 2, 3, 4, 5, 6 ), whichc
c
 1    c1 = ( 1.0d0, 0.0d0 )
      c2 = ( 0.0d0, 0.0d0 )
      c3 = ( 0.0d0, 0.0d0 )
      c4 = ( 0.0d0, 0.0d0 )
      c5 = ( 0.0d0, 0.0d0 )
      c6 = ( 0.0d0, 0.0d0 )
      RETURN
 2    c1 = ( 0.0d0, 0.0d0 )
      c2 = ( 1.0d0, 0.0d0 )
      c3 = ( 0.0d0, 0.0d0 )
      c4 = ( 0.0d0, 0.0d0 )
      c5 = ( 0.0d0, 0.0d0 )
      c6 = ( 0.0d0, 0.0d0 )
      RETURN
 3    c1 = ( 0.0d0, 0.0d0 )
      c2 = ( 0.0d0, 0.0d0 )
      c3 = ( 1.0d0, 0.0d0 )
      c4 = ( 0.0d0, 0.0d0 )
      c5 = ( 0.0d0, 0.0d0 )
      c6 = ( 0.0d0, 0.0d0 )
      RETURN
 4    c1 = ( 0.0d0, 0.0d0 )
      c2 = ( 0.0d0, 0.0d0 )
      c3 = ( 0.0d0, 0.0d0 )
      c4 = ( 1.0d0, 0.0d0 )
      c5 = ( 0.0d0, 0.0d0 )
      c6 = ( 0.0d0, 0.0d0 )
      RETURN
 5    c1 = ( 0.0d0, 0.0d0 )
      c2 = ( 0.0d0, 0.0d0 )
      c3 = ( 0.0d0, 0.0d0 )
      c4 = ( 0.0d0, 0.0d0 )
      c5 = ( 1.0d0, 0.0d0 )
      c6 = ( 0.0d0, 0.0d0 )
      RETURN
 6    c1 = ( 0.0d0, 0.0d0 )
      c2 = ( 0.0d0, 0.0d0 )
      c3 = ( 0.0d0, 0.0d0 )
      c4 = ( 0.0d0, 0.0d0 )
      c5 = ( 0.0d0, 0.0d0 )
      c6 = ( 1.0d0, 0.0d0 )
      RETURN
      END
      SUBROUTINE FFTCOS( values, coefs,  N )
c
c tested  using FFTEST6/13/87
c
c finds the fourier cosine coefficients of a function whose first quarter
c period is given, and whose even numbered wavenumbers are absent.
c It takes advantage of the known symmetry to multiply the
c number of data points by 4, so that from n points, n nonzero coeff's
c are found.
c
      IMPLICIT UNDEFINED ( a - z )
c
      DOUBLE COMPLEX values(1), coefs(1)
      INTEGER n, n2pl, n4pl, iml
      DOUBLE PRECISION x(2048), y(2048), work(2048)
      DOUBLE PRECISION normlz
c
c
      INTEGER ifail, i
c
c usually normalization ( for non-const modes ) is sqrt(n)/2 , but
c we actually have 4n data points...
c
      normlz = dsqrt( dfloat(n) )
      n2pl = n + n + 1
      n4pl = n + n + n2pl
c
      DO 3 i = 1, n
         x(i) = dreal( values( i ) )
         y(i) = dimag( values( i ) )
 3    CONTINUE
c
      x(n+1) = 0.0d0
      x(n2pl) = -x(1)
      x(n2pl+n) = 0.0d0
      y(n+1) = 0.0d0
      y(n2pl) = -y( 1 )
      y(n2pl+n) = 0.0d0
c
      DO 1 i = 2, n
         iml = i - 1
         x(n4pl - iml) =  x(i)
         x(n2pl-iml) = -x(i)
         x(n2pl+iml) = -x(i)
         y(n4pl - iml) =  y(i)
         y(n2pl-iml) = -y(i)
         y(n2pl+iml) = -y(i)
1     CONTINUE
c
      CALL C06FCF( x, y, n*4, work, ifail)
c
      DO 2 i = 1, n
         coefs( i ) = dcmplx( x( 2*i ) / normlz, y( 2*i ) / normlz )
 2    CONTINUE
c
      RETURN
      END
      SUBROUTINE COSUM( coefs, values,  N )
c
c tested  using FFTEST 6/13/87
c
c finds the  first quarter period of a function whose fourier
c cosine coefficients are given, and whose even numbered wavenumbers are
c absent.
c
      IMPLICIT UNDEFINED ( a - z )
c
      DOUBLE COMPLEX values(1), coefs(1)
      INTEGER n, i2, n4p2, i2ml, n4
      DOUBLE PRECISION x(2048), y(2048), work(2048)
      DOUBLE PRECISION normlz
c
c
      INTEGER ifail, i
c
c usually normalization ( for non-const modes ) is sqrt(n)/2 , but
c we actually have 4n data points...
c
c Also, we conjugate imaginary parts before use... and on return
c
      normlz = dsqrt( dfloat(n) )
c
      n4   = 4 * n
      n4p2 = n4 + 2
c
      DO 3 i = 1, n
         i2 = 2 * i
         i2ml = 2 * i - 1
         x(i2) = dreal( coefs( i ) ) * normlz
         y(i2) = dimag( coefs( i ) ) * normlz
         x(n4p2-i2) = x(i2)
         y(n4p2-i2) = y(i2)
         x(i2ml) = 0.0d0
         y(i2ml) = 0.0d0
         x(n4-i2ml) = 0.0d0
         y(n4-i2ml) = 0.0d0
 3    CONTINUE
c
      CALL C06FCF( x, y, n*4, work, ifail)
c
      DO 2 i = 1, n
         values( i ) = dcmplx( x( i ), y( i ) )
 2    CONTINUE
c
      RETURN
      END
      PROGRAM FFTEST
c
c This program tests FFTCOS, the fast fourier cosine transformer, and
c COSUM, the fast cosine series sum'er.  This version gives a point source
c to the first, compares the transform to the known one, and then
c inverts the transform.
c
      IMPLICIT UNDEFINED ( a - z )
c
      DOUBLE PRECISION dx
cccc      DOUBLE PRECISION rfun, ifun
      INTEGER n, wavnum, i
      DOUBLE COMPLEX   vals(512), cofs(512), nvals(512), mycofs(512)
      DOUBLE PRECISION  pi, pio2
c
      data pi / 3.14159265358979323844d0 /
c
cccc      rfun(dx) = 3.0d0*dcos( (2*wavnum-1)*dx*pi/2.0d0 )
cccc      ifun(dx) = 5.0d0*dcos( (2*wavnum-1)*dx*pi/2.0d0 )
cccc                 +3.0d0*dcos( (2*wavnum+1)*dx*pi/2.0d0 )
c
      pio2 = pi/2.0d0
c
cccccccccccccccccc100   PRINT *, "number of points, wave num?"
c
100   PRINT *, "number of points, location of source?"
      READ(5,*) n, wavnum
c
      dx = 1.0d0/dfloat( n )
      do 1 i = 1, n
c
         if( i .eq. wavnum+1 ) THEN
            vals( i ) = ( 1.0d0, 2.0d0 )
         ELSE
            vals( i ) = ( 0.0d0, 0.0d0 )
         ENDIF
c
         mycofs(i) = ( 1.0d0, 2.0d0 ) *
                     2.0d0*dcos( pio2*(2*i-1)*dfloat(wavnum)/ dfloat(n) )
                       / dfloat(n)
         IF( wavnum .eq. 0 ) mycofs(i) = mycofs(i) / 2.0d0
c
cccc              vals( i ) = dcmplx(rfun(dfloat(i-1)*dx), ifun(dfloat(i-1)*dx))
1     CONTINUE
c
      WRITE(6,99)( i, vals(i), i = 1, min( 32,n ) )
      CALL fftcos( vals, cofs, n )
c
      print *,"n, wavnum = ", n, wavnum, " transform-my version:"
      write(6, * ) (i, cofs(i)-mycofs(i),   i = 1, min(n,16))
c
      CALL cosum( cofs, nvals, n )
c
      PRINT *, "inverse transform - old values"
      WRITE(6, *) (i, vals(i)-nvals(i), i = 1, min(n,16))
      GO TO 100
99    FORMAT( "values to be tformed", /,
                        8( 4(i3,2x,f5.1,2x,f5.1,2x), / ) )
      END
      PROGRAM MULTZ8
c
c version 1, 6/21/87, number of points in y-direction now 513, 7/25/87
c*******************************************************************
c
c  This program evaluates the values of the field variables ( below ) given the
c values of the coefficients of the homogeneous solutions.  The added
c particular solutions ( if prtadd .ne. 0 ) correspond to Jz(z=0) = 1-(y/l1)^4.
c
c*******************************************************************
c
      IMPLICIT UNDEFINED ( a - z )
c
      DOUBLE PRECISION B11, B12, B21, B22, BC, UNIAXM, THIKNS
      DOUBLE PRECISION NUVAL, PHIOVL
      PARAMETER  ( b11 = 1.0d15, B12 = 1.0d7, B21 = 1.0d7, B22 = 1.0d0 )
      PARAMETER  (  BC = B12 * B21 / ( B11 * B22 )  )
      PARAMETER  ( UNIAXM = 5.0d5, THIKNS = 1.0d-3 )
      PARAMETER  ( NUVAL = 0.4d0, PHIOVL=0.8d0 )
c
c Bij are the coupling coefficients in MKS units:Ns/m^4, Vs/m^2, N/Am,and Ohm m
c BC is the electrokinetic coupling coefficient.
c UNIAXM = the uniaxial modulus 2 G + lambda in N/m^2.
c THIKNS = the thickness of the layer in meters.
c NUVAL = Poisson's ratio
c PHIOVL = porosity
c
      DOUBLE COMPLEX vals( 513 )
      REAL           mags( 513, 129 ), args( 513, 129 ), szval( 129 )
c
      DOUBLE PRECISION  zval( 129 ), l, l1ovrl
      DOUBLE PRECISION  f, omega, delt, nu, phi0, alpha0, n, r
      DOUBLE PRECISION  kn(128), kninv(128), jn( 128 )
      DOUBLE PRECISION  chkn(128),shkn(128),cothkn(128)
      DOUBLE COMPLEX    lambda, lambdn(128)
c
c l is the ratio of the quarter period to the THIKNS of the tissue
c l1ovrl is the duty cycle ratio L1/L of electrode to open space on the surface
c f = frequency for which calculations are performed ( user specified )
c omega = 2*pi*f
c delt = y-wavenumber * thickness ( "delta-hat" ),  = ( 2*wavnum-1)*pi/ 2*l
c n = 1 - 2 nu
c nu = Poisson's ratio
c phi0 = porosity
c alpha0 = solid volume fraction = 1/phi0   - 1
c r = frequency paramater, prop to omega, ( diffn bdry lyr thick ) **-2...
c dltinv = 1/delt
c kn(i) - delt @ wavnum = i, kninv = 1/kn
c jn = Fourier coefs of Jz(z=0), now set up for jz = 1 - (y/l1)^4
c lambda = dynamic decay parameter ("LAMBDA2") of homogeneous solutions
c
      DOUBLE COMPLEX cvec( 6, 128 ), c1( 128 ), c2( 128 ), c3( 128 )
      DOUBLE COMPLEX                 c4( 128 ), c5( 128 ), c6( 128 )
      DOUBLE PRECISION  temp, y( 513 ), kmax, hammng, hconst, hcoef
      INTEGER                varnum
      CHARACTER*200 header
      CHARACTER*20 cfname
      CHARACTER*20 vfname
      CHARACTER*20 grdfil
```

```
c
c ci(wavnum) = coef cf ith hmg soln of wave number n
c cvec( n,m ) = cn( m ), n = 1, 2, 3, 4, 5, 6
c y = values of y at which to evaluate
c z = value of z ( in -1 <= z <= 0 ) at which to evaluate
c kmax = max wavnumber, used for hamming window coef, hammng
c varnum = number of the field variable to be evaluated and written on disk
c according to   1  2  3  4  5  6  7  8  9        10 11 12
c                uy uz Vy Vz vy vz p  s  shear    jy jz  phi
c header = file headers
c cfname = coefficient Ci's values' file's name
c vfname = function values' file's name
c grdfil = file with values of z at which to evaluate
c
      INTEGER modes, nypts, wavnum, ynum, whichc, znum, nzpts
c
c modes = number of modes kept
c nypts = number of values of y at which to evaluate
c whichc is 1, ...6 depending on which hmg sln is being considered
c
      DOUBLE PRECISION hold, temp, csh, snh
      DOUBLE COMPLEX i
      DOUBLE PRECISION pi
c
      PARAMETER ( pi = 3.14159265358979323844d0 )
      PARAMETER (  i = ( 0.0d0, 1.0d0 )  )
c
c---------------------------------------------------------------
c
c set up default param values
c
      nu = NUVAL
      n = 1.0d0 - 2.0d0* nu
      phi0 = PHIOVL
      alpha0 = 1.0d0 / phi0 - 1.0d0
c
c
 1    WRITE(6,*)"name of input file for c vectors?"
      READ(5,"(a)") cfname
      IF( cfname .eq. 'q' .or. cfname .eq. '' ) STOP
      OPEN(1,file=cfname,form="unformatted",status="old",err=1)
      READ(1)header
      READ(header,*) modes, f, llovrl, l
      READ(1)( ( cvec( whichc,wavnum ),
                     whichc = 1, 6 ),  wavnum = 1, modes )
      CLOSE(1)
      WRITE(6,*)"header line is"
      WRITE(6,*)header
      WRITE( 6,* ) "variable options are:  1=uy, 2=uz, 3=Vy, 4=Vz, "
              // "5=vy, 6=vz, 7=p, 8=s, 9=shear, 10=jy, 11=jz, 12=phi"
      WRITE(6,*)"number of the variable to be evaluated>>?"
      READ( 5, * ) varnum
c
c calculate parameter values for each of the wavenumbers, so it only has
c to be done once... cf. eqns V-44 and VIII-15, 33, 43, 47, 48
c
      omega = 2.0d0 * pi * f
      temp = omega * ( B11 * THIKNS*THIKNS / UNIAXM ) / phi0
      r = temp * 2.0d0* (1.0d0 - nu )    * phi0
c
```

```
     DO 101 wavnum = 1, modes
        delt = dfloat( 2* wavnum - 1 ) * pi / ( 2.0d0 * l )
        kn( wavnum ) = delt
        kninv( wavnum ) = 1.0d0 / delt
        hold =  llovrl * delt
        csh = dcos( hold )
        snh = dsin( hold )
        hold = 1.0d0 / hold
        jn(wavnum) = - 8.0d0* (                hold*csh/delt
    ~                         - 3.0d0*hold*hold*snh/delt
    ~                         - 6.0d0*hold**3   *csh/delt
    ~                         + 6.0d0*hold**4   *snh/delt )
        lambda = cdsqrt( 1.0d0 - i * temp / ( delt*delt ) )
        lambdn( wavnum ) = lambda
        shkn( wavnum ) = ( dexp(delt) - dexp(-delt) ) / 2.0d0
        chkn( wavnum ) = ( dexp(delt) + dexp(-delt) ) / 2.0d0
        cothkn(wavnum) = chkn( wavnum ) / shkn( wavnum )
 101 CONTINUE
c
c Get a grid with resolution appropriate to the number of modes kept
c and keeps 1 period of the action.  NOTE that y goes from 0 to 2*l ("L",
c not necessarily = 1 ).
c
  3   WRITE(6,*)"name of file with vert grid points?"
      READ( 5,"(a)") grdfil
      OPEN(2, file="/bb/jrs/grids/"//grdfil, status="old",err=3 )
      READ(2,"(a)") header
      WRITE(6,*)"grid file header is ", header
      READ(header,*)nzpts
      DO 1015 znum = 1, nzpts
         READ(2,*) zval( znum )
         szval( znum ) = zval( znum )
1015  CONTINUE
      CLOSE(2)
c
      WRITE(6,*)'how many y points for evaluation?'
      READ(5,*) nypts
      DO 102 ynum = 1, nypts
         y( ynum ) = 2.0d0 * l * dfloat( ynum -1 ) / dfloat( nypts-1 )
 102  CONTINUE
c
 2    WRITE(6,*)"name of output file for function values?"
      READ(5,"(a)") vfname
      OPEN(1,file=vfname, form = "unformatted", status="new",err=2)
      WRITE(header,*)nypts, nzpts, varnum, modes, f, llovrl, l,
     ~   "= nypts, nzpts, varnum, modes, f, llovrl, l: multz8 output"
     ~ //": z values, magnitudes, phases (single prec)"
      WRITE(1)header
      WRITE(1)( szval( znum ), znum = 1, nzpts )
c
c for hamming window info, see R. W. Hamming, DIGITAL FILTERS, 1983, pp104-106.
c
      kmax = kn( modes )
      hconst = .523d0 + 0.076d0 / dfloat( modes )
      hcoef  = 1.0d0 - hconst
c
      DO 103 wavnum = 1, modes
         hammng = hconst + hcoef * dcos( pi*kn(wavnum)/kmax )
         jn( wavnum ) = jn  (    wavnum ) * hammng
         cl( wavnum ) = cvec( 1, wavnum ) * hammng
         c2( wavnum ) = cvec( 2, wavnum ) * hammng
         c3( wavnum ) = cvec( 3, wavnum ) * hammng
         c4( wavnum ) = cvec( 4, wavnum ) * hammng
         c5( wavnum ) = cvec( 5, wavnum ) * hammng
         c6( wavnum ) = cvec( 6, wavnum ) * hammng
  103 CONTINUE
c
      DO 105 znum = 1, nzpts
c
         CALL MONEZ( zval(znum), y, nypts, modes, f, nu, phi0, r, BC,
     ~            varnum, c1, c2, c3, c4, c5, c6,
     ~            kn, kninv, lambdn, shkn, chkn, cothkn, jn, vals )
c
         DO 104 ynum = 1, nypts
            mags( ynum, znum ) = cdabs(vals(ynum))
            args( ynum, znum ) = datan2( dimag(vals(ynum)),
     ~                                   dreal(vals(ynum)) )
  104    CONTINUE
         IF( mod( znum, 8 ) .eq. 0 )
     ~                 print *,"multz8 thru point",znum,"of",nzpts
 105  CONTINUE
c
      WRITE(1)( ( mags( ynum,znum ), ynum = 1, nypts ),
     ~                               znum = 1, nzpts )
      WRITE(1)( ( args( ynum,znum ), ynum = 1, nypts ),
     ~                               znum = 1, nzpts )
      CLOSE(1)
      GO TO 1
      END
      SUBROUTINE MONEZ( z, y, nypts, modes, f, nu, phi0, r, BC,
     ~                  varnum, c1, c2, c3, c4, c5, c6,
     ~                  kn, kninv, lambdn, shkn, chkn, cothkn, jn, vals )
c
c version 1 6/21/87
c*****************************************************************
c
c  This program evaluates the values of a single field variables at a single
c value of z given the values of the coefficients of the homogeneous
c solutions, and the nondimensional coefficients.
c
c*****************************************************************
c
      IMPLICIT UNDEFINED ( a - z )
c
      DOUBLE PRECISION z, y( 1 ), f, nu, phi0, r, bc
      INTEGER nypts, modes, varnum
      DOUBLE COMPLEX c1( 1 ), c2( 1 ), c3( 1 )
      DOUBLE COMPLEX c4( 1 ), c5( 1 ), c6( 1 )
      DOUBLE COMPLEX lambdn( 1 )
c
c z - value of depth at which to evaluate, -1 <= z <= 0
c y - list of y-values at which to evaluate
c f - frequency at which to evaluate
c nu - Poisson's ratio
c phi0 - porosity
c r - frequency paramater, prop to omega, ( diffn bdry lyr thick )**-2...
c bc - electrokinetic coupling parameter: b12*b21 / ( b11*b22 )
c
c according to    1  2  3  4  5  6  7  8  9       10 11 12
c                 uy uz Vy Vz vy vz p  s  shear   jy jz  phi
c
c nypts - number of y vals
c modes - number of modes kept
c varnum - number of the field variable to be evaluated and written on disk
c according to    1  2  3  4  5  6  7  8  9       10 11 12
c                 uy uz Vy Vz vy vz p  s  shear   jy jz  phi
c
c ci(n) - coefficient of homogeneous soln of type i for wavenum n
c lambda - diffusion bndry layer exponent/"complex decay coef"
c
      DOUBLE PRECISION  kn(1),kninv(1)
      DOUBLE PRECISION  shkn(1), chkn(1), cothkn(1), jn(1)
      DOUBLE COMPLEX vals( 1 )
      DOUBLE COMPLEX uyhp, uzhp, svyhp, svzhp
      DOUBLE COMPLEX Vyhp, Vzhp, php, shp
      DOUBLE COMPLEX shearhp, jyhp, jzhp, phihp
c
c kn(i) - ith wavnumber "delt"
c kninv - 1/kn
c shkn - sinh( kn ), chkn - cosh, cothkn...
c jn - nth Fourier coef of the forcing current
c
c vals - the values to be returned: at a given value of z, each y
c
c uy, uz - horiz and vertical solid matrix displacement
c svy, svz  - horiz and vertical lab-frame fluid velocity
c Vz, Vz  - horiz and vertical relative  fluid velocity
c p - fluid pressure
```

```
c eta = normal compressive force assuming p = 0 ( s*(0), with p = 0 )
c s = normal compressive force = p - eta
c shear = sigma( y,z ) at z = 0
c jy, jz = horiz, vert current densities.
c xxxhp = homogeneous or particular solution for xxx for current wavenumber
c
      DOUBLE PRECISION  delt, dltinv, alpha0, n, thisjn
      DOUBLE COMPLEX    lambda
c
c delt = y-wavenumber * thickness ( "delta-hat" ),  = ( 2*wavnum-1)*pi/(2*1)
c n = 1 - 2 nu
c alpha0 = solid volume fraction = 1/phi0   - 1
c thisjn =  value of jn for current n
c lambda = dynamic decay parameter ("LAMBDA2") of homogeneous solutions
c
      INTEGER ynum, wavnum
c
c ynum, wavenum  = loop indecies
c
      DOUBLE PRECISION  shd,chd,cothd
      DOUBLE PRECISION  sins(513),coss(513),thssin,thscos
      DOUBLE PRECISION  nux, phi0x, rx
c
c      chd =  cosh( delt ), chkn( n ) = chd( delt = kn(n) )
c      shd =  sinh(kn)
c      cothd =coth(kn)
c
      DOUBLE COMPLEX     zero
      INTEGER parity, parlst(12)
c
      COMMON / prtcom /  shd, chd, cothd
      COMMON / homcom /  delt, dltinv, lambda, n, nux, phi0x, alpha0, rx
c
      PARAMETER  ( zero = ( 0.0d0, 0.0d0 ) )
c
      data parlst / 1,0,1,0,1,0,  0,0,1,1,0,0 /
c
c---------------------------------------------------------------
c
      nux = nu
      phi0x = phi0
      rx = r
      n = 1.0d0 - 2.0d0* nu
      alpha0 = 1.0d0 / phi0 - 1.0d0
c
c find out if this variable is even or odd
c
      parity = parlst( varnum )
c
      DO 102 ynum = 1, nypts
         vals( ynum ) = zero
 102  CONTINUE
c
      DO 106 wavnum = 1, modes
         delt = kn( wavnum )
         dltinv=kninv(wavnum)
         lambda = lambdn( wavnum )
         IF( parity .eq. 0 ) THEN
            DO 103 ynum = 1, nypts
               coss( ynum ) = dcos( delt*y(ynum) )
 103       CONTINUE
        ELSE
           DO 1035 ynum = 1, nypts
              sins( ynum ) = dsin( delt*y(ynum) )
1035       CONTINUE
        ENDIF
c
c add homogeneous solution contributions
c varnum = number of the field variable to be evaluated and written on disk
c according to   1  2  3  4  5  6  7  8  9        10 11 12
c                uy uz Vy Vz vy vz p  s  shear    jy jz  phi
c
        IF( varnum .ne. 10 .and. varnum .ne. 11 ) THEN
           CALL HMG6( z, c1(wavnum), c2(wavnum), c3(wavnum),
    ~                    c4(wavnum), c5(wavnum), c6(wavnum),
    ~         uyhp, uzhp, svyhp, svzhp, Vyhp, Vzhp, php, shp, shearhp )
           DO 104 ynum = 1, nypts
              IF( parity .eq. 0 ) THEN
                 thscos = coss(ynum)
              ELSE
                 thssin = sins(ynum)
              ENDIF
c
              GO TO ( 1,2,3,4,5,6,7,8,9,104,104,12 ), varnum
 1               vals(ynum)=vals(ynum) + uyhp * thssin
               GO TO 104
 2               vals(ynum)=vals(ynum) + uzhp * thscos
               GO TO 104
 3               vals(ynum)=vals(ynum) + Vyhp* thssin
               GO TO 104
 4               vals(ynum)=vals(ynum) + Vzhp* thscos
               GO TO 104
 5               vals(ynum)=vals(ynum) + svyhp* thssin
               GO TO 104
 6               vals(ynum)=vals(ynum) + svzhp* thscos
               GO TO 104
 7               vals(ynum)=vals(ynum) + php * thscos
               GO TO 104
 8               vals(ynum)=vals(ynum) + shp * thscos
               GO TO 104
 9               vals(ynum)=vals(ynum) + shearhp* thssin
               GO TO 104
12               vals(ynum)=vals(ynum) - bc * php * thscos
c
 104       CONTINUE
        ENDIF
c
c add particular solution contributions, note modification of sins and coss
c to account for jn
c varnum = number of the field variable to be evaluated and written on disk
c according to   1  2  3  4  5  6  7  8  9        10 11 12
c                uy uz Vy Vz vy vz p  s  shear    jy jz  phi
c
        IF( varnum .ne. 3 .and. varnum .ne. 4 ) THEN
           shd = shkn( wavnum )
           chd = chkn( wavnum )
           cothd = cothkn( wavnum )
           thisjn = jn( wavnum )

           CALL PRTSLN( z, uyhp, uzhp, svyhp, svzhp, php, shp,
                          shearhp, phıhp, jyhp, jzhp )
c
           DO 107 ynum = 1, nypts
              IF( parity .eq. 0 ) THEN
                 thscos = coss(ynum) * thisjn
              ELSE
                 thssin = sins(ynum) * thisjn
              ENDIF
c
              GO TO ( 91,92,107,107,95,96,97,98,99,910,911,912),varnum
c
 91              vals(ynum) = vals(ynum) + uyhp * thssin
               GO TO 107
 92              vals(ynum) = vals(ynum) + uzhp * thscos
               GO TO 107
 95              vals(ynum) = vals(ynum) + svyhp* thssin
               GO TO 107
 96              vals(ynum) = vals(ynum) + svzhp* thscos
               GO TO 107
 97              vals(ynum) = vals(ynum) + php * thscos
               GO TO 107
 98              vals(ynum) = vals(ynum) + shp * thscos
               GO TO 107
 99              vals(ynum) = vals(ynum) + shearhp* thssin
               GO TO 107
 910             vals(ynum) = vals(ynum) + jyhp * thssin
               GO TO 107
 911             vals(ynum) = vals(ynum) + jzhp * thscos
               GO TO 107
 912             vals(ynum) = vals(ynum) + phihp * thscos
c
 107       CONTINUE
        ENDIF
c
106     CONTINUE
        RETURN
        END
```

Appendix C

Notation

Any variable not found elsewhere may be listed under "A," standing for "any field variable."

Variable	Units	Description
A^A	–	solution for field variable A (A is any field variable) for problem "A" of figure 6.3
A^B	–	solution for field variable A (A is any field variable) for problem "B" of figure 6.3
A^H	–	homogeneous ($\vec{J} = \vec{0}$) solution for A
A_i^H	–	$i^{\underline{\text{th}}}$ order long-wave approximation for A^H
$A_l^m(z)$	–	the $l^{\underline{\text{th}}}$ homogeneous solution for variable A at wavenumber k_m
A^P	–	particular solution for A, where A is any field variable
$A^{Sm}(z)$	–	symmetric solution for wavenumber k_m for field variable A
A_i	–	i^{th} order long-wave approximation for A
a_J	m	length equivalent to imposed current density, $J_0\frac{\delta^{*2}b_{12}}{G+\lambda_L}$
b_{11}	$\frac{Ns}{m^4}$	phenomenological coupling coefficient, zero-current fluid resistivity
b_{12}	$\frac{N}{Am}$	phenomenological coupling coefficient, $= b_{21}$ by Onsager Reciprocity
b_{21}	$\frac{Vs}{m^2}$	phenomenological coupling coefficient, $= b_{12}$ by Onsager Reciprocity
b_{22}	Ωm	phenomenological coupling coefficient, zero-flow resistivity
b_e	–	electrokinetic coupling coefficient, $\frac{b_{12}b_{21}}{b_{11}b_{22}}$
C_l^m	–	coefficient of the $l^{\underline{\text{th}}}$ homogeneous (symmetric) solution
$\vec{E}$	V/m	electric field strength
f	Hz	frequency of imposed surface disturbance, $\omega/2\pi$
G	$\frac{N}{m^2}$	shear modulus (drained first Lamé coefficient – *cf.* [91]) of solid matrix
i	–	$\sqrt{-1}$

Variable	Units	Description
$\vec{J}$	$\frac{A}{m^2}$	current density vector field
J_0	$\frac{A}{m^2}$	amplitude of imposed current density
j_m	–	Fourier cosine coefficients of $\bar{\jmath}_z$
j_y	–	non-dimensionalized Fourier transformed J_y
$\bar{\jmath}_y$	–	non-dimensionalized J_y, J_y/J_0
$\bar{\jmath}_y^m(z)$	–	y-directed current density for wavenumber k_m
j_z	–	non-dimensionalized Fourier transformed J_z
$\bar{\jmath}_z$	–	non-dimensionalized J_z, J_y/J_0
$\bar{\jmath}_z^m(z)$	–	z-directed current density for wavenumber k_m
k	m^{-1}	wavenumber of imposed surface disturbance
$k_1 \ldots k_6$	–	coefficients of homogeneous solution vectors
k_7, k_8	–	coefficients of particular solution vectors
l	–	non-dimensional quarter-period of field variables: dimensional dimensional period is $4l\delta^*$
l_1	–	non-dimensional electrode half-width, actual width is $2l_1\delta^*$
M	–	number of Fourier modes kept in truncated series
n	–	$1 - 2\nu$
p	–	non-dimensionalized Fourier transformed pressure $\mathcal{P}$
$\bar{p}$	–	non-dimensionalized $\mathcal{P}$, $\mathcal{P}e^{i\omega t}[J_0\delta^* b_{12}]^{-1}$
p_a, p_b	–	the two possible long-wave approximations to p
p_m^B	–	Fourier coefficients for $\bar{p}^B(z = 0)$
$\mathcal{P}$	$\frac{N}{m^2}$	Pressure corrected for osmotic differences, fluid force per unit total area
$\mathcal{P}_{ln}^m$	–	homogeneous coefficients (C_m^l) corresponding to one unit of pressure at $y = l(n-1)/M$, $z = 0$
r	–	non-dimensional frequency parameter
r	–	radial coordinate in cylindrical polar coordinates (§2.3.2 only)

Variable	Units	Description
s	—	non-dimensionalized Fourier transformed S
$\bar{s}$	—	non-dimensionalized S, $Se^{i\omega t}[J_0\delta^* b_{12}]^{-1}$
s_m^B	—	Fourier coefficients for $\bar{s}^B$
S	$\frac{N}{m^2}$	normal vertical compressive stress, $-\sigma_{33}$
S_{ln}^m	—	homogeneous coefficients (C_m^l) corresponding to one unit of normal stress at $y = l(n-1)/M$, $z = 0$
$\mathrm{snc}_n\,(y)$	—	periodic version of the "sync" function ($\sin x/x$) defined by equations 6.17
t	s	time
T_n	s	amount of time required to solve an n by n system of linear equations with complex coefficients
$\vec{u}$	—	non-dimensionalized Fourier transformed $\vec{u}^s$
$\vec{u}^s$	m	displacement vector of solid matrix
u_r	m	radial displacement, cylindrical polar coordinates
u_θ	m	angular displacement, cylindrical polar coordinates
u_y	—	non-dimensionalized Fourier transformed u_y^*
$\bar{u}_y$	—	non-dimensionalized u_y^*, $u_y^* e^{i\omega t}/a_J$
u_y^*	m	horizontal ($y-$) displacement of solid matrix
u_z	—	non-dimensionalized Fourier transformed u_z^*
$\bar{u}_z$	—	non-dimensionalized u_z^*, $u_z^* e^{i\omega t}/a_J$
u_z^*	m	vertical ($z-$) displacement of solid matrix
$\vec{v}^s$	m/s	lab-frame local velocity of solid matrix, $\partial_t \vec{u}^s$
$\vec{v}^f$	m/s	lab-frame local velocity of fluid
v_y	—	non-dimensionalized Fourier transformed v_y^*
$\bar{v}_y$	—	non-dimensionalized v_y^*, $v_y^* e^{i\omega t}[J_0 \frac{b_{12}}{b_{11}}]^{-1}$
v_y^*	m/s	y-component of $\vec{v}^f$
v_z	—	non-dimensionalized Fourier transformed v_z^*
$\bar{v}_y$	—	non-dimensionalized v_z^*, $v_z^* e^{i\omega t}[J_0 \frac{b_{12}}{b_{11}}]^{-1}$
v_z^*	m/s	z-component of $\vec{v}^f$

Variable	Units	Description
$\vec{V}^*$	m/s	velocity of fluid relative to solid, $\vec{v}^f - \vec{v}^s$
V_y	–	non-dimensionalized Fourier transformed V_y^*
$\bar{V}_y$	–	non-dimensionalized V_y^*, $V_y^* e^{i\omega t}[J_0 \frac{b_{12}}{b_{11}}]^{-1}$
V_y^*	m/s	y component of relative fluid velocity, $\vec{V}^*$
V_z	–	non-dimensionalized Fourier transformed V_z^*
$\bar{V}_z$	–	non-dimensionalized V_z^*, $V_z^* e^{i\omega t}[J_0 \frac{b_{12}}{b_{11}}]^{-1}$
V_z^*	m/s	z component of relative fluid velocity, $\vec{V}^*$
W^*	$N \cdot m/s$	work done on solid per unit time and unit length in x-direction
X^H	–	homogeneous solution vector
X^P	–	particular solution vector
x^*, y^*, z^*	m	fixed lab-frame Cartesian coordinates
$\{y,z\}$	–	the y- or z-component or derivative of a field
z	–	z^*/δ^*, the top of the surface is $z = 0$, the bottom $z = -1$
$\hat{z}$	–	kz^*
α	–	solid volume fraction: volume of solid per unit volume of fluid
α_0	–	undisturbed solid volume fraction, $1/\phi_0 - 1$
δ	–	non dimensional thickness, $k\delta^*$
δ^*	m	undeformed thickness of the layer
δ_{ij}	–	the Kronecker δ function
Δ	–	$k\Delta^*$
Δ^*	m	diffusion boundary layer thickness
ϵ	Farads $/m$	permitivity of bulk conductor model
$\underline{\underline{\epsilon}}$	–	small strain tensor of solid matrix
θ	–	angle coordinate in cylindrical polar coordinates
λ	m^{-1}	wavelength of imposed surface disturbance, $2\pi/k$
Λ	–	homogeneous solution exponential decay coefficient
λ_L	$\frac{N}{m^2}$	second Lamé coefficient of solid matrix (drained – *cf.* [91])
ν	–	Poisson's ratio of solid matrix (drained – *cf.* [91])

Variable	Units	Description
π	$\frac{N}{m^2}$	osmotic pressure in interstitial fluid (or 3.14159...)
Π_n	–	value of the pressure at $y = (n-1)/M$, $z = 0$ for problem "B"
ρ	$\frac{C}{m^3}$	macroscopically averaged bulk charge density of the medium
$\rho^{s,f}$	kg/m^3	"apparent" density [83]: mass of solid (fluid) per unit total volume
$\rho_T^{s,f}$	kg/m^3	"true" density [83]: mass of solid (fluid) per unit solid (fluid) volume
σ	mho/m	bulk conductivity in rigid conductor model
$\underline{\underline{\sigma}}$	$\frac{N}{m^2}$	stress tensor, total force per unit total area
σ_l^m	–	*cf.* A_l^m for σ_{yz}
$\bar{\sigma}_{yz}^*$	$\frac{N}{m^2}$	shear stress
$\bar{\sigma}_{yz}$	–	non-dimensional σ_{yz}^*, $\sigma_{yz}^* e^{i\omega t}[J_0\delta^* b_{12}]^{-1}$
Υ_n	–	value of the normal stress at $y = (n-1)/M$, $z = 0$ for problem "B"
ϕ	–	non-dimensionalized Fourier transformed electrical potential
$\bar{\phi}$	–	non-dimensionalized electrical potential Φ, $\Phi e^{i\omega t}[j_0\delta^* b_{22}]^{-1}$
ϕ_0	–	undisturbed porosity, $1/(\alpha_0 + 1)$
ϕ_a, ϕ_b	–	the two possible long-wave approximations to ϕ
ϕ_f	–	porosity: volume of fluid per unit total volume.
Φ	V	electrical potential field
ω	s^{-1}	angular frequency of imposed disturbance

Bibliography

[1] Abramowitz, M., and I. A. Stegun, eds., "Handbook of Mathematical Functions with Formulas, Graphs, and Mathematical Tables," Dover, New York, 1972.

[2] Abarbanel, S., Gottlieb, D., and E. Tadmor, "Spectral Methods for Discontinuous Problems," Inst. for Computer Applications in Sci. and Eng. (ICASE) report #85-38, NASA #CR-177974, NASA, Virginia, 1985.

[3] Armstrong, C. G., W. M. Lai, and V. C. Mow, "An Analysis of the Unconfined Compression of Articular Cartilage," *J. Biomech. Eng.*, **106**:165, 1984.

[4] Bassett, C. A., and R. J. Pawluk, "Electrical Behavior of Cartilage During Loading," *Science,* **178**:982, 1972.

[5] Bender, C. M., and S. A. Orszag, *Advanced Mathematical Methods for Scientists and Engineers*, McGraw-Hill, New York, 1978.

[6] Biot, M. A., "Le Prolbème de la Consolidation des Matières Argileuses sous une Charge," *Ann. Soc. Sci. Bruxelles*, **B55**:110-113, 1935.

[7] __________, "General Theory of Three-Dimensional Consolidation," *J. Appl. Phys.*, **12**:155, 1941

[8] __________, "Theory of Elasticity and Consolidation for a Porous Anisotropic Solid," *J. Appl. Phys.*, **26**:182, 1955.

[9] __________, "General Solutions of the Equations of Elasticity and Consolidation for a Porous Material," *J. Appl. Mech.*, **78**:91, 1956.

[10] __________, "Thermoelasticity and Irreversible Thermodynamics," *J. appl Phys.*, **27**:240, 1956.

[11] __________, "Theory of Propagation of Elastic Waves in a Fluid–Saturated Porous Solid. I. Low–Frequency Range," *J. Acoust. Soc. Am.*, **28**:168, 1956.

[12] ———, "Mechanics of Deformation and Acoustic Propagation in Porous Media," *J. appl Phys.*, **33**:1482, 1962.

[13] ———, "Generalized Theory of Acoustic Propagation in Porous Dissipative Media," *J. Acoust. Soc. Am.*, **34**:1254, 1962.

[14] Boyce, W. E., and R. C. DiPrima, *Elementary Differential Equations and Boundary Value Problems*, 3rd ed., Wiley, New York, 1977.

[15] Biot, M. A., and D. G. Willis, "The Elastic Coefficients of the Theory of Consolidation," *J. App. Mech.*, **24**:594, 1957.

[16] Bowen, R. M., "Theory of Mixtures," in *Continuum Physics*, A. E. Eringen, ed., vol. 3, pp. 1-127, 1976.

[17] Burridge, R., and J. B. Keller, "Poroelasticity Equations Derived from Microstructure," *J. Acoust. Soc. Am.* **70**:4, 1981.

[18] Chandler, R. N., "Transient Streaming Potential Measurements on Fluid–Saturated Porous Structures...," *J. Acoust. Soc. Am.*, **70**:116, 1981.

[19] Chandler, R. N., and D. L. Johnson, "The Equivalence of Quasistatic Flow in Fluid–Saturated Porous Media and Biot's Slow Wave in the Limit of Zero Frequency," *J. appl Phys.*, **52**:3391, 1981.

[20] Cleary, M. P., "Fundamental Solutions for a Fluid–Saturated Porous Solid," *Int. J. Solids Structures*, **13**:785, 1977.

[21] Craine, R. E., A. E. Green, and P. M. Naghdi, "A Mixture of Viscous Elastic Materials with Different Constituent Temperatures," *Quart. J. App. Math.*, **23**:171-184, 1970.

[22] Currie, I. G., *Fundamental Mechanics of Fluids*, McGraw-Hill, New York, 1974.

[23] Darcy, H., *Les Fontaines Publiques de la Ville de Dijon*, Dalmont, Paris, p. 590, 1856.

[24] Degroot, S. R., and P. Mazur, "Nonequilibrium Thermodynamics in Biophysics," North Holland, Amsterdam, 1969.

[25] Eisenberg, S. R., Sc. D. thesis, *Nonequilibrium Electromechanical Interactions in Cartilage: Swelling and Electrokinetics*, M.I.T. Department of Electrical Engineering and Computer Science, 1983.

[26] Eisenberg, S. R., and A. J. Grodzinsky, " Swelling of Articular Cartilage and Other Connective Tissues: Electromechanochemical Forces," *J. Orthop. Res.*, **3**:148, 1985.

[27] Eisenberg, S. R., and A. J. Grodzinsky, "The Effect of Chemical Transients on the Non–Equilibrium Swelling Behavior of Articular Cartilage and Other Connective Tissues," *1983 Advances in Bioeng.*, D. L. Bartel, ed., New York, ASME, p. 102.

[28] Eisenberg, S. R., and A. J. Grodzinsky, "Electromechanical Micromodel of Articular Cartilage," in *Proc. ASME Biomech. Symp.* , D. Butler *et al.*, eds., Albuquerque, NM, AMD vol. 68, p. 85, 1985.

[29] Fatt, I., and T. K. Goldstick, "Dynamics of Water Transport in Swelling Membranes," *J. Colloid Sci.*, **20**:962, 1965.

[30] Fraeijs de Veuveke, B. M., "A First Course in Elasticity," F. A. Ficken, translator. Springer - Verlag, New York, 1979.

[31] Frank, E. H., Ph. D. Thesis, *Electromechanics of Normal and Degenerated Cartilage: Poroelastic Behavior and Electrokinetic Mechanisms*, M. I. T. Department. of Elec. Eng. and Comp. Sci., 1987.

[32] Frank, E. H., and A. J. Grodzinsky, "Streaming Potential Detection of Cartilage Degeneration Kinetics in Vitro," *Proceedings of the Third Annual Conference of the Bioelectrical Repair and Growth Soc.*, **3**:16, 1983.

[33] Frank, E. H., A. J. Grodzinsky, T. J. Koob, and D. R. Eyre, "Streaming Potentials: A Sensitive Index of Enzymatic Degradation in Articular Cartilage," (in press).

[34] Frank, E. H., and A. J. Grodzinsky, "Cartilage Electromechanics I: Electrokinetic Transduction and the Effects of Electrolyte pH and Ionic Strength," *J. Biomech.*, **20**:615-627, 1987.

[35] Frank, E. H., and A. J. Grodzinsky, "Cartilage Electromechanics II: A Continuum Model of Cartilage Electrokinetics and Correlation with Experiments," *J. Biomech.*, **20**:629-639, 1987.

[36] Frank, E. H., N. G. Kavesh, and A. J. Grodzinsky, "Continuum Theory and Measurement of Cartilage Electrokinetics: Relevance to Stimulation of Chondrocyte Biosynthesis," in *Bioelectrical Repair and Growth*, E. Fukada, S. Inoue, T. Sakou, H. Takahashi, and N. Tsuyama, eds., Nishimura Press, Japan, 1985.

[37] Frankel, J., "On the Theory of Seismic and Seismoelectric Phenomena in a Moist Soil", *J. Phys.*, 8:4, p. 230, 1944.

[38] Friedman, M. H., "Free Swelling of Biological Tissue: the Corneal Stroma," *Chem. Eng. Prog. Symp. Ser.*, 66:33, 1970.

[39] Friedman, M. H., "General Theory of Tissue Swelling with Application to the Corneal Stroma," *J. Theor. Bio.*, 30:93, 1971.

[40] Gladwell, G. M. L., *Contact Problems in the Classical Theory of Elasticity*, Sijthoff and Noordhoff, Germantown, Maryland, 1980.

[41] Godfrey, D. E. R., *Theoretical Elasticity and Plasticity for Engineers*, Thames and Hudson, London, 1959.

[42] Gottlieb, D., and S. A. Orszag, "Numerical Analysis of Spectral Methods: Theory and Applications," Soc. of Ind. and App. Math, Philadelphia, 1977.

[43] Green, A. E., and P. M. Naghdi, "The Flow of Fluid Through an Elastic Solid," *Acta Mechanica*, 9:329, 1970.

[44] Grodzinsky, A. J., "Electromechanical and Physicochemical properties of Connective Tissue," *CRC Critical Rev. in Biomed. Engin.*, 9:133, 1983.

[45] Gross, D., and W. S. Williams, "Streaming Potential and the Electromechanical Response of Physiologically Moist Bone," *J. Biomech*, 15:277, 1982.

[46] Hamming, R. W., "Digital Filters," Prentice-Hall, New Jersey, 1983.

[47] Hamming, R. W., "Numerical Methods for Scientists and Engineers," McGraw-Hill, New York, 1962.

[48] Haus, H. A., and J. R. Melcher, *Electromagnetic Fields and Energy*, course notes for MIT course 6.013, 1985 (to be published by Prentice-Hall, New Jersey).

[49] Hayes, W. C., L. M. Keer, G. Herrmann, and L. F. Mockros, "A Mathematical Analysis for Indentation Tests of Articular Cartilage," *J. Biomech.*, 5:541, 1972.

[50] Hedbys, B. O., and S. Mishima, "Flow of Water in the Corneal Stroma," *Exptl. Eye Res.*, 1:262, 1962.

[51] Hoch, D. H., *et al.*, "Early Changes in Material Properties of Rabbit Articular Cartilage After Meniscectomy," *J. Orthop. Res.*, 1:4, 1983.

[52] Holmes, M. H., W. M. Lai, and V. C. Mow, "Singular Perturbation Analysis for Stress Relaxation Test of Articular Cartilage," *J. Biomech Eng.* **107**:206, 1985.

[53] Jackson, J. D., "Classical Electrodynamics," John Wiley and Sons, New York, 1975.

[54] Johnson, D. L., "Elastodynamics of Gels," *J. Chem. Phys.*, **77**:1531, 1982.

[55] Katchalsky, A., P. F. Curran, *Nonequilibrium Thermodynamics in Biophysics*, Harvard University Press, 1967.

[56] Kavesh, N. G., B. S. thesis, *Electromechanical Transduction Properties of Bovine Articular Cartilage*, M. I. T. Department. of Elec. Eng. and Comp. Sci., 1984.

[57] Kosteuch, J. D., K. R. Foster, and S. R. Pollack, "Dielectric Properties of Fluid-Saturated Bone – The Effect of Variation in Conductivity of Immersion Fluid," *IEEE Trans. Biomed. Eng.*, **BME-31**: 369, 1984.

[58] Kwan, S. C., W. M. Lai, and V. C. Mow, "Permeability of Soft, Hydrated Tissues under Finite Deformation," in *1985 Biomechanics Symposium,* AMD-68, D. Butler, T. K. Hung, and R. E. Mates, eds., ASME, New York, pp. 79-80, 1985.

[59] Kwan, S. C., W. M. Lai, and V. C. Mow, "Response of Articular Cartilage Layer Subjected to a Spreading Pressure Distribution Simulating Walking," in *1983 Biomechanics Symposium,* ASME, New York, page 9, 1985.

[60] Lai, W. M., and V. C. Mow, "Drag–Induced Compression of Articular Cartilage During A Permeation Experiment," *Biorheology*, **17**:111, 1980.

[61] Lai, W. M., V. Roth, and V. C. Mow, "Effect of Nonlinear Permeability and Rate of Compression on the Stress Behavior of Articular Cartilage," *J. Biomech. Eng.*, **103**:61, 1981.

[62] Lee, R. C., Ph. D. Thesis, *Cartilage Electromechanics: The Relationship of Physicochemical to Mechanical Properities*, M. I. T. Department. of Elec. Eng. and Comp. Sci., 1979.

[63] Lee, R. C., A. J. Grodzinsky, and M. J. Glimcher "The Electromechanics of Normal and Chemically Modified Articular Cartilage," in *Electrical Properties of Bone and Cartilage: Experimental Effects and Clinical Applications*, C. T. Brighton *et al.*, eds., Grune and Stratton, New York, 1979, pp. 47-56.

[64] Lee, R. C., E. Frank, A. J. Grodzinsky, and D. K. Roylance, "Oscillatory Compressional Behavior of Articular Cartilage and its Associated Electromechanical Properties," *J. Biomech. Engin.*, **103**:280, 1981.

[65] Levich, V. G., *Physicochemical Hydrodynamics*, Prentice-Hall. New Jersey, 1962.

[66] Levinson, N., and R. M. Redheffer, *Complex Variables*, Holden-Day, San Francisco, California, 1970.

[67] Lotke, P. A., J. Black, and S. Richardson, "Electromechanical Properties of Human Articular Cartilage," *J. Bone & Joint Surg.*, **54-A**:1040, 1970.

[68] Mak, A. F., "The Apparent Viscoelastic Behavior of Articular Cartilage – The Contributions from the Intrinsic Matrix Viscoelasticity and Interstitial Fluid Flows," *J. Biomech. Engin.*, **108**: 123-130.

[69] Mak, A. F., W. M. Lai, and V. C. Mow, "Indentation of Articular Cartilage: A Biphasic Analysis," in *1982 Advances in Bioengineering*, L. Thibault, ed., ASME, New York, p. 71.

[70] Malvern, L. E., *Introduction to the Mechanics of a Continuous Medium*, Prentice-Hall, New Jersey, 1969.

[71] Mankin, H. J., and K. D. Brandt, "Biochemistry and Metabolism of Cartilage in Osteoarthritis," in *Osteoarthritis, Diagnosis and Management*, F. W. Moskowitz, D. S. Howell, V. M. Goldberg, and H. J. Mankin, eds., W. B. Saunders, Philadelphia, 1984, pp. 43-79.

[72] Maroudas, A., "Transport through Articular Cartilage and some Physiological Implications," in *Normal and Osteoarthrotic Articular Cartilage,"* S. Y. Ali, M. W. Elves and D. H. Leaback, eds., Institute of Orthopaedics, London, 1974.

[73] __________, "Fluid Transport in Cartilage," *Ann. Rheum. Dis.*, **34**: Suppl. 2, p. 77, 1975.

[74] __________, "Physicochemical Properties of Articular Cartilage," in *Adult Articular Cartilage*, M. A. R. Freeman, ed., Pitman Medical, Kent, England, p. 215 - 290, 1979.

[75] __________, "Balance between Swelling Pressure and Collagen Tension in Normal and Degenerate Cartilage," *Nature*, **260**:808-809, 1976.

[76] __________, "'Free' and 'Exchangeable' or 'Trapped' and 'Non-exchangeable' Water in Cartilage," *J. Orthop. Res.*, **5**:133-138, 1987.

[77] Mathews, J., and R. L. Walker, "Mathematical Methods of Physics," Benjamin/Cummings, Massachusetts, 1970.

[78] McCutchen, C. W., "The Frictional Properties of Animal Joints," *Wear*, 5:1, 1962.

[79] Mckibbin, B., and A. Maroudas, "Nutrition and Metabolism," in *Adult Articular Cartilage*, M. Freeman, ed., Pitman Medical, Kent England, pp. 461-486, 1979.

[80] McNamee, J., and R. E. Gibson, "Displacement Functions and Linear Transforms Applied to Diffusion through Porous Elastic Media," *Quart. J. of Mech. and App. Math.*, **13**:98-111, 1960.

[81] Melcher, J. R., *Continuum Electromechanics*, MIT Press, Cambridge, MA, 1981.

[82] Morgenthaler, A. W., S. M. Thesis, *Electromechanical Response of Articular Cartilage Subject to Enzymatic Degradation*, M. I. T. Deparment. of Elec. Eng. and Comp. Sci., 1987.

[83] Mow, V. C., S. C. Kuei, W. M. Lai, and C. G. Armstrong, "Biphasic Creep and Stress Relaxation of Articular Cartilage in Compression: Theory and Experiments," *J. Biomech. Eng.*, **102**:73, 1980.

[84] Mow, V. C., M. H. Holmes, and W. M. Lai, "Fluid Transport and Mechanical Properties of Articular Cartilage: A Review," *J. Biomechanics*, **17**:377, 1984.

[85] Mow, V. C., and W. M. Lai, "Recent Developments in Synovial Joint Biomechanics," *SIAM Review*, **22**:275-317, 1980.

[86] Mow, V. C., and J. M. Mansour, "The Nonlinear Interaction Between Cartilage Deformation and Interstitial Fluid Flow," *J. Biomech.*, **10**:31, 1977.

[87] Mow, V. C., and J. M. Schoonbeck, "Contribution of Donnan Osmotic Pressure towards the Biphasic Compressive Modulus of Articular Cartilage," *Trans. Thirtieth Orthop. Res. Soc.*, **9**: 262, 1984.

[88] Muir, I. U. M., "Articular Cartilage," in *Adult Articular Cartilage*, M. A. R. Freeman, ed., Pitman Medical, Kent, England pp. 145 - 214, 1979.

[89] Muskhelishvili, N. I., "Some Basic Problems of the Mathematical Theory of Elasticity," J. R. M. Radok, translator, P. Noordhoff Ltd., Groningen, the Netherlands, 1963.

[90] Onsager, L., "Reciprocal Relations in Irreversible Processes. I," *Phys. Rev.*, **37**:405, 1931.

[91] Rice, J. R., and M. P. Cleary, "Some Basic Stress Diffusion Solutions for Fluid-Saturated Elastic Porous Media with Compressible Constituents," *Rev. Geophys. and Space Phys.*, **14**:227, 1976.

[92] Sachs, J. R., and A. J. Grodzinsky, "A Mathematical Model of an Electromechanically Coupled Poroelastic Medium Driven by an Applied Electric Current," (to appear).

[93] Sachs, J. R., and A. J. Grodzinsky, "A Mathematical Model of an Electromechanical Probe of a Coupled Fluid-Solid System II: Mechanical Boundary Conditions," (to appear).

[94] Salzstein, R. J., S. R. Pollack, A. F. Mak, and N. Petrov, "Electromechanical Potentials in Cortical Bone: Part I: A Continuum Approach," (submitted).

[95] Salzstein, R. J., and S. Pollack "Electromechanical Potentials in Cortical Bone: Part II: Experimental Analysis," (submitted).

[96] Streeter, Victor L., ed., "Handbook of Fluid Dynamics," Mcgraw-Hill, New York, 1961.

[97] Tanaka, T., and D. Fillmore, "Kinetics of Swelling of Gels," *J. Chem. Phys.*, **70**:1214, 1979.

[98] Tanaka, T., L. O. Hocker, and G. B. Benedek, "Spectrum of Light scattered from a Viscoelastic Gel," *J. Chemical Phys.*, **59**:5151, 1973.

[99] Terzaghi, K., "Die Berechnung der Durchaßigkeitsziffer des Tones aus dem Verlauf der hydrodynamischen Spannungserscheinungen," *Sitzungsber. Akad. Wiß. Wien Math.-Naturwiß. Kl., Abt.*, **2A**, 132, 105, 1923.

[100] Timoshenko, S. P., and J. N. Goodier, "Theory of Elasticity," McGraw-Hill, New York, 1970.

[101] Torzilli, P. A., "The Influence of Cartilage Conformation on its Equilibrium Water Partition," *J. Orthop. Res.*, **3**:473-483, 1985.

[102] Torzilli, P. A., and V. C. Mow, "On the Fundamental Fluid Transport Mechanic]sms through Normal and Pathological Articular Cartilage During Function – I. The Formulation," *J. Biomech.*, **9**:541-552, 1976.

[103] Torzilli, P. A., and V. C. Mow, "On the Fundamental Fluid Transport Mechanic]sms through Normal and Pathological Articular Cartilage During Function – II. The Analysis, Solution, and Conclusions," *J. Biomech.*, 9:587-606, 1976.

[104] Woolley, D. E., "Mammalian Collagenases," in *Extracellular Matrix Biochemistry*, K. A. Piez and A. H. Reddi, eds., Elsevier, New York, 1984.

[105] Yasuda, I., "Fundamental Aspects of Fracture Treatment," *J. Kyoto Med. Soc.*, 4:395-406, 1953.

[106] Yih, C.-H., *Fluid Mechanics*, West River Press, Ann Arbor, Michigan, 1979.

[107] Zaretsky, I., L. Mouayad, and J. Melcher, "Modal Approach to Obtaining Continuum Properties from Interdigital Electrode Dielectrometry," *LEES Technical Report*, number **TR86-019**, Mass. Inst. of Tech., Cambridge, Mass., 1986 (submitted, *IEEE Trans on Elec. Insul.*).

Biographical Note

I was born to American parents in Paris, France on November 19, 1959. After a stint of 13 years at the University of Chicago Laboratory Schools, I left for Brown University in the fall of 1977. In June, 1981 I received my Sc. B. and Sc. M. degrees in applied math, the Rohn-Truell Award for Outstanding Achievement in Applied Math, and associate membership in Σ Ξ. During the summers of my years at Brown I worked variously as a computer programmer, engineering lab assistant and general fixit, and professional musician. After graduation, I worked as a lab assistant in a solar energy engineering lab, and as a percussionist in classical and jazz ensembles. I also studied Japanese martial arts.

I entered M.I.T. in September, 1982. To support my research habit, I was a National Science Fellow and a teaching assistant for graduate courses on methods of applied math.